Copyright is owned by the Author of the thesis. Permission is given for a copy to be downloaded by an individual for the purpose of research and private study only. The thesis may not be reproduced elsewhere without the permission of the Author.

ANDESITIC PLINIAN ERUPTIONS AT MT. RUAPEHU (NEW ZEALAND): FROM LITHOFACIES TO ERUPTION DYNAMICS

A thesis presented in partial fulfilment of the requirements for the degree of

Doctor of Philosophy

in

Earth Science

at Massey University (Palmerston North, Manawatu)

New Zealand

Natalia Pardo Villaveces

2012

Mt. Ruapehu is Te Whare Toka o Paerangi (The House of Stone of Paerangi, Ngāti Rangi ancestor), Matua te Mana (The Powerful One; "Mana" means prestige and enduring, spiritual power) in Ngāti Rangi maori culture. The Waikato-iti stream, in the Rangipō Desert, is Te Onetapu (sacred place) where Ngāti Rangi people rise their "karakia" to the volcano, their ancestor.

Dedicated to the Ngāti Rangi Iwi on behalf of all the indigenous communities living around active volcanoes in the world, who constantly teach us about the unfolding of life, the dynamic interdependence between people and the environment, and how to integrate all sources of knowledge to consciously and truly build sustainable communities

He Ruruku: Mai ara rā!

Mai ara rā! Mai ara rā!
Mai ara rā te Tupua!
Mai ara rā te Tawhito!

Tēnei au
Tēnei au te rangahau ana, ki te ao, ki te pō
Kia Ranginui e tū iho nei,
Kia Papatuānuku e takoto ake nei.

Mai ara rā, mai whea ra tōku ahunga mai?
Tāhuri whakataumaha, huri whakamāmā
E te Kāhui Maunga ko wai ra koe?

Inā, Matua Te Mana te aunahi pītataata mātahi
Pikimai Rawea te kai-kukume ake matua whenua rō wai

Te rongo nei ia hīhī,
Te rongo nei ia hāhā me huka tātairango.
Tina, tina toko te manawa ora, he manawa ora!

Ko te Roi-a-Rangi mo Rua-te-Tipua
Ko te Roi-a-Rangi nō Nukuhau e
Te pātukituki ka tū whakahirahira Kāhui Maunga mā.

Ko toka pokohiwi ka hora maru tapu, e Ngā Turi-o-Murimotu
Te ahi kā o Paerangi i te Whare Toka
Te puta mai te Kāhui-o-Rangi, te Kāhui-a-Rua
Tōna hekenga mai i Te Wai-ā-Moe ki Paretetaitonga
Ko te ara hekenga, ko te ara hokinga mo ngā uri kōtuku
Ka tuku, ka tuku atu i ngā hau kaha ia Parakakariki, ia Mouwhakaarahia

Hei tohu, hei whakaatu ki te ao!
Whiti, whano, hara mai te toki!
Haumia! Hui e!
Taiki e![1]

[1] Karakia (i.e. prayer) offered by Ngati Rangi Iwi to Mt. Ruapehu, their ancestor. Provided by Che Wilson, Ohakune 2011, Aotearoa.

ABSTRACT

A new detailed stratigraphy was developed for a sequence of pyroclastic deposits including the largest known eruptions associated with Mt. Ruapehu, deposited in the period ~27-10 ka BP cal. From the largest Plinian eruption deposits in this sequence, subtle lithofacies variations within componentry, pumice textures and sedimentary features were used to identify a systematic change in eruptive conditions over time. Early eruptions involved steady eruption columns, while younger eruptions involved unsteady, collapsing columns. Isopach and Isopleth (pumice and lithic) mapping of most widespread and distinctive units show that the largest explosive eruptions known from this volcano attained peak column heights between 22 and 37 km, with mass discharge rates reaching 10^7-10^8 kg/s.

To characterise the conditions controlling the style of Plinian eruptions at this andesitic volcano, and to explain the systematic variation in column stability over time, five key units were sampled in detail, exemplifying the major contrasting lithofacies. The sampled tephras underwent grain-size analysis, along with quantification of componentry, porosimetry and density on particles of a range of size classes, as well as 2D and 3D microtextural analyses of juvenile pumice clasts to define vesicularity and crystallinity. In addition, physiochemical factors such as melt-evolution and volatile-contents were determined by analysing bulk pumice, glass-inclusions and residual glasses with electron microprobe and FTIR-spectroscopy.

Bulk compositions of these tephras vary from basaltic-andesite to andesite (56-62 wt.%, SiO_2), and had minimum pre-eruptive H_2O contents of 4-5 wt.%. The evolution of eruption behaviour over time was not correlated to any progressive change in bulk geochemical properties, but instead resulted from variations in physical processes within the conduit. Ascending magmas experienced heterogeneous bubble nucleation, and later-erupted units showed increasing degrees of rheological heterogeneities developed across the conduit. Differences between units were due to changes in the magma decompression rates, the degree of bubble-crystal-melt interactions and bubble shearing, as well as the composition of the residual melt. Conditions that led to the most variable physical states of the magma reaching the fragmentation level resulted in the highest variability in pumice textures, the greatest range in styles of fragmentation, and the most unstable eruption columns.

A new model describing the pre-eruptive magma storage region, conduit processes, magma fragmentation, and pyroclastic dispersal during Plinian eruptions at Mt. Ruapehu is proposed. This hypothesises that eruption column unsteadiness and collapse occurs when magma shear reaches extreme levels along the conduit under conditions of low isolated porosity (<3 vol.%). This situation also generates the worst-case hazard scenarios expected for Ruapehu, eruptions, where Plinian columns of over 30 km may produce widespread tephra fall, as well as partially collapse to generate pyroclastic density currents of over 15 km runout.

ACKNOWLEDGMENTS

This thesis would not have been possible without the guidance and the help of several people who, in one way or another, contributed and extended their valuable assistance in the preparation and completion of this study. I would first like to acknowledge my first teacher of Volcanology, Héctor Cepeda, for keeping alive from afar my passion for volcanoes and question our role as scientists within any local community. He also dragged my attention to explore this side of the world, Aotearoa (New Zealand). Professor Claus Siebe (UNAM-Mexico), who encouraged me to come and continue my studies in Volcanology, suggesting without hesitation Professor Shane Cronin as my supervisor. My utmost gratitude goes to Professor Shane Cronin who continuously motivated me and supported me along the difficult PhD process, providing excellent guidance, lessons, discussions and encouragement, together with his patience with my "Colombian English" and exhaustive final edition. He, together with my other co-supervisors, Drs. Alan Palmer and Karoly Németh, and Associate Professor Ian Smith, helped me to keep up every day's motivation in the research. I will always be grateful to Alan Palmer for all his assistance and guidance during the extensive field-work and data collection phases of this study. Dr. R.B. Stewart (Massey University), Dr. Ben Kennedy (Canterbury University), and Dr. Katherine Cashman (University of Oregon, U.S.A.) are greatly thanked for the examination of this thesis, all the comments, discussions, and suggestions that significantly improved the final version.

Some of the most difficult tasks of this project would definitely not have been possible without the teachings, hospitality and guidance of Dr. Heather Wright (USGS, California, USA). During and after the X-ray synchrotron analyses at California, she always found time to discuss and review my ideas until outputs were reached that we could trust. Also, Dr. C. Ian Schipper (ISTO-CNRS, Orléans, France), who arrived at the precise moment to rescue me from the frustrating sample preparation for FTIR measurements and taught me that patience, persistence, and having fun are the best ingredients to be successful in any lab procedure.

This study was financed by the New Zealand Foundation for Research Science and Technology, (now the Ministry of Science and Innovation, NZ Natural Hazards Research Platform) programme, "Living with Volcanic Risk" and by a Massey University Doctoral Research Scholarship. I am also grateful for the support of the Tongariro Natural History Society through a Memorial Award. H. Keys, J. Johnson (Department of Conservation), and the Range Control staff of the NZ National Army camp at Waiouru are thanked for allowing access to the Tongariro National Park and Army land.

I also thank Alastair McDowell for his training and aid during the CT-scanning at Lawrence Berkeley National Laboratory (Berkeley, California). Dr. C. Ian Schipper for scanning the samples at ISTO-CNR (University of Orléans, France), along with Dr. Alan Burgisser and ERC grant 202844 under the European FP7, for providing the facilities within this micro-CT laboratory. Dr. Anja Moebis, for helping with the complex FTIR sample preparation, and together with Professor Bob Stewart and Dr. C.I. Schipper, for discussing and developing the corresponding methodology at Massey University. Drs. Anja Moebis and Clel Wallace, thank you for teaching me how to deal with the serious mission of thin sectioning pumice and polishing. Mr. Doug Hopcroft and Dr. Jianyu Chen are gratefully acknowledged for their collaboration with the Scanning Electron and Confocal microscopes. A very special acknowledgment goes to Ritchie Sims, at University of Auckland, who made every second of the tedious microprobe analysis fun and enriching. His help and friendship were always there. I am extremely grateful to Ian Furkert, Bob Toes, Matthew Irwin, and Mike Bretherton for bringing all their best energy and enthusiasm while assisting me in the different laboratory procedures. It was very

important to be surrounded by their kindness and smiles, which made the long journeys in the lab peaceful and joyful. I also thank them for making me stop sometimes and forcing me to go home.

Dr. R.B. Stewart, Dr. G. Lube, and Dr. J. Procter, as well as Professors V. Neall, and M. Bebbington, for their helpful lessons and discussion. All the PhD-students, friends and staff of Volcanic Risk Solutions of Massey University were extremely helpful and supportive. I am very grateful to Dr. Marco Brenna, Dr. Gert Lube, Ms. Emma Phillips, Dr. Jon Procter, and Dr. Ting Wang for their support in the field. Thanks to Marco, Ting, and Gert for being always there in my moments of panic, especially with software and calculations. This project could not have achieved the desired progress without the efficiency, promptness, and help of Dr. Kate Arentsen, who dealt with most of the exhaustive logistics. She, and Dr. A. Moebis greatly contributed to the final edition and formatting. My gratitude goes also to Moira Hubbard and Liza Haarhoff for all their assistance and kindness with administrative issues during the PhD.

Chapter reviews by Dr. Claus Siebe (UNAM-Mexico), Dr. Guido Giordano (Italy), Dr. Roberto Sulpizio (Italy), an anonymous reviewer, Dr. Setsuya Nakada, and Dr. James White, were gratefully received and proved extremely useful for improving the quality of the resulting manuscripts. The final publications are available at www.springerlink.com.

Warm and special gratitude to my “kiwi brother”, Andy Dolling, for being so present and filling my soul with joy, poetry, and music, needed to survive the PhD. Through the ukulele and drums he always found a way to keep me singing, creating, and smiling even in the most difficult moments. Along with him, all my friends in Whanganui, Mike and Loraine Dolling, Ron Riddel and Saray Torres, Chika and Richie Janutka, and David Griffiths who became a beautiful and supportive family in this country. Niji, Kiwa, and Kaho Janutka, thank you all for remind me to keep my inner child alive and strong, even while doing a PhD.

Vilma Rodríguez, German Molano, and Alvaro Martínez, for helping me to keep connected with my roots, my dreams, my reasons, my questions. They have been a wonderful example and reference; a grounding point, guiding me in my own personal search within this hybrid Colombian personality dancing between arts, science, and social justice. Erica Lattughi and Matiu Te Huki, for opening a new perspective of freedom and possibilities, nurturing my will to choose our own path and work with love for our dreams. Erica, Jen Hyde, and Korty Wilson, for supporting and helping me to contribute to the real, physical, daily world by reinforcing the meaning of community and sustainable living while we conduct scientific research. Jaime Dorner and Marisol Vargas, for opening the paths of theatre, allowing me to keep vibrant the creative artistic world, contributing to balance the scientific days and to keep exploring the depths, multiplicity, and possibilities of the human being. I also thank my first friends and flatmates, Sadia Tahir and Mazidah Abdul Rahman, who created a beautiful and supportive connection between women from different countries and cultures arriving to a common place, Te Papaioea (Palmerston North). Also to newer friends in this town, including Angela and Gabor Kereszturi, as well as my wonderful flat-mate, friend, and supportive shoulder, Javier Agustín-Flores. Thank you all for listening and sharing.

Last, but not least, my thanks to my wonderful, missed family in Colombia and overseas, for giving me strength, believing in my dream, and letting me fly with my own wings.

Table of Contents

List of figures

List of tables

List of abbreviations

Abbreviation	Meaning
Locations and Stratigraphic Units	
Fm.	Formation
TVZ	Taupo Volcanic Zone
TgVC	Tongariro Volcanic Centre
CL	Crater Lake
Rhyolitic tephras (Okatania Caldera):	
Ok	Okareka Tephra
Rw	Rerewhakaaitu Tephra
Wh	Waiohau tephra
Mt. Ruapehu andesitic tephras:	
HP	Hokey Pokey Eruptive Unit
Mgt	Mangatoetoenui Eruptive Unit
Sw	Shawcroft Eruptive Unit
Oru	Oruamatua Eruptive Unit
Ak	Akurangi Eruptive Unit
Okp-Ph	Okupata-Pourahu Eruptive Unit
L-	Lower
M-	Middle
U-	Upper
Mt. Tongariro andesitic tephras:	
Pk	Pahoka Tephra
Rt	Rotoaira lapilli
LA	Lithofacies Association
PDC	Pyroclastic density current
cal yr BP	Calibrated years before present
ka BP cal.	kilo-annum before present (calibrated)
Eruption parameters	
V	Tephra volume [km^3]
Vp	Proximal tephra volume [km^3]
Vt	Total tephra volume [km^3]
T	Deposit thickness [cm]
T_0	Extrapolated thickness at the vent [cm]
A	Area [km^2]
A_{ip}	Break-in-slope distance [km]
k	slope
H_b	Eruption column neutral buoyancy level [km]
H_t	Eruption column total height [km]
b_c	Clast half-distance
b_t	Thickness half-distance
D	Fragmentation Index of Walker (1973)
Q	Volume discharge rate [m^3/s]
MDR	Mass discharge rate [kg/s]
M	Eruption magnitude
Sh	Shape factor
Grain-size parameters	
M	Mode
Md	Median
σ_G	Graphic standard deviation
S_{Kg}	Graphic asymmetry
Mz	Mean
σ_i	Inclusive standard deviation
S_{ki}	Inclusive graphic asymmetry
K_g	Kurtosis

Density and porosity parameters	
δ_{bulk}	Bulk density [$g \cdot cm^{-3}$]
δ_{skel}	Skeletal density [$g \cdot cm^{-3}$]
δ_{sol}	Solid density [$g \cdot cm^{-3}$]
φ_{bulk}	Bulk porosity [vol.%]
φ_{conn}	Connected porosity [vol.%]
φ_{iso}	Isolated porosity [vol.%]
Textural parameters	
N_v	Vesicle number density [cm^{-3}]
nv	vesicle number density per size class [cm^{-3}]
N_x	Mafic crystals number density [cm^{-3}]
VVD	Vesicle volume distribution
CVVD	Cumulative vesicle volume distribution
VSD	Vesicle size distribution
CVSD	Cumulative vesicle size distribution
CVD	Mafic crystals volume distribution
CCVD	Mafic crystals Cumulative volume distribution
CSD	Mafic crystals size distribution
CCSD	Mafic crystals Cumulative size distribution
Mt	Magnetite
Pl	Plagioclase
Px	Pyroxene
Cpx	Clinopyroxene
Opx	Orthopyroxene
Mt	Magnetite
Ox	Oxides
Gx	Glomerocryst
Others	
ε	Molar absorptivity coefficient [Liters/(mol x cm^{-2})]
LOI	Water from loss on ignition
ΔP	Decompression rate
ΔP_{SS}	Supersaturation pressure
Pc	Closure pressure
GT	Growth rate in a given timescale
n_o	Number of initial nuclei
L	Dominant diameter
Ves	Vesicle
Qz-Ab-Or	Quartz-Albite-Orthoclase

Techniques and equipment	
SEM	Scaning Electron Microscope
BSE	Back-scatter electron image
µ-CT	X-ray microtomography
FTIR	Fourier Transform infra-red
EMPA	Electron Microprobe
XRF	X-ray fluorescence spectrometry
LA-ICP-MS	Laser Ablation Inductively Coupled Mass Spectrometry

Institutions	
LBNL	Lawrence Berkeley National Laboratory at Berkeley (CA, USA)
ISTO	Institut des Sciences de la Terre d'Orléans l'Université d'Orléans (France)

CHAPTER 1. Introduction

1.1 Research problem and motivation

The causes, processes and consequences of explosive volcanism along subduction zones, together with their implications to human society and the environment, are an important aspect of current research in volcanology (Jeanloz 2000; Cashman and Cronin 2008; Cashman and Giordano 2008). The introduction of volatiles (mainly water) released from the subducting slab into the mantle wedge, lowering its solidus and causing partial melting of the mantle material, results in the generation of hydrous, volatile-rich magmas, which are potentially much more explosive than their anhydrous counterparts (Lambert and Wyllie 1972; Gill 1981).

The eruptions of Mt. St Helens (U.S.A., 1980-1986), Redoubt (U.S.A., 1989-1990), Mt. Pinatubo (Philippines, 1991), Chichón (México, 1992), Crater Peak (U.S.A., 1992), and Chaitén (Chile, 2007-2008), clearly show that long-lived andesitic to dacitic composite volcanoes produce frequent and violent eruptive events, representing the greatest volcanic threat to human populations (Woods 1995; Simkin and Siebert 2000; Carn et al., 2009; Lara 2009). In this context, knowledge of the factors controlling the related eruptive styles and mechanisms, volumes, magma discharge rates, and resultant products (e.g. transport and deposition) during the geological and historical record of these systems is extremely important to understand and quantify the potential hazards.

Most of the field studies regarding processes taking place during highly explosive eruptions, including magma degassing and fragmentation mechanisms and thresholds, as well as eruption column dynamics and plume dispersion, have mainly focused on rhyolitic and basaltic systems (**Chapter 1.2**). Also, most of these studies have been centred on very specific questions and methodologies, and a clear link between microscopic observations of pyroclasts and field characteristics is lacking. This thesis will apply and develop the concepts pointed out above for the characterization of large explosive volcanic eruptions of intermediate composition ($55<SiO_2<65$ %) at subduction-zone volcanoes. For this purpose, and considering the excellent exposure of the geological record, this study will be centred

at Mt. Ruapehu, the most active andesitic volcano of New Zealand. The **objective** will be to determine the range and upper limits of the physical processes taking place in the volcanic conduit, vent and eruptive plume. This includes determination of the limits of peak column heights, volumes, magma discharge rate, the investigation of magma degassing and fragmentation mechanisms, and the implication of these factors for eruption column stability. All of these issues will be addressed in correlation with potential external controlling factors, such as conduit and vent geometry modifications and interaction with external water (Cioni et al., 2003; Houghton et al., 2004).

Research on andesitic volcanoes of New Zealand has been principally focussed on the effusive activity and petrology of the related lavas and domes (e.g. Cole 1978; Hackett 1985; Cole et al., 1986; Graham and Hackett 1987; Hackett and Houghton 1989; Graham et al., 1990; Hobden et al., 1996; Stewart et al., 1996; Hobden 1997; Waight et al., 1999; Gamble et al., 2003; Price et al., 2005), along with the most frequent vulcanian-strombolian and phreatomagmatic historical eruptions (Cronin et al., 1997a; Cronin et al., 1998; Nakagawa et al., 2002). However, the studies of Donoghue (1991), Donoghue et al., (1995a, b; 1997; 1999), Wilson et al. (1995), Cronin et al. (1996a, c), Cronin and Neall (1997), Nairn et al. (1998), Nakagawa et al. (1998), and Hitchcock and Cole (2007) prove that explosive eruptions 10 to 100 larger in magnitude and eruption rate than historical events have occurred at these volcanoes (Neall et al., 1995).

This thesis will provide a contribution to the knowledge on the physical controls and characteristics of subplinian-Plinian eruptions at such andesitic volcanoes, and the related maximum hazard scenarios expected for North Island of New Zealand.

The principal **aims** are:

i. To define the magmatic and environmental factors controlling the largest magnitude eruptions from Mt. Ruapehu.

ii. To quantify the variability of eruptive parameters, including eruption volume, column height, and mass-eruption rates from the largest eruptions known at this volcano.

iii. To quantify the variability of magma vesiculation and fragmentation in these eruptions.

iv. To identify the magmatic supply and rise processes involved in these events.

v. To document the potential hazard posed by the maximum likely eruption from one of the most active andesitic volcanoes in New Zealand.

The thesis comprises a printed document with eight chapters, along with specific data sets included in ten digital appendices (**A-J**). A complete description of the **methods** used to address the proposed aims is detailed in **Chapter 2.** This Chapter is followed by a detailed analysis of the **field characteristics and lithofacies** of the largest eruptions known to be sourced at Mt. Ruapehu: in **Chapter 3**, the reconstruction of the eruptive sequences, the general picture of Plinian and subplinian behaviour of this volcano and the identification of the largest events are presented. The quantification of **eruptive parameters** and examination of their variability during these largest events are presented in **Chapter 4**. The microtextural and geochemical characteristics of the eruptive units representing contrasting lithofacies and eruption column behaviour are addressed in **Chapter 5**, with particular attention to the understanding of processes driving magma towards **fragmentation**. Afterwards, 3D techniques applied to characterise the variability of pumice textures within each selected eruptive unit are presented in **Chapter 6**, which focuses on the processes occurring within the conduit, including magma **vesiculation and degassing**. The integration of the multiple field, microtextural, and geochemical results obtained here is **discussed** in **Chapter 7**, which provides a new understanding of the interconnected processes occurring from the storage system towards the conduit, fragmentation level, plume dynamics, and final deposition. A summary of the main **conclusions** is finally presented in **Chapter 8**.

The reader must be aware that individual chapters were written in the form of papers for publication (**Chapters 3** and **4** are published). Therefore, some repetition might be found, particularly within the introductions of each chapter.

1.2 Literature review

The first approaches to the systematic study of explosive volcanic eruptions were focused on their classification (Walker 1973) and interpretation of the eruptive column dynamics, particle transport and deposition (Wilson 1976; Carey and Sparks 1986; Fagents and Wilson 1992). From this work, the basic parameters of column height, eruptive volume, muzzle velocity and magma discharge rate, allow the construction of theoretical models that can be used to characterize an explosive eruption based on data measured in the field. In the last three decades, significant advances in the understanding of the physics of explosive volcanic eruptions have been made (Freundt and Rosi 1998; Gilbert and Sparks 1998; Sigurdsson et al., 2000). Important approaches to extend from this include investigation of pre-eruptive conditions (Johnson et al., 1994; Gardner et al., 1995; Rutherford and Devine 1996; Rutherford et al., 1998), volatile content, speciation and behaviour in magmas (Lange 1994; McMillan 1994; Symonds et al., 1994). Pioneering publications on explosive volcanic eruption mechanisms over the last two decades have centred on magma vesiculation processes (Klug and Cashman 1994), coupled and decoupled magma degassing and permeability (Klug and Cashman 1996; Rust and Cashman 2004; Gonnermann and Manga 2007; Wright et al., 2007; Mueller et al., 2008; Takeuchi et al., 2009), the effects of magma decompression and degassing time scales (Jaupart 1998), pre- and syn-eruptive magma rheology modifications (Hess and Dingwell 1996; Stix et al., 1997; Giordano and Dingwell 2003; Lavallée et al., 2008), syn-eruptive degassing-induced crystallization (Gardner et al., 1998; Hammer et al., 1999; Cashman and Blundy 2000), and the complexity of conduit dynamics (Wilson et al., 1980; Macedonio et al., 1994; Polacci et al., 2001, 2003; Cioni et al., 2003; Rosi et al., 2004; Wright and Weinberg 2009) including localized strain, heating by viscous dissipation, as well as crystal fragmentation and resorbtion at the conduit walls (Rust et al., 2004; Kennedy et al., 2005; Gonnermann and Manga, 2005). Finally, important contributions have been attained experimentally on magma fragmentation, the characteristic process occurring during explosive volcanic eruptions. For instance, bubble overpressure has been identified as a primary factor required to overcome the strength of the denser magma, leading to its rupture via layer-by-layer bursting of vesicles (Spieler et al., 2004b; Scheu et al., 2006).

1.2.1 Subplinian and Plinian eruptions

At active, convergent plate margins, typical of the Pacific Ring of Fire, the main cause of magma generation is the drop of the mantle and crust **solidus** temperature by the addition of volatiles. In this tectonic environment, considerable amounts of water derived from the subducting lithosphere, mainly carried within the crystal structures of hydrated minerals, are incorporated into the mantle; (Jeanloz 2000; Perfit and Davidson 2000; Parfitt and Wilson 2008). The volume, frequency, and style of eruptions resulting from subduction processes are largely dependent on the volumes of magma generated by the mantle/crust melting, and the depth, spatial and temporal distribution of its production in the source region (Asimow 2000). The amount of melt produced in subduction zones largely depends on the flux of volatiles (mainly water) from the subducting slab (Morris et al. 1990; Schmidt and Poli 1998).

Magma Ascent and Fragmentation: explosive eruptions occur when rising magma is transformed from a liquid with dispersed crystals and gas bubbles into a gas with dispersed liquid drops and solid particles (McBirney and Murase 1970; Klug and Cashman 1996), rapidly accelerating towards the surface and ejected from a vent (Walker 1973; Wilson et al., 1980; Fisher and Schmincke 1984). Magma fragmentation can be generated by two principal mechanisms which can act separately, or in a feedback manner; these are termed magmatic and phreatomagmatic processes. In the first case, the "explosiveness" of the magma is due to "internal" magma conditions, primarily the rapid exsolution and expansion of the dissolved volatiles (mainly H_2O and CO_2) as the magma approaches the surface and the confining lithostatic pressures decrease. This leads to the conversion of potential energy into kinetic energy (Wilson et al., 1980; Carey and Sparks 1986). Subsequently, gases and pyroclasts are accelerated towards the Earth's surface in eruptive plumes that can reach several tens of kilometres in height (McBirney 1973).

Magmatic eruptions can be triggered by overpressure in the magma storage region due to injection of fresh, hot, magma or due to volatile enrichment in the melt phase during cooling and crystallization (Wallace 2001). Alternatively, they can result from the

unloading of shallow magma following a sudden partial or total collapse of an overlying volcanic edifice (Lipman and Mullineaux 1981, in: Carey et al., 1995).

In the phreatomagmatic case, explosions result from the interaction of the rising magma with external water. This process is described as a fuel-coolant interaction (Wohletz 1983), during which the magma thermal energy is converted into kinetic and mechanical energy at thin films at the magma-water interface over very short time-scales (less than milliseconds). This process leads to abrupt quenching, chilling and subsequent brittle failure of a magma, and sudden external water vaporization. The change in volume due to rapid steam expansion is very large, resulting in mechanical work, which is expressed as magma and country-rock fragmentation, crater excavation, tephra dispersion, and acoustic and seismic perturbations (Wohletz and Sheridan 1983; Fisher and Schmincke 1984; Wohletz 1986; Cas and Wright 1987; Wohletz and Heiken 1992).

In the absence of significant interaction with external water, it is the content (wt%) of dissolved volatiles in the magma that provides the driving force for explosive volcanic eruptions; the formation of bubbles increases both the bulk magma buoyancy and the magma chamber overpressure, controlling the eruption dynamics (Gonnermann and Manga 2007). Exsolution rates depend on the relative solubility of each volatile species, which depends, in turn, on the confining pressure, the magma composition and temperature (Cas and Wright 1987). As the magma rises, it may cross the volatile saturation curve and the accompanying decompression triggers volatile supersaturation and exsolution as separated bubbles (i.e. ***first boiling***). Otherwise, a rising magma may cool and the anhydrous mineral phases begin to crystallize, increasing the volatile saturation of the residual melt (Blake 1984; Tait et al., 1989; Navon and Lyakhovsky 1998). The increased vapour pressure leads to volatile exsolution (***second or retrograde boiling***). Therefore, the vesiculation of a volatile-saturated, rising magma (Johnson et al., 1994; Wallace et al., 1995) begins with **bubble nucleation** (Sparks 1978; Cashman et al., 2000), defined as the aggregation of molecules to form the smallest stable gas bubble that can overcome the magma surface tension (Sparks 1978; Toramaru 1989; Sparks et al., 1994). In the case of **homogeneous nucleation**, high volatile supersaturation levels are reached and the vesiculation is delayed until magma reaches high levels in the conduit. In these conditions, the exsolution level is

far above the saturation level (Cioni et al., 2000). In the case of **heterogeneous nucleation** there are no kinetic barriers to overcome and the nucleation is initiated at the contact of existing impurities within the magma (Navon and Lyakhovsky 1998); therefore, the exsolution occurs at lower degrees of supersaturation, or even at the saturation level (Toramaru 1989; Mangan and Sisson 2000; Gardner and Denis 2004). In either case, high rates of bubble nucleation drive a "catastrophic over-pressurization and volume expansion" (*Op.cit*) responsible for explosive magma fragmentation (Gonnermann and Manga 2007).

Once nucleated, bubbles begin to **grow** deep in a conduit, initially following an exponential trend that is mainly controlled by the magma viscosity. Following this is a parabolic growth trend, controlled by volatile diffusion rates, and finally at higher conduit levels, bubble growth becomes expansion-dominated (Cashman et al., 2000). Bubble growth by decompression, which accompanies magma ascent, follows thermodynamic gas laws: the decreasing pressure over the bubble causes an increase of bubble volume (i.e. expansion). Bubble growth by coalescence depends on the availability of bubbles to interact, allowing melt drainage by the capillary stresses in the films and plateau borders that separate bubbles (Cashman and Mangan 1994; Mangan and Cashman 1996). Bubble coalescence is particularly important in low-viscosity, slow-rising magmas, and it plays a significant role in developing magma permeability, which is a crucial condition in determining the eruptive style and potential eruptive style transitions (Klug and Cashman 1996; Klug et al., 2002; Rust and Cashman 2004). In more silicic and viscous magmas, bubble coalescence requires time to overcome viscosity-barriers (Cashman and Mangan 1994). In addition, bubble growth is strongly affected by the presence of neighbouring bubbles and by the crystallinity of the magma: crystal contents greater than 25-30 % induce non-Newtonian behaviour, and bubbles start to deform by shear. Commonly, the magma viscosity at this stage is high enough to prevent an efficient separation between liquid and bubbles (Cashman et al., 2000).

The solubility-and-diffusivity-controlled volatile exsolution process during magma ascent and decompression is commonly referred to as "degassing" (Gonnermann and Manga 2007). In general, basaltic magma compositions are less viscous and more prone to **decoupled degassing**, where bubbles migrate faster than the surrounding melt, while more

silicic magmas involve kinetic barriers, where bubbles are relatively immobile with respect to the melt and **coupled degassing** is more likely (Wilson et al., 1980; Sparks et al., 1994; Papale et al., 1998; Sable et al., 2006). Coupled degassing is not only a function of composition, but it is also strongly affected by the ascent rate (e.g., high ascent rates delay degassing), decompression rate (high if triggered by flank or caldera collapses), and groundmass crystallization (Sable et al., 2006). An open-system degassing results in the magma outgassing (i.e. loss of gas; Eichelberger 1995; Klug and Cashman 1996; Hammer et al., 1999). If outgassing cannot keep pace with the eruption timescales (closed-system), the gas is not physically separated from the melt prior to fragmentation, and disruption and explosive fragmentation of the supersaturated magma is inevitable (Bursik 1993; Hammer et al., 1999; Gonnermann and Manga 2007).

The resulting eruptive style of any particular volcano is intimately related to the rheology of the magma, which determines the relative rates of bubble and crystal nucleation, growth, ascent, and gas loss, and its relation to the bulk magma ascent rate. In general, delayed bubble nucleation leads to rapid magma expansion and **fragmentation**, generating explosive eruptions (Cashman et al., 2000). If the bubble growth rate keeps pace with the rising rate, or if bubbles interconnect, enhancing the magma permeability required for gas lateral and/or vertical escape, the magma can reach the surface without fragmenting, resulting in effusive eruptions (Cashman et al., 2000; Rust and Cashman 2004). If the bubble growth rate is faster than the ascent or lateral gas escape rates, the volatile-rich magma accelerates and reaches the fragmentation level, producing explosive eruptions. Traditionally, it was thought that fragmentation would only occur when the bubble content reached 70-80 vol.% (Sparks 1978; Woods 1995). However, recent investigations on pumice textures, combined with experimental and numerical modelling, have pointed out that the magma can fragment at even lower or higher vesicularities (Houghton and Wilson 1989; Klug and Cashman 1996; Spieler et al., 2004b; Scheu et al., 2006). Fragmentation at low vesicularities (~64 vol.%) is particularly likely if shearing processes are high along with elevated degrees of magma chamber overpressure (Gardner et al., 1996). Experimental research has shown that the fragmentation threshold is inversely proportional to the porosity and it is largely affected by permeability at high porosity values. Chemical

composition, crystallinity and bubble size distribution are not critical factors (Spieler et al., 2004a).

The magmatic fragmentation mechanism can be acceleration-dominated or decompression-dominated (Cashman et al., 2000): at one end of this continuum, the nucleated bubble and growing bubbles decrease the bulk magma density, allowing bubble expansion and subsequent mixture acceleration. As magma rises rapidly, it experiences high strains and the tensile strength is exceeded either by fluid instabilities or brittle fracture. Fluid instabilities are commonly developed in low-viscosity magmas, yielding to rapid acceleration, and bubble growth advances up to form a high speed moving foam; bubble walls become so thin and unstable that they can easily break. At the other end of the spectrum, rapid decompression of highly viscous magmas at shallow depths yields to rapid changes in bubble internal pressure and sudden expansion, generating fragmentation waves that propagate downward. If the strain rate applied to the mixture exceeds the liquid viscous relaxation rate (i.e. time needed for the liquid to retain equilibrium under an applied strain), the bubbly magma crosses the **glass transition**; that is, the transition from a viscous flow to structural failure (Dingwell and Webb 1989; Dingwell 1998; Gonnermann and Manga 2007). Consequently, the magma responds with brittle behaviour to the applied strain, disintegrates and rapidly accelerates, leading to high eruptive columns (Alidibirov and Dingwell 1996; Mader 1998; Houghton et al., 2004). Typically, in Plinian to subplinian eruptions, both rapid acceleration and decompression act in concert (Cashman et al., 2000). Experimental research has demonstrated that the depth of fragmentation strongly depends on the balance between the speed of fragmentation (as the wave propagates layer-by-layer down to the conduit) and the speed of magma ascent; and this balance may influence the steadiness of the resulting eruption (Spieler et al., 2004b). Changes in the balance between both speeds determine fluctuations in the fragmentation depth with time. Moreover, the fragmentation speed is directly influenced by porosity and, therefore, changes in the porosity of the magma across the coduit determines fluctuations in the spatial position of the fragmentation front (Scheu et al., 2006).

In summary, the disruption of magma is largely dependent on the volatile content, magma rheology and strain rate exerted on it (Wilson 1999). Numerical modelling also suggests

that fragmentation may be either brittle or ductile (Proussevitch et al., 1993; Mader 1998), where the latter might occur via progressive thinning of liquid layers. Such strain-induced fragmentation during sustained eruptions has also been discussed by Papale (1999).

Considering that real volcanic systems are not closed, the analysis of the physical conditions of erupting magmas must also include the degree of interaction with surrounding hydrothermal systems and the capability of the conduit to allow groundwater inflow. During phreatomagmatic eruptions, the resulting stress waves prompt higher deformation rates compared to the melt bulk modulus (Morrissey and Mastin 2000). The fragmentation can also be triggered by magma viscous deformation in response to the tensional stress generated by sudden water vaporization and the accompanying fluid-instabilities. In this case, the fragmentation process depends on the water/magma ratio, interaction depth, mode of interaction, magma ascent rate (Heiken 1972; Lorenz 1973; White 1991; Zimanowski et al., 1997), and water source (e.g., crater lakes or aquifers). Generally the fragmentation efficiency during the fuel-coolant interaction is greater than in pure, dry, magmatic eruptions (Walker 1973).

During high magma ascent rates and magma discharge, conduit wall abrasion and scouring commonly takes place; moreover, under-pressurizing magma by unsteady conduit walls' collapse has been also well documented by Wilson et al., (1980), Macedonio et al., (1994) and Kennedy et al. (2005). Collapses of the conduit walls are expected to occur at the fragmentation level, where differences in lithostatic and magmatic pressures are the largest, in the order of MPa (Papale et al., 1998). Those collapses are also caused by decreasing dissolved water content, higher chemical evolution of the anhydrous magmas, and increasing crystal content, which ultimately control melt viscosity. Increasing lithic content is a function of conduit erosion and magma discharge rate (Taddeucci and Wohletz 2001); lithic content increases if conduit widening increases at steady discharge rates. If conduit walls collapse, lithic-content increases but the deposit usually reflects a decrease in the mass discharge rate.

Plinian and subplinian eruptive plumes and resulting deposits: prior to fragmentation, the mixture in contact with the conduit walls is mostly the melt and crystal fractions. There, a great part of energy is used in doing work to overcome the magma

viscous flow and the friction between the magma and the walls, especially in narrow dikes. Above the fragmentation level, most of the mixture in contact with the conduit walls has significantly lower viscosity and is composed of gas. From this point, an abrupt drop in friction takes place and the energy previously used in overcoming friction becomes an extra input to increase the kinetic energy, maintaining the system conservation of energy and momentum (Spieler et al., 2004b). Consequently, the fragmented magma is suddenly accelerated towards the surface through a vent at a speed (exit velocity) that can reach several hundreds of meters per second (Wilson et al., 1980; Parfitt and Wilson 2008), depending on the gas content, and forms eruptive plumes.

In the case of highly explosive conditions, usually characterized by initially delayed bubble nucleation (due to kinetic barriers) and coupled degassing (Wilson et al., 1980; Jaupart and Allegre 1991; Papale et al., 1998; Cashman et al., 2000), the dissolved volatiles reach the supersaturation level, and exsolution processes such as bubble nucleation occur in a runaway fashion accompanied by major acceleration, driving the melt through the glass transition (Papale 1999; Sable et al., 2006). According to computer simulations, choking occurs at the conduit exit, thought to be located at the base of the crater where the flow velocity is equivalent to the local speed of sound (Papale et al., 1998). Fragmentation can be complex, and might involve different mechanisms, where the proportion of fine ash (<63 mm) increases with the intensity of the eruption and correlates with the fragmentation efficiency (Cashman et al., 2000).

Resulting Plinian and subplinian eruptive columns (**Fig. 1.1**) are characterized by:

1) a gas thrust region at the base, driven by the explosive fragmentation momentum and rapidly interacting with the atmosphere;

2) a convective region, driven by the buoyancy resulting from the entrainment of atmospheric air into the gas-pyroclast mixture and subsequent thermal exchange. Here, the magma discharge rate controls the thermal energy input. These processes continue and the plume rises until the mixture reaches a density equal to the atmosphere at a level named Height of Neutral Buoyancy (H_B);

3) the umbrella region, where the mixture rises above H_B driven by its momentum until a maximum height (H_T), while spreading laterally, influenced by the local winds, and mainly behaving as a density current (**Fig. 1.1**) (Carey and Sparks 1986; Bursik et al., 1992; Rosi 1998; Cioni et al., 2000). Therefore, density and grain size sorting takes place in the plume, with smaller and lighter particles carried to greater heights and released at greater distances from the vent (Wilson 1976).

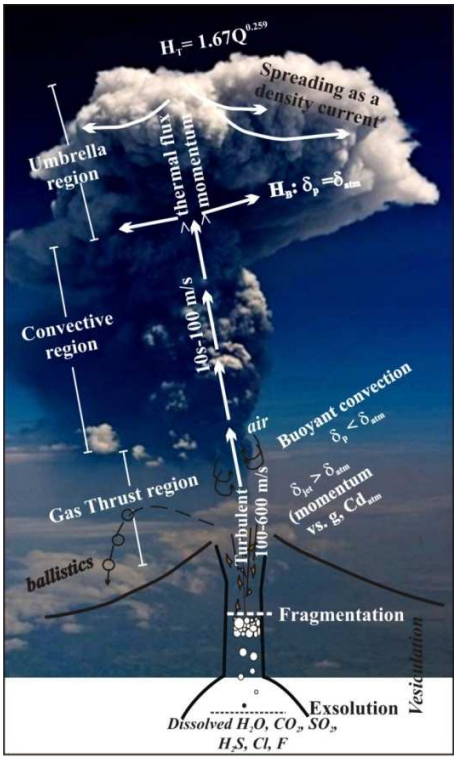

Figure 1.1 Typical Plinian-suplinian eruptive column, showing the three distinctive regions mentioned in the text. After Cioni et al. (2000).

H_T: Total column height
Q: Volume discharge rate
H_B: Neutral Buoyancy level
δp/atm: density of the pyroclastic mixture and atmosphere respectively
g: gravity
Cd: Drag force

Due to the great dispersal potential of Plinian and subplinian eruptions, and considering the instantaneous accumulation with respect to the geological time, the resulting sheet-like, mantling fallout deposits can be used as chronostratigraphic markers (Lowe et al., 2008). The accumulation of massive to stratified beds with increasing sorting with distance is the main result of fallout from the umbrella cloud. Typically, the decrease of thickness and grain-sizes with distance from the vent has been described as following an exponential or a power law (Walker 1973; Pyle 1989; Fierstein and Nathenson 1992). This has been explained as the result of the deposition of coarser and ballistic fragments derived from the margins of the eruptive column in proximal areas, to finer fragments accumulated from the umbrella region in more distal areas, according to the corresponding particle terminal fall

velocities (Wilson 1976; Wilson et al., 1980; Carey and Sparks 1986; Rosi 1998). Therefore, ballistic particle distribution is independent of column height and their range is solely determined by the initial muzzle velocity and ejection angle (Wilson 1972; Rosi 1998). Anomalous secondary thickness and deviation from typical log-normal, unimodal grain-size distribution can occur, as the result of ash aggregation effects during heavy rains or during phreatomagmatic eruptions (Carey and Sigurdsson 1989; Brazier et al., 1983; Woods 1995).

Massive, ungraded beds have been commonly interpreted as the result of continuous magma discharge driving steady convective columns. Proximal interbedded ash layers could represent small collapses from the margins (c.f., Cioni et al., 2003). On the other hand, distinctive stratification marked by contrasting grain sizes and depositional processes (e.g., interlaying of ash fallouts and pyroclastic density current deposits) have been documented as related to unsteadiness in the magma discharge and oscillating convective columns, typically formed during subplinian eruptions (Sieh and Bursik 1986; Bursik 1993; Cioni et al., 2000; 2003). Alternatively, they can be explained as the result of deposition from different transport regimes of pyroclastic density currents (i.e., suspension ash decoupled from the main pyroclastic density current dominated by turbulence and traction).

On the resulting pyroclasts: volatile saturation levels, eruption dynamics and conduit processes are recorded by juvenile pumice and scoria textures (Cashman and Mangan 1994; Gardner et al., 1996, 1998; Hammer et al., 1999; Polacci et al., 2001; Wright and Weinberg 2009; Bouvet de Maisonneuve et al., 2009). A critical parameter to be determined from pumice texture is the vesicularity, expressed as bubble volume fraction, since it has been suggested as a measure of the volume fraction of the gas phase. When the vesicularity is less than 74 %, the magma behaves as a bubble suspension, while for greater vesicularities it is a true “foam” (Navon and Lyakhovsky 1998). The 74 % defines the critical value at which gas reaches its maximum packing when bubbles are spherical, undeformed, and uniform in size. The existence of Plinian deposits with pumice containing vesicularities lower than 70 % and higher than 80 % led to the development of alternative models (Houghton and Wilson 1989; Klug and Cashman 1996; Mangan and Cashman 1996) to those previously proposed by Sparks (1978). On one hand, extreme vesicularities (>90 %)

have been explained as the result of a redistribution of bubbles into elongated “tubes”, or reticulitic patterns to reach maximum packing, and rapid acceleration into the fragmentation level (Mangan and Cashman 1996; Mader 1998; Cashman et al., 2000). On the other hand, low vesicularities (<60 %) have been interpreted as the result of rapid decompression, or as limited bubble growth due to syn-eruptive degassing and microlite crystallization prior to fragmentation (c.f., Gardner et al., 1998). Therefore, high densities of small bubbles may reflect high supersaturation levels, a late stage of supersaturation of a relatively degassed magma, or heterogeneous nucleation on existing impurities (Cashman et al., 2000). In this context, vesicularity alone is not definitive for fragmentation thresholds, and is largely dependent on magma viscosity (Mader 1998), permeability and overpressure at the fragmentation front (Spieler et al., 2004a) .

Bubble number density (Nd_b), which is the number of bubbles per volume unit, and total vesicularity are two useful parameters in the estimation of volatile saturation at the moment of nucleation and fragmentation, respectively (Cashman and Mangan 1994). Blower et al. (2002), reviewed the significance of the bubble size distribution (BSD) of magmas, derived from the analysis of the vesicle size distributions (VSD) of juvenile clasts (Mangan and Cashman 1996). The BSD can be unimodal, polymodal, or commonly shows an exponential or power law trend, giving information on nucleation and growth rates, the extent of bubble coalescence, magma ascent rate and volatile supersaturation (Klug et al., 2002). Usually, the number of peaks identified in the unimodal to polymodal BSDs is interpreted as corresponding discrete, nucleation events (e.g., Sparks and Brazier 1982; Whitham and Sparks 1986; Orsi et al., 1992; Klug et al., 2002). Slow, pre-eruptive degassing within the magma chamber generates the largest bubble size population (~60 μm); syn-eruptive degassing produces bubbles typically between 5 and 50 μm (Whitham and Sparks 1986; Mader 1998).

Variations in pumice vesicularity and volatile content must be carefully interpreted, since juvenile clasts do not quench instantaneously with fragmentation, and post-fragmentation processes, such as coalescence, bubble expansion and collapse, can occur in a ~60s time-interval, depending on the erupting mixture viscosity (Gardner et al., 1996; Klug et al., 2002). Collapse is unlikely in magmas with viscosities higher than 10^5 Pa·s, and expansion

is unlikely for magmas with viscosities higher than 10^9 Pa·s. Bubble coalescence enables interconnected pathways to form for gas escape, which can evolve to bubble shrinkage and distortion (Saar and Manga 1999; Burgisser and Gardner 2005). Microfractures and small voids between microlites can also enhance permeability development (Walker 1989). In this context, it is extremely useful to describe bubble shapes in the juvenile clasts; for example, complex bubble shapes commonly result from coalescence, while angular and wrinkly contours of small bubbles can reflect bubble collapse and local magma shrinkage after coalescence (Sable et al., 2006).

The discussion above has to be contextualized into the andesitic composition. Acid, rhyolitic, low-temperature magma should be suddenly quenched at the vent exit, whereas basic, basaltic, high-temperature magma can remain in the liquid state while transported in the column (Toramaru 1990). Thus, andesitic magmas are expected to behave in an intermediate way, where the bulk viscosity is largely determined by the competence between crystals and melt viscosity (e.g., Whittington et al., 2009). It is important to highlight that the place and time where the magma quenches is critical in the interpretation of pumice textures.

Some authors have stated that magma close to, or at, conduit margins is more prone to degassing and crystallizing, developing a larger viscosity and lower ascent rates (e.g., Cioni et al., 2000; Houghton et al., 2004; Sable et al., 2006). In these models, the velocity profile, inferred by heterogeneity in vesicularity, assumes slow-moving zones on the margins and fast-moving zones at the conduit axis, allowing a longer residence time for magma located at the margins, where mature vesicularity and microlite crystallization is more likely. As fragmentation occurs, the different magma portions travel along different flow lines with different ascent rates, experiencing a range in decompression rates, degassing and crystallization histories (Houghton et al., 2004; Sable et al., 2006).

Other models propose different viscosity and magma rheology distribution across the conduit, considering the complexity of conduit processes and geometry in governing the magma flow (Scandone and Malone 1985; Woods and Koyaguchi 1994; Macedonio et al., 1994; Cashman and McConnell 2005): shear brecciation near the conduit walls, shear heating and shear localization (Wright and Weinberg 2009), permeable gas flow and

conduit walls instability are all critical factors. Recent research has reinforced the possibility of developing high temperatures due to viscous dissipation along the conduit walls, allowing lower viscosity regions where brittle deformation is unlikely (Polacci et al., 2001, 2003; Polacci 2005; Rosi et al., 2004; Costa and Macedonio 2005). This process is related to the capillary number (*Ca*), which compares the bubble dimensions, strain rate and shear viscosity to the surface tension of the mixture: if *Ca* >1, the bubbles deform and provide free-slip surfaces, decreasing the relative viscosity of the mixture; whereas if *Ca*<1 the bubbles behave as rigid bodies, increasing the relative viscosity (Rust and Manga 2002; Stein and Spera 2002). The increase of *Ca* may occur locally, developing shear bands and localizing the strain rate, triggering the glass transition of the sheared magma portion (Wright and Weinberg 2009).

Documented cases: Plinian eruptive phases can be produced in any polygenetic volcano, irrespective of any specific magma composition. Although they are expected to be more typical of silicic, highly viscous magmas, Holocene and historical Plinian eruptions ranging from basaltic (e.g. the ~30 ka Fontana Tephra and the 2120 ± 120 yr BP Masaya Triple Layer produced by Masaya volcano in Nicaragua: Williams 1983; Wehrmann et al., 2006; Pérez et al., 2009; Tarawera-1886 A.D., New Zealand: Nairn and Cole 1981) to rhyolitic (e.g., Taupo-1850 ± 10 yr BP, New Zealand: Froggatt & Lowe 1990), and even trachytic-trachyandesitic (e.g., Chichón-1982 and 1320-1433 A.D., Mexico: Sigurdsson et al., 1984; Macías et al., 2003) and phonolitic to tephriphonolitic compositions (e.g. Vesuvio-79 A.D. Italy: Carey and Sparks 1986; Gurioli et al., 2005) have been documented worldwide.

Two of the best documented Plinian eruptions of andesitic stratocones are the 1980 Mt. St. Helens event in the United States (Carey et al., 1995; Cioni et al., 2000) and the Mt Pinatubo, 1991 eruption (Koyaguchi and Tokuno 1993; Hoblitt et al., 1996; Hammer et al., 1999; Polacci et al., 2001). Other examples include: the 122 BC eruption of Mt. Etna in Italy (Del Carlo and Pompilio 2004); the 800 yr BP eruption of Quilotoa volcano in Ecuador (Rosi et al., 2004); the 12.1 ka and the 10.5 ka eruptions at Nevado de Toluca in Mexico (Arce et al., 2003; 2005); the ~14.1 ka Tutti Frutti (Siebe et al., 1997; Sosa-Ceballos et al., 2012) and the ~5 ka “Ochre Pumice” (Arana-Salinas et al., 2010) Plinian eruptions at Popocatépetl volcano in Mexico.

Similarly to other compositions research indicates that composite volcanoes also require conditions favourable for generating coupled degassing and corresponding delayed nucleation during magma ascent.

Experiments and numerical modelling: despite the scale problem, extensive numerical modelling and experiments have been carried out in the last two decades to simulate Plinian and subplinian explosive volcanic eruptions. Eruptive plume dynamics and tephra dispersal (Bursik 1993; 1998; Woods 1995; Rosi 1998; Bonadonna et al., 1998; Sulpizio et al., 2005), conduit dynamics (e.g., Macedonio et al., 1994; Jaupart 1998; Papale et al., 1998; Papale 1999), and degassing and fragmentation mechanisms (e.g. Melnik 2000; Neri et al., 1998, 2002) have been all extensively considered.

Mader (1998) summarized the most relevant experimental approaches that have considered nucleation (e.g., Sugioka and Bursik 1995), gas expansion (Anilkumar et al., 1993), exsolution (e.g. Mader et al., 1994), and fragmentation mechanisms (e.g. Zimanowski et al., 1991). The tendency of explosive eruptions to develop high bubble number densities (up to 10^7 mm^{-3}) and bimodal bubble size distributions have been tested with decompression experiments by Larsen and Gardner (2000), Cluzel et al. (2008), and Toramaru (2006).

Decompression experiments in shock tubes have been widely used to understand the reliability of either homogeneous or heterogeneous nucleation, and to study fragmentation conditions, although they have mainly considered rhyolitic compositions (Martel and Schmidt 2003; Mangan et al., 2004). It is noteworthy that simultaneous homogeneous and heterogeneous nucleation in the same eruption is also possible, as demonstrated by Marziano et al. (2007). Namiki and Manga (2005) demonstrated that vesicularity determines the potential energy that provides the expansion velocity of the bubbly magma during rapid decompression; large potential energies result in faster expansion and constributes to magma fragmentation. However, the control of permeability on fragmentation has been extensively modelled and highlighted as a more dominant parameter than vesicularity (Klug and Cashman 1996; Saar and Manga 1999; Rust and Cashman 2004; Mueller et al., 2005; Mueller et al., 2008; Takeuchi et al., 2009).

1.2.2 The Tongariro Volcanic Centre (TgVC)

The research area (**Fig. 1.2**) is mainly constrained to the Tongariro National Park and the Waiouru Army training area, where two of New Zealand's most active andesitic volcanoes are located: Mt. Ruapehu and Mt. Tongariro. The former is a large (110 km^3), 2797 m high composite volcano, located at the southern end of the Taupo Volcanic Zone (TVZ) (Cole 1979; Cole et al., 1986; Hackett 1985; Graham and Hackett 1987; Hackett and Houghton 1989; Gamble et al., 1993; Graham et al., 1995; Cronin et al., 1996a). K/Ar dating on Ruapehu lavas suggests that the eruptive activity dates back to 340 ka (Gamble et al., 2003), with four major cone-building stages reported at >120, 120-60, 60-15, and 15-0 ka (Hackett and Houghton 1989). However, recent $^{40}Ar/^{39}Ar$ dating indicates major "pulses" at 180-250, 115-160, 50, 20 and <15 ka (Gamble et al., 2003). Mt. Tongariro is a smaller (75 km^3) andesitic massif consisting of several coalescing volcanic cones (Mathews 1967; Hobden et al., 1996; Hobden 1997). K/Ar dating indicates major cone-building stages at 210–200, 130–70 and from 25 ka to the present (Hobden et al., 1996). Gamble et al., (2003) report major stages occurring at 10, 25, 70-130, 180-230, and 260-280 ka, pointing out that both volcanoes might have been initiated simultaneously (with a maximum age of 340 ka), but showing major cone-building stages at separate time intervals. From the lithostratigraphic record, the major explosive activity of Mt. Ruapehu took place during the late Pleistocene (~60-10 ka BP cal.; Topping 1973; Donoghue et al., 1995b; Cronin et al., 1996a), while the major explosive activity related to Mt. Tongariro occurred between ~11 and ~9 ka BP cal. (Nairn et al., 1998).

The general geology of Ruapehu and Tongariro volcanoes is compiled within the New Zealand Geological Survey Bulletin (Gregg 1960), and synthesized in Gregg (1961). Both Mt. Ruapehu and Mt. Tongariro, together with Kakaramea-Tihia and Pihanga are collectively referred to as the Tongariro Volcanic Centre (TgVC; Cole and Nairn 1975; Cole 1978).

Pleistocene and Holocene products of Mt. Ruapehu comprise extensively described lava flows (Graham and Hackett 1987; Hackett and Houghton 1989; Waight et al.,1999; Gamble et al., 2003), fallout and rare ash-flow deposits (Topping 1973; Donoghue 1991; Donoghue

et al., 1995a, b; Donoghue et al., 1999; Moebis et al., 2011), lahar deposits (Palmer 1991; Cronin et al., 1996a; Donoghue and Neall 2001), and debris-avalanche deposits (Lecointre et al., 1998). The pyroclastic deposits identified as the products of the largest explosive eruptions of Mt. Ruapehu in the geological record correspond to the 27,097 ± 957 cal years BP to ~10,000 cal years BP Bullot Formation (Donoghue 1991; Donoghue et al., 1995b). The historical activity has been mainly characterized by lahar generation (e.g., Cronin and Neall 1997; Cronin et al., 1997a; Neall et al., 2001; Lecointre et al., 2004; Lube et al., 2009; Procter et al., 2010), small and frequent phreatic, phreatomagmatic eruptions and rare dome-building events (Healy et al., 1978, in Cronin et al., 1997a; Nairn et al., 1979; Hackett and Houghton 1989), related to the South Crater (Cole and Nairn 1975), which is currently occupied by an acidic crater lake (Christenson and Wood 1993).

The largest explosive events known for Mt. Tongariro comprise a ~11 ka BP cal., multi-vent Pahoka-Mangamate eruptive sequence described by Nairn et al., (1998; after Topping 1973, 1974; Donoghue et al., 1995b). The authors mapped the lapilli units and related them to simultaneously or sequentially erupting vents, producing Plinian dispersals. From this sequence, the Pahoka Tephra (Topping 1974; Kohn and Topping 1978; Donoghue et al., 1995b; Nakagawa et al., 1998) is particularly interesting due to its contrasting lithofacies with respect to the typical Bullot Fm., Mt. Ruapehu eruptions. Donoghue et al., (1995b) mapped the respective isopachs, confirming Mt. Tongariro as the most plausible source and a SE dispersal axis with a calculated volume of 0.28 km^3; however, Nairn et al., (1998) presented newer data, locating the source at the present position of Saddle Cone, and identified a NE dispersal axis with a calculated volume of 0.4 km^3. This problem will be addressed in **Chapter 4**.

Spinks et al., (2005) studied the structural control on volcanism in the intra-arc rift of the Taupo Volcanic Zone (TVZ), and proposed that segments dominated by an extensional component are associated with caldera formation and larger eruptive volumes, while segments dominated by dextral shear are related to stratovolcanoes and lower eruptive volumes. The inverse correlation between the dextral transtension component and the eruptive volume/style was then explained as the response to the control of the upper-crustal tectonics on the location of magma storage: greater extension accommodates larger magma

volumes. In this context, most of the andesite petrogenesis studies on the TgVC point to complex mixing and mingling processes taking place in intricate magma storage and plumbing systems (Graham and Hackett 1987; Gamble et al., 1999; Cole et al., 2000; Price et al., 2005).

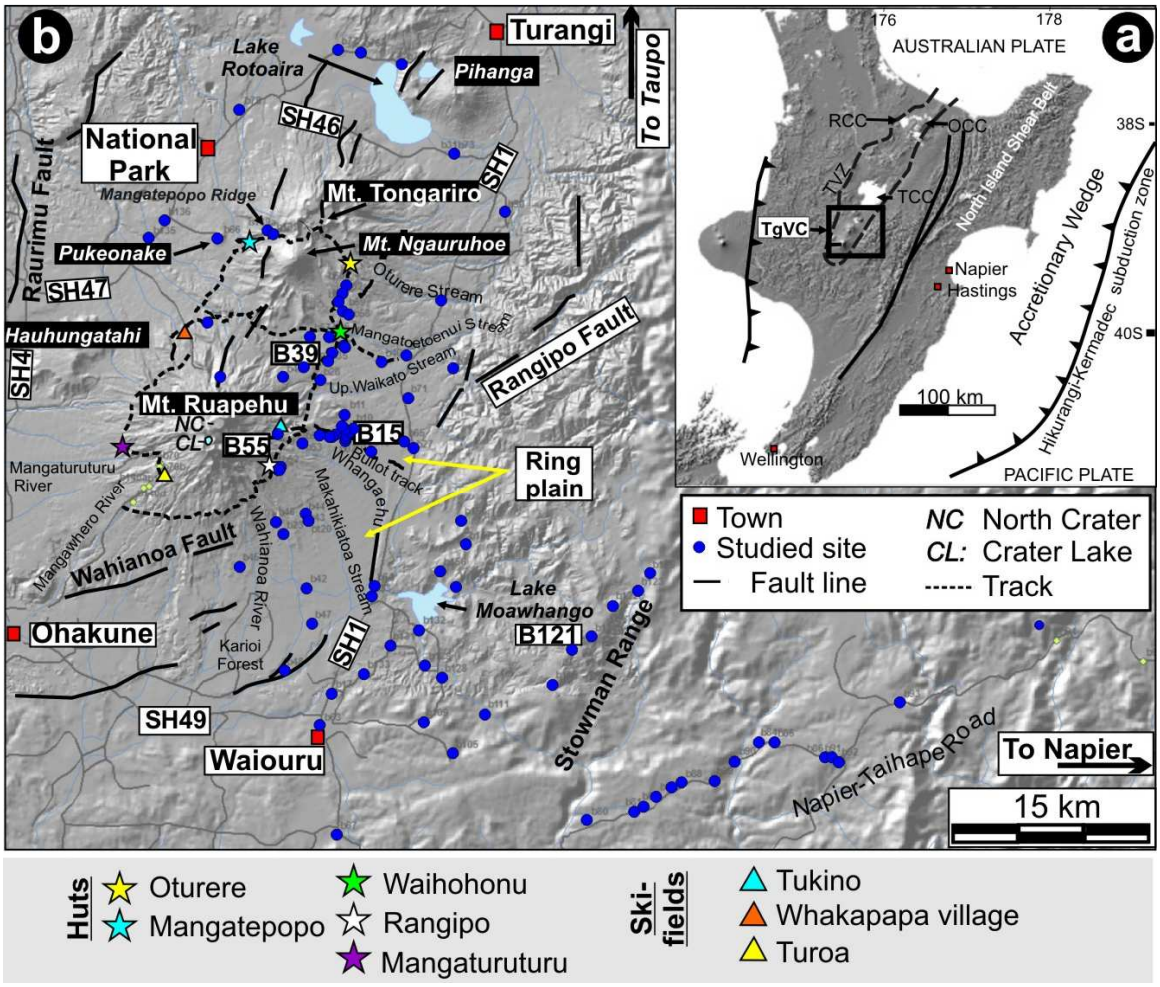

Figure 1.2 Study area. a) North Island of New Zealand tectonic setting (modified from Reyners et al. (2006) and Villamor et al. (2010)), showing the Hikurangi-Kermadec subduction margin. TVZ: Taupo Volcanic Zone, with andesitic Tongariro Volcanic Centre (TgVC) and the rhyolitic Okataina (OCC), Rotorua (RCC), and Taupo calderas (TCC); b) TgVC comprises Mt. Ruapehu and Mt. Tongariro composite volcanoes. SH: State highways connect the urban centres (red squares). Study sites indicated by blue circles; main reference type sections labelled as "B".

Price et al., (2005) carried out an integrated approach to understand the temporal evolution of andesites and rhyolites of the TVZ. The authors propose the generation of andesitic

magmas from the interaction of mantle-derived magmas with lower crustal melts and restites, when mantle-derived mafic magmas intrude and underplate the crust (Harrison and White 2006). The great short-term geochemical variability of lava-flow sequences are consistent with complex, dyke-sill systems with scattered, separated magma reservoirs throughout the crust and upper mantle feeding eruptions at TgVC (Gamble et al., 1999; Nakagawa et al., 1999, 2002; Waight et al.,1999; Price et al., 2005). In this way, eruptions are thought to be related to contemporaneous and chemically different magma batches mixed and mingled at various depths and stages; variability seems to increase with time (Hobden et al., 1999) and appears to be related to progressively lower magma production rates (Gamble et al., 2003; Price et al., 2005).

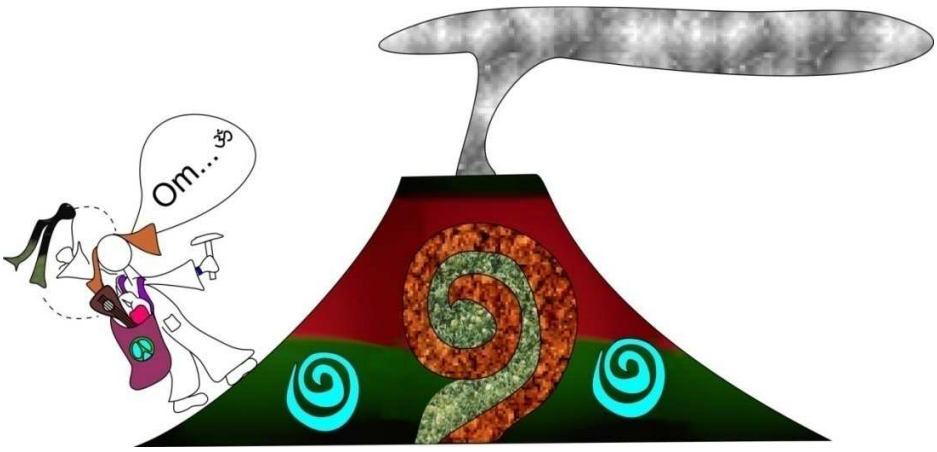

Unlocking the secrets of Ruaumoko[2].
S.J.Cronin and N.Pardo collective artwork, 2012

The introduction above comprised a background of the main topics addressed and discussed in this study, within the context of Mt. Ruapehu. In the next chapter, the reader will find the methodological approach to attain the aims stated above (pp. 2-3).

[2] God of volcanoes and earthquakes, the youngest son of Papatuanuku (Mother Earth) in Māori Mythology.

CHAPTER 2. Methodology

2.1 Fieldwork and physical parameters

The pyroclastic deposits that represent the largest explosive eruptions known from the Mt. Ruapehu geological record are mapped within the Bullot Formation, dated between 27,097 ± 957 cal years BP and ~10,000 cal years BP (Donoghue 1991; Donoghue et al., 1995b). The best exposures of these units are found on the eastern flanks of the volcano and upper Ring Plain, where detailed description of 158 stratigraphic profiles was carried out (**Appendix A**). Bed geometry, sedimentary structures, including contact types, bed forms and stratification, paleochannels, dunes, lenses, grain-size grading, and syn-depositional deformation structures (e.g., impact sags) were carefully recorded. Textural parameters, such as clast framework (matrix supported vs. clast-supported), particle sorting, roundness, sphericity, colours, pumice vesicularity and crystal content, size, and shape, as well as accidental clast types were initially macroscopically described in the field with the aid of a 10x hand lens.

This detailed description provided the key criteria for the interpretation of the particle transport and deposition mechanisms, as well as the identification of the range in types of eruptive units and time breaks bounding pyroclastic deposits. Pauses between eruption events are based on the recognition of paleosols and inter-eruptive fluvial architectural elements, such as incised channels filled with fluvial deposits, or sheet-like overbank/flood-plain units (Fisher and Schmincke 1984; Miall 1996). Paleoclimate is an important issue to consider with respect to development of paleosols and the preservation of primary pyroclastic deposits in the geological record at Mt. Ruapehu. During emplacement of the Bullot Fm., conditions varied from harsh periglacial climates during the last glacial period, along with warmer and wetter conditions in interglacial periods (Lowe et al., 2008). Hence, pedogenetic processes were highly limited, affecting the types of soils developed (Cronin et al., 1996b), and the preservation potential of tephra units during periods of extensive snow/ice cover was low, with extensive tephra remobilization by meltwaters and “snow slurry lahars” (Cronin et al., 1996a; 1997a). In addition, complex interactions occurred

between tephras, snow, ice, and water, affecting the form and nature of deposits (Manville et al., 2000). Here, syn-eruptive lahars or fluvial deposits are referred to as those generated synchronously with the eruptive activity (i.e. included in the eruptive unit); those following tephra accumulation (i.e. bounding eruptive units) will be referred to as inter-eruptive units.

The first tasks in the field were to characterise the unique lithofacies for each stratigraphic unit, necessary for stratigraphic correlation. The deposits corresponding to the five largest eruptions were identified and selected according to their significantly contrasting lithofacies that may be taken as representing end-member conditions and triggering controls in similar eruptive styles. A total of 100 detailed (mm resolution) stratigraphic profiles were drawn and analyzed, and 58 more were used for further correlation and mapping. In each location, the maximum thickness and the three maximum axes of the largest five pumice and lithic clasts (c.f., Rosi et al., 2001) of the corresponding pyroclastic fall deposits were measured to construct **isopach and isopleth maps**. Contours were digitally drawn on a 20 m resolution DEM, using ArcMap 9, to facilitate calculation of distances, areas, and circularity (expressed here as a shape factor: $Sh = ((4\pi Area)/ Perimeter^2)$). During each procedure, the manual results were compared to contours derived from automatic interpolations (e.g. Natural neighbour/Kriging) generated within Surfer 8 (Golden Software) to better determine the dispersal axis. Long axes were measured from the vent and following the distortion of the corresponding contour; maximum short axes were measured in three different points perpendicular to the longest axis within an error of ±6 %.

The **fallout tephra volume (V)** was estimated from both irregularly shaped, whole deposit isopachs and from the approximated ellipses following Pyle (1989) modified by Fierstein and Nathenson (1992), Bonadonna et al., (1998) and Sulpizio (2005), to compare the effect of thickness extrapolation to an infinite area. Plots of thickness (Tk) logarithm vs. the square root of the area ($A^{1/2}$) enclosed by the corresponding isopach were produced. From the resulting straight-line graph, the extrapolated thickness (T_o) at the vent ($A^{1/2} = 0$) was determined, as well as the slope (k) of the line considering the thickness at two points *a* and *b*:

$$-k = (\ln T_b - \ln T_a)/ A_b^{1/2} - A_a^{1/2} \quad [1]$$

Following Pyle (1989), V was calculated independently of the isopach shape, as:

$$V = 2T_o/k^2 \quad [2]$$

Equation 2 was valid in the case of a single line segment in the graph. However, in most of the cases tephra-fall deposits did not show a simple exponential or power-law decay in thickness with distance, and instead show multiple (often two to three) segments with different slopes in ln (thickness) vs (area)$^{1/2}$ plots. When two segments are distinguished, the break-in-slope is referred as A_{ip} and the relationship is described as:

$$T_{ip} = T_0 e^{(-k\sqrt{A_{ip}})} \quad [3]$$

Bonadonna and Houghton (2005) obtained a general formula for volume calculations where the field data are arranged in *n* segments, expressed as:

$$\frac{2T1_0}{k_1^2} + 2T1_0\left[\frac{k_2A_{ip1}+1}{k_2^2} - \frac{k_1A_{ip1}+1}{k_1^2}\right]e^{(-k_1A_{ip1})} + 2T2_0\left[\frac{k_3A_{ip2}+1}{k_3^2} - \frac{k_2A_{ip2}+1}{k_2^2}\right]e^{(-k_{12}A_{ip2})} + \cdots + 2T\,(n-1)_0\left[\frac{k_{n3}A_{ip(n-1)}+1}{k_{3n}^2} - \frac{k_{(n-1)}A_{ip(n-1)}+1}{k_{(n-1)}^2}\right]e^{(-k_{(n-1)}A_{ip(n-1)})} \quad [4]$$

where T n_0, -k_n and A_{ipn} are the intercept, slope and break-in-slope, respectively, of the segment *n*. Bonadonna et al., (1998) explained the segmentation of these plots as a reflection of varying thinning rates with distance related to the accumulation of particles of different settling behaviour according to their sizes. Then, A_{ip} corresponds to the point where the sedimentation from the umbrella cloud changes from high to intermediate Reynolds number particles, and A_{ip} increases as column height increases. Research by Sulpizio (2005) further elucidated the different methods to obtain erupted volumes according to the properties of the deposit, in terms of preservation and data availability. For Mt. Ruapehu, the proximal-intermediate distance data are available, and then k_1 and A_{ip} should be re-calculated considering that high-Reynolds Number (*Re*) particles have a narrow range of settling velocities compared to low Reynolds Number particles. Since the exact proportion of the proximal (Vp) vs. total volume (Vt) ratio, minimum volumes are best obtained assuming $\frac{V_p}{V_t} < 0.3$ and:

$$\sqrt{A_{ip}} \approx 3.34k^{-0.96}, \quad [5]$$

$$k_1 = 1.61\sqrt{A_{ip}^{-1.02}}\,, \qquad [6]$$

and the volume can be calculated applying Bonadonna et al. (1998; see equation 4).

Following Pyle's (1989) method, the distance at which the thickness decreases to one half of its maximum value is referred to as "thickness half-distance" (b_t), which describes the morphology of the deposit. Likewise, the distance at which the maximum clast diameter halves with respect to its maximum value is termed the "clast half-distance" (b_c), and reflects the corresponding column height. The b_c/b_t ratio gives information about the particles dispersion, considering both the column height and wind effects. High b_c/b_t indicates rapidly thinning deposits with most of the particles accumulated close to the vent, while low b_c/b_t should correspond to widely dispersed deposits (Pyle 1989). In this context, b_c/b_t gives an estimation of the **fragmentation index** and allows the classification of the eruptive style. A traditional calculation of the fragmentation index (D), by extrapolating the area enclosed by the 0.01 T_{max} isopach (Walker 1973), was also obtained.

The eruptive column height (H_t) was determined using the crosswind range and downwind range obtained from the isopleths data and following the model of Carey and Sparks (1986). The column heights obtained by plotting the downwind and crosswind ranges of 8 mm and 16 mm clasts of known density were then averaged to estimate the mean column height and wind speed. In parallel, the **level of neutral buoyancy (H_b)** was obtained following Pyle (1989) by obtaining the parameter b_c, since:

$$-b_c \approx 0.41\, H_b/(H_b^{1/2} - 7.3)\,, \qquad [7]$$

And the total height H_t can be estimated following Sparks's (1986) model:

$$H_t \approx H_b/0.7\,, \qquad [8]$$

Finally, total column height was also calculated following Sulpizio (2005), considering that H_t is proportional to the proximal thinning rate (k) and:

$$H_t = 7.6k^{-0.47}, \qquad [9]$$

Once H_t was estimated, the **volume discharge rate (Q)**, given in m^3/s, was obtained following Sparks (1986) as:

$$Q = \left(\frac{Ht}{1.67}\right)^{3.86}, \quad [10]$$

The mass discharge rate (MDR) is the mass (in kg) erupted through the vent per time unit (seconds), and it was obtained graphically using the model of Sparks (1986) and Sparks et al. (1997). By measuring the weight (in grams) of overnight dried (at 100^0C) samples with a KERN-HCB SOK20 high precision balance for a known volume of bulk-deposit (in cm^3), a rough idea of the deposit density was obtained (cf. Arana-Salinas et al., 2010), from which whole-deposit mass was calculated:

$$Total\ Mass = (deposit\ density) * (Erupted\ volume) \quad [11]$$

The total mass is also a measure of erupted magnitude (M), expressed by Pyle (2000) as:

$$M = Log\ (Total\ Mass) - 7 \quad [12]$$

The resulting eruptive parameters obtained for the five largest eruptive units identified within the Bullot Fm., are shown in **Appendix B** and **Chapter 4**.

2.2 Laboratory

2.2.1 Grain size analysis

For practical proposes, pyroclast sizes were described in the field using the simple Udden (1914) scale modified by Wentworth (1922). In the laboratory, higher precision allowed detailed classification according to Sohn and Chough (1989). Pyroclastic fallout deposits samples of ~1 kg were firstly dried, weighed, and manually sieved at 0.5 ϕ intervals, between -5 and 4.5 ϕ. Gentle hand-shaking was carried out for pumice clasts in order to avoid pumice breakage. The grain-size distribution and sorting was then analyzed with the aid of the SFT- Kware software (Wohletz et al., 1989). In order to make data comparable, grain-size parameters were normalized to the total weight of clasts smaller than -5 ϕ and

coarser grain-sizes were treated separately since they represent fragments derived from a different transport mechanism (i.e. ballistics). In each distribution, the statistical parameters were obtained following Inman (1952), by quantifying the mode (M), the median (Md), the graphic standard deviation (σ_G), graphic skewness (SK_g); and following Folk and Ward (1957) by obtaining the mean (Mz), inclusive graphic standard deviation (σ_i), inclusive graphic skewness (SK_i), and the kurtosis (K_g). The sorting classification was estimated qualitatively in the field and quantitatively using the σ_i values, following the criteria of Cas and Wright (1987). Results are presented in **Appendix C**.

The description and quantification of pumice textures, as well as the lithic content and classification of pyroclastic deposits have been widely used for the characterization and estimation of eruptive parameters and the reconstruction of magma rheology in the conduit (Whitham and Sparks 1986; Houghton and Wilson 1989; Klug and Cashman 1994; 1996; Gardner et al., 1996; Polacci et al., 2001, 2003; Polacci 2005). The methods described below were applied for samples representative of the selected eruptive units and samples were preferentially analysed, corresponding to locations along the dispersal axis of the selected units.

2.2.2 Componentry

Component analysis was performed on the selected sieved samples, which were cleaned with multiple immersions in distilled water inside an ultrasound bath for 30 min to 1 hr. Glass, crystal and lithic contents were determined in the 0.5, 1, 2, and 3 ϕ size fractions (<1 mm) of individual phases, considering that the fine ash size fraction gives information close to the fragmentation mechanism. A total of 300 particles per size class were counted with the aid of a Leica Wild MZ8 binocular microscope (**Appendix E and Chapter 5**). The classification criteria common for all the samples consisted of the separation of juvenile pumice/scoria, dense fresh lithics, and altered accidental lithics. Detailed classification varied according to the properties of individual deposits, but generally comprised clast morphology, surface, vesicle content, shape and size, crystal content, habit and size, and

clast colour. In order to make data comparable, component classes were normalized to the total number of particles per size class. This step allowed a further approach to the characterization of the juvenile clasts' textures at the scale permissible by the binocular microscope. Hence, preliminary ideas regarding vesiculation, fragmentation, and conduit processes could be attained and were used to select subsequent subsamples for further analyses.

2.2.3 Gas-Pycnometry: pumice density and porosity

Pumice clasts were sampled from the deposits of the main Plinian phases of the eruptive units that represent contrasting lithofacies associations.

Each selected fallout deposit was sampled at regular intervals (separated in the vertical axis by 5 clasts), with a minimum total of 30 juvenile fragments between 8 and 32 mm per interval, completing 60 to 100 juvenile clasts per unit. In this study, the pumice textures are qualitatively described as finely vesicular if >90 % of vesicles are <2 mm and coarsely vesicular if larger. Vesicularity is described according to Houghton and Wilson (1989). These samples were further classified according to their macrotextures (**Table 2.1**), cleaned in distilled water, dried, and were kept in a desiccator for skeletal and bulk density determination. Ten samples of each eruptive unit were crushed with an agate mortar and only in the case of very dense clasts were milled with a tungsten carbide ring grinder.

After classification of macrotextures within each fallout, a representative clast of each type within each unit was sectioned and polished for inspection under optical microscope (**Appendix D**), backscattered secondary electron (BSE) imaging, glass analysis with electron microprobe (**Appendix F**), and porosity measurements (**Appendix G**).

Table 2.1 Macrotextural classification of pumice rocks collected from Mt. Ruapehu, Late Pleistocene, Plinian eruptions.

Type	General characteristics	Subtype	
1	Highly vesicular, vitrophyric clasts with subspherical vesicles showing smooth outlines and thin walls	1a	Foamy. highly vesicular clasts dominated by subspherical vesicles <2 mm in diameter
		1b	Expanded. Subspherical to irregular large vesicles
2	Fluidal, highly to moderately vesicular, crystal-bearing clasts with strongly orientated, elongated (i.e. ellipsoidal) vesicles, commonly aligned with the longest axes of phenocrysts	2a	Finely vesicular to microvesicular (<2 mm in diameter). Vesicles show irregular outlines and variable wall-thickness
		2b	Coarsely vesicular (>2 mm in diameter). Vesicles show smooth outlines and thin walls
3	Fibrous, porphyritic, microlite-rich, often colour-banded	3a	Microvesicular, occasionally colour-banded
		3b	Coarsely vesicular (>2 mm in diameter), often colour-banded
4	Dense-microvesicular, microlite-rich clasts with highly distorted, often aligned vesicles only visible in the microscope and usually showing thick walls, pinched shapes and angular terminations.		

Bulk Density: the selected pumice clasts are too small and irregular in shape to be cored to produce regular cylinders (e.g., Klug and Cashman 1994); therefore, Archimedes experiments were carried out following Houghton and Wilson (1989), in order to calculate the bulk density. All samples were previously dried at 50°C for 24 hrs, and their weight was then recorded as S_D. For a first set of samples, each clast was impregnated in melted, ultra-refined paraffin wax of known density (0.9 g/cm^3). The best results of rapid coating and minimum penetration of the wax into the pumice pores were obtained when the wax was not too hot and fluid, usually around 45°C-50°C; at that temperature, the wax rapidly solidifies when the clast is removed and it is viscous enough to avoid extensive penetration into the pumice pores. A thin thread was attached to the clast during this process to hang the coated pumice for further drying and weighing in a suspension balance.

A copper reference mass was used to ballast the coated pumice in distilled water (Density δ=1.000 g/cm^3), and the volume was estimated using the Archimedes Principle. Initially, the ballast was suspended in air on a precision balance and the resulting weight was recorded as $\mathbf{B_D}$. Then, it was submerged in a beaker containing distilled water and the resulting weight was recorded as $\mathbf{B_W}$. The forces acting on the object are in equilibrium and the buoyancy $\mathbf{B_1}$ is:

$$B_1 = B_{\mathbf{D}} - B_W \qquad [13]$$

B_1 is equivalent to the volume of the displaced fluid (i.e. Distilled water) and also equivalent to the volume of the ballast, recorded as **Vb**. Each coated sample was then

suspended in a precision balance and the resulting weight in air was recorded as $\mathbf{C_D}$. The weight of the wax was obtained by:

$$Wx_D = C_D - S_D \quad [14]$$

Knowing the density of the wax, we calculated the respective volume, which was recorded as **Vx**.

Subsequently, the ballast was attached to the coated sample and the weight in air of the whole system was recorded as $\mathbf{CSB_D}$. This assemblage was further introduced in the distilled water and the weight recorded as $\mathbf{CSB_W}$. The resulting buoyancy B_2 is:

$$B_2 = CSB_{\mathbf{D}} - CSB_W \quad [15]$$

B_2 is equivalent to the volume of the coated sample with the ballast, recorded as **Vcsb**. The volume of the sample Vs is then obtained by:

$$Vs = Vcsb - Vb - Vx \quad [16]$$

This is the bulk volume of the sample and is used to calculate the bulk density, as:

$$\delta_{bulk} = S_D/Vs \quad [17]$$

During the last part of this project, a new Micrometrics GeoPyc 1360 envelope density analyzer was acquired by Massey University, which applies the Archimedes experiment within a quasi-fluid displacement medium composed of microspheres having a high degree of flowability (DryFlo-Micromeritics). Envelope volumes were assumed to be equivalent to bulk volumes and were further used to calculate the corresponding bulk density of each clast.

Skeletal and solid Density: these parameters were obtained on previously dried pumice samples with a Quantachrome helium ultrapycnometer, using pure nitrogen as the flowing gas. Five to six runs per sample were carried out to minimize the standard deviation. The pressure of the equipment was set at 19-19.5 psi, with a gas flow rate fast enough to achieve that pressure between 30 and 60 s, but slow enough to establish an increasing rate of 0.1 psi per grade, once the desired pressure was achieved. Each analysis was carried out

using the automatic equilibration time, and either the vacuum flow system (1 minute of vacuum) or the pulse mode for the gas inflow (4 pulses per run), showing no significant differences in the results. For powder samples only the pulse mode was performed.

In a porous material, such as a pumice clast, the He-pycnometer measures the volume accessed by the flowing gas. It only accesses the connected pores of the sample and the resulting density is known as the skeletal density δ_{skel}. In order to consider the isolated pores, it was necessary to crush some of the samples and run the analysis of the powder to obtain the solid density δ_{sol}, being always $\delta_{sol} > \delta_{skel}$. It is noteworthy that best results were obtained when at least three-quarters of the sample container was filled with the powder. δ_{sol} corresponds to the dense rock equivalent (DRE) used in the calculations of total porosity performed by Houghton and Wilson (1989).

Standard deviations per analysis vary between 0.0004 and 0.2 %. However, errors between 1 % and 5 % were estimated most commonly. Rarely some irregularly-shaped and weathered samples gave variability up to 16 % from repeated measurements of the same sample, by changing its orientation. This issue is probably due to the heterogeneity in shape and texture of the samples, as well as the presence of a clay coat around the clasts (resulting from weathering), which can lead to variations in the accessible gas volumes with the orientation of the sample in the holder. This problem can be minimized when coring samples into regular cylinders. Further variations were also evidenced when slightly changing the flow rate into the He-pycnometer and room temperature, but in general, the experiments were considered as reproducible. The level of confidence in the measurements was tested by calibrating the pycnometer with steel, non-porous spheres of known volume and by frequently repeating the measurement of an andesitic pumice sample of Taranaki volcano, previously analyzed with a similar machine at the University of Oregon by Platz (2007). Foliated or strongly anisotropic samples were positioned in at least three mutually perpendicular orientations in the pycnometer.

Porosity: with all the different density data, the following calculations were carried out to estimate bulk or total (φ_{bulk}), connected (φ_{conn}), and isolated (φ_{iso}) porosities of each sample,

by using the bulk volume, the volume accessible by the flowing gas (He_{vol}), and the solid density, following Klug and Cashman (1996), Klug et al. (2002), and Wright et al. (2007):

$$\varphi_{conn} = \frac{(\text{Bulk volume} - He_{vol})}{\text{Bulk volume}} \quad [18]$$

$$\varphi_{bulk} = \left(1 - \left(\frac{\text{Bulk volume}}{\text{Solid density}}\right)\right) * 100 \quad [19]$$

$$\varphi_{iso} = \varphi_{bulk} - \varphi_{conn} \quad [20]$$

In the absence of a gas permeameter, the permeability of each sample could only be qualitatively considered, based on descriptions of bubble coalescence, shear, development of tubular textures, and presence of microfractures.

Pumice clasts showing inner vesicularity and/or crystallinity gradients were avoided in order to exclude post-fragmentation effects (e.g., Mangan and Cashman 1996). Thomas and Sparks (1992) demonstrated that clasts larger than 1.6 cm in diameter do not cool significantly while transported in the eruptive column, and for clasts close to 6.4 cm, it takes 10 to 15 s in the fallout to cross the glass transition. Similarly, Klug and Cashman (1994) estimated that these lapilli sizes would have 50 s available for post-fragmentation expansion and bubble coalescence.

2.2.4 Pyroclast 2D microtextures and ash morphology: optical and scanning electron microscopy

Three to six pumice clasts from the modal grain size of each selected unit, which usually corresponds to the -4 ϕ and -3 ϕ fractions, were thin sectioned and polished for optical microscopy, backscatter imaging, and ulterior chemical analysis with microprobe (**Appendix D**). The selection was based on the textural classification performed with the binocular microscope, since there is not a direct classification given by the density and total

porosity data obtained with the He-Pycnometer (also noticed by Polacci et al., 2001; Polacci 2005; Rosi et al., 2004; Sable et al., 2006).

Sectioning and polishing were carried out by Neville Orr at GNS-Science (Lower Hutt, New Zealand). Previously dried pumice samples were impregnated into a two component epoxy resin (EpoTek), placed under repeated vacuum to ensure the resin penetrated all possible voids, and dried at 50°C for 24 hrs, or until the epoxy was completely solid (e.g. Toramaru 1990). Afterwards, the samples were ground with 250, 400, 600, and 1000 grade silicon carbide grits, mounted on glass, cut, ground again down to ~30 μm, and further polished with consecutively 6, 3 and 1 μm diamond pastes. Since the epoxy only reaches the interconnected bubbles, three to five impregnations were required as the samples were ground, in order to preserve the bubble walls as much as possible.

The thin sections were analyzed with a polarizing optical microscope (NIKON Eclipse E600W POL). Porphyritic textures were described following Winter (2010) as: Fine-grained if phenocrysts are <1 mm diameter, medium-grained if between 1-5 mm, and coarsed-grained for phenocrysts >5 mm. Digital images were captured using a 5 mega-pixel Nikon digital camera at different magnifications. Each contrasting textural end-member was further carbon-coated for microprobe analysis and acquisition of backscatter secondary electron images with a Scanning Electron Microscope (SEM) at the Microscopy Imagery Centre at Massey University, running with 20 kV accelerating voltage and a 55 μA beam current, at a 11.3 mm working distance. A minimum of six images were taken to characterize each clast.

Careful attention was given to the identification of different stages of bubble coalescence, retraction films, bubble wall wrinkling, and “donut” textures to refine the interpretation by comparison with published data (e.g., Cashman and Mangan 1994; Klug and Cashman 1996; Gardner et al., 1998; Polacci 2005; Bouvet de Maisonneuve et al., 2009). Phenocrysts and microlite size, shape, habit, colour and optical properties were similarly analyzed. However, the low contrast for components of Ruapehu andesitic samples did not allow the separation of feldspars (e.g. Hammer et al., 1999) from the surrounding glass matrix. Therefore, microlite volume fraction, number density, and average size were only

determined for mafic minerals. Crystal sizes were classified as phenocrysts (>150 μm), microphenocrysts (150-50 μm), and microlites (<50 μm).

For additional morphology observation of ash shards, more than 50 individual grains were hand-picked per eruptive unit, ranging from the 2 ϕ and the 3 ϕ fraction. Grains were cleaned in distilled water using an ultrasound bath, mounted in a double taped stub, and subsequently covered with gold for imaging with the SEM, running with 20 kV accelerating voltage, 55 μA beam current, at a 8.8 mm working distance. An average of 30 grains per level within each selected eruptive unit (~100 per unit) were analyzed, with a total of 511 grains counted and studied (see **Appendix E**).

2.3.5 Pyroclast 3D micro- textural analysis

One of the key problems in volcanology, and particularly in tephra analyses, is the 3D extrapolation of 2D information. Stereological assumptions are rather common and have been used to obtain volumetric measurements, such as the bubble and crystal content, size distribution, volumetric density, etc (e.g., Underwood 1970; Toramaru 1990; Sahagian and Proussevitch 1998; Higgins 2000; Blower et al., 2001; Proussevitch et al., 2007, 2011). However, experimental techniques have been tested in the last decade, giving valuable information that simplifies the analyses and gives a more realistic approach when combined with 2D textural analyses on digital images. Mercury porosimetry (Whitham and Sparks 1986) and the recently applied X-ray computed microtomography (Ketcham and Carlson 2001; Song et al., 2001; Gualda and Rivers 2006; Polacci et al., 2006; Degruyter et al., 2010; Giachetti et al., 2010; Zandomeneghi et al., 2010; Giachetti et al., 2011) give 3D reconstructions of the bubble network in pumice samples, which allow the best quantification of parameters such as the porosity, permeability, hydraulic tortuosity, and pore-size and throat (i.e. pore aperture) size distributions, which are crucial to understand the state of magma prior to fragmentation (Saar and Manga 1999; Blower et al., 2001; Costa 2006).

High resolution X-ray synchrotron and computed microtomography (μCT): According to the textural variability within each unit, two (for the less variable) to five (for the more heterogeneous) clasts per unit were cored for 3D imaging at the X-ray tomography beamline (number 8.3.2) of the Advance Light Source group at Lawrence Berkeley National Laboratory at Berkeley (LBNL-California), and at the Institut des Sciences de la Terre d'Orléans, l'Université d'Orléans (ISTO-France). A total of 13 samples were studied to cover the range of textures observed in the stratigraphic record and observed in 2D. Cylinders of 1 cm diameter were produced for the coarsely vesicular samples, whereas 5 mm diameter cylinders were produced for the most finely vesicular samples.The advantages of this method are enormous compared to the extremely time-consuming analyses of polished thin sections, particularly considering that it is non destructive, requires no sample preparation other than to adjust the sample to a size that fits in the apparatus, and the dataset acquisition can be obtained in less than 1 hr (Gualda and Rivers 2006; Polacci et al., 2006). High-resolution X-ray computed Tomography (μCT) allows the visualization of the interiors of solid objects, and the acquisition of digital information on their 3D geometry and properties by obtaining multiple views over a range of angular orientations (Mees et al., 2003). The technique is based on the X-ray linear attenuation properties of solid materials; as the X-rays pass through a sample, the signal is attenuated as a function of the X-ray beam energy, the density of the material, and particularly the average atomic number of the material (Ketcham and Carlson 2001; Ketcham 2005). The attenuation of a monoenergetic beam passing through a homogeneous material is described by Beer's Law: $\mathbf{I=I_0\ exp(-\mu x)}$, where $\mathbf{I_0}$ is the initial X-ray beam intensity, **I** is the resulting intensity after its interaction with a sample characterized by a linear attenuation coefficient **μ**, along a path of length **x**. In 3D analysis, each pixel of the three-dimensional image matrix corresponds to a volume element (voxel) (Ketcham 2005; Polacci et al., 2006; Degruyter et al., 2010).

The images produced are X-ray tomographic radiographs, where the brightness is proportional to the atomic number (Z): an image element will appear bright-white at higher Z and dark grey at lower Z (hence pore spaces appear black). A stack of 2D images is then generated as .tiff formatted bitmap files, corresponding to 6 to 20 GB of data generated per sample. At LBNL-California, the beamline 8.3.2 is a super bend magnet source, with a

local magnetic field of 4.37 Tesla, a 400 mA ring current, and 1.9 GeV of ring energy; the high magnetic field drives the critical energy of the source up to 10.5 KeV. The source size is 220 x 30 µm fwhm (w x h), and analyses are carried out within a "hutch", 20 m away from the source. The x-rays enter the hutch with a beam size of 40 x ~4.6 mm (w x h) and interact with the sample, which is mounted on a rotation stage. Each radiograph is then taken by rotating the sample 0.2 degrees at a time. The stacks of image "slices" were reconstructed with Octopus v8 (IIC UGent, Zwijnaarde, Belgium) and processed for 3D visualization and quantification with Avizo Fire 6.1 and 6.2 (VSG-Visualization Sciences Group, Zuse Institute Berlin). The grayscale value of a particular voxel is the result of the average attenuation of all the elements enclosed within it. Hence, the discrimination among different elements/components according to their grayscale tone is limited by the sampling resolution (Gualda and Rivers 2006). A detailed description of the equipment is found in **Appendix H.1**.

Dr. C. Ian Schipper (ISTO) scanned pumice lapilli with a Phoenix Nanotom 180 X-ray computed microtomograph (µ-cT) at Institut des Sciences de la Terre d'Orléans (ISTO; CNRS-l'Université d'Orléans, France). Totals of 2000-2300 scans of each clast were collected during 360^{o} rotation, using a tungsten filament and molybdenum target. Operating voltages were in the range 80 to 100 keV, with currents of 50-90 nA. Voxel edge lengths ranged from ~2 to 4 µm (**Table 2.2**).

Table 2.2 Samples used for X-ray microtomography study, from the Mangatoetoenui (Mgt), Shawcroft (Sw), Oruamatua (Oru), Lower and Upper Okupata tephras (L-U-Okp).

Unit	Sample	Lab	Sample volume used (mm^3)	Pixel size (µm)	Sample field of view ($pixels^2$) (x # images)	Subvolumes size (mm^3) (x # subvolumes)
Mgt	IX1b-1b	LBNL	67	4.4	2961 * 2805 (x 420)	9-21 (x4)
	IX1b-2a	LBNL	68	4.4	3526 * 3505 (x667)	10-34 (x4)
	IXe-1	ISTO	38	3.6	1911 x 1983 (x 879)	9-10 (x4)
Sw	Sw-2b	LBNL	71	4.4	3552*3636 (x591)	11-17 (x5)
	Sw-5b	ISTO	68	4.4	1958*1934 (x 1261)	16-18 (x4)
Oru	M-Oru-2a	ISTO	33	3.5	1878*1953 (x1398)	5-9 (x4)
	M-Oru-3a	ISTO	24	3.5	1948*1978 (x1817)	5-7 (x4)
	M-Oru-4a	ISTO	42	4.2	2024*1650(x1428)	9-11 (x4)
L-Okp	Ph16a-5a	ISTO		4.2	1938*1992 (x1952)	(x20)
U-Okp	B13-Ph161c-6a	ISTO	55	4.0	2055*2016 (x1953)	14 (x4)
	B50Ph16b-3a	ISTO	41	4.2	1989*1926 (x2023)	13-14 (x3)
	B50Ph16b	ISTO	7	2.0	1929*1932 (x1617)	2 (x4)
	Ph-2-1d-5x	LBNL	2	2.0	3216*3500 (x1768)	0.5-1 (x3)

Each sample was cored to a 0.5 to 1 cm diameter cylinder (up to 1 cm high) and image stacks of the dimensions indicated as "Sample field of view" were obtained. Sample volume used refers to the sample volume used for 3D image processing and quantification. Pixel size refers to the resolution limit. Subvolumes size indicates the maximum size of each sample subvolume that could be analysed, limited by the computer power.

Raw scans were reconstructed into stacks of greyscale images with an offline PC microcluster running Phoenix datosx rec reconstruction software.

Image visualization and processing: for three subvolumes of samples scanned at LBNL, subsets of image stacks were loaded in Avizo Fire 6.2, facilitated by computers at LBNL that allow up to 10 GB of data to be loaded and manipulated. The first 3D image was obtained to broadly visualize the overall pumice texture and to select sub-volumes of interest in order to crop the images and produce a dataset small enough to carry on the image processing. A similar procedure was carried out for the rest of the samples at Massey University with the free software Image-J (National Institute of Health, NIH) by using the BoneJ and 3D Particle Analyser plugins of those packages. A detailed description of the method is presented in **Appendix H.2**.

In general, the heterogeneity of each sample was larger than the maximum possible size of the virtually cored subvolume, which is limited by the computer capacity. Hence, three to four subvolumes were virtually produced within each scanned sample and the individual results were later merged into a single data-set to cover the entire clast. For the purposes of the current study, image processing comprised the following five general steps: 1) adjust brightness/contrast; 2) image filtering (median-smoothing); 3) segmentation, including: (a) thresholding and generation of binary images, (b) morphological processes such as dilation followed by erosion and hole-filling, and (c) pore-separation; the latter involved the application of a step-by-step watershed process (semi-automatic, comprising the generation of distance maps, image inversion and subtraction when using Avizo Fire 6.2; and automatic when using Image J). This last step was carried on to separate vesicles that were connected by fine apertures (i.e. virtual de-coalescence).

Values reported here are limited by the resolution of the synchrotron and μCT cameras (c.f., Giachetti et al., 2011), causing features (e.g., bubble walls) smaller than the pixel size

(~4 μm) to be lost. Therefore, the pixel size was reduced to 2 μm for the most finely vesicular clasts causing a decrease in sample size. This volume reduction may truncate large features (e.g., vesicles and crystals). Furthermore, multiple subvolumes are needed to characterize a sample, which requires a large amount of computer power and time.

Quantitative results were produced as .xsl files, from which vesicle volume and size distributions (VVD, VSD) were obtained (**Appendix H.3; Chapter 6**). Cumulative vesicle volume and size distributions (CVVD; CVSD) are also presented, following the suggestions of Klug et al. (2002). These authors considered that the linear relationships of ln(n) vs. L require simple vesiculation under constant rates of nucleation and growth, which is rather unlikely, particularly under rapid decompression (e.g. Adams et al., 2006). Hence, cumulative curves represent a better estimation of the overall integrated result of bubble nucleation through time (i.e. records the rate and timing of nucleation of vesicles during the ascent of a parcel of magma), allowing more comparable results.

For best qualitative observation in 3D a set of video files were produced with Image-J (**Appendix H.4**).

2.2.6 Dissolved volatiles

Fourier Transform IR-spectroscopy (FTIR): the Fourier Transform infra-red technique (micro-FTIR) has been rarely used in pumice samples, due to the great difficulty of sample preparation, and the error that can be incorporated in the readings, related to the microlites and vesicles that might be present along the beam path. However, if the sample preparation is successful and crystal and bubble corrections are performed, analysis on selected juvenile, fresh ash fragments allows the identification and estimation of the dissolved volatile contents in the glass, which is representative of the volatile content of the erupting magma at the moment of fragmentation (Stolper 1982; Dixon et al., 1997; Wright et al., 2007). In addition, this technique has been widely used on melt inclusions in olivine, quartz, pyroxenes and feldspars to estimate the pre-eruptive volatile content (Frezzotti 2001).

Given that bulk tephra and groundmass glass reveal little about the initial abundance of volatiles in the pre-eruptive magma, glass inclusions hosted in phenocrysts were chosen for

micro-FTIR measurements and estimation of pre-eruptive volatile content (Lowenstern 1995). The minerals identified in most of the samples are augite, hypersthene and plagioclase, all having good cleavage, which is problematic for exploring melt inclusions for entrapped volatiles. However, pyroxenes were targeted due to their transparency and potentially long crystallization histories. They were hand-picked from the sieved 2, 1, and 0.5 mm size fractions. Further selection of crystals was made under the polarizing microscope after checking for melt inclusions, and the selected crystals were glued on a petrographic slide using crystal bond and ground with 600 grit paper until glass inclusions were intersected. Afterwards, the exposed surface was polished using 3 μm and 1 μm diamond grit-impregnated papers (Schipper 2010). Then, the slide was heated at 50°C to melt the crystal bond and turn the wafer to repeat the procedure on the other side (e.g., Nichols and Wysoczanski 2007). Each double polished sample was prepared to a maximum thickness chosen to allow analysis (15-93 μm). The thickness was measured with a micrometer, with precision of ± 10 μm (1σ); however, considering the heterogeneity of the surface, we estimated the local thickness for each inclusion within each crystal based on the spectrographic interference colours chart (Kerr 1977). The utility of this method was corroborated with a confocal microscope at the Microscopy Imagery Centre at Massey University for two samples, whose measured thicknesses were within ± 2 μm (1σ) relative to the values obtained by optical estimations.

A total of 10 crystals per unit (x 4 units) were successfully double polished, each one with several glass inclusions: for the Mangatoetoenui Eruptive Unit 25 points were targeted, providing 16 readable spectra; for Shawcroft Eruptive Unit 35 points yielded 16 clean spectra; Oruamatua Eruptive Unit 49 (13 reliable), and Okupata-Pourahu Eruptive Unit 29 (15 reliable for the L-Okp and 7 only for the U-Okp). The main limitations during this study comprised the small size of the inclusions and the minimum thickness required for their double-exposure, which limited accurate IR absorption.

The micro-FTIR analyses were carried out with a Nicolet Continuum FTIR microscope with a Nicolet 6700 spectrometer at Massey University. A minimum of 512 scans were taken at a resolution wavelength of 4 cm^{-1} in different spots of the same wafer, at minimum

apertures of 15 μm, in order to maximize reproducibility. The analyses were carried out with a liquid-nitrogen-cooled MCT detector and KBr beam splitter.

The spectra were analyzed in the absorptivity dominium with the OMNIC FT-IR software. The identification of absorption bands at ~3550 cm^{-1}, for total H_2O, and 1630 cm^{-1} for OH^- groups was based on the experimental studies of wate

r speciation reported by Stolper (1982), Newman et al. (1986), and Ihinger et al. (1994). The peak amplitude was measured after subtracting the background established with straight line fits. H_2O content ($C\ (H_2O)$) in wt.% was calculated using the Beer-Lambert Law (Libowitzky and Rossman 1997):

$$C\left(H_2O\right)=\frac{A\times 1.8}{t\times D\times \varepsilon} \qquad [21]$$

where A corresponds to the absorption peak amplitude measured directly from the infra-red spectra in cm^{-1}; 1.8 is the H_2O molecular weight already converted in the corresponding units; t is the thickness of the sample given in cm, D is the dacitic to rhyolitic glass density given in g/cm^3 and calculated by following Lange and Carmichael (1987), Lange (1997), Ochs and Lange (1997), and Best (2003); ε is the molar absorptivity coefficient given in $L/(mol\ x\ cm^{-2})$ (e.g. Ihinger et al., 1994; Devine et al., 1995; Libowitzky and Rossman 1997; Wallace and Anderson 1998; Ohlhorst et al., 2001; King and Holloway 2002; Mandeville et al., 2002). Absorbance coefficients were obtained from published experimental data in andesitic, dacitic, and rhyolitic glass: ε_{3570}=63 ($Lmol^{-1}cm^{-2}$) for dacitic inclusions (Whittington et al., 2009) and ε_{3570}=56 ($Lmol^{-1}cm^{-2}$) for rhyolitic inclusions (Newman et al., 1986); ε_{1630}=55 ($Lmol^{-1}cm^{-2}$) was used for rhyolitic inclusions (Newman et al., 1986) but there are no ε_{1630} values available in the literature for dacitic compositions. Therefore, values calculated for Fe-bearing andesites (ε_{1630}=42.34 in Mandeville et al., 2002) and rhyolites (Newman et al., 1986) are used.

For this study a statistical representation was preferred to careful and detailed selection of the inclusions, trying to avoid leaking structures from the resultant analysis (**Appendix I**). The glass composition of glass inclusions was determined by Electron microprobe (see below).

2.2.7 Geochemistry

Textural characteristics were integrated with chemical analyses to reconstruct the physical properties of the melt. All the chemical data (**Appendix F**) were further recalculated and normalized on an anhydrous basis for further plotting.

Electron microprobe (EMPA): major elements of glass and minerals were obtained from carbon coated, polished thin sections using a JEOL JXA-840 electron probe micro-analyser (EMPA) at the University of Auckland. Analytical data were gathered using a Princeton Gamma Tech Prism 2000 Si (Li) EDS X-ray detector, a 2 µm focused beam an accelerating voltage of 15kV, a beam current of 800pA and 100s live count time. A defocused beam of 20 µm in diameter was used for glass to minimise alkali loss (Nielsen and Sigurdsson 1981). The main focus of this study regarded glass compositions, and the KN-18 glass standard was used as a monitor during glass analyses. 10 points per sample were enough to characterize microlite-poor groundmass glass, and 30 to 52 points were probed to minimize error in the microlite-rich samples.

A similar process was carried out to analyze the glass inclusions that "survived" the manipulation during FTIR analyses. Double polished crystals were mounted on to a glass slide using double tape, and all glass inclusions that could be identified by contrasting backscattered electron properties were analysed. Not all inclusions could be analyzed because of damage of crystals and surfaces during FTIR procedures, storage, and mounting. FTIR images were carefully matched to BSE images to identify those inclusions that could be successfully analysed with both techniques. All probed points giving glass composition totals lower than 94 % or higher than 99 % were excluded from analysis. A careful and detailed selection of glass inclusions is outside the aims of this study and it is noted that low volatile contents or high silica contents could result from post-entrapment growth of the host crystal from trapped melt and diffusion of species through the host crystals (Lowenstern 1995).

X-ray fluorescence spectrometry (XRF): five fresh pumice fragments picked from each different stratigraphic level in the same pyroclastic deposit were crushed for whole-rock

chemical analyses by X-ray fluorescence (XRF). 10 to 20 clasts per deposit were selected with a total of 68 samples analyzed. Approximately 4 g of powder was weighed into pre-weighed ceramic crucibles, and left in an oven at 105^{o}C for ~24 hours/overnight to measure the water loss of the sample. The combined powder and crucible was then reweighed, and the crucibles put in a furnace at 850^{o}C overnight. When cooled for ~20 minutes, these were reweighed to obtain a loss on ignition (LOI) value, which indicates volatile content in the sample. 6 ± 0.0005 g of Lithium Borate Spectrachem 12-22 flux was weighed into glass bottles, and 2 ± 0.0005 g of the ignited sample powder added to this, and mixed. The flux and discs are fused by heating the mixture to 1100^{o}C, then freezing the molten material to form a homogenised glass disc.

Major element concentrations were determined with a Siemens SRS 3000 sequential X-ray spectrometer with a Rh tube, which uses Brucker SPECTRA-plus software (V1.51). The method follows that of Norrish and Chappell (1977), with a reproducibility of ±1 % (1σ). For trace elements 34 international standards are used for calibration and samples were analyzed using pressed powder pellet (Norrish and Chappell, 1977; in Platz, 2007), with theoretical detection limits of 1-2 ppm. La, Ce and Th were measured for overlap corrections and reproducibility is 2σ <5 % for all elements except Ba, La, Ce, Pb and Th.

Laser Ablation Inductively Coupled Mass Spectrometry (LA-ICP-MS): trace elements were analyzed by LA-ICP-MS (Pearce et al., 2007) by fusion on an Iridium strip heater under an Argon atmosphere. The analyses were carried out A/Prof. Ian Smith at the Research School of Earth Sciences, Australian National University. The samples were measured on a quadrupole ICP-MS coupled to an ArF 'Excimer' laser system (Eggins et al., 1998a, b). Ablation was carried out in a stratified atmosphere of Ar and He, excluding Ar from the area of ablation (Eggins et al., 1998a). The scan speed was set to 20 µm/sec and and the quadrupole ICP-MS was calibrated using a pre-prepared sample of NST612. An analysis of BCR-2 was run every 30 samples. Data reduction uses calculations input into a spreadsheet created by ANU to convert average peak for each element in counts per second into ppm. This spreadsheet uses the NST612 analyses at each end of the stack side, as well as the silica content of the sample as determined by XRF.

CHAPTER 3. Tephrostratigraphy of the Bullot Formation and characterisation of the largest explosive eruptions of Mt. Ruapehu

*This chapter presents the detailed tephrostratigraphy of the ~27-10 ka BP cal., Bullot Formation and its volcanological interpretation. Within this record, 33 distinct eruptive units were identified, which were grouped into six periods that reflect important variations in eruptive behaviour, particularly in column stability. The deposits of the largest explosive eruptions were classified into three lithofacies associations (**Fig. 3.1**), each one suggesting a different behaviour of the eruptive column. A systematic change in the dominant lithofacies association over time was identified, indicating a transition from earlier eruptions producing non-collapsing but oscillatory columns, to eruptions generating steady columns, and younger eruptions producing unsteady, collapsing columns. In addition, there is a new understanding of the last Plinian event, previously referred as the Okupata Tephra and Pourahu Member (c.f., Donoghue 1991; Donoghue et al., 1995a, 1999). This and the next chapter revise the previous stratigraphy and define a new maximum eruption size for Mt. Ruapehu.*

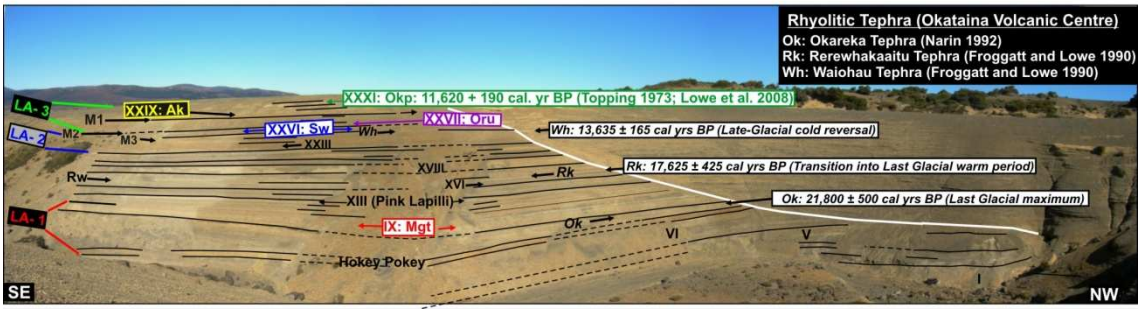

Figure 3.1 Deposits of the Bullot Formation at location B1 (i.e. Type location of Donoghue 1991; **Appendix A**). LA; Lithofacies Association type as will be defined in this Chapter. In Roman numbers some of the main pyroclastic beds are indicated. M1, M2, and M3, as well as the Hokey Pokey Lapilli and Pink Lapilli correspond to the marker beds identified by Donoghue (1995b). The position of rhyolitic ash marker beds is shown in white boxes. Mgt: Mangatoetoenui; Sw: Shawcroft; Oru: Oruamatua; Ak: Akurangi are new eruptive units defined in this study. Okp: Okupata Tephra (Topping 1973).

3.1 Introduction

The original definition of the Bullot Formation (Donoghue 1991) comprises only the deposits overlying the 27,097 ± 957 cal years BP, rhyolitic Kawakawa Tephra. However, it is important to emphasize that similar deposits indicating Plinian to subplinian events were also common prior the accumulation of this tephra (**Fig. 3.2**). The pre-Kawakawa pyroclastic deposits of Mt. Ruapehu are only locally preserved at location B14 (**Appendix A**), and are equivalent in age to the volcaniclastic deposits

reported in the Ring-Plain and along the Upper Waikato Stream by Cronin et al. (1996a). The study presented here is focused on the lithostratigraphic record overlying the Kawakawa tephra and precise correlation was only possible for the eruptive units younger than the Hokey Pokey Tephra (Donoghue 1991; Donoghue et al., 1995). Eruptive units between the Kawakawa Tephra and the Hokey Pokey Tephra (*Hokey Pokey Lapilli* defined by Donoghue 1991) were only found at locations B1, B14, and B27 (**Appendix A**).

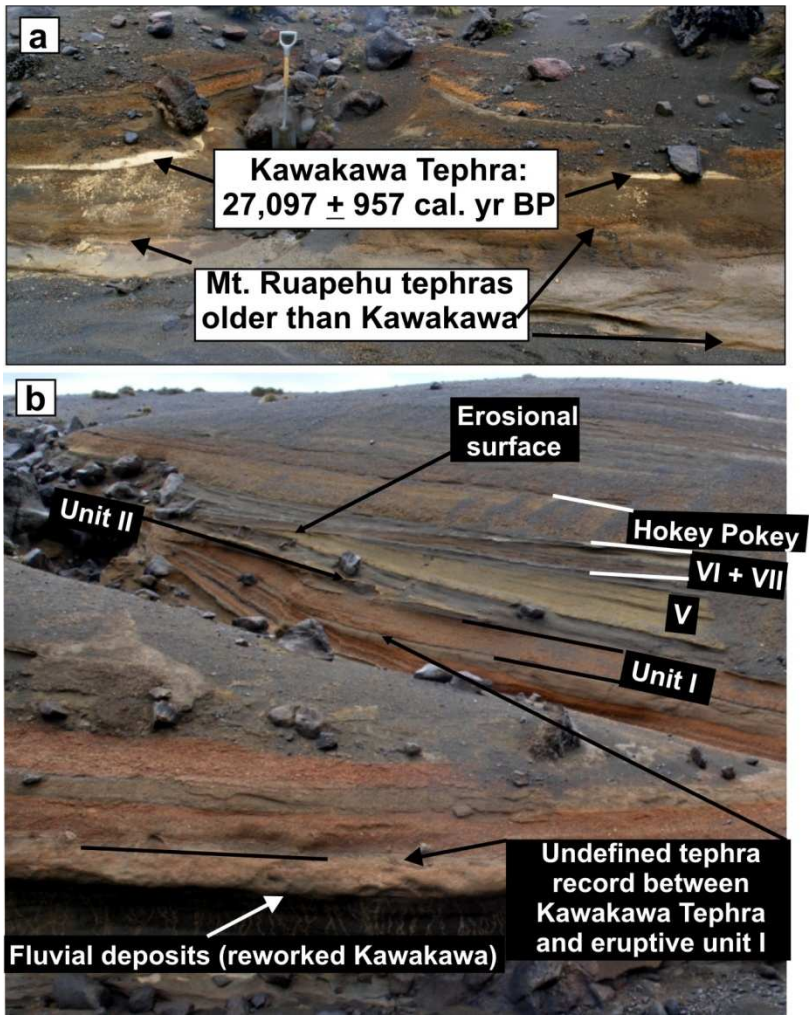

Figure 3.2 Deposits at location 14 (**Appendix A**), not included within the original definition of the Bullot Formation but indicating similar eruptive behavior. Thick pumice lapilli fall beds are found below: **a)** the Kawakawa Tephra or fluvial deposits reworking this tephra, and **(b)** the deposits described by Donoghue (1991) and Donoghue et al. (1995b) as the first unit (I) of the Bullot Formation.

An earlier version of this Chapter was published by Pardo et al. (2012a; **Appendix J.1**) and reports the principal findings obtained from detailed field work, lithostratigraphic correlation and definition of the eruptive sequences. The contributions of each author to the study were as follows:

Natalia Pardo (Principal researcher):

- Field stratigraphy, sampling and interpretation
- Manuscript preparation and writing

Dr. Shane J. Cronin (Chief supervisor):

- Introduction and assistance in the field
- Editing and discussion of the manuscript

Dr. Alan S. Palmer (co-supervisor):

- Field assistance and sampling
- Editing and discussion of the manuscript

Dr. Karoly Németh (co-supervisor):

- Field assistance and discussion

3.2 Reconstructing the largest explosive eruptions of Mt. Ruapehu, New Zealand: Lithostratigraphic tools to understand subplinian-Plinian eruptions at andesitic volcanoes

Natalia Pardo[a], Shane J. Cronin[a], Alan S. Palmer[a], Karoly Németh[a]

[a]Institute of Natural Resources, Massey University, Palmerston North, New Zealand

3.2.1 Abstract

The tephra record of Mt. Ruapehu comprised between 27,097 ± 957 and 11,620 ± 190 cal years BP, allowed the determination of the largest-scale explosive eruptions sourced at the most active New Zealand andesitic volcano. From the lithostratigraphic analysis, a systematic change in the explosive behaviour has been identified. Deposits of eruptions between ~ 27,097 ± 957 and 17,625 ± 425 cal years BP, suggest stable but oscillatory eruptive columns, characterized by crystal-poor, foamy to expanded pumice clasts. From the end of this period and up to 13,635 ± 165 cal years BP eruptive columns were steady and conduit wall erosion was extreme. Following 13,635 ± 165 cal years BP and up until 11,620 ± 190 cal years BP, pyroclastic deposits show evidence for unsteady eruption conditions and collapsing columns, characterized by extremely heterogeneous and coarse-grained porphyritic pumice clasts, ranging from microvesicular to fibrous textures, including colour-banded clasts. After ~11 ka BP cal., there was an abrupt transition in the dominant eruptive behaviour at Mt Ruapehu, since which time eruptions have been an order of magnitude lower in intensity and volume. These data demonstrate long-period transitions in eruption behaviour at an andesitic stratovolcano, which is critical to understand if realistic time-variable hazard forecasts are to be developed.

Keywords: andesitic tephras, explosive volcanism, eruptive unit, fallouts, lithofacies, lithofacies association, tephrostratigraphy

3.2.2 Introduction

With populations increasing near andesitic volcanoes around the globe, attention of physical volcanologists over the past four decades has been focused on defining the

range and scale of eruptive hazards at these volcanoes and forecasting most-likely eruptive scenarios. The most frequent activity of andesitic volcanoes is effusive volcanism, low-magnitude explosive events, and the generation of lahars. Isolated larger-scale eruptions also attest to the rare, but at times catastrophic activity generated by this type of volcano, such as Somma Vesuvius (Italy, AD 79; e.g., Gurioli et al., 2005), Askja (Iceland, 1875; e.g., Carey et al., 2010), Colima (Mexico, 1913; e.g., Saucedo et al., 2010), Mt. St. Helens (U.S.A., 1980; e.g., Lipman and Mullineaux 1981), Chichón (Mexico, 1982; Macías et al., 2003), Mt. Pinatubo (Philippines, 1991; Koyaguchi and Tokuno 1993), and Chaitén (Chile, 2007-2008; Carn et al., 2009; Lara 2009). Such large-scale eruptions represent a real threat to society (Cashman and Blundy 2000; Simkin and Siebert 2000). Such eruptions also represent the "extreme" potential of individual volcanic centres and understanding these maximum limits is an important step to completing a full and robust volcanic hazard assessment.

On the North Island of New Zealand (**Fig.1.2**), the largest explosive volcanic eruptions occur from Quaternary rhyolitic eruptive centres, particularly Okataina and Taupo calderas (Wilson et al., 1988; Wilson et al., 1984; 1995; Graham et al., 1995). Research on the coeval andesitic volcanoes has principally concentrated on their effusive activity and petrology (e.g., Cole 1978; Hackett 1985; Cole et al., 1986; Graham and Hackett 1987; Hackett and Houghton 1989; Graham et al., 1990; Hobden et al., 1996; Stewart et al., 1996; Hobden 1997; Waight et al., 1999; Gamble et al., 2003; Price et al., 2005), along with the tephras and lahars produced by their most frequent vulcanian-strombolian and phreatomagmatic historical eruptions (Houghton et al., 1987; Cronin et al., 1997a; 1998; Nakagawa et al., 2002; Bonadonna and Houghton 2005). Donoghue (1991), Donoghue et al. (1995a, b), Neall et al. (1995), Wilson et al. (1995), Cronin et al. (1996a), Donoghue et al. (1997), Cronin and Neall (1997), Nairn et al. (1998), Nakagawa et al. (1998), Donoghue et al. (1999), and Hitchcock and Cole (2007) have also described some aspects of explosive eruptions that may be two to three orders of magnitude larger than recent examples.

This paper provides a detailed tephrostratigraphic analysis of the largest known explosive eruptions from Mt. Ruapehu between 27,097 ± 957 and 11,620 ± 190 cal years BP. These new data help elucidate the nature of the largest-scale explosive eruptions that we can expect from New Zealand andesitic volcanoes, and to shed light

on the physical mechanisms of subplinian and Plinian eruptions at similar subduction-related andesitic volcanic systems elsewhere.

The tephra record described here was previously thought to consist of indiscernible lapilli beds lacking diagnostic field characteristics (c.f., Donoghue et al., 1995b), but we show that key criteria can distinguish and allow us to correlate them permitting construction of isopach and isopleth maps (**Chapter 4**). These criteria can be applied when other chronostratigraphic and paleosol markers are absent and/or deposit geochemistry is affected by weathering.

3.2.3 Geological Setting

The research area (**Fig. 1.2**) lies within the Tongariro Volcanic Centre (TgVC) at the southern end of the late Pliocene to Quaternary, NNE-SSE trending Taupo Volcanic Zone (TVZ), one of the most magmatically active regions on Earth (Gregg 1960, 1961; Cole and Nairn 1975; Cole 1978; Cole et al., 1986; Reyners et al., 2006).

Mt. Ruapehu and Mt. Tongariro (including Mt. Ngauruhoe) are two of the most active, low-K andesitic-dacitic New Zealand volcanoes. They are located within the Mt. Ruapehu graben where faulting and volcanism appear closely related (Narin et al., 1998; Villamor et al., 2010). Mt. Ruapehu (i.e. Rua "pit", pehu "to explode"; in Te reo Maori language) is a large (110 km^3), 2797 m high, composite volcano, comprising several overlapping craters, progressively younger towards the south (Hackett 1985; Graham and Hackett 1987; Hackett and Houghton 1989; Graham et al., 1995; Wilson et al., 1995; Cronin et al., 1996a; Gamble et al., 2003). Mt. Tongariro (i.e. riro "carried away", tonga "south wind") is a slightly smaller (75 km^3) composite volcano consisting of several coalescing volcanic cones, with Mt. Ngauruhoe the most recently active (Hobden et al., 1996; Hobden 1997; Moebis 2010; Moebis et al., 2011). Gamble et al. (2003), pointed out that both volcanoes might have initiated simultaneously (with a maximum age of 340 ka), but major cone-building stages occurred at different times.

Pleistocene and products of Mt. Ruapehu comprise well described lava flows (Graham and Hackett 1987; Hackett and Houghton 1989; Waight et al., 1999; Gamble et al., 2003), and fall deposits, plus rare pyroclastic density current deposits (Topping 1973;

Donoghue 1991; Donoghue et al., 1995a, b, 1999; Bonadonna and Houghton 2005; Moebis et al., 2011), lahar deposits (Cronin et al., 1996a; Donoghue and Neall 2001), with debris-avalanche deposits (Palmer and Neall 1989; Lecointre et al., 1998; McClelland and Erwin 2003). The largest eruptions of Mt. Ruapehu date back to the late Pleistocene (Topping 1973; Donoghue et al., 1995b; Cronin et al., 1996a, b) and their deposits are included within the Bullot Formation (Donoghue 1991). Historical activity has been centred at the South Crater (Cole and Nairn 1975), which is currently occupied by an acidic Crater Lake (Christenson and Wood 1993), mainly characterized by lahar generation (e.g., Cronin and Neall 1997; Cronin et al., 1997a; Neall et al., 2001; Lecointre et al., 2004; Lube et al., 2009; Procter et al., 2010), small and frequent phreatic, phreatomagmatic eruptions, and rare dome-building events (Nairn et al., 1979; Houghton et al., 1987; Hackett and Houghton 1989; Cronin et al., 1997a; Kilgour et al., 2010).

3.2.4 The largest explosive eruptions recorded at Mt. Ruapehu

A total of 158 locations exposing the Bullot Formation were described, primarily to the east of Mt. Ruapehu (**Appendix A**). West of the volcano only one location, the Pukeonake spatter cone, contained a coherent tephra sequence of this age, with a few other localities showing one or two units. The most distal locations where the tephras can be distinguished and correlated along the apparent dispersal axis are 80 km east of Crater Lake (**Fig.1.2**).

Bed geometry and sedimentary structures, including contact types, bed forms and stratification, paleochannels, dune structures, clast-concentration lenses, grain-size grading, and syn-depositional deformation structures (e.g., impact sags) were carefully studied. Matrix supported vs. clast-supported facies, sorting and composition were qualitatively described in the field, with particular attention given to the characteristics of pumice, scoriae and lithic fragments, including colour, shape, vesicle and crystal contents, sizes, shapes, and fabric (e.g., frothy, foliated, fibrous and mottled). These data were used to interpret particle transport and deposition mechanisms, key field criteria to distinguish the lithofacies classes of eruptive units. Boundaries to eruptive units are major discontinuities within this region marking significant repose periods in

the eruptive activity: these include loess, paleosols, and deeply incised paleochannels filled with thick fluvial deposits synchronous to epiclastic deposits at other locations, indicating the reestablishment of the landscape and the return of sedimentary processes to the background conditions existing before the eruption (c.f., Manville et al., 2009). During the emplacement of the Bullot Formation in high-elevation sites studied (500-1600 m elevation) syn-depositional conditions ranged from harsh periglacial climates during the last glacial period, to warmer and wetter conditions during the transition into the Holocene (Lowe et al., 2008). Hence, pedogenetic processes were highly limited, affecting the types of soils developed (Cronin et al., 1996c); also reduced preservation of tephra units emplaced onto extensive snow/ice cover occurred, with widespread tephra remobilization by melt-waters and snow-slurry lahars (Cronin et al., 1996a, 1997a; Manville et al., 2000). Here, the discrimination between syn-eruptive volcaniclastic deposits (synchronous with the eruptive activity) and inter-eruptive post-eruptive volcaniclastic deposits, based on their geometry, sedimentary structures, and lithology (following Smith 1991; Manville et al., 2009) was crucial to establish the hierarchy of discontinuities formed under glacial-periglacial conditions during accumulation of the Bullot Formation. Minor discontinuities, such as local scouring, gradational and sharp contacts given by contrasting grain-size, sorting, clast-support framework, bed-structure, or lithic vs. pumice content mark changes in the eruptive style and/or transport/emplacement mechanism, and do not signify major time breaks. Beyond 20-25 km from Crater Lake, many of the proximally separate beds merge into compound depositional units bounded by major discontinuities.

Thirty three eruptive units bounded by thick loess and/or paleosols (**Figs. 3.1, 3.3; Appendix A**) could be correlated between many of the studied sites, ranging from the Hokey Pokey lapilli defined by Donoghue et al. (1995b), to the ~11 ka BP cal., Pahoka Tephra defined by Topping (1973). Regional stratigraphic markers supporting correlations include the rhyolitic Okataina-sourced: 21,800 ± 500 cal years BP Okareka Tephra (during the Last Glacial maximum), 17,625 ± 425 cal years BP Rerewhakaaitu Tephra (marking the onset of a transition into a late-glacial warm period), and 13,635 ± 165 cal years BP Waiohau Tephra (marking a late-glacial cold reversal) (Froggat and Lowe 1990; Newnham et al., 2003; Lowe et al., 2008).

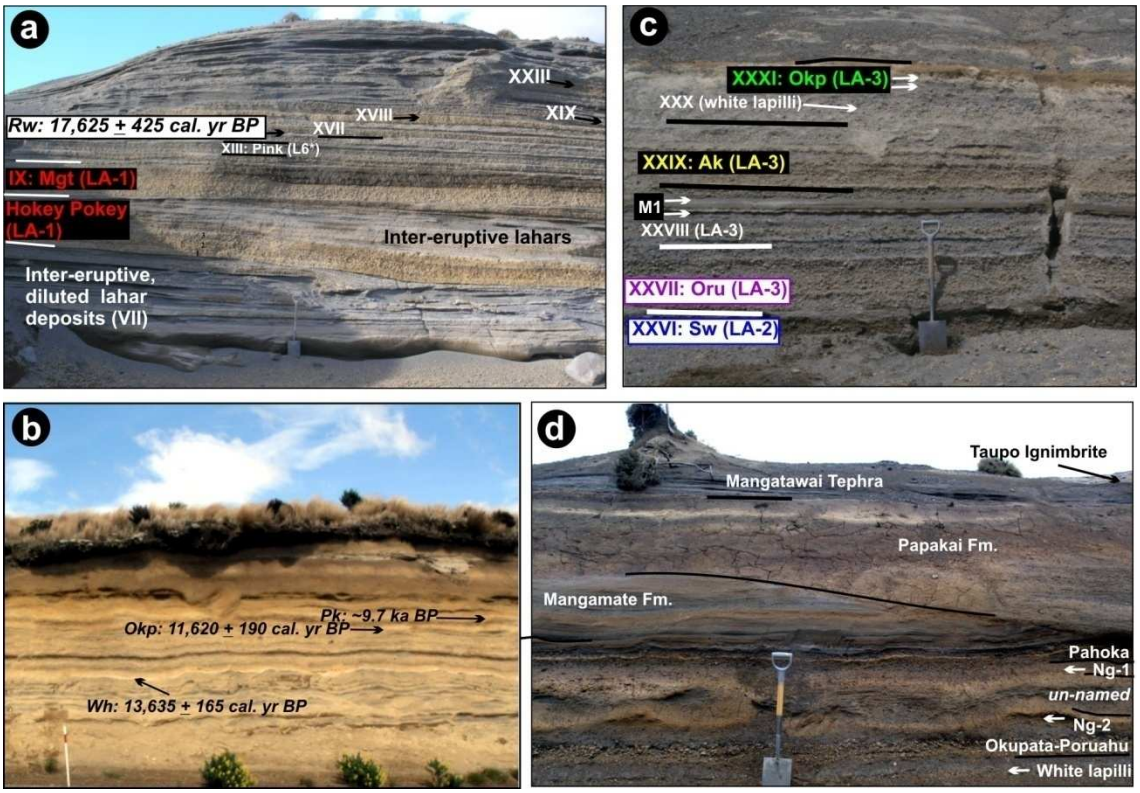

Figure 3.3 Bullot Formation as seen on the eastern Ring Plain: **a)** lower part of the studied sequence, 15 km from Crater Lake; **b)** middle part of the sequence, 17 km from Crater Lake. Important markers are shown: the Okataina caldera Rerewhakaaitu (Rw) and Waiohau (Wh) tephras, Mt. Ruapehu Okupata Tephra (Okp), and Mt. Tongariro Pahoka Tephra (Pk); **c-d)** upper part of the sequence, 15-17 km from Crater Lake. Ng-1-2: Ngamatea Lapilli 1-2 as defined by Donoghue (1991) are the last subplinian eruptions from Mt. Ruapehu before the onset of the most explosive period of Mt. Tongariro, represented by the Pahoka-Mangamate sequence, as redefined by Nairn et al. (1998).

Below, a detailed tephrostratigraphy is presented in chronological order with particular detail given on the most widespread, thick and coarse-grained, pyroclastic fall deposits related to subplinian and Plinian eruptions, mainly from Mt. Ruapehu. The oldest unit that could be successfully correlated in the studied area is the Hokey Pokey Eruptive Unit (**Figs.3.1, 3.2, 3.3a; Appendix A**). Several outcrops along the Upper Waikato Stream expose weathered pumice lapilli beds below the Hokey Pokey Eruptive Unit and even below the ~27 ka BP cal., Kawakawa tephra (Cronin et al., 1996c; Wilson 2001; Lowe et al., 2008), showing that large explosive events from Mt. Ruapehu were common, at least from ~55 ka BP cal. (Cronin et al., 1997b).

The grain-size terms ash, lapilli, blocks, and bombs are here only used to describe primary deposits. Silt, sand, and gravel are here restricted to descriptions of volcaniclastic and epiclastic deposits (see White and Houghton 2006 classification for

the equivalent diameters). Both grain-size and bed thickness dimensions are given as exposed in the Ring Plain, between 9 and 15 km from Crater Lake.

The Hokey Pokey Eruptive Unit (HP)

The HP unit is bounded by thick lahar deposits and loess, and was erupted immediately before the 21,800 ± 500 cal years BP rhyolitic Okareka Tephra (**Fig. 3.4**). It is well exposed at the base of the studied deposits, mantling the underlying topography and decreasing in thickness and grain-size towards the east. Up to four distinct pyroclastic, clast-supported, well sorted, pumice lapilli beds (**Fig. 3.4**), bounded with sharp to locally erosive contacts by thin volcaniclastic deposits of variable thickness (**Figs. 3.3a** and **3.4**), were distinguished within the first 15 km E, NE, and SE from Mt. Ruapehu.

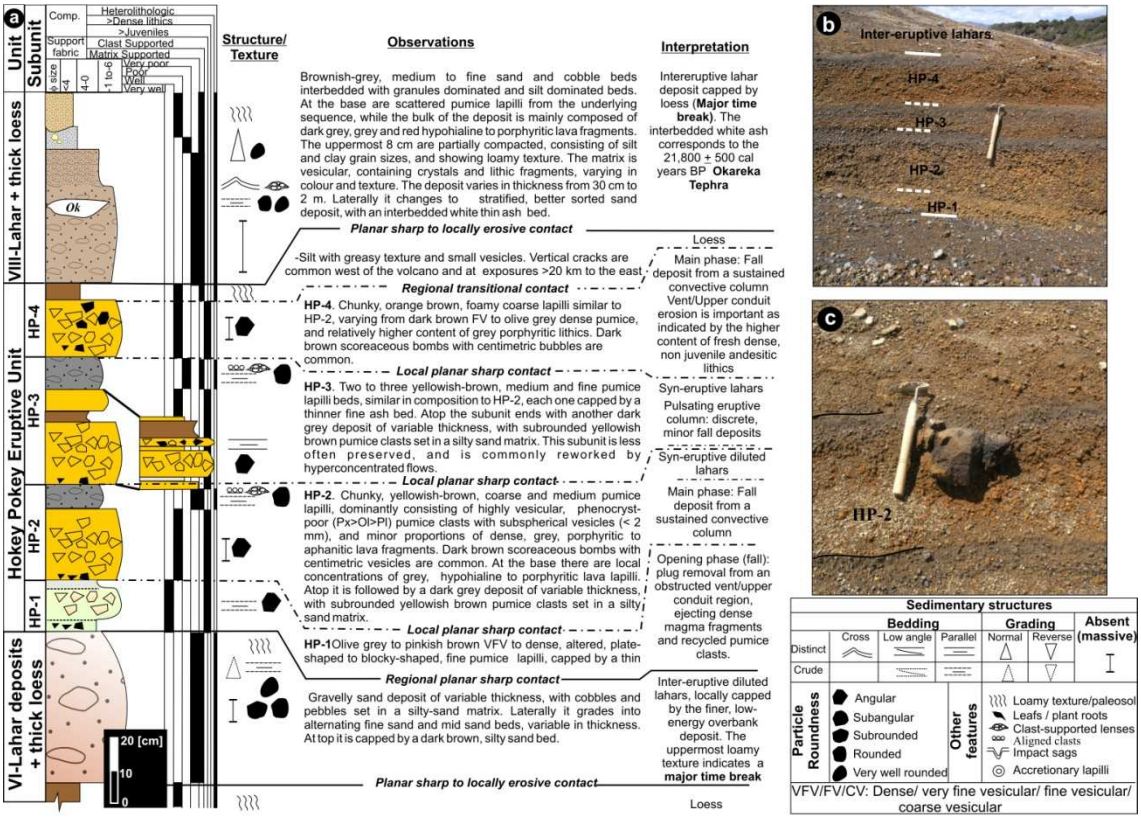

Figure 3.4 Hokey Pokey eruptive unit: **a)** general stratigraphic profile of the Hokey Pokey eruptive unit **b)** HP subunits (HP-1 to 4) ~9 km from the vent, with the main lapilli fall deposits and interbedded, thinly stratified diluted lahars and fluvial deposits; **c)** bread-crust bombs in the main Plinian fall deposits are common in the first 10 km from the vent. Solid lines represent regionally exposed, major discontinuities limiting eruptive units, and dashed lines indicate locally exposed, minor discontinuities separating deposits of eruptive phases/pulses within the same unit.

Eruptive period	Pre-Okareka tephra	Rangipo			Tukino	Karioi				Ohinewairua		Taurewa
Unit	Hokey Pokey (L3*)	IX (L4*)	XIII (XIII-1 = L6*)	XVIII (XVIII-4 = L8*)	XIX (L11*)	XXIII (L13*)	XXIV (L14*)	XXV (L15*)	XXVI (Sw/ L16*)	XXVII (XXVII-1 = L17*)	XXVIII (L18**)	XXXI (Okp**)
Age (Donoghue et al. 1995b)	< 21,800 ± 500 cal. years BP	< 21,800 ± 500 cal. years BP		< 17,625 ± 425 cal. years BP					< 113,635 ± 165 years BP			11,620 ± 190 cal. years BP
Bed colour	Strong yellowish brown	Pale brown	Pinkish-brown	Strong yellowish brown	Dark brown base, orange top	Strong iron-stained, orange-brown				Pale brown to greyish-brown		Pinkish-white to white
Lithofacies association type	LA-1	LA-1	Not end-member; hybrid 2B and 3	LA-1	LA-2b	LA-2a				LA-3		
Juvenile Pumice	91 %. Frothy, finely vesicular , subspherical vesicles < 2 mm	60% Foliated, ellipsoidal to tube-like vesicles < 1 cm	60 -20% Very finely vesicular to dense, distorted vesicles < 1mm	78-90% Frothy, finely vesicular , subspherical vesicles < 2 mm	49% Expanded, coarsely vesicular > dense. Sbspherical vesicles 1cm	68% Dense to very finely vesicular with subspherical to ellipsoidal vesicles < 1mm			57%	37% Very heterogeneous, from finely to coarsely vesicular, some colour banded and fibrous, with elongated and some highlly distorted vesicles		33%
Whole-rock SiO_2 [%]	52.37	57.42	L6*54.71	L8*49.62	55.44	51.34	53.15	53.31	Sw: 57.6	L17: 53.17	L18: 57.39	52.15-57.73
Glass matrix SiO_2 [%]	60.02	66.94	L6*61.59		62.07	69.48		61.7		L17: 73.33	L18: 66.17	67.52-74.17
Bulk density [g/cm^3]	1.25	$*\delta_{bulk}$: 0.99 g/cm^3 0.65-1.56				$*\delta_{bulk}$: 1.35 1.39				$*\delta_{bulk}$: 1.40 1.33		$*\delta_{bulk}$: 1.16 0.92-1.33
Bulk vesicularity [%]	43-78	47-74				54-57				55		56-71
Phenocrysts	5% (Cpx + Opx + Pl>> Ol) < 1mm	30% (Cpx + Opx> Pl) < 5 mm	<5% (Cpx + Opx > Pl) < 2 mm	<15% (Cpx + Opx > Pl) < 5 mm	<4% (Cpx + Opx + Pl) < 5 mm	4% (Pl> Opx + Cpx) < 1 mm			6%	38 % (Pl+ Opx + Cpx>>Qz) < 7 mm give mottled, coarse-poprphyritic texture		44%
Non-Juvenile Lithic clasts	6% (mainly fresh, dark grey, fine grained porphyritic andesites, rare hydrothermally altered volcanics)	2% (mainly fresh, dark and pale grey, coarse-grained porphyritic andesites)	Variable, lithic-rich beds up to 80% mainly fresh, dark and pale grey, coarse-grained porphyritic)	Variable, lithic-rich beds up to 25% fresh, dark and grey, coarse-grained porphyritic > aphanitic Hydrothermally altered)	47% concentrated at top: porphyritic to aphanitic Hydrothermally altered	30% Highly hydrothermally altered dense volcanic lithics, varying in colour and texture: red, grey, olive grey, bluish-brown, orange, purplish-brown and yellow, aphanitic to coarse-grained porphyritic. Some meta-sedimentary			37%	25% Coarse-grained porphyritic grey andesites > orange and red, hydrothermally altered aphanitic lithics >> metasedimentary grawackey		23%
Predominant pumice type	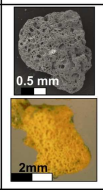	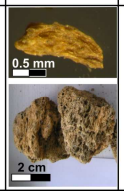			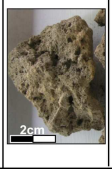					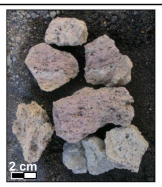		

Table 3.1 Correlation of the eruptive units defined here with the published stratigraphy and main field characteristics of key eruptive units of this study. Donoghue's (1991) equivalent nomenclature of the lapilli beds representing Plinian phases within each eruptive unit are shown in brackets. Whole-rock and glass composition are taken from Donoghue et al. (2007). Componentry, density and vesicularity proportion as expressed as average vol.% from gas-pycnometry measurements (**Appendix G**). The average bulk density of the whole deposit ($*\delta_{bulk}$) is reported in g/cm^3 for some of the units.

Beyond this distance, the eruptive unit consists of only a single pumice lapilli bed (i.e. Hokey Pokey lapilli defined by Donoghue 1991) with characteristics described for HP-2 and HP-4 in figure 3.4, bounded by compacted loess, and recognized as a useful regional marker. The capping loess contains patches of the Okareka tephra. Distinguishing features are the strong "chunky" appearance, and the predominance of yellowish-brown, equant-shaped, frothy, finely vesicular, phenocryst-poor (<5 %) pumice clasts (**Table 3.1**), with dominantly sub-spherical vesicles of restricted size (<2 mm).

Interpretation: the HP unit is interpreted as resulting from four distinct eruptive phases producing widespread fall deposits separated by pauses long enough for syn-eruptive lahars and fluvial reworking to occur, locally channelling the deposits. Donoghue (1991) reported whole rock and glass SiO_2 contents for the Hokey Pokey lapilli around 52 and 60 wt. %, respectively (**Table 3.1**). The main depositional axis for this unit is to

the ENE, but there are not enough exposures to produce isopach maps due to common syn- and post-eruptive reworking by stream-flows, snow melt, and lahars.

Rangipo Eruptive Period

This eruptive period produced seven eruptive units, each consisting of pyroclastic deposits followed by inter-eruptive, epiclastic sequences (fluvial deposits and loess) very well exposed on the Rangipo desert.

Unit IX: this well bedded unit (**Figs. 3.1, 3.3a, 3.5 and 3.6; Appendix A**) is widely distributed on the eastern volcano slopes and ring plain, comprising four distinct, topography-mantling beds that thin and fine towards the NE and SE. The lowermost lapilli fall bed (subunit IX-1) is up to 40 cm thick, has a distinctive grey porphyritic lithic lapilli concentration at its base and is characterized by yellowish-brown to pale brown pumice lapilli, fining upward and capped by a greenish grey fluvial sand deposit. Above this is a second prominent, ungraded, pale brown, pumice lapilli fallout (subunit IX-2), which is capped by a thinner (<7 cm) firm orange-brown, fine ash fall deposit (**Figs. 3.5 and 3.6**). Beyond 20 km from source all beds merge. Distinguishing features of the eruptive unit are the normal grading of IX-1, the dark brown, very coarse, strongly foliated pumice clasts with elongate vesicles up to 1 cm (**Table 3.1**) giving a fluidal texture, and the high content of green pyroxene glomerocrysts.

Interpretation: Unit IX represents at least four eruptive phases (**Fig. 3.6**) beginning with a conduit/plug or dome clearing explosion, producing the monolithologic lithic-rich base. After this, a sustained column developed, producing the first main, gradually waning pyroclastic fall bed. This deposit (IX-1) corresponds to the L4 tephra (**Table 3.1**) identified by Donoghue (1991) and is defined here as the Lower Mangatoetoenui eruptive unit (L-Mgt).

A brief-inter episode hiatus occurred, accompanied by fluvial action, before production of the highest eruptive plume of the sequence, which deposited the very coarse-grained and massive IX-2a fall bed. This column dissipated and deposited the uppermost mantling ash-bed (IX-2b), followed by subsequent aeolian and fluvial reworking. The bedset IX-2 is defined here as the Upper-Mangatoetoenui eruptive unit (U-Mgt). Unit IX (i.e The Mangatoetoenui eruptive unit: Mgt) immediately overlies the Okareka

Tephra, and has two depositional lobes, directed north-eastward and south-eastward (**Chapter 4**).

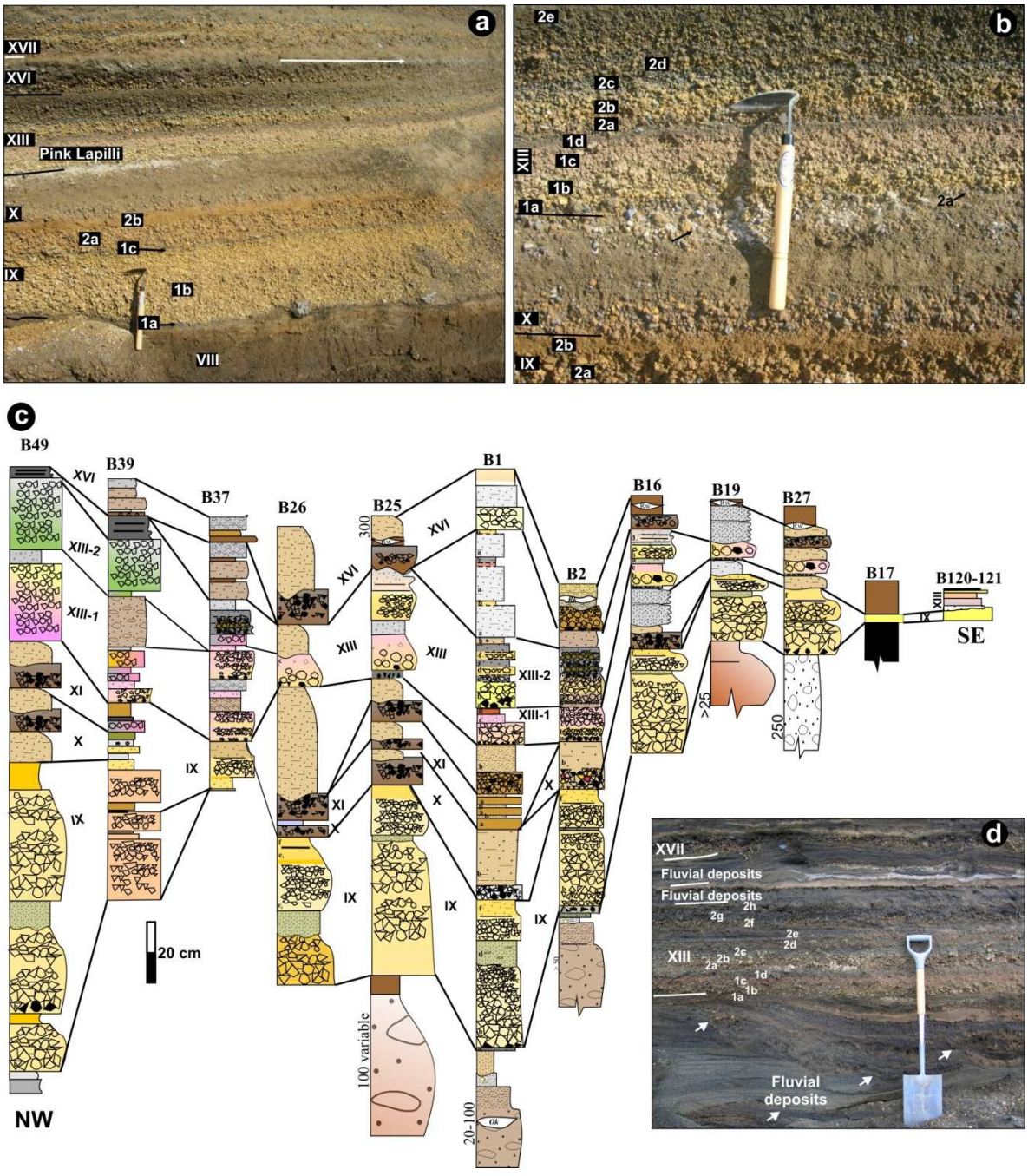

Figure 3.5 Post-Okareka, pre-Rerewhakaaitu eruptive units IX to XVI as: **a)** exposed within 10 km from source, showing the inner distinctive subunits as described in the text. The white arrow points the 17,625 ± 425 cal years BP rhyolitic marker; **b)** detailed deposits overlying unit IX, with the distinctively pink fall bed of eruptive unit XIII; **c)** NW-SE stratigraphic correlation from unit IX to XVI; **d)** exposure at a small tributary to the Upper Waikato stream, showing the lateral facies variation of the inter-eruptive fluvial deposits: thick fluvial sequences commonly fill paleochannel structures (arrows).

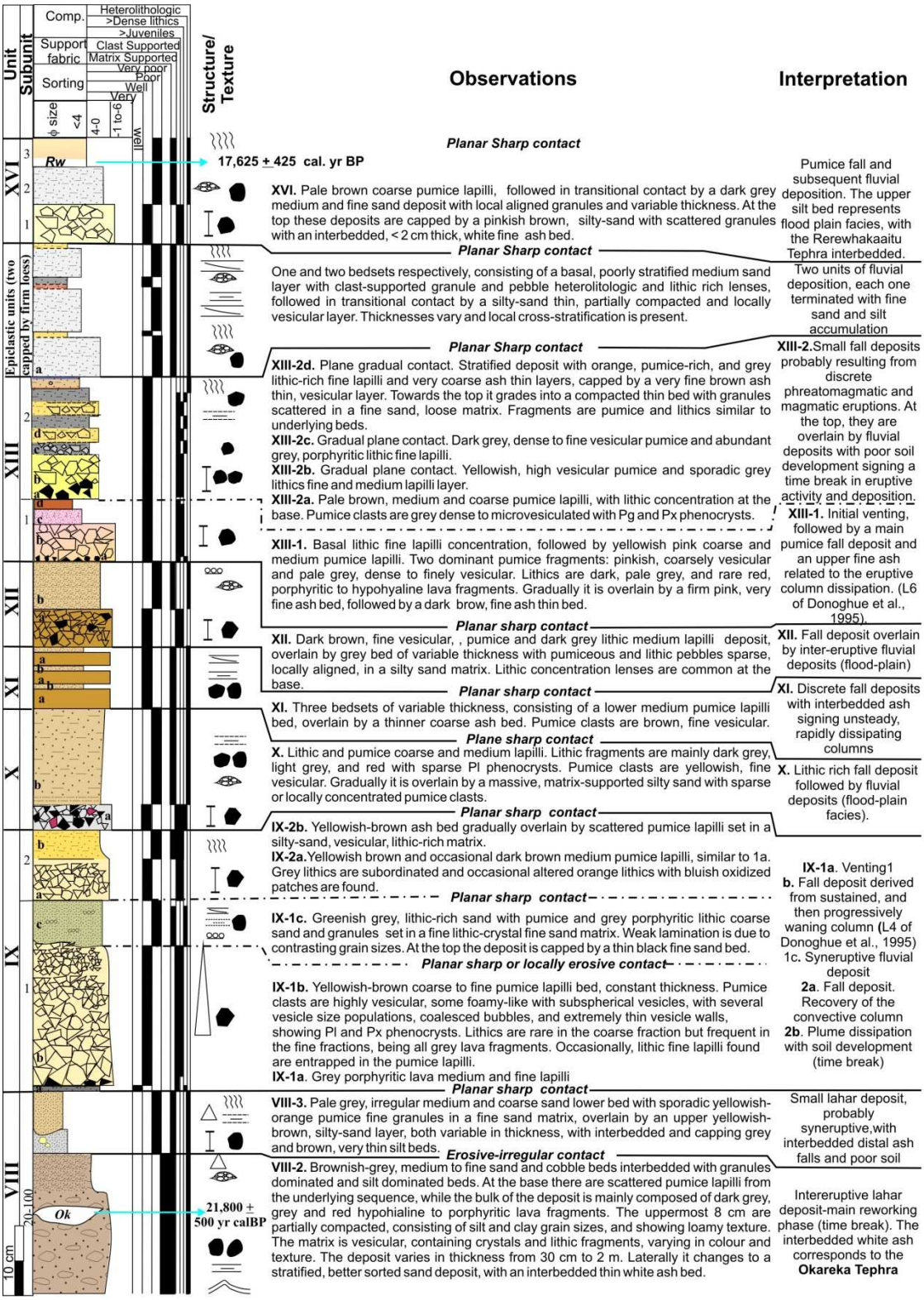

Figure 3.6 General stratigraphic profile showing the eruptive units IX to XVI, accumulated between the Okareka Tephra (Ok) and the Rerewhakaaitu Tephra (Rw). The legend for the sedimentary structures is the same as in **Fig. 3.4**. Solid lines represent regionally exposed, major discontinuities delimiting eruptive units, and dashed lines indicate locally exposed, minor discontinuities separating deposits of eruptive phases/pulses within the same unit.

Eruptive Units X, XI, and XII: these units (**Figs. 3.5 and 3.6**) are predominantly massive along the dispersal axis and crudely bedded away from it. Each eruptive unit consists of a clast-supported, well sorted, angular coarse and medium pale-brown pumice lapilli bed of constant thickness (<10 cm), followed by inter-eruptive hyperconcentrated flows and fluvial sand deposits, and loess. Unit X is particularly enriched in dark-grey, light-grey and red hypohyaline to porphyritic lithics.

Interpretation: each pyroclastic massive bed is interpreted as a discrete fall deposit. A particularly significant eruption pause occurred after the deposition of unit XII lapilli fallout, marked by the incision of paleochannels and widespread thick sedimentary sequences on the Ring Plain, and an angular erosional discontinuity in the proximal areas (**Fig.3.7**).

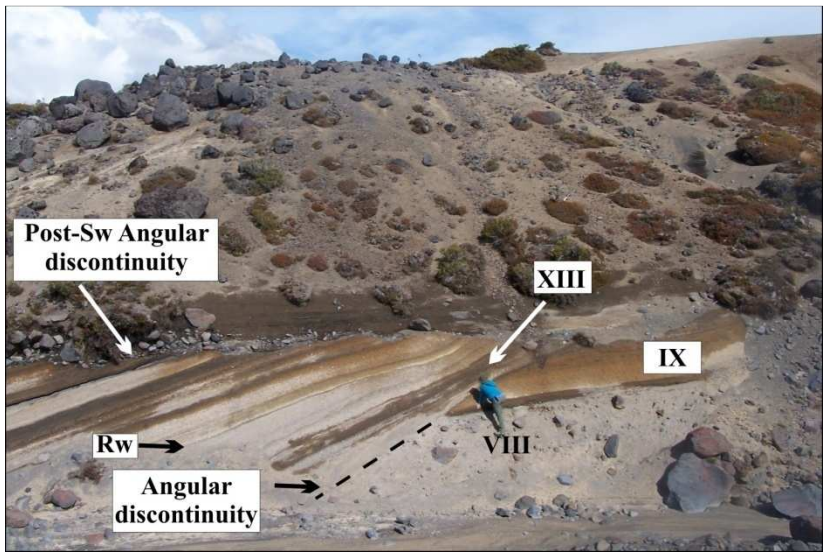

Figure 3.7 Proximal deposits on the eastern slopes of Mt. Ruapehu showing angular discontinuities. There is one distinctive above which unit XIII was deposited. Rw: 17,625 ± 425 cal years BP, rhyolitic Rerewhakaaitu Tephra marker.

Eruptive Unit XIII: this unit crops out in almost every studied location and is one of the best markers among Mt. Ruapehu tephras due to its unique pinkish-brown colour (**Figs. 3.5, 3.6**). It comprises two subunits: the lowermost (XIII-1) has a distinctive, lithic-rich, fine lapilli base (XIII-1a; < 3 cm thick) and consists of pale grey, dense to finely vesicular pumice (**Table 3.1**). XIII-1a is overlain by a distinctive pinkish-brown, massive coarse lapilli bed (XIII-1b; < 15 cm), characterised by coarsely vesicular pumice clasts, grading upward into pink ash (XIII-1c < 5 cm). Locally, a capping thin brown fine ash bed is also preserved (XIII-1d).

The second subunit (XIII-2) is also very distinctive, and consists of alternating, massive, well sorted, clast-supported, pastel-coloured, fine pumice lapilli and dark grey, lithic-dominated coarse and fine ash beds: in the latter, lithic content reach up to 80 % and juvenile clasts are vesicle-poor, blocky-shaped. The subunit is capped with brown loamy loess (XIII-2e).

Interpretation: Unit XIII resulted from multiple eruptive phases, beginning with a conduit/vent clearing explosive phase (XIII-1a), during which a plug of porphyritic lava and grey, dense pumice was removed. This was followed by sustained ejection of highly vesicular magma, producing the widespread, coarsely vesicular pink pumice fall deposit XIII-1b. The eruption included a pulsatory phase, with alternating pumice-rich lapilli beds and fine grained lithic-rich ash beds, suggesting probable interaction between magma and external water. Following eruptive activity, fluvial re-deposition and loess accumulation began.

Locally, two minor discrete fall deposits and intervening syn-eruptive lahar deposits overlie unit XIII (**Fig. 3.5d**). In most locations the primary deposits were completely reworked by fluvial action, as indicated by thick sand and gravel sequences showing rapid transitions between channel and overbank silt facies. The eruptive activity was only clearly renewed with the deposition of a pale brown, pumice, coarse lapilli bed (Unit XVI; **Fig. 3.6**; **Appendix A**), directly overlain by a thin loess containing pockets of the rhyolitic 17,625 ± 425 cal years BP Rerewhakaaitu Tephra, sourced from the Okataina Caldera.

Units XVII and XVIII: these lapilli units (**Figs. 3.8, 3.9**) are widely distributed across the E and SE sectors of the volcano and are easily distinguished by their yellowish brown and occasionally orange-brown bed colours, the strong-yellow, coarsely vesicular, phenocryst-poor pumice with dark brown interiors, and the presence of hydrothermally altered, red lithics in some of the beds. Unit XVII directly overlies the Rerewhakaaitu Tephra, and its inner stratification is defined by alternating lapilli and coarse but thin ash beds or laminae (**Fig. 3.8b**). Unit XVIII is well exposed at proximal sites on the north-eastern slopes and pumice clasts from the uppermost beds occur commonly on the surface slopes around Rangipo Hut (**Fig. 1.2**). It is partially or completely reworked on the eastern slopes and Ring Plain. In the upper reaches of the Mangatoetoenui stream (**Fig. 1.2**), six, distinct strong yellow to orange lapilli beds

occur, with two packages (Lower and Upper-XVIII) separated by syn-eruptive fluvial deposits.

The three lower pumice lapilli beds (Lower-XVIII) are relatively thinner than those above, and very similar in pumice fabric, and accidental lithics to unit XVII below. The uppermost three lapilli beds (Upper-XVIII) are more widely preserved (**Fig. 3.8c**), and dominantly composed of pale yellow, finely vesicular, phenocryst-rich pumice lapilli, with rare lithic clasts. Locally, in the upper Mangatoetoenui catchment area, a massive, matrix-supported, poorly sorted blocks and lapilli deposit (**Fig. 3.10**), with highly variable thickness occurs in the same stratigraphic position as the fifth lapilli bed, completely replacing it.

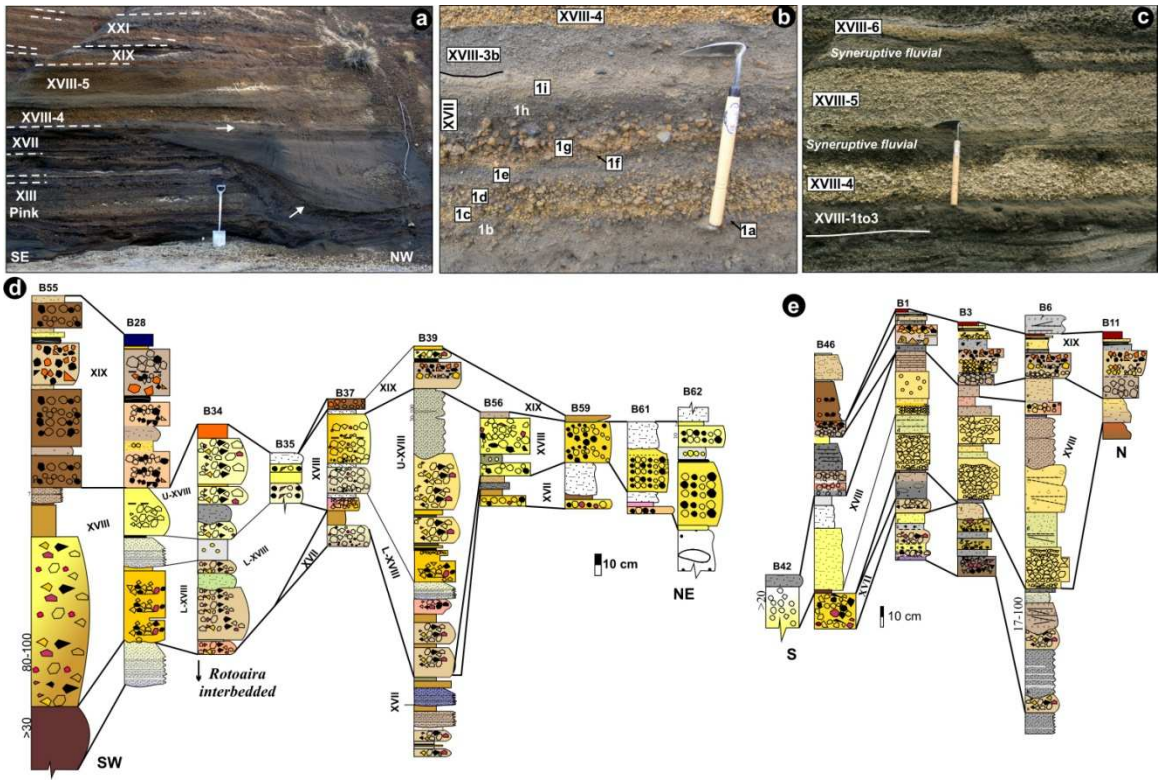

Figure 3.8 Fall deposits of units XIII to XIX as **(a)** exposed at medial distances. Interbedded fluvial deposits lateral facies variation is evident, with thicker sequences filling paleochannels; **b)** zoom of the lithic-rich unit XVII; **c)** zoom of the lithic-poor Upper XVIII unit; **d-e)** stratigraphic correlation from unit XVII to XIX.

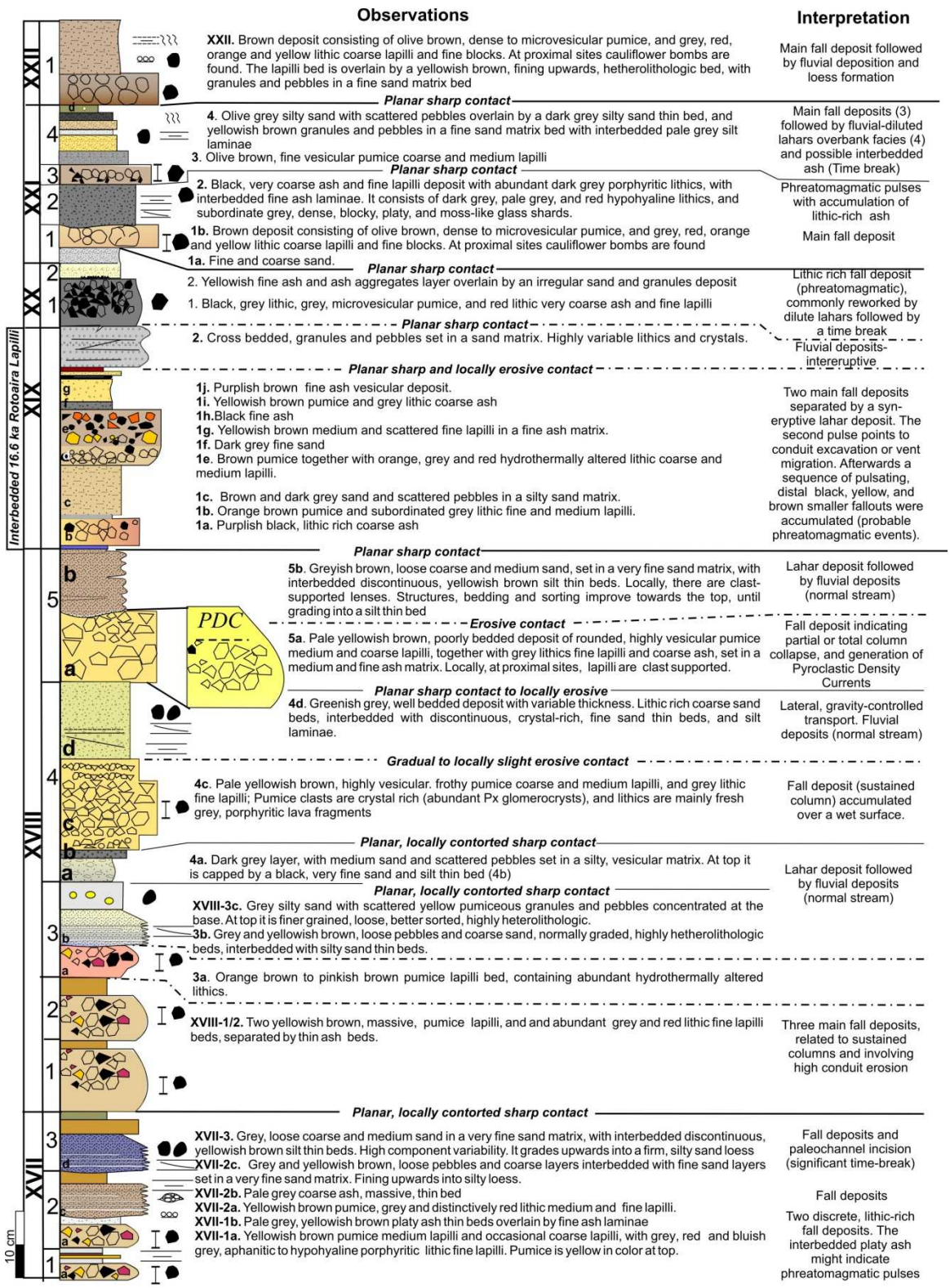

Figure 3.9 General stratigraphic profile showing the eruptive units XVII to XXII, as described in the text. The legend for the sedimentary structures is the same as in **Fig. 3.4**. Solid lines represent regionally exposed, major discontinuities limiting eruptive units, and dashed lines indicate locally exposed, minor discontinuities separating eruptive phases/pulses within the same unit.

Interpretation: Unit XVII (**Fig. 3.9**) is very different from earlier eruptives in this sequence, particularly in pumice textures and differentially hydrothermally altered lithologies. The termination of the eruptive unit is marked by fluvial deposits and a highly eroded paleosurface, with a locally preserved, weak capping paleosol.

Unit XVIII (**Fig. 3.9**) signals a renewal of eruptive activity and involved at least six eruptive phases: the first three were characterized by relatively short-lived, sustained columns, producing lapilli fall deposits capped by ash from the dissipating plumes that progressively decreases in lithic content. Following the third phase, syn-eruptive lahars reworked most of the primary fall deposits to the east. Afterwards, three major eruptive events took place producing sustained eruptive columns accumulating the massive lapilli beds XVIII-4 to 6 (**Fig. 3.9**). Based on descriptions by Donoghue (1991), XVIII-4 possibly corresponds to her L8 tephra.

The XVIII-5 (**Fig. 3.9**) event was accompanied by partial column collapse producing pyroclastic density currents (PDC) as evidenced by the matrix-supported, poorly sorted pyroclastic, channelized deposit of variable thickness found on the upper Mangatoetoenui Stream (**Fig. 3.10**). Primary PDC deposits were only found along this stream down to 6 km from the North Crater; at 8 km (location B28; **Appendix A**) deposits are pumice-dominated but begin to present well defined, parallel and cross stratification, and intense rounding, suggesting partial, syn-eruptive reworking by hyperconcentrated flows.

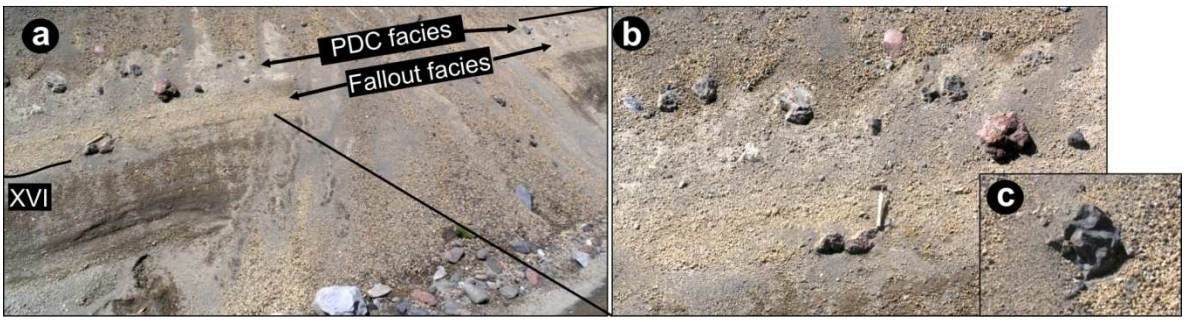

Figure 3.10 Units XVII and XVIII at location B49 (Appendix A) showing pyroclastic density current (PDC) facies, characterised by: **a)** poorly sorted, matrix-supported, block (bombs) and pumice lapilli deposits; blocks and bombs (**b**) have different degrees of oxidation and vesicularity, usually showing vesicular cores and dense rims with radial joints (**c**).

Unit XVIII is the only one indicating eruption column collapse producing PDC among eruptive units older than 13,635 ± 165 cal years BP. Primary pyroclastic deposits were followed by lahars, which removed much of the primary tephra sheet to the east. These volcaniclastics grade up to stream-flow deposits, indicating a gradual stabilisation of the landscape.

Tukino Eruptive Period

This period produced three eruptive units (XIX to XXI), comparatively thin but very coarse-grained and well exposed in the Tukino ski field area (**Fig. 1.2**).

Units XIX to XXII: these units are very useful stratigraphic markers within 20 km of Crater Lake, and are characterized by coarse lapilli, block-and-bomb beds less than 10 cm thick, interbedded with thin dark grey and purplish brown, fine ash beds (**Figs. 3.9** and **3.11a**). Unit XIX is well bedded, and easily recognized by a concentration of dark brown, coarse vesicular, phenocryst-poor, scoriaceous lapilli and bombs at its base, and a concentration of orange, vesicular pumice and orange to grey, hydrothermally altered, porphyritic lithic lapilli (**Table 3.1**). This bed is capped by a distinct thinly laminated, purplish brown and black ash deposit (<5 cm).

Units XX and XXI are very similar, separated by a weak paleosol, each one consisting of two, distinctively coarse-grained beds; the primary beds of unit XX are commonly reworked and replaced by hyperconcentrated-flow deposits. The lapilli beds forming unit XXI are more prominent and widely distributed, characterised by coarsely vesicular, scoriaceous bombs, finely vesicular brown pumice coarse lapilli, and abundant hydrothermally altered lithic coarse lapilli and blocks. Both lapilli/block beds are separated by a distinctively laminated, black ash deposit (**Figs. 3.9, 3.11b, c**).

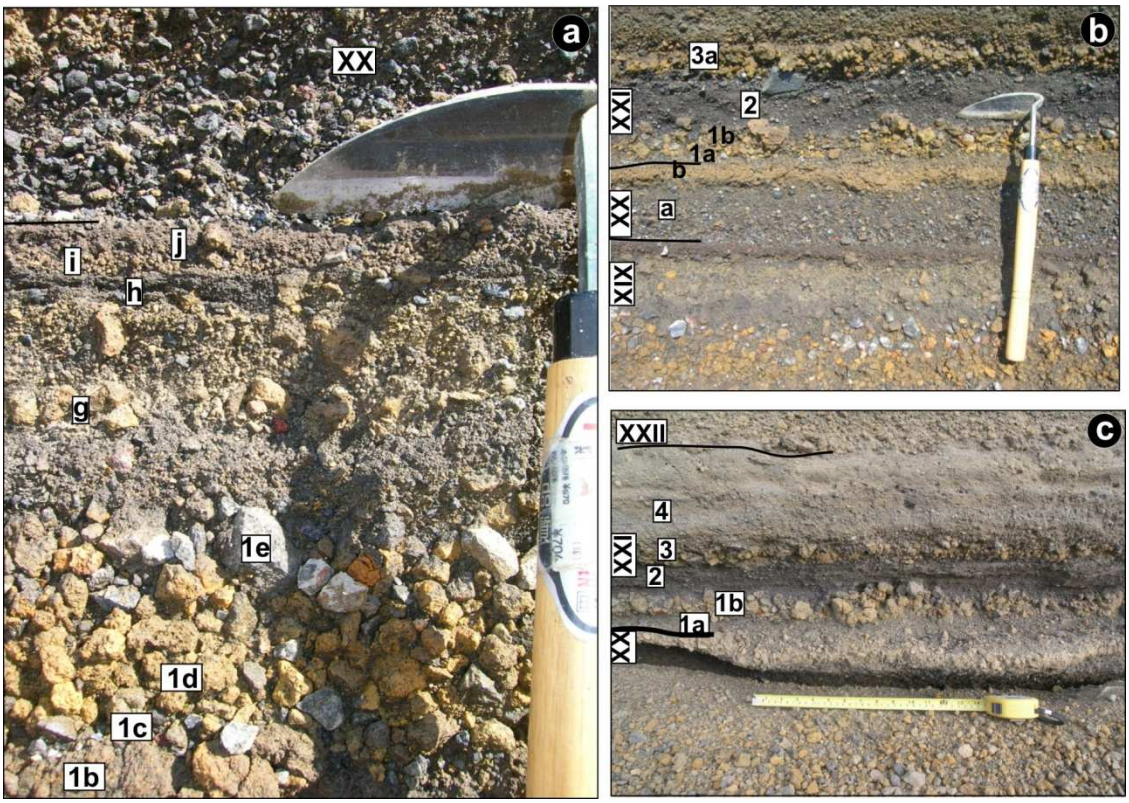

Figure 3.11 Deposits signalling the beginning of the Tukino Eruptive Period: **a)** zoom in eruptive unit XIX. **b** and **c** show the overlying units XX and XXI, with the distinctive dark grey, dilute lahar depositional facies.

Interpretation: Unit XIX began with two short-lived, high eruptive columns, producing coarse pumice lapilli fallout and cauliflower bombs (XIX-1b and 1d). The dominantly brown, coarsely vesicular, phenocryst-poor scoreaceous juvenile fragments contrast to previously erupted highly and finely vesicular, frothy pumice. Subsequently the eruptive style changed, to lower magnitude events, probably involving phreatomagmatic phases. This is evidenced by the small-scale, thin, fine-grained, yellowish, pumice rich, black-lithic rich, and purplish brown vesicular laminated ash above. Post-eruptive fluvial activity is recorded by the matrix-supported, cross-bedded heterolithologic deposits on several locations around the ring plain. The ~17 ka BP cal., Rotoaira Lapilli (Topping 1973; Shane et al., 2008), from Mt. Tongariro, is interbedded within units XVIII to XIX on the NNE slopes of Mt. Ruapehu, and completely replaces XIX north of the Waipakihi road and along the Lake Rotoaira road (SH46). It represents the youngest of the three known major eruptive episodes sourced at Mt. Tongariro between 26 and 12 ka BP cal. (Shane et al., 2008).

Unit XX represents increasing eruptive intensity and the accumulation of hyperconcentrated flows along several distributaries on the eastern and southern ring plain. Unit XXI signals a return to the eruptive conditions existing in unit XIX, with the generation of high but short-lived eruptive columns involving significant conduit erosion, with probable inflow of groundwater, as inferred from the abundance of hydrothermally altered lithics and interbedded, lithic rich, fine-grained, black blocky-ash fallouts. Afterwards, successive accumulation of syn-eruptive lahars (fine grained facies) and compacted, loamy loess suggest the cessation of the eruptive activity.

The last eruptive event within the Tukino eruptive period is marked by the clast-supported, pale brown, pumice lapilli bed of unit XXII (**Fig. 3.9; Appendix A**), which is very similar to units XI, XII, and XVI.

Karioi Eruptive Period

This period produced four widely distributed eruptive units (XXIII to XXVI), which are unique in the sequence examined (**Appendix A**). They are characterised by the distinctive strongly coloured, iron-stained orange lapilli beds that are rich in a variety of coloured lithics including a variety of hydrothermally altered, aphanitic to porphyritic variants (**Figs. 3.1, 3.2a, and 3.12a, b**). Pumice clasts show dark brown interiors, are usually very finely vesicular to dense and phenocryst-poor (Pl > Px vs. Px > Pl in previous units). Each coarse lapilli bed is commonly preceded by olive grey, pale yellow or red, thin, laminated, fine platy-shaped ash beds, some containing accretionary lapilli (**Fig.3.12; Appendix A**).

Bread-crust bombs are present within units XXIII, XXV and XXVI as far as 9 km from the vent. Unit XXIV is less prominent, relatively finer grained, well bedded and commonly eroded. The silty-sand, firm deposit separating units XXV and XXVI contains the regionally distributed, 13,635 ± 165 cal years BP rhyolitic Waiohau Tephra.

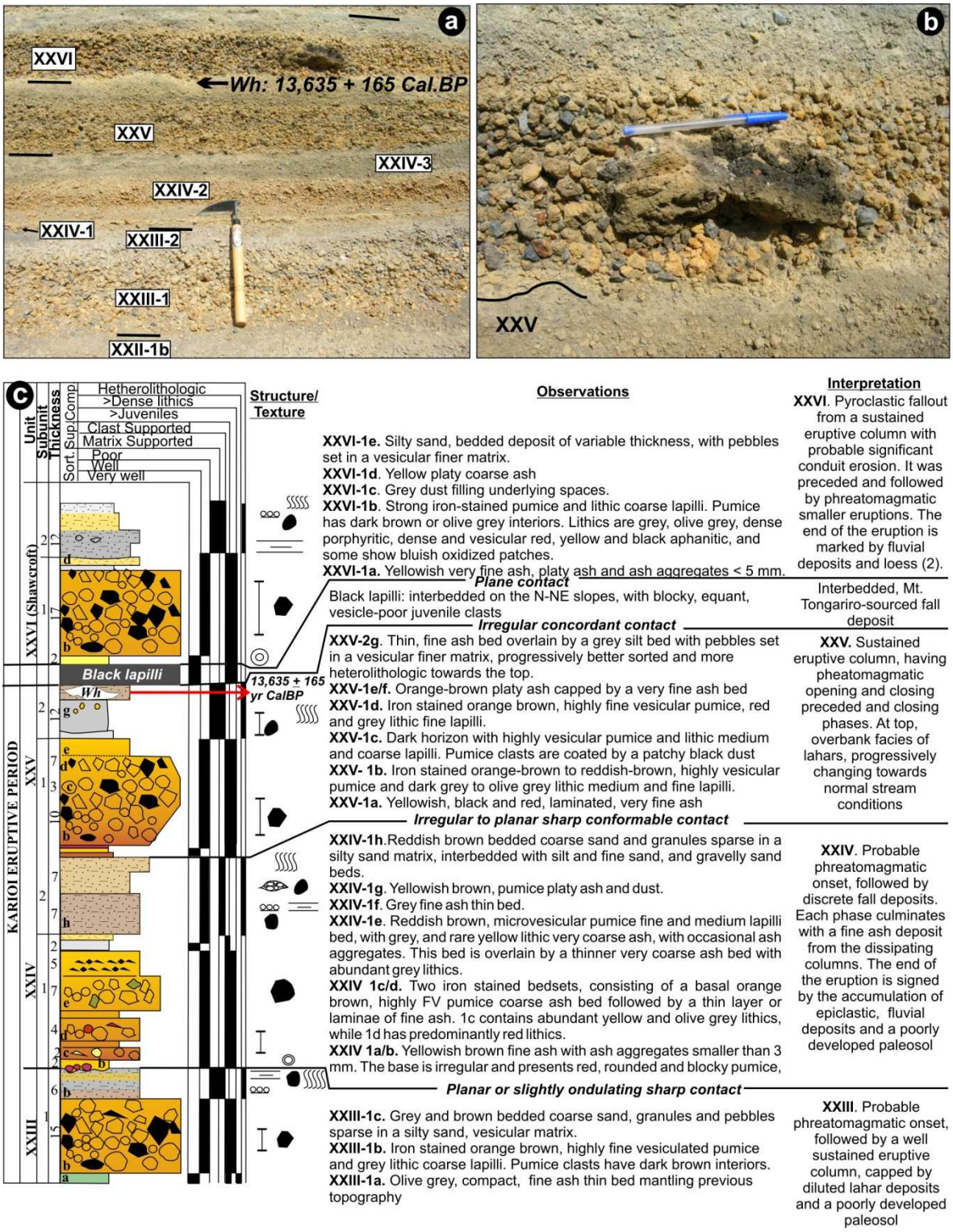

Figure 3.12 a) Eruptive units grouped within the Karioi Eruptive Period (XXIII to XXVI) highly distinctive in their high lithic content and lithic type variability; **b)** zoom into the Shawcroft lapilli (Plinian phase of eruptive unit XXVI), presenting bread-crust bombs of ~30 cm in diameter 10 km downwind the main SE depositional lobe; **c)** detailed stratigraphic profile of the eruptive units XXIII to XXVI comprising deposits of the *Karioi Eruptive Period*.

Interpretation: these units reflect fall deposition from high and sustained eruptive columns (except for unit XXIV, which may reflect more pulsating conditions), accompanied by significant conduit abrasion as evidenced by the high lithic content and variability (**Table 3.1**). The primary deposits suggest a general SE dispersal axis and a minor NE lobe, and are overlapped by inter-eruptive lahar deposits grading upward into dilute stream-flow deposits beneath loess. The main lapilli fall units XXIII, XXIV, and XXV are tentatively correlated with Donoghue's (1991) L13, L14, and L15 tephras, while the lapilli bed within eruptive unit XXVI corresponds to her "Shawcroft Lapilli".

On the NE slopes of Mt. Ruapehu, a distinctively clast-supported, massive, well sorted, black dense lapilli deposit is interbedded between the Waiohau Tephra and the Shawcroft lapilli (**Appendix A**); it rapidly decreases in grain size and thickness south-eastwards. It is preliminarily interpreted as evidence of a previously unknown event of large-scale explosive volcanism at Mt. Tongariro, between the ~17 ka BP cal., Rotoaira Lapilli and the ~11 ka BP cal., Pahoka-Mangamate sequence defined by Nakagawa et al. (1998), and Shane et al. (2008).

Ohinewairua Eruptive Period

This period produced three eruptive units (XXVII to XXIX) as far as 72 km SE of the volcano, which are widespread and distinctive.

Units XXVII, XXVIII, and XXIX: these are well bedded units (**Figs. 3.1, 3.3c, 3.13, Appendix A**), contrasting with underlying dominantly massive or thickly bedded units. Each unit consists of three to four clast supported, coarse pumice lapilli beds (<20 cm), usually bounded by firm, thin fine ash beds of constant thickness containing accretionary lapilli, and by loose, matrix-supported, well-sorted, heterolithologic sand deposits with local cross-bedding, erosive basal contacts, and clast-supported lenses. Each eruptive unit is capped by a firm, silty-sand paleosol. Pumice clasts are pale brown, coarse and porphyritic, varying from dense to coarsely vesicular, some fibrous and colour-banded fabrics (**Table 3.1**), with 15-20 % of black pyroxene phenocrysts (2-7 mm). Single subunits are distinctive in lithic content and lithic variability, varying

from monolithologic beds with olive grey porphyritic lithics to beds containing multicoloured, hydrothermally altered lithics. The distribution of the deposits suggests a main ESE dispersal axis, with a minor secondary lobe towards the ENE (**Chapter 4**).

Laterally, and along the Upper Waikato stream (**Fig. 1.2**), some of the clast-supported lapilli beds are completely replaced by massive, matrix-supported, poorly sorted beds, showing abrupt thickness variation: they contain rounded dark brown coarse pumice lapilli and volcanic lithic blocks of different colours and porphyritic textures, set in a fine ash pumice-crystal matrix (XXVII beds in **Figs. 3.13d, e; Appendix A**).

Unit XXVIII is well exposed in proximal locations, but the primary deposits are commonly replaced by deposits of streams and diluted lahars in medial and distal sites. It is distinguished by the uppermost mantling, firm, yellowish-grey, thinly laminated bed (<10 cm), which corresponds to the M1 marker identified by Donoghue et al. (1995b): it consists of alternating pumice-rich and lithic-rich, platy ash thin beds and laminae, some containing accretionary lapilli, which are very similar to the typical Holocene deposits of Mt. Ruapehu. Juvenile clasts are distinctively poorly vesicular and block-shaped.

Unit XXIX (**Figs. 3.1, 3.3c, 3.13**) is distinguished by its stratigraphic position above the M1 marker, and the abundance of hydrothermally altered, yellowish to orange, porphyritic to aphanitic lithics within the lowermost, coarse lapilli bed (XXIX-1a).

Interpretation: Units XXVII to XXIX suggest pulsating and unsteady eruptive columns, with opening and closing phases producing the thin, accretionary lapilli-rich, platy ash beds. The lateral variation into matrix-supported facies of variable thickness and restricted distribution indicate partial collapse of the unsteady eruptive columns and the generation of pyroclastic density currents.

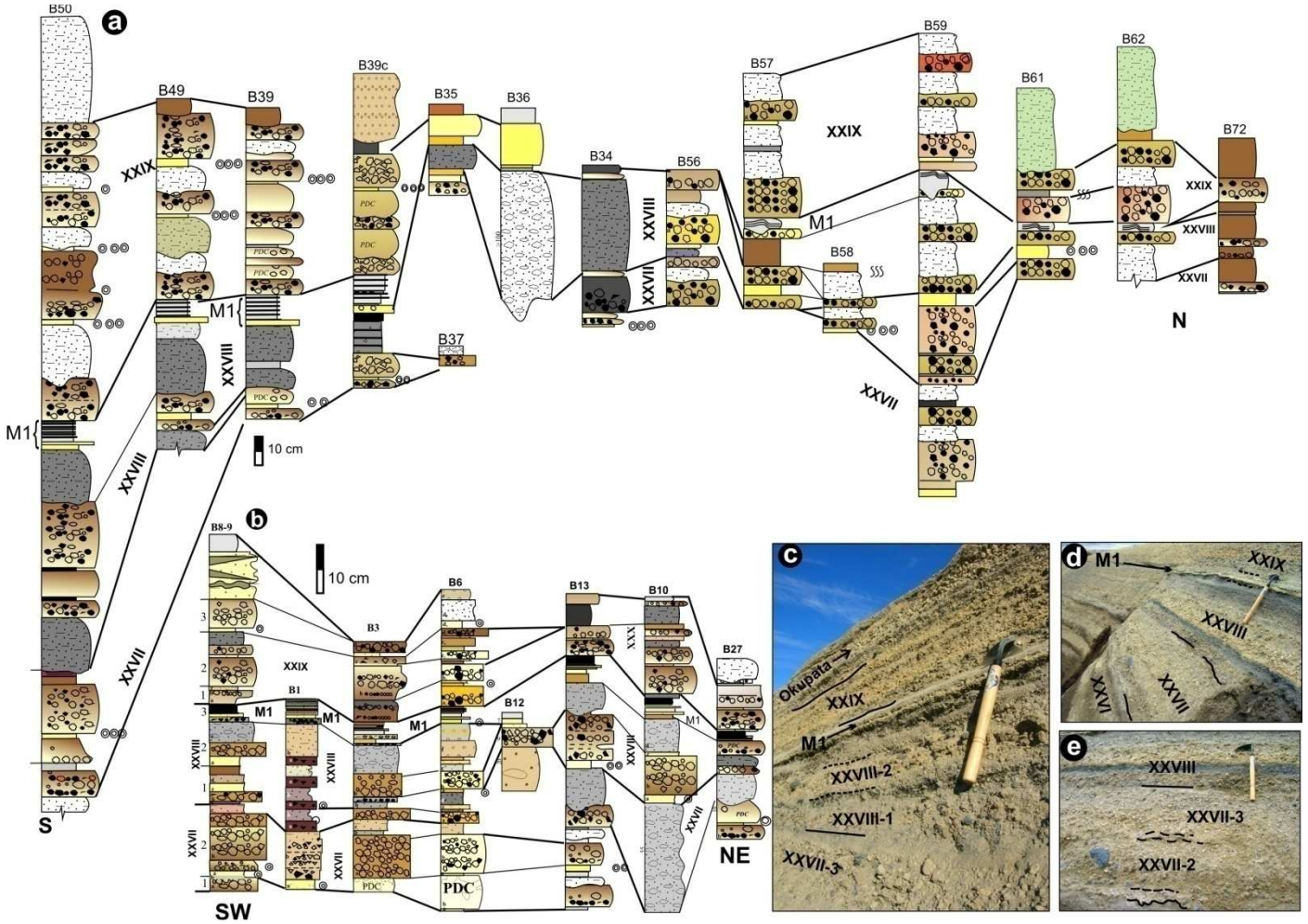

Figure 3.13 a-b) Stratigraphic correlation of units XXVII to XXIX, characterized by well bedded deposits shown in **c**-to-**e; e)** Matrix supported facies of unit XXVII, interpreted as resulting from pyroclastic density currents.

PDC deposits within unit XXVII, here named **Oruamatua Eruptive Unit**, were mainly found along the Upper Waikato drainage (<20 cm thick) down to 10 km from North Crater (locations B3, B6, **Appendix A**); thin (10 cm), veneer deposits were also locally found as far as 15 km east (location B27, **Appendix A**) and 10 km northeast (location B39, **Appendix A**) from the vent. PDC deposits within unit XXIX, here named **Akurangi Eruptive Unit**, are exposed along the Mangatoetoenui Stream, as far as 8 km from North Crater (location 39, **Appendix A**). There, up to five PDC units <11 cm were distinguished (**Appendix A**). Exposures located at 11 km (location B36) from the vent along this catchment already show lahar deposits (i.e. hyperconcentrated flows) in the same stratigraphic position. Thin (<10 cm) veneer deposits were found along the Upper Waikato Stream as far as 10 km (location B3).

Although a specific study on the PDC deposits is needed, the current knowledge indicates that channels flowing parallel and close to the current Upper Waikato Stream were the main flow paths during the Oruamatua eruption, with some outflows towards the Mangatoetoenui stream. PDC produced during the Akurangi eruption mainly flowed along channels parallel and close to the current Mangatoetoenui stream with some outflows towards the Upper Waikato stream. Minimum PDC run out distances were between 10-15 km east and northeast from the vent, and hyperconcentrated flow deposits predominate at greater distances.

Syn-eruptive and inter-eruptive dilute lahars are represented by the heterolithologic deposits interbedded with or completely replacing the pyroclastic beds.

The M1 marker (**Appendix A**) within this sequence indicates a contrasting eruptive style, comparable to those that have dominated the most recent history of Mt. Ruapehu (e.g., 1995/96 events; Cronin et al., 2003).

Taurewa Eruptive Period

This period groups four eruptive units and it corresponds to a correction and re-definition of the "Taurewa Eruptive Episode" defined by Donoghue et al. (1999). It includes the Okupata Tephra (Topping 1973) and coeval PDC deposits referred as the

"Pourahu" pyroclastic flow by Donoghue (1995a, b), as well as the overlying Ngamatea-1 and Ngamatea-2 fall units defined by Donoghue (1991).

White Lapilli Eruptive Unit (XXX): the most complete outcrop for this unit occurs in the Tukino ski field area (**Fig. 1.2**), overlying the uppermost dark grey hyperconcentrated flow deposit culminating unit XXIX (i.e. Akurangi eruptive unit). Three subunits can be distinguished (**Fig. 3.14**), the lowermost two only exposed at proximal sites (location B55, **Appendix A**). The uppermost subunit (XXX-3) is widely distributed, and distinguished by a thin (<7-10 cm), bright-white, clast-supported, massive pumice lapilli, with abundant, hydrothermally altered lithics. At most localities on the ring plain and east of Ruapehu, this bed directly overlies a paleosol developed above unit XXIX and is commonly overlain by a dark-grey to brownish-grey, matrix-supported, poorly sorted, normally graded silty sand, with scattered sub-rounded pebbles and granules set and locally aligned in a vesicular silty-sand matrix. Laterally and longitudinally this heterolithologic sand deposit shows a basal erosive contact onto the white lapilli bed and shows variations from weak bedding to well-developed cross-bedding structures, grading up into partially indurated greasy silt.

Interpretation: this unit shows evidence for discrete eruptive phases (**Fig. 3.14**), beginning with a short-lived eruptive column producing the first lapilli fall subunit (XXX-1), followed by pyroclastic surges (XXX-2) and a main, sustained eruptive column, represented by the thickest and coarsest-grained, widely distributed uppermost white lapilli fallout (XXX-3). Pyroclastic surge deposits were only found at a distance $\leq$5 km from South Crater. The white lapilli bed is easily recognized on the central-southern ring plain by its colour and stratigraphic position, and consequently is a helpful local marker. A significant time break after the accumulation of unit XXX is evidenced by a relatively thick (~20 cm), pale brown to pale grey paleosol (**Fig. 3.14a**).

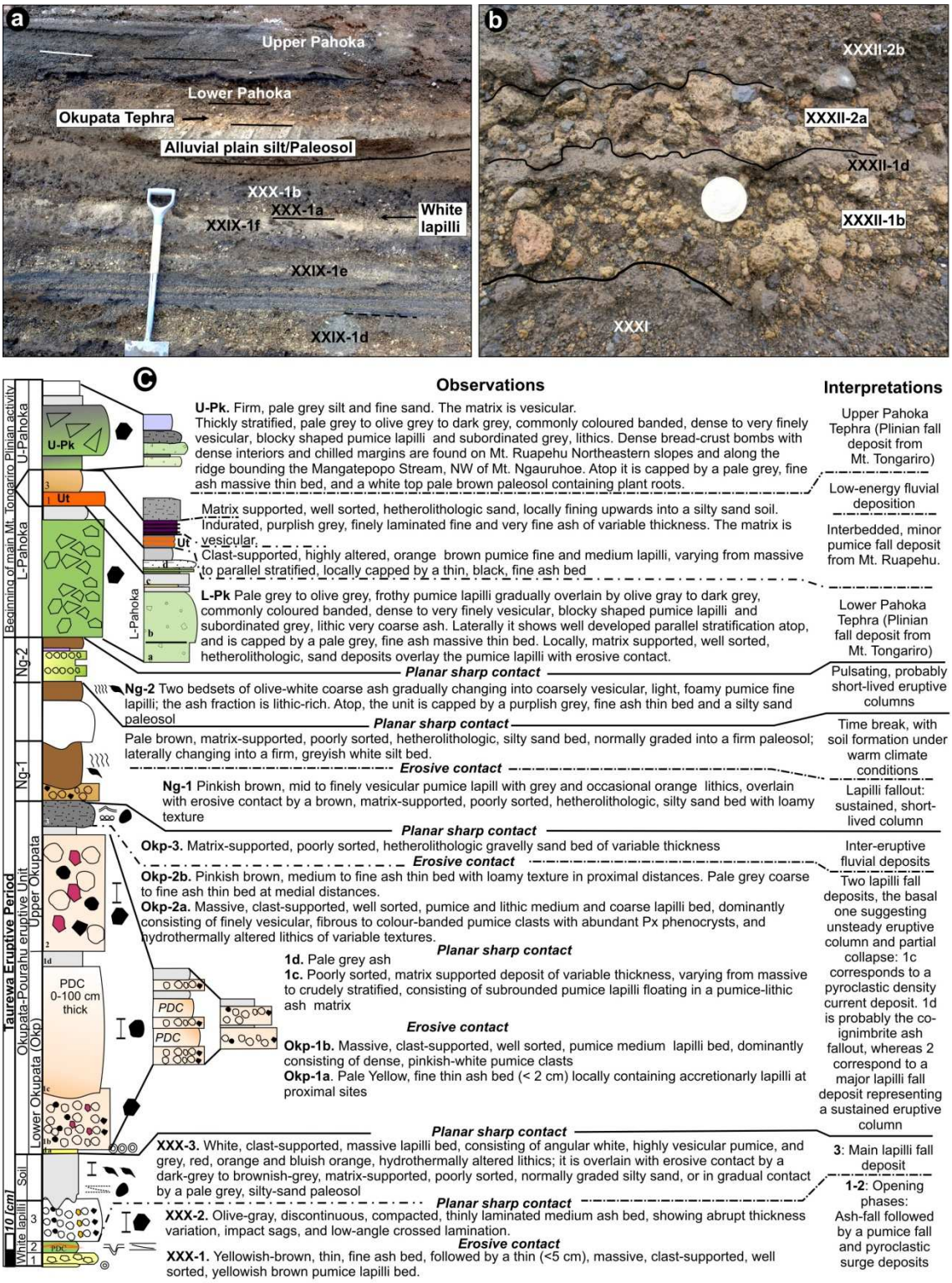

Figure 3.14 a) Uppermost part of the studied stratigraphic record, showing the distinctive white lapilli fallout bed of unit XXX and the widely distributed Okupata Tephra (zoomed in **b)**, both formed during the Taurewa Eruptive period; **c)** general stratigraphic profile showing the youngest studied eruptive units (XXX-XXXII) of Ruapehu covered by the Mt. Tongariro sourced Pahoka Tephra. The pyroclastic density current deposits (PDC) of the unit XXXI corresponds to the Pourahu pyroclastic flow of Donoghue et al. (1995a).

Okupata-Pourahu Eruptive Unit (XXXI): this unit (**Fig.3.3d, 3.14, Appendix A**) is one of the best regional markers due to its wide distribution, pinkish-white pumice clasts, and stratigraphic position. The most complete profiles are at proximal locations (locations B39, B49, B50; **Appendix A**), beginning with a locally exposed thin fine-ash bed containing accretionary lapilli, overlain by two distinctive, pale brown, massive, clast-supported, well sorted, medium and coarse pumice lapilli beds, each one mantled by a thin greyish brown, fine ash. The pumice clasts are coarsely-porphyritic, pinkish white to pinkish grey, showing a distinctive fibrous fabric varying from finely to coarsely vesicular, and a mottled appearance given by ~20-25 % of black pyroxene phenocrysts (**Table 3.1**). Finely vesicular to dense, brown and bluish grey, finely porphyritic and colour-banded pumice lapilli are also common, as well as accidental, orange and red, hydrothermally altered lithic clasts.

A poorly sorted, matrix-supported deposit varying in thickness, and interfingered between the clast-supported beds was locally found long the Whangaehu valley (Location B55), as reported by Donoghue et al. (1995a, b, 1999); it reaches 30-60 cm on the eastern slopes below the Round the Mountain track (locations B39, B49; **Figs. 3.15a-c**), and along the Mangatoetoenui stream, found as thin beds (<6 cm) as far as 20 km from South Crater (location B72; **Fig. 3.15d**). It consists of sub-rounded pumice lapilli chaotically distributed in a finer matrix, decreasing in grain size and increasing in matrix proportions with distance.

The pyroclastic deposits are overlain through a sharp and locally erosive contact by a dark grey fluvial sand deposit and a firm, pinkish brown, loamy soil containing plant roots. At distal locations both clast-supported beds merge into one and the capping soil is distinctively dark brown, consistently containing abundant plant roots.

Interpretation: at the studied locations, the lithofacies indicate at least two phases of pyroclastic fall deposition. Partial or complete column collapse, inferred from the interfingered matrix-supported pumice deposit, generated pyroclastic density currents related to the first fall bed. A sustained column is represented by the second, thick and lithic-rich fall deposit. The end of the eruptive activity is marked by fluvial deposits and a soil.

The whole unit is condensed distally into a single clast-supported bed, reported by other authors as the Okupata Tephra (11,620 ± 190 cal years BP; Topping 1973; Donoghue et

al., 1995b, 1999; Donoghue and Neall 2001; Lowe et al., 2008), and marks the establishment of a vegetation similar to current plant communities, suggesting the onset of early Holocene warmth in central North Island (Newnham and Lowe 2000; Lowe et al., 2008).

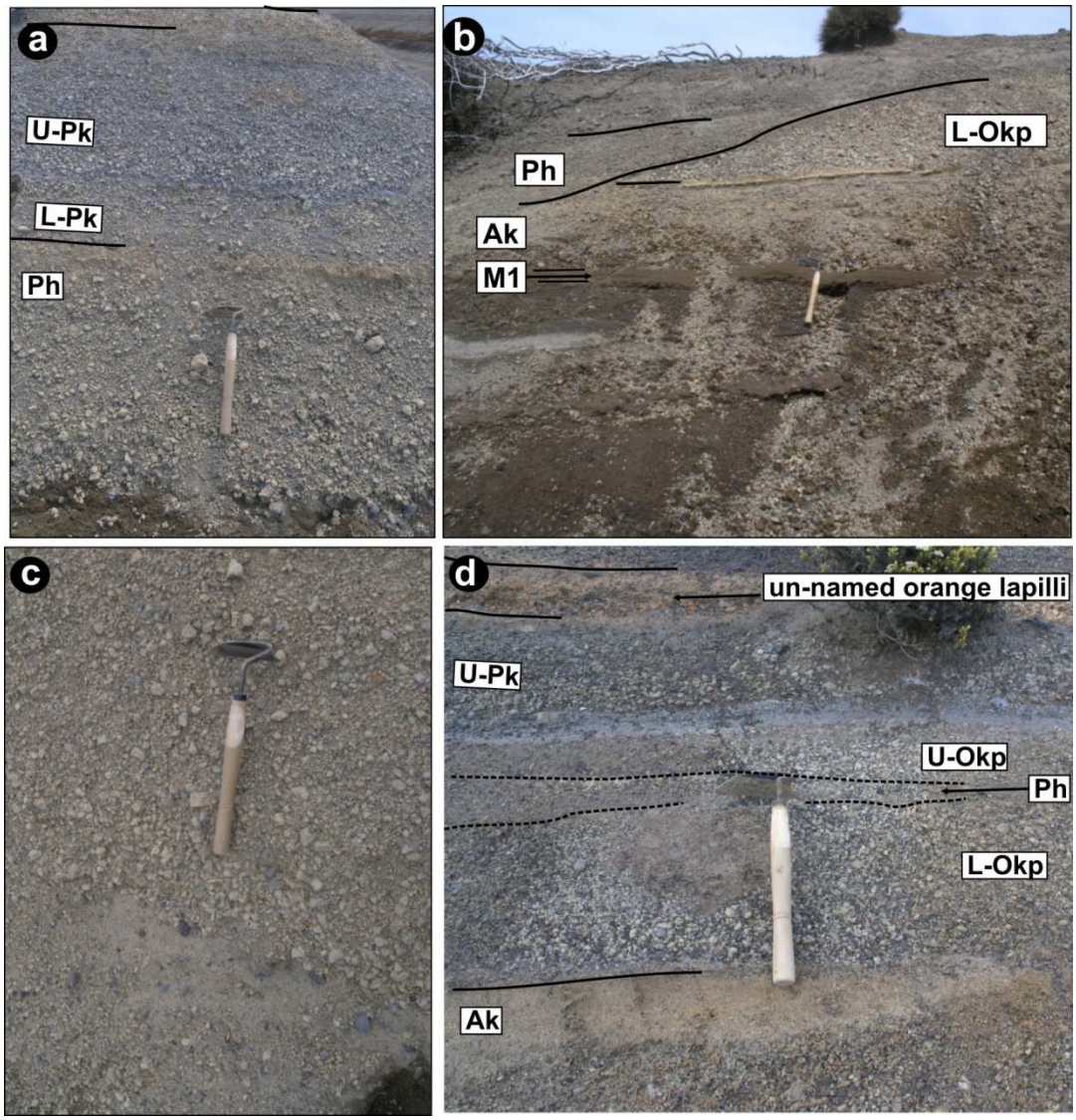

Figure 3.15 Pyroclastic density current (PDC) deposits within the Okupata-Pourahu eruptive unit (Okp-Ph), characterised by poorly sorted **(a)**, channel-infilling **(b)**, matrix-supported pumice lapilli and blocks **(c)** facies, varying in thickness with distance **(d)**.

Donoghue et al., (1999) identified the pyroclastic density current facies of this unit and referred to it as the "Pourahu Member", whereas they restricted the term "Okupata Member" to the fall deposits. The name Okupata-Pourahu is here given to the eruptive unit comprising two major fallouts separated by a pyroclastic flow deposit and/or its "co-ignimbrite" ash (**Fig. 3.14b**). The more restricted distribution and significantly

thinner deposits compared to units XXVII and XXIX suggest that it was not the largest eruption produced by Mt. Ruapehu in the Late Pleistocene (**Chapter 4**).

Afterwards, progressively thinner, finer grained lapilli deposits, separated by progressively thicker paleosols were formed, corresponding to the **Ngamatea lapilli** 1 and **2** units (Donoghue et al., 1995a, b). Thin (<10 cm), unnamed, orange lapilli beds similar to the typical fallouts of Bullot Fm. are found interbedded with (**Fig. 3.14a**) and also overlying (**Fig. 3.15a, b**) the Mt. Tongariro sourced Pahoka Tephra. After the Okp-Ph unit, subsequent Plinian-subplinian events occurring at the Tongariro Volcanic Centre were dominantly generated by Mt. Tongariro, while Mt. Ruapehu underwent a drop of several orders of magnitude in the volume of its eruptions and its dominant eruptive style became more phreatomagmatic, producing smaller eruptions similar to the observed 1995-1996 events (Donoghue et al., 1995b; Donoghue and Neall 2001; Cronin et al., 2003).

3.2.5 Physical volcanology implications: towards an understanding of Subplinian-Plinian eruptions at Mt. Ruapehu

Lithofacies analysis

Considering the features described above, the main distinguishing field criteria for correlating Mt. Ruapehu fall beds (**Fig. 3.16**) are: 1) bed colour, 2) pumice textures (including size, shape, dominant vesicle sizes and fabric, phenocrysts content, size and fabric), 3) lithic content and lithic types, and 4) bed structure (massive, bedded, graded). Integration of the regional rhyolitic stratigraphic markers is fundamental to cross-check correlations.

Based on the same field criteria, three contrasting lithofacies associations were recognized: **1)** thickly bedded eruptive units, comprising multiple massive to normally graded, yellowish brown, pumice-dominated lapilli beds. Some of them contain a basal, monolithologic horizon consisting of angular, coarsely porphyritic fresh lithics or angular to rounded dense pumice clasts. Juvenile pumice clasts in the thickest, coarsest, and most widespread beds representing the main eruptive phases (Plinian-subplinian)

vary in the same stratigraphic level from finely vesicular, foamy-like pumices to coarsely vesicular, foliated and rare expanded fabrics (**Table 3.1**). Pumice clasts contain 2 to 11 % of large (1-5 mm) clinopyroxene, orthopyroxene, and plagioclase phenocrysts and glomerocrysts. Lithic content is the lowest of all lithofacies (<7 %). In proximal to medial locations (as far as 9 km from the vent, along the dispersal axis), 30 cm-sized bread-crust bombs are common. The best examples are the Hokey Pokey, IX (i.e. **Mangatoetoenui**), upper XVIII, and XXIV eruptive units.

2) Eruptive units containing one or a few, distinctively lithic-rich, massive beds with 30-35 % of multicoloured, hydrothermally altered, aphanitic to finely porphyritic lithic clasts, and up to 5 % of accidental, metasedimentary clasts from the Tertiary "basement". Crude stratification develops across the deposit, particularly away from the dispersal axis. The coarsest and thickest beds are usually underlain by a thin, massive or laminated red, yellowish, purplish or olive grey, platy-shaped coarse ash to fine ash bed, occasionally containing accretionary lapilli. Lithofacies association 2 is further subdivided into two categories. In **2A** units the coarsest bed reaches 25 to 30 cm of thickness at medial distances and pumice fragments are usually iron-stained with dark brown interiors and are typically dense to very finely vesicular (**Table 3.1**). Most of the pumice clasts have subspherical to ellipsoidal, oriented and aligned vesicles smaller than 0.5 mm, and variable amounts (<8 %) of fine-sized (<1 mm) phenocrysts and glomerocrysts (Pl>Px). Bomb-sized clasts show bread-crust textures and are found as far as 13 km along the dispersal axis. Eruptive units XXIII, XXV, and XXVI (i.e **Shawcroft**) are good examples of this category. Within the **2B** category the main (i.e. coarsest and thickest) bed is half the thickness of those in the 2A type. Juvenile clasts are commonly fresh, dark brown, very coarsely vesicular, expanded to strongly foliated, and phenocryst-poor, whereas bomb-sized clasts show cauliflower structures, and are mainly restricted to proximal sites. 2B is also characterized by the presence of thin, interbedded, dark grey to black, blocky coarse ash, lithic-rich laminated beds. Units XIX and XXI are examples of this category.

3) Well bedded eruptive units, comprising multiple, thinly stratified, pale-brown to white pumice lapilli beds with variable lithic content (10-25 %). Clast-supported pyroclastic deposits mantling previous paleotopography are laterally interfingered with matrix-supported, paleotopography-controlled pyroclastic deposits. The coarsest and thickest clast-supported beds are usually underlain and capped by thinner (<5 cm) fine

ash, mantling beds containing accretionary lapilli. Relatively lithic-rich beds contain fine to coarse porphyritic lithics, variable in colour, texture, and hydrothermal alteration. Pumice clasts are highly heterogeneous within a single stratigraphic level, and distinct from other lithofacies associations: textural end-members include dense, pale brown pumice with ~20 % of microphenocryst-smaller than 1 mm, pinkish-white finely vesicular with ~20 % phenocrysts smaller than 0.5 mm, and colour-banded, coarse-porphyritic, finely to coarsely vesicular, fibrous pumice with strongly distorted vesicles and black pyroxene phenocrysts between 2 and 7 mm. The best examples correspond to the tephras produced during XXVII, XXVIII, XXIX, and the youngest Okupata-Pourahu eruptive units. Unit XVIII is the only case of this type older than 13,635 ± 165 cal years BP (i.e., Waiohau Tephra).

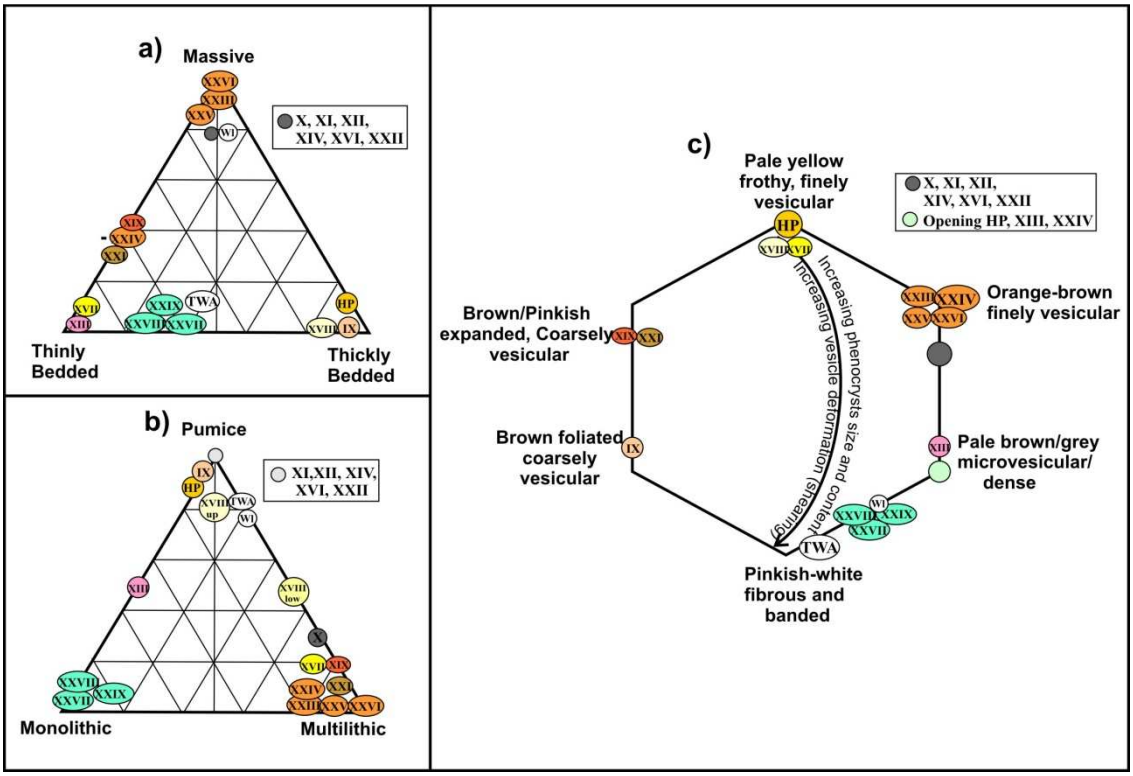

Figure 3.16 Classification diagrams of the studied Mt. Ruapehu units, based on key field criteria for lithofacies correlation: **a)** bed structure; **b)** dominant component; **c)** pumice colour, directly linked to pumice textures as shown.

From lithofacies to preliminary eruptive dynamics

Massive, ungraded beds, such as those represented by lithofacies association 1 and 2 have been commonly interpreted as the result of continuous magma discharge driving steady (non collapsing) convective columns (c.f., Cioni et al., 2003). The grading within

unit IX mantling lapilli beds records progressive changes in column height, then waning and final dissipation with ash deposition. The main difference between lithofacies association type 1 and type 2 is the lithic content and composition, with relatively larger lithic grain sizes and deposit density at a fixed locality for lithofacies association type 2. The lithic-poor lithofacies association type 1 suggests open/clear conduit conditions during the main eruptive phases, whereas the lithic-rich and lithic-bearing nature of lithofacies association type 2 reflects conduit obstructions, development of new conduits, or important constraints on conduit geometry, such as intense conduit wall abrasion during high magma ascent and discharge rates, vent migration (e.g., Wilson et al., 1980; Macedonio et al., 1994; Papale et al., 1998; Taddeucci and Wohletz 2001), and/or conduit implosion (e.g., Kennedy et al., 2005). On the other hand, distinctive stratification marked by contrasting grain sizes and depositional processes (e.g., interlayering of ash-fall and pyroclastic density current deposits), typical of lithofacies association type 3, has been documented as related to unsteadiness in the magma discharge and oscillating convective columns (Sieh and Bursik 1986; Bursik 1993; Cioni et al., 2000, 2003). The characteristically colour-banded pumice clasts, the presence of larger and more abundant phenocrysts, and the occurrence of dense, plate-like (c.f., Palladino et al., 2008) pumice clasts suggest contrasting probable degassing mechanisms from the other lithofacies associations, which will be discussed later in **Chapter 6**.

Considering the entire composite stratigraphic section reconstructed for the first 20 km along the dispersal axis from Mt. Ruapehu, 66 % of individual tephras from the 27-10 ka BP cal., period contain lapilli-sized particles (the remainder are ash-grade). Most (46 %) of the pumice lapilli-rich pyroclastic beds are 5-10 cm thick and contain a variable amount of dense juvenile porphyritic clasts, suggesting violent but short-lived eruptions. Around 29 % of the beds are <5 cm thick, and contain abundant accretionary lapilli (15 %), and either represent relatively smaller phreatomagmatic eruptions, or eruptions during rain/cloudy periods. A minority (6 %) comprise aligned lithic or altered microvesicular pumice lapilli, suggesting explosive phases during which the vent/upper conduit was obstructed by a porphyritic, degassed magma plug. These thin beds typically represent the opening phases of major subplinian-Plinian eruptive events, which produced 20 % of the studied tephra record. If we only consider the largest explosive phases, 58 % of them suggest dominantly dry eruptions leading to sustained

eruptive columns, 26 % involved unsteady, collapsing columns dominantly preceded and followed by smaller phreatomagmatic phases; whereas 16 %, also combined with phreatomagmatic or ash-producing intervening phases, are particularly lithic-rich and suggest sustained columns (**Table 3.2**).

Table 3.2 Synthesis of the general characteristics of the different lapilli and ash fall beds found in the studied stratigraphic record.

Lapilli dominated beds	**> 10 cm, usually < 50 cm**	**Sustained lithic rich**	3	Separating the domain of sustained columns (mainly dry, showing lithofacies association 1) and a domain of collapsing columns combined with phreatomagmatic smaller eruptions (lithofacies association 3)
		Collapsing columns	5	Following and preceding accretionary lapilli or fine phreatomagmatic ash thin beds. Main phases showing lithofacies association 3, more frequent at top of the stratigraphic record
		Sustained lithic-poor	11	Following and preceding conduit/vent plugs. Main phases of lithofacies association 1, dominant in the oldest eruptions
		Short-lived lithic rich	10	Individual phases, particularly at the beginning or at the end of lithofacies associations 1 and 3, bounded/combined with thick phreatomagmatic sequences separating the older domains of lithofacies associations 1 and the younger domain of lithofacies association 2
	<10 cm beds	**Short-lived lithic poor**	34	Phases within lithofacies associations 1 or 3,or isolated beds, non related to any particular trend
		Laminated ash: alternating dry/wet phreatomag -matic	12	After removal of plug and main phase of eruptive units characterized by lithofacies association 1; or isolated eruptions after major conduit geometry modifications (XIX, XXVII, XXVIII; XXIX,) and before or immediately opening a lithic-rich lapilli bed of lithofacies association 2 (XXV)
Ash dominated beds	**Few mm to 5 cm thick laminae/beds**	**Purplish to olive grey fine ash/dust**	5	Opening and closing short lithofacies association 2 (XXI, XVII, XXIII). Probably phreatomagmatic
		Accretionar y lapilli and ash aggregates bearing thin ash beds	9	Opening phases of lithofacies associations 2 and 3; can be linked to the main eruptive phase or isolated, preceding the main phase
		Fresh, highly vesicular	35	Eruptive columns waxing/ waning
		(monolitho-logic): Dome/ Upper conduit	2	Opening phases of lithofacies association1
		Altered/ dense (recycled?) pumice	4	Opening phases of lithofacies association 1 (rare 3); can be followed by phreatomagmatic ashes before the main eruptive phase

Numbers correspond to the total of individual beds of that particular type found in the record, between 4 and 80 km from the source.

In terms of timing, 36 % of the largest explosive eruptions are represented by lithofacies association type 1, in the older part of the record, while another 36 % contributed to lithofacies association type 3 in the younger part of the record. Deposits of these extremely explosive phases are separated by deposits dominated by lithofacies association type 2 within the intermediate part of the record (**Table 3.2**).

3.2.6 Discussion

When the entire stratigraphic record is qualitatively visualized in terms of inferred relative eruptive behaviour/style with time (**Fig. 3.17**), a transition from older (immediately below and above the Okareka Tephra) explosive eruptions characterized by steady eruptive columns to younger events (post Waiohau Tephra) characterized by unsteady, partially collapsing columns can be seen. The two periods were separated by an interval (between 17,625 ± 425 cal years BP and shortly after 13,635 ± 165 cal years BP), during which eruptive columns were steady, but extremely violent (high) and involved large proportions of country rock fragments (increasing in unit XVII, reaching a maximum in units XXIII-to-XXVI, and decreasing afterwards). These changes are also signalled by a variation in the dominant pumice macro-texture within the coarsest, thickest, and most widespread deposit of each eruptive unit. Older deposits are dominated by highly vesicular pumices varying from foamy (subspherical vesicles) to fluidal (oriented oblate-ellipsoidal vesicles), whereas younger deposits are dominated by coarse-grained porphyritic extremely heterogeneous pumice fabrics, including colour-banded and dense varieties. In between, the lithic-rich deposits are dominated by micro-porphyritic, dense to micro-vesicular pumice clasts (**Table 3.1; Fig. 3.16**).

Microscopic and geochemical analyses of pumice clasts will be presented in **Chapters 5-7**, but it is possible from field lithofacies analysis to propose an initial hypothesis. The observations presented in this Chapter suggest that Mt. Ruapehu's eruptive behaviour has systematically changed since ~25ka. Initially, it was characterized by stable magma bodies being suddenly unloaded by the explosive removal of domes and/or degassed magma plugs, with expansion and formation of highly vesicular, foamy pumice clasts under dry conditions (e.g., Hokey Pokey lapilli). Along with the transition from the Last Glacial to the present interglacial, around 17,625 ± 425 cal years BP, magma-water

interaction was enhanced, which is probably related to aquifer recharge by increased precipitation and melt-water infiltration (e.g., XVII, increasing in XIX-XXI units).

Opening phreatomagmatic phases shortly preceded the climactic explosive events and/or alternated within major phases. Reductions in magma overpressure enhanced conduit wall collapses, promoting the incorporation of different types of lithics during the subsequent large-scale events. The high lithic variability and incorporation of metasedimentary clasts reflect probable fluctuation of the fragmentation level depth for lithofacies association 2. These conditions prevailed until sometime after 13,635 ± 165 cal years BP (the last event being the Shawcroft eruptive unit-XXVI). From this time until ~10 ka BP cal., the studied tephras indicate that melts were slightly more siliceous than in previous events (**Table 3.1**), with the generation of oscillating eruptive columns and pyroclastic density currents. The repose period between eruptive units increased with time, and paleosol development was progressively enhanced by the establishment of warm Holocene climatic conditions. The Okupata Tephra represents the last Plinian event known from Mt. Ruapehu (Donoghue et al., 1995b), immediately followed by dacitic domes and the collapse of the NW sector (~9 ka BP cal., Murimotu debris avalanche (Palmer and Neall 1989; McClelland and Erwin 2003). Since then, and clearly since ~3 ka BP cal., the eruptive activity has been centred in Crater Lake, being very different in magnitude and style, with small-scale, relatively more frequent phreatomagmatic eruptions and the accumulation of thin ash tephras (Donoghue 1991; Donoghue et al., 1997).

Although further, multidisciplinary research is needed, a tight correlation between eruptive magnitude and local tectonic activity might explain this abrupt change: Villamor et al., (2010) found a significant drop in the Rangipo fault-slip rate from 2-9 mm/yr to 0.2 mm/yr at ~14 ka BP cal., from paleoseismology data. Therefore, a pulsating rifting process (also suggested for Tongariro by Nairn et al., 1998), characterized by fast fault slip-rates at low recurrence intervals (large fault displacements for a short period), might have favoured the accommodation of large magma volumes under southern TVZ stratovolcanoes. The segmented nature of the Rangipo fault zone could explain the shift of large-scale volcanism towards the north, from Ruapehu to Tongariro, at around ~11 ka BP cal.

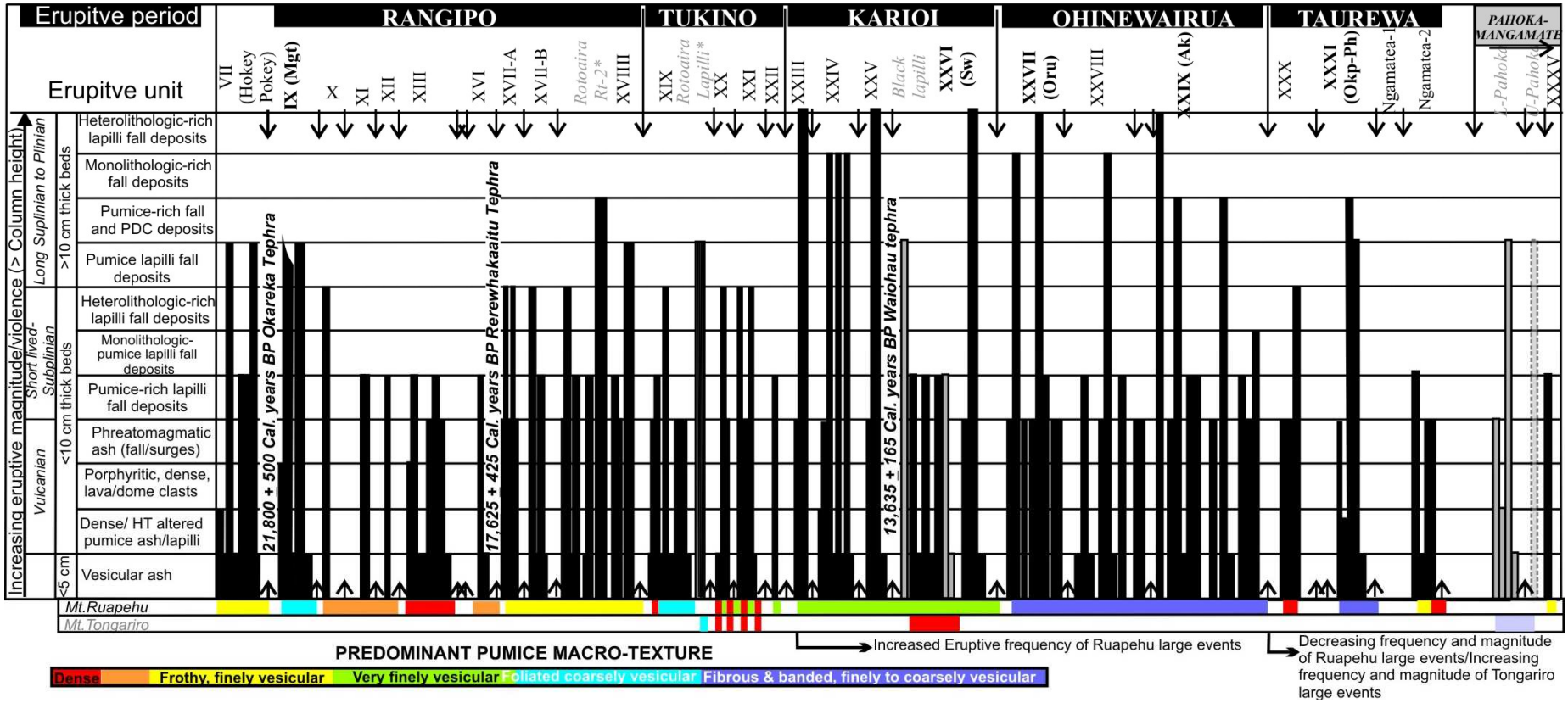

Figure 3.17 Schematic interpretation of the studied stratigraphic record, to visualize in a comparative way, the most plausible eruptive styles for Mt. Ruapehu's explosive activity between the time of accumulation of the Hokey Pokey lapilli (younger than 27,097 ± 957 cal years BP and older than 24,800 ± 500 cal years BP), and the 11,620 ± 190 cal years BP Okupata Tephra. The Plinian activity of Mt. Tongariro is firstly identified in the interbedded Rotoaira units (as identified by Shane et al., 2008), followed by the here named "black lapilli", and clearly beginning the series of major eruptions that produced the ~11 ka BP cal., Pahoka-Mangamate eruptive sequence (Narin et al., 1998). The newly defined eruptive units: Mangatoetoenui (Mgt), Shawcroft (Sw), Oruamatua (Oru), Akurangi (Ak), and Okupata-Pourahu (Okp-Ph) typically represent contrasting lithofacies associations and related eruption behaviour.

The examined record is consistent with the observations on subplinian and Plinian eruptions of calc-alkaline magmas at stratovolcanoes elsewhere, with eruption cycles typically culminating in dome emplacement episodes, and explosive conditions re-establishing after dome disruption phases, which are often marked by a basal, lithic-rich tephra horizon (e.g., Bursik 1993; Hammer et al., 1999; Wright et al., 2007). Similarly, opening and closing phreatomagmatic eruption phases, generating dilute pyroclastic density currents, are widely documented, such as the Mt. Pinatubo 1991 eruption, Philippines (Hammer et al., 1999), the 800 yr BP Quilotoa eruption, Ecuador (Rosi et al., 2004), the 79 AD Vesuvius eruption (Gurioli et al., 2005), the 10.5 ka Nevado de Toluca, México (Arce et al., 2003), or the 4965 yr BP Popocatépetl, México (Arana-Salinas et al., 2010). Hence, it seems that viscous disruptions of "rigid" bodies, such as domes or degassed magma plugs, or brittle disruptions caused by sudden magma-water interactions are efficient promoters of major explosive eruptive phases when sufficient volumes of volatile-saturated magmas are stalled in the mid to upper crust.

The quantification of the eruptive parameters, volumes, and column heights indicated by the contrasting lithofacies and the high pumice textural heterogeneity (**Chapter 4)** will help to elucidate eruption-controlling factors.

3.2.7 Conclusions

Examination of the stratigraphic record within the Bullot Formation of Mt. Ruapehu's largest explosive eruptions has helped to improve our understanding of the maximum probable eruptive scenarios expected from the Tongariro Volcanic Centre. The correlation of individual lapilli beds cropping out as far as 80 km from the current vent of Mt. Ruapehu allowed the identification of major lithofacies, and to define thirty three eruptive units produced during six eruptive periods. The oldest two of these are: 1) ~23,000 and 21,800 ± 500 cal years BP, during which the *Hokey Pokey Eruptive Unit* formed; and 2) The *Rangipo Eruptive Period*, which comprises eight units erupted between 21,800 ± 500 cal years BP and ~17 ka BP cal. These early phases were characterized by the generation of sustained Plinian to subplinian eruptive columns, involving frothy to foliated, finely vesicular pumice clasts and low contents of lithics. The pumice is predominantly similar in texture and type, except for the initial phases of

the youngest XVIII unit. The third, *Tukino Eruptive Period* from ~17 ka BP cal., to 13,625 ± 165 cal years BP (up to unit XXII defined in this study), produced four eruptive units from Mt. Ruapehu, with the Mt. Tongariro-sourced Rotoaira Lapilli (Topping 1973) interbedded. This period was dominated by comparatively short-lived subplinian columns, involving weakly fragmented, coarsely vesicular pumice and scoria clasts, and variable contents of hydrothermally altered lithics, generally decreasing in content towards the youngest units. The fourth, *Karioi Eruptive Period*, (units XXIII to XXVI), slightly after 13,625 ± 165 cal years BP, was characterized by sustained eruptive columns involving high contents of hydrothermally altered lithics of variable texture and finely vesicular pumice. The *Ohinewairua Eruptive Period* produced three units (XXVII to XXIX), characterized by unsteady, oscillating eruptive columns, commonly producing pyroclastic density currents; Lithic content is variable, but commonly lower than within the Karioi Period. Pumice clasts are commonly very finely vesicular and coarsely porphyritic, occasionally showing banded textures. The sixth eruptive period, the re-defined *Taurewa Eruptive Period* (unit XXX to unit Ngamatea Lapilli 1, as defined by Donoghue et al., 1995 a, b) also produced the 11,620 ± 190 cal years BP, Okupata Tephra. This period was characterized by relatively short-lived subplinian-Plinian eruptive columns, except the re-defined Okupata-Pourahu unit, which consists of thick fall and pyroclastic density current deposits, with distinctively pinkish white to white fibrous and banded pumice.

From a hazards perspective, it can be seen that this volcano undergoes significant variations in hazard type and magnitude over time. Hence, time-varying approaches, rather than simple event frequency averages are needed to adequately forecast future eruption potential. The deposits described here represent an earlier phase of activity at Mt. Ruapehu, which terminated around 11 ka BP cal. The shift towards the Holocene and historical contrasting eruptive magnitude and styles appears linked to the shifting of the main vent location towards the south (Crater Lake), and changes in the local volcano-tectonic setting (c.f., Villamor et al., 2010).

MASSEY UNIVERSITY
GRADUATE RESEARCH SCHOOL

STATEMENT OF CONTRIBUTION TO DOCTORAL THESIS CONTAINING PUBLICATIONS

(To appear at the end of each thesis chapter/section/appendix submitted as an article/paper or collected as an appendix at the end of the thesis)

We, the candidate and the candidate's Principal Supervisor, certify that all co-authors have consented to their work being included in the thesis and they have accepted the candidate's contribution as indicated below in the *Statement of Originality*.

Name of Candidate: Natalia Pardo Villaveces

Name/Title of Principal Supervisor: Professor Shane J Cronin

Name of Published Research Output and full reference:

Pardo N, Cronin SJ, Palmer A, Németh K (2012a) Reconstructing the largest explosive eruptions of Mt. Ruapehu, New Zealand: lithostratigraphic tools to understand subplinian-Plinian eruptions at andesitic volcanoes. Bull Volcanol 74: 617-640. doi:10.1007/s00445-011-0555-z.

The final publication is available at www.springerlink.com

In which Chapter is the Published Work: Chapter 3 and Appendix J.1

Please indicate either:

- The percentage of the Published Work that was contributed by the candidate:

  and / or

- Describe the contribution that the candidate has made to the Published Work:

  Natalia Pardo carried out the field stratigraphy, sampling, interpretation of the deposits, as well as the manuscript preparation and writing

Natalia Pardo
Digitally signed by Natalia Pardo
DN: cn=Natalia Pardo, o=Massey University, ou=INR, email=N.Pardo@massey.ac.nz, c=NZ
Date: 2012.05.04 12:12:24 +12'00'

Candidate's Signature

7/05/2012
Date

Shane J Cronin
Digitally signed by Shane J Cronin
DN: cn=Shane J Cronin, o=Massey University, ou=Institute of Natural Resources, email=s.j.cronin@massey.ac.nz, c=NZ
Date: 2012.05.10 10:16:04 +12'00'

Principal Supervisor's signature

10/5/2012
Date

*This Chapter presents the spatial distribution of five eruptive units representing the largest explosive eruptions known in the Late Pleistocene record of Mt. Ruapehu. This data was used to infer the most probable vent location and to quantify the variability of eruptive parameters (**Appendix B**) within Plinian eruptive styles.*

In addition, the debate regarding the source of the Pahoka Tephra (Nairn et al., 1998; after Topping 1973, 1974; Donoghue et al., 1995b) was addressed. This unit is, particularly interesting due to its contrasting lithofacies respect with the typical Bullot Fm., Mt. Ruapehu eruptions.

4.1 Introduction

After establishing the eruptive sequence in **Chapter 3**, the following eruptive units were chosen to represent each one of the contrasting lithofacies association types: **a)** Unit IX, formally named as **Mangatoetoenui Eruptive Unit (Mgt)**, exemplifies lithofacies association type (LA) 1, and represents the case of non-collapsing but **oscillatory** (i.e. varying in height with time) eruptive columns; **b)** Unit XXVI, referred as the **Shawcroft Eruptive Unit (Sw)** exemplifies LA-2 and represents the case of **steady** eruptive columns; **c)** Units XXVII, named here as the **Oruamatua Eruptive Unit (Oru)**, XXIX, named here as the **Akurangi Eruptive Unit (Ak)**, and the re-defined **Okupata-Pourahu Eruptive Unit (Okp-Ph)** were selected to exemplify LA-3. This last type was the most common at the end of the Late Pleistocene, before the transition to the Holocene, mostly Vulcanian-Strombolian and phreatomagmatic eruptions. Their significance in terms of hazard implications is crucial, since these units represent the case of **unsteady, collapsing** columns producing dangerous pyroclastic density currents (PDC). Moreover, their quantification, together with the previously shown stratigraphic redefinition, demonstrate that the Okupata and Pourahu Members defined by Donoghue et al., (1999) do not represent the largest Plinian event of Mt. Ruapehu. By contrast, Oru and Ak point out the largest eruption volumes, column heights, and MDR values, proving that these were the most violent eruptions. Consistently, Oru and Ak provide information of the worst hazard scenario we could expect from Mt. Ruapehu.

An earlier version of this Chapter was published by Pardo et al., (2012b; **Appendix J.2**) and the corresponding data are presented in the **Appendices B, F, G**. The contributions of each author to the study were as follows:

Natalia Pardo (Principal researcher):

- Field data collection and mapping
- Digital mapping, calculation of eruptive parameters, and interpretation
- Manuscript preparation and writing

Dr. Shane J. Cronin (Chief supervisor):

- Field assistance
- Editing and discussion of the manuscript

Dr. Alan S. Palmer (co-supervisor):

- Field assistance
- Editing and discussion of the manuscript

Dr. Jonathan Procter:

- Field assistance
- GIS assistance and data projection on Digital Elevation Models (DEM)
- Editing and discussion of the manuscript

Dr. Ian Smith (co-supervisor):

- Provided chemistry data
- Discussion of the manuscript

4.2 Andesitic Plinian eruptions at Mt. Ruapehu: Quantifying the uppermost limits of eruptive parameters

Natalia Pardo[a], Shane J. Cronin[a], Alan S. Palmer[a], Jonathan Procter[a], Ian Smith[b]

[a] Institute of Natural Resources, Massey University, Private Bag 11222, Palmerston North 4442, New Zealand

[b] School of Environment, The University of Auckland, Private Bag 92019, Auckland, New Zealand

4.2.1 Abstract

New tephro-stratigraphic studies of the Tongariro Volcanic Centre (TgVC) on the North Island (New Zealand) allowed reconstruction of some of the largest andesitic, explosive eruptions of Mt. Ruapehu. Large eruptions were common in the Late Pleistocene, before a transition to strombolian-vulcanian and phreatomagmatic eruptive styles that have predominated over the past 10,000 years. Considering this is one of the most active volcanoes in New Zealand and the uppermost hazard limits are unknown, the pyroclastic deposits corresponding to the five largest eruptions since ~27 ka BP cal., were identified and mapped. The selected eruptive units are also characterized by distinctive lithofacies associations correlated to different behaviours of the eruptive column. In addition, the source of the ~11 ka BP cal., Pahoka Tephra, identified by previous authors as the product of one of the largest eruptions of the TgVC, is clarified. The most common explosive eruptions taking place between ~13.6 and ~11 ka BP cal., involved strongly oscillating, partially collapsing eruptive columns up to 37 km high, at mass discharge rates up to 6 x 10^8 kg/s and magnitudes of 4.9, ejecting minimum estimated volumes of 0.6 km^3. Our results indicate that this volcano (as well as the neighbouring andesitic Mt. Tongariro) can generate Plinian eruptions similar in magnitude to the Chaitén 2008 and Askja 1875 events. Such eruptions would mainly produce pyroclastic fallout covering a minimum area of 1700 km^2 ESE of the volcano, where important tourism, agricultural, and military activities are based. As for the 1995/96 eruption, our field data indicate that complex wind patterns were critical in controlling the dispersion of the eruptive clouds, developing sheared, commonly bilobate plumes.

Keywords: explosive volcanism, eruptive parameters, isopach, isopleths, physical volcanology, pyroclast

4.2.2 Introduction

Understanding the physical processes controlling Plinian eruptions at subduction-related composite volcanoes is critical for estimating the associated maximum potential hazard from them (Jeanloz 2000). The term Plinian (Escher 1933; Walker and Croasdale 1971), traditionally refers to the extremely energetic eruptive style characterized by large dispersal areas and intermediate to high fragmentation index (Walker 1973; Wilson 1976; Rosi 1998; Cioni et al., 2000). During these eruptions, large volumes of pyroclasts (0.1-10 km^3, corresponding to 10^{11}-10^{13} kg) are ejected at high speeds from the vent (100-400 m/s), at extreme mass discharge rates (10^6-10^8 kg/s) (Cioni et al., 2000). The resulting eruptive column reaches tropospheric to stratospheric heights (~30 km) and can be maintained for tens of hours (Wilson 1976).

Magma degassing processes, fragmentation depth and mechanisms, syn-and-inter-eruptive conduit geometry conditions, vent migration, physical and chemical changes in magma storage zones, and magma rheology modifications along the conduit are all potential factors determining the eruptive behaviour of Plinian columns (Wilson et al., 1980; Papale and Dobran 1993; Varekamp 1993; Macedonio et al., 1994; Cioni et al., 2003; Sulpizio 2005). The 27,097 ± 957 cal years BP to ~10,000 cal years BP tephro-stratigraphic record of Mt. Ruapehu (New Zealand) provides a clear example of the variability and complexity of Plinian styles experienced by a single andesitic volcano, where contrasting lithofacies associations are inferred to reflect variable magmatic (i.e. vesiculation state, composition and volatile content of the erupting magma, fragmentation mechanisms) and environmental conditions (i.e conduit/vent geometry, inflow of external water into the conduit), ultimately affecting the steadiness of the eruptive column and tephra dispersion (Pardo et al., 2012a; **Chapter 3; Appendix J.1**). In this chapter, new isopach and isopleth maps are presented, and quantify the main corresponding physical eruptive parameters of the five eruptive units representing the largest explosive eruptions known in the Late Pleistocene record of Mt. Ruapehu. These units were also selected to represent contrasting lithofacies association types to study the variability within Plinian eruptive styles. These new data allow establishment of the uppermost hazard limits and the maximum eruptive scenarios expected from the largest and most active andesitic volcano of New Zealand.

Around 10 % of New Zealand's national economy is concentrated in the Central North Island, and the surroundings hold ~24 % of the country's population (The Treasury 2010). As demonstrated by the 1995/1996 eruptions, even very small tephra falls from this volcano may disperse ash broadly over agricultural areas, along with towns and cities and key infrastructure lifelines (Cronin et al., 1998, 2003; Johnston et al., 2000). Mt. Ruapehu is also located within the Tongariro National Park, a UNESCO World Heritage area that is one of the most visited tourist attractions in the country. In addition, up to ten thousand people can be present at any one time on the ski fields of Mt. Ruapehu during the winter season (Kilgour et al., 2010). The populated centres surrounding the park include Turangi (3441 inhabitants) to the north, Ohakune (1101 inhabitants), Waiouru (1383 inhabitants) and Taihape (1788 inhabitants) to the South (Statistics New Zealand 2007, 2009).

The quantification of eruptive parameters was carried out according to the methodology explained in **Chapter 2.1**, and pumice vesicularity was described and measured according to the methods presented in **Chapter 2.2.3**. Pumice textures will be referred to as: 1) Foamy; highly vesicular clasts dominated by subspherical vesicles <2 mm in diameter. 2) Fluidal; highly to moderately vesicular clasts with strongly orientated, elongate (i.e. ellipsoidal) vesicles, commonly aligned with the longest axes of phenocrysts. 3) Microvesicular; dense clasts with highly distorted, often aligned vesicles that are only visible under microscope and usually show pinched shapes and angular terminations.

To evaluate the magma fragmentation mechanisms involved in the studied eruptives, the morphology of clean juvenile ash grains picked from the 3 ϕ size fraction was analysed, according to the methods described in **Chapter 2.2.4**.

4.2.3 Mt. Ruapehu Plinian eruption lithofacies associations

Mt. Ruapehu's eruptive behaviour has systematically changed since ~27 ka BP cal., from older explosive eruptions characterized by steady eruptive columns, to younger events characterized by unsteady, partially collapsing columns (**Chapter 3; Appendix J.1**). These stages were separated by an interval between 17,625 ± 425 cal years BP and shortly after 13,635 ± 165 cal years BP, when eruptive columns were steady, but powerful and involved large proportions of accessory and accidental lithic fragments. Each one of these eruptive

behaviours has been inferred by analysing pyroclastic deposits with contrasting lithofacies associations, which were classified into three main types: *Type 1 association* comprises a few (<3) overlapping fall deposits characterized by massive to normally graded, clast-supported, pumice lapilli beds and scarce porphyritic lithics. Usually, the initial eruptive products include a basal concentration of fresh andesitic lithics or angular to rounded dense pumice clasts. Juvenile pumice textures in the thickest, coarsest, and most widespread beds representing the main eruptive phases are highly vesicular, varying within the same stratigraphic level from finely vesicular-foamy pumices, to coarsely vesicular-fluidal textures and rare microvesicular (nearly dense), crystal-rich textures. Lithic content and lithological variability are significantly lower in comparison with the other lithofacies associations.

Type 2 association comprises one or a few, distinctively lithic-rich, thick, ungraded fall deposits with abundant, multicoloured, hydrothermally altered, aphanitic to finely porphyritic lithic clasts. Crude stratification is present across the deposits, particularly away from the dispersal axis. The coarsest and thickest beds are usually underlain by a thin, massive or laminated red, yellowish, purplish or olive grey, platy coarse ash to fine-ash bed, locally containing accretionary lapilli. The main part of an individual eruptive unit is typically represented by a single thick, coarse-grained bed consisting of clast-supported pumice fragments that are iron-stained with dark brown interiors, typically highly and finely vesicular, microphenocryst-bearing, varying from foamy to micro-fluidal, and microvesicular (nearly dense). Bombs showing bread-crust (as far as 15 km from the vent) or cauliflower structures (as far as 5 km from the vent) are common.

Type 3 association deposits comprises multiple, well-stratified fall deposits of contrasting grain-size interfingered with thin pyroclastic density current deposits. Lapilli fall beds are commonly bounded by thin (<3 cm) fine ash beds containing abundant accretionary lapilli. Pumice textures are the most heterogeneous among all lithofacies associations, varying from incipiently vesicular to moderately and highly vesicular, typically fibrous and coloured-banded.

The new stratigraphic analysis presented in **Chapter 3** shows the systematic change from older, typically type 1 to younger, typically type 3 eruptive units. Based on their lithofacies analysis, for this study, the following coarsest, thickest and most widely distributed eruptive units within each lithofacies association type were chosen for further quantification: eruptive unit IX (Mangatoetoenui Eruptive Unit) represents lithofacies association type 1, unit XXVI

(Shawcroft Eruptive Unit) represents lithofacies association type 2, and eruptive units XXVII (Oruamatua Eruptive Unit), XXIX (Akurangi Eruptive Unit), and XXXI (Okupata-Pourahu Eruptive Unit) together exemplify the lithofacies association type 3, which was the most common produced between 13,635 ± 165 and 11,000 cal years BP, immediately before the transition to lower magnitude Holocene eruptions.

The lowermost unit of the ~11 ka BP cal., Pahoka-Mangamate Sequence (Nairn et al. 1998), known as the Pahoka Tephra, was also mapped to clarify its source, which had been attributed variously to Mt. Ruapehu, Mt. Tongariro, or a vent located between the two, known as the "Saddle Cone" (Topping 1973; Donoghue 1991; Nairn et al., 1998).

Type 1: Thickly bedded, lithic-poor association (Mangatoetoenui Eruptive Unit)

Field characteristics: the Mangatoetoenui Eruptive Unit (Mgt) consists of two, clast-supported and well-sorted pyroclastic subunits (lower L-Mgt and upper U-Mgt) that mantle previous topography (**Fig. 4.1**), separated by a volcaniclastic, cross-bedded sand deposit (IX-1d in **Fig. 4.1**), which is very well sorted, but varies considerably in thickness and sedimentary structures laterally and distally. The L-Mgt consists of two fall beds (**Fig. 4.1**): the basal, thin lithic-lapilli deposit (IX-1a) was only identified to the east and disappears beyond 10 km from the source. The overlying main, medium and coarse pumice lapilli bed (IX-b), gradually fines upwards to fine lapilli and very coarse ash (IX-1c), and is widely exposed over the entire study area. The U-Mgt comprises two massive beds, also mantling previous topography. The lower is the thickest and coarsest (IX-2a), and is capped by the thinner ash bed IX-2b (**Fig. 4.1**), which commonly grades into loess upward. The L-Mgt is mainly characterized by highly and coarsely vesicular pumice clasts (average vesicularity = 80 %; average pumice density = 0.64 g/cm^3. See **Appendix G**) showing strong alignment of ellipsoidal vesicles and phenocrysts in a dark brown glass groundmass. The U-Mgt is characterized by microvesicular to dense, crystal-rich clasts (total vesicularity = 64 %; average pumice density = 1.28 g/cm^3), containing distorted, in some instances pinched vesicles, and entrapped lithics.

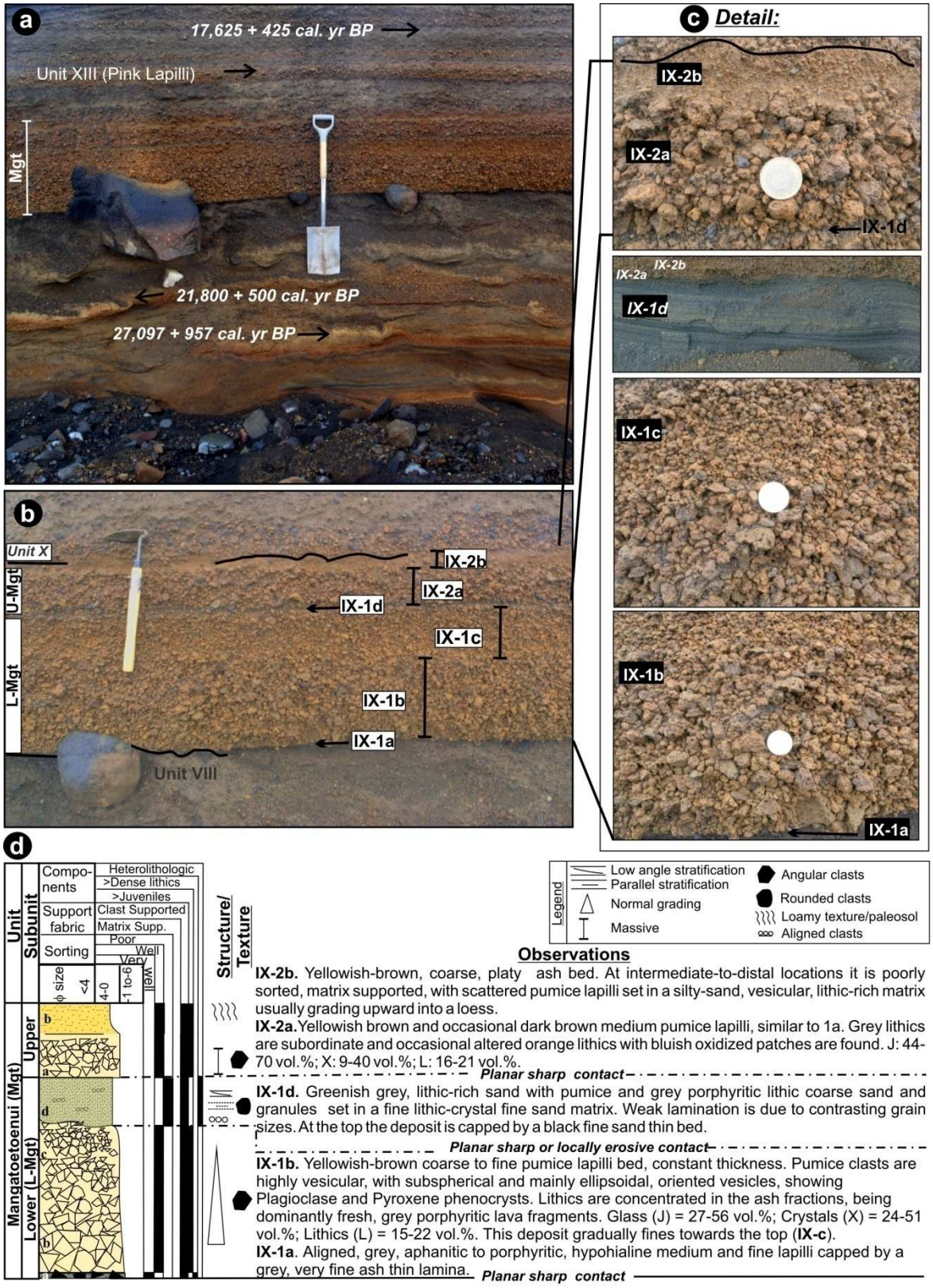

Figure 4.1 Lithofacies association type 1, represented by the Mangatoetoenui Tephra. a) Stratigraphic position within the Bullot Fm., above the 21,800 ± 500 cal years BP, rhyolitic Okareka Tephra; b) Exposure 15 km from source showing normally graded L-Mgt and massive U-Mgt pumice lapilli beds, locally separated by syn-eruptive fluvial deposits (IX-1d); c) Phases distinguished in proximal areas by contrasting grain-sizes; d) Composite stratigraphic profile. Relative proportion of juvenile glass (J), crystals (X), and lithics (L) are given for the main Plinian deposits as vol.% based on component analysis of 300 grains within 1, 2, and 3 ϕ size fractions.

Within any particular stratigraphic level, all the textural types from highly vesicular, foamy-like to fluidal and even microvesicular, dense juvenile clasts can be found. The phenocryst association is plagioclase (Pl) ± orthopyroxene (Opx) ± clinopyroxene (Cpx) >>Magnetite (Mt), with most of the pyroxenes forming glomerocrysts. Juvenile pumice bulk composition ranges from basaltic andesite to andesite (SiO_2: 56.2-58.3 wt.%, normalized to dry basis), without showing significant variations with time (**Appendix F.1**). The non-juvenile lithics are recognized by their grey colour, microporphyritic texture, and absence of vesicles, containing variable amounts of Pl phenocrysts within a microlitic groundmass, very similar to the older andesitic lavas exposed on the slopes of the volcano reported by Graham and Hackett (1987).

Interpretation: the Mangatoetoenui Eruptive Unit represents at least four eruptive phases. The eruption began with a conduit/vent clearing, probably phreatic explosion, producing the monolithologic lithic-rich bed IX-1a (e.g. Bursik 1993; Hammer et al., 1999; Wright et al., 2007). The restricted deposits suggest that this opening phase was a laterally directed explosion. Subsequently, a sustained eruptive column arose, producing the first main fall deposit (IX-1b), then gradually waned over time as indicated by the normal grading (IX-1c). During a brief inter-phase hiatus small, scour and fill channels formed in and locally reworked previous deposits (IX-1d), before resumption of a buoyant eruptive plume deposited the very coarse-grained and massive IX-2a fall bed of the U-Mgt. The uppermost ash-bed (IX-2b) was probably accumulated from the dissipating cloud, and further reworked by aeolian and fluvial processes. Beyond 17 km from the source, both L-and-U-Mgt subunits merge into a single fall bed.

Isopach and Isopleth maps: Isopach and Isopleth maps for individual phases could not be constructed, but were developed for the combined pyroclastic fall deposits. Thickness distributions (**Appendix B.1**) show two clear depositional lobes, the largest one directed towards the southeast (found as far as 35 km from source) and a more restricted one to the northeast, deflected distally towards the north (**Fig. 4.2a**). The two lobes are also evident in both lithic and pumice clast isopleths (**Appendix B.2; Figs.4.3a, b**). By tracing the axes of approximated ellipses extrapolated from field data, the most probable vent for the Mangatoetoenui Eruptive Unit is the North Crater of Mt. Ruapehu.

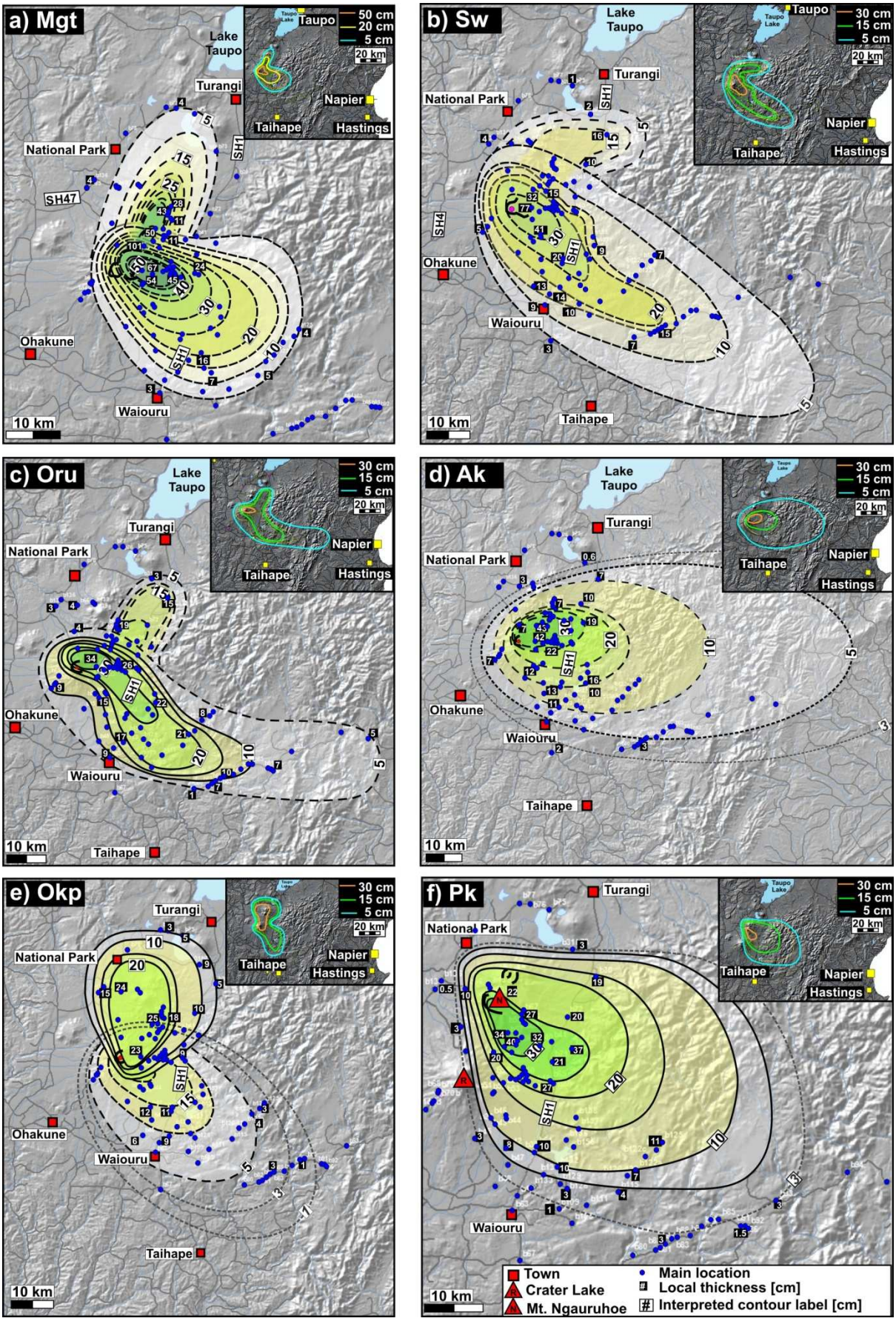

Figure 4.2 *See caption in the next page.*

Figure 4.2 Isopach maps for: **a)** Mgt-Mangatoetoenui Eruptive Unit (lithofacies association-type 1); **b)** Sw-Shawcroft Eruptive Unit (lithofacies association-type 2); **c)** Oru-Oruamatua Eruptive Unit; **d)** Ak-Akurangi Eruptive Unit; **e)** Okp-Lower and Upper Okupata tephras(c-e: lithofacies association-type 3); **f)** U-Pk-Mt. Tongariro sourced Upper Pahoka Tephra (N: current Ngauruhoe vent; R: current Mt. Ruapehu Crater Lake). Contours are labelled within white squares and shown in centimetres (cm), drawn on a proximal 5 m DEM combined with a distal 20 m DEM. In black squares some of the local average field data values are shown (see **Appendix B.1**). Upper right sub-quadrants show the contours interpreted from field data to illustrate the dispersion axes in relation to intermediate-distal urban areas (e.g. Napier, Hastings).

Type 2: Massive-lithic rich (Shawcroft Eruptive Unit)

Field characteristics: the Shawcroft Eruptive Unit (Sw) overlies the regional marker identified as the rhyolitic 13,635 ± 165 cal years BP Waiohau Tephra (Donoghue et al., 1995b) and is distinguished by a thick, multi-coloured, lithic-rich, massive, coarse lapilli and bomb-rich bed, defined as "Shawcroft lapilli" by Donoghue et al., (1995b) bounded at the base and top by finer grained thin beds. The lowermost, lithic-rich, platy ash (**Fig. 4.4**), commonly with accretionary lapilli (XXVI-1a) is only exposed within 8 km of the vent. Bread-crust bombs in the Shawcroft lapilli (XXVI-1b) bed (**Fig. 4.4c**) are found on the eastern slopes of the volcano, up to 10 km from Crater Lake. At localities within 4 km of the vent, on the northern wall of the upper Whangaehu valley, there is an interbedded firm deposit (XXVI-1s bed, **Fig. 4.4**), which consists of a lower, yellow coarse ash bed, which is matrix-supported, well sorted, shows low-angle cross-lamination, and contains abundant accretionary lapilli (**Fig. 4.4d-f**). The yellow ash bed is overlain by a dark grey, firm, vesicular fine ash bed showing crude lamination. Both of these yellow and grey beds vary laterally in thickness and show impact sags (**Fig. 4.4d-e**).

Textural variability of juvenile pumice within a single stratigraphic level is more restricted than in Mgt. Pumice ranges from dark brown, microvesicular to yellowish-brown, micro-fluidal clasts (average vesicularity = 63 %; average pumice density = 1.25 g/cm^3; **Appendix G**), with fine (<1 mm) pyroxenes (Px), (Opx ± Cpx ± Pl)-glomerocrysts and non-juvenile, probably accessory andesitic lithics. The mineral association for both types is Pl>Opx±Cpx>>Mt. Juvenile pumice bulk composition is basaltic-andesitic to andesitic (SiO_2: 57.0-58.4 wt.%, normalized to dry basis; see **Appendix F.1**). Non-juvenile lithic clasts vary from fresh grey andesites to multicoloured, hydrothermally altered lithics and occasional metasedimentary lithics.

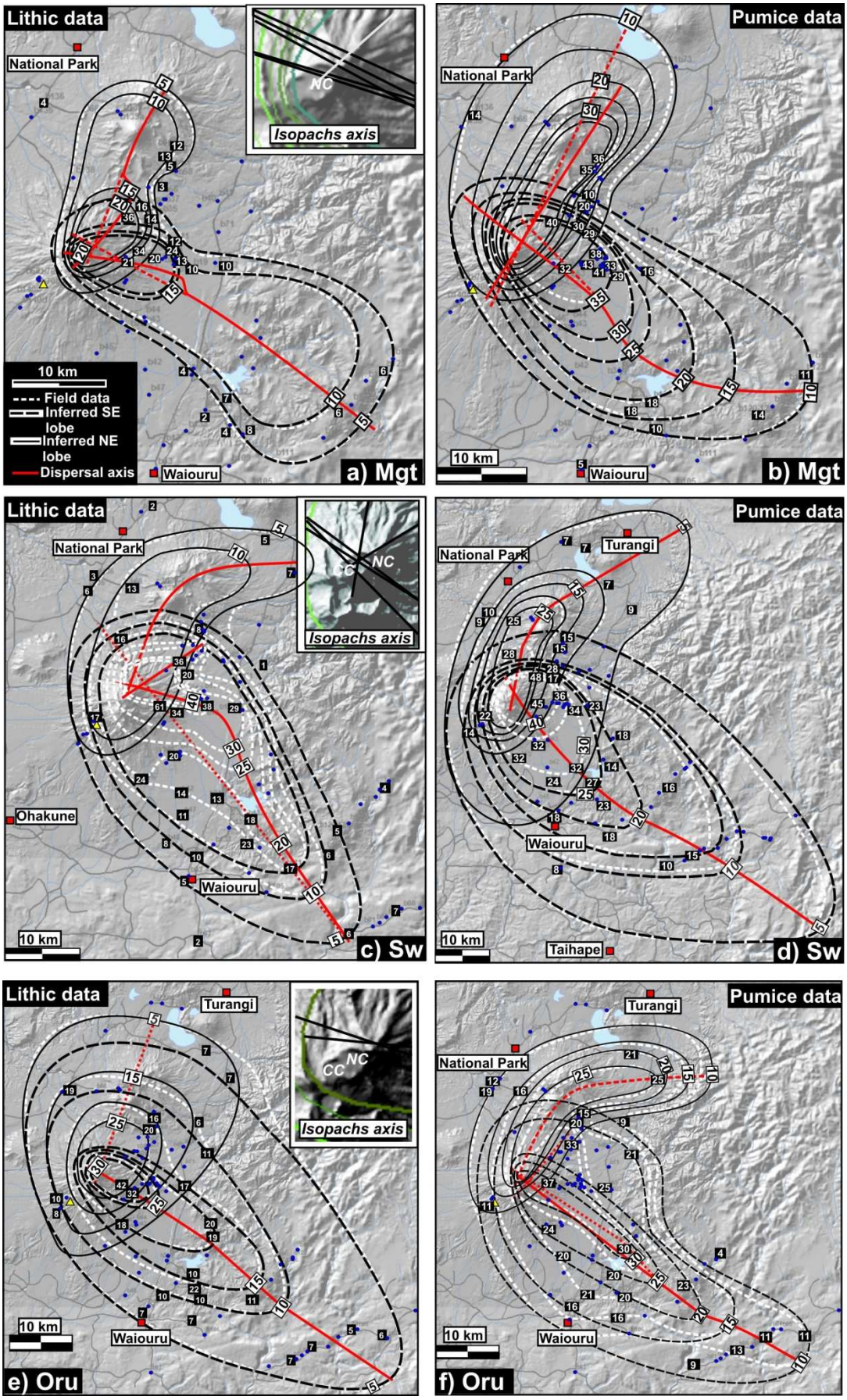

Figure 4.3 *See caption below.*

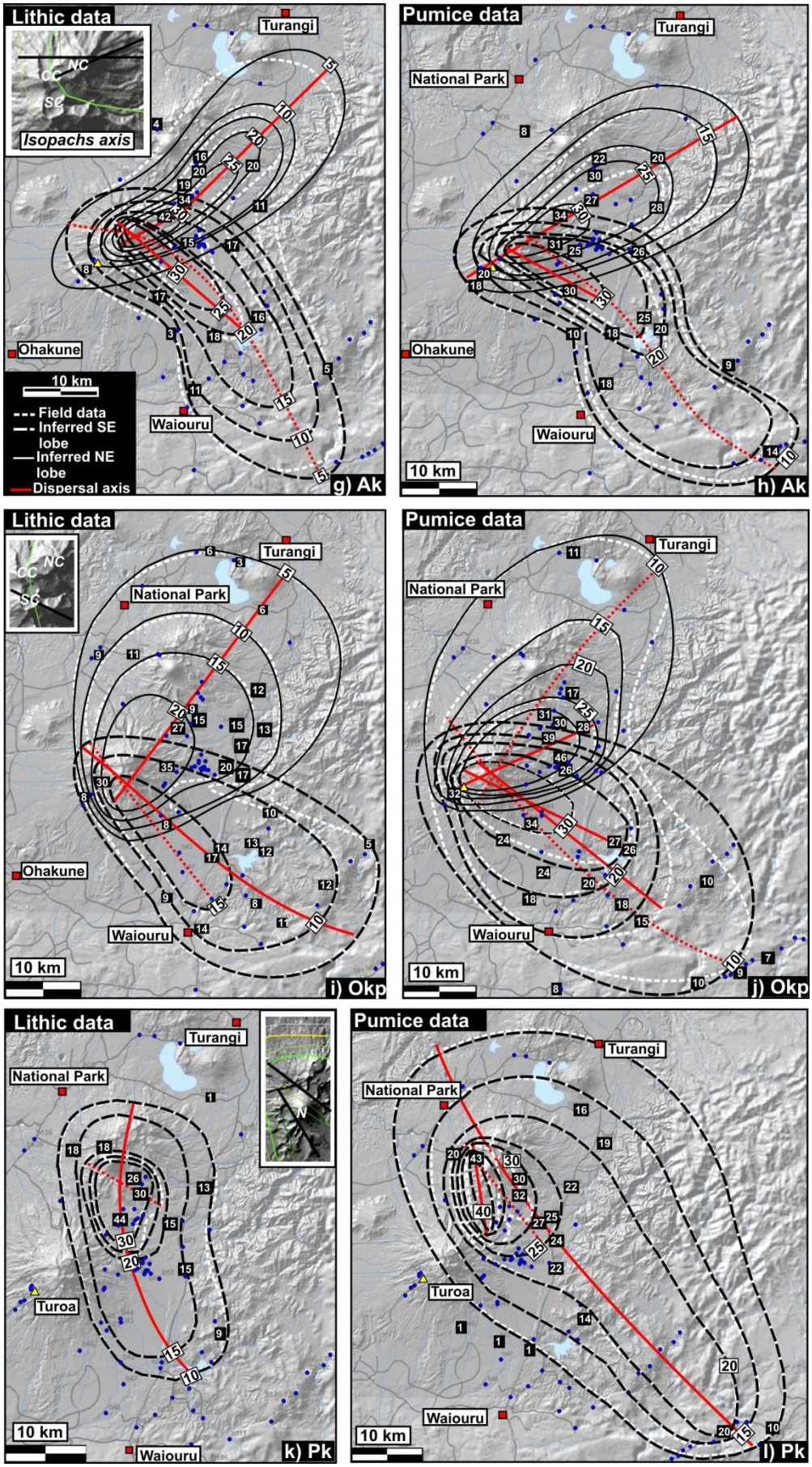

Figure 4.3 [cont] *See caption below.*

Figure 4.3 Isopleth maps showing the distribution of lithic and pumice clast diameter in mm: **a-b)** Mangatoetoenui; **c-d)** Shawcroft; **e-f)** Oruamatua; **g-h)** Akurangi; **i-j)** Okupata; **k-l)** U-Pahoka. The axis of the tephra lobe, traced from isopachs (in red), is extrapolated towards the source, suggesting North Crater as the most probable vent for most units, but not the youngest Okupata tephras, which originated from a vent closer to Crater Lake, and the Pahoka tephra which was produced by Mt. Tongariro. NC: North crater, CC: Central Crater, SC: South Crater, N: Mt. Ngauruhoe (see **Appendix B.2** for complete field data set).

At intermediate and proximal locations, there are at least four thin fine ash beds on top of the Shawcroft lapilli (**Fig. 4.4b**), but at distal locations, it is directly covered by a poorly sorted, silty-sand, heterolithologic, crystal-rich deposit of variable thickness, grading into loess at top (XXVI-e in **Fig. 4.4b, g**).

Interpretation: the Shawcroft lapilli is a widespread fall deposit from a sustained eruptive column, preceded (XXVI-1a) and followed (XXVI-1c-d) by smaller, phreatomagmatic eruptions that deposited the bounding thin, fine-grained, lithic-rich, platy ash beds. Although in most locations the main phase (XXVI-1b) is represented as a single bed, there may have been two fall phases/pulses, separated by emplacement of the laminated pyroclastic surge deposits that crop out in proximal locations (**Fig. 4.4f**). The abundant lithic fragments and their diversity indicate intense erosion of the hydrothermally altered regions of the conduit. Post-eruptive sedimentary processes (XXVI-1e) deposited massive gravelly-sand and parallel-bedded, silty-sand from high-discharge floods. Beyond 15 km from the vent, only the Shawcroft lapilli is preserved, immediately capped by post-eruptive volcaniclastic sediments or a weak paleosol.

Isopach and Isopleth maps: Isopach and Isopleth maps of the main eruptive phase (XXVI-1b) (**Figs. 4.2b; Appendix B**) show a main lobe towards the southeast, and a short, secondary lobe to the northeast. The two lobes are also evident in both lithic and pumice clast isopleths (**Figs.4.3c, d**). The maps suggest that the vent probably located between the southern sector of North Crater and the Central Crater.

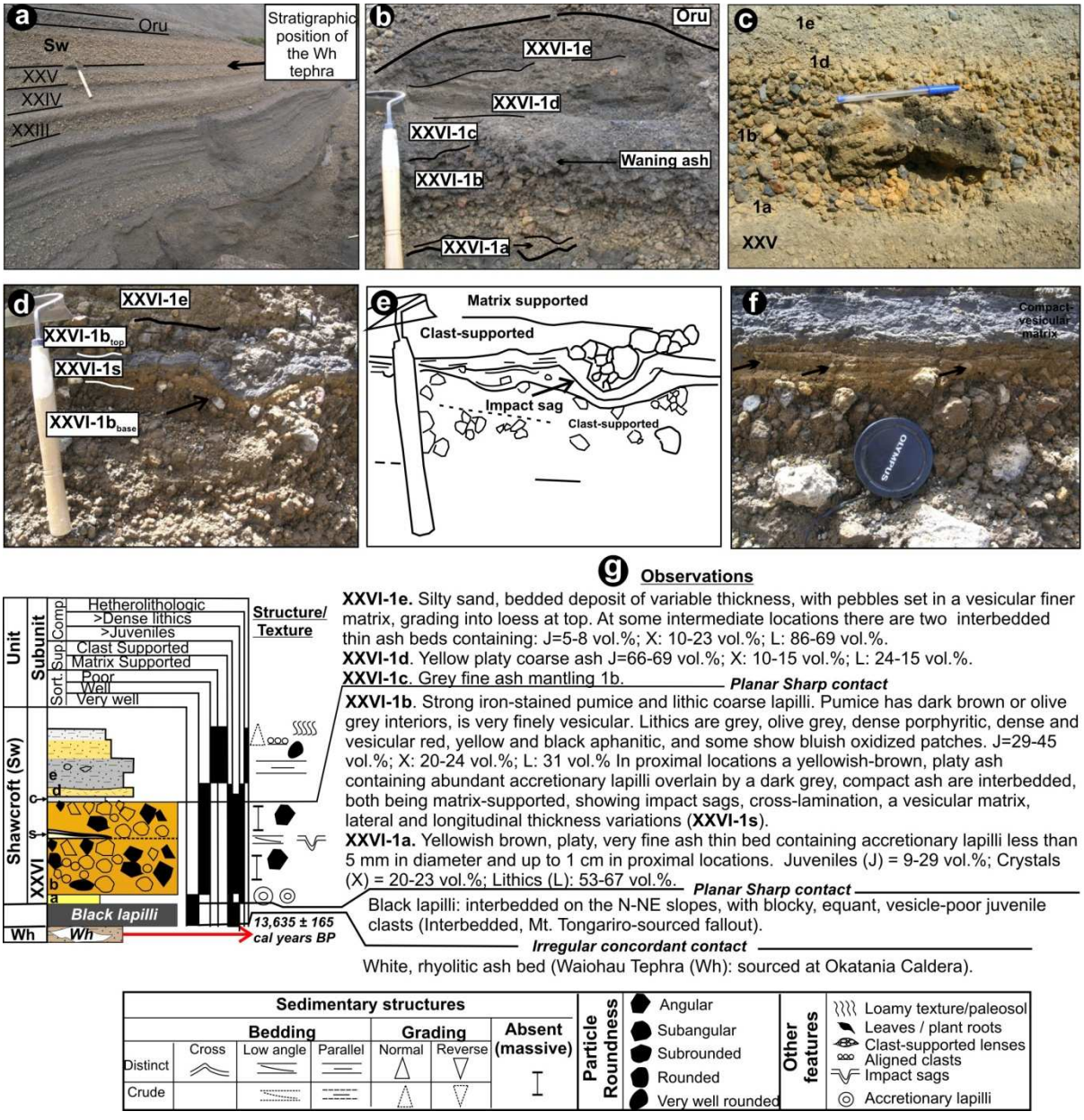

Figure 4.4 Lithofacies association type 2, represented by the Shawcroft Eruptive Unit (Sw); **a)** Stratigraphic position above the 13,635 ± 165 cal years BP, rhyolitic Waiohau Tephra (Wh); **b)** close-up view at 10 km from the vent showing the deposits of individual phases; **c)** Typical lithic-rich, coarse grained lithofacies of the main phase (i.e. Shawcroft lapilli) with bread-crust bombs up to 30 cm in diameter; **d)** Proximal outcrop (5 km) showing cross-laminated pyroclastic surge deposits (XXVI-1s) interbedded within the main lapilli fall deposits. Note the impact-sag (sketched in **e**), under a ballistic clast, the crossed lamination and accretionary lapilli (arrows) in **f**; **g)** Composite stratigraphic profile. Relative proportion of juvenile glass (J), crystals (X), and lithics (L) are given for the main Plinian deposits as vol. % based on component analysis of 300 grains within 1, 2, and 3 ϕ size fractions.

Type 3: Thinly Bedded (Oruamatua, Akurangi, and Okupata-Pourahu eruptive units)

Lithofacies association type 3 deposits are the most abundant below the transition to the typically phreatomagmatic and phreatic deposits of the Holocene. The three thickest of these, units are XXVII (here named Oruamatua Eruptive Unit), XXIX (Akurangi Eruptive Unit), and XXXI (Okupata-Pourahu Eruptive Unit).

Field characteristics: the Oruamatua Eruptive Unit (Oru) consists of three pyroclastic subunits, here distinguished as Lower (L-Oru), Middle (M-Oru), and Upper (U-Oru), (**Figs. 4.5** and **4.6**), with distinctive tephras separated by syn-eruptive, thin hyperconcentrated flow deposits. The L-Oru is lithic-rich and mantles older topography. The non-juvenile fragments comprise fresh, grey and brown, coarse porphyritic lava fragments, multi-coloured, hydrothermally altered porphyritic to aphanitic clasts, and occasional metasediments (**Figs. 4.5** and **4.6**). The M-Oru (**Fig. 4.5d**) shows important facies variations along the Upper Waikato stream (**Fig. 1.2**), where the clast-supported, well sorted pumice lapilli bed is completely replaced by a massive, matrix-supported, very poorly sorted deposit showing abrupt thickness variation (**Fig. 4.6**). The U-Oru (**Figs. 4.5e, 4.6**) mantles the M-Oru and it is distinguished by the widespread, lowermost yellowish-brown platy ash bed ($U\text{-}Oru_{3a}$ in **Fig. 4.6**) containing abundant, reversely graded accretionary lapilli. Lateral variation of the main clast-supported pumice lapilli facies ($U\text{-}Oru_{3b}$; **Fig. 4.6**) to poorly sorted, matrix-supported facies is also evidenced along paleo-valleys.

The entire Oruamatua unit is distinguished from previous units by having typically pale brown, crystal-rich (porphyritic), moderately to poorly microvesicular pumice clasts (average vesicularity = 58 %; average pumice density = 1.26 g/cm^3; **Appendix G**). Locally, and predominantly in the M-Oru, there are pinkish-brown pumice clasts varying from coarsely vesicular-fluidal to finely vesicular-fibrous texture and colour-banded, microvesicular clasts. Phenocryst content and size are large relative to other lithofacies association types and the general mineral assemblage is Pl>>Opx>Cpx>>Mt. Juvenile pumice bulk composition lies within the andesite field, showing a wider spread of silica content than older units (SiO_2: 57.33-60.14 wt.%, normalized to dry basis; **Appendix F.1**). At exposures >30 km from the vent, individual subunits merge into a single, mantling clast-supported fine lapilli bed.

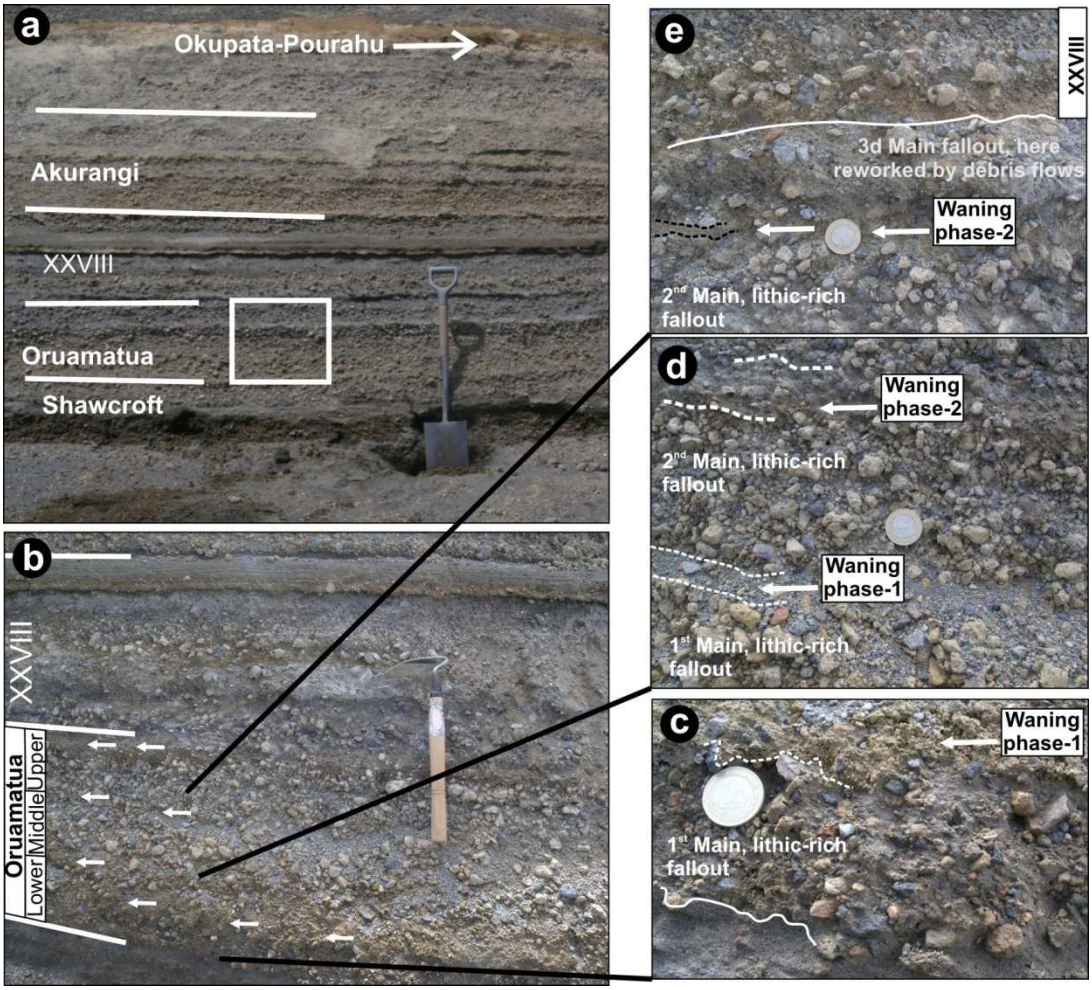

Figure 4.5 Bedded lithofacies association type 3, Oruamatua and Akurangi eruptive units: **a)** Relative stratigraphic position above Sw; **b)** Individual subunits representing different eruptive phases within the Oruamatua eruptive: **c)** Lithic-rich Lower-Oru **d)** Middle-Oru showing three bedsets indicating three main fallout phases separated by fine ash (oscillating columns or wandering plume effects) **e)** Upper-Oru, partially reworked here (B15 in **Appendix A**).

The younger Akurangi eruptive unit (**Figs. 4.5a, 4.6**) is also widely distributed, and consists of four distinct pyroclastic subunits very similar to Oru, locally separated by matrix-supported, poorly sorted deposit with hetherolithologic granules and pebbles set in a lithic-crystal sand matrix (**Figs. 4.2d, 4.6**). The youngest Okupata-Pourahu Eruptive Unit (**Fig. 4.7**) was described by Topping (1973) and Donoghue et al. (1999). Pumice clasts are highly vesicular, typically fibrous, often colour-banded, and coarsely porphyritic. The phenocryst assemblage is Pl>Opx>Cpx>Mt. Our field data (**Fig. 4.7c**) indicate this unit consists of two main fall deposits: the Lower-Okupata (L-Okp) tephra (total vesicularity = 62 %; average pumice density = 1.15 g/cm^3; **Appendix G**), and the Upper-Okupata (U-Okp) tephra (average vesicularity = 71 %; average pumice density = 0.92 g/cm^3), locally separated by the Pourahu

pyroclastic flow deposit (Donoghue et al., 1999), or by its correlative co-ignimbrite ash (Ph-$_{1d}$ in **Fig. 4.6b**). Juvenile pumice bulk composition is the most variable of all the studied units, with most of the samples plotting inside the basaltic-andesite and andesitic fields (SiO_2: 56.1-61.6 wt.%, normalized to dry basis; **Appendix F.1**). Non-juvenile lithics include fresh, coarsely porphyritic grey andesites, and red to orange, hydrothermally altered, porphyritic clasts. The pyroclastic deposits are capped by reworked volcaniclastic units and a paleosol (**Fig. 4.7c**). At distal locations the unit is condensed into a single mantling clast-supported bed, known as the Okupata Tephra (11,620 ± 190 cal years BP; Topping 1973; Donoghue et al., 1995a, b; Lowe et al., 2008), which was emplaced at the onset of the early Holocene warming in Central North Island (Newnham and Lowe 2000).

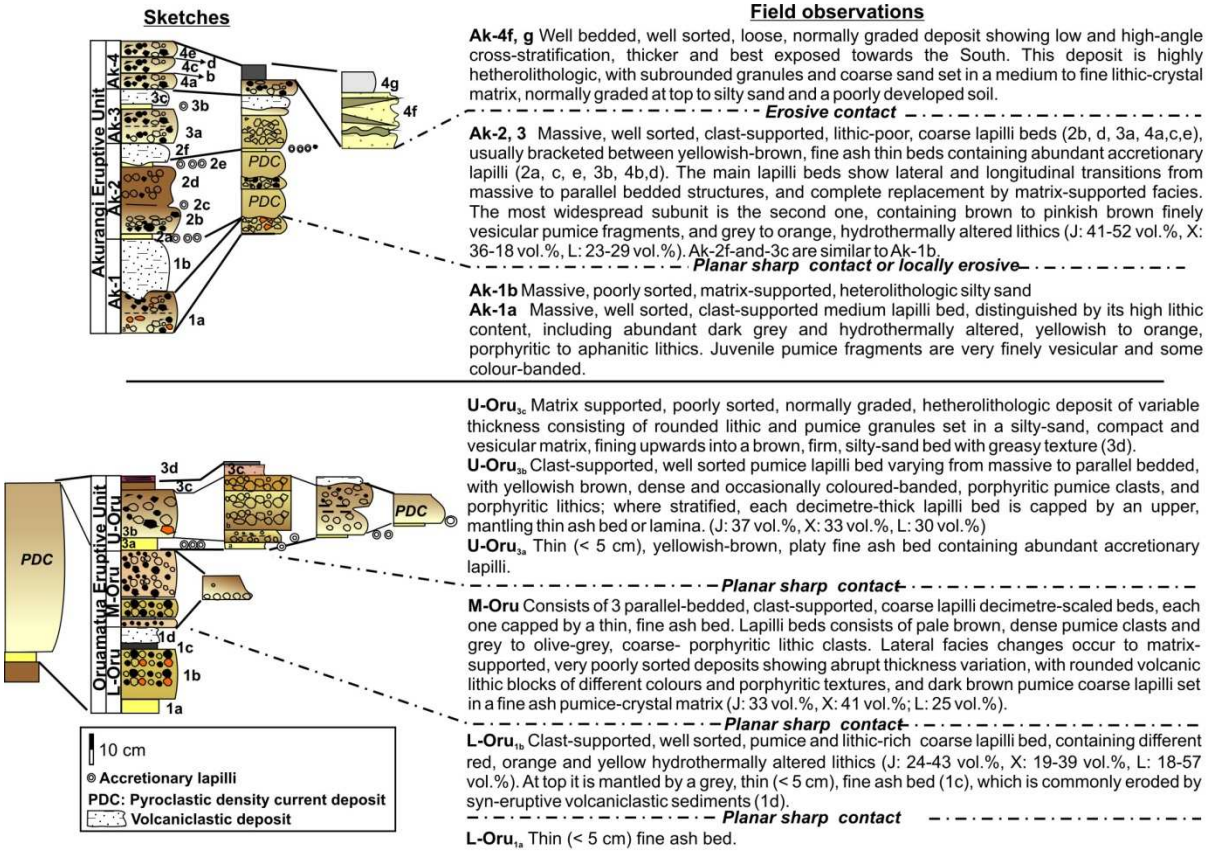

Figure 4.6 Stratigraphic profile from the Oruamatua and Akurangi eruptive units showing lateral variation from fall to pyroclastic density current deposits (PDC).

Interpretation: bedding in this type suggests pulsating and unstable eruptive columns (c.f. Sieh and Bursik 1986; Bursik 1993; Cioni et al., 2003; Sulpizio et al., 2005). In the case of the Oruamatua and Akurangi units, the main Plinian phases represented by the coarsest grained, thickest, and widely exposed fall beds, were usually preceded by opening

phreatomagmatic events producing thin, fine grained, accretionary lapilli-rich beds. The opening phases cleared the conduit and allowed subsequent decompression, driving the main Plinian phases (e.g., Arce et al., 2003; Rosi et al., 2004; Gurioli et al., 2005; Hammer et al., 1999). Matrix-supported facies of variable thickness and limited distribution were accumulated from pyroclastic density currents and indicate partial column collapse. Syn-eruptive and inter-eruptive reworked volcaniclastic deposits are intercalated with the pyroclastic beds.

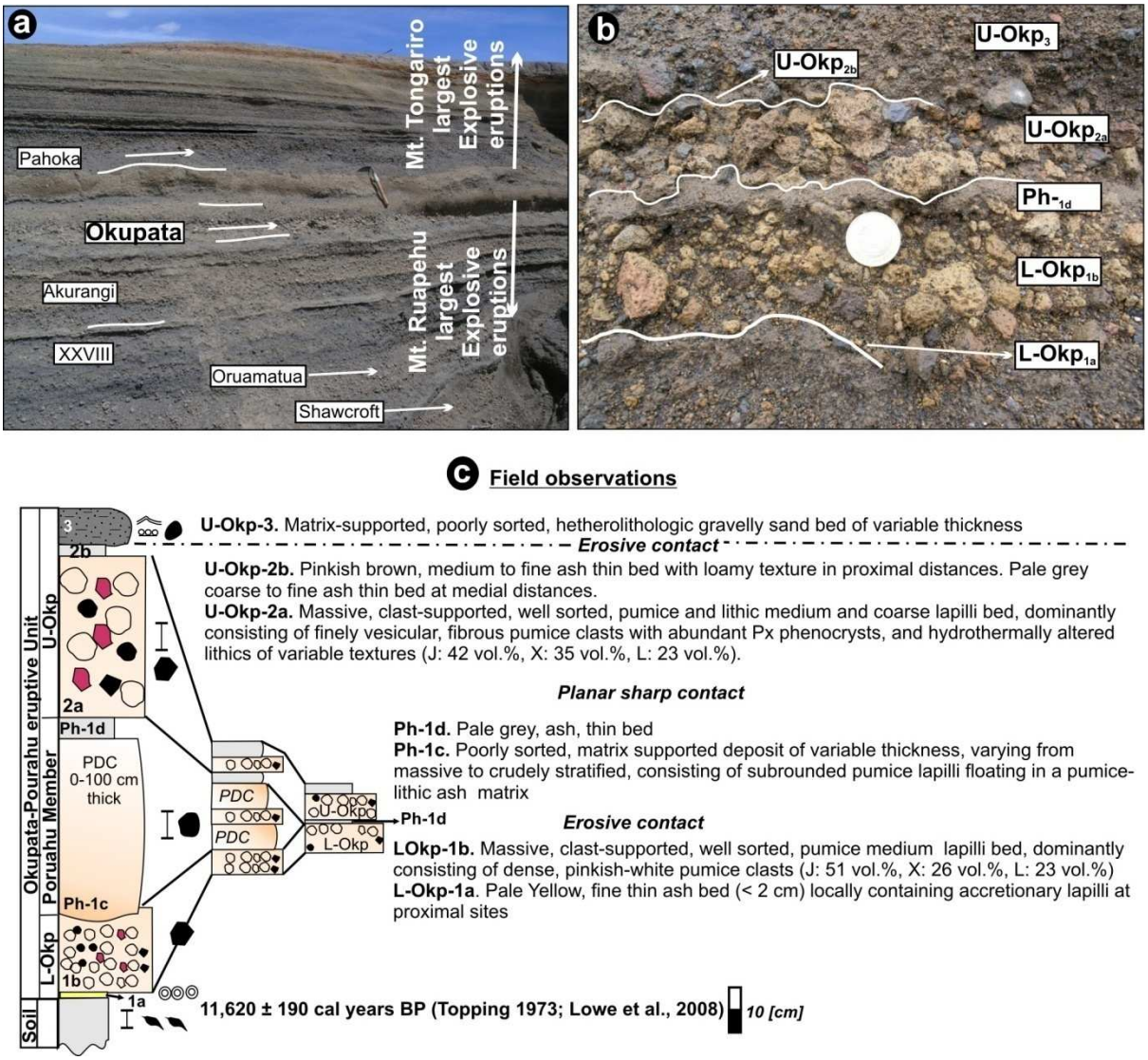

Figure 4.7 Uppermost studied units, comprising: **a)** the last known Plinian deposit sourced at Mt. Ruapehu (Okp-Ph) and the first Plinian deposit of the Pahoka-Mangamate explosive period of Mt. Tongariro (Upper Pahoka Tephra); **b)** detail of the two main fall deposits forming the Okupata-Pourahu eruptive unit (L-and-U-Okp), separated by a co-ignimbrite ash at proximal locations (and in the same stratigraphic position as the pyroclastic flow deposit named Pourahu member by Donoghue et al., 1999; Ph-1d bed); **c)** composite stratigraphic profile (See legend Fig. 4.4). Relative proportion of juvenile glass (J), crystals (X), and lithics (L) are given for the main Plinian deposits as vol.% based on component analysis of 300 grains within 1, 2, and 3 ϕ size fractions.

Isopach and Isopleth maps: because individual phases within each eruptive unit could not be discerned at medial-to-distal locations, isopach and isopleth maps were constructed for the total thickness of fall beds of each unit (**Figs. 4.2c, d, e**). Field data (**Appendix B.1**) suggest a main depositional lobe towards the southeast, and a short lobe to the northeast. These lobes are also evident in both lithic and pumice clast isopleths (**Figs.4.3e, f; Appendix B.2**). The most probable vent is the North Crater of Mt. Ruapehu. Isopach data of the Akurangi Eruptive Unit can be explained by drawing a single lobe with a dispersal axis towards the East (**Fig 4.2d**); however, isopleths indicate two lobes (**Figs. 4g, h**). This apparent discrepancy might reflect the effect of different wind patterns in a vertically stratified atmosphere with overlapping lobes producing a composite deposit, and the limited exposure in the eastern area. The dispersion axis of the deposits suggests a vent located between central and north craters. Isopach maps constructed with the merged thickness data of L-and-U-Okp tephras (**Fig. 4.2e**) show two lobes, one towards the north and the other one towards the south-east. Isopleth data (**Appendix B.2**) indicate a shift in the vent position to the southern crater of Mt. Ruapehu (**Fig. 4.3i, j**).

The Pahoka Tephra

Field characteristics: in addition to the units exposed above, clearly from Mt. Ruapehu, the ~11 ka BP cal., Pahoka Tephra (Topping 1974) was proposed to be sourced from Mt. Tongariro (Topping 1974; Donoghue et al., 1995b), before being re-assigned to a vent between Mt. Ruapehu and Mt. Tongariro, beneath the "Saddle Cone" lavas (Nairn et al., 1998). New field data show that this eruption produced two subunits, here termed Lower and Upper Pahoka (L-Pk and U-Pk, respectively; **Fig. 4.8; Appendix A**). The L-Pk comprises two thin, very fine grained and commonly eroded mantling beds, whereas the overlying three beds are grouped within the U-Pk, which is the only one that can be mapped well. The latter corresponds to the Pahoka Tephra reported by Topping (1973), and is characterized by blocky-shaped, dark olive-grey, and commonly colour-banded, microvesicular juvenile fragments (Pl>>>Cpx+Opx>Ol). Lithic clasts are dark grey, vesicular to dense, coarsely porphyritic to aphanitic lava fragments, dark red and orange, hydrothermally altered, aphanitic lithics, with the majority coated with ash and fine lapilli. At proximal locations

dense bombs up to 15 cm occur, showing chilled, cracked crusts (**Fig. 4.8**). At distal locations the unit is condensed into a thinly laminated, compact, olive-grey ash.

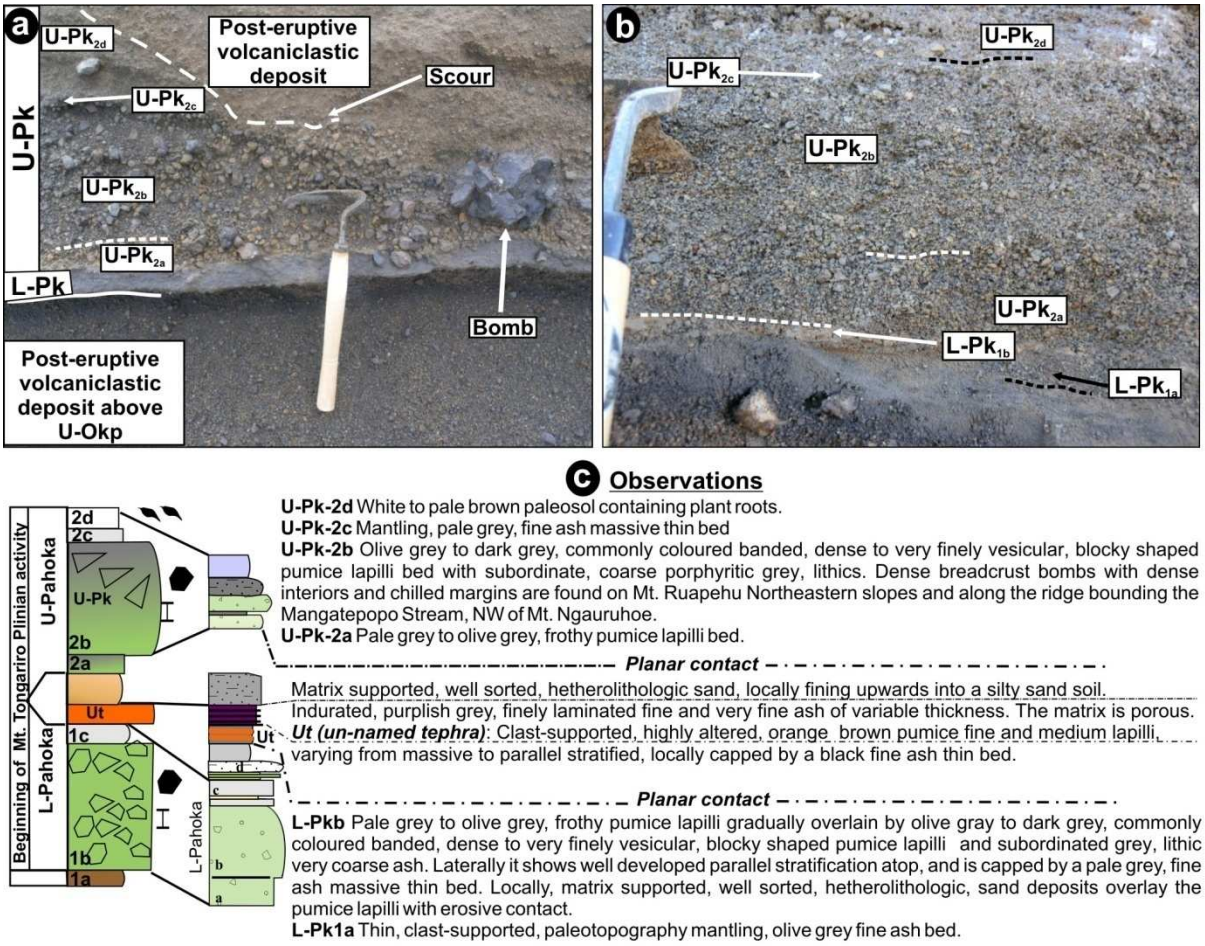

Figure 4.8 Upper Pahoka Tephra as exposed **a)** In proximal locations (< 6 km from source) on the northeastern slopes of Mt. Ruapehu. Note the dense, chilled bombs **b)** Typical facies at intermediate locations (13.5 km from source), showing the detailed textures representing the phases described in the text.

Interpretation: the unit represents at least five eruptive phases producing fall deposits of contrasting grain-size, the first two grouped within the L-Pk. The U-Pk_{2a} bed indicates that an opening event ejected degassed microlite-rich, foamy magma, probably from a conduit plug or collapsed magma foam. This event led to further magma decompression and development of the main Plinian column accumulating the U-Pk_{2b} fall deposit. The uppermost U-Pk_{2c} bed comprises ash accumulated from the dissipating cloud, and is overlain by post-eruptive hyperconcentrated flow deposits (U-Pk_{2d}) in the E-NE area.

Isopach and Isopleth maps: the new mapping data indicate that the Upper Pahoka Tephra was sourced from Mt. Tongariro (proto-Ngauruhoe). Isopachs show a clear lobe towards the

southeast (**Fig. 4.2f**), while isopleths show irregular proximal contours and regular mid-distal contours, supporting this source (**Fig. 4.3k, l**). There is no evidence supporting a source location between Mt. Ruapehu and Mt. Tongariro at the "Saddle Cone". The coarse bombs exposed on the north-eastern slopes of Mt. Ruapehu are enclosed within the same isopach/isopleths from Tongariro, including the extensive bomb field found on Mangatepopo Ridge (**Fig.1.2**).

4.2.4 Ash morphology

Ash particles (**Fig. 4.9**) indicate that the fragmenting magma had variable vesicularity. The Mangatoetoenui unit (**Fig. 4.9a**), the Okupata tephra (**Fig. 4.9e**) and the Mt. Tongariro-sourced Pahoka Tephra (**Fig. 4.9f**) are dominated by highly vesicular pumice with cuspate glass shards. Besides highly vesicular clasts, poorly to non-vesicular, platy and blocky ash grains with conchoidal fractures and v-shaped pits are present in the Shawcroft (**Fig. 4.9b**), Oruamatua (**Fig. 4.9c**), and Akurangi (**Fig. 4.9d**) units. There is high lithic content (up to 31 vol.% in the 3 ϕ size fraction) and up to 24 vol.% of the shards (normalized to total juvenile content) are only weakly vesicular, but the combination of distinctive quenching cracks together with abundant stepped-surfaces that would unequivocally indicate thermo-hydraulic explosions (e.g. Büttner et al., 1999; Dellino et al., 2001) is lacking. The fragmentation mechanisms will be discussed in **Chapter 5** but, as a preliminary hypothesis, these observations indicate that magma-water interaction occurred but did not play a major role in fragmenting the magma compared to decompression.

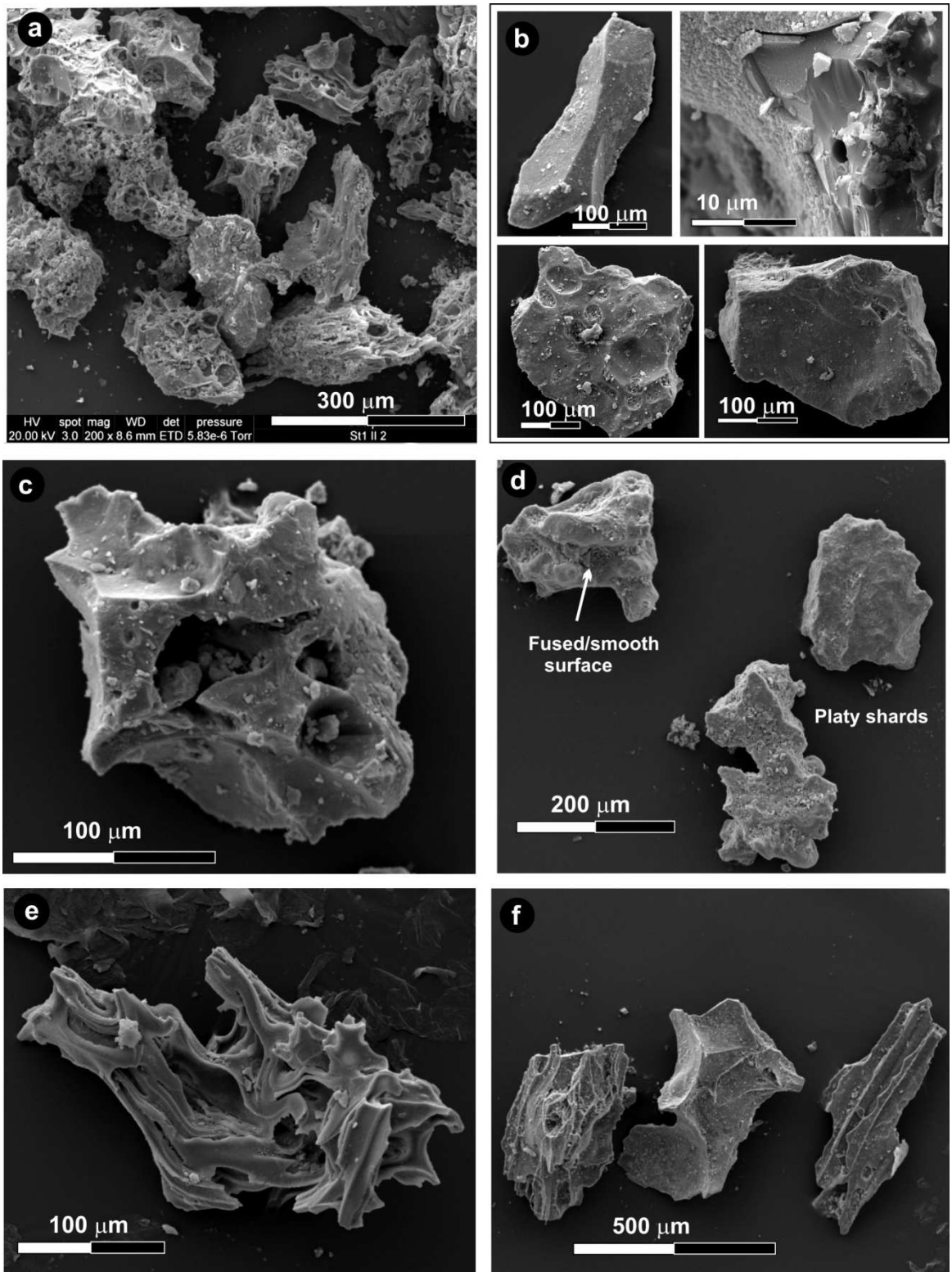

Figure 4.9 SEM images of juvenile ash grains: **a)** Mgt juvenile, highly vesicular glass shards; **b)** Sw poorly vesicular glass shards. Note the conchoidal fracture and sharp edges zoomed on the uppermost-right image; **c)** Oru coarsely vesicular shards with thick vesicle walls around large, irregular vesicles **d)** Ak platy-shaped and poorly vesicular glass shards; **e)** Okp fibrous glass shards; **f)** Mt. Tongariro Pk glass shards.

4.2.5 Eruptive parameters

The thickness of the studied fall units exponentially decrease over distance (**Fig.4.10**). Most of them show two linear segments when Log_{10} thickness (Log_{10} T) is plotted against distance, expressed as the square root of the isopach area ($A^{1/2}$), as is typical Plinian columns (Bonadonna et al., 1998). Isopach geometries are mostly bilobate, except for the Akurangi and Pahoka units (**Fig.4.2, Table 4.1**). The Mangatoetoenui, Okupata, Akurangi, and Pahoka units are characterized by nearly elliptical isopachs with wide radial expansion (aspect ratios >0.5 and shape factors >0.8), whereas the Shawcroft and Oruamatua units have elongate isopachs with narrower radial expansion (aspect ratios <0.5 and shape factors <0.65). In general, NE lobes are shorter than the main SE ones, except for Okupata tephras, which have a large lobe dispersed towards the north. The thinning rate of the SE lobes is highest for the Mangatoetoenui (5 cm isopach: 37.5 km from source) and L-and-U Okupata units (5 cm isopach: 33.9 km from source), and lowest in the Oruamatua eruptive unit (5 cm isopach: 76.5 km from source). The Shawcroft, Akurangi, and the Upper Pahoka units have intermediate values (5 cm isopach: 58.5 km, 68.5 km, and 52.1 km from source, respectively).

Eruptive Volumes

Due to limitations of exposure, individual units could only be traced reliably to the 5 cm isopach, out to ~80 km from source (**Figs. 1.2, 4.2**). Therefore, volume calculations (**Table 4.2**) are minimum estimates and significant volumes in distal areas are not accounted for. Depending on the method applied, the thinning rate used (k total or k_0-proximal), and the isopach shape (i.e. working with individual lobes or with whole-deposit contours), total volumes differ by between 8 and 31 %. If working with separate lobes the sum of the individual volumes show no significant difference relative to data taken from whole-deposit isopachs. However, to avoid possible overlapping when combining two lobes and based on irregular shapes of the erupted clouds, as shown by the Chaitén 2008 eruption (Lara 2009; Watt et al., 2009), the approximation of isopachs to perfect ellipses was avoided and the discussion is restricted to the results obtained from the irregular-shaped, whole-deposit maps. For the total data set (1 line-segment only), volumes calculated following Sulpizio (2005) and the traditional Pyle method (1989; modified by Fierstein and Nathenson 1992) are very similar (± 4-10 %); if integrating multiple segments (Bonadonna et al., 1998) and using the proximal thinning rate (k_0) in the Sulpizio (2005) method, calculated volumes differ by 1 to

16 %, except for Shawcroft and Pahoka units, where volumes are 30 and 57 % higher if applying the Sulpizio (2005) approach.

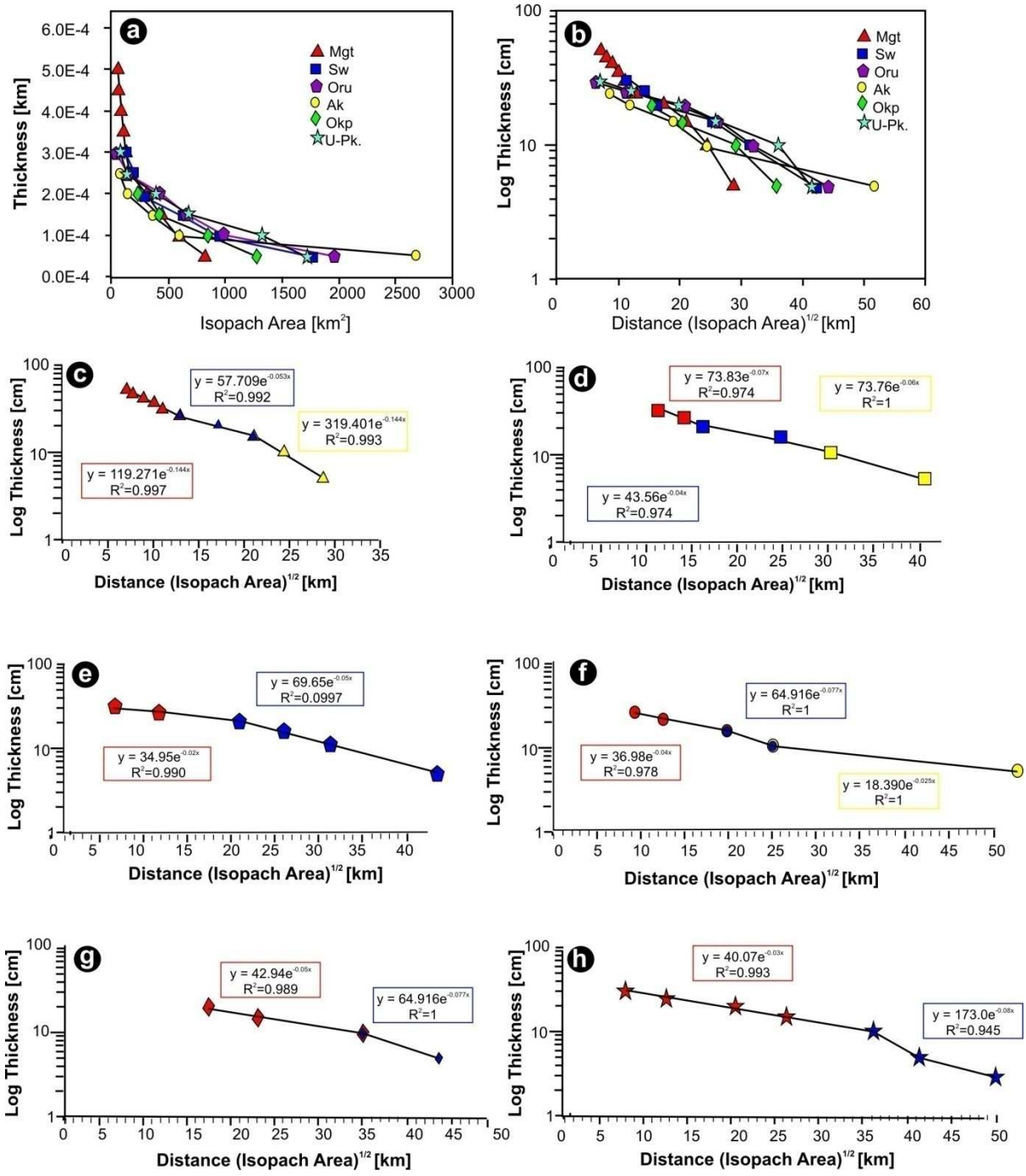

Figure 4.10 Whole-deposit isopach data plots for each eruption showing: **a)** thickness vs. Isopach area; **b)** Log (T) vs. Distance expressed as (Isopach Area)$^{1/2}$. Individual eruptive units show two to three individual segments with different slopes: **c)** Mangatoetoenui (Mgt); **d)** Shawcroft (Sw); **e)** Oruamatua (Oru); **f)** Akurangi (Ak); **g)** Combined Lower and Upper Okupata (Okp); **h)** Upper Pahoka (U-Pk). Colours in **c-h** separate different segments (S): proximal S_0 (red), proximal-intermediate S_1 (blue), and in some cases intermediate-distal S_2 (yellow).

Table 4.1 Isopach data for individual units and resulting geometrical values calculated with ArcGis 9.0 for the whole deposit and for individual lobes. T: thickness, A: area, P: perimeter, Sh: shape factor, ASE: area of the southeast lobe, ANE: area of the northeast lobe.

	WHOLE DEPOSIT			SE lobe						NE lobe					
T [cm]	A [km^2]	$A^{1/2}$	Sh	A_{SE} [km^2]	$A_{SE}^{1/2}$ [km]	Long axis	Short axis	Aspect ratio	Sh	A_{NE} [km^2]	$A_{NE}^{1/2}$ [km]	Long axis	Short axis	Aspect ratio	Sh
Mangatoetoenui Eruptive Unit (Mgt)															
50	52	7.2	0.6	37	6.1	11.0	3.1	0.3	0.5	16	4.0	7.9	2.7	0.3	0.6
45	63	8.0	0.8	47	6.8	12.0	3.7	0.3	0.7	23	4.8	8.5	2.7	0.3	0.6
40	83	9.1	0.5	59	7.7	12.5	4.3	0.3	1.0	44	6.7	13.9	2.5	0.2	0.6
35	105	10.3	0.5	73	8.6	13.0	5.4	0.4	0.8	52	7.2	14.4	2.7	0.2	0.6
30	126	11.2	0.5	98	9.9	14.1	6.8	0.5	0.8	63	7.9	14.6	3.0	0.2	0.6
25	169	13.0	0.6	166	12.9	15.6	8.6	0.6	0.8	79	8.9	15.8	3.5	0.2	0.6
20	293	17.1	0.6	264	16.3	22.6	12.8	0.6	0.8	102	10.1	17.2	5.0	0.3	0.6
15	442	21.0	0.6	403	20.1	27.2	16.0	0.6	0.9	146	12.1	19.0	5.5	0.3	0.7
10	596	24.4	0.6	526	22.9	30.6	19.2	0.6	0.9	208	14.4	21.7	6.1	0.3	0.7
5	824	28.7	0.6	696	26.4	34.2	23.5	0.7	0.9	315	17.7	26.5	7.6	0.3	0.7
Shawcroft Eruptive Unit (Sw)															
30	128	11.3	3.0	71	8.4	12.9	7.7	0.6	0.8	52	7.2	8.4	4.6	0.5	0.9
25	204	14.3	1.5	160	12.6	22.8	7.3	0.3	0.6	101	10.0	9.3	5.8	0.6	1.0
20	268	16.4	0.9	216	14.7	24.2	8.5	0.4	0.7	152	12.3	10.9	7.9	0.7	0.9
15	651	25.5	0.3	491	22.2	45.4	13.2	0.3	0.5	299	17.3	12.9	12.5	1.0	0.5
10	973	31.2	0.1	739	27.2	47.0	18.0	0.4	0.6	470	21.7	16.8	13.1	0.8	0.6
5	1764	42.0	0.0	1403	37.5	60.0	24.1	0.4	0.7	670	25.9	18.3	18.9	1.0	0.6
Oruamatua Eruptive Unit (Oru)															
30	38	6.2	0.7	55	7.4	14.6	4.2	0.3	0.6	33	5.7	9.3	4.5	0.5	0.7
25	133	11.5	0.5	151	12.3	28.8	4.9	0.2	0.4	47	6.8	10.3	4.9	0.5	0.7
20	438	20.9	0.4	377	19.4	38.5	10.5	0.3	0.5	136	11.7	20.0	6.8	0.3	0.6
15	684	26.2	0.5	555	23.6	43.0	14.3	0.3	0.5	245	15.7	29.9	8.6	0.3	0.5
10	1009	31.8	0.5	827	28.8	52.1	19.8	0.4	0.6	385	19.6	30.4	10.9	0.4	0.6
5	1965	44.3	0.5	1742	41.7	52.4	20.7	0.4	0.6	555	23.6	32.0	14.9	0.5	0.7
Akurangi Eruptive Unit (Ak)															
25	76	8.7	0.8	88	9.4	13.3	7.3	0.5	0.9						
20	141	11.9	0.8	157	12.5	18.1	9.8	0.5	0.9						
15	360	19.0	0.9	347	18.6	25.9	16.6	0.6	0.9						
10	587	24.2	0.9	625	25.0	30.4	23.1	0.8	0.9						
5	2684	51.8	0.9	2576	50.8	69.0	13.6	0.2	0.9						
L-and-U-Okupata Eruptive Unit (Okp)															
20	243	15.6	0.7	43	6.6	10.5	5.7	0.5	0.9	240	15.5	23.3	13.0	0.6	0.8
15	396	19.9	0.5	173	13.2	19.1	10.5	0.5	0.9	349	18.7	25.4	18.0	0.7	0.9
10	839	29.0	0.5	394	19.8	26.3	17.1	0.7	0.9	552	23.5	28.1	24.0	0.9	0.9
5	1274	35.7	0.6	927	30.4	31.9	26.8	0.8	0.9	754	27.5	30.4	30.4	1.0	0.9
U-Pahoka Eruptive Unit (UPk)															
30	53	7.3	0.8	7	11.0	6.2	0.6	0.8							
25	144	12.0	0.7	12	19.3	8.4	0.4	0.7							
20	402	20.0	0.9	20	24.2	18.9	0.8	0.9							
15	673	25.9	0.9	26	31.2	25.1	0.8	0.9							
10	1315	36.3	0.9	36	44.0	36.2	0.8	0.9							
5	1727	41.6	0.9	42	51.9	40.5	0.8	0.9							

The calculated minimum erupted volumes for the selected units range between 0.2 and 1.2 km^3 using the range of methodologies described above. Following the Sulpizio (2005) method and considering the uncertainties given by the lack of distal isopach data, calculated volumes range between 0.3 and 0.6 km^3, assuming Vp/Vt < 0.3 (**Table 4.2**).

Table 4.2 Eruptive volumes in km^3 obtained using methods from different authors, considering 1 single segment, multiple segments, as well as the data from whole-deposits and as obtained from individual depositional lobes.

Unit	Pyle (1989, modified by Fierstein and Nathenson 1992, and Bonadonna et al. 1998)								Sulpizio (2005)															
	Whole deposit		SE Lobe		NE Lobe		Combined lobes		Whole deposit using k vs Aip1/2			Whole deposit using k0 vs Aip1/2			SE + NE lobes using k vs Aip1/2			SE + NE lobes using k0 vs Aip1/2			Observed BS_{12} [km]	Observed BS_{23} [km]	$Aip^{1/2}$calc (k) (Sulpizio 2005)	$Aip^{1/2}$calc (k0) (Sulpizio 2005)	0.01 Tmax (Vol 1 segment)	D [km^2] Walker (1973)
	1 seg	mult.seg.	1 seg	mult.seg.	1 seg	mult.seg.	1seg	mult	Vp/Vt<0.3	0.3<Vp/Vt<0.7	Vp/Vt>0.7	Vp/Vt<0.3	0.3<Vp/Vt<0.7	Vp/Vt>0.7	Vp/Vt<0.3	0.3<Vp/Vt<0.7	Vp/Vt>0.7	Vp/Vt<0.3	0.3<Vp/Vt<0.7	Vp/Vt>0.7						
Mgt	0.2	0.2	0.2	0.2	0.1	0.1	0.3	0.3	0.3	1.9	1.5	0.2	0.4	1.1	0.3	0.8	2.3	0.4	1.2	3.5	12.5	21.1	31.4	25.4	1.0	2254
Sw	0.5	0.3	0.3	-	0.2	0.1	0.5	0.4	0.6	1.0	3.0	0.3	0.6	4.8	0.6	1.0	3.1	0.6	1.1	3.3	16.0	27.6	59.3	38.7	0.6	8483
Oru	0.4	0.4	0.3	0.3	0.1	0.1	0.5	0.4	0.5	0.9	2.7	0.8	1.1	3.0	0.6	1.1	3.2	1.1	1.8	5.4	20.9	20.9	62.9	107.1	0.5	9600
Ak	0.5	0.6	-	-	-	-	-	-	0.6	1.0	3.0	0.4	0.7	2.2	-	-	-	-	-	-	19.4	24.3	80.8	61.6	0.3	16184
Okp	0.3	0.2	0.1	0.1	0.2	0.2	0.3	0.3	0.4	0.6	1.8	0.4	0.8	2.2	0.4	0.8	2.3	0.5	1.0	2.9	29.2	-	45.7	58.4	0.6	4943
UPk	0.4	0.4	-	-	-	-	-	-	0.5	0.9	2.8	1.2	1.9	5.7	-	-	-	-	-	-	29.3	-	59.3	96.8	0.5	8483

k: slope (thinning rate) when all data are fit within a single curve; k_0: slope of the proximal segment when multiple segments are identified (maximum case). A_{ip}= observed isopach area at the inflexion point when multiple segments are considered. Vp: proximal volume. Vt: total volume. $A_{ip}^{1/2}$= distance from vent expressed as the square root of the isopach area in km. The suffix "calc" stays for calculated when using Sulpizio (2005) method. BS_{12}: break in slope between the first two segments; BS_{23}: break in slope between the second and third segments. D: Dispersal index obtained by extrapolating the area enclosed within the $0.01T_{max}$ isopach (Walker 1973). T_{max}= maximum thickness. Eruptive units: Mangatoetoenui (Mgt), Shawcroft (Sw), Oruamatua (Oru), Akurangi (Ak), Okupata Tephras (Okp*), and Upper Pahoka Tephra (UPk).

Isopleths and classification of the eruptions

Lithic and pumice isopleths (**Fig.4.3**) are irregularly shaped and suggest two directions of dispersion, similar to the corresponding isopachs. The Mangatoetoenui unit (**Fig. 4.3a, b**) has a main lobe towards the SE (0.5 cm isopleths reach 35 km), and a shorter lobe towards the NE. The Shawcroft contours are more irregularly shaped (**Fig. 4c, d**), with proximal lithic isopleths toward the east, but more distal <3 cm isopleths are deflected towards the southeast (0.5 cm isopleths extend 42 km). The secondary Shawcroft NE-lobe is well defined by

pumice and lithic lapilli isopleths, and is bent in distal reaches to the east. The highly irregular shapes of proximal lithic isopleths might reflect multiple vents. The Oruamatua Eruptive Unit (**Fig. 4.3e, f**) has a main lobe towards the SE (0.5 cm: 57 km from the vent) and a smaller lobe towards the NE, which is best reflected by pumice isopleths. For the Akurangi Unit (**Fig. 4.3g, h**) and the Okupata tephras (**Fig. 4.3i, j**) the NE-lobe is straight and as large as the SE-lobe. For the whole deposit, both isopleths and isopachs, all studied units fit within the Pyle (1989) Plinian classification (**Fig 4.11a, Table 4.3**). Estimated dispersal areas inside the 0.01 T_{max} isopach (c.f., Wilson 1976) are greater than 2000 km^2.

Table 4.3 Geometrical parameters obtained from whole-deposit isopach and isopleths data.

Unit	Mangatoetoenui				Shawcroft				Oruamatua			Akurangi				(L+U) Okupata			Upper Pahoka		
	1Seg	S0	S1	S2	1Seg	S0	S1	S2	1Seg	S0	S1	1Seg	S0	S1	S2	1Seg	S0	S1	1Seg	S0	S1
bt	4.0	3.2	6.2	2.7	7.8	5.0	8.7	6.1	8.3	14.5	6.5	4.0	3.2	6.2	2.7	6.0	7.7	3.8	7.8	13.0	4.9
bc (lithics)	6.5	6.5	6.5	6.5	5.6	5.6	5.6	5.6	9.8	9.8	9.8	5.8	5.8	5.8	5.8	9.8	9.8	9.8	6.5	6.5	6.5
bc/bt*	1.6	2.0	1.1	2.4	0.7	1.1	0.6	0.9	1.2	0.7	1.5	1.4	1.8	0.9	2.1	1.6	1.3	2.6	0.8	0.5	1.3
bc (pumice)	7.8	7.8	7.8	7.8	9.1	9.1	9.1	9.1	13.0	13.0	13.0	7.0	7.0	7.0	7.0	9.8	9.8	9.8	19.6	19.6	19.6
bc/bt^	1.9	2.4	1.3	2.9	1.2	1.8	1.0	1.5	1.6	0.9	2.0	1.7	2.2	1.1	2.6	1.6	1.3	2.6	2.5	1.5	4.0

Following the terminology of Pyle (1989): bt= "thickness half-distance" is the distance at which the thickness decreases to one half of its maximum value, which describes the morphology of the deposit; bc = "clast half-distance" is the distance at which the maximum clast diameter halves with respect to its maximum value, reflecting the corresponding column height. Hence, bc/bt gives an estimation of the fragmentation index. 1Seg: considering all data as one single segment; S0-2: Individual segments as separated by colours in **Fig. 4.10**.

Column Heights, mass discharge rates, and eruptive magnitude

A two-lobe geometry explains best fits the field data, and column height (H_T) was calculated for each individual lobe. SE-lobes suggest relatively higher H_T, varying from 21 to 37 km by either Sulpizio (2005) or Carey and Sparks (1986) methods. On the other hand, the NE-lobes indicate columns between 17.5 and 28 km. In general, column heights obtained by all applied methods reached stratospheric levels.

When plotting cross-wind vs. down-wind maximum ranges (**Fig. 4.11b**) as done by Carey and Sparks (1986), most of the data imply strong winds (>>30 m/s), except during deposition of the Oruamatua eruptive unit (10 to 15 m/s). Volume discharge rates (Q) calculated from column heights obtained with the Sulpizio (2005) method are on the order of ~10^4 m^3/s, except for the Oruamatua and Akurangi units (**Fig. 4.11c, d**), which are up to one order of magnitude higher (~10^5 m^3/s). Corresponding mass discharge rates (MDR) vary between ~10^7 to 10^8 kg/s (**Figs. 4.11c, d**), as is characteristic of Plinian eruptions.

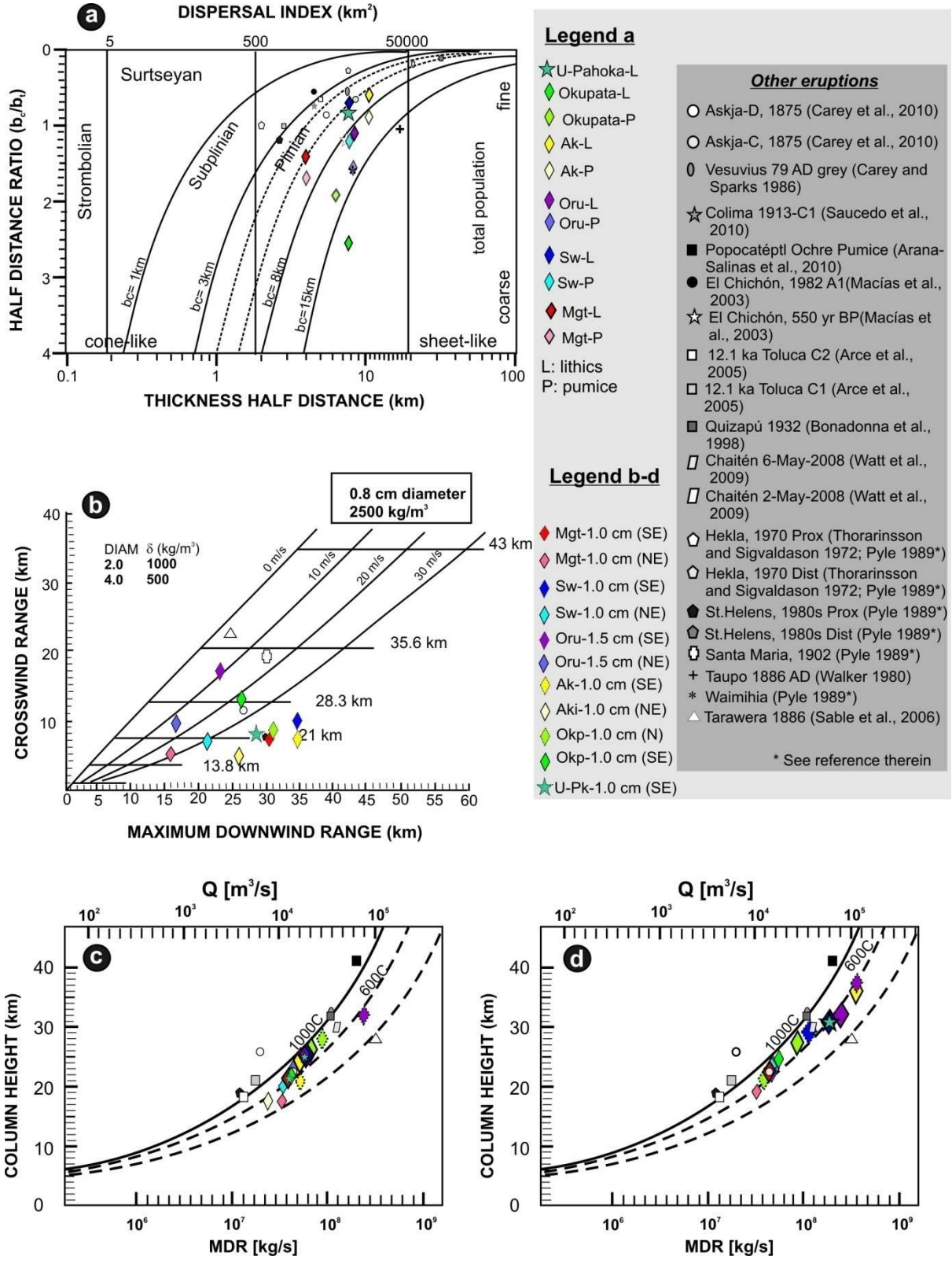

Figure 4.11 Classification schemes for the studied eruptions: **a)** Isopach and Isopleth data in the Pyle (1989) diagram lie within the Plinian field; **b)** Isopleth data in the Carey and Sparks (1986) diagram for column height and wind-speed, based on 0.8 cm-diameter lithic clasts data; **c-d)** Sparks (1986) diagram to determine Mass discharge rates considering column heights obtained with the Carey and Sparks (1986) method **(c)** and Sulpizio (2005) method **(d)**. Other eruption parameters are respectively plotted for comparison.

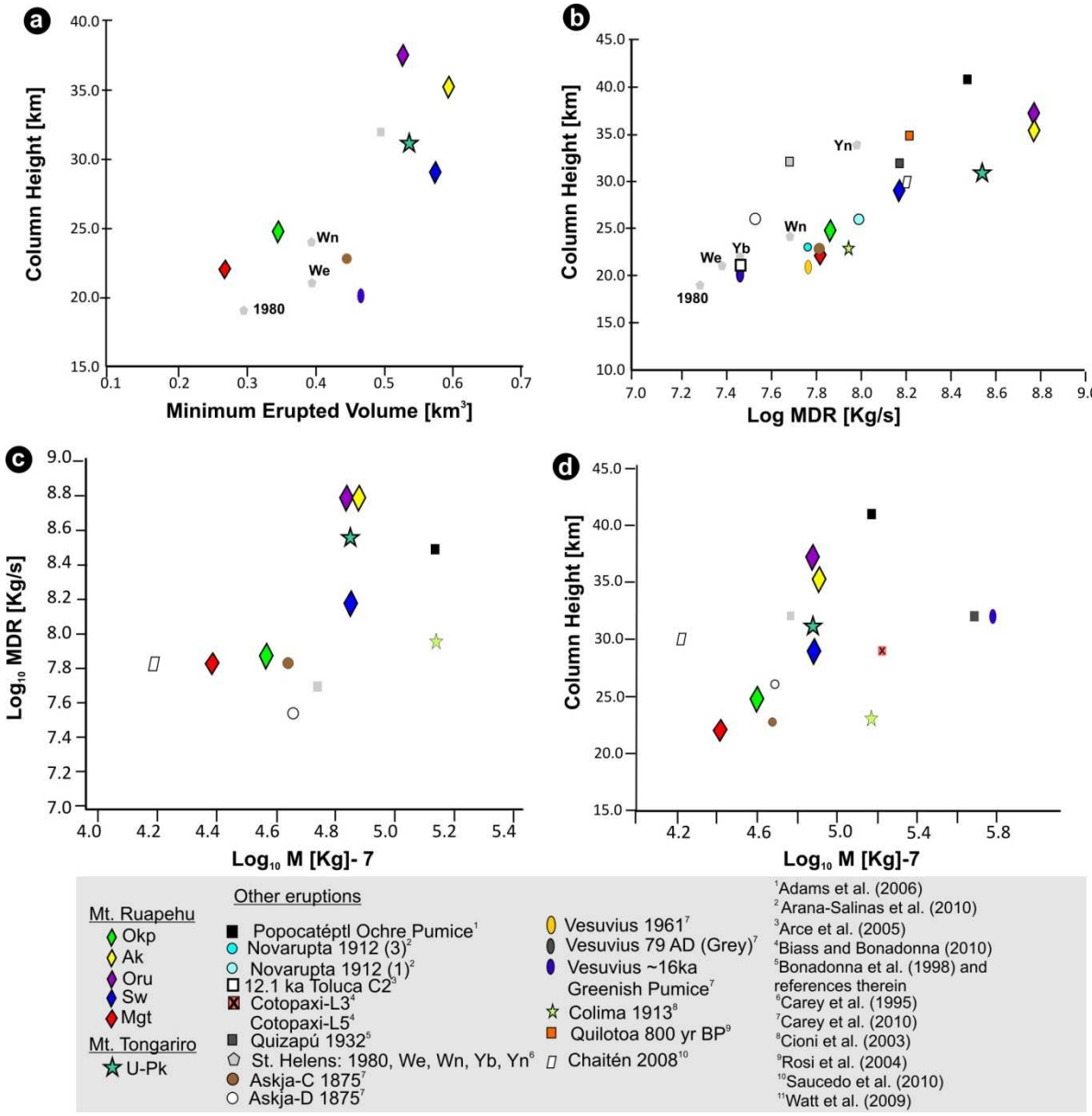

Figure 4.12 Comparison of eruptive parameters with others published for Plinian eruptions at andesitic volcanoes worldwide. Our data indicate: **a)** increasing column heights with erupted volume as obtained from the whole deposit of each unit and **b)** with MDR; **c-d)** eruptive intensity (MDR) and column height vs. magnitude (M = Log (Mass of the deposit in kg) – 7), with higher intensities **(c)** and column heights **(d)** reached at larger magnitudes.

Table 4.4 Estimated eruptive parameters considering the volume (expressed as a minimum value Vol*) calculated by using the method of Sulpizio (2005).

	Unit	Mgt	Sw	Oru	Ak	Okp	U-Pk
Column Heights (Ht) [km]	***Vol* [km^3]***	0.3	0.6	0.5	0.6	0.4	0.5
	Ht-Sparks (1986)	21.4	25.0	25.0	24.3	26.0	25.0
	Ht-Sulpizio (2005)	22.8	31.1	32.0	36.2	27.4	31.1
	Ht_{SE}: Sulpizio (2005)	22.0	29.0	37.2	35.3	24.8	31.1
	Ht_{NE}: Sulpizio (2005)	18.9	23.4	23.4	-	21.3	-
	Ht_{SE}: Carey and Sparks (1986)	21.0	25.0	32.0	21.0	22.0	21.5
	Ht_{NE}: Carey and Sparks (1986)	17.5	20.0	23.0	17.5	28.0	-
Volume discharge rate (Q) [m^3/s]	***Q: Sparks (1986)***	1.9E+04	3.4E+04	3.4E+04	3.1E+04	4.0E+04	3.4E+04
	Q: Sulpizio (2005)	2.4E+04	8.0E+04	8.9E+04	1.4E+05	4.9E+04	8.0E+04
	Q_{SE}: Sulpizio (2005)	2.1E+04	6.1E+04	1.6E+05	1.3E+05	3.3E+04	-
	Q_{NE}: Sulpizio (2005)	1.2E+04	2.7E+04	2.7E+04	-	1.8E+04	-
	Q_{SE}: Carey and Sparks (1986)	1.8E+04	3.4E+04	8.9E+04	1.8E+04	2.1E+04	1.9E+04
	Q_{NE}: Carey and Sparks (1986)	8.7E+03	1.5E+04	2.5E+04	8.7E+03	5.3E+04	-
Mass Discharge rate (MRD) [kg/s]	***MDR: Sparks (1986)***	6.0E+07	7.8E+07	7.5E+07	7.0E+07	8.0E+07	7.8E+07
	MDR: Sulpizio (2005)	6.8E+07	3.5E+08	4.5E+08	6.0E+08	9.2E+07	3.5E+08
	MDR_{SE}: Sulpizio (2005)	6.8E+07	1.5E+08	6.0E+08	6.0E+08	7.5E+07	-
	MDR_{NE}: Sulpizio (2005)	5.5E+07	7.0E+07	7.0E+07	-	6.0E+07	-
	MDR_{SE}: Carey and Sparks (1986)	6.0E+07	7.8E+07	4.3E+08	7.2E+07	6.2E+07	6.0E+07
	MDR_{NE}: Carey and Sparks (1986)	5.5E+07	5.8E+07	7.0E+07	4.0E+07	9.8E+07	-
Eruptive magnitude (M)	***Vol (m^3)***	3.0E+08	6.0E+08	5.0E+08	6.0E+08	4.0E+08	5.0E+08
	Wet Deposit density (kg/m^3)	990.2	1348.6	1449.6	1380	1156.7	1441
	Total Mass (kg)	2.97E+11	8.09E+11	7.25E+11	8.28E+11	4.63E+11	7.21E+11
	M =(Log_{10}Mass)-7	4.5	4.9	4.9	4.9	4.7	4.9

Eruptive units: Mangatoetoenui (Mgt), Shawcroft (Sw), Oruamatua (Oru), Akurangi (Ak), Combined Lower and Upper Okupata tephras (Okp*), and Upper Pahoka Tephra (U-Pk). $Ht_{SE,NE}$: total column height for the southeast and northeast lobe, respectively. Q: volume discharge rate; the suffix SE or NE stays for estimated Q based on the southeast or northeast lobe Ht data. MDR: mass discharge rate; the suffix SE or NE stays for estimated MDR based on the southeast or northeast lobe Ht data. M: eruptive magnitude calculated from the total mass of the deposit.

When plotting H_T vs. Q and vs. MDR (**Figs. 4.11c, d**), all data indicate magma eruption temperatures between 600°C and 1000°C, as expected (cf. Sparks 1986). Independently of the input data (whole-deposit or individual lobe) and the method used to obtain H_T values, the Mangatoetoenui Unit has the smallest H_T and MDR values, and the Oruamatua the highest (**Fig. 4.12**). The magnitudes M estimated by the Pyle (2000) method are >4.9 (apart from Mangatoetoenui M >4.4 and Okupata >4.6), similar to other Plinian eruptions (**Table 4.4** and **Fig. 4.11**).

4.2.6 Discussion

A segmented distribution of tephra thickness over distance for Plinian fall deposits was explained by Bonadonna et al. (1998), as the result of the deposition of particles having different Reynolds-numbers (*Re*). The pumice and lithic clasts accumulated during the main eruptive phases of each selected unit correspond to high and intermediate *Re* particles (coarse ash and lapilli), lifted to 15-35 km in the atmosphere, which suggests that most of the particles were incorporated in the turbulent-flow regime of the eruptive cloud and were accumulated according to their inertial settling velocities, independent of air viscosity (cf. Bonadonna et al., 1998). Hence, thinning rate is better described by exponential laws than by power laws (**Fig. 4.10**).

Using the method of Pyle (1989; modified by Fierstein and Nathenson 1992), integrating multiple segments usually provides a smaller volume than working with a single segment. This might be due to the fact that most of our data lie within proximal and medial regions, where the last segment usually has a faster thinning rate than the most proximal segments (**Fig.4.9b**). Data published for other eruptions (e.g. Hudson-1991; Cerro Negro-1971; Sulpizio 2005) suggest that this is a common feature for the first 50 km, before the deposit begins to display the typical exponential or power-law thinning trend with distance (c.f. Walker 1973; Pyle 1989, Fierstein and Nathenson 1992). This is likely due to particle aggregation, with accretionary lapilli beds reflecting the efficiency of high columns in promoting fine-particle aggregation (Watt et al., 2009). Alternatively it may reflect poor preservation of the complete fall sequence at every location, and/or fluctuating winds during each eruptive phase. Most tephras described here are >5 cm thick and within the lapilli to very coarse ash grade (1-64 mm in diameter), hence the Sulpizio (2005) method, in which the

break in slope is calculated from the proximal-intermediate dataset, is more appropriate. It is impossible however, to define the actual relationship between proximal (Vp) and total volume (Vt), and thus possible ranges are presented in **Table 4.2**. These data show that the Mangatoetoenui Unit is the smallest described (0.3 km^3), with the others having volumes ~0.5-0.6 km^3. Erupted volumes of the multi-bedded lithofacies association type-3 units (Oruamatua, Akurangi and Okupata) do not account for the associated co-Plinian pyroclastic density current deposits.

The asymmetrical and irregular shapes of isopleths reflect the strong influence of the local wind pattern. The bilobate isopachs and isopleths (**Figs. 4.2 and 4.3**) suggest two predominant wind directions (north-westerlies and south-westerlies), varying: **a)** with time, so that pauses between eruptive pulses/phases cannot be distinguished, or **b)** with altitude in the atmosphere, so that higher portions of the plume could have been affected by north-westerlies, and the lower portion by south-westerlies. Both options are very likely in the North Island, where wind direction and speed can significantly change within a few hours (cf. Cronin et al., 1998; Turner and Hurst 2001).

The deflection of the dispersal axis reconstructed from both lithic and pumice data of the Shawcroft Unit (**Figs. 4.3a, c**), and pumice data from the Oruamatua Unit (**Fig. 4.3f**) suggests important cross-wind effects in these cases, causing bending of the plume. Deflections of the eruptive plume axis and multiple lobes have been recently documented from field data and simulated maps for other high-latitude volcanoes, such as Katla-1676 ± 12 and ~3600 yr BP (Larsen et al., 2001), Askja-1875 (Carey et al., 2010), and Hudson-1991 (Kratzmann et al., 2010); the complexity of tephra dispersion, strong contour distortion, axis bending, and the influence of shifts in the wind-direction over a short time interval (hours), were well exhibited by the eruption of Chaitén (Chile) in 2008 (Lara 2009; Watt et al., 2009).

Our data are consistent with similar eruptions at other andesitic-dacitic stratovolcanoes (**Figs. 4.11, 4.12**). It is clear that the lack of distal data containing low-*Re* particles information (cf. Bonadonna et al., 1998), and the Late Pleistocene windy, poorly vegetated periglacial conditions unfavourable for tephra preservation, are crucial factors in causing significant underestimations of erupted volumes.

When plotting H_T and Log_{10} MDR vs. erupted magnitude, expressed as (Log_{10} (Total Deposit Mass) -7), a weak positive correlation indicates that larger column heights and eruptive intensities correlate with larger eruptive magnitudes (**Fig. 4.12**). Mangatoetoenui and

Okupata eruptions were the least violent of those studied, whereas Shawcroft, Oruamatua, and Akurangi were the most violent explosive eruptions known from Mt. Ruapehu. All of the most violent eruptions produced deposits between 13,635 ± 165 cal years BP and ~11 ka BP cal. These units show a characteristic basal thin, fine-ash bed linked to a phreatomagmatic opening phase, as interpreted for lithofacies associations 2 and 3. They also show the highest content of non-juvenile, highly hydrothermally altered lithics in the deposits of the Plinian phases, indicating strong conduit erosion (e.g. Wilson et al., 1980; Macedonio et al., 1994) during the eruption and probably the disruption of a pre-existing hydrothermal system (e.g. Varekamp 1993; Thouret et al., 2002). Juvenile shards in the 3 ϕ size fraction (**Fig. 4.9**) in the Shawcroft, Oruamatua, and Akurangi units contain poorly vesicular, blocky shards showing conchoidal fractures and rare stepped surfaces (c.f. Buttner et al., 1999; Dellino et al., 2001), which occur together with the highly vesicular shards. This implies some degree of magma-water interaction occurred, but its role in fragmentation is not well understood.

Our study reveals that Mt. Ruapehu is capable of producing events of magnitudes 4 to 5. The characterization and quantification of Late Pleistocene events (the last one close to ~11,620 ± 190 cal years BP) indicate that the greatest hazard scenario expected for this volcano involves Plinian columns similar to those produced during the eruptions of Askja 1875 (Carey et al., 2010) and Chaitén 2008 (Lara 2009; Watt et al., 2009).

4.3.7 Conclusions

Deposits of five Plinian-style eruptions were quantified, corresponding to three contrasting lithofacies associations in the geological record of Mt. Ruapehu. These represent the most violent eruptions known for this volcano. Isopach and isopleth maps indicate that the North Crater was the main active vent during the Late Pleistocene, responsible for all eruptions, except for the last one (11,620 ± 190 cal years BP), which may have its source at or near the South Crater. Erupted volumes varied from at least 0.3 to 0.6 km^3, column heights ranged between 22 and 37 km, volume discharge rates from ~10^4-10^5 m^3/s, mass discharge rates from ~10^7-10^8 kg/s and estimated magnitudes (M = Log_{10} Deposit mass [kg] -7) from 4.4 and 4.9. All of these values are characteristic of Plinian eruptions, two to three orders of magnitude larger than eruptions occurring over the past ~3 ka BP cal. (c.f. Donoghue 1991; Donoghue et al., 1995b).

Tephra dispersal patterns were complex, the result of high to intermediate *Re* particles dispersed within the turbulent portion of an ash cloud subject to strong cross-winds and wandering plume effects.

Based on our results, the Oruamatua and Akurangi eruptions were the strongest produced by Mt. Ruapehu in the Late Pleistocene and represent the maximum probable scenario expected for this volcano. These units indicate that the most violent eruptions occurred when porphyritic magma bodies suddenly decompressed, involving high erosion of the conduit under high mass-discharge rates, and producing unsteady, partially collapsing eruptive columns. Dilute and concentrated pyroclastic density currents represent the greatest hazard down the main proximal catchments, and coarse grained tephras (lapilli size) can fall over distances ~30 km, reaching the town of Waiouru.

Future mitigation strategies should consider the potential illustrated in this study for high-intensity eruptions in combination with the low frequency of such large events, and a population that has never experienced such an eruption.

MASSEY UNIVERSITY
GRADUATE RESEARCH SCHOOL

STATEMENT OF CONTRIBUTION TO DOCTORAL THESIS CONTAINING PUBLICATIONS

(To appear at the end of each thesis chapter/section/appendix submitted as an article/paper or collected as an appendix at the end of the thesis)

We, the candidate and the candidate's Principal Supervisor, certify that all co-authors have consented to their work being included in the thesis and they have accepted the candidate's contribution as indicated below in the *Statement of Originality*.

Name of Candidate: Natalia Pardo Villaveces

Name/Title of Principal Supervisor: Professor Shane J Cronin

Name of Published Research Output and full reference:

Pardo N, Cronin SJ, Palmer A, Procter J, Smith I (2012b, in press). Andesitic Plinian eruptions at Mt. Ruapehu: quantifying the uppermost limits of eruptive parameters. Bull Volcanol. doi: 0.1007/s00445-012-0588-y

The final publication is available at www.springerlink.com

In which Chapter is the Published Work: Chapter 4 and Appendix J.2

Please indicate either:

- The percentage of the Published Work that was contributed by the candidate:

  and / or

- Describe the contribution that the candidate has made to the Published Work:

  Natalia Pardo carried out the field data collection and mapping, digital mapping and calculation of eruptive parameters, as well as the manuscript preparation and writing

Natalia Pardo
Digitally signed by Natalia Pardo
DN: cn=Natalia Pardo, o=Massey University, ou=INR, email=N.Pardo@massey.ac.nz, c=NZ
Date: 2012.05.04 12:13:12 +12'00'

Candidate's Signature

7/05/2012
Date

Shane J Cronin
Digitally signed by Shane J Cronin
DN: cn=Shane J Cronin, o=Massey University, ou=Institute of Natural Resources, email=s.j.cronin@massey.ac.nz, c=NZ
Date: 2012.05.10 10:17:20 +12'00'

Principal Supervisor's signature

10/5/2012
Date

Magma composition, fragmentation, and pyroclastic deposition

This chapter presents the petrography of the pyroclasts found within the Plinian deposits illustrated in ***Chapter 4****. Local grain-size distribution, ash componentry, juvenile ash morphology, bulk-rock, and groundmass glass composition analyses are shown and discussed. From these data, the fragmentation mechanism could be inferred and the magma characteristics are discussed in correlation with external factors to address the implications of fragmentation on eruption column stability. The corresponding methodology is explained in* ***Chapters 2.2.1, 2.2.2, 2.2.4*** *and* ***2.2.7****.*

5.1 Introduction

A key concept in explosive volcanic eruptions is the magma fragmentation. That is, the transformation from a liquid with dispersed crystals and gas bubbles into a gas with dispersed liquid drops and solid particles (e.g., McBirney and Murase 1970; Klug and Cashman 1996), rapidly accelerating towards the surface and ejected from a vent (Walker 1973; Wilson et al., 1980; Fisher and Schmincke 1984). The investigation on the fragmentation mechanism (i.e., magmatic vs. phreatomagmatic) and styles (brittle or ductile: Proussevitch et al., 1993; Mader 1998; decompression-dominated: Alidibirov and Dingwell 2000; Cashman et al., 2000; Spieler et al., 2004a,b; or induced by shear: Papale 1999) is a key factor to understand: (1) "internal" magma conditions, such as volatile content (Wilson et al., 1980; Carey and Sparks 1986) and rheological state of the magma shortly at the onset of the eruption (Dingwell 1998); and (2) "external" conditions, such as the degree of interaction with surrounding hydrothermal systems and the conduit capability of allowing groundwater inflow (Heiken 1972; Lorenz 1973; White 1991; Zimanowski et al., 1997; Cioni et al., 2003; Houghton et al., 2004).

The physical properties of Plinian eruptions (McBirney 1973; Klug and Cashman 1996; Rust and Cashman 2004), magma fragmentation mechanisms and thresholds have been mainly focused on the rhyolitic and basaltic end-member magmas, mostly associated with caldera volcanism (Klug et al., 2002; Polacci et al., 2003). This study applies and develops the concepts exposed above to investigate the case of intermediate, andesitic compositions ($55<SiO_2<65$ %). This chapter provides a detailed description of the Mangatoetoenui, Shawcroft, Oruamatua, and Okupata-Pourahu eruptive units, quantified in **Chapter 4**, and representing the range of contrasting behaviour of Plinian eruption columns throughout the Late Pleistocene history of Mt. Ruapehu (**Chapter 3**). In order to understand the correlation

between the distinctive lithofacies associations identified in the field (**Chapters 3, 4**) and the eruptive dynamics, grain-size, componentry, microscopic texture (optical and SEM), and geochemical analyses (**Chapter 2**) are here presented and discussed. Magma fragmentation mechanisms and styles are addressed in correlation with the existing data on the limits of peak column heights, erupted volumes, and magma discharge rates (**Chapter 4**).

5.2 Results: Contrasting Plinian behaviour at Mt. Ruapehu

Based on the quantification of the eruptive parameters shown in **Chapter 4**, microscopic analyses will be presented for: **a)** the **Mangatoetoenui Eruptive Unit (Mgt)**, representing the case of non-collapsing but **oscillatory** (i.e. in height) eruptive columns (lithofacies association type LA-1); **b)** the **Shawcroft Eruptive Unit (Sw)**, representing the case of **steady** eruptive columns (LA-2); **c)** the **Oruamatua Eruptive Unit (Oru)** and the **Okupata-Pourahu Eruptive Unit (Okp-Ph)**, representing the case of **unsteady, collapsing** columns. The observations and interpretations presented here for the Orauamatua eruptive unit are also representative of the **Akurangi Eruptive Unit (Ak)**.

5.2.1 Non-collapsing, oscillatory columns of intermediate height (20-25 km): The Mangatoetoenui eruptive unit

Lithofacies: deposits representing the four eruptive phases identified within the Lower Mangatoetoenui subunit (L-Mgt) and the three phases of the Upper-Mangatoetoenui subunit (U-Mgt) were analyzed. The type location for this description is B15 (**Fig. 5.1; Appendix A**), 10 km east of the vent (North Crater of Mt. Ruapehu). As previously discussed in **Chapter 4**, the exposed L-Mgt facies represents a short-lived, vent/conduit opening phase, rapidly followed by the first Plinian eruption, comprising waxing, climactic and waning phases. After a short time interval represented by fluvial deposits (in some localities), the U-Mgt signals a resumption of eruptive activity with the second Plinian eruption also comprising three phases (**Fig.5.1**).

The deposits produced from individual eruptive phases are characterized by a unimodal, negatively skewed grain-size distribution (**Table 5.1; Fig. 5.2; Appendix C**), typical of coarse-grained, poorly to well sorted pyroclastic fall deposits (c.f., Cas and Wright 1987).

The polymodal distribution of the uppermost ash bed within the U-Mgt indicates that the original fall deposit was partially reworked by post-eruptive fluvial or aeolian processes.

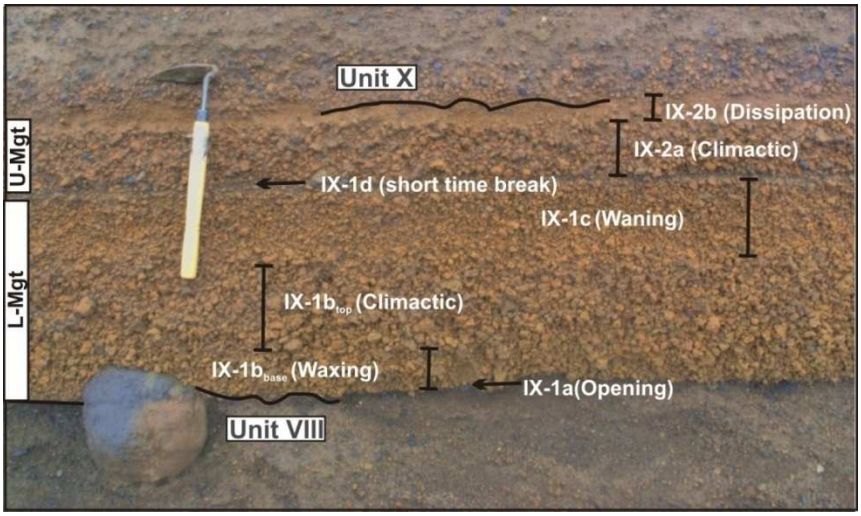

Figure 5.1 Mangatoetoenui Eruptive Unit, consisting of two main subunits separated by a thin fluvial deposit (IX-1d) marking a short-time break in the eruptive activity. The L-Mgt indicates a vent/conduit opening phase (IX-1a) immediately followed by the main Plinian event (IX-1b-and-c). The second Plinian (IX-2) deposit locally overlies a thin fluvial deposit (B15, in **Appendix A**).

Table 5.1 Statistical results of grain-size analyses carried on for each eruptive unit at localities B50 and B14 (9-10 km from the vent; **Appendix A**). L/U-Mgt: Lower/Upper Mangatoetoenui; Sw: Shawcroft; Oru: Oruamatua; L/U-Okp: Lower/Upper Okupata Tephra; Ph: Pourahu.

Unit	Sample	Inman Statistics			Folk & Ward (1957)				Classification		
		Median Diameter (Md_ϕ)	Graphic Standard deviation (σ_ϕ)	Graphic skewness (SkG)	Graphic Mean (Mz)	Inclusive Graphic Standard deviation (σ_i)	Inclusive Graphic Skewness (Sk_i)	Graphic Kurtosis (KG) Folk (1980)	Sorting (Cas and Wright 1987)	Skeweness	Kurtosis
L-Mgt	B14-IX-1a	-3.3	1.7	0.6	-2.7	2.0	0.6	2.0	Poorly sorted	Coarse grains domain	Very leptokurtic
	B14-IX-1b	-3.3	1.1	0.2	-3.1	1.6	0.4	1.9	Well sorted		
	B14-IX-1c	-2.5	1.3	0.3	-2.3	1.6	0.4	1.6			
U-Mgt	B14-IX-1e	-3.2	1.7	0.5	-2.6	2.0	0.6	1.9	Poorly sorted		
	B14-IX-1f	0.4	2.4	0.2	0.7	2.2	0.1	1.0		Nearly symmetric	Mesokurtic
Sw	B50-5b	-3.6	1.5	0.3	-3.3	1.9	0.4	1.7	Well sorted	Coarse grains domain	Very leptokurtik
	B50-5c	-3.8	1.1	0.4	-3.5	1.5	0.5	2.4			
Oru	B50_B_XXVII-1	-2.6	1.4	0.1	-2.5	1.5	0.2	1.1			Leptokurtik
	B50_B_XXVII-2 (PDC)	1.5	3.1	-0.7	0.1	2.8	-0.6	0.6	Poorly sorted	Mixed coarse and fines populations, with a tail in the coarse sizes	Very platikurtik
	B50_B_XXVII-3	-2.4	2.8	0.5	-1.4	2.5	0.5	1.0		Coarse grains domain	Mesokurtic
L-Okp	B50-Ph-1	-1.7	1.7	0.0	-1.7	1.6	0.1	0.8	Well sorted		
Ph	B50-16A	-2.1	2.6	0.1	-2.0	2.5	0.2	0.9	Poorly sorted	Mixed coarse and fines populations, with a tail in the coarse sizes	Platikurtic
U-Okp	B50-16B	-3.6	3.0	0.6	-2.4	2.8	0.6	0.8			

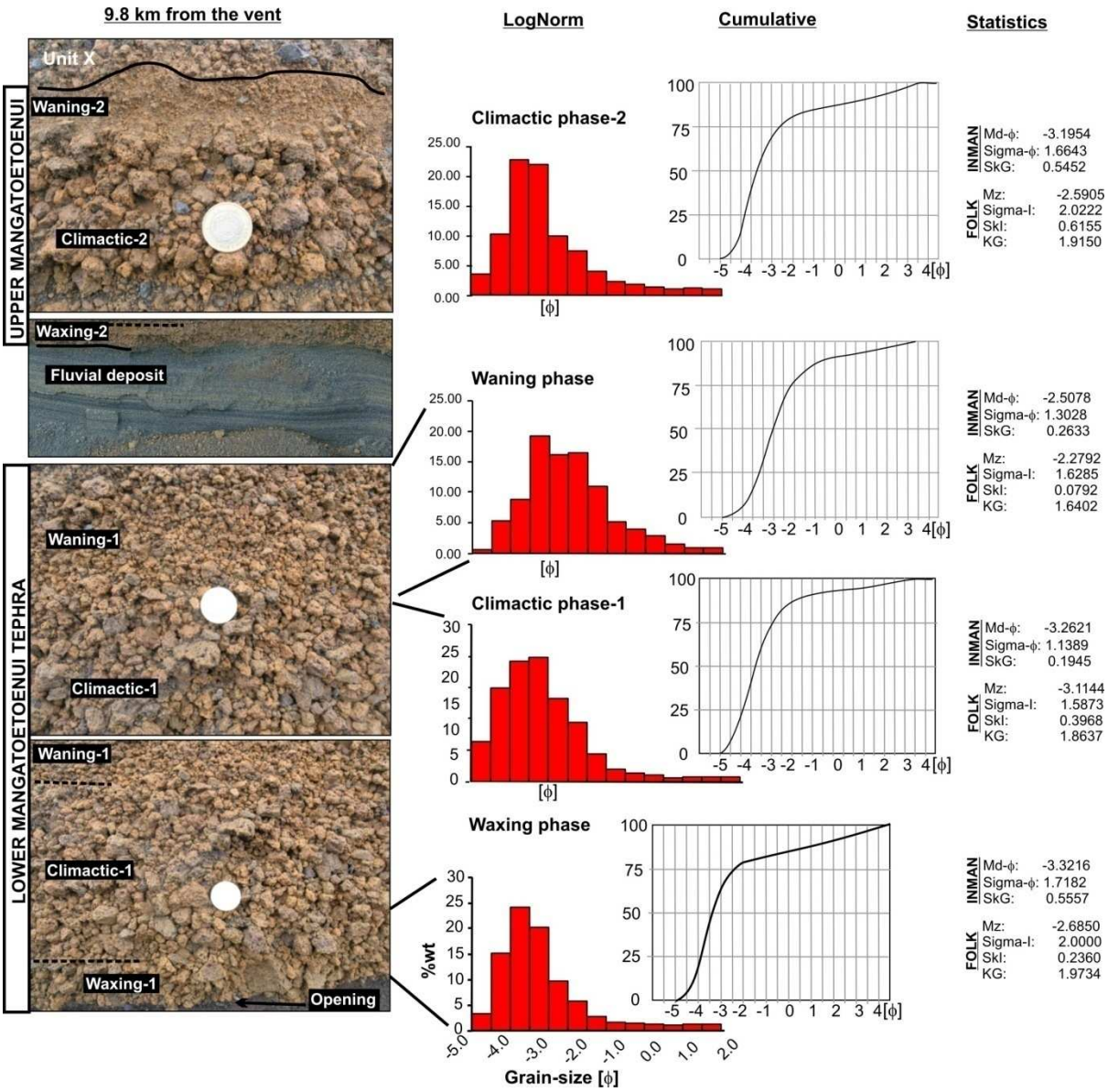

Figure 5.2 Detail of the Mangatoetoenui Eruptive Unit and inferred eruptive phases. Grain-size distribution histograms for the main eruptive phases are shown, with the corresponding cumulative curve and statistic parameters as calculated with SFT software. Results are typical of pyroclastic fall deposits.

Pumice textures: most of the -5 ϕ lapilli sampled from the Plinian fall deposits show dense, phenocryst rich rims and highly vesicular cores with sub-spherical bubbles from 3 mm to 1 cm in diameter, increasing in size towards the centre of each clast. This observation indicates advanced post-fragmentation bubble expansion, coalescence and degassing, and thus this size fraction was avoided for further vesicularity measurements. The dominant medium lapilli size fraction (-4.5 to -3 ϕ; **Appendix D.1)** consists of juvenile clasts showing highly heterogeneous textures within the same stratigraphic level (**Fig. 5.3a,b; 5.4**): **a)** subangular to equant, crystal-poor, **foamy** pumice clasts characterized by subspherical vesicles of different

sizes, separated by thin walls and showing different degrees of coalescence in the groundmass glass (**Fig. 5.3c; 5.4a, d, g**); **b)** Angular to subangular, crystal-bearing, anisotropic pumice clasts with **fluidal** texture formed by the alignment of ellipsoidal to strongly elongated vesicles and phenocrysts in a microlite-bearing groundmass (**Fig. 5.3d, 5.4b, e, h**); **c)** Angular, crystal-rich, **microvesicular** pumice clasts (**Fig. 5.3e**) with highly distorted vesicles, commonly showing pinched edges, in a microlite-rich groundmass. Fluidal and foamy clasts are dominant in the L-Mgt (**Fig. 5.3a**), whereas the microvesicular, crystal-rich clasts predominate in the U-Mgt (**Fig. 5.3b, 5.4c, f, i**).

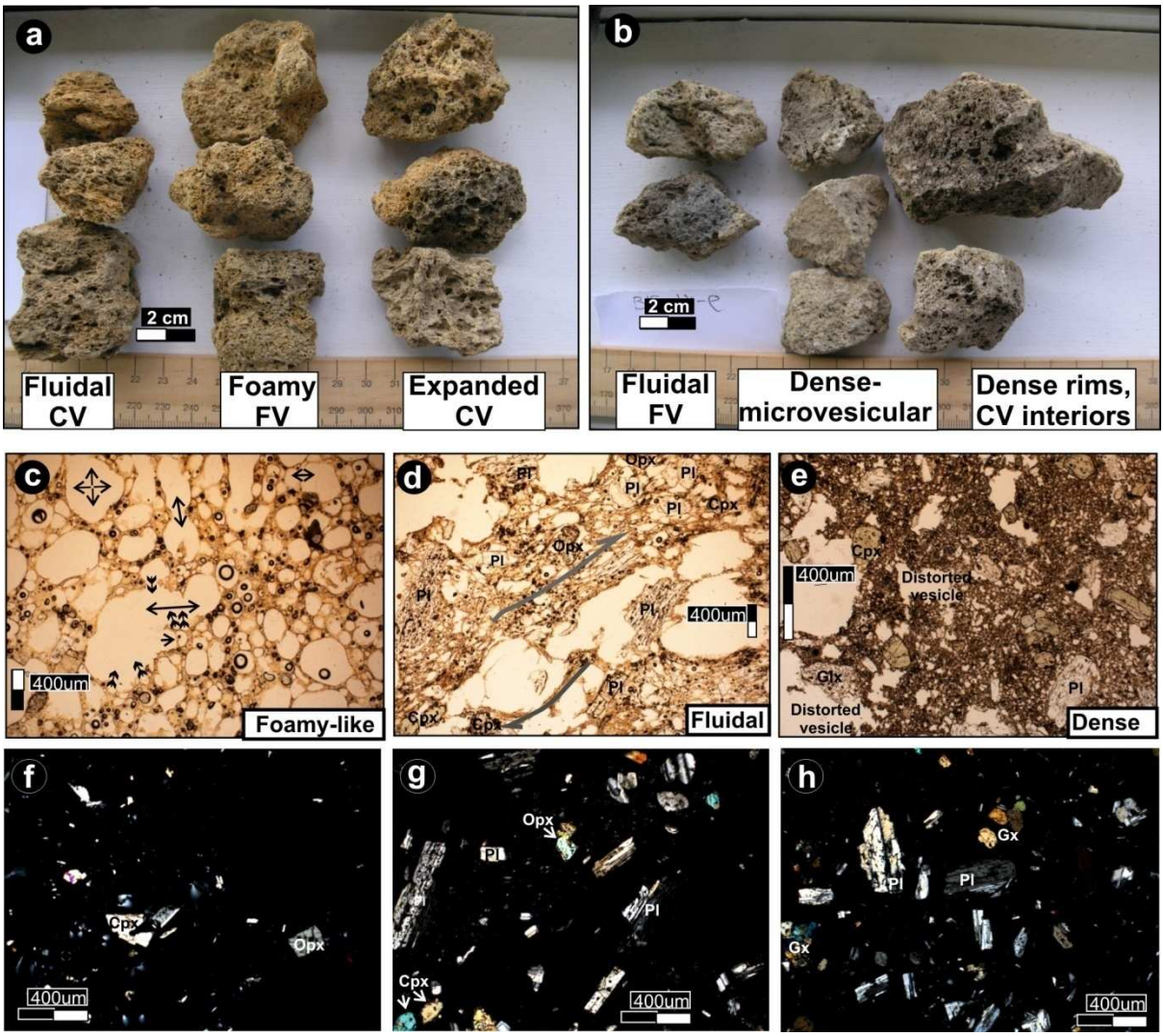

Figure 5.3 Pumice types identified at the same stratigraphic level within: **a)** L-Mgt and **b)** U-Mgt. Note contrasting vesicle sizes. Thin sections from three end-members are shown, including: **c)** foamy end-member with subspherical vesicles between 50 and 200 μm in diameter, and with smooth vesicle outlines and thin walls. Different degrees of coalescence are illustrated: single-direction arrows show the initial stages of slight vesicle wall deformation, while double-direction arrows point out aperture throats and interconnection. This pumice is transitional to coarsely vesicular, expanded types; **d)** fluidal pumice clasts with strong alignment and elongation of vesicles, parallel to tabular phenocrysts; **e)** crystal-rich, microvesicular end-member with highly irregular and distorted micro-vesicles showing abrupt terminations and refolded shapes. Note the increase in phenocrysts, glomerocrysts (Gx), and microlite content from a typical foamy (**f**), fluidal (**g**), to microvesicular (**h**) texture.

All clast types distinguished in 2D images are fine-grained and porphyritic, containing subhedral and anhedral orthopyroxenes (Opx), clinopyroxenes (Cpx), and subhedral to euhedral plagioclase (Pl), commonly showing oscillatory zoning and occasionally sieve textures (**Fig. 5.5a-i**). These mineral phases occur both as free crystals and as glomerocrysts (Gx), particularly in the fluidal and microvesicular pumice clasts. Oxide microphenocrysts (Ti-Magnetite: Mt) are scarce and usually enclosed within vesicles (**Fig.5.5j, k**). This "bubble-wall texture" was identified in 2D and 3D images, reflecting the wetting character of Ti-Mt oxides (c.f., Navon and Lyakhovsky 1998).

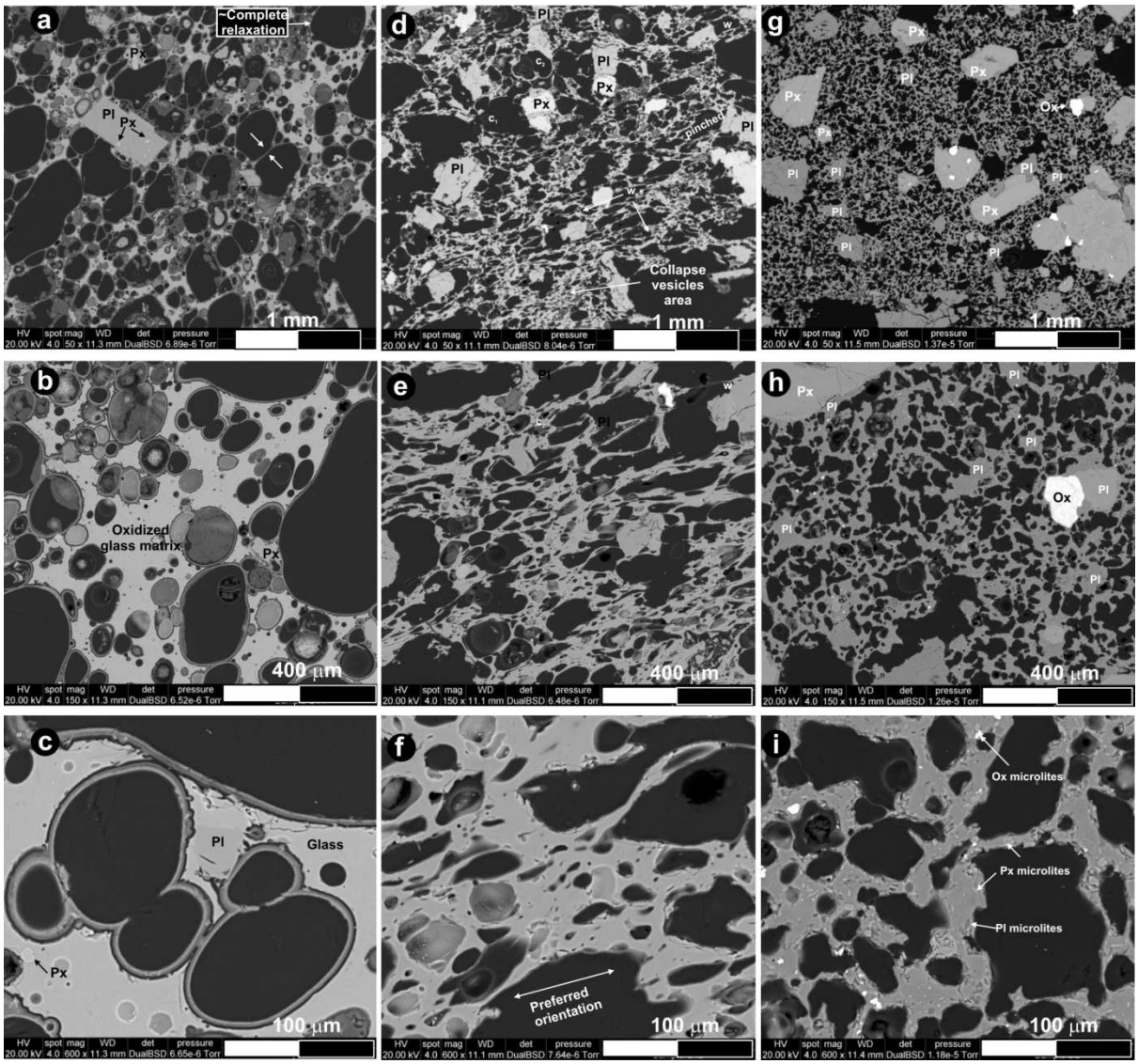

Figure 5.4 Back scatter electron images (BSE), at three different magnifications, showing pumice samples with contrasting textures, varying from: **a-c)** foamy with subspherical vesicles showing thin walls and smooth outlines; **d-f)** fluidal texture formed by aligned and oriented vesicles showing thick walls, some wrinkled. Vesicles are irregular, most of them showing pinched edges; **g-i**) microvesicular texture within the U-Mgt, with abundant and larger phenocrysts and greater oxides content (ox). Microlite content is also high and vesicles are extremely distorted, most of them showing collapse structures.

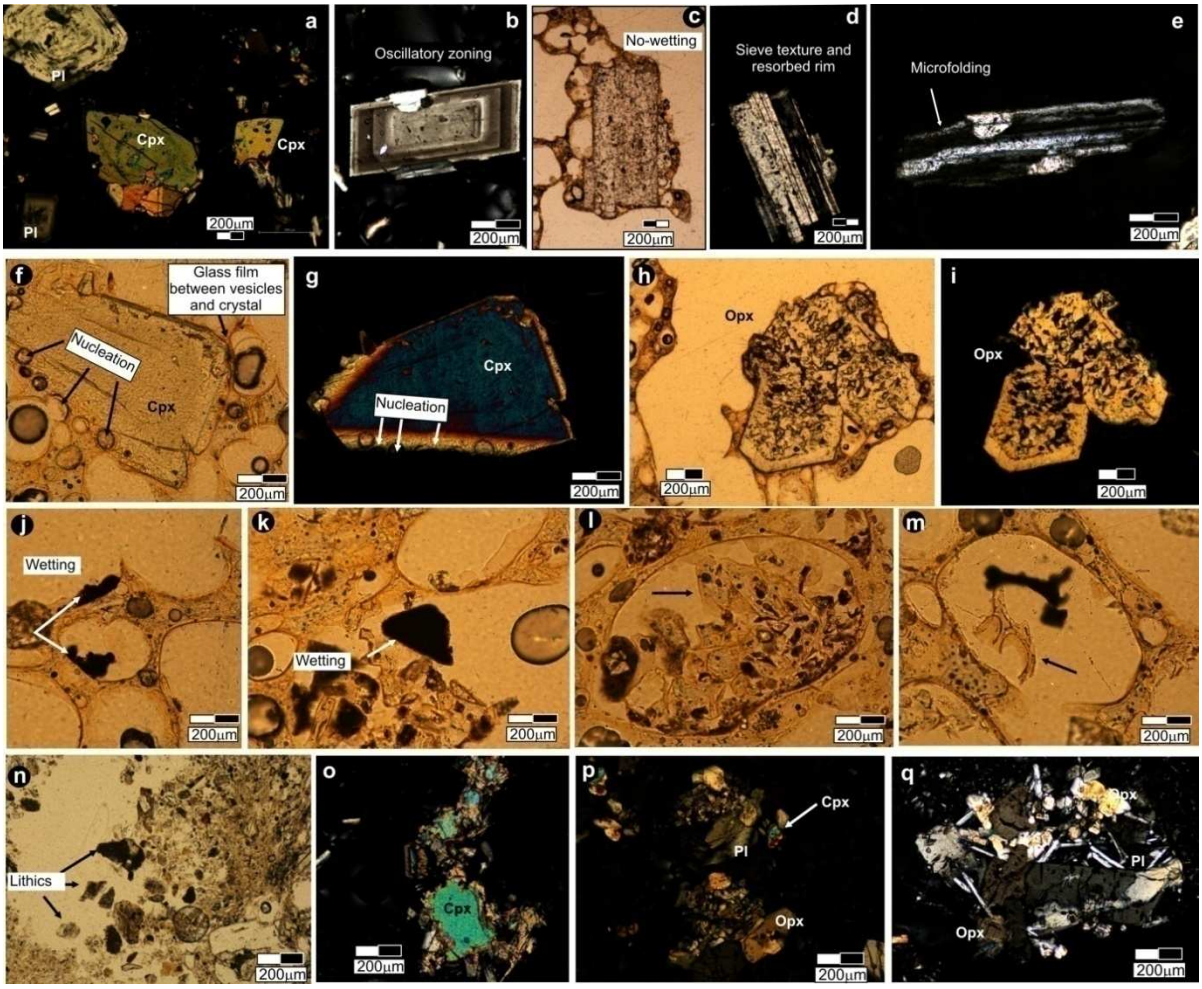

Figure 5.5 Main crystal phases in the Mgt unit (**a**). Plagioclase phenocrysts are commonly euhedral, zoned (**b**), subhedral sieved (**c, d**), an occasionally show plastic micro-deformation (**e**). Clinopyroxenes are commonly subhedral to anhedral and occasionally show "bubble wall-texture" (**f, g**). Orthopyroxenes (**h, i**) are commonly euhedral to subhedral, sieved, and vesicles do not seem to wet the crystal. Oxides are commonly embedded within vesicles (**j, k**). Vesicles embedding pumice fragments (**l**) or glass shards (**m**) are common. Non juvenile fragments are mainly volcanic aphanitic (**n**) or microphaneritic andesites (**o-q**).

Before proceeding, it is important to clarify that the term "fluidal texture" refers to pumice clasts with deformed i.e., elongated and oriented) vesicles and has no direct implication on the fluidity of the magma itself.

Component analysis and ash-size fractions: bulk grain counts (**Chapter 2**) were carried out with component categories including: juvenile glass, free crystals, and lithics (**Appendix E.1**). The relative proportions of each component vary over time and also with size fraction (**Fig. 5.6**). Juvenile clasts were counted and classified into foamy, fluidal, and microvesicular types (**Fig. 5.7**), according to their predominant vesicle size and shape, and crystal content. These textural divisions can also be recognized down to the fine ash fraction (**Fig.5.8**). When

analyzing the size fractions ≤0 ϕ (**Fig.5.6**), the relative contents of juvenile glass, free crystals, and lithics do not show significant variations with grain size, but vary with stratigraphic position. The content of low-density fragments (glass + crystals) increases and dense lithic clast content decreases upward in each tephra analysed. In the coarse-ash fractions, most of the juvenile pumice clasts (22-31 vol.%) are crystal-poor and highly vesicular (foamy + fluidal types).

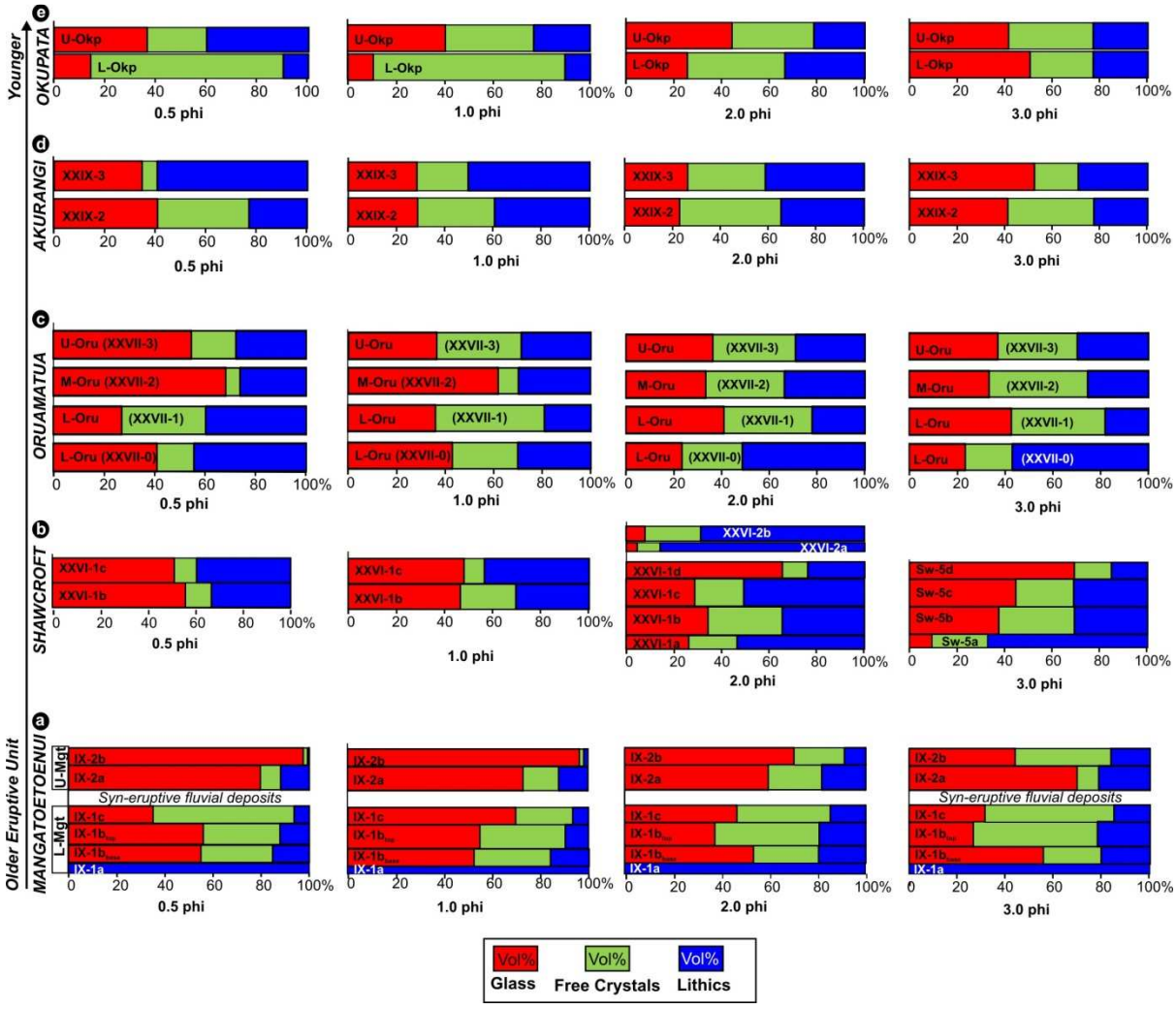

Figure 5.6 Bulk componentry analysis for ash size fractions ≤0 ϕ, based on 300 grains counted per size fraction and normalized as vol.%. Analyzed eruptive units from oldest to youngest are: **a)** Mangatoetoenui, **b)** Shawcroft, **c)** Oruamatua, **d)** Akurangi, **e)** Okupata.

In the L-Mgt, the content of highly vesicular clasts increases upward, while crystal-rich, microvesicular pumice clasts become less common. In the U-Mgt, relative proportions of these components remain approximately constant throughout the unit. Within the 3 ϕ size class relative proportions of glass morphologies (**Fig. 5.8b-j; 5.9**) do not show a significant

variation with stratigraphic position in each tephra. Instead, there is a clear predominance of highly vesicular, foamy (~40 %) and fused-shaped (Sheridan and Wohletz 1983) pumice shards (26-32 %) having smooth surfaces (i.e., "melted"; c.f., Wohletz and Krinsley 1982; Wohletz 1983), relative to poorly vesicular glass shards (24-28 %). In this size fraction, Pelée's tears are also present (<6 %) within the L-Mgt (**Appendix E.1**).

Five types of non-juvenile lithic clasts were distinguished (**Fig.5.8k-p; 5.10a**): **L1) recycled material** from the vent (δ_{bulk} = 0.7 g/cm^3): comprises lithic aggregates formed by heterolithologic, multi-coloured, **subrounded** lithic fragments and **altered**, **rounded** pumices bound by a black, oxidized, amorphous groundmass (**Fig. 8k**). **L2)** Lithics derived from lava flows, comprising **fresh** to slightly altered, dark (**Fig. 5.8l**) and pale grey (**Fig. 5.8m**), coarsed-grained porphyritic **andesites** (δ_{bulk} = 2.09 and 2.77 g/cm^3, respectively). **L3)** Moderately altered, brownish grey (δ_{bulk} = 2.24 g/cm^3), subrounded, fine-grained porphyritic lava fragments (**Fig. 5.8n**) and **partially altered** coarse porphyritic andesites (δ_{bulk} = 2.74 g/cm^3). **L4)** Lithics derived from the **hydrothermally altered** (δ_{bulk} = 1.28 to 2.55 g/cm^3) levels of the conduit, comprising: red, purple, bluish-grey, orange, and yellowish-white, highly altered volcanic clasts, varying from aphanitic, poorly vesicular lava fragments to coarsed-grained porphyritic clasts (**Fig. 5.8o**). **L5)** Phaneritic lithics comprising: coarse-grained, Opx±Cpx±Pl **glomerophyric** fragments, either sourced from deep plutons or to crystal accumulations on the walls of the magma reservoir (**Fig. 5.5o-q**); and rare highly altered, friable, white, **sediments** (**Fig. 5.8p**) derived from the Tertiary basement (c.f., Graham et al., 1990).

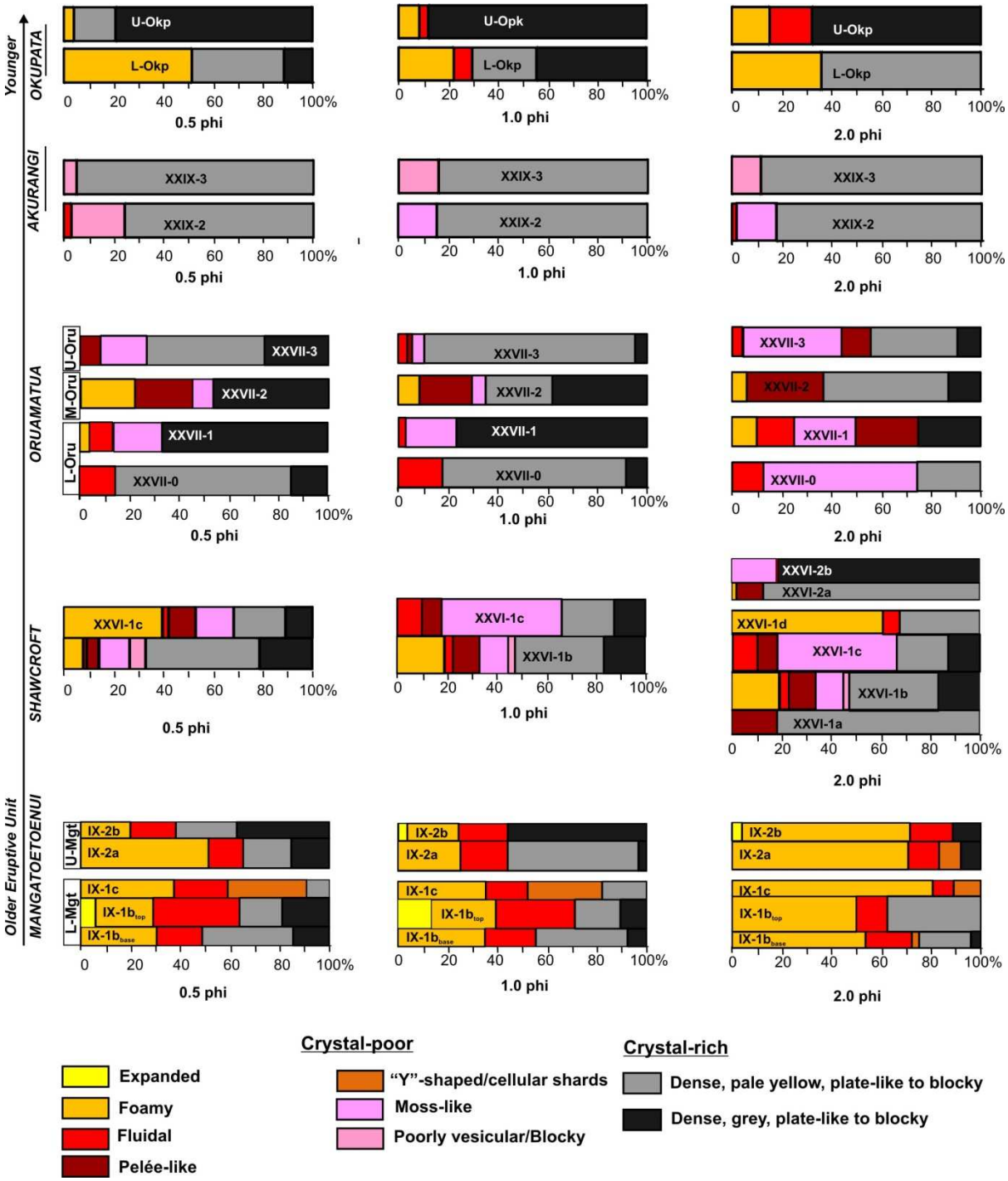

Figure 5.7 Relative proportions of the different glass morphology normalized over total glass content as vol.%.

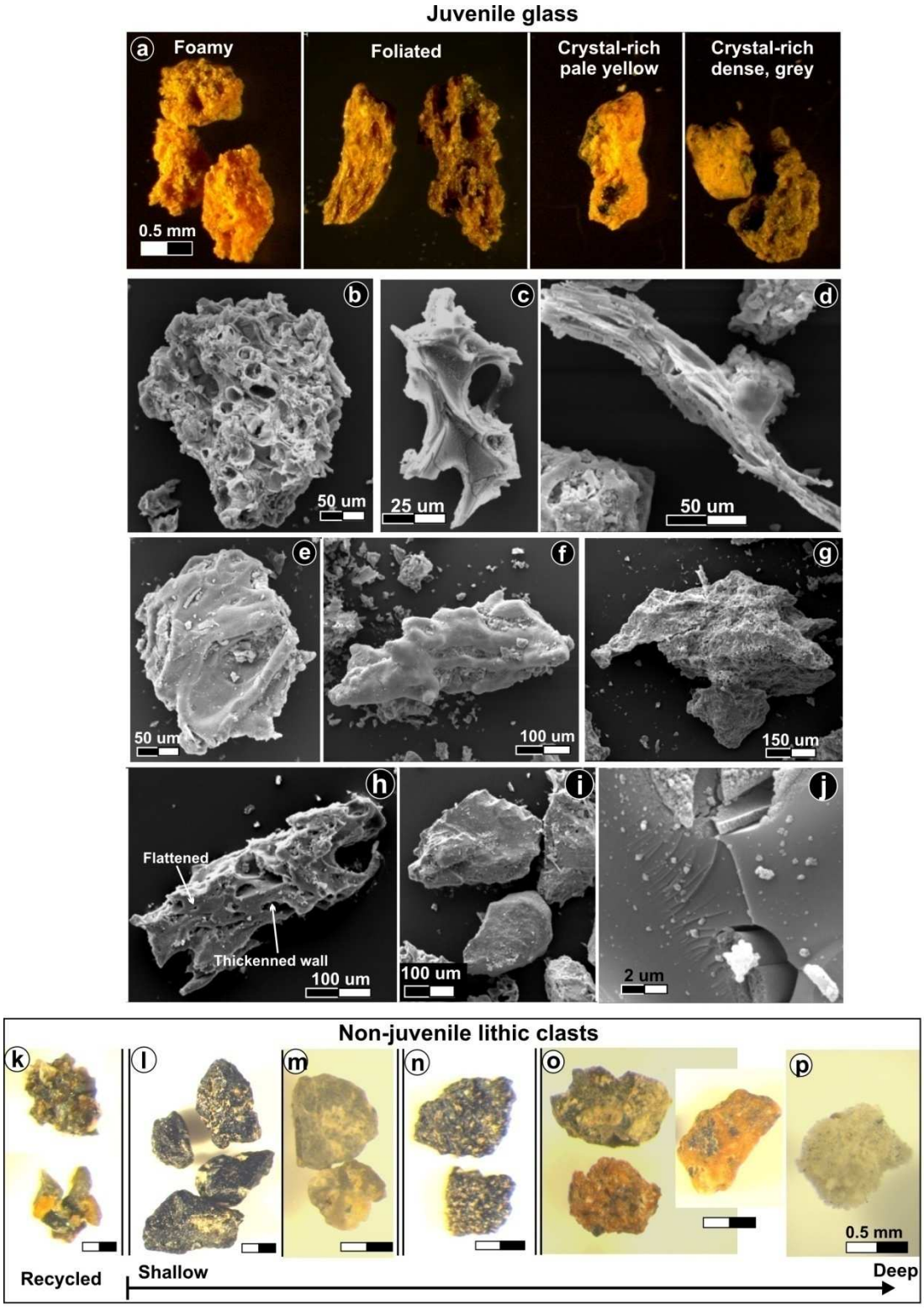

Figure 5.8 a) Main pumice clasts classes identified within the Mangatoetoenui Unit, under binocular microscope; **b)** foamy, highly vesicular pumice shard with subspherical vesicles; **c)** cuspate glass shard derived from bubble bursting; **d)** fibrous shard; **e)** fluidal-shaped glass with ellipsoidal vesicles having thick walls; **f)** fused-shaped pyroclast with smooth, "melted" surfaces; **g)** platy, poorly vesicular glass; **h)** poorly vesicular clast with flattened vesicles having over-thicken walls; **i)** blocky shaped, non vesicular shards; **j)** conchoidal fractures on glass surfaces; **k)** lithic aggregates, probably recycled from the vent walls/floor; **l)** dark grey, fresh andesites; **m)** pale grey, fresh andesites; **n)** partially altered, vesicular lavas; **o)** hydrothermally altered volcanic ranging from aphanitic to porphyritic; **p)** altered accidental white sedimentary clast.

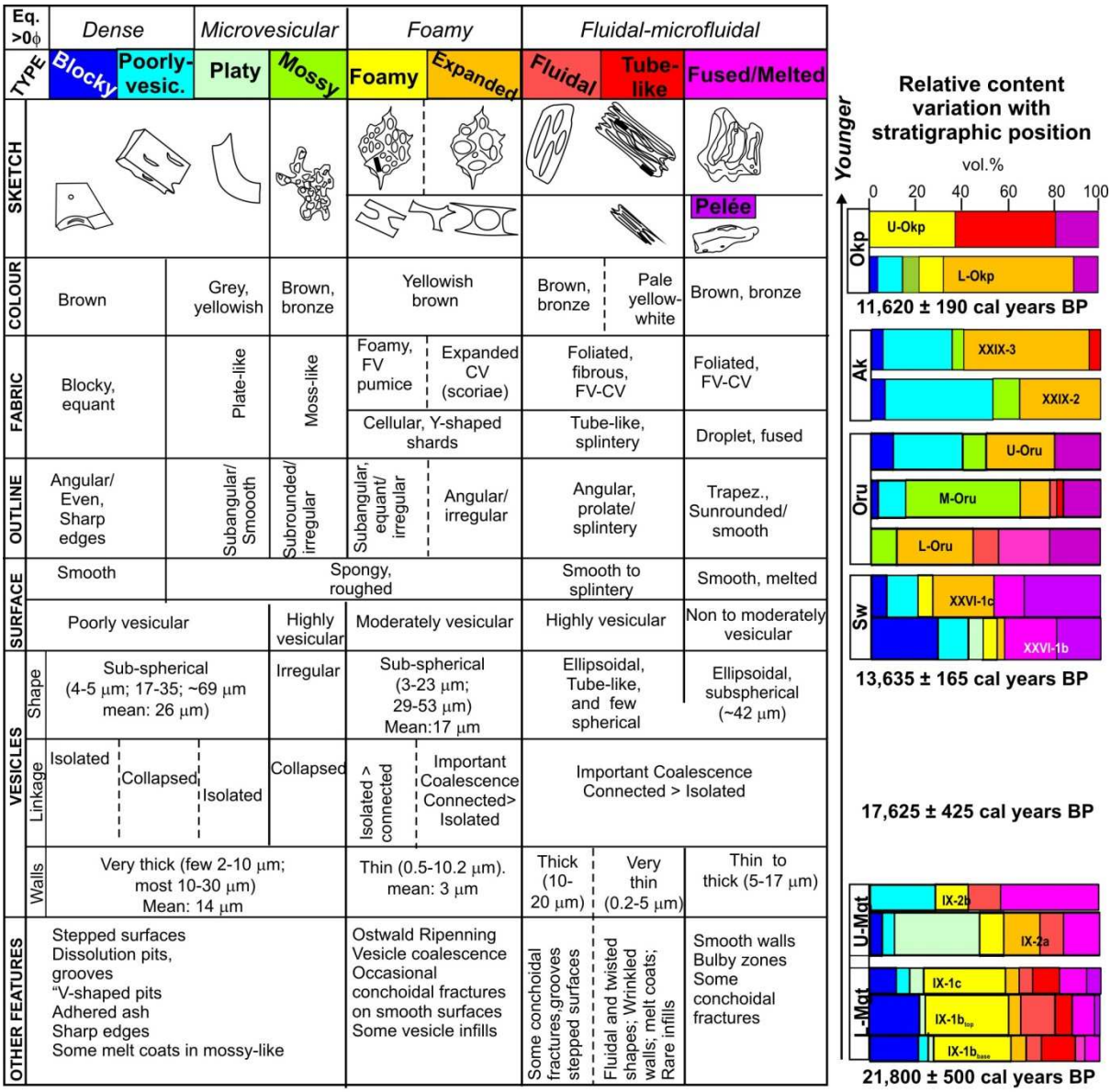

Figure 5.9 Juvenile ash morphological types identified within the 3 ϕ size fraction of the eruptive units selected for this study. Observations were carried on with a FEI Quanta 200 Environmental Scanning Electron Microscope (SEM) on gold coated ash particles at 20 kV. The relative proportions within this size fraction over time are shown to the right. Calibrated radiocarbon ages correspond to interbedded rhyolitic tephras as reported by Froggatt and Lowe (1990), Newnham et al. (2003), and Lowe et al. (2008). For the complete stratigraphy refer to **Chapter 3**, **Appendices A** and **J.1**. Eq.>0 ϕ: equivalent very coarse ash and lapilli-sized textural types.

The fresh, hypohyaline clasts derived from the vent or the uppermost part of the conduit decrease with time in the fine fraction and are restricted to the opening phase and the L-Mgt (**Fig. 5.10a**). Lithics derived from shallow levels (fresh andesites) and highly hydrothermally altered zones reach their maximum in the fine fractions of the waning phases, whereas the climactic phases are characterized by a mixed population with nearly equal proportions of all the different lithologies (**Appendix E.1**).

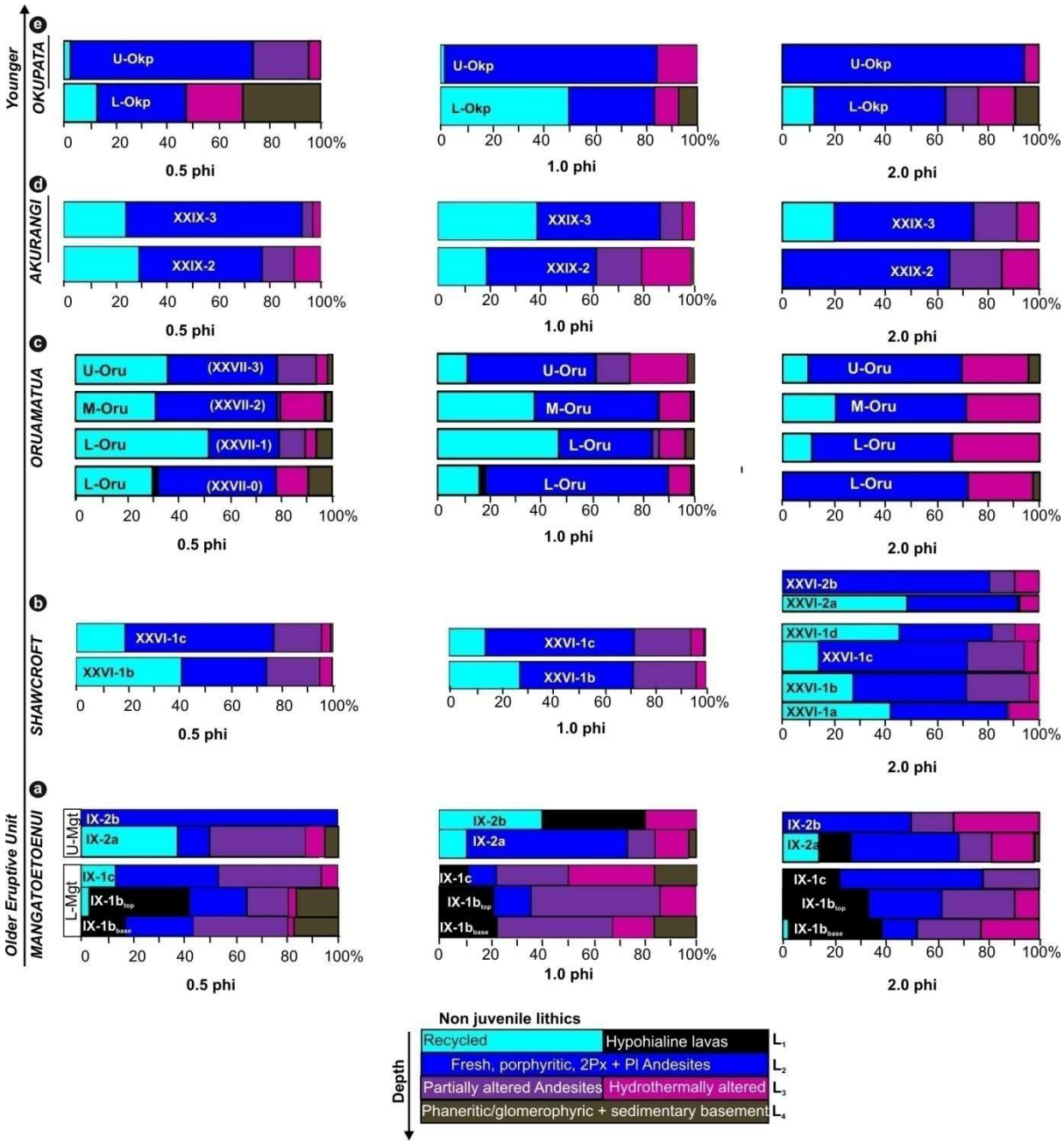

Figure 5.10 Relative proportions of non juvenile lithic clasts types normalized over total lithic content as vol.%. Units and subunits are shown in stratigraphic order from base **(a)** to top **(e)**.

In summary, **the Lower Mangatoetoenui Tephra** lithofacies and its relation to the parent eruption was interpreted as follows:

Opening phase (IX-1a): the onset of the eruption is marked by a monolithologic fall deposit, consisting of aligned fresh, angular, black, aphanitic to porphyritic, hypohyaline, andesitic medium lapilli (**Fig. 5.1**), capped by a thin, grey, very fine-ash lamina.

Waxing phase (IX-1b$_{base}$): the onset of the Plinian phase is represented by an overlying, medium pumice lapilli (Mz = -2.7 ϕ), forming a poorly sorted fall deposit (**Figs. 5.1, 5.2; Appendix C; Table 5.1**). This unit is dominated by pumice (54 ± 2 vol.%), which is mainly characterized by finely vesicular foamy and crystal-rich microvesicular fabrics (**Figs.5.6, 5.7; Appendix D.1**). The crystal content is slightly higher in the finest grain-size fraction with pyroxene glomerocrysts being more abundant than plagioclase (**Appendix E.1**). Non-juvenile hypohyaline clasts derived from the shallowest, vent/conduit regions are concentrated in the finest grain-size fractions, followed by partially altered and highly hydrothermally altered volcanic lithics and minor proportions of fresh, porphyritic andesites (**Fig. 5.8**).

Climactic phase (IX-1b$_{main}$): the peak of the Plinian phase (IX-1b) is represented by a medium to coarse, well sorted lapilli bed (Mz = -3.1 ϕ) (**Figs. 5.1, 5.2; Appendix C**), with texturally heterogeneous pumice clasts at any stratigraphic level (**Figs.5.3, 5.4; Appendix D.1**). This bed shows the maximum variability of components, with glass, crystal, and lithic contents being approximately equal in proportion (**Fig. 5.6; Appendix E.1**). Coarsely vesicular, fluidal pumice clasts dominate the coarse ash fractions, but crystal-bearing, microvesicular to poorly vesicular pumice clasts are more highly represented in the finest fraction (**Fig.5.7**). In addition, this bed shows the highest total lithic content of the entire L-Mgt, with approximately equal proportions of clasts derived from the vent and/or uppermost conduit region (fresh andesites), and partially altered to highly hydrothermally altered clast content in the finest size class (**Fig. 5.10a**).

Waning phase (IX-1b$_{top}$): is represented by a normally graded, well sorted, medium lapilli bed (Mz = -2.3 ϕ), forming the uppermost deposit of the L-Mgt (**Figs. 5.1, 5.2**). It shows the lowest lithic contents within all size-fractions. Juvenile clasts slightly dominate over crystal and lithic contents (**Fig. 5.69; Appendix E.1**) and are characterized by highly vesicular pumice and glass shards, whereas the crystal-rich, microvesicular juvenile content is significantly lower than previous phases, being absent in the finest size fraction (**Fig. 5.7**).

Within the 0.5 and 1.0 ϕ fractions, this deposit has the highest content of hydrothermally altered lithics and glomerocrysts. However, in the finest fraction fresh, dark-grey, Opx±Cpx±Pl-bearing, porphyritic andesites dominate the non-juvenile lithology (**Fig. 5.10a**).

On the other hand, the **Upper Mangatoetoenui Tephra** is characterized (**Fig. 5.1**) by the strong predominance of crystal-rich, microvesicular juvenile pumice and crystals relative to the L-Mgt (**Fig.5.3; Appendix D.1**). The overall lithic content is very similar to the L-Mgt subunit (36-64 %), (**Fig. 5.6**) with a clear predominance of fresh andesites (**Fig. 510; Appendix E.1**).

Waxing and climactic phase (IX-2a): after a short time period following the deposition of the L-Mgt tephra, represented by localized fluvial deposits, the onset of the second Plinian eruption is manifested by a thin coarse-ash bed, capped by a thin lamina representing a short-lived waxing phase deposit. This was immediately followed by the accumulation of the main, coarse, poorly sorted lapilli (Mz = -2.6 ϕ) fall deposit (**Fig. 5.2**).

Waning phase and dissipation cloud (IX-2b): the overlying coarse ash deposit (Mz = 0.4 ϕ) reflects the final deposit of the dissipating column (**Figs. 5.1, 5.2**), and is commonly reworked by fluvial and aeolian processes. Coarsely vesicular and microvesicular, grey, crystal-rich pumice fabrics, as well as non-juvenile, hydrothermally altered lithics and partially altered andesites are more abundant here than in the climactic phase (**Fig. 5.7, 5.10a; Appendix E.1**).

In the 3 ϕ size fraction (**Fig. 5.9**) there is a progressive upward reduction of the highly vesicular pumice and glass shards relative to the L-Mgt, and an increase in the fused-shaped, poorly vesicular end-member, with ellipsoidal vesicles having very thick walls and smooth, fluid-form surfaces (e.g., **Fig. 5.8f**).

Chemical Composition: juvenile pumice whole-rock XRF analyses (**Chapter 2.2.7; Appendix F.1**) indicate that the Mgt unit has a restricted bulk andesitic composition (SiO_2: 56.20-58.29 wt.%, normalized to dry basis), without showing significant variations over time/depth. Groundmass glass composition (**Appendix F.2**) shows two distinct groups, correlated with pumice texture and specifically, with the crystal content (**Fig. 5.11**): **(1)** andesitic (SiO_2: 56-60 wt.%), corresponding to the crystal-poor fabrics of the L-Mgt; and **(2)**

dacitic (SiO_2: 61-65 wt.%) associated with the crystal-bearing fluidal and microvesicular textures. By contrast, glass inclusions in pyroxene phenocrysts are mainly dacitic to rhyolitic (**Appendix F.3**), with 67-70 wt.% SiO_2, which is much more silicic than the residual groundmass glass.

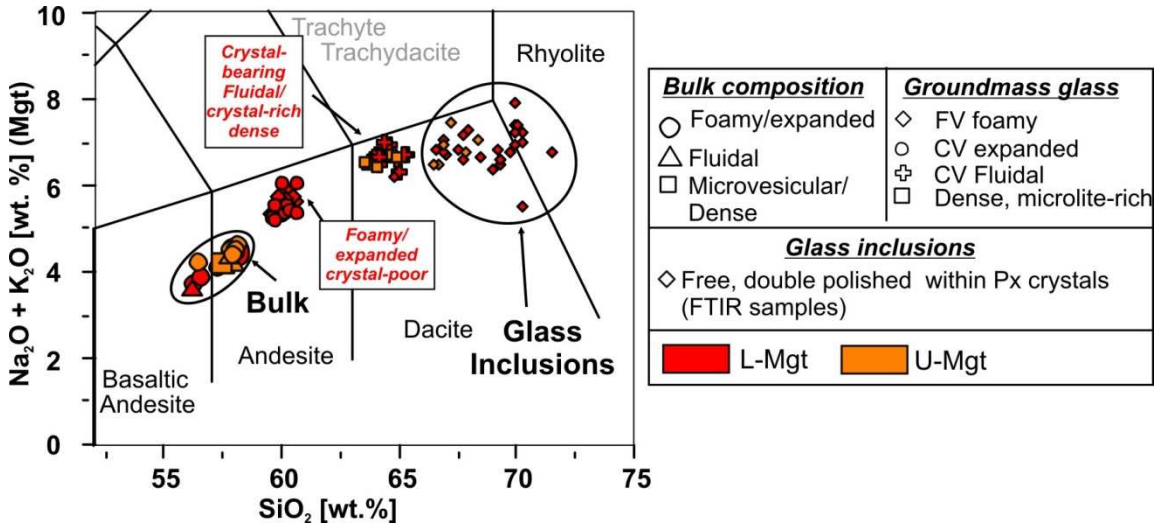

Figure 5.11 Total alkalis vs. silica (TAS) diagram (Le Bas et al., 1986) showing the bulk and glass composition of juvenile clasts within the Mgt unit as well as glass inclusions trapped within pyroxene crystals. The variability of groundmass glass composition within the L-Mgt is related to the heterogeneous textures (i.e. crystal content), whereas the homogeneous, more silica-rich glass composition of the U-Mgt reflects the higher crystal content of predominantly microvesicular pumice clasts.

Discussion: the observations above suggest that the Mangatoetoenui eruption resulted from the explosive fragmentation of a basaltic-andesitic to andesitic magma, rapidly rising from depth without opportunity for extensive crystallization. Textures of the largest plagioclase phenocrysts (complex zoning, occasional resorption borders, sieve textures, and rare euhedral rims) indicate convection within the reservoir and/or fast decompression linked to fast ascent rates (c.f., Nelson and Montana 1992). Price et al. (2005) reported dacite to rhyolite glass inclusions and groundmass glass compositions for Mt. Ruapehu andesites, with major and trace element compositions similar to the typical Taupo Volcanic Zone rhyolites and dacites. Similarly, melt inclusions analysed in this study indicate that Cpx phenocrysts coexisted with a rhyolitic melt early in the magmatic history, before being entrapped within the andesitic-dacitic melt of the Mgt magma. Price et al. (2005) found that Pl, Opx, and possibly Cpx compositions of xenoliths and host-andesites overlap, indicating that phenocrysts in andesite lavas were probably derived from the disaggregation of crustal xenoliths or from previous magma batches. The accidental lithic fragments found in the component analysis of the

Mangatoetoenui unit show the same mineral assemblage as the juvenile pumice clasts and free crystal phases, pointing towards an analogous model for the origin of tephra phenocrysts. The highly evolved glass inclusions trapped within pyroxene hosts, compared to the composition of glass groundmass, supports a hypothesis of pyroxene phenocrysts crystallizing in an earlier different storage system to the erupting bulk melt.

The lithic fallout at the onset of the Mgt eruption suggests that an initial phreatic phase removed a vent/conduit plug, triggering sudden magma decompression that fed the first Plinian eruptive column. Most of the fragmented ash was derived from decompression of expanding bubbles within viscous regions of the magma, where spherical to subspherical vesicles could act as rigid objects (c.f., Rust and Manga 2002; Rust and Cashman 2011; Stein and Spera 2002). These were followed by ash particles derived from regions in the rising magma where vesicles were elongated in response to acceleration and shear. A minor proportion of particles with smooth surfaces (including some Pelée's tears; Shimozuru 1994), show that ductile deformation occurred locally after fragmentation (i.e. under slow quenching rates) with particles derived from the regions of highest ascent rate and extreme exit velocity. Rare and gradually diminishing, crystal-rich, very finely to poorly vesicular clasts (**Fig. 5.9**) derived from marginal degassed regions of the conduit close to the walls, where ascent rate was slower, permeability enhanced, and degassing-induced crystallization was triggered (c.f., Massol and Jaupart 1999). Larger contents of crystal, microlites and lithics provide higher overall viscosity in the regions close to the conduit walls (c.f., Adams et al., 2006). The presence of all pumice morphology types within a particular stratigraphic level has been reported in similar deposits of Plinian eruptions around the world (e.g., Lirer et al., 1973; Waitt et al., 1981; Hoblitt and Harmon 1993; Gardner et al., 1998; Polacci et al., 2001; Taddeucci and Wohletz 2001; Klug et al., 2002; Sable et al., 2006), suggesting that the rising magma comprised laterally adjacent zones of differing volatile saturation, degassing history, viscosity, and ascent rate that reached the fragmentation level at the same time. In addition, in the low-viscosity magma producing the L-Mgt, gas volume fraction should have exceeded a critical value in order to attain fragmentation (c.f., Verhoogen 1951; Proussevitch et al., 1993).

Within the L-Mgt, the crystal, lithic and glass contents do not change with grain-size (**Fig. 5.6**), but vary systematically with stratigraphic position (i.e., over time). Higher contents of low-density components (**Figs. 5.7, 5.9**) and the depletion in microvesicular juveniles and total lithic contents (**Fig. 5.6**) are present within the deposits accumulated during waning

phases. This indicates that component distribution during the L-Mgt could have been controlled by changes in the fragmentation level (i.e., deepening with time; c.f., Spieler et al., 2004a). Additional distribution of components with depth could be due to density-segregation and deposition of particles according to their settling velocities. During the waxing and climactic phases, the finely fragmented lithics of fresh andesite "shallow country rock" increase during the eruption, whereas hydrothermally altered lithics decrease, possibly indicating that greater near-surface crater erosion was caused during the waxing phase. The contrasting lithologies reached near equal proportions during the climactic phase, suggesting the attainment of a homogeneous mixture.

A predominance of fluidal textures in the L-Mgt lapilli is consistent with the development of permeable networks with bubble connectivity enhanced by coalescence (Cashman and Mangan 1994; Klug and Cashman 1996), and regions subject to differential shear (Massol and Jaupart 1999; Wright and Weinberg 2009): studied textures indicate magma discharge rate and vesiculation rate decreased with time, leading towards the waning phase. This is consistent with the uppermost, normally graded deposits of the L-Mgt (**Fig. 5.1**), which reflect a decreasing eruptive column height during the eruption.

The U-Mgt juvenile pyroclasts indicate a second major eruption phase after a short repose interval (IX-d bed in **Figs. 5.1,** and **5.2**), where magma was texturally more mature (i.e. degassed, as indicated by abundant collapsed vesicles and higher crystal content) than during the L-Mgt. This suggests that the magma remaining after the first Plinian phase was temporarily stored in at shallow levels or had slower ascent rates, promoting undercooling and degassing that progressively enhanced crystallization (c.f., Tuttle and Bowen 1958; Nakada and Motomura 1995; Hammer et al., 1999). The dominant platy morphologies of the finely fragmented ash of the U-Mgt (**Fig. 5.9**) and the restricted vesicle size and low vesicularity of the U-Mgt, microlite-rich clasts suggests a more viscous magma compared to the L-Mgt. This suggests that decompression stresses around over-pressured bubbles exceed the tensile strength of the melt leading to fragmentation (c.f., McBirney and Murase 1970; Alidibirov 1994; Koyaguchi and Mitani 2005; Koyaguchi et al., 2008; Rust and Cashman 2011) at a shallower level than L-Mgt. In other words, the relatively more "dense" U-Mgt magma required higher fragmentation thresholds than L-Mgt magma (c.f., Spieler et al., 2004b). The increased coarsely-vesicular ash, fused-shaped fragments (with thick vesicle walls and smooth surfaces) and poorly vesicular clasts (with flattened vesicles and thick vesicle walls) towards the top of the U-Mgt (**Figs. 5.8e, h, 5.9**), suggest eruption of

progressively more degassed magma. This process could result in decreasing magma discharge rate with time, reduction of conduit diameter, ultimately leading to the termination of the eruption (c.f., Massol and Jaupart 1999).

For both L-and-U-Mgt, the dominant shapes of fine ash particles are strongly indicative of dry magmatic fragmentation with glass shards commonly derived from subspherical and ellipsoidal vesicle walls (**Fig. 5.8c, d**; c.f., Heiken 1972; Fisher and Schmincke 1984). The scarce, poorly vesicular, blocky shaped shards (**Fig.5.8h, i**) might be related to outgassed portions of the magma or the fragmentation of thick walls of collapsed vesicles. Rare conchoidal fractures (**Fig.5.8j**) might be the result of shock waves caused by the decompression, rather than magma-water interaction. Considering the predominance of highly vesicular pumice shards and low-lithic contents, external water interaction with magma was negligible during the Mangatoetoenui Plinian eruption.

5.2.2 Steady and sustained, high (> 29 km) columns: Shawcroft Eruptive Unit

Lithofacies: this eruptive unit consists of a main lapilli fall deposit bounded by two thin, fine ash beds representing distinct eruptive phases, which can be recognized in most of the studied locations (**Appendix A**). Two further thin and poorly preserved ash and fine lapilli fall beds locally occur at the top of the sequence in proximal areas, representing closing phase fallouts that were commonly reworked by hyperconcentrated flows and fluvial action (**Fig. 5.12**). The type location for this description is B50 (**Fig.5.12a; Appendix A**), with comparable units at B06 (**Fig.5.12b; Appendix A**), 8.9 and 9.7 km east of the vent (i.e. The North Crater of Mt. Ruapehu), respectively.

As previously described (**Chapters 3, 4**), the opening phase of the Shawcroft Eruptive Unit (Sw) is marked by a thin, pale yellow, fine platy ash fall bed (XXVI-1a bed in **Figs.5.12a, b**) containing abundant ash aggregates (c.f., Brown et al., 2010). This deposit is overlain by the thickest and coarsest-grained, lithic-rich, lapilli fall deposit (XXVI-1b bed in **Figs.5.12a-c**) representing the climactic Plinian phase. The deposit of this phase is characterized by a massive, medium lapilli fall bed (Mz = -3.6 ϕ), showing a unimodal, negatively skewed grain-size distribution (**Figs.5.12a, b; Table 5.1; Appendix C**), typical of coarse-grained,

well sorted (σ_I = 1.5) fall deposits. The total deposit appears in most places to be a single unit, but at one proximal location, pyroclastic-surge deposits are interbedded within it, implying that it may have two phases (**Fig.5.12d**).

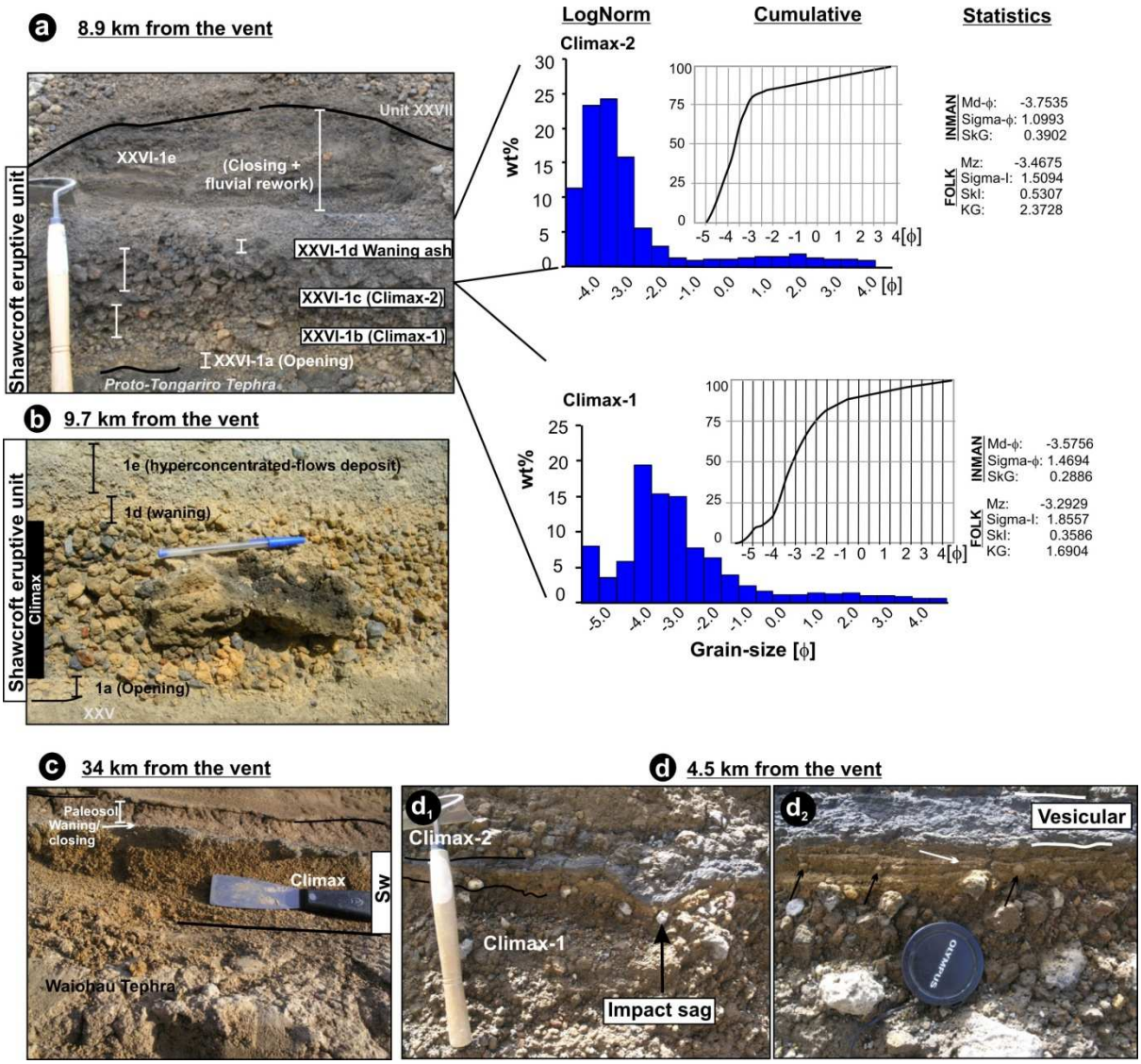

Figure 5.12 Detail of the Shawcroft Eruptive Unit deposits and inferred eruptive phases. Note the contrasting grain sizes among fallout beds in **a**, **b**, and **d**, indicating varying eruptive styles between phases. Lateral variations with distance include proximal parallel bedding (**a**), massive facies at medial and distal locations along the dispersal axis (**b** and **c**), and proximal pyroclastic surge deposits interbedded within the fallout beds (**d**) showing impact sags (arrow in $\mathbf{d_1}$), low-angle cross laminations and accretionary lapilli ($\mathbf{d_2}$). Grain-size distribution diagrams for the main eruptive phases are shown, with the corresponding cumulative curve and statistic parameters as calculated with SFT software.

Two eruptive pulses are indicated by only very subtle evidence at ~8.9 km from the vent, where a moderately well sorted (σ_I = 1.8) lapilli passes through a transitional contact up to a well-sorted unit (**Fig. 5.12a; Appendix C**).

The massive lapilli bed is usually capped by a thin, fine ash bed (XXVI-1d bed in **Figs.5.12a, b**) commonly well preserved up to ~34 km from the vent (waning phase), and in turn, overlain by a 7 cm-thick medial ash paleosol (**Fig.5.12c**). Occasionally, and only at proximal locations (<9 km from the vent), three to four thin, black fine ash beds are interbedded with thin, pale brown, silty-sand. The black ash units probably represent further, minor, closing phases of this eruption sequence, but the deposits are mostly reworked by hyperconcentrated-flows and fluvial activity (**Fig.5.12a**).

Pumice textures: the dominant medium lapilli size fraction (-4.5 and -3 ϕ; **Appendix D.2**) consists of very finely vesicular, fine-porphyritic, pumice clasts showing less heterogeneous fabrics within any stratigraphic level, when compared to the Mgt unit (**Fig. 5.13**). Juvenile clasts were classified into rare and proximally distributed **(a)** crystal-poor, subangular, equant, coarsely vesicular, **expanded** textural type. These are characterized by elongated vesicles between 100 and 800 μm, with smooth outlines and thin walls, showing varying degrees of coalescence (**Fig. 5.13c**). The dominant texture is (**b) microvesicular**, glomerophyric, with high microcryst and microlite contents, ellipsoidal ≤100 μm showing smooth outlines and rare larger vesicles with irregular shapes and sharp outlines. Some vesicles in these particles have very thick vesicle-walls, pinched terminations, concave, refolded or flattened shapes (**Fig. 5.13e, 5.14a-c**). The third type of particles are **(c)** glomerocryst-rich and microlite-rich, **dense** clasts (**Fig.5.13f-g**) with highly distorted vesicles rarely exceeding 100 μm, frequently showing pinched edges.

Phenocrysts in all juvenile clast types vary from euhedral to subhedral, and the mineral assemblage is Pl>Opx±Cpx>Mt. The largest Pl phenocrysts (~0.4 mm-1.5 mm) show oscillatory zoning (**Fig. 5.15a**), resorption borders (**Fig. 5.15b**), alteration rims, and are commonly found as Px-Pl or Pl-only glomerocrysts. Several Pl phenocrysts are characterized by fractures parallel to the largest axis, with individual crystal fragments separated by ≤70 μm (**Fig. 5.15c**). Pyroxenes are found within large (~1 mm) 2-Px+Pl cumulates (**Figs. 5.15d-e**) or as small (Opx: 159- 250 μm, Cpx: <44 μm) free crystals. Cpx phenocrysts commonly show rounded outlines and host glass inclusions (**Fig. 5.15f**).

Subrounded, non juvenile hypocrystalline, fine-grained andesitic lithics (**Fig. 5.15g, h**) and microphaneritic diorites (**5.15i**) with rounded outlines are commonly embedded in the groundmass glass of microvesicular and dense lapilli.

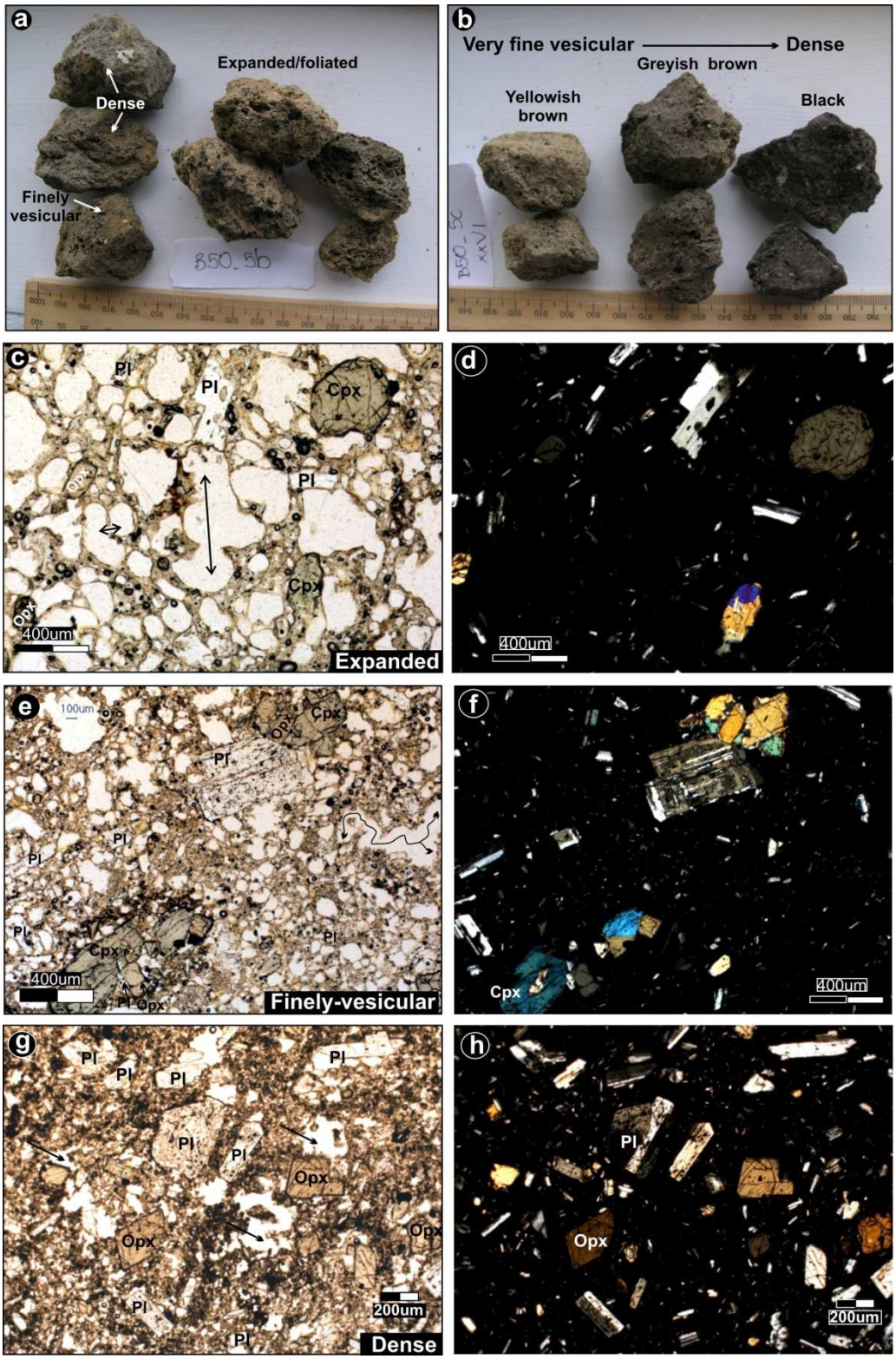

Figure 5.13 Pumice fabrics identified at the same stratigraphic level within the Shawcroft lapilli at: **a)** the base and **b)** top of the deposit. Three main textural end-members are shown, varying from: **c-d)** foamy to expanded clasts with subspherical vesicles between 100 and 800 μm in diameter, having smooth vesicle outlines and thin walls. Different degrees of coalescence are illustrated: double-direction arrows point out aperture throats and interconnection paths; **e-f)** finely vesicular, glomerocrystic, microvesicular clasts with some irregular vesicles

(contorted arrow) and higher microlite content than **c**; **g-h)** crystal-rich, porphyritic, dense end-member with highly irregular and distorted micro-vesicles and abundant microlites.

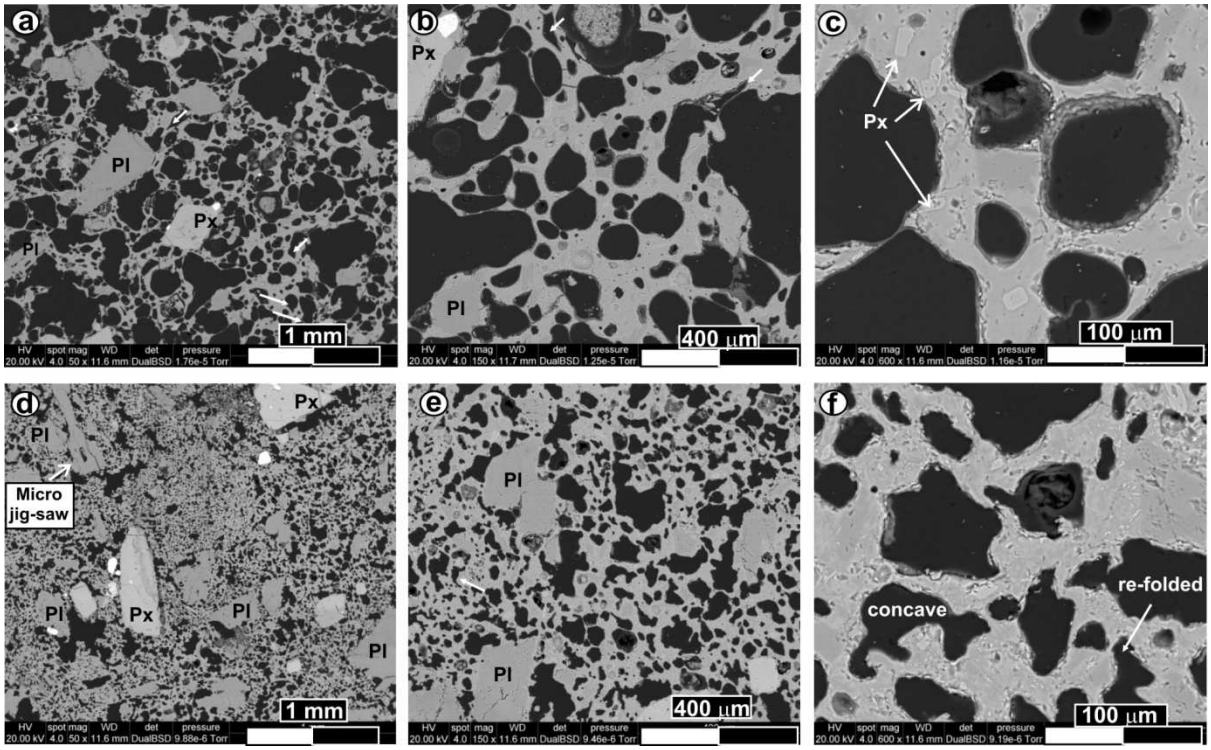

Figure 5.14 Back-scatter electron images (BSE) of pumice samples of the Shawcroft lapilli at three different magnifications: **a-c)** microvesicular with subspherical vesicles showing thick walls and irregular, occasionally sharp edges (white arrows in **a, b**). The groundmass glass contains feldspar and pyroxene microlites **(c)**. **d-f)** Dense end-member with highly distorted vesicles showing thick walls and relatively higher microlite content.

Component analysis and ash-size fractions: relative proportions of each component vary with stratigraphic level, but only slightly with size fraction (**Fig. 5.6; Appendix E.1**). When analyzing the size fractions ≤ 0 ϕ (**Fig. 5.6; Appendix E.1**), there is a significantly higher total lithic content than in the Mgt (up to 31 % in the 3 ϕ size fraction). In addition, the juvenile fragments (**Fig.5.16**) have very low vesicularity compared to the Mgt pumice clasts. Within the coarse ash fraction (**Fig.5.16a**), pale brown and grey, moss-like, phenocryst-rich particles predominate. In the fine ash fraction (**Fig.5.16b-m**) the main distinguishing feature of the Sw is the presence of fused-shaped (c.f., Wohletz and Krinsley 1982) glass shards and Pelé's tears with smooth surfaces (**Fig.5.16f**) and high proportions (24 vol.% of total glass content) of poorly vesicular to non-vesicular, blocky-shaped shards with local conchoidal fractures, grooves, and local stepped surfaces (**Fig.5.16g, i**).

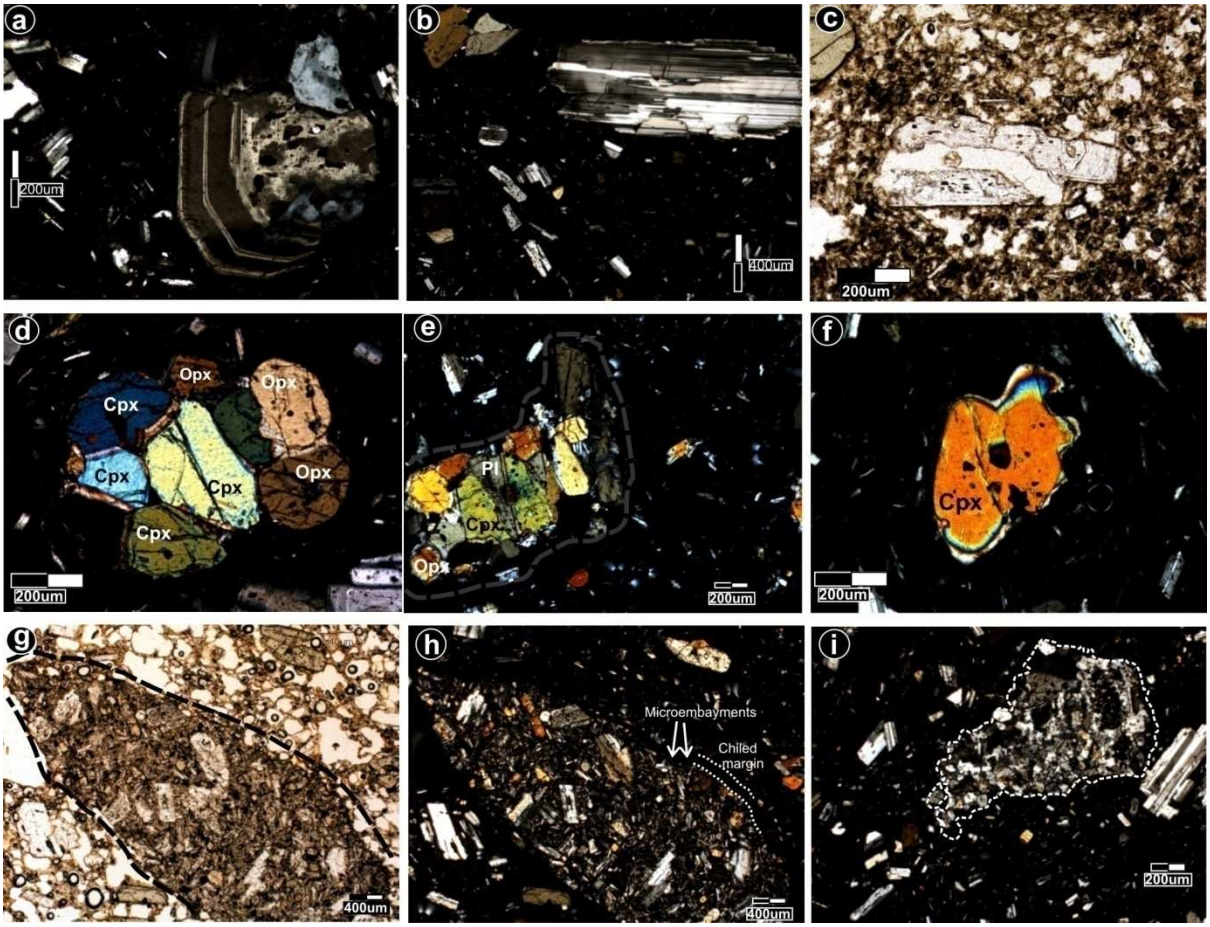

Figure 5.15 a-b) Plagioclase phenocrysts within the Shawcroft lapilli showing: **a)** the complex glomerophyric texture of largest sized Pl, where the core has a sieved texture, glass inclusions, and a subrounded outline; this core is mantled by a subhedral crystal with oscillatory zoning; **b)** border resorption indicated by the rounded outline of the phenocryst, which also has complex intergrowths and twins; **c)** example of a cracked Pl where individual fragments are pulled apart; **d-e)** mafic cumulates consisting of subhedral to anhedral Cpx and Opx, with interstitial Pl and rare Mt; **f)** rounded clinopyroxene with local embayments indicating resorption; **g-i)** non juvenile, entrapped lithics distinguished by a contrasting texture and sharp outline, varying from andesites **(g-h)** to microphaneritic diorites **(i).**

The relative proportions of juvenile glass, free crystal and non-juvenile lithics (**Fig. 5.6**) do not vary significantly with grain size, but change with stratigraphic position. This trend is best represented in the 3 ϕ fraction (**Appendix E.1**). In general, opening phases are lithic-rich and closing, lithic poor, while glass contents are the highest in the waning phase. An almost equally proportioned mixture of components occurs in the interval associated with the climactic phase (**Fig. 5.6**).

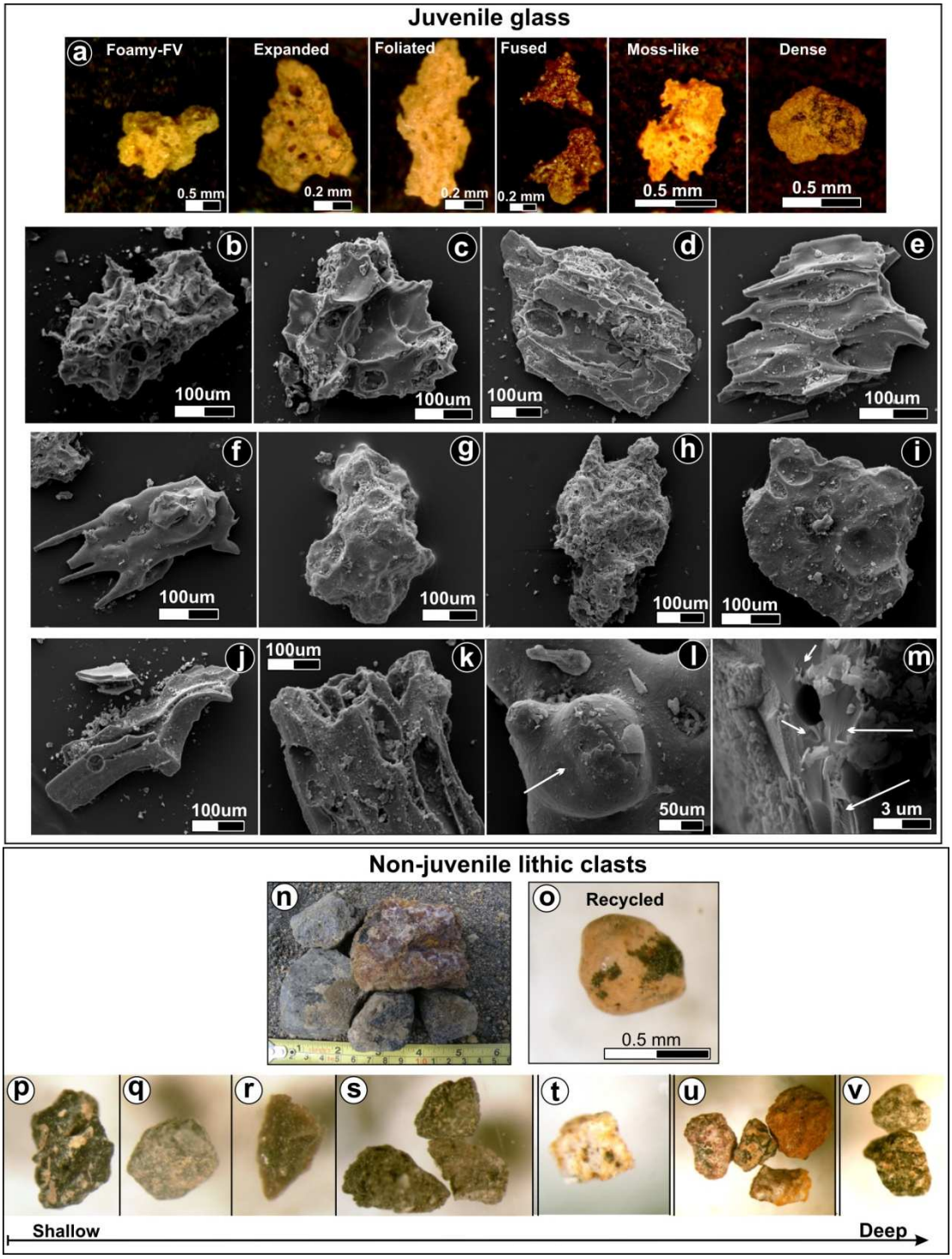

Figure 5.16 a) Main pumice textures identified within the Shawcroft eruptive unit, as seen under binocular microscope; **b)** foamy, highly vesicular particles with subspherical vesicles; **c)** expanded; **d)** fluidal; **e)** fluidal glass with ellipsoidal vesicles having thick walls and smooth surfaces; **f)** Pelée's tear or particle with re-melted surface; **g)** poorly vesicular glass; **h)** poorly vesicular clast with flattened altered, mossy-like surface; **i)** blocky shaped, poorly to non vesicular shards; **j)** glass shard derived from bubble bursting; **k)** fluidal shard with tube-like vesicles; **l)** fluidal, bulbous surface with unburst vesicles (arrow); **m)** step-fractured glass surface with conchoidal fractures, grooves, and "V"-shaped pits (arrows); **n)** typical lithic lapilli; **o)** altered, rounded, recycled pumice from the vent walls/floor; **p)** dark grey andesites; **q)** pale grey, fresh andesites; **r)** brown, fresh Pl+Cpx, hypohyaline andesite (note that they are not necessarily accidental but could also derived from the degassed magma at the base of the conduit; however it contributes to the low-temperature material of the erupting mixture); **s)** brown, vesicular lava; **t)** altered accidental white (Rhyolitic?) pumice; **u)** hydrothermally altered lavas ranging from aphanitic to porphyritic in texture, and **v)** microphaneritic lava clasts.

Within the coarse ash fraction, dense pumice clasts are more abundant in the opening phase, gradually decreasing with time, whereas moss-like and foamy-like particles become common over the climactic and waning phases. The closing phases (XXVI-2a and 2b in **Fig.5.7**) are dominated by poorly vesicular particles. Within the 3 ϕ ash fraction (**Fig. 5.9**), the main Plinian phase contains abundant fused-shaped shards with smooth surfaces and Pelée's tears (**Fig. 5.16f**) at the base and increasing foamy and expanded shards towards the top.

The non-juvenile lithics identified within Sw (**Fig. 5.16n-v**) are the same as within the Mgt unit, along with rounded recycled, altered pumice clasts (**Fig.5.16o**) (up to 28 % of lithics) in the opening and closing phase deposits. Fresh, andesitic lava fragments are the most common and the content remains constant over time (~25 %; **Fig. 5.16p-r**). Other components include partially altered lava clasts (up to 11 % in the Plinian phase; **Fig. 5.16s**), and minor proportions of highly hydrothermally altered clasts (~3 %, or lower in the Plinian phase; **Fig. 5.16t-v**).

In summary, the **Shawcroft eruptive unit** is characterized as follows:

Opening phase (XXVI-1a): the lowermost thin, accretionary lapilli-rich ash bed is extremely lithic-rich (up to 67 % in the 3 ϕ fraction) with progressively less juvenile and higher lithic contents within the finer size fractions (**Figs. 5.6; 5.7**). Most of the glass fragments (up to 82 % of glass) are highly altered, subrounded phenocryst-rich and poorly vesicular, with rare ellipsoidal vesicles and thick walls. The fresh glass content is low (9 % in the 3 ϕ fraction), mostly made up by non-vesicular, fused-shaped shards and Pelée's tears with smooth surfaces, and moss-like shards. Non juvenile fragments are dominantly recycled pumice clasts from earlier Ruapehu tephras (43 %), fresh andesites (22 %), minor proportions of partially altered lava clasts and highly hydrothermally altered lithics (2 %).

Plinian phase (XXVI-1b; 1c): this produced the thickest and coarsest grained bed and contains the highest contents of juvenile fragments (**Fig. 5.7; Appendix E.2**). The juvenile component rises from 38 % to 45 % upward, whereas the lithic content remains constant (31 %). Fresh dark brown, Pelée's tears and fused-shaped shards with ellipsoidal vesicles, and moderately to poorly-vesicular shards are common in the finest fractions at the base of the deposit (**Fig. 5.9**); moderately vesicular (expanded) pumice shards, fibrous and "Y"-shaped glass shards increase towards the top (**Fig. 5.9**). The relative proportions of fresh andesitic lava lithics and highly hydrothermally altered lithics increase upward, along with the

appearance of rare phaneritic, dioritic clasts (**Fig. 5.10b**). Further geochemical analyses, excluded in this study, are needed to identify what proportion of the fresh andesites are juvenile clasts sourced from the base of the conduit, or accidental. To date their content is included within the accidental fragments.

Waning phase (XXVI-1d): this deposit consistently shows the highest low-density, juvenile and lithic contents (**Fig. 5.6**). It contrasts to the underlying deposits, in being rich in fresh, foamy, highly vesicular clasts (**Fig. 5.7**) with fluidal texture and smooth surfaces. Most non-juvenile fragments are recycled pumice clasts (**Fig. 5.10b**).

Chemical composition: juvenile pumice whole rock analyses (**Appendix F.1**) indicate that the Shawcroft unit has a restricted andesitic bulk lapilli composition (SiO_2: 57.02-58.4 wt.%, dry basis), without significant variations over stratigraphic height (time). Groundmass glass compositions are also restricted in range (**Appendix F.2**; SiO_2: 60.62-64.22 wt.%) with weak trend of microlitic, dense textured glasses towards higher silica contents (**Fig. 5.17**). Glass inclusions in Cpx and Opx have dacitic compositions (**Appendix F.3**; SiO_2: 64.25-67.74 wt.%).

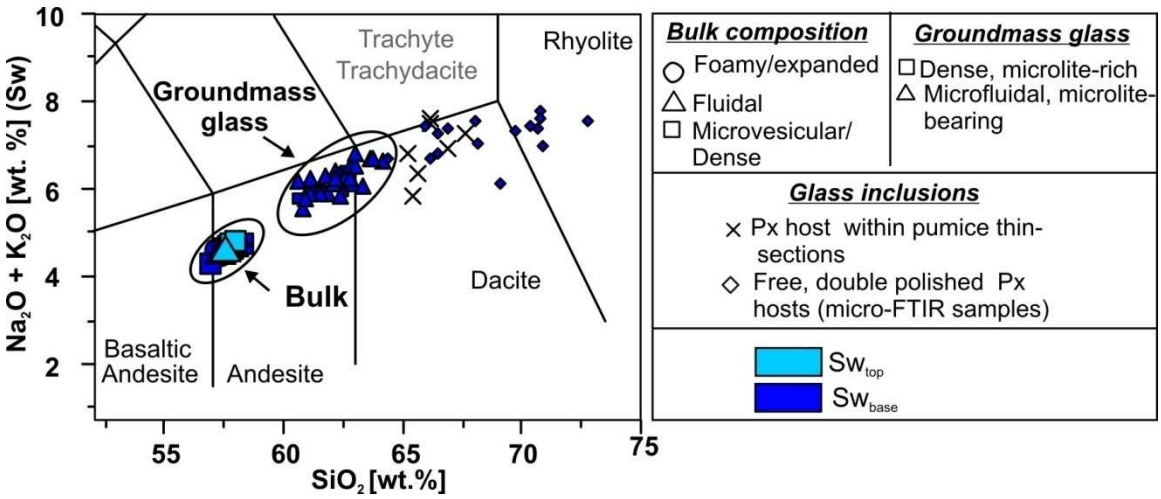

Figure 5.17 Total alkalis vs. silica (TAS) diagram (Le Bas et al., 1986) showing the bulk and glass composition of juvenile pumice clasts within the Sw lapilli. The homogeneity in pumice textures relative to Mgt samples is also reflected by a single cluster of groundmass glass compositions. Glass inclusions are consistently more silicic than groundmass glass (dacitic to rhyolitic).

Discussion: according to these observations, the erupting Shawcroft magma was very similar in bulk composition to that during the Mgt episode. Similar to the Mgt case, glass inclusions are higher in silica than groundmass/lapilli glass, which is inconsistent with normal patterns

of fractional crystallization (c.f., Lowenstern 1995). The Sw magma had a similar degassing history, storage periods, and/or ascent rates to the U-Mgt conditions. Contrasting with the Mgt, the Sw magma was both chemically and texturally homogeneous.

The typically microporphyritic pumice clasts of the Sw have subspherical to slightly distorted vesicles that are significantly smaller than in the Mgt unit (**Fig. 5.14**). This indicates restricted vesicle growth within a microlite-bearing melt, inducing volatile saturation and bubble gas overpressure (c.f., Martel and Schmidt 2003; Woods 1995). The lithic content within the finest size fractions, together with variation in glass shard morphology types with grain-size and stratigraphy, suggests that the initial opening phase was shallow-phreatomagmatic. This is interpreted as an explosive interaction of slowly rising magma and deep groundwater to produce the basal ash fallout containing abundant accretionary lapilli. The opening phase generated a sudden decompression of the underlying viscous andesitic magma, which was probably already saturated in volatiles due to the extensive crystallization of anhydrous phases. This decompression led the violent release of the over-pressured small bubbles and subsequent fragmentation. Excavation and erosion (e.g., Macedonio et al., 1994; Woods 1995) of the hydrothermally altered conduit walls promoted entry of hot geothermal fluids (c.f., Papale et al., 1998; Houghton et al., 2004). Although fine lithics are abundant and poorly vesicular shards with grooves are found, there is a lack of distinctive quenching cracks and stepped-surfaces (c.f., Büttner et al., 1999; Dellino et al., 2011). This observation indicates magma probably interacted with external fluids, perhaps aiding fragmentation, but a true fuel-coolant interaction did not occur. Based on pumice lapilli and ash textures, the decreasing content of dense fragments with stratigraphic position indicates progressive deepening of the fragmentation interface with time during the main Plinian event. The closing phases (**Fig. 5.7**), signal a return to shallow fragmentation (>dense particles; c.f., Spieler et al., 2004a).

The fused-shaped shards and Pelée's tears that characterize this unit are indicative of post-fragmentation ductile behaviour due to slow quenching rates (c.f., Toramaru 1990) and probably high exit-velocities (c.f., Shimozuru 1994). These features probably reflect highly effective heat flow conditions during the Sw eruption (c.f., Wilson et al., 1978) and are consistent with the high altitude reached by the eruptive column producing Sw (which was ~7 km higher than that reconstructed for Mgt unit; **Chapter 4**).

Although the typical Sw lapilli deposit is massive, an interbedded surge deposit was found at one proximal location (B50 **Appendix A**), providing evidence for marginal column collapses and the generation of pyroclastic density currents simultaneously with the central sustained column. Towards the end of the eruption, the degassing rate was probably faster than magma ascent/discharge rate, leading towards smaller-scale closing phreatomagmatic phases (**Fig. 5.12a**).

5.2.3 Unsteady and collapsing, high (> 30 km) columns: Orumatua Eruptive Unit

Lithofacies: eruptive units younger than the Shawcroft change in character, as exemplified by the Oruamatua eruptive unit (**Chapter 3**). Together with the analogous Akurangi Eruptive unit they represent the most violent events produced by Mt. Ruapehu, before the transition toward the significantly smaller events and less violent styles experienced by this volcano throughout the Holocene.

The Oruamatua eruptive unit (**Fig. 5.18**) is subdivided into three main pyroclastic subunits (Lower, Middle, and Upper), distinguished by proximal-medial (5-20 km) deposit characteristics (locations B1, B6, B13, B16B50, in **Appendix A**). Individual subunits are bounded by fine-grained diamictons, typically lensoidal, poorly sorted and heterolithologic sand and pebbles set in a lithic-crystal sand matrix. These deposits are interpreted to represent syn-eruptive, hyperconcentrated flows occurring due to tephra reworking during short pauses in the eruption (**Chapters 3-4**). At more distal locations (e.g. B72, B132 in **Appendix A**), the tephra fall consists of a single massive, clast-supported, fine pumice lapilli bed.

The Lower Oruamatua tephra (L-Oru): deposits representing the onset of the Oruamatua eruptive unit begin with a thin (<5 cm) mantling, fine-ash bed, overlain by a widespread $\leq$ 20 cm thick, massive, clast-supported, well sorted (σ_I = 1.5), medium lapilli bed (Mz = -2.6 ϕ). This unit is highly distinctive because pumice lapilli is only marginally more abundant than lithics (~45 %), the latter of which contain common red, orange and yellow hydrothermally altered andesites (XXVII-1 bed in **Fig. 5.18**). This deposit usually shows a negatively skewed grain-size distribution (**Fig. 5.18; Table 5.1; Appendix C**), typical of coarse-grained fall deposits. This lapilli bed is capped by a thin, dark-grey fine ash. Shower bedding occurs at

exposures laterally away from the dispersal axis (e.g. B59, **Appendix A; Figs. 4.2** and **4.3**). A brief respite in the pyroclastic deposition sequence is marked by hyperconcentrated flow deposits, forming silts and sand-dominated, lensing beds, filling hollows and exhibiting high-angle cross stratification, aligned pebbles along with clast-supported zones.

The Middle Oruamatua Tephra (M-Oru): the resumption of eruptive activity is evidenced by a second, medium-coarse pumice lapilli bed (XXVII-2 bed in **Fig. 5.18**), which is massive at proximal locations, and distinctively shower-bedded at medial locations. It usually consists of coarse ash to fine lapilli (Mz = 0.1 ϕ), which is poorly sorted (σ_I = 2.8) and characterized by a bimodal grain-size distribution (**Fig. 5.18; Table 5.1; Appendix C**).

Each lapilli bed within the M-Oru is capped by a thin, fine platy ash bed. The unit also shows lateral and longitudinal facies variations. Along the Upper Waikato stream, the fall bed is replaced by a massive, matrix-supported, very poorly sorted pumice-rich deposit, showing abrupt thickness variations (**Fig. 3.13; Chapter 3**). It contains rounded, heterogeneous and multicoloured lithic lava blocks with porphyritic textures (~30 %), and dark brown pumice coarse lapilli set in a fine ash pumice and crystal-fragment matrix. Its sedimentary characteristics (**Chapter 3**) are indicative of accumulation from a pyroclastic density current (PDC) flowing parallel and close to the current Upper Waikato Stream.

The Upper Oruamatua Tephra (U-Oru): the U-Oru has a distinctive basal 1-5 cm-thick, yellowish-brown, platy-ash fall bed (XXVII-3a), containing abundant accretionary lapilli that coarsen upward. It is capped by a clast supported, massive deposit (XXVII-3b), grading from poorly sorted (σ_I = 2.5) fine lapilli (Mz = -1.4 ϕ), at the base, up to well sorted (σ_I = 1.6), medium lapilli (Mz = -2.4 ϕ) at the top in proximal localities. It becomes shower-bedded at medial sites, with each ~10 cm lapilli bed being capped by a thin, mantling ash bed. Lithics are common (~29 %) and consist of coarse to fine-grained porphyritic, olive grey and rare vesicular red lava clasts. Locally, this subunit also laterally passes into a matrix-supported facies, with poorly sorted pumice lapilli set in a fine ash matrix (indicative of pyroclastic density current deposition). At the top, XXVII-3 is mantled by fine ash and at proximal locations (~5 km), the fine ash is thicker, finely laminated, and shows low-angle cross lamination, and a vesicular matrix.

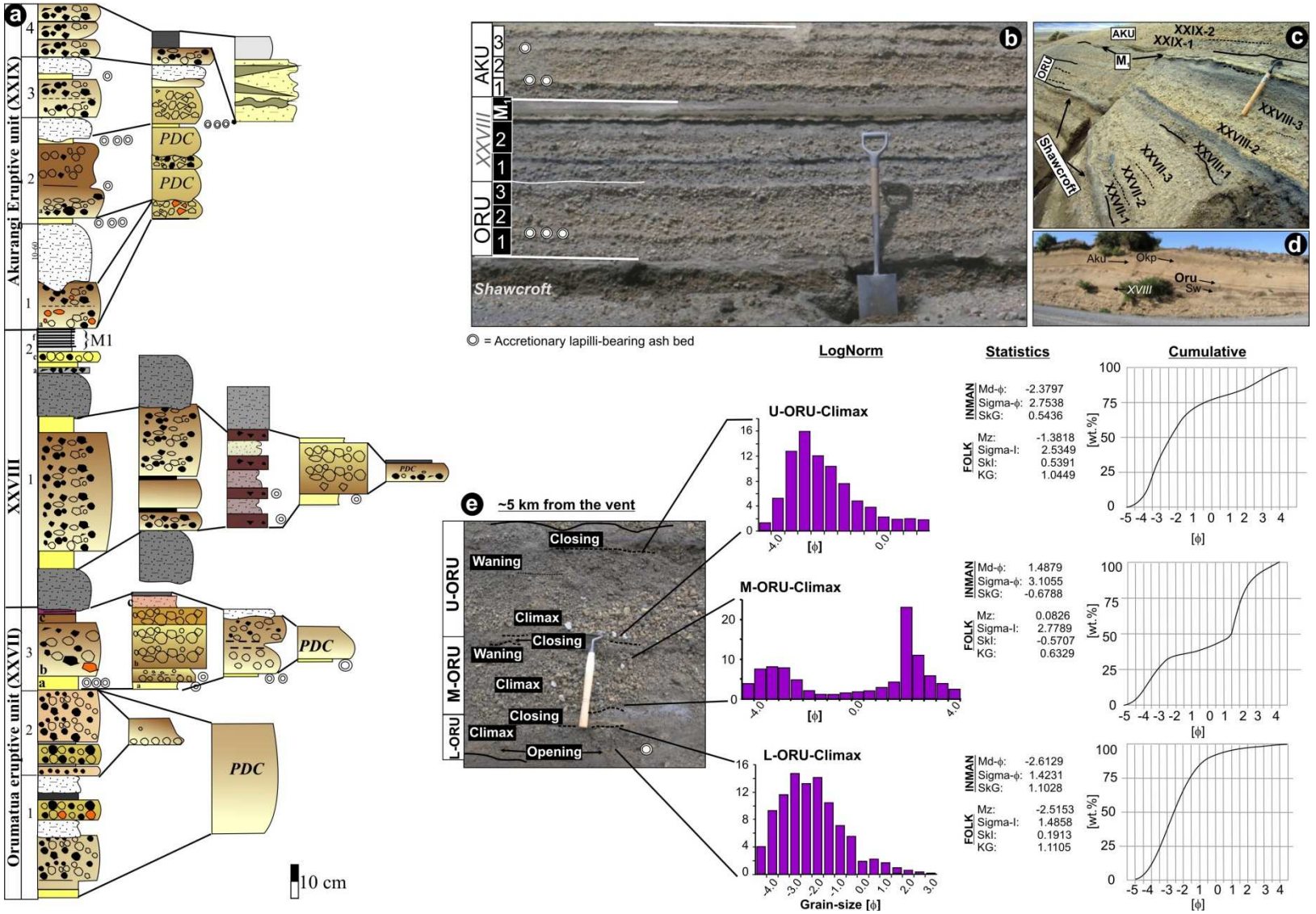

Figure 5.18 (*see caption next page*)

Figure 5.18 a) Detail of the stratigraphic sections comprising the Oruamatua (Oru) and Akurangi (Ak) eruptive units, including the inferred eruptive phases (see details in **Chapter 3**); **b)** note the stratified (shower-bedded) nature of these units, with multiple parallel beds contrasting in grain-size; **c)** PDC facies (XXVII-2) interbedded within fallouts; **d)** stratigraphic position at ~17 km from the vent; **e)** grain-size distribution histograms for the main eruptive phases within Oru are shown, with the corresponding cumulative curve and statistical parameters as calculated with SFT software. Results are typical of pyroclastic fall deposits, although the M-Oru shows transitions to matrix-supported deposits, with polymodal distributions consistent with the accumulation of Pyroclastic flows.

These features are interpreted to indicate deposition from pyroclastic surges, associated with the topographically controlled, poorly sorted pyroclastic density current/pyroclastic flow deposits described earlier. At medial localities the main, lapilli fall bed is overlain by post-eruptive, sand-dominated hyperconcentrated flow deposits (**Chapters 3, 4; Appendix A**).

Pumice textures: typical Oru fall deposits are characterized by highly heterogeneous pumice clasts, including microfibrous, colour-banded, and microlite-rich, dense textures (**Fig. 5.19a; Appendix D.3**). Non banded pumice clasts (**Fig. 5.19b-e**) dominate and vary from **(a)** crystal-bearing, **microvesicular pumice** to crystal-rich, **dense** clasts (**Fig. 5.19b,c**) having distorted vesicles with thick walls, to **(b) microfibrous,** microlite-rich clasts **Fig. 5.19d**) with highly sheared vesicles having thin, commonly wrinkled walls; some vesicles have pinched terminations (**Fig. 5.19e**). Differences between the microfibrous and dense clasts are best seen in BSE images (**Fig. 5.20**). In hand-specimen, most of the vesicles are $\leq$0.5 mm, although rare expanded clasts with ellipsoidal vesicles >5 mm can also be found. The mineral assemblage is Pl>>>Opx>Cpx>Mt. Occasionally, and mainly at proximal locations, a third contrasting clast type **(c)** is **coloured-banded**, dense to microfibrous and characterized by the local alignment of sheared vesicles and phenocrysts. The difference in colour bands (**Fig. 5.19f, g**) corresponds to textural variations, mainly in terms of vesicle shape and size, crystal size, and microlite content (Table D1 in **Appendix D.3**). The mineral assemblage is the same in each band.

Phenocrysts are relatively large compared to the pumice clasts analyzed in older eruptive units (2.0 x 0.8 mm in average). Pl phenocrysts show seriated textures and are commonly euhedral to subhedral, some showing sieve textures. Cracks in plagioclase are both parallel and perpendicular to the longest axis (**Fig. 5.21b**). Pyroxenes vary from subhedral to anhedral, with Cpx commonly forming glomerocrysts with Opx, Pl and magnetite (Mt). Most of the Opx are twined (**Fig. 5.21c**).

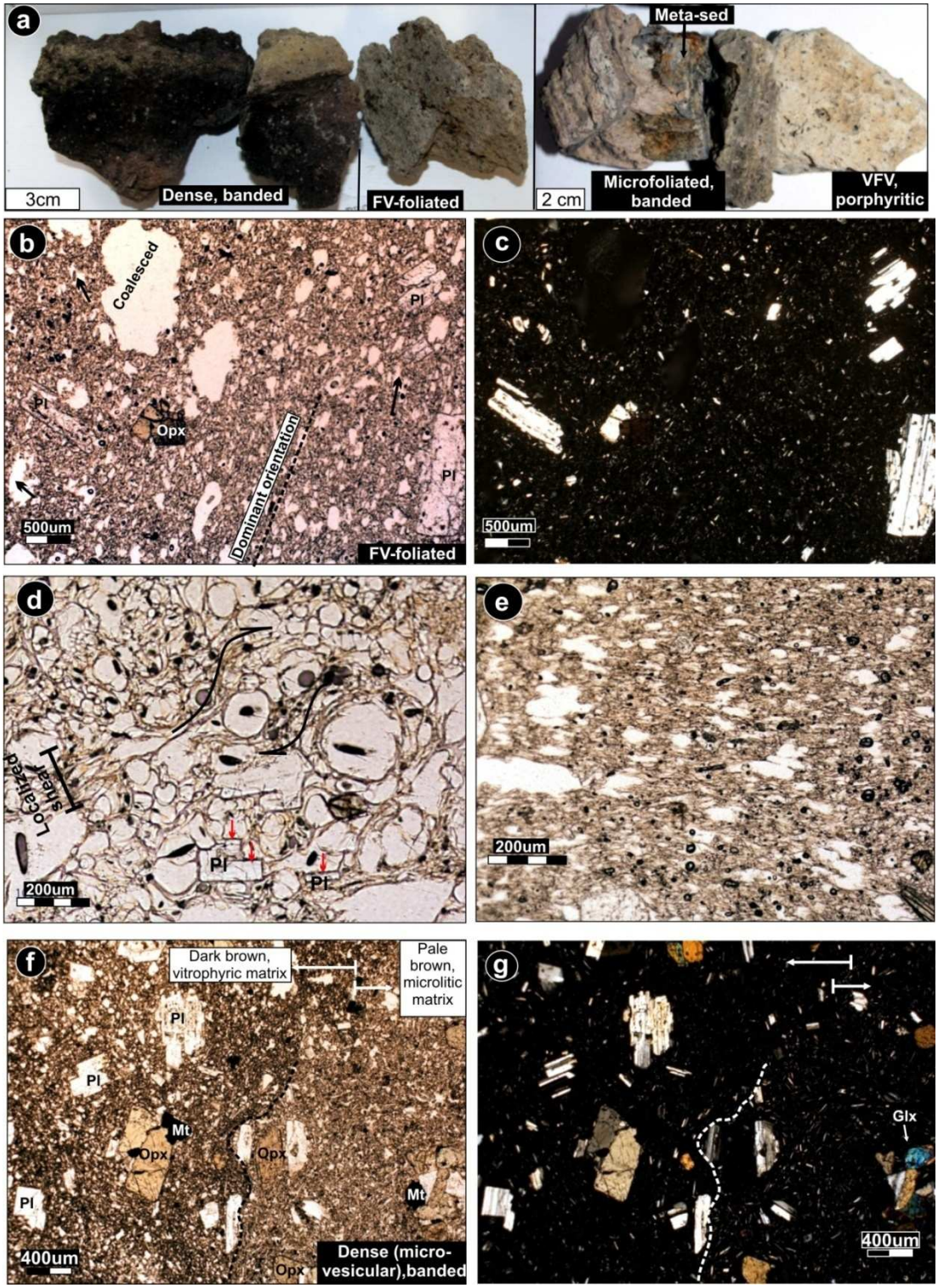

Figure 5.19 a) Macrotextural variations within the same stratigraphic level of the Oruamatua Tephra. **b)** Dense, microfluidal textural end-member, usually pale, grayish brown in colour. Note the alignment of elongated vesicles. Some vesicles are highly distorted or show abrupt termination (arrows), which is in part due to the high microlite content (**c**). Different degrees of vesicle deformation can be traced, from: **d)** localized shear bands evident at higher magnitudes, with sigmoid-like and distorted vesicles (arrows), contrasting to neighboring spherical vesicles. Note the sharp edges of some of the vesicles dictated by the neighboring crystals (red arrows); to **e**) extremely flattened and refolded vesicles with irregular outlines; **f)** banded microvesicular texture, common in the U-Oru. Note the difference between the dark brown and the pale brown bands. Under crossed polarizer (**g**) the bands are distinguished by the microlite content.

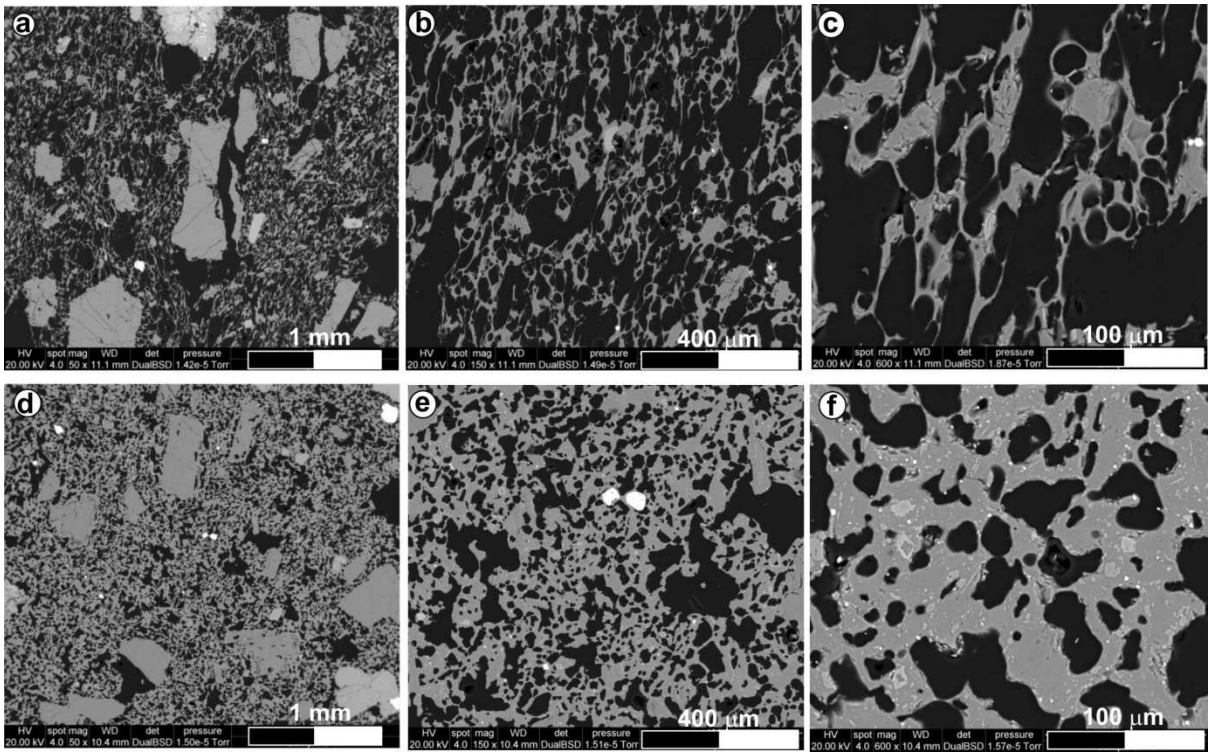

Figure 5.20 Backscattered electron images of the main contrasting textures within the Oruamatua unit, including a-**c)** microfibrous, coarsely porphyritic clasts with feldspars phenocrysts showing micro jig-saw structures **(a)**, and elongated vesicles, some with pinched edges **(b)** and thin vesicle walls **(c)**; **d-f)** dense textures are coarsely porphyritic **(d)**, vesicles are extremely distorted, showing pinched edges **(b)** and very thick walls in a microlite-rich glass groundmass **(f)**.

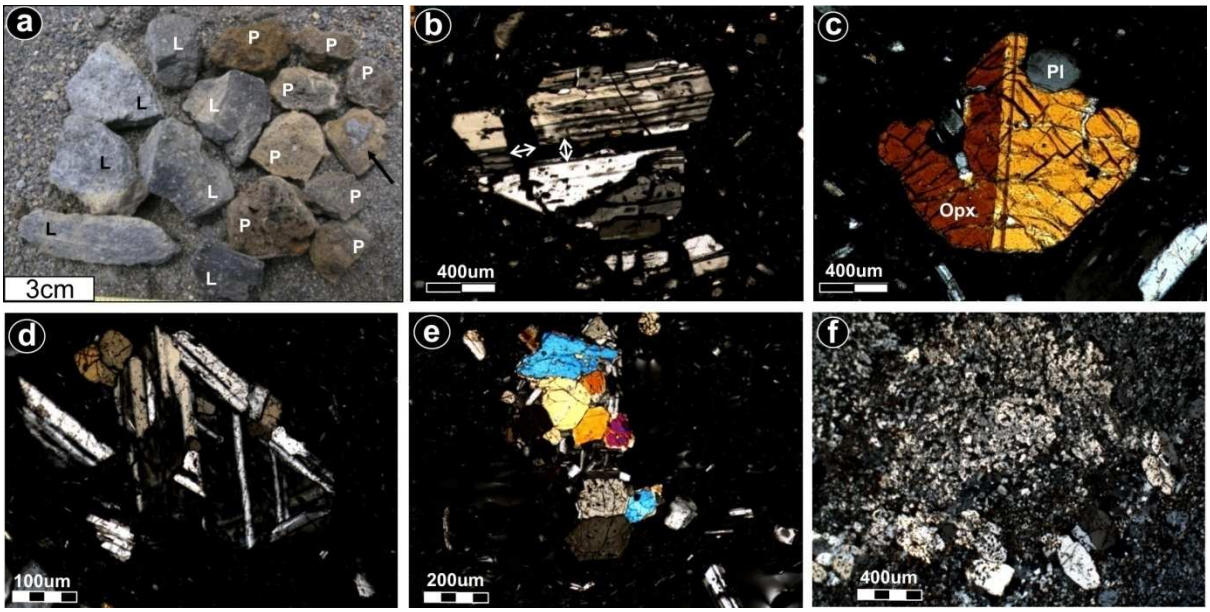

Figure 5.21 a) Typical lithic (L) and juvenile (P) Oru lapilli in the field. Note that lithic clasts are commonly entrapped within pumice clasts (arrow); **b)** euhedral to anhedral plagioclase phenocrysts show cracks oriented both parallel and perpendicular to the longest axis, with individual fragments pulled apart a few microns (see arrows); **c)** euhedral orthopyroxene with twining; **d)** euhedral Pl-Glomerocrysts with a few anhedral Orthopyroxene microcrysts; **e)** glomerophyric 2-Px+Pl texture; **f)** metasedimentary clast embedded in a dense clast.

Entrapped lithic clasts are common (**Fig. 5.21a**), varying from igneous, microphaneritic, 2-Px+Pl aggregates (**Fig. 5.21e**), to accidental, metasedimentary quartzitic siltstones (**Fig. 5.21f**), which represent fragments detached from the tertiary basement (Graham et al., 1990). Traces of corroded olivine xenocrysts are also found.

Component analysis and ash-size fractions: the components identified within Oru are the same types identified within Sw. The relative proportions of each component vary with stratigraphic position and weakly with size fraction (**Figs. 5.6, 5.7, 5.10c; Appendix E.3**). In the size fractions ≤0 ϕ (**Fig.5.6**), Oru has a very high total lithic content (up to 66 %), in the early and late phase deposits, with lower contents between.

Glass fragments are predominantly finely vesicular-to-dense, with significantly higher crystal contents than previous units. Within the ash fraction the following classes were identified: **a)** Dark brown, fresh, moderately vesicular (**expanded**) clasts with fluidal surfaces (**Figs. 5.22ae**); **b)** varying from **foamy**, finely vesicular clasts with subspherical vesicles (~11 μm, 32, >50 μm) to **microfibrous** having thin vesicle walls and ranging in colour from white to bronze, some oxidized to orange (**Fig. 5.22b, f**). **c)** Equant, **moss-like** particles with irregular-shaped vesicles (~7, ~25, ~45 μm) having very thick walls (8-25 μm), particularly concentrated in the 2 ϕ fraction (**Fig. 5.22c, g**) ; **d)** Pale brown and pale grey, crystal rich, blocky to **plate-shaped** (c.f., Palladino et al., 2008), occasionally subrounded, dense particles (**Fig. 5.22d, h**). These morphologies were identified also in the 3 ϕ fraction, together with fluidal shards showing ellipsoidal and oriented vesicles (**Fig. 5.22i, j**), fused-shaped shards or few dense particles with melted surfaces (**Fig. 5.22k**), and occasionally blocky-shaped shards (**Fig. 5.22l**). Flattened vesicles are common (**Fig. 5.22m**) along with micro-scale surface features, such as conchoidal fractures, grooves, local "V"- shaped pits (**Fig. 5.22n, o**), and stepped surfaces (**Fig. 5.22p**).

The main distinguishing feature of the Oru unit is the presence of types **c** and **d** particles, commonly showing distorted vesicle shapes with thick walls, and the very high content of hydrothermally altered lithics (**Fig. 5.22s**) in the finest size fractions (up to 23 %, **Appendix E.3**).

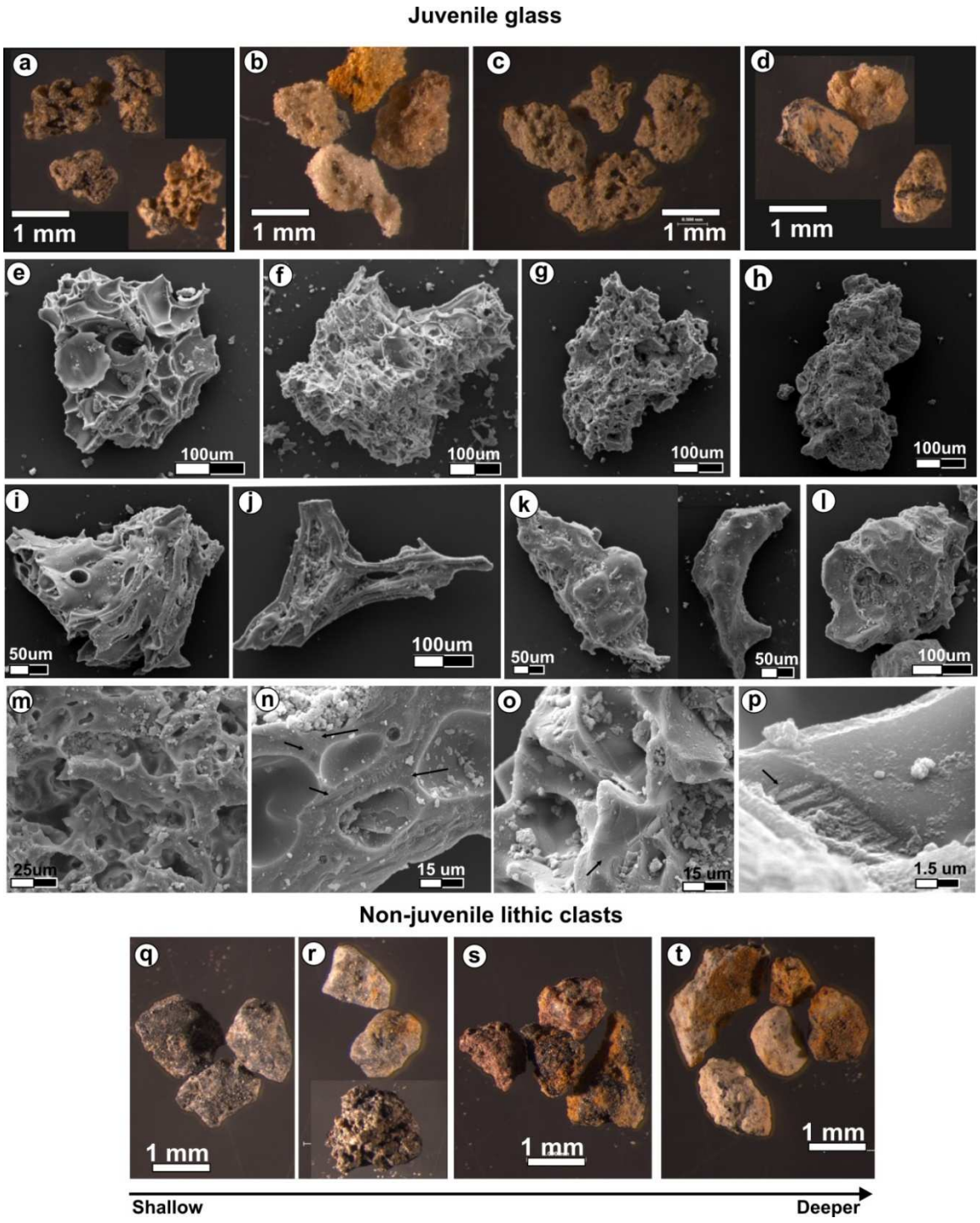

Figure 5.22 Main ash components identified within the Oruamatua Unit, under a binocular microscope: **a)** highly vesicular particles; **b)** microfibrous particles with different colours due to different microlite content and degree of oxidation; **c)** grey, microvesicular to dense particles with sharp edges; **d)** crystal-rich, dense, coarse-grained porphyritic (glomerophyric) particles. Ash particles within the 3 ϕ fraction under SEM include: **e)** foamy to expanded, highly vesicular pumice shard with subspherical vesicles; **f)** fibrous shard; **g)** scoreaceous particle having distorted vesicles with thick walls; **h)** typical mossy-like end-member, poorly vesicular and with occasional melted surfaces. Shards derived from bubble-wall rupture include: **i-j)** tube-like; **k)** Dense particles with melted surfaces, and **l)** blocky-shaped shards. In detail, **m)** shows the flattened vesicles having over-thickened walls within **g**. Conchoidal fractures are common (arrows in **n** and **o**) as well as stepped surfaces **(p)**. Accidental clasts include: **q)** fresh, dark and pale grey andesites; **r)** partially altered dense and vesicular

andesites; **s)** hydrothermally altered volcanic ranging from aphanitic to porphyritic lavas; **t)** altered accidental white sedimentary clasts.

The main difference with the older Sw unit is the incorporation of high contents of more deeply derived accidental lithics, some of them sedimentary (**Fig. 5.22t**) and sourced from the tertiary "basement". These deep-sourced lithics are particularly concentrated in the opening and closing phase deposits (**Fig. 5.10c**).

For the purpose of this study, and considering the high number of individual beds in many locations, only the main lapilli fall deposits of the **Oruamatua Plinian phases** were detailed as follows:

L-Oru: the lithic content of the first Plinian phase shows the highest values in the finer grain sizes, hence the glass and crystal contents are correspondingly the lowest (**Fig. 5.6**). Most of the glassy coarse ash particles at the base of the L-Oru (XXVII-0 bed) correspond to moderately vesicular grains with irregular vesicles showing thick walls. Other morphology types include: dense, moss-like, platy to prismatic particles (**Figs. 5.22c, g, h**), with fewer fibrous pumice clasts (**Fig. 5.22b, f, i, j**). At the top of the L-Oru (XXVII-1 bed), highly vesicular fragments (**Fig. 5.22a, e**) are incorporated, including some expanded grains and fused-shaped particles (**Fig. 5.22k**). The finely fragmented non-juvenile components are mainly fresh, andesitic lava (17-41 %) (**Appendix E.3**). Glass shards (**Fig. 5.9**) are predominantly highly vesicular and foamy (**Fig. 5.22e, g**), with subordinate coarsely vesicular fluidal pumice shards showing smooth surfaces (**Fig. 5.22i-k**).

M-Oru: the second major Plinian phase (XXVII-2 bed) is very similar to the L-Oru, except that phaneritic and microphaneritic clasts derived from deeper levels in the conduit are scarce to absent (**Fig. 5.10c**). Within the coarse ash fractions, dense particles with melted surfaces, resembling collapsed-bubble textures, become important in all size fractions (**Fig. 5.7**). Within the 3 ϕ size fraction (**Figs. 5.9, 5.22h**), mossy-like, poorly vesicular, platy to blocky-shaped shards are more common. Glass shards are characterized by conchoidal fractures, local grooves, stepped surfaces, and impact pits (**Fig. 5.22m-p**).

U-Oru: the last Plinian phase (XXVII-3 bed) is distinctive by the high content of accidental lithic clasts derived from deep regions (**Fig. 5.10c**) and highly vesicular, glass shards with thick walls in the fine ash size fraction (**Fig. 5.9**). Poorly vesicular and blocky-shaped shards with sharp edges, local stepped surfaces, conchoidal fractures, grooves, and impact pits (**Figs. 5.9, 5.22l**) are common.

Chemical composition: juvenile pumice whole rock analyses (**Appendix F.1**) plot within the andesitic field (**Fig. 5.23**), showing a wider range relative to earlier units (SiO_2: 57.33-60.14 wt.%, dry basis). This variation is not systematic over stratigraphic level (i.e. time). Groundmass glass compositions (**Appendix F.2**) of the main Plinian phase (M-Oru) are rhyolitic, consistent with the high crystallinity of pumice samples relative to previous eruptive units (SiO_2: 70.08-74.92 wt.%). Contrasting with previous units, glass inclusions (**Appendix F.3**) in Cpx and Opx are more mafic than the residual glass, varying from dacitic to low-silica rhyolitic (SiO_2: 65.3 and 69.15 wt.%).

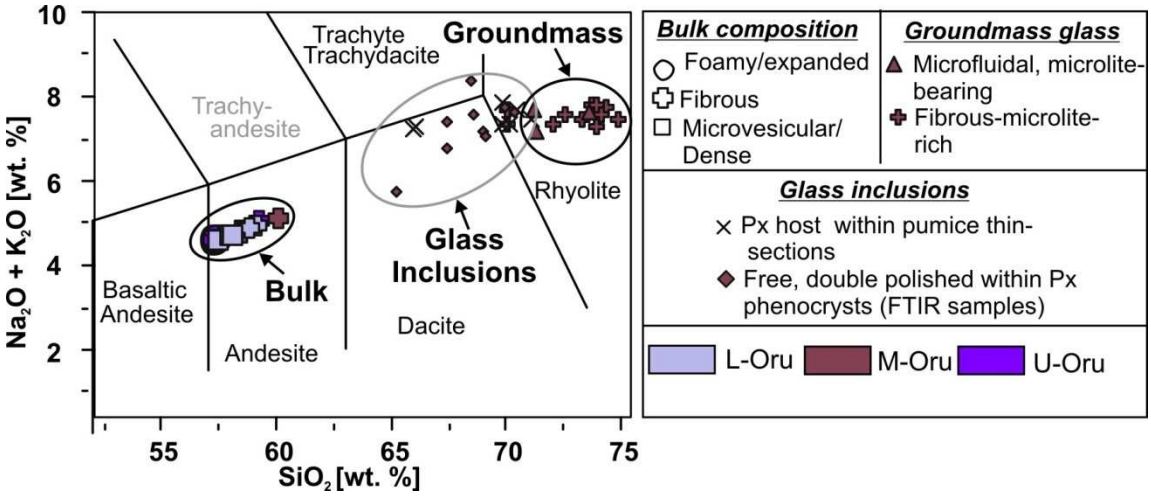

Figure 5.23 Total alkalis vs. silica (TAS) diagram (Le Bas et al., 1986) showing the bulk and glass composition of juvenile pumice clasts within the Oru unit as well as the glass inclusions in pyroxene crystals. Note that the high groundmass glass silica contents are consistent with more crystal-rich textures relative to earlier eruptive units, as well as glass inclusions being more mafic than groundmass glass.

Discussion: the Oruamatua unit signals a change from stable to unsteady eruptive columns from Mt. Ruapehu. These oscillating and collapsing columns also generated significant pyroclastic density currents (**Chapters 3, 4**). The main phases of the Oru were preceded and followed by phreatomagmatic explosions, producing thin, accretionary lapilli rich, and platy ash fall beds. The magma was slightly more siliceous than previous units and contrasting to them, glass inclusions are more mafic than residual groundmass glass, consistent with post-entrapment fractional crystallization of plagioclase, orthopyroxene and clinopyroxene (c.f., Lowenstern 1995; Signorelli et al., 1999). The high crystal and microlite contents, high bulk-rock SiO_2 contents, and evolved residual melt compositions suggest a prolonged storage at shallower levels than during the Mgt and Sw episodes (c.f., Cashman and Ferry 1998; Papale et al., 1998).

The Lower Oruamatua tephra: the initial highest lithic content, the concentration of lithics within the finest grain-sizes, and the presence of deep-derived lithic fragments indicate that the first, major Plinian phase of the Oru reamed out the lower conduit associated with intense fragmentation. The relatively higher vesicularity of the finest glass shards compared to those erupted in subsequent phases of this episode suggests that this was the most volatile-rich magma batch.

The Middle Oruamatua tephra: after a short repose period, the eruptive activity recommenced, with the generation of an extremely unsteady eruptive column. The disappearance of deep-derived lithics and vesicular (i.e., fluidal) textures, and predominance of dense, poorly-vesicular, mossy-like ash textures suggest a shallower fragmentation level relative to the first climactic phase. The abundance of vesicular grains with flattened vesicles showing thick walls (**Fig. 5.9**) suggests that this magma was more degassed than L-Oru. Depletion in the volatile content could allow the inflow of external water into the conduit, improving fragmentation efficiency (i.e., smaller grain-size). These conditions favoured the unsteadiness of the column, contributing to column collapses and the subsequent generation of pyroclastic density currents.

The Upper Oruamatua tephra: after a brief repose period, the eruptive activity recommenced. The U-Oru componentry suggests that the fragmentation level might have deepened once again, involving more vesicular magma and incorporating deep microphaneritic and sedimentary clasts (**Fig. 5.10c**), whereas the access of external water (evidenced by the increased blocky shard content in **Fig. 5.9**) contributed to unsteady and collapsing columns. Excluding the lithic-rich opening phase, the increase in lithic content from the L-Oru towards the U-Oru within the finest ash fraction (**Fig. 5.6**), suggests a progressive enlargement of the conduit/vent. This process favoured access of external water and unsteadiness of the eruptive column (c.f., Kaminski and Jaupart 1997).

Overall, the high crystal content and silica-rich glass of the Oru eruptive unit suggests more viscous conditions prevailed than during previous eruptive units described here. The variability of pumice textures and ash morphologies is more pronounced than the Mgt unit. Localized shear in the conduit generated strong vesicle elongation and banding, which would have modulated the rheology of the mixture (c.f., Massol and Jaupart 1999; Stein and Spera 2002; Wright and Weinberg 2009). The entire Oru unit is characterized by crystal-rich clasts with irregular vesicle shapes and very thick vesicle walls within a microlitic groundmass.

These features are indicative of mature textures, suggesting advanced degree of degassing and vesicle collapse prior to fragmentation. The different textures indicate a complex, heterogeneous magma rheology across the conduit, with even more effective segregation of rheological zones than in the Mgt eruption.

The dense and banded pumice clasts with very high microlite content in the groundmass and the progression from vesicular towards more moss-like and ultimately dense, blocky-shaped particles (**Fig. 5.9**), indicate that magma reaching the fragmentation level was progressively degassing over the course of this eruption episode. Variable porosity (and therefore, in density) of magma across the conduit could have contributed to an irregular fragmentation surface, with density variations across the conduit affecting the position of the fragmentation front (c.f., Spieler et al., 2004a).

5.2.4 Unsteady, collapsing columns of intermediate height (<25 km): Okupata-Poruahu eruptive unit

Two subunits (Lower and Upper Okp tephras; **Appendix A**) consist of deposits from multiple eruptive phases, each characterized by different transport and accumulation mechanisms (**Chapters 3, 4; Fig. 3.24; Appendix A**).

Lithofacies: the onset of the eruptive activity is marked by a proximally exposed, thin fine ash bed containing accretionary lapilli (*opening phase*; **Fig. 5.24a**). The basal ash is mantled by a distinctive, pale brown to white, massive, clast-supported, fine and medium lapilli bed (Mz = -1.7). The grain-size distribution at proximal sites is nearly symmetric, well sorted (σ_I = 1.6), but platikurtic (**Fig. 5.24f; Table 5.1; Appendix C**). Pumice clasts are extremely finely vesicular to dense, commonly coloured-banded, and rarely coarsely vesicular, fibrous, and porphyritic. This bed (XXXII-1a: *Plinian phase-1*; **Fig. 5.24a**) is thicker and coarsens towards the N-NW, where it is characterized by a basal concentration of extremely light, microvesicular, plate-shaped (c.f., Palladino et al., 2008) pumice lapilli, gradually passing to more expanded but distinctively fibrous textures.

At the Tukino ski field (**Fig. 5.24b**), locally on the upper eastern slopes and along the Whangaehu River valley, the lowermost fallout bed is partially or totally replaced by a matrix-supported, poorly sorted (σ_I = 2.5) deposit (**Fig. 5.24b-d**), consisting of subrounded

pumice lapilli and rare bombs distributed in a finer ash matrix (i.e., Poruahu pyroclastic flow deposit identified by Donoghue et al., 1995a). The grain-size distribution is distinctively polymodal and platikurtic (**Fig. 5.24g; Table 5.1; Appendix C**). Its distribution and thickness is topographically-controlled and restricted along the Whangaehu valley, thickening in paleovalleys, decreasing in total grain size and increasing in matrix proportion with distance (**Chapter 3**). Where the pyroclastic flow deposit (PDC) occurs it is capped by a thin, pale grey fine ash, which otherwise directly mantles the fall deposit (**Fig. 5.24a**). The capping grey ash may represent a "co-ignimbrite" ash associated with emplacement of the PDC.

Overlying the PDC deposit (**Appendix A**) or the related co-ignimbrite ash (**Figs. 5.24a, c, d**), there is a second massive, clast-supported, medium lapilli bed (Mz = -2.4). At proximal-to-medial distance exposures it is poorly sorted (σ_I = 2.8), showing a negatively skewed grain-size distribution (**Fig. 5.24h; Table 5.1; Appendix C**), typical of coarse-grained fall deposits (XXXII-2a: *Plinian phase-2*; **Figs. 5.24a,c**). It is thicker and coarser-grained towards the E and SE. Non-juvenile lithic lapilli are common within the first 20 km, with dark-grey, fresh, coarse porphyritic andesites, as well as orange and red, hydrothermally altered lithics. It is capped by a thin ash bed (XXXII-2b in **Fig. 5.24d**), or directly overlain with a sharp and locally erosive contact by a dark grey, matrix-supported, poorly sorted, hyperconcentrated flow deposit containing rounded lithic pebbles set in a vesicular silty-sand matrix (XXXII-2c bed in **Fig. 5.24a**).

At more distal locations (east and south of location 34, **Appendix A**), the PDC deposit is absent and the fallouts (i.e., Lower-and-Upper Okupata tephras) merge into a single, well sorted fallout bed, having a clear unimodal, negatively skewed grain-size distribution (**Table 5.1; Appendix C**).

Over the entire area, the Okp-Ph eruptive unit is capped with a firm, pinkish brown, silty-sand paleosol, locally containing plant roots. At distal locations this paleosol is distinctive by its dark brown colour, marking an eruptive break at the onset of the Holocene warming, immediately before the large Plinian eruptions of the neighbouring Mt. Tongariro occurred (i.e. Pahoka eruptive unit; **Fig. 5.24e**).

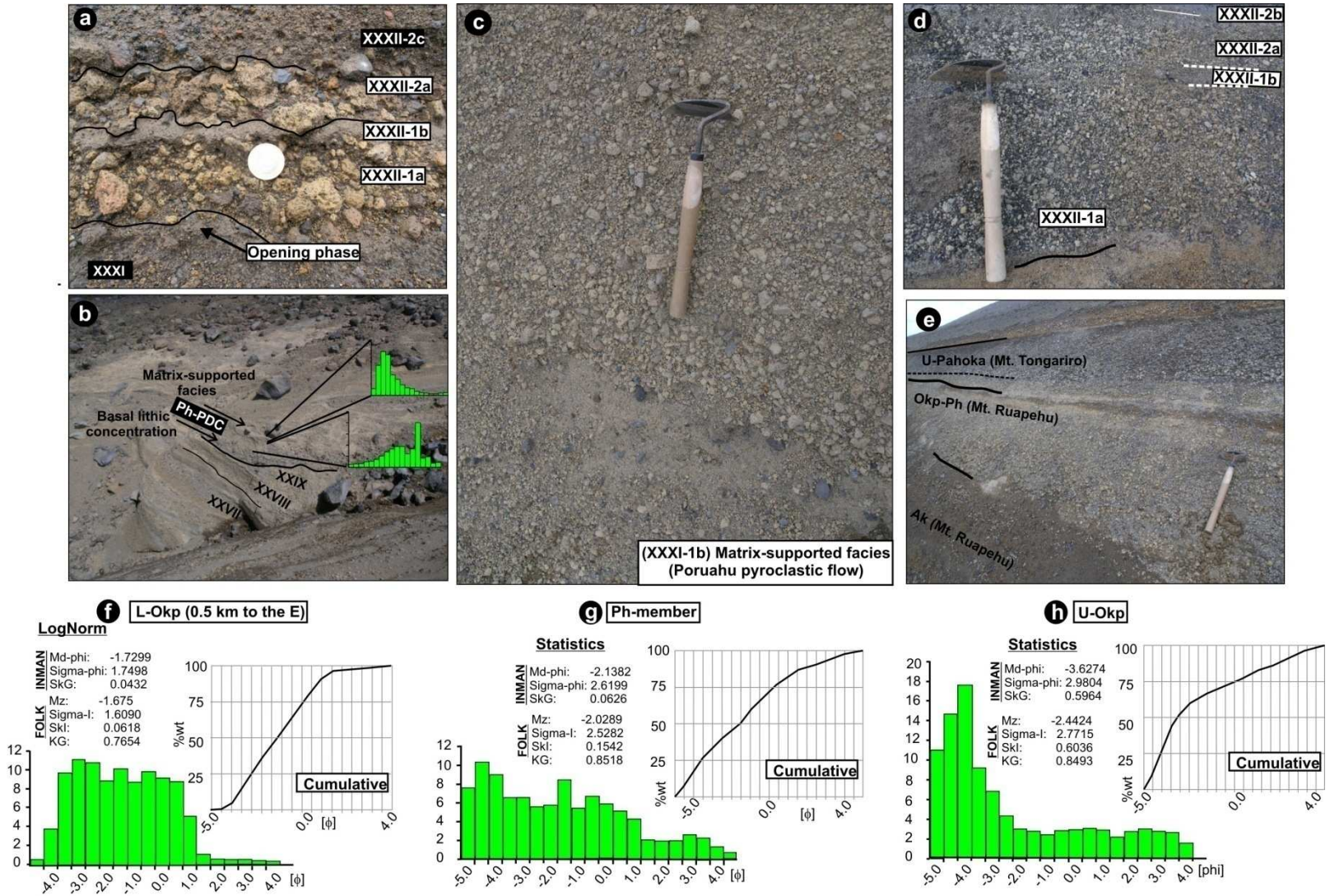

Figure 5.24 Exposures of the Okp-Ph unit. Proximal locations are shown at: **a)** 11.2 km from the vent to the E; **b)** 5.5 km to the East, showing pyroclastic density current facies in the upper Whangaehu valley; **c)** 7.4 km to the NW; **d)** 12.3 km to the NE; and **e)** 9.4 km from the vent to the NE; **f-h)** grain-size distribution of the different subunits as analyzed from samples taken 0.5 km from the vent (proximal facies).

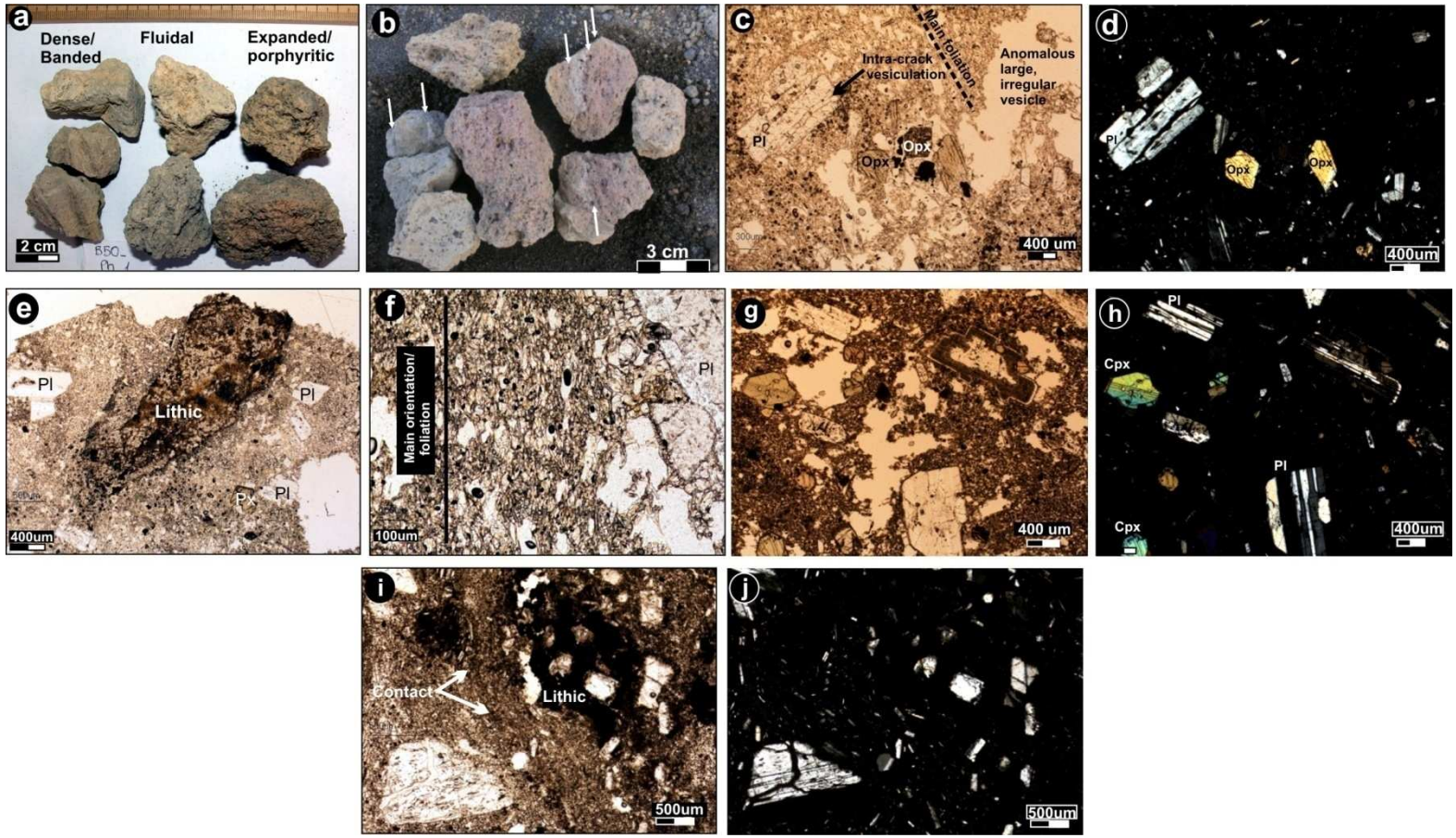

Figure 5.25 Typical juvenile pumice clasts within the **a)** Lower and **b)** Upper Okupata Tephras, characterized by **c-d)** highly vesicular clasts with irregular vesicles, some of them showing pinched edges. Anomalous large vesicles are found, showing advanced stages of interconnection. Feldspars are the dominant crystal phase, commonly showing cracks parallel and perpendicular to the longest axis and vesicle elongation/orientation; **e-f)**. Pale, microfibrous textures with an accidental sedimentary clast; **g-h)** dark, dense, end-member, with large phenocrysts and highly irregular vesicles having sharp edges and pinched terminations; **i-j)** banded texture imparted by differences in glass colour, vesicle-crystal sizes and content. Note the irregular boundary and the predominance of feldspar as pheno and microcrysts, occasionally showing jigsaw microstructure.

Pumice textures: the Okp-Ph unit is characterized by an extreme variability in juvenile clasts textures, both vertically and horizontally across the unit (Figs. 5.25a, b; Appendix D.4). The pumice lapilli are predominantly fibrous, with very thin vesicle walls. In most of the pumice clasts, vesicles vary from ellipsoidal to flattened shapes, with pinched terminations, and even extremely distorted forms. Anomalous large vesicles also occur, commonly showing irregular and sharp outlines (Fig. 5.26). Pumice fabrics vary from: **a)** pale brown to pinkish white, irregular-shaped, **fibrous**, finely vesicular porphyritic clasts, with rare large vesicles, (**Figs. 5.25c, d**); vesicle size may vary with larger vesicles occurring in lapilli with smaller crystals. **b)** Plate-like, pale brown, and pale pinkish brown, **microfibrous**, microporphyritic lapilli (**Fig. 5.25e, f**). Aligned, elongated vesicles are common, forming localized shear zones (90 to 220 μm wide). **c) Dense**, grey and dark pinkish brown, isotropic clasts with large phenocrysts, and low microlite contents compared to the other pumice types (**Fig. 5.25g, h**). **d) Colour-banded, microlite-rich**, microfibrous clasts with aligned, highly elongated and irregular vesicles.

The contacts between bands of different colours are irregular (**Fig. 5.25i, j**), following the main orientation of elongated vesicles and tabular crystals. Differences between bands are due to variations in crystal size and content, vesicle size and shape (**Table D2** in **Appendix D.4**). Local shear zones are present, particularly along band boundaries, shown by intensely distorted vesicles and folding or fracturing of some plagioclase phenocrysts. The textural differences are also seen in BSE images (**Fig. 5.26**), where vesicle-wall wrinkling and distortion (i.e. refolding and shearing) is common in fibrous clasts, and vesicles with thick walls and pinched terminations are frequent in the denser clasts.

Similar to the Oru and Ak units, phenocrysts are large and subhedral (long axis up to 8 mm) in the Okp-Ph unit, with mineral assemblage of Pl>>>Cpx>Opx>Mt. Most of the plagioclase phenocrysts are microfractured, with cracks perpendicular to the vesicle elongation and crossed by glass fibers (**Fig. 5.27a, b**). Pyroxenes are rarely found as free crystals, rather mostly occurring within glomerocrysts (**Fig. 5.27c, d**). Accidental lithics are common, distinguished in thin sections by their contrasting dark colour under parallel polarizer, rounded outline, corroded borders, and alteration (**Figs. 5.25e, f**). Microporphyritic lithics are commonly micro-fractured (**Fig. 5.27f**).

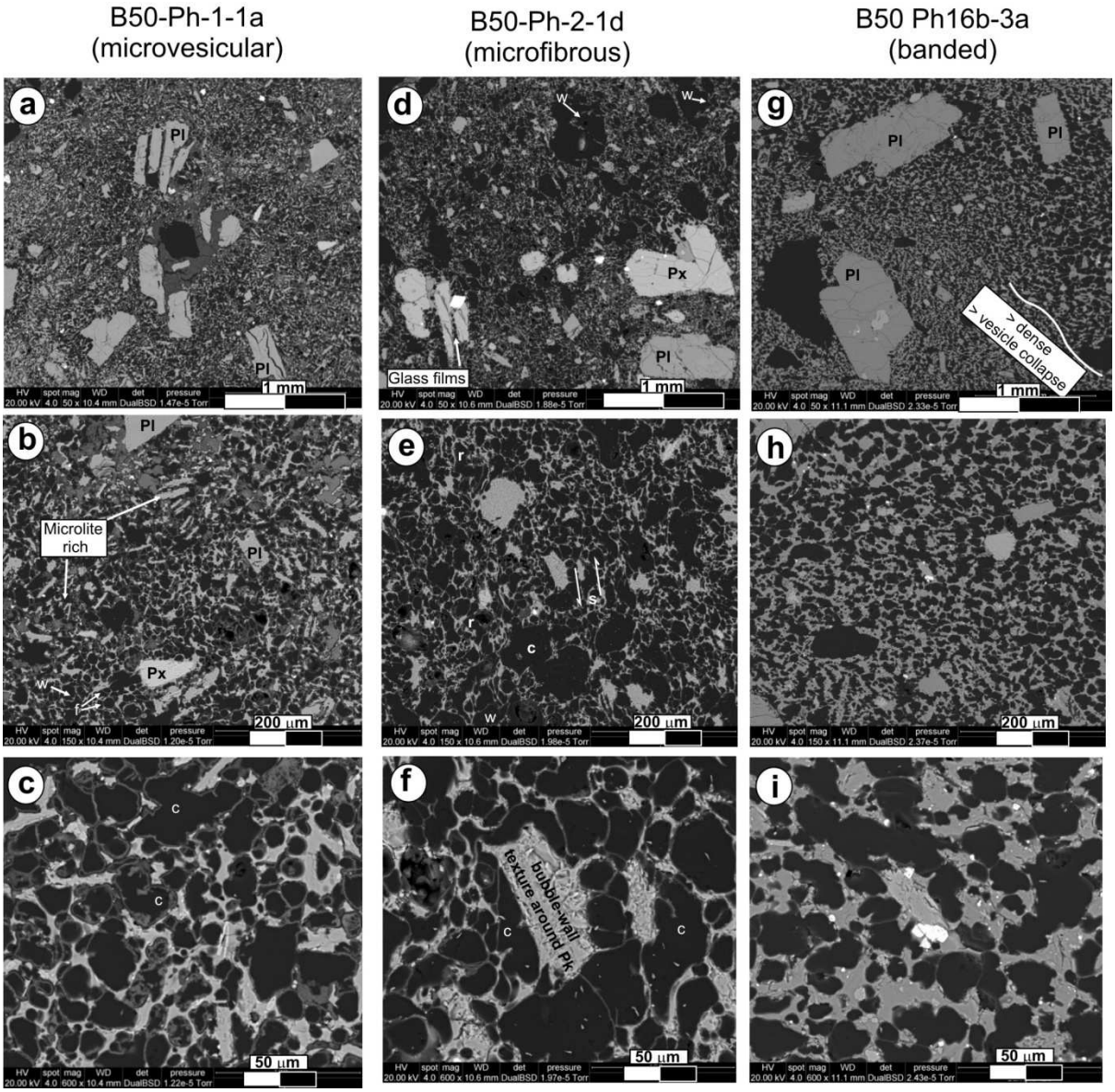

Figure 5.26 a) Typical microlite-rich, porphyritic, microvesicular texture of the L-Okp, with feldspars commonly showing micro-jigsaw cracks; note the high microlite content in **b**, small subspherical and larger irregular vesicles in **c**. **d)** Typically microfibrous, coarsely porphyritic texture of U-Okp with very thin, commonly wrinkled vesicle walls. Vesicles are commonly elongated, refolded or sheared **(e)**, and different degrees of coalescence occur **(f)**. **g)** Dense, colour-banded texture of U-Okp, where bands correspond to different size and shape of vesicles. Some bands corresponds to zones of significant vesicle collapse as shown by highly distorted pores **(h)** with sharp edges, some evidencing coalescence in a microlite-rich groundmass glass **(i)** w: wrinkled thin vesicle walls; f: flat walls; c: coalesced vesicle; r: refolded vesicle; s: localized shear.

Component analysis and ash-size fractions: the relative proportions of glass, crystals, and dense lithics within the L-and-U Okupata tephras vary with both grain-size and stratigraphic position (**Fig. 5.6**). Glass shards (**Fig. 5.28a-d**) are typically porphyritic, highly vesicular (much more so than Oru, Ak; **Chapter 3**). Within the L-Okp tephra, crystals are concentrated within the coarse ash size fractions (up to 80 %), decreasing within finer classes which have

higher glass and lithic contents. Within the 0.5 to 2 ϕ size classes, juvenile pumice (up to 40 %) and lithics (up to 40 %) are more abundant in the U-Okp. The total lithic content is equal for both subunits in the finest 3 ϕ analyzed class (23 %; **Fig. 5.6; Appendix E.4**).

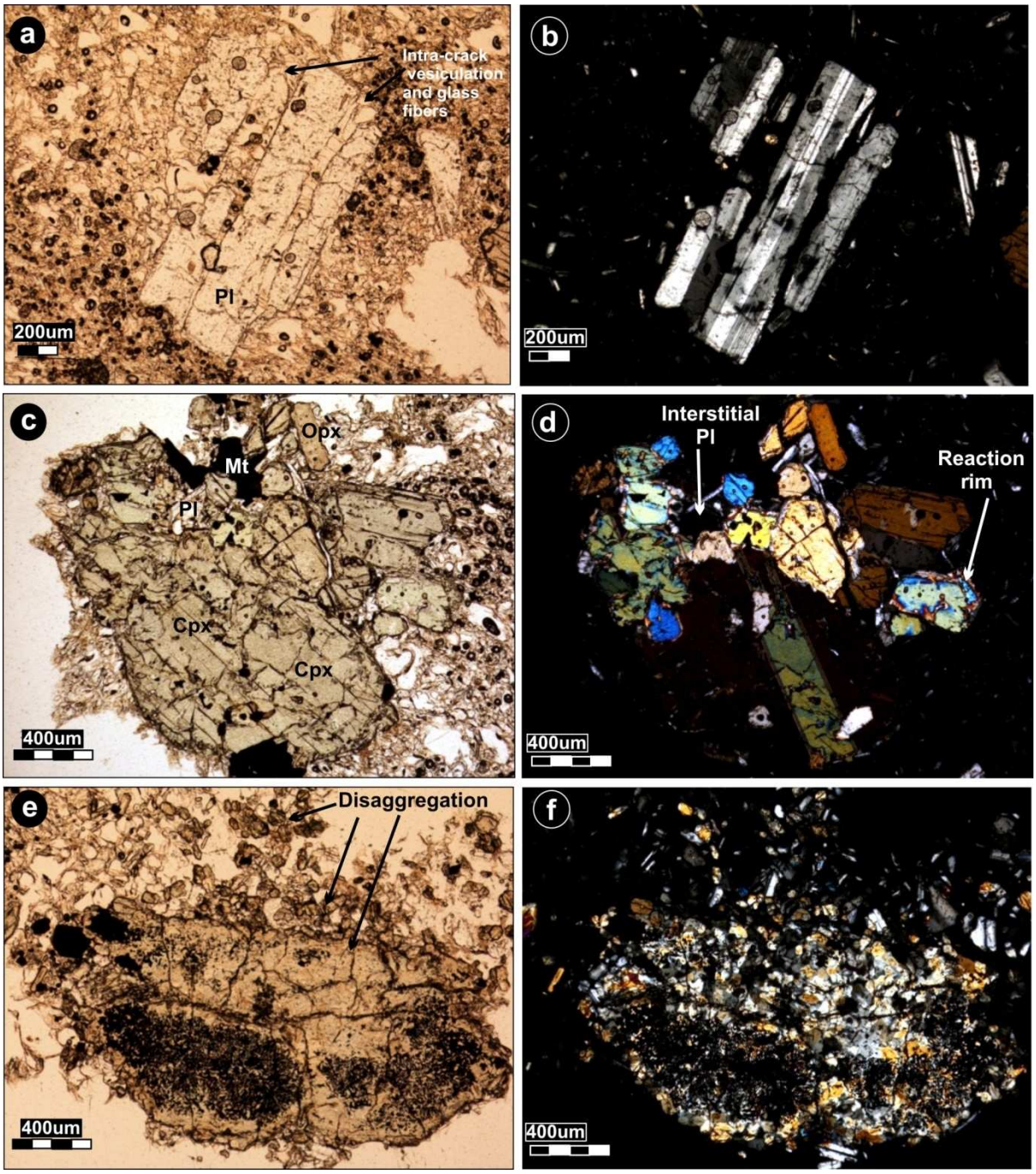

Figure 5.27 Photomicrographs **a-b)** showing a broken plagioclase crystals, illustrating how the cracks served as vesiculation sites and formation of glass fibres; **c-d)** common glomerophyric texture with 2Px, interstitial Pl and Mt. **e-f)** Microphaneritic lithic clast entrapped in the groundmass glass, where individual components are seen under crossed-polarizer (**f**). Note that the border is broken and individual grains look detached from the main lithic.

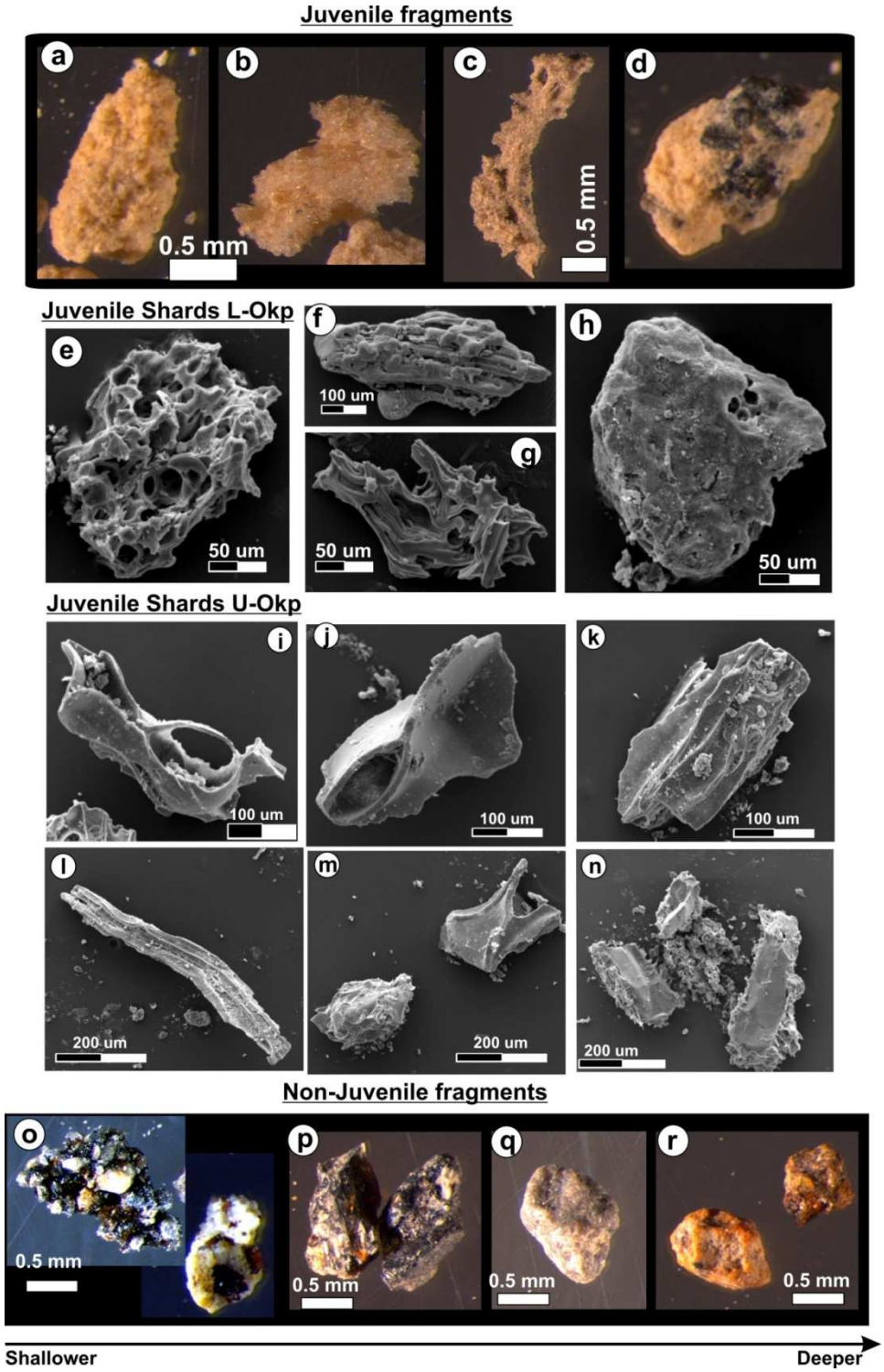

Figure 5.28 a-d) Main pumice clasts classes identified within the Okupata-Pourahu eruptive Unit, as seen under a binocular microscope; **a)** microvesicular pumice with subspherical vesicles; **b)** fibrous, microlite-rich pumice; **c)** dark brown, expanded to mossy-like pumice having irregular vesicles with thick walls; **d)** dense, porphyritic clast. Juvenile shards within the L-Okp comprise: **e**) highly vesicular, scoreaceous shards; **f-g)** fluidal glass with ellipsoidal vesicles having thick walls and "melted" surfaces. **h)** Poorly to non-vesicular shards with occasional melted surfaces. The U-Okp unit is characterized by: **i-j)** cuspate glass shard derived from bubble bursting; **k,l)** fluidal and tube-like shard derived from walls of elongated vesicles; **m)** the top-right shard is similar to "**i-j**", and bottom-left shard is "drop-like" glass with smooth surfaces (e.g., Wohletz and Krinsley 1982); **n)** typical "bubble-wall" texture around Px-phenocrysts; **o)** lithic aggregates, probably recycled from the vent walls/floor; **p)** dark grey, porphyritic andesite; **q)** pale grey, fresh andesites; **r)** hydrothermally altered clasts.

Among the juvenile glass coarse-ash sized particles (**Fig. 5.7**), the L-Okp has more highly vesicular clasts (**Fig. 5.28a**), than the variable textures in U-Okp (**Fig. 5.28c, d**). Within the U-Okp, fibrous to tube-like fragments (**Fig. 5.28b**) are well reflected only within the finest size classes. Within the highly fragmented particles size (≤3 ϕ), the textural trends are different (**Fig. 5.9**): glass shards within the L-Okp have highly heterogeneous morphologies (**Fig. 5.28e-h**), whereas the U-Okp has a restricted range and a clear predominance of "bubble-wall' glass shards (**Fig. 5.28i-j**) and fibrous shards (**Fig. 5.28k, l**).

The non-juvenile lithology is more heterogeneous within the L-Okp (**Fig. 5.10e**) than in the U-Okp, varying from oxidized crystal-ash aggregates (**Fig. 5.28o**), probably corresponding to recycled material from the vent, to dark and pale grey, porphyritic, andesitic clasts (**Fig. 5.28p, q**) coarse-grained and altered, along with minor proportions of highly hydrothermally altered clasts (**Fig. 5.28r**).

Chemical composition: juvenile pumice whole rock analyses (**Appendix F.1**) are basaltic-andesite to andesite, consistent with published data (Donoghue et al., 1995a, 1999) and show the largest chemical variation for whole-rock data among the units of this study (SiO_2: 56.08-61.63 wt.%, dry basis). These chemical variations show no clear correlation with pumice texture (**Fig. 5.29**). In general, L-Okp samples are more mafic than U-Okp samples.

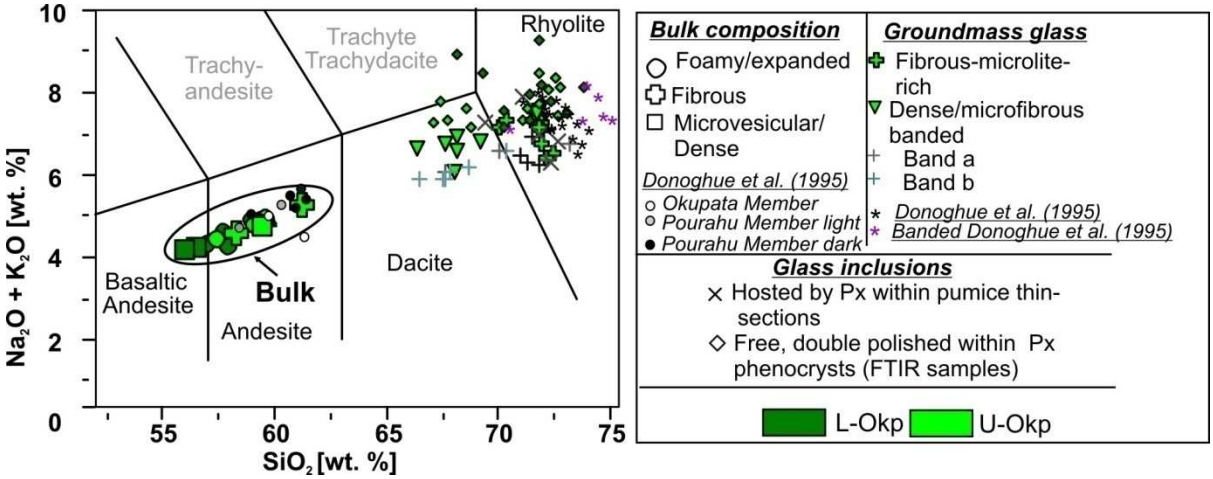

Figure 5.29 Total alkalis vs. silica (TAS) diagram (Le Bas et al., 1986) showing the bulk and glass composition of juvenile pumice clasts within the Okp unit. Note the large compositional span within the same unit, and the high glass groundmass silica content consistent with more crystal-rich textures relative to previous eruptive units. Data are consistent with previous published analyses (Donoghue 1991; Donoghue et al., 1995a).

Bulk analyses reported by Donoghue (1991; Donoghue el al., 1995a) from the pyroclastic flow deposit interfingered between L-and-U-Okp (i.e. Pourahu Member) lie within the trend of the U-Okp tephra. Glass compositions vary between dacitic to rhyolitic according to crystal content between samples and between bands within a banded sample (**Appendix F.2**; SiO_2: 66.47-73.23 wt.%). All the glass compositions reported by Donoghue (1991) plot within the rhyolitic field. The glass inclusions within Px and Pl probed in this study (**Appendix F.3**) also vary from dacitic to rhyolitic (L-Okp SiO_2: 67.2-72.0 wt.%; U-Okp SiO_2: 68.2-73.8 wt.%).

Discussion: the Okupata-Pourahu unit resulted from two main phases. In general, the erupting magma was both chemically and physically more heterogeneous than previous eruptive units as described above. The similarity of groundmass glass and glass inclusions (**Fig. 5.25**) may indicate that inclusions remained in contact with the melt until shortly prior to the eruption by leaking and capillary paths through crystal cleavage and/or twin planes (c.f., Stewart and Pearce 2004; Signorelli et al., 1999; Cashman and McConnell 2005).

Considering the large content and size of phenocrysts, the highly siliceous, microlite-rich melt, and the dominant pumice textures with distorted vesicles, it is likely that the state of the magma before the eruption was highly viscous and degassed. Textures and highly evolved groundmass glass suggest that magma storage was shallow and prolonged.

Donoghue et al. (1995a; 1999), argued that the textural features of this eruption and the PDC generation were related to mingling between a hot, mafic, andesitic magma (containing rare, quenched olivine microcrysts) that injected into a shallow-resting, cooler, less dense, andesitic magma. Although mixing still a possible process during Okupata-Poruahu magmatism (i.e., evolved groundmass glass relative to melt inclusions may be a result of shallow microlite crystallization rather than a change in the pre-existent magma storage conditions/depth), this is not directly determining the resulting pumice textures and column behaviour. The data presented here indicate that banded textures and differences in bands are more related to physical conditions of the magma (i.e. vesicle shear, amount of microlites), rather than chemical variations. Pumice banding in Okp-Ph (as well as in the Oru and Ak) unit is more related to the rheological properties of the magma within the conduit, rather than due to magma mixing or mingling in the storage system.

The textures and geochemical data of the Oru (also explaining Ak) and Ok-Ph units can be explained by: **(1)** heating and self-mixing effects within the crystal-rich magma reservoir, as have been documented in cases where mafic magmas intrude at the bottom of a shallower reservoir without physical mixing (c.f., Murphy et al., 2000; Couch et al., 2001). In this case, the proximity of a deeper rising magma can trigger vesiculation and overpressure to initiate the eruption (c.f., Huber et al., 2011). **(2)** Local heterogeneous rheological conditions of the viscous magma reaching the base of the conduit were accentuated within and along the conduit by differential crystal and vesicle content, as well as variable vesicle shapes. The complex rheology of crystal-bubble suspensions rising into volcanic conduits at differential ascent rates, producing banding textures, and developing advanced shear inducing fragmentation have been extensively documented in viscous, siliceous magmas (e.g., Rosi et al., 2004; Gonnermann and Manga 2005). Contrasting magma flow viscosity across the conduit could also promote complex dynamics along the contacts of rheological contrast, including zones close to conduit walls.

Seismological investigations on highly viscous magmas demonstrate that shear stresses along conduit walls are capable to trigger seismicity and produce variable viscosity according to failure and healing cycles, affecting overpressure (Hale and Mühlhaus 2007). Therefore, it is probable that high overpressure acting on a highly heterogeneous magma (model 2) across the conduit led to fragmentation at different depths (c.f., Spieler et al., 2004a), promoting column unsteadiness.

The lowermost, accretionary-lapilli rich ash signals the onset of the eruption, leading to sudden decompression of magma deeper in the conduit. Plate-like, microvesicular vitrophyric pumice lapilli at the base of the L-Okp and the predominance of finely vesicular ash suggest the pre-existence of a magma "foam" capping the conduit, which was unloaded at the beginning of this phase. This, in turn led to the decompression of the underlying, crystal-rich, heterogeneous, porphyritic magma. The different textures of the dominant andesitic, porphyritic, non-juvenile clasts to the previous eruptions, combined with isopach and isopleth data (**Chapter 4**) indicate that vent had moved to the south (near the present-day Crater Lake). The variability of accidental lithics (**Fig. 5.10e**) is consistent with major crater and conduit erosion during L-Okp. Decreasing magma volatile contents during the eruption was driven by syn-eruptive degassing and crystallization along sheared zones (as reflected by the

high microlite content), which could also promote column collapse and the generation of a PDC at the end of L-Okp.

A buoyant eruptive column was re-established after a brief interval, producing the U-Okp. High lithic contents (**Fig. 5.6**) indicate ongoing conduit erosion during this phase (c.f., Macedonio et al., 1994). The abundance of bubble wall glass shards, fibrous, and fused-shaped shards in the 2 ϕ and 3 ϕ fractions of the U-Okp suggest a lower degree of magma fragmentation relative to earlier eruptive units. This is also reflected by the low ash content (**Fig. 5.24f**) and the low half distance ratio estimated from the deposit (**Chapter 4**). The crystal concentration at the base of the unit reflects the transport-accumulation process, with pyroxenes and glass being density sorted.

Fibrous and tube-like pumice fine particles become common in the U-Okp, suggesting that the erupting magma was subject to extreme strain along the conduit. Fluidal surfaces and smooth glass coatings of pumice particles (**Fig. 5.28f**), indicate that the melt was in some cases still deformable after fragmentation. The range of fragmentation mechanisms is evidenced by the polymodal grain-size distribution (**Fig. 5.24f, h**), probably involving feedback between rapid decompression, acceleration (e.g., Cashman et al., 2000), and shear-induced fragmentation (e.g., Dingwell 1996; Mader et al., 1996; Papale 1999; Zhang 1999). The latter is supported by the typical plate-like and fibrous ash morphologies similar to those described by Palladino et al. (2008). Ash and lapilli particles with deformed vesicles and wrinkled vesicle walls indicate permeability was developed before fragmentation (c.f., Cashman and Mangan 1994; Klug and Cashman 1996).

5.3 Conclusions

Magmas involved in the Mangatoetoenui and Shawcroft eruptions were of similar basaltic-andesitic to andesitic bulk composition, with glass inclusions in pyroxenes being more siliceous than residual groundmass glass. This is inconsistent with fractional crystallization (Lowenstern 1995) and suggests that pyroxene phenocrysts coexisted with a rhyolitic melt early in the magmatic history. Subsequently, these phenocrysts were then entrapped within the andesitic-dacitic Mgt and Sw melts. By contrast, the magma involved in Oruamatua eruption was slightly more siliceous and variable, and the glass inclusions hosted in pyroxenes were more mafic than residual glass. This fits with fractional crystallization of

plagioclase, orthopyroxene and clinopyroxene within the same storage system. However, the more evolved residual melt composition may be due to magma shallow stalling and microlite crystallization. Therefore, future detailed studies on groundmass glass and melt inclusions could help to define if this unit was related to a shallower storage system compared to those of the Mgt and Sw episodes, or of differences are only due to shallow conduit processes. The magma erupted during the Okupata-Pourahu eruption episode was chemically and physically more heterogeneous than previous units. In this case, groundmass glass and inclusions have similar compositions, suggesting that inclusions remained in contact with the melt until shortly prior to the eruption.

Pumice textures and ash morphologies indicate that the Lower Mangatoetoenui eruption phase resulted from fragmentation of a low-viscosity, rapidly rising and expanding magma without opportunity of extensive crystallization (L-Mgt). The Upper Mangatoetoenui eruption phase and Shawcroft eruption episode involved a relatively more dense magma than the Lower Mangatoetoenui phase. Pumice textures and ash morphologies of Mgt and Sw indicate that decompression-dominated fragmentation led to magma failure. Denser magmas also could imply a shallower fragmentation level, or higher fragmentation thresholds than the highly vesicular L-Mgt magma.

During Oruamatua, Akurangi, and Okupata-Pourahu eruption episodes, pumice textures indicate that localized shear produced strong vesicle elongation and banding, modulating the rheology across the conduit (c.f., Massol and Jaupart 1999; Stein and Spera 2002; Wright and Weinberg 2009). These eruption episodes involved more viscous magmas than previous eruptions, with pumices containing high crystal contents and highly siliceous, microlite-rich glass groundmass. Ash morphologies suggest that, besides decompression, shear stresses also induced fragmentation (c.f., Mader et al., 1996; Papale 1999; Zhang 1999), and in the particular case of the Oruamatua (and probably Ak) episode, the interaction with external water improved fragmentation efficiency.

Interestingly, the inferred range of fragmentation mechanisms correlates with the changes in the stability of the Plinian columns over the Late Pleistocene (**Chapter 3**): **(1)** in the case studied for oscillating but non-collapsing columns (Mgt), the coexistent of highly vesicular and fluidal morphologies and the lowest content of dense particles suggest that the fragmentation front was irregular, with variations in depth according to the local porosity/density of the magma. **(2)** The case studied for steady eruption columns (Sw) involved, instead, a chemically and rheologically homogeneous magma. Decompression-

dominated fragmentation affected most of the magma, causing extreme excavation and erosion of the hydrothermally altered levels of the conduit. Although this could allow the access of geothermal fluids (c.f., Papale et al., 1998; Houghton et al., 2004), ash micro-structures suggest that the thermal contrast between fluids (i.e. magma and geothermal fluids) was not enough to drive important phreatomagmatism. In this case, despite degassing, sufficient volatile content remained available for bubble growth favouring a sustained column. **(3)** In the case of eruptions related to collapsing columns (Oru, Ak, Okp), the extreme variability of ash morphologies at any stratigraphic level, including dense particles, reflect extreme irregularity of the fragmentation depth (c.f., Spieler et al., 2004a). Besides decompression, shear-induced fragmentation and phreatomagmatism also played a significant role. The higher viscosity of magmas within this case could favour large frictional forces along conduit walls. Together with large differences in pressure between the magma reservoir and the vent, these processes promoted conduit wall collapses and dramatic changes in conduit geometry leading to column collapse.

The hypothesis emerging from this chapter is that, the higher the rheological heterogeneity of the magma at the fragmentation level, the greater the likelihood for column collapse and PDC generation. This hypothesis will be addressed in the following chapter, together with the vesiculation history and degassing processes occurring within the conduit.

CHAPTER 6. Magma degassing and conduit dynamics

This chapter presents the 3D textural characterization of the pumice textures found within Mangatoetoenui, Shawcroft, Oruamatua, and Okupata-Pourahu eruptive units, in order to understand the physical conditions of the magma within the conduit. From vesicle and mafic crystal data, conduit processes are inferred with particular attention to the degassing mechanisms and the conditions leading to different degrees of rheological heterogeneity at the fragmentation level. The 3D textural analyses of different pumice textures are linked to the corresponding eruption style inferred for each unit, and vesiculation processes are discussed in terms of their implications for column stability.

6.1 Introduction

The identification and characterisation of factors and processes governing explosive volcanic eruptions is critical to understand triggering mechanisms, expected eruption behaviour and causes implied in the transitions from one eruptive style to another. Eruption dynamics (i.e. magnitude, intensity, duration, and column steadiness) are determined by processes occurring in the storage region, the volcanic conduit, and the vent. Within the storage region, gas overpressure can build and may drive eruptions (e.g., Cashman and McConnell 2005). Within the volcanic conduit, magma decompression, degassing-induced crystallization and fragmentation occur (e.g., Gardner et al., 1999; Hammer et al., 1999; Blundy and Cashman 2005). These processes control magma rheology (a function of melt, solid and volatile contents) through a variety of feedback mechanisms (e.g., Stein and Spera 1992; Mader 1998; Mangan and Sisson 2000, Rust and Manga 2002). Also, external factors such as conduit wall collapse and/or inflow of groundwater may influence eruption dynamics. Vent geometry and changes during eruptions regulate the exit velocity and consequently can influence eruption column stability (c.f., Houghton et al., 2004).

In the absence of significant interaction with external water, the content of dissolved volatiles in the magma provides the driving force for explosive volcanic eruptions (Sparks 1986). Volatile exsolution increases magma chamber overpressure, controlling the eruption dynamics (Gonnermann and Manga 2007). Complex bubble-crystal interactions are common in silicic magmas and must be considered for interpretations of the magma relative viscosity within the conduit (Thomas et al., 1994; Saar and Manga 1999; Stein and Spera 2002; Wright and Weinberg 2009). Moreover, changes in the rheology of the magma control transitions in the eruption intensity and style, from explosive to effusive and vice-versa (e.g., Cashman and McConnell 2005; Sable et al., 2006; Platz et al., 2007).

Pyroclast textures have been extensively studied in the last four decades as records of the complex dynamics of volatile exsolution during ascent from the chamber to the surface. Toramaru (1990) recognized that the morphology and texture of vesicular juvenile clasts reflects physical properties of magma, such as viscosity, surface tension, and volatile diffusivity, providing valuable information on magma vesiculation processes. Variations in textures and composition within the stratigraphic sequence reflect transitions in the eruptive dynamics with time (e.g., Jaupart 1998; Gurioli et al., 2005; Belien et al., 2010). A wide range in pumice textures at the same stratigraphic level has been extensively documented in Plinian to subplinian deposits, highlighting heterogeneity in magma rheology and/or in flow conditions across and along the conduit, which can be related to heterogeneous flow conditions (e.g., Lirer et al., 1973; Waitt et al., 1981; Hoblitt and Harmon 1993; Gardner et al., 1998; Hammer et al., 1999; Polacci et al., 2001; Taddeucci and Wohletz 2001; Klug et al., 2002). Hence, the localization of pyroclasts and hence the gas distribution inside the conduit can be reconstructed from pumice textures (Sable et al., 2006; Wright et al., 2007; Bouvet de Maisonneuve et al., 2009; Kennedy et al., 2005). Moreover, correlations between groundmass glass composition and magma ascent/decompression rates have been demonstrated in decompression experiments by Hammer et al. (1999), Mangan and Sisson (2000), and Cichy et al. (2011).

The style of eruptive activity at a volcano is largely related to the timing and nature of gas exsolution and escape from magma during ascent (Martel and Schmidt 2003, Cichy et al., 2011). Based on comparison with experimental studies and natural systems, the textures of vesicles preserved in volcanic clasts can be used to infer conditions of magma expansion. Experimental modelling of heterogeneous bubble nucleation have demonstrated that high crystal number densities allow bubble nucleation around crystals at low volatile supersaturation pressures (<5 MPa in Hurwitz and Navon 1994; <20 MPa in Gardner et al., 1999; Gardner 2007). Homogeneous bubble nucleation in the absence of crystals (c.f., Mangan and Sisson 2000; Cluzel et al., 2008), on the other hand, requires extremely high supersaturation pressures (~170MPa in Hamada el al., 2010). Vesicle number densities (N_v) are used to determine the bubble nucleation mechanism; homogeneous bubble nucleation typically results in pumice with high N_v (~10^8-10^{10} cm^{-3}), whereas heterogeneous nucleation produces low (<10^8) N_v (Cashman et al., 2000; Gardner 2007; Cluzel et al., 2008). From experiments on rhyolitic melts, Mourtada-Bonnefoi and Laporte (1999) report bubble number densities of 10^7-10^9 cm^{-3} for homogeneous nucleation, whereas Hurwitz and Navon (1994)

and Gardner et al. (1999) report 10^6-10^8 cm^{-3} values for heterogeneous nucleation. Mangan and Sisson (2000) demonstrated that both homogeneous and heterogeneous nucleation rates can be comparable in some cases, and that N_v are highly dependent on the saturation pressure and degree of H_2O supersaturation (ΔPss~), with total N_v values of ~10^3-10^6 cm^{-3} for ΔP_{ss}~130-150 MPa. Hence, the nucleation rate and mechanism (heterogeneous or homogeneous), as well as the resulting N_v are largely determined by the magma decompression rate (Toramaru 1995, 2006; Mourtada-Bonnefoi and Laporte 2004; Hamada et al., 2010). The nucleation mechanism, in turn, dictates the degassing efficiency (equilibrium vs. disequilibrium) by establishing the depth of gas exsolution (Mangan and Sisson 2000).

In the last three decades, textural analysis of vesicular clasts has been increasingly common in order to investigate processes of magmatic degassing in explosive eruptions (e.g., Houghton and Wilson 1989; Klug and Cashman 1994; Gardner et al., 1996; Shea at al., 2010). For instance, if the vesicle size distributions (VSD) represent the state of the magma at the moment of quenching, frequency plots give hints on bubble nucleation events and the nature of coalescence (e.g., Sparks and Brazier 1982; Kulg and Cashman 1994; Polacci et al., 2003). Based on theoretical models presented by Cashman and Ferry (1988), the linear part of the VSD should correspond to the vesicles originating from primary nucleation and growth, whereas the tail of the curves corresponds to late modifications of the original distribution (e.g., Cashman and Mangan 1994; Mangan and Cashman 1996; Klug et al., 2002; Adams et al., 2006; Polacci et al., 2008, Shea et al., 2010). However, the discussions have been mainly centred on the Plinian basaltic and rhyolitic end-members and based on extrapolations from 2D datasets, potentially misclassifying the 3D geometry of interconnected pores (Giachetti et al., 2011). Recent studies have demonstrated X-ray synchrotron and computed microtomography (μCT) of volcanic samples provides direct characterization of the 3D structure of pyroclasts and omits the need for critical assumptions about pore shape when transforming from 2D to 3D (e.g., Song et al., 2001; Ketcham and Carlson 2001; Polacci et al., 2006; Wright et al., 2006; Polacci et al., 2008, 2009a, b; Degruyter et al., 2010).

In this chapter, the main concepts of magma vesiculation and degassing processes outlined above were applied and developed in the Plinian fall deposits of intermediate composition sourced at Mt. Ruapehu. The characteristics of the dominant pumice textures within each of these tephras were quantified using the 3D information provided by X-ray synchrotron and

computed μCT, to infer the degassing processes occurring during these eruptions and their influence on the resulting eruptive style. Pumice clasts were sampled from the deposits representing the main Plinian phases of the Mangatoetoenui (Mgt), Shawcroft (Sw), Orumatua (Oru), and Okupata-Poruahu (Okp-Ph) eruptions of Mt. Ruapehu (**Chapters 4** and **5**).

The analysis of 3D microtomography images is difficult (c.f., Gualda et al., 2010a, b; Baker et al., 2010), including possible errors induced by the computed de-coalescence process, the difficulty of selecting, processing, and merging representative (large enough) subvolumes to characterize a whole clast, as well as the exclusion of the largest sized vesicle populations in order to improve image resolution (c.f., Giachetti et al., 2011). However, this method of characterization was preferred, in combination with gas-pycnometry and qualitative observations in 2D back scatter electron (BSE) images, to avoid assumptions about vesicle shapes and dimensions to convert data from 2D images into 3D measurements. The methodology employed for the 3D textural data acquisition and characterization of pumice lapilli are explained in **Chapters 2.2.3** and **2.3.5**.

In the context of this study, "pumice" is defined as a highly, finely vesicular glass foam of volcanic origin (quenched glass), independent of its bulk composition (Fisher and Schmincke 1984; Whitham and Sparks 1986), indicative of explosive fragmentation of a highly viscous, volatile rich magma.

6.2 Results

The following textural characterisation within each eruptive unit is presented in stratigraphic order.

6.2.1 The Mangatoetoenui Unit Pumice textures

Density and porosity: gas-pycnometry analyses (**Appendix G; Fig.6.1; Table 6.1**) reveal that the L-Mgt medium-sized lapilli have bulk porosities of 66-91 % (average = 80 %). The lapilli become generally less porous upwards (63-81 %; average = 77 %), in parallel with the normal grading of the deposit. Bulk densities vary widely from 0.38 to 1.36 $g \cdot cm^{-3}$ (average = 0.64 $g \cdot cm^{-3}$), and higher in the unit this range narrows to 0.63-1.19 $g \cdot cm^{-3}$ (average = 0.80 $g \cdot cm^{-3}$). The U-Mgt lapilli contain many denser particles, with bulk porosities varying from

15 to 78 % (average = 64 %) and consistently higher densities (0.64 to 2.67 g·cm^{-3}; average = 1.28 g·cm^{-3}).

Within the L-Mgt, connected and bulk porosity (**Fig.6.1e**) are not directly correlated, due to a wide range in isolated porosities (0-20 %), especially at high bulk porosity (>70 %). Within the U-Mgt, connected and bulk porosity show a better correlation, with isolated porosities being <10 %. In U-Mgt, microfluidal, crystal-bearing lapilli have higher isolated porosities than expanded, coarsely-vesicular clasts. Porosity and density distributions are asymmetric, with bulk density distributions very leptokurtic to leptokurtic (L-Mgt: Skeweness (Sk) = 1.85; U-Mgt: Sk = 1.74) and isolated porosity mesokurtic (L- Mgt: Sk = 0.79; U-Mgt: Sk = 0.45). Bulk porosity distributions are also leptokurtic (L-Mgt: Sk = -1.10; U-Mgt: Sk = -1.78), while those of connected porosity are positively skewed (L-Mgt: Sk = -0.26, ~mesokurtic; U-Mgt: Sk = -1.80, petokurtic). Bulk and isolated porosity distributions have low variance relative to connected porosity, which has a broad mode.

3D-Textures: three samples from the Mgt were scanned with high resolution X-ray techniques (**Chapter 2.2.5**). Sample IX-1b-1b from the L-Mgt represents a typical **foamy** texture (**Figs. 6.2a-e**), with 72 % vesicles and 4% mafic crystals *(+1 % plagioclase feldspar*). Another L-Mgt sample, IX-1b-2a represents a typical **fluidal** texture (**Fig. 6.2f-i**) with 70% vesicles and 11 % mafic crystals (*+7 % plagioclase feldspar*). Finally, a U-Mgt sample was analysed to represent a **microfluidal** (**Fig. 6.2j-m**) texture (IX-1e-2) with 51 % vesicles and 14 % mafic crystals (*+4 % plagioclase feldspar*) (**Appendices H.3.1, H.4.1**).

The L-Mgt samples (**Appendices H4.1a,b**) have vesicles with smooth outlines that are spherical to ellipsoidal (**Fig. 6.2b**) in the foamy lapilli, and large and highly elongated in the fluidal sample (**Fig. 6.2h**). Cross sections of both samples show the elongated vesicles are aligned, especially in the fluidal textures, although tube-like texture does not occur (**Fig.6.2c, d, h, i**).

The degree of vesicle coalescence is variable (**Fig. 6.2b, c, g, h**) and mainly occurs in the direction of elongation. Vesicle walls may be flat to slightly curved, suggesting similar internal pressures in neighbouring vesicles (c.f., Cashman and Mangan 1994; Burgisser and Gardner 2005). In other cases vesicle walls may be extremely thin (<4 µm CT-resolution limit) or are ruptured. Wrinkled walls (e.g., Klug and Cashman 1996; Klug et al., 2002) occur only in the fluidal textured sample. Large, irregularly shaped vesicles formed by the coalescence of small ones, but showing incomplete recovery of the spherical shape (i.e.

retraction; Cashman and Mangan 1994), have pore aperture widths from ~66 to 100 μm perpendicular to elongation, and 66 to 308 μm in parallel views.

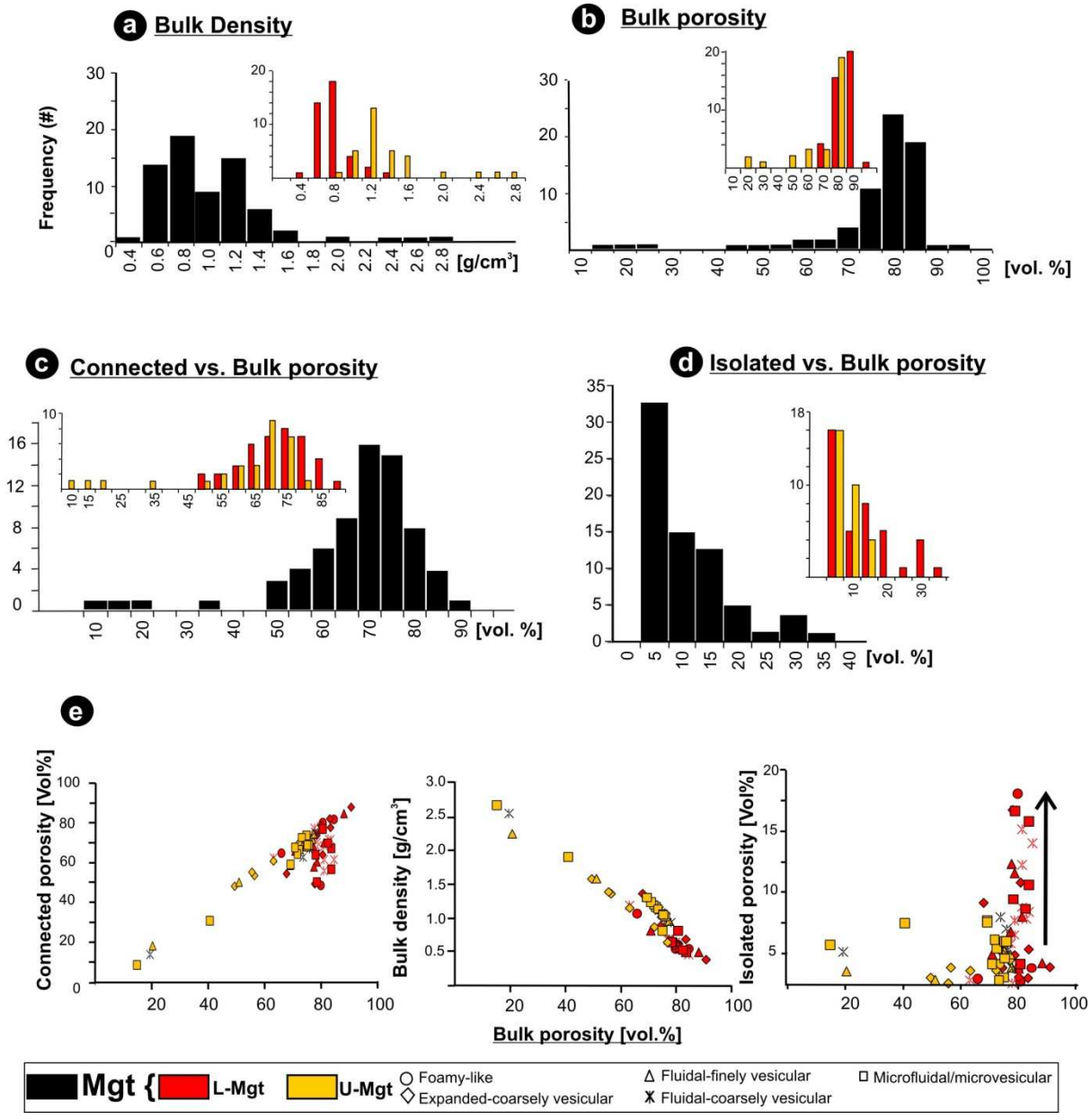

Figure 6.1 Porosity and density frequency distributions within lapilli of the Mangatoetoenui unit. The individual parameters were obtained from measurements of: **a)** bulk sample volume and envelop density; **b)** connected + isolated porosities relative to the bulk sample volume; **c)** skeletal density; **d)** solid density determined in milled samples; **e)** comparative plots of individual parameters against bulk porosity. Black histograms illustrate all data (n= 69), while red shows that of L-Mgt and yellow the U-Mgt.

Table 6.1 Summary Table of density and porosity measurements using Gas-pycnometry and Envelope pycnometry (see methodology **Chapter 2.2.3** and results in **Appendix G**). Mgt: Managtoetoenui unit; Sw: Shawcroft unit; Oru: Oruamatua Unit; Okp-Ph: Okupata-Pourahu eruptive unit.

Mgt	Bulk density [g/cm^3]	Skeletal density [g/cm^3]	Solid density [g/cm^3]	Bulk porosity [vol.%]	Connected porosity [vol.%]	Isolated porosity [vol.%]
MIN	0.38	1.05	2.70	14.9	8.4	0.2
MAX	2.67	4.15	4.24	91.0	88.2	31.2
AVERAGE	**0.93**	**2.70**	**3.47**	**73.0**	**64.9**	**8.1**
L-Mgt$_{base}$	0.64	2.23	3.21	79.9	68.8	11.1
L-Mgt$_{top}$	0.80	3.06	3.50	76.9	74.0	2.9
U-Mgt	1.28	3.24	3.78	64.4	59.5	4.8
Foamy	0.86	2.74	3.32	73.9	67.5	6.4
Fluidal	0.88	2.60	3.42	73.8	65.5	8.3
Microfluidal	1.08	2.83	3.72	70.7	60.9	9.7
Total measured samples						*70*
Sw	**Bulk density [g/cm^3]**	**Skeletal density [g/cm^3]**	**Solid density [g/cm^3]**	**Bulk porosity [vol.%]**	**Connected porosity [vol.%]**	**Isolated porosity [vol.%]**
MIN	0.19	1.30	2.80	47.8	1.2	0.1
MAX	2.81	3.47	3.70	94.9	94.0	12.5
AVERAGE	**1.25**	**3.10**	**3.39**	**62.8**	**59.3**	**3.5**
Sw-base	1.27	3.14	3.53	63.5	59.2	4.3
Sw-Top	1.23	3.06	3.26	62.1	59.4	2.7
Foamy	1.16	3.21	3.48	66.3	63.3	2.9
Microfluidal	1.25	3.04	3.33	61.9	59.0	3.0
Dense	1.29	3.12	3.43	62.4	58.0	4.4
Total measured samples						*99*
Oru	**Bulk density [g/cm^3]**	**Skeletal density [g/cm^3]**	**Solid density [g/cm^3]**	**Bulk porosity [vol.%]**	**Connected porosity [vol.%]**	**Isolated porosity [vol.%]**
MIN	0.01	2.45	2.82	3.3	1.3	0.0
MAX	2.86	3.59	3.93	99.6	99.6	7.3
AVERAGE	**1.26**	**2.87**	**2.99**	**57.8**	**56.0**	**1.8**
L-Oru	1.33	2.84	2.95	55.0	53.2	1.8
M-Oru	1.13	2.91	3.02	62.6	61.1	1.9
U-Oru	1.29	2.86	3.01	56.9	54.8	2.1
Foamy	1.27	2.87	2.96	57.1	56.0	1.1
Fluidal	1.17	2.88	3.03	61.6	59.6	
Fibrous	1.17	2.87	3.00	60.7	59.0	1.9
Dense	1.32	2.86	2.99	55.9	53.8	2.1
Total measured samples						*100*
Okp-Ph	**Bulk density [g/cm^3]**	**Skeletal density [g/cm^3]**	**Solid density [g/cm^3]**	**Bulk porosity [vol.%]**	**Connected porosity [vol.%]**	**Isolated porosity [vol.%]**
MIN	0.31	2.06	2.78	10.2	9.7	0.0
MAX	2.60	3.22	4.73	90.1	89.7	14.9
AVERAGE	**1.04**	**2.90**	**3.10**	**66.2**	**64.0**	**2.2**
L-Okp	1.15	2.91	3.03	61.8	60.0	1.8
U-Okp	0.92	2.90	3.17	70.7	68.1	2.6
Foamy	1.10	2.86	2.95	62.0	60.9	1.1
Fibrous	0.92	2.90	3.13	70.6	68.2	2.4
Dense	1.21	2.91	3.07	60.3	58.3	2.1
Total measured samples						*60*

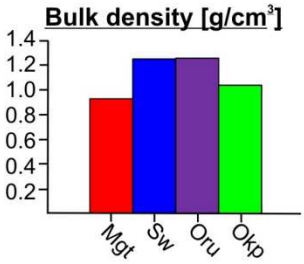

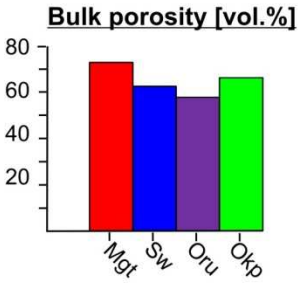

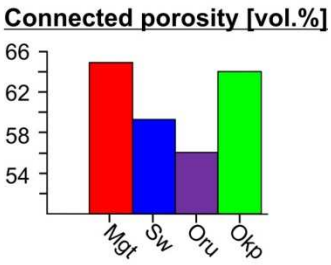

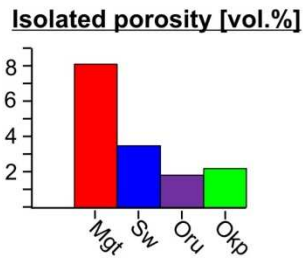

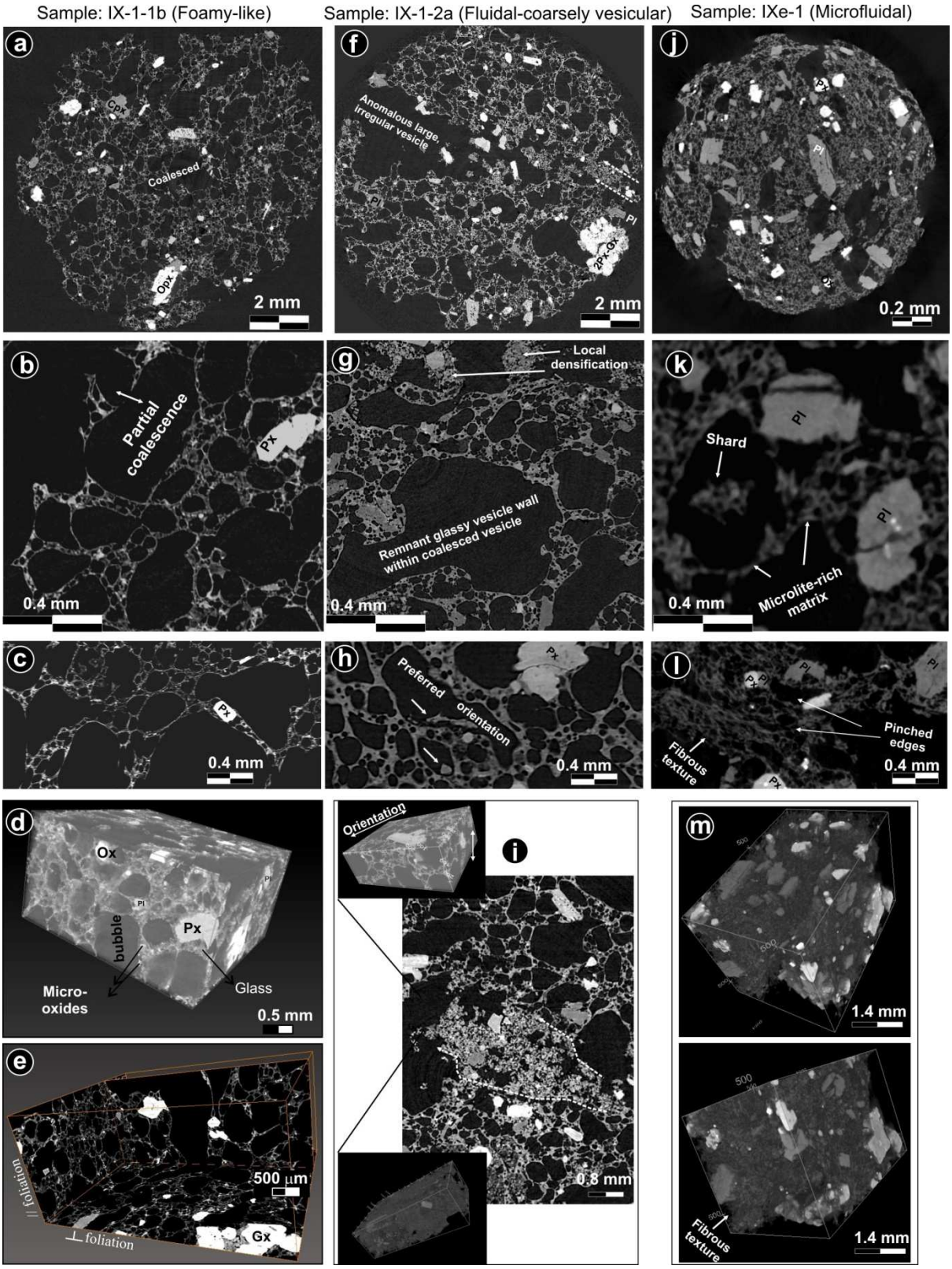

Figure 6.2 Reconstructed X-ray images as orthoslices and rendered subvolumes of three lapilli samples from the Mgt unit: **a-e)** shows crystal-poor, foamy lapilli with subspherical vesicles having thin walls; **f-i)** shows crystal-bearing, fluidal texture with elongated vesicles having thicker walls. White arrows in H point out glass shards included within a vesicle. Dashed arrows in (**i**) show a region of internal heterogeneity in the sample; **j-m)** illustrate a porphyritic, microfluidal pumice clast. **a-i** are synchrotron images (1 pixel = 4.5 µm), and **j-m** are computed µ-CT images (1 pixel = 3.6 µm).

Vesicle shapes within the microfluidal and crystal-rich U-Mgt sample (**Figs. 6.2j-m**) are more complex, usually distorted by having pinched edges, and show a clear orientation parallel to elongation (**Fig. 6.2l; Appendix H4.1c**).

All samples show a few irregularly shaped, anomalously large vesicles (>1600 μm in maximum diameter) that could not be included in the image analysis. However, these are not important for interpretations of degassing mechanisms, since they are thought to result from pre-eruptive nucleation and growth within the deeper magma chamber or extensive coalescence (Orsi et al., 1992). In addition, pores ≤1 μm are considered to be connection points or apertures between vesicles, rather than true bubbles (Sparks and Brazier 1982; Whitham and Sparks 1986). In microtomographic studies very small objects cannot be resolved (Shea et al., 2010), which can be seen in vesicle size distribution (VSD) deviations from linearity at sizes ≤10 μm.

Plagioclase with sieved textures (low attenuation, dark grey similar to glass matrix), pyroxenes (light grey with intermediate attenuation), and Ti-Mg oxides (white, high attenuation) were successfully identified, but only clinopyroxenes (Cpx), orthopyroxenes (Opx), and oxides (Ox) could be separated by greyscale thresholding. These mineral phases will be referred as mafic crystals throughout the text, and calculated crystal number densities will be restricted to them. Plagioclase (Pl) phenocrysts are commonly broken apart, with microjigsaws cracks separating individual a few microns (**Fig. 6.2k; Appendix H4.1c**), similar to those reported by Kennedy et al., (2005).

Textural parameters for each analysed subvolume (2-27 mm^3) from any single sample (~60 mm^3) show no significant variations, except for the foamy sample, which shows both skewed vesicle volume distribution (VVD) and polymodal VVD (**Table 6.2; Appendix H.3.1**). Despite this, samples are generally homogeneous and distributions from merged subvolumes are consistent with individual samples ones; hence merged data-sets are here considered to best characterize each sample (**Fig. 6.3**). In addition, the low values of the logarithm of vesicle number density per vesicle size class ($\ln(n_v)$) at vesicles <10 μm in diameter, within the VSD and CVSD, is attributed to a resolution limitation.

The quantitative analysis of vesicles indicates that vesicularity decreases with increasing mafic crystallinity and decreasing dominant vesicle size. Vesicle number density (N_v) is

constant (3×10^5 cm^{-3}), whereas mafic crystal number densities (N_x, vesicle-free) are slightly higher. N_x (vesicle-free) is one order of magnitude larger than N_v.

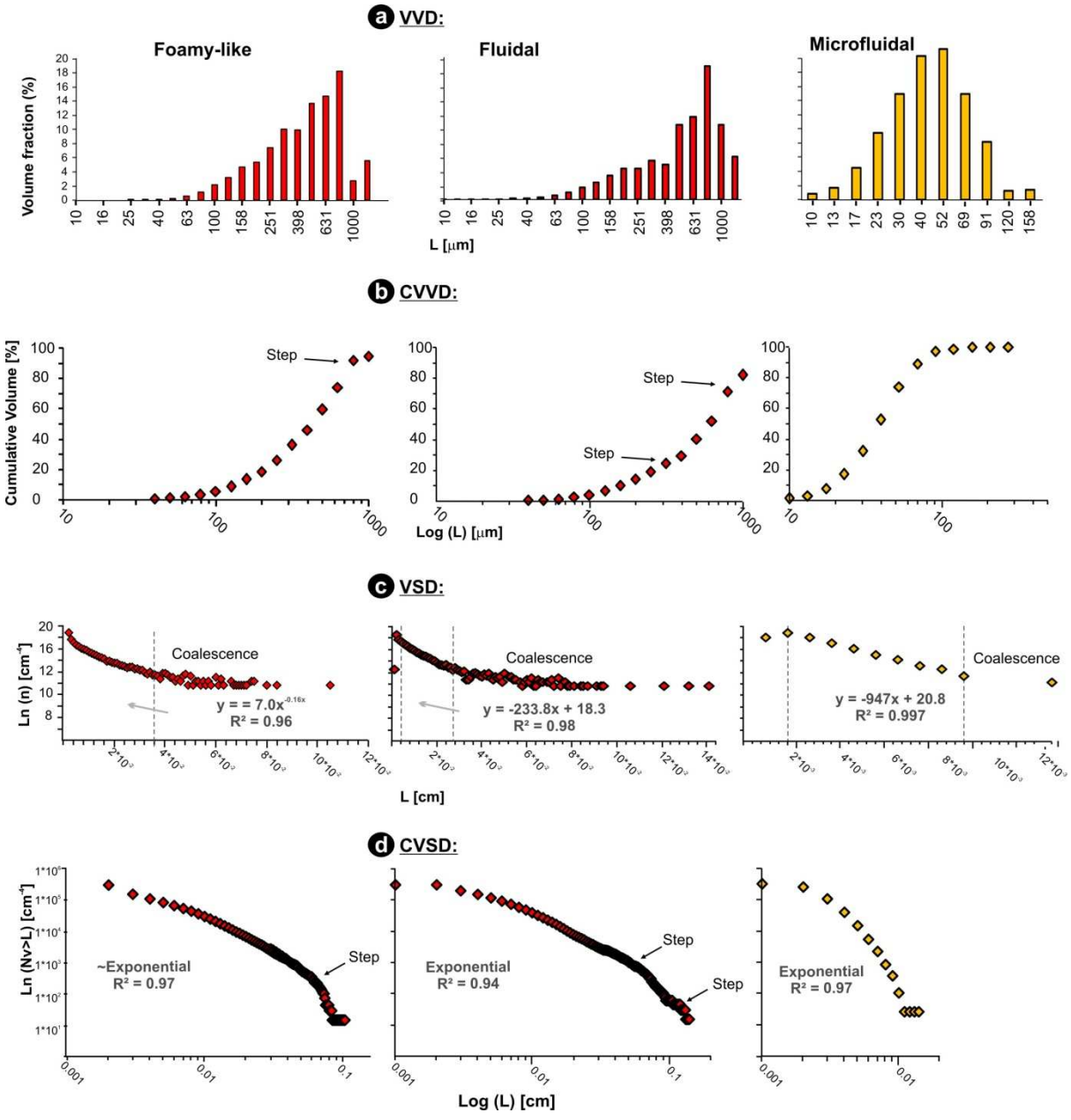

Figure 6.3 3D Quantitative analysis of: **a)** Vesicle Volume Distribution (VVD); **(b)** Cumulative Vesicle Volume Distribution (CVVD); **(c)** Vesicle Size Distribution (VSD); and **(d)** Cumulative Vesicle Size Distribution (CVSD) obtained from X-ray synchrotron and computed micro-CT 3D images. Arrows point steps in the CVVD and CVSD curves interpreted to represent coalescence (foamy and microfluidal case) or multiple events of nucleation and growth (fluidal case). Note that the length scale in the histograms is linear, not logarithmic.

Table 6.2 Summary of X-ray microtomography results on merged subvolumes of each sample.

Unit	Sample	Type	Vol [mm^3]	#	φ [Vol.%]	χ [Vol.%]	Nv [cm^{-3}]	Nx [cm^{-3}]	NPx [cm^{-3}]	Nox [cm^{-3}]	-1/GT	GT [cm]	n_o	Nt [cm^{-3}]	L [mm]	VVD	CVSD	Interpretation	CVD	CCSD	Interpre-tation
L-Mgt	IX-1b-1	1a	67	20142	72	18	3.0×10^5	3.9×10^6	4.2×10^6 (29%)	-	-	-	-	-	-	**Skewed**	~Exp.	One nucleation event + coalescence and hindered growth	**Polymodal**	-	MLT
	IX-1b-2a	2b	68	21170	70	16	3.1×10^5	3.0×10^6	4.3×10^6 (61%)	5.3×10^5 (0.2%)	224	4.5E-03	18	8.1E-02	0.045	P**olymodal** skewed	Exp.	Two nucleation events and coalescence	**Polymodal**	-	MLT
U-Mgt	IX-1e-2	2a	37	12068	51	37	3.2×10^5	1.5×10^6	9.7×10^4 (10%)	5.8×10^4 (0.6%)	986	1.0E-03	21	2.1E-02	0.010	**Broad mode**	Exp.	Single stage of nucleation and growth (minor coalescence)	**Polymodal**	PL	MLT
Sw-b	Sw-5b-2b	2a	71	37811	59	13	5.3×10^5	6.6×10^6	5.7×10^6 (14%)	1.7×10^5 (0.9%)	204	4.9E-03	18	8.6E-02	0.049	**Skewed**	Exp.	One nucleation event + ripening or hidnered growth + coalescence + minor collapse	**Polymodal**	PL	MLT
	Sw-5b-4	4	68	10980	52	22	1.6×10^5	8.7×10^5	8.3×10^5 (15%)	4.5×10^4 (1.0%)	914	1.1E-03	20	2.2E-02	0.011	**Bimodal**	PL	One nucleation event modified by coalescence	**Polymodal**	PL	MLT
Oru	Oru2a	2a	33	17403	50	6	5.3×10^5	1.4×10^6	1.7×10^6 (6%)	9.2×10^4 (0.9%)	953	1.0E-03	21	2.2E-02	0.010	**Skewed**	Exp.	Single stage of nucleation and growth + coalescence	**Polymodal**	PL	MLT
	Oru 3a	3a	24	12415	51	20	5.2×10^5	3.4×10^6	1.8×10^6 (8%)	6.1×10^4 (0.5%)	1181	8.5E-04	21	1.8E-02	0.008	**Skewed**	Exp.	Single nucleation event + minor coalescence and local collapse	**Polymodal**	PL	MLT
	Oru 4a	4	42	9449	52	15	2.3×10^5	1.6×10^6	2.3×10^6 (23%)	1.1×10^5 (0.6%)	1167	8.6E-04	21	1.8E-02	0.009	**~Bimodal**	Exp.	Two nucleation events + coalescence	**Polymodal**	PL	MLT
L-Okp	Ph16a-5a	4	226	70732	52	8	3.1×10^5	6.9×10^5	1.5×10^5 (3%)	2.8×10^4 (0.4%)	1009	9.9E-04	20	2.0E-02	0.010	**Flattened, broad**	PL	Two nucleation events modified by coalescence and collapse	**Polymodal**	PL	MLT
U-Okp	B13-Ph16-1c-6a	4	55	41805	32	25	$7.6x\ 10^5$	1.8×10^6	3.6×10^5 (14%)	3.4×10^4 (0.5%)	599	1.7E-03	20	3.4E-02	0.017	**One main mode (masks skewed VVD)**	Exp. To PL	Two nucleation events modified by coalescence and collapse	**Polymodal**	PL	2 events
	B50 Ph16b-3a	4	41	1252	61	59	3.1×10^4	2.6×10^6	6.8×10^5 (6%)	1.5×10^5 (1.3%)	896	1.1E-03	18	2.0E-02	0.011	**2 populations, one skewed**	Exp.	Two nucleation events modified by coalescence and collapse	**Polymodal**	PL	MLT
	B50Ph16b_1	3b	7	7883	43	16	1.2×10^6	3.8×10^6	3.2×10^6 (19%)	2.1×10^5 (1.7%)	1709	5.9E-04	22	1.3E-02	0.006	**Polymodal**	Exp.	Two nucleation events modified by coalescence and collapse	**Polymodal**	Exp.	MLT
	Ph-2-1d-5x	3b	2	10032	41	27	5.3×10^6	7.7×10^6	-	-	556	1.8E-03	24	4.3E-02	0.018	**Polymodal**	~Exp.	Two nucleation events modified by coalescence and collapse			MLT

Legend: #= number of measured vesicles φ = vesicularity; χ = mafic crystallinity; N_v = vesicle number density; N_x = mafic crystal number density (vesicle-free); N_{px} = pyroxene number density (vesicle-free); N_{ox} = magnetite number density (vesicle-free); G = mean growth rate; T= timescale of nucleation and growth; n_o = initial bubble nuclei; Nt = total vesicle number density; L= vesicle dominant diameter; VVD = Vesicle volume distribution; CVSD = Cumulative vesicle size distribution; CVD = mafic crystal volume distribution; CCSD = Cumulative mafic crystal size distribution. Exp. = Exponential trend; PL = Power-law trend. MLT = Multiple nucleation and growth; CN = Continuous nucleation. See text and **Appendix H** for more explanation and texture type nomenclature.

Each textural type shows a distinctive shape of VVD, cumulative vesicle volume distribution (CVVD), VSD, and cumulative vesicle size distribution (CVSD) (**Fig. 6.3; Table 6.2; Appendix H.3.1 and H.3.5**). All VSD show a nearly linear segment for the small vesicle-class sizes, followed by a flat tail at larger sizes; a pattern best developed in the L-Mgt samples. Estimated GT (G: mean growth rate; T: time scale of nucleation and growth) is in the order of 45 μm for the expanded samples (L-Mgt foamy and fluidal) and 10 μm for the U-Mgt microfluidal clast, whereas the estimated initial number of nuclei per cm^3 increases from 18 in the L-Mgt to 21 in the U-Mgt.

The mafic crystal size distributions of all samples are very similar, with polymodal crystal volume distributions (CVD), stepped crystal size distributions (CSD), and cumulative crystal size distributions (CCSD) reflecting two to three crystal size populations and dominant mafic crystal diameters in the order of 12 μm (**Appendix H.3.1**).

Volatile content obtained of melt inclusions: FTIR spectra were obtained from both sides of five double-exposed glass inclusions hosted in clino-and-orthopyroxene crystals from the L-Mgt (**Chapter 2.2.6; Table 6.3; Fig. 6.4; Appendix I**). Glass compositions were measured with electron microprobe from 25 inclusions within the five crystals, varying from 65 to 73 wt.% (normalized), with densities between 2.51 and 2.60 $g \cdot cm^{-3}$. Dissolved total H_2O content calculated from the absorption peak at ~3550 cm^{-1} ranges between 2.1 and 5.2 wt.%. Molecular H_2O content calculated from the absorption peak at ~1630 cm^{-1} ranges between 1.0 and 2.4 wt.%. FTIR spectra were obtained from seven inclusions within orthopyroxenes of the U-Mgt and electron microprobe glass compositions were obtained in six inclusions, ranging from 67 to 68 wt.% (normalized); corresponding glass densities vary between 1.2 and 3.58 $g \cdot cm^{-3}$. Calculated total H_2O content vary from 1.2 to 3.6 wt.%, with molecular H_2O ranging between 0.3 and 1.9 wt.% (**Appendix I**).

Variation of silica concentration of glass inclusions within a single crystal are related to the position within the crystal, with compositions increasingly evolved towards the outer rim, consistent with crystallization of the host during melt evolution (c.f., Blundy and Cashman 2001). Variations of volatile content in the L-Mgt samples correlate with inclusion shape, with highest total H_2O obtained in rounded inclusions and lowest values from irregular and cracked inclusions, which might have leaked (c.f., Tait 1992).

Table 6.3 Summary of microprobe and micro-FTIR analyses of glass inclusions for the Mangatoetoenui Unit.

Sample	Host	# runs	SiO_2	TiO_2	Al_2O_3	FeO	MnO	MgO	CaO	Na_2O	K2O	P_2O_5	Calc Density [g/cm^3]	H_2O total @ 3550	H_2O mol @ 1630	Observations	Temperature ^{0}C (2Px geothermometer)	Liquid density [g/cm^3]	Calc. Saturation P [MPa]	Minimum saturation depth [km]	Melt viscosity [Pa*s]
Lower Mantatoetoenui Unit																	1120				
Residual Melt																		2.8			0.4-0.5
IXb-4-1	Opx	2*	70.35	0.63	13.58	4.30	0.11	0.96	2.78	3.77	3.22	0.31	2.52	**5.25**	**2.41**	Rounded		2.4	192	**7**	0.6
IXb-11-1	Opx	2*	67.61	0.78	15.46	3.84	0.00	1.12	4.13	3.75	3.05	0.25	2.55	2.06	1.26-1.64	Leaking		2.5	42	2	0.6
IXbX2	Opx	5	68.49	0.63	14.64	4.63	0.09	1.12	3.27	3.27	3.52	0.34	2.55								
IXbX3	Cpx	3	68.48	0.82	14.85	4.09	0.01	1.03	3.10	3.37	3.82	0.43	2.54								
IXbX4	Opx	3	70.34	0.73	13.66	4.31	0.09	0.93	3.00	3.67	3.04	0.23	2.53								
IXbX5	Cpx	8	68.54	0.78	14.53	4.05	0.07	1.11	3.54	3.65	3.39	0.35	2.54								
IXbX9	Cpx	3	69.01	0.63	14.30	4.16	0.11	1.14	3.66	3.52	3.25	0.24	2.54	3.26	1.19	Irregular shaped		2.5	91	3	
IXbX10	Cpx	3	69.59	0.81	14.09	3.88	0.05	1.14	3.42	3.82	2.97	0.24	2.53								
Average		*25*	*69.05*	*0.73*	*14.39*	*4.16*	*0.07*	*1.07*	*3.36*	*3.60*	*3.28*	*0.30*	*2.54*					2.5			
IX-1-1	Cpx	2*												3.40	1.09-1.41	Elongated, cracked			98	4	
IX-6-1	Cpx	2*												2.76	1.03-1.34	Subangular			69	3	
Upper Mantatoetoenui Unit																					
Residual Melt																		2.8			0.5
IXe-2-1	Opx	1*	66.72	1.01	14.84	4.66	0.02	1.52	4.38	3.75	2.72	0.37	2.54	1.95	0.72-0.93	Irregular shaped		2.5	38	1	
IXe-8-3	Opx	1*	66.98	0.85	14.43	5.05	0.04	1.51	3.66	3.96	3.00	0.51	2.53	1.79	0.98-1.28	Rounded		2.5	32	1	
IXe-2	Opx	3	67.69	0.88	14.76	4.31	0.14	1.21	3.84	3.77	3.01	0.40	2.56								
Ixe-8	Opx	3	66.96	0.78	15.42	4.37	0.04	1.27	3.81	3.59	3.38	0.38	2.55								
Average	*Opx*	*6*	*67.09*	*0.88*	*14.86*	*4.60*	*0.06*	*1.38*	*3.92*	*3.77*	*3.03*	*0.42*	*2.55*					2.5			
IXe-1-1	Opx	1*												2.50	1.2-1.36	Irregular shaped			59	2	
IXe-3-1	Opx	1*												1.22	0.29-0.37	Rounded			16	1	
IXe-4-1	Opx	1*												1.82	0.37-0.48	Rounded			34	1	
IXe-8-1	Opx	1*												**3.58**	**1.47-1.91**	Rounded			**106**	**4**	
IXe-8-2	Opx	1*												2.04	0.63-0.82	Subrounded, elongated			41	1	
Shawcroft Eruptive Unit																	1013				

Chemical data are given in wt.%; H_2O contents measured at 3550 and 1630 cm^{-1} are given in wt.%. Calc. Saturation P = Calculated saturation pressure following Newman and Lowenstern (2002). Calc density = calculated density based on glass composition.

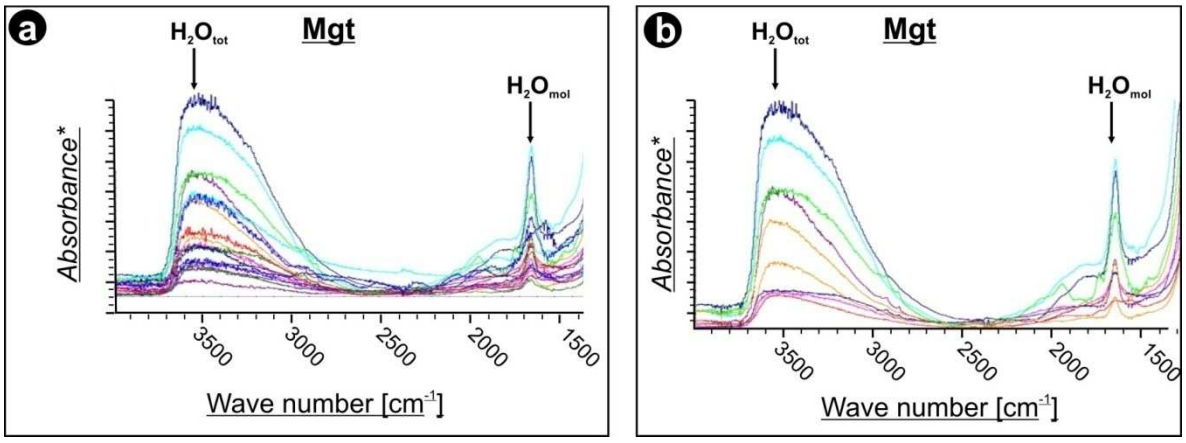

Figure 6.4 Mid-Infrared spectra obtained using an FTIR microscope in glass inclusions hosted in Cpx and Opx within the Mangatoetoenui (Mgt) eruptive unit: **a)** total spectra showing the main peaks of total and molecular water; **b)** filtered data showing those spectra that are free of "noise". Y-axis corresponds to absorbance (*), not to scale (See appendix A for absorbance values of individual spectra).

Within the U-Mgt, rounded inclusions of similar glass composition have variable volatile contents, suggesting polybaric crystallization (c.f., Blundy and Cashman 2001). Therefore, the values reported here must be regarded as a minima and the best approximation of the total H_2O content during pyroxene crystallization could be 5.2 wt.% in the L-Mgt, and 3.6 wt.% for the U-Mgt.

Interpretation: the glass inclusions have higher silica contents than groundmass glass (**Chapter 5.2.1**), which is counter the expected crystallisation-induced evolution in these composition magmas. Hence, the FTIR results cannot be regarded as pre-eruptive volatile contents, but instead provide information of a pre-existing, evolved storage system located at minimum depths of 7 km (for L-Mgt) and 4 km (for U-Mgt), where the pyroxenes crystallized. These pyroxenes were later carried into the erupting magma on its way to eruption.

Although the VSD are exponential, the moderate vesicle number densities of 10^5 cm^{-3} and higher mafic crystal number densities (N_x) suggest that heterogeneous bubble nucleation (c.f., Mangan and Sisson 2000) was predominant. This is confirmed by magnetite number densities as high as $10^5 cm^{-3}$ and in agreement with observations made from optical analysis in thin sections (**Fig. 5.5; Appendix D.1**), where oxides are completely embedded within vesicles. The foamy and fluidal textural types of the L-Mgt unit suggest very dynamic flow conditions in comparison to the microfluidal U-Mgt and, in general, L-Mgt lapilli textures and glass composition indicate it had a lower viscosity than the U-Mgt melt (**Appendix H.4.1**).

The main difference between textural types within L-Mgt may relate to the mafic crystal content and number densities. The foamy lapilli textures indicate one nucleation event modified by coalescence and hindered growth processes, whereas the coarsely vesicular fluidal lapilli textures with polymodal VVD had multiple nucleation phases and growth processes. L-Mgt textures indicate that coalescence was responsible for the final vesicle size distributions. Local vesicle shearing resulted from differential expansion (yz views in **Appendix H.4.1**) where vesicle growth deformed the surrounding melt.

The analyses of U-Mgt micofluidal lapilli have a single mode of the VVD, steep CVVD, nearly linear VSD, and exponential CVSD. Hence, a single nucleation and growth event rapidly following decompression (c.f., Navon and Lyakhovsky 1998; Lyakhovsky et al., 1996; Gardner et al., 1998) explains most of these features. A second vesicle population may also occur due to coalescence, producing the tails in VSD and CVSD. However, this is outside the detectable upper-limit of the subvolumes. The U-Mgt greater crystal content compared to L-Mgt probably restricted bubble growth, contributing to the overall increase in viscosity.

Microtextural variations found within any stratigraphic level give hints on conduit processes, whereas variations with stratigraphic position (from L-to-U-Mgt) indicates variation in

vesiculation and degassing processes with time. Bubble diffusion and expansion processes occurred differently across the conduit during the L-Mgt phase. A single bubble nucleation and growth is favoured in the central, rapidly ascending, crystal-poor magma where bubbles grow under high decompression rates. Multiple stages of bubble nucleation and growth occur in crystal-bearing portions closer to the conduit margin where interaction with other bubbles and phenocrysts complicated expansion. In these slower-rise sites, bubble elongation and shearing is promoted, and crystals provided more effective sites for bubble nucleation. This is in agreement with observations of Klug and Cashman (1994), who found different VVD and VSD within samples of the same deposit, suggesting different eruption paths, ascent rates and exsolution rates within the conduit.

During the short repose time between L-and-U-Mgt (**Chapters 4, 5**) most of the magma was subject to a slower decompression rate or experienced a shallow arrest. Degassing was enhanced, allowing extensive crystallisation and increasing magma viscosity. Vesiculation occurred as a single, late event under fast decompression and bubble growth was highly restricted by crystals. Predominantly long-axis cracks in feldspars parallel to vesicle elongation, similar to those reported by Kennedy et al., (2005) indicate that under rapid decompression the magma near the conduit wall decompressed laterally, with fractures opening parallel to the conduit flow.

6.2.2 Shawcroft Eruptive Unit Pumice textures

Density and porosity: the Shawcroft (Sw) lapilli from the Plinian phase analyzed for porosity and density measurements (**Appendix G; Table 6.1; Fig.6.5**) show similar average values at the bottom and top of the deposit. The bulk densities span a greater range from 0.19 to 2.81 g·cm^{-3} (average = 1.27 g·cm^{-3}) at the base, compared to 0.88 to 1.72 g·cm^{-3} at the top (average = 1.23 g·cm^{-3}). Bulk porosities range between 48 and 95 % at the base of the deposit (average = 63.5%), with only $\leq$13 % isolated pores. At the top of the lapilli bed, bulk porosities range from 46 to 72 % (average = 62.1 %), with $\leq$9 % isolated porosity.

Bulk density (**Fig. 6.5a**) and porosity (**Fig. 6.5b**) distributions within Sw samples have narrower peaks, and are more symmetric than those of the Mgt unit. The connected porosity distribution (**Fig. 6.5c**) is asymmetric, positively skewed, with a distinct mode around 70 %,

and the isolated porosity distribution is polymodal, and negatively skewed (**Fig. 6.5d**). Connected porosity is directly correlated with bulk porosity, independently of the pumice texture (**Fig. 6.5e**). All porosities, and particularly the isolated porosity, are lower than in the Mgt samples (**Table 6.1**).

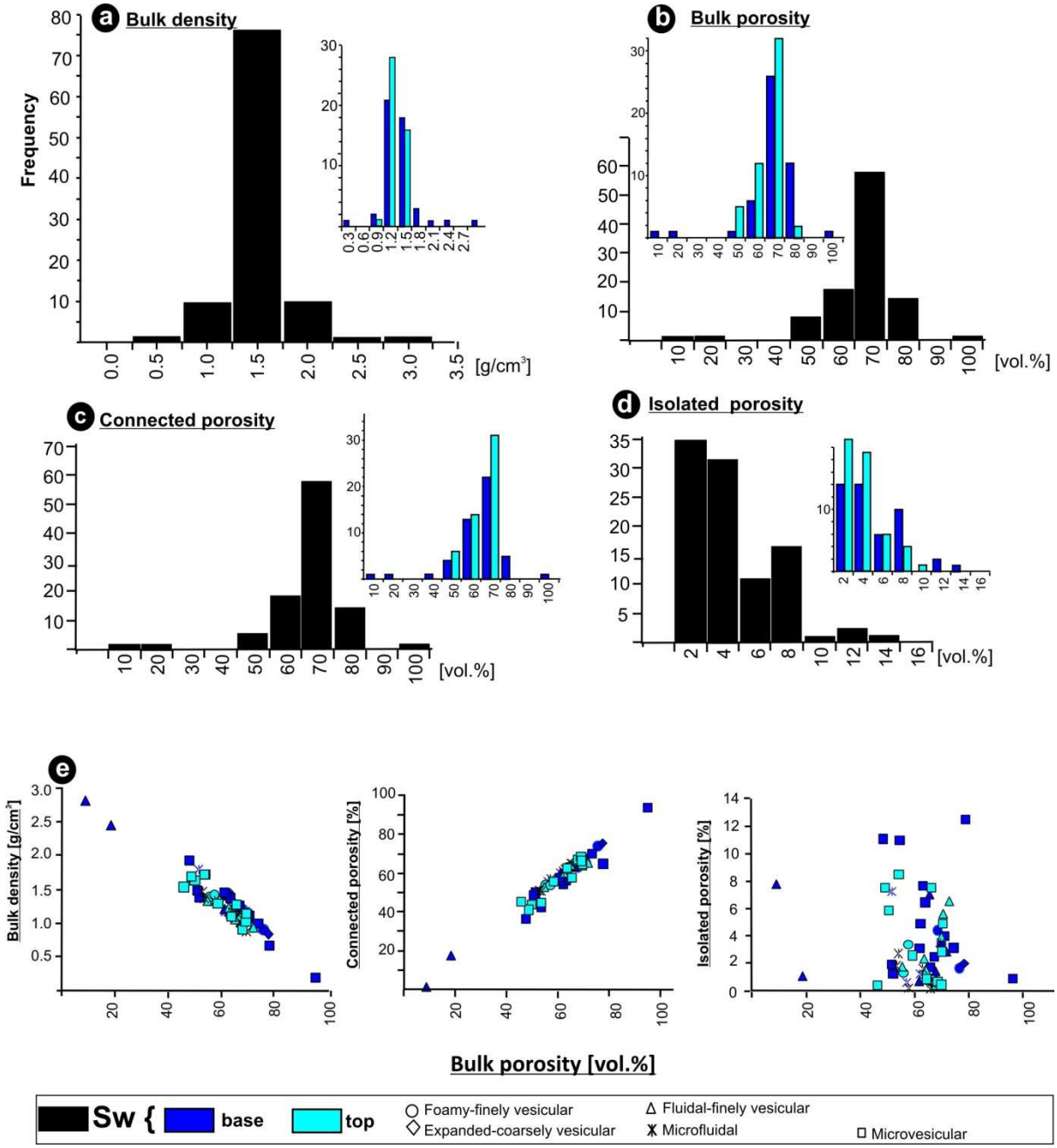

Figure 6.5 Porosity and density frequency distributions within the Shawcroft Lapilli. The individual parameters were obtained from measurements of: **a)** bulk sample volume and envelop density; **d)** connected + isolated porosities relative to the bulk sample volume; **c)** skeletal density **d)** solid density determined in crushed samples; **e)** comparative plots of individual parameters against bulk porosity. Black histograms illustrates all samples measured (n=98), dark blue are basal samples, and cyan are from the top of the fall deposit.

3D-Textures: two samples were selected for X-ray scanning: Sw-5b-2b represents the **microvesicular** texture (**Fig. 6.6a-d**), with 59 % vesicles and 6 % mafic crystals (+ *9 % felsic*); and Sw-5b-4 is a sample of the **dense** end-member (**Fig. 6.6e-h**), with 51 % vesicles and 7 % mafic crystals (+ *15 % felsic*) (**Appendices H.3.2, H.4.2**).

Both types show very similar, small, dominantly irregular vesicles of 80-180 μm in diameter in 2D orthoslices. Different degrees of coalescence but, contrary to Mgt, no complete shape relaxation is evident. Pore aperture widths vary between ~44 to 180 μm. As seen in 2D thin sections, vesicles are irregular and elongated, occasionally terminating in a tear or V-form (**Fig. 6.6b,f**). Vesicle outlines are sharp and irregular due to high plagioclase phenocryst and microlite content compared to Mgt samples. Vesicle walls are significantly thicker than Mgt samples and vary from flat to slightly curved. Cracked feldspars and clinopyroxene crystals are common (**Figs. 5.15c; 6.6c, g**), and are filled with thin melt fibers (glass) and small vesicles in some cases (**Appendix H.4.2b**).

The textural parameters of merged subvolumes (**Table 6.2**) of each sample have similar characteristics to the individual subvolumes (**Appendix H.3.2; Fig. 6.7**). Total vesicularity is significantly lower than foamy and fluidal textures observed in the L-Mgt, and more similar to the microfluidal clast analyzed from the U-Mgt. N_x is one order of magnitude higher ($7x10^6$ cm^{-3}) than N_v in the Sw microvesicular lapilli, but similar to N_v in the dense Sw type. Each textural type shows a distinctive VVD, CVVD, VSD, and CVSD shape (**Fig. 6.7**). The VSD of the microvesicular type shows an inflection towards higher $\ln(n_v)$ values at smaller sizes, a linear portion for vesicles 55-125 μm, and a long, flat tail for larger vesicle sizes. The CVSD is exponential. On the other hand, the VSD of the dense clast (**Fig. 6.7c**) shows a flat tail for vesicles larger than 130 μm. The CVSD (**Fig. 6.7d**) is steep and follows a power-law. Estimated GT is in the order of 49 μm for the microvesicular clast and 11 μm for the dense clast, whereas the estimated initial number of nuclei per cm^3 increases from 18 at the base of the deposit to 20 at the top (**Table 6.2**).

The crystal size distributions of all samples show polymodal CVD, stepped CSD, and power-law CCSD reflecting two to three crystal size populations (**Appendix H.3.2**).

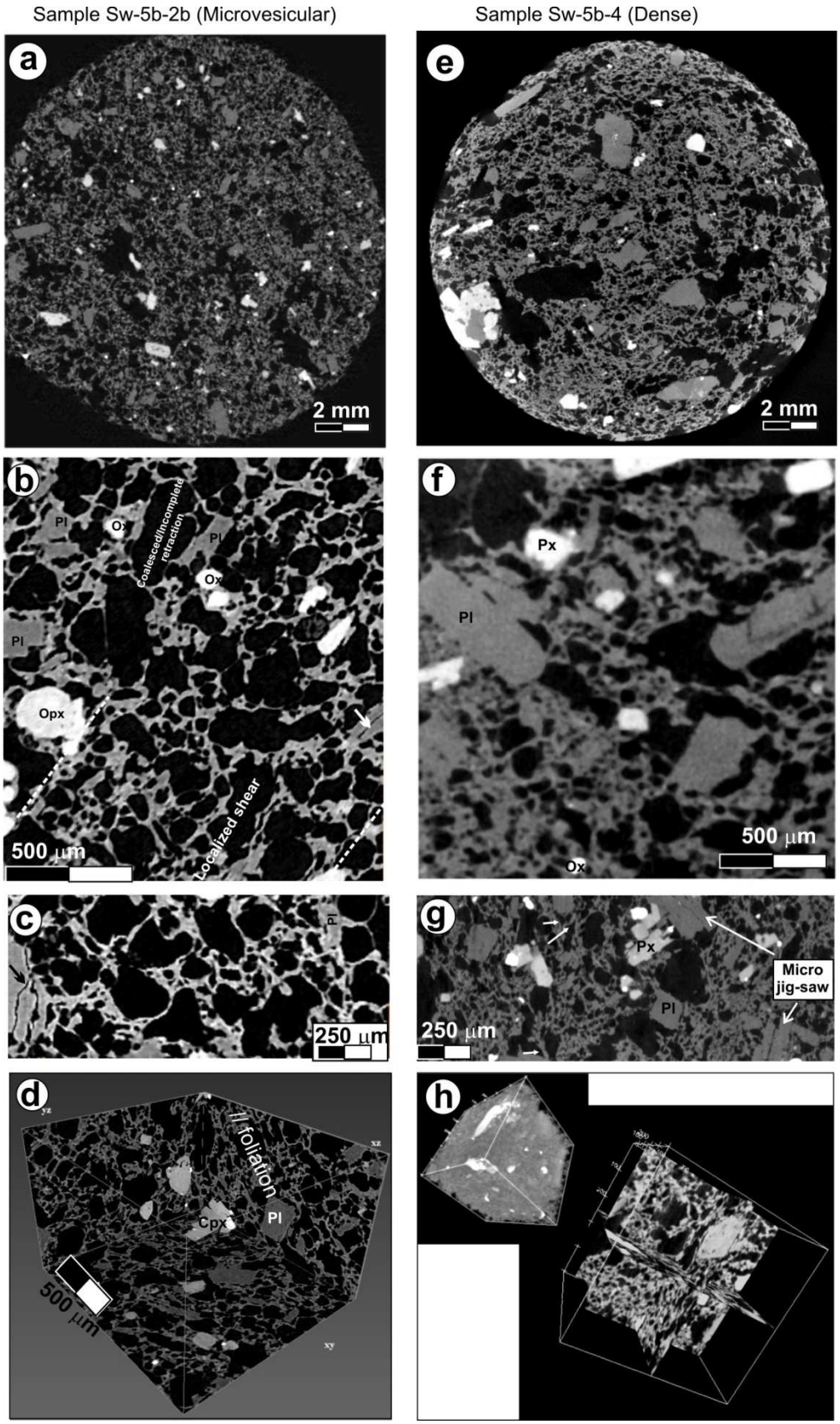

Figure 6.6 Reconstructed X-ray images as orthoslices and rendered subvolumes of two different textures**: a-d)** porphyritic, microvesicular pumice clast; (**e-h**) porphyritic, microlite-rich, dense clast; note the presence of micro jigsaw feldspars (arrow in **c**, **g**); **a-d** are synchrotron images (1 pixel = 4.5 μm), and **e-h** are computed micro-CT images (1 pixel = 4.4 μm).

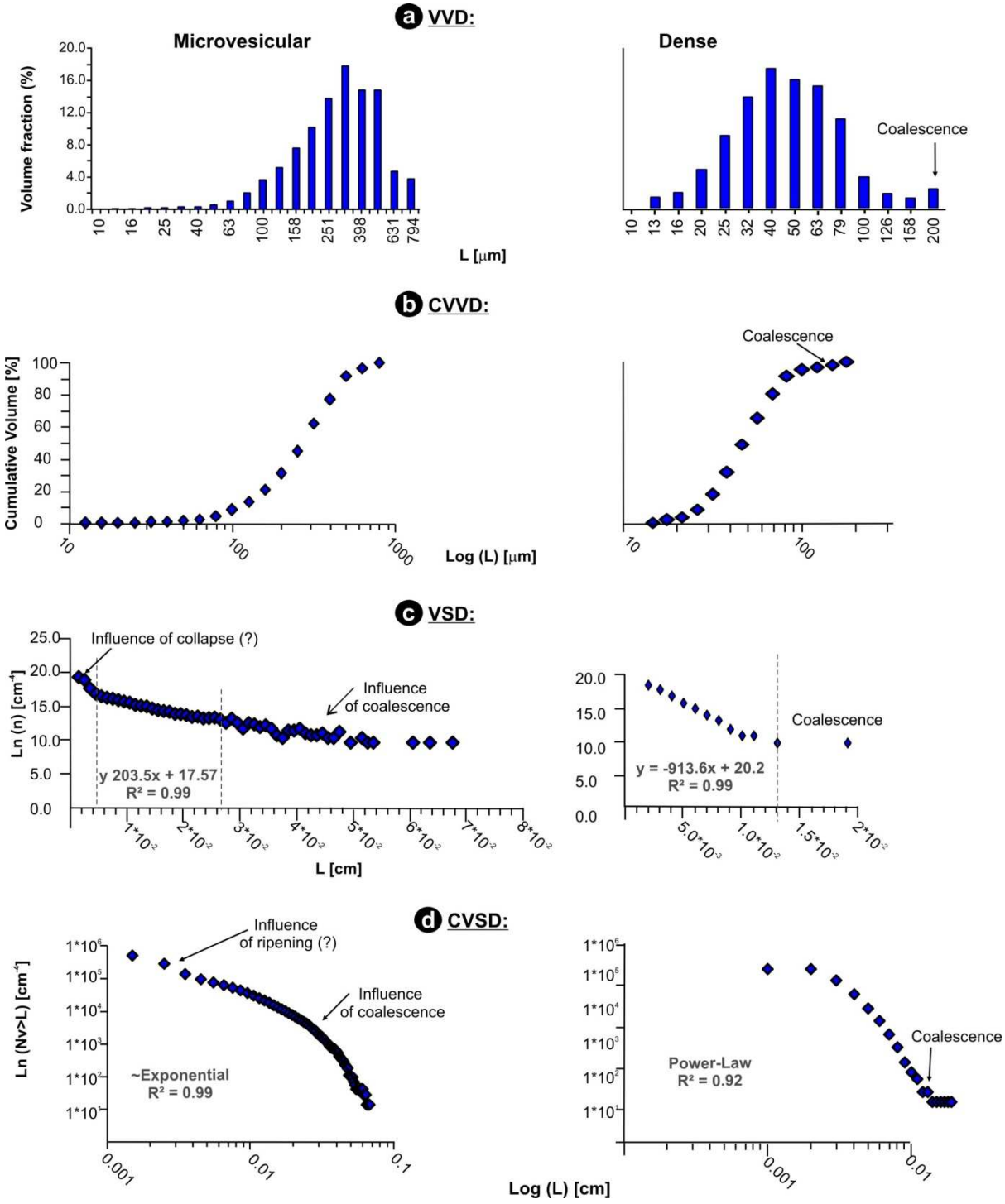

Figure 6.7 3D determinations of: **a)** Vesicle Volume Distribution (VVD), **(b)** Cumulative Volume Distribution (CVVD), **(c)** Vesicle Size Distribution (VSD), and **(d)** Cumulative Vesicle Size Distribution (CVSD).

Volatile content obtained in melt inclusions: FTIR spectra were obtained from both sides of 14, double-exposed glass inclusions hosted in clino-and-orthopyroxene crystals (**Table 6.4; Appendix I; Fig. 6.8**). Glass compositions were obtained using electron microprobe from 16 different inclusions, varying from 64 to 71 wt.% SiO_2 (normalized), with corresponding glass densities between 2.49 and 2.63 g·cm^{-3}. Only considering the spectra with minimum noise, dissolved total H_2O content calculated from the absorption peak at ~3550 cm^{-1} ranges between 1.3 and 5.4 wt.%. Molecular H_2O content calculated from the absorption peak at ~1630 cm^{-1} ranges between 0.5 and 1.9 wt.%.

Table 6.4 Summary of microprobe and micro-FTIR analyses on glass inclusions for the Shawcroft eruptive unit. Chemical data are given in wt.%; H_2O contents measured at 3550 and 1630 cm^{-1} are given in wt.%.

Sample	Host	# runs	SiO_2	TiO_2	Al_2O_3	FeO	MnO	MgO	CaO	Na_2O	K2O	P_2O_5	Calc Density [g/cm^3]	H_2O total @ 3550	H_2O mol @ 1630	Observations	Temperature ^{0}C (2Px geothermometer)	Liquid density [g/cm^3]	Calc. Saturation P [MPa]	Minimum saturation depth [km]	Melt viscosity [Pa*s]
Shawcroft Eruptive Unit																	1013				
Residual Melt																		2.8			0.5
Swa-1-3	Opx	1*	64.47	0.96	15.84	5.64	0.01	1.73	4.49	3.91	2.73	0.21	2.55	1.79	0.75-0.97	Subangular		2.5	32	1	0.5
Swa-3a-2	Cpx	1*	72.84	0.76	12.13	3.52	0.06	0.74	2.17	3.44	4.08	0.25	2.49	2.58	1.18	Rounded		2.4	61	2	0.7
Swa-5-1	Opx	1*	70.87	0.56	13.83	3.26	0.20	0.68	2.46	3.98	3.76	0.40	2.50	3.30	0.77	Irregular/cracked		2.4	92	3	0.7
Swa-5-2	Opx	1	70.83	0.66	13.85	3.47	0.05	0.92	2.60	4.12	3.44	0.07	2.51			Rounded, cracked		2.4			
Sw-12a-1	Opx	1*	66.23	0.95	15.50	4.54	0.00	1.57	4.23	4.39	2.28	0.32	2.58	1.81	0.59-0.76	Irregular, cracked		2.5	33	1	0.6
Swa-1	Opx	4	65.30	1.02	14.99	5.62	0.16	1.51	4.15	3.83	3.10	0.32	2.60								
Swa-5	Opx	6	70.15	0.62	14.25	3.63	0.10	0.83	2.88	3.90	3.48	0.16	2.52								
Swa-13	Opx	4	67.70	0.79	15.19	3.88	0.16	1.27	3.79	3.99	2.95	0.27	2.55								
Average		*14*	*68.55*	*0.79*	*14.45*	*4.20*	*0.09*	*1.16*	*3.35*	*3.95*	*3.23*	*0.25*	*2.54*					2.5			0.6
Swa-1-1	Opx	1*												1.30	0.46-0.59	Elongated, close to crack			18	1	
Swa-1-2	Opx	1*												1.27	0.46-0.59	Rounded, small, close to crack			17	1	
Swa-3a-1	Cpx	1*												**5.42**	1.91	Rounded, close to crack			**198**	**7**	
SwA-9a-1	Cpx	1*												5.04	1.59	Irregular shaped			178	6	
SwA-9a-2	Cpx	1*												4.70	1.16	Small. Rounded			161	6	
Sw-13a-1	Opx	1*												1.79	0.54	Rounded, close to crack			32	1	
Sw-13a-2	Opx	1*												2.84	0.62	Elongated, close to crack			71	3	

Some of the crystals are zoned (**Appendix I**) and more mafic glass-inclusion compositions occur towards the outer rim of the crystal. Although oscillatory zonation is common in plagioclase and resorption borders are frequent in both feldspars and pyroxenes (**Appendix D.2**), without a detailed study of the mineral chemistry it is impossible to determine whether reheating of the melt occurred, or simply convection of crystals within the reservoir (e.g., Murphy et al., 2000). Lower volatile contents were obtained in inclusions close to crystal cracks, indicating possible leaking (c.f., Lowenstern 1995, Frezzotti 2001). Overall, glass inclusions of similar composition gave variable water contents, suggesting polybaric crystallization occurred (c.f., Blundy and Cashman 2001). The minimum value of total H_2O in the magma were pyroxenes crystallized is 5.4 wt.%.

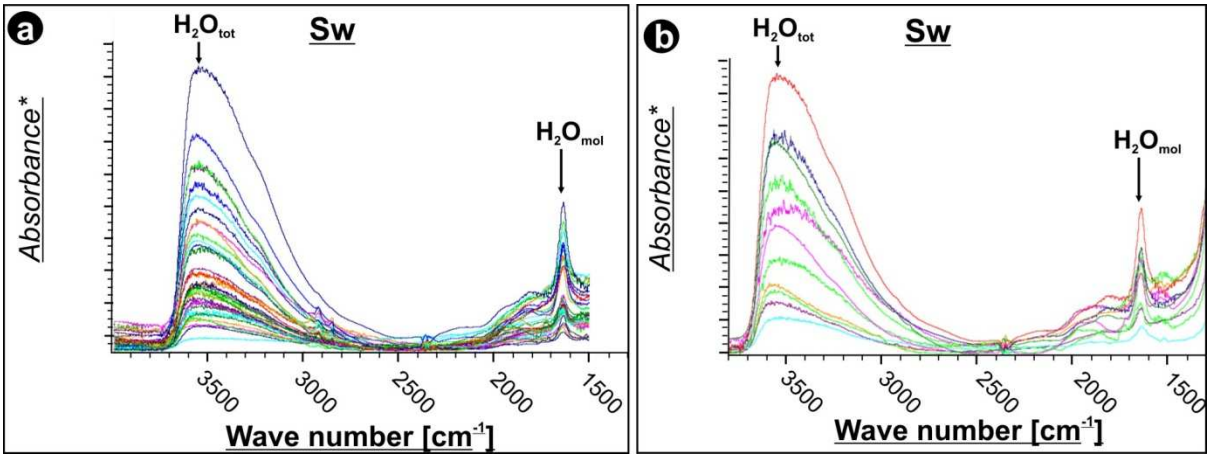

Figure 6.8 Mid-Infrared spectra obtained in glass inclusions hosted in Cpx and Opx within the Shawcroft (Sw) eruptive unit: **a)** total spectra showing the main peaks of total and molecular water; **b)** filtered data showing spectra free of "noise". Y-axis corresponds to absorbance (*), not to scale. See appendix A for individual values.

Interpretation: the more evolved composition of the glass inclusions relative to the groundmass glass (**Chapter 5.2.2**) indicates either: **a)** phenocrysts coexisted with a rhyolitic melt early in the magmatic history and were later entrapped within the erupting Sw magma; or **b)** post-trapping evolution occurred, including melt crystallisation or chemical exchange with the host crystal (c.f., Frezzotti 2001). Detailed analysis of inclusions would need to be undertaken to prove either hypothesis, but in either case, the water contents measured by FTIR cannot be pre-eruptive volatile contents, but rather give information about the entrapped melt at the moment of pyroxene crystallisation.

Both microvesicular and dense Sw lapilli textures suggest that vesicle growth and shapes were highly restricted by other vesicles and crystals. Refolded vesicle shapes suggest multiple stages of deformation before fragmentation. Compared to Mgt-foamy and fluidal types, the irregularity of vesicle shapes and the thicker vesicle walls of Sw samples suggest a longer degassing history in the latter before fragmentation. This interpretation is also supported by the presence of microlites (**Fig. 5.13**), which commonly form in response to degassing during decompression (c.f., Klug and Cashman 1996; Hammer et al., 1999). High viscosity is additionally suggested by high average bulk densities and low average bulk porosities (**Table 6.1**), as well as the wide range of connected porosity. Permeable gas escape was also responsible for local vesicle collapse. The narrow density and porosity distribution modes suggest that the magma was, not only chemically but also physically homogeneous, under a uniform state of degassing, crystallization, and with a uniform ascent rate.

The main difference between textural types within the Shawcroft unit corresponds to different N_x at similar vesicularity. The significantly larger N_x of the microvesicular type is correlated with a more complex bubble growth process, which included hindered growth, coalescence and minor collapse. The last two processes are indicated from inflections in the VSD and CVSD (**Figs. 6.7c, d**). The dense type show more heterogeneity between individual subvolumes (**Appendix H.3.2**). Coalescence appears to be responsible for a broader mode in VVD, the inflection of the CVVD, and the flat tail of the VSD curves (c.f., Cashman and Mangan 1994; Mangan and Cashman 1996; Klug et al., 2002; Adams et al., 2006; Polacci et al., 2008, Shea et al., 2010). However, both VSD and the power-law CVSD are also consistent with a single stage of nucleation. In some of the subvolumes a slight shift of the CVVD to coarser vesicles might result from hindered growth or ripening effects (c.f., Cashman and Mangan 1994). The local effects of vesicle collapse might be responsible for the "shrinkage" of the CVSD (**Fig. 6.7d**), which shows a "sigmoidal" shape (c.f., Shea et al., 2010). Therefore, variations between subvolumes of a particular sample are probably dictated by the local effect of bubble ripening/hindered growth, coalescence, and local collapse.

Contrary to the Mgt unit, the Sw samples indicate a common degassing path for most of the magma body, which ascended at relatively constant rate. These conditions favoured continuous bubble nucleation, but growth was highly limited by crystal content and N_x, under decompression rates lower than Mgt eruption. Coalescence was prompted without enough time for relaxation, and where local permeable paths developed, bubble collapse occurred.

Similar to Mgt, the presence of cracks within phenocrysts indicates a very late decompression wave, the volumetric expansion of the entire mixture, and the rapid quenching of the magma shortly after crystal breakage. Considering the higher crystallinity and microlite content in Sw samples, volatile loss could have acted as a feedback mechanism allowing over-pressurization of small, constrained bubbles, which could not relax under high decompression rates (c.f., Dingwell 1996; Deubener et al., 2003), fragmenting the magma at lower vesicularities compared to Mgt (c.f., Spieler et al., 2004a,b).

6.2.3 The Oruamatua Unit pumice textures

Density and Porosity: the Oruamatua lapilli clasts from the Plinian phase (**Appendix G; Table 6.1; Fig.6.9**) have the lowest connected porosities and isolated porosities of all studied units. The average bulk density varies from 1.33 $g \cdot cm^{-3}$ in the L-Oru, to 1.13 $g \cdot cm^{-3}$ in the M-Oru, returning to 1.29 $g \cdot cm^{-3}$ in the U-Oru. Bulk and connected porosities are the lowest in the L-Oru (55 and 53 %, respectively) and reach maximum values in the M-Oru (63 and 61 %, respectively), before returning for the U-Oru (57 and 55 % respectively).

Bulk density (**Fig. 6.9a**) and porosity (**Fig. 6.9b**) distributions within Oru samples have weakly defined peaks, reflecting a physical heterogeneity. Bulk density and porosity distributions are nearly symmetric. Connected porosity distribution is nearly symmetric and ranges between 60 to 75 % (**Fig. 6.9c**), with isolated porosity (**Fig. 6.9d**) $\leq$7 %. There is a positive linear correlation between connected and bulk porosities (**Fig.6.9e**).

3D-Textures: three samples from the M-Oru bed were scanned, one to represent **a) microfluidal lapilli** with 50 % vesicles and 3 % mafic crystals (*+ 10 % feldspars*); **b) microfibrous** lapilli with 51 % vesicles and 9 % mafic crystals (*+ 10 % feldspars*); and **c) microvesicular-dense** pumice clasts with 52 % vesicles and 5 % mafic crystals (*+ 22 % feldspars*) (**Fig. 6.10; Appendices H.3.3, H.4.3**).

All the samples are very finely vesicular, coarsely porphyritic, and contain highly irregular vesicles with sharp edges. Microfluidal lapilli textures (**Appendix H.4.3a**) are characterized by anomalously large, irregularly shaped pores (**Fig. 6.10a, c**), the thickest vesicle walls (**Fig. 6.10b**) and the largest modal vesicle diameter (10 μm). Microfibrous lapilli (**Appendix H.4.3b**) have the thinnest vesicle walls and the largest N_x (**Fig. 6.10f**). Microvesicular-dense clasts (**Appendix H.4.3c**) have the most distorted and smallest pores together with the lowest N_v (**Fig. 6.10j**). In all cases, feldspar and pyroxene phenocrysts show cracks both parallel (**Fig. 6.10g,** yz view in **Appendix 4.3b**) and perpendicular (**Fig. 6.10f, j**) to the crystal long axes.

Samples are homogeneous and merged subvolumes (**Table 6.2; Fig. 6.11**) match the distributions from individual subvolumes (**Appendix H.3.3**), except for the microvesicular textures. In the latter case, advanced coalescence is indicated by the broad VVD mode in the

merged volume (**Fig. 6.11a**), which masks the polymodal VVD seen in individual subvolumes (**Appendix H.3.3**).

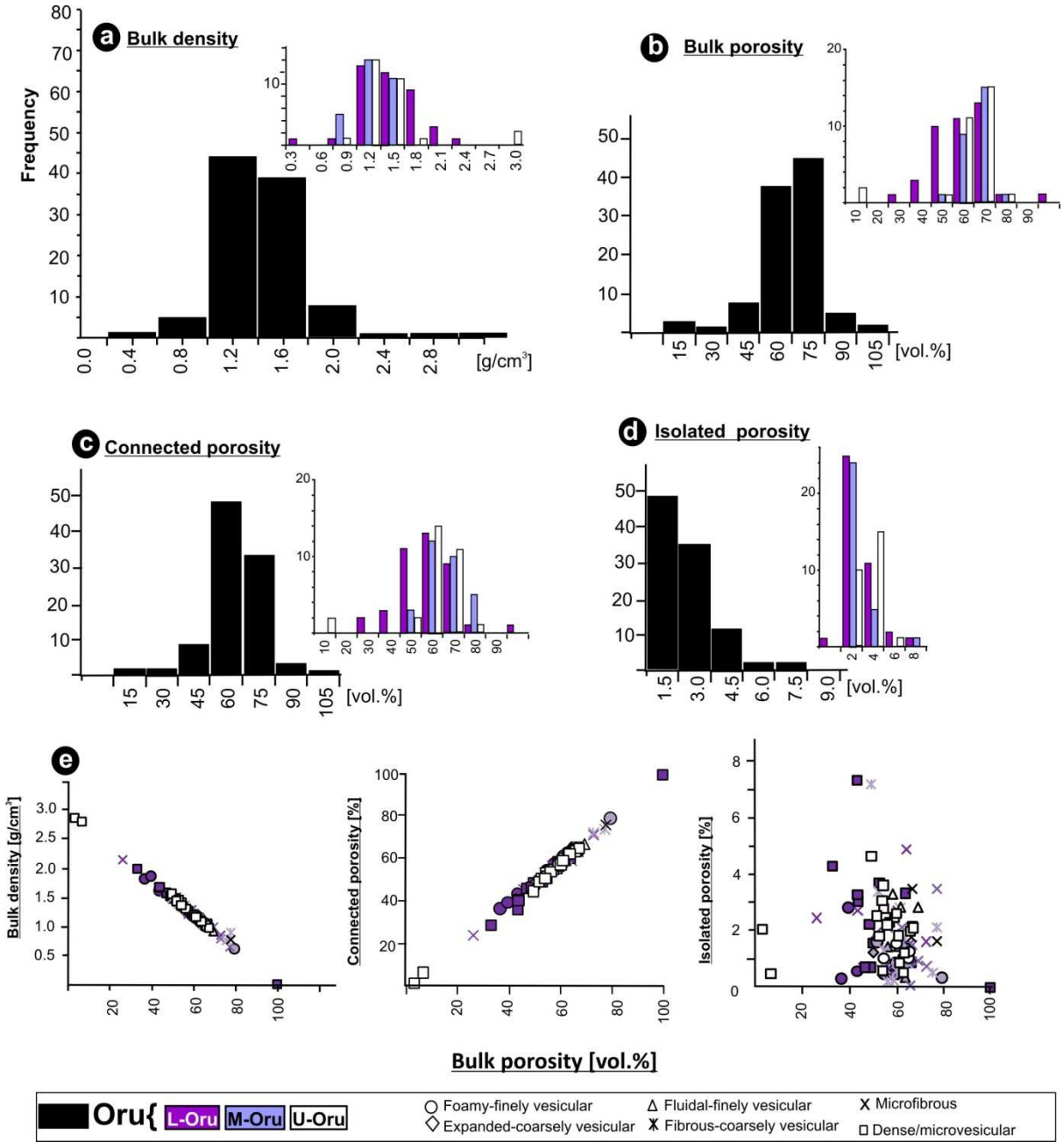

Figure 6.9 Porosity and density frequency distributions within the Oruamatua eruptive unit. The individual parameters were obtained from measurements of: **a)** bulk sample volume and envelop density; **b)** connected + isolated porosities relative to the bulk sample volume; **c)** skeletal density; **d)** solid density determined in crushed samples; **e)** comparative plots of individual parameters against bulk porosity. Black histograms are for all analyses (n = 99), while others show the individual analyses from the different stratigraphic positions.

In general, total vesicularity and mafic crystal content is similar to the dense lapilli of Sw and all samples have small modal vesicle diameters of 8-10 μm. N_v ($2\text{-}5\times10^5$ cm^{-3}) is similar to Sw, decreasing with increasing total vesicularity. N_x are one order of magnitude higher

(vesicle-gree) than N_v ($1\text{-}2\times10^6$ cm^{-3}) an order of magnitude larger than N_v. Differences in VVD, CVVD, VSD, and CVSD shapes between clast types are less obvious than in previous units.

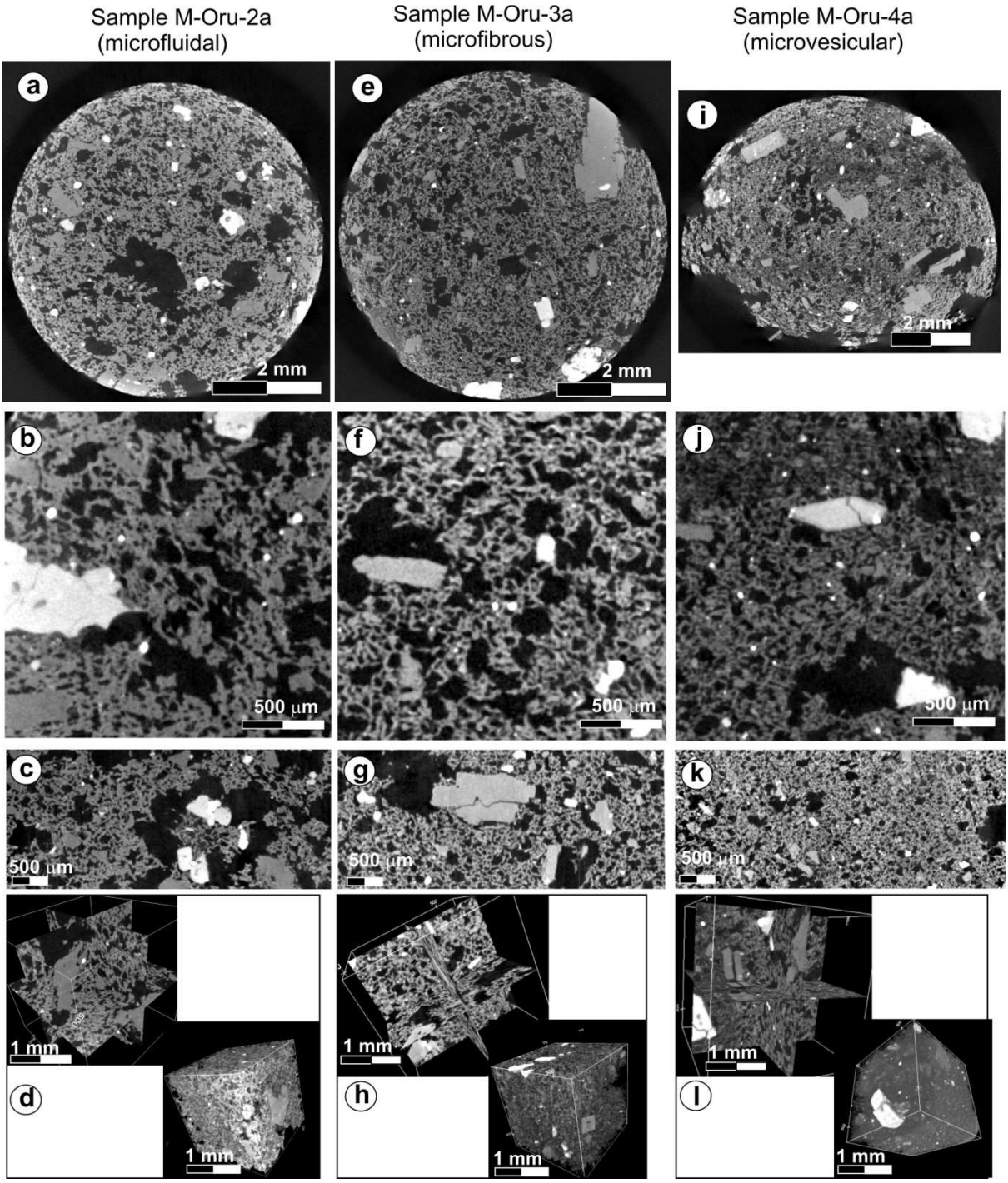

Figure 6.10 Reconstructed X-ray images as orthoslices and rendered subvolumes of three different textures**: a-d)** microvesicular; **e-h)** microfibrous; **i-l)** dense. All samples were scanned with the μCT (1 pixel = 3.5, 3.1, and 4.2 μm respectively).

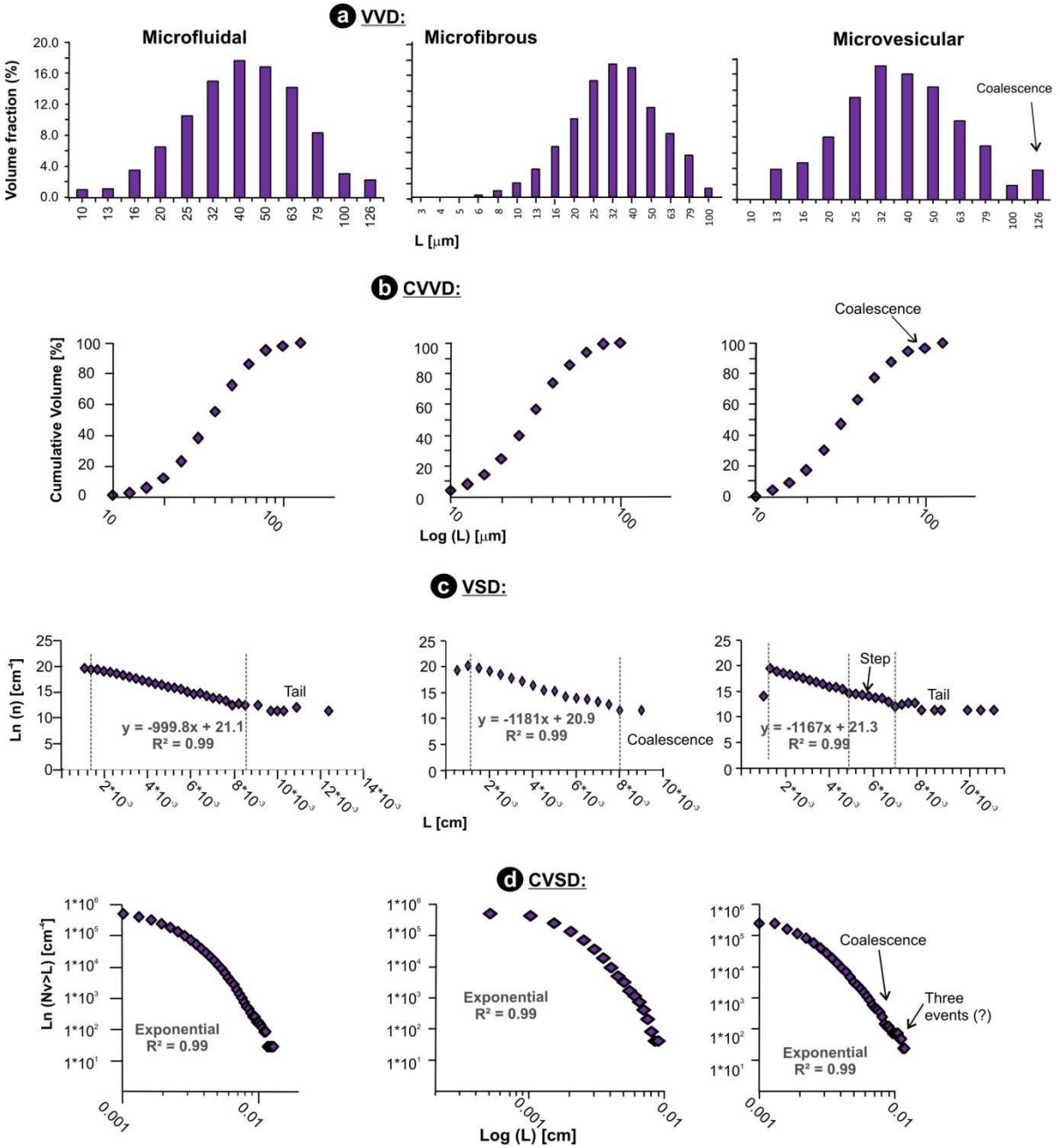

Figure 6.11 3D Quantitative results for: **a)** vesicle volume (VVD), **(b)** cumulative volume (CVVD), **(c)** vesicle size (VSD), and **(d)** cumulative vesicle size (CVSD) distributions obtained from μ-CT.

The main variations arise in the VVD shape; unimodal in the microfluidal clast, skewed in the microfibrous lapilli, and bimodal to polymodal in the microvesicular clast (**Fig. 6.11a, b**). All the VSDs (**Fig. 6.11c**) have a flat tail (>80 μm), and all CVSD (**Fig. 6.11d**) are exponential. Estimated GT values vary from 9 to 10 μm, being lower in the crystal-rich microfibrous clast and consistently higher in the relatively crystal-poor, microfluidal clast (**Table 6.2**). Initial number of nuclei per cm^3 is nearly constant for all samples (21).

Similar to previous units, the mafic crystal size distributions of all samples are very similar, with polymodal CVD, stepped CSD, and power-law CCSD reflecting multiple mafic crystal-size populations with a modal diameter of 11 μm (**Appendix H.3.3**). There is also a separate population of anomalously large phenocrysts (>700 μm in the microfluidal and >350 μm in the microfibrous clast).

Volatile content of melt inclusions: FTIR spectra were obtained in 12 glass inclusions hosted in clino- and- orthopyroxene crystals picked from the M-Oru lapilli bed (**Table 6.5; Appendix I; Fig. 6.12**). Glass compositions using electron microprobe were obtained for 9 different inclusions, varying from 65 to 70 wt.% SiO_2 (normalised), corresponding to glass densities between 2.51 and 2.65 g·cm^{-3}. Only considering the spectra with minimum noise, dissolved total H_2O content calculated from ~3550 cm^{-1} peak ranges between 0.7 and 1.8 wt.%. Molecular H_2O content calculated from the absorption peak at ~1630 cm^{-1} ranges between 0.2 and 0.8 wt.%.

Table 6.5 Summary of microprobe and micro-FTIR analyses on glass inclusions for the Oruamatua eruptive unit. Chemical data are given in wt.%.

Sample	Host	# runs	SiO_2	TiO_2	Al_2O_3	FeO	MnO	MgO	CaO	Na_2O	K2O	P_2O_5	Calc Density [g/cm^3]	H_2O total @ 3550	H_2O mol @ 1630	Observations	Temperature °C (2Px geothermometer)	Liquid density [g/cm^3]	Calc. Saturation P [MPa]	minimum saturation depth [km]	Melt viscosity [Pa*s]
Oruamatua Eruptive Unit																	974				
Residual Melt																		2.7		0	0.7
Oru-2-1	Cpx	2*	70.03	0.69	13.69	3.93	0.00	0.99	2.63	4.03	3.68	0.32	2.52	1.72	0.42	Rounded, cracked		2.7	32	1	0.6
Oru-13-1	Opx	2*	69.02	1.12	13.87	4.26	0.06	1.18	3.14	3.75	3.37	0.23	2.54	1.53	0.80	Subrounded		2.5	26	1	0.6
Oru-13-2	Opx	1*	69.15	0.94	13.05	4.38	0.02	1.47	3.73	3.66	3.36	0.24	2.55	1.38	0.61	Irregular, with oxide		2.5	21	1	0.6
Oru-5	Opx	1	70.42	0.76	13.84	3.55	0.08	0.66	2.69	3.82	3.78	0.40	2.51							0	
Oru-15	Opx	2	66.37	0.81	12.05	5.03	0.14	3.30	5.78	3.44	2.75	0.34	2.58							0	
Oru-16	Opx	1	68.63	0.84	14.60	4.41	0.06	0.80	3.00	3.75	3.76	0.15	2.55							0	
Average		*9*	*68.94*	*0.86*	*13.52*	*4.26*	*0.06*	*1.40*	*3.50*	*3.74*	*3.45*	*0.28*	*2.54*					2.5		0	
Oru-4-1	Cpx	1*												0.95	0.24	Irregular shaped, thin, external			10	0	
Oru-4-2	Cpx	1*												1.69	0.70	Elongated inner			31	1	
Oru-5b-3	Opx	1*												0.66	0.23	Small, rounded			5	0	
Oru-17	Cpx	1*												**1.84**	0.58	Small, rounded			36	**1**	

The data show a decrease in volatile content with lower silica-content in glass (**Table 6.5**) and inclusions are more mafic in the interior relative to the crystal rim (**Appendix I**). These results are consistent with concentration of volatiles in the residual glass as crystallization proceeds during magma evolution (c.f., Signorelli et al., 1999; Blundy and Cashman 2001; Frezzotti 2001). The minimum value of total H_2O in the magma were pyroxenes crystallized is 1.8 wt.%.

With similar glass composition, inner-crystal inclusions have higher volatile contents than those near the rim, which could indicate degassing or variation due to analytical limitations of small-sized inclusions.

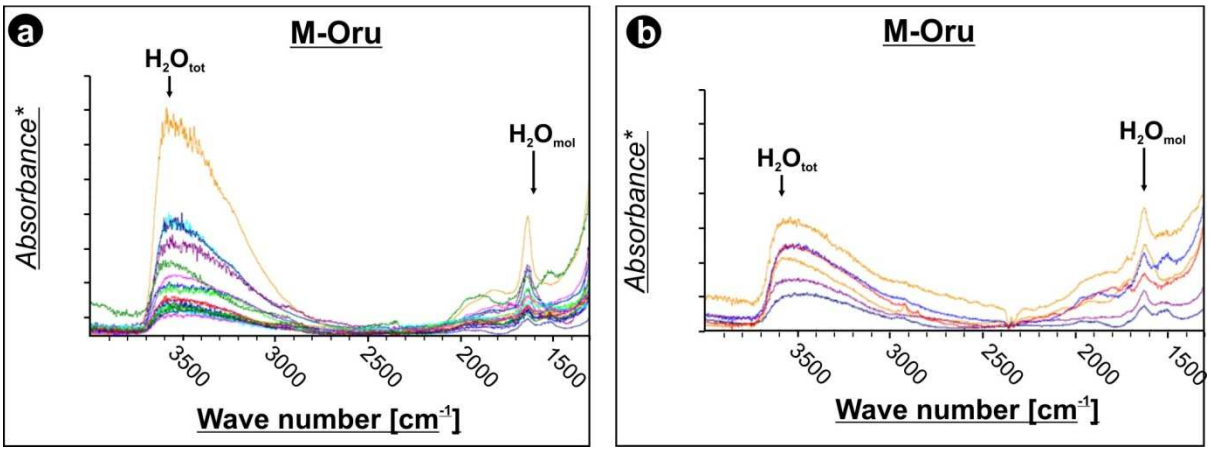

Figure 6.12 Mid-Infrared spectra obtained in glass inclusions hosted in Cpx and Opx within Mid-Oruamatua eruptive unit: **a)** total spectra showing the main peaks of total and molecular water **b)** filtered data showing those were "noise" was less present. Y-axis corresponds to absorbance (*), not to scale (See appendix A for absorbance values of individual measurement).

Interpretation: contrary to previous units and based on groundmass chemical data (**Chapter 5.2.3**), measured volatile content in the Oruamatua unit likely corresponds to the original minimum, pre-eruptive conditions (1.8 wt.% of total H_2O). Alternatively, if groundmass glass high silica content is only due to the higher microlite content relative to older units, differences in melt composition relative to Mgt and Sw may be only due to shallow conduit crystallization. Based on thermodynamic models and experimental data of H_2O solubilities in rhyolitic melts presented by Holloway and Blank (1994), Wallace and Anderson (2000), and following Newman and Lowenstern (2002), Oru inclusions appear to be degassed or indicate a minimum pre-eruptive storage depth of 1 km (**Table 6.5**).

More evolved melt chemistry (**Chapter 5.3.3**) and larger crystal content relative to Mgt and Sw suggest Oru magma was relatively more degassed, where vesicle growth and shape were highly affected by neighbouring vesicles and crystals. The high microlite content, distorted vesicle shapes and thick vesicle walls suggest significant degassing before fragmentation. All data is consistent with a single stage of nucleation and growth for the microfluidal and microfibrous samples, and at least two nucleation stages for the microvesicular clast (best represented in the individual sub-volumes; **Appendix H.3.3**). Coalescence is responsible for broad modes in VVD, the inflection of the CVVD (particularly in the dense clast), and the

flat tail of the VSD curves. Vesicle collapse inferred from qualitative observations is represented by stepped curves in the CVSD of microfibrous and microvesicular clasts (**Fig. 6.11d**), suggesting advanced permeability (c.f., Klug et al., 2002). Within the M-Oru, the main difference between textures was due to heterogeneous bubble growth mechanisms.

The Oru magma was more complex than that of the Sw unit, due to more effectively packed gas-pockets within highly elongated vesicles. Shearing of vesicles could cause segregation of portions of different ascent rates, especially towards the conduit walls. Similar processes have been documented for other volcanoes by Rust and Manga (2002), Rosi et al. (2004), Sable et al. (2006), and Wright and Weinberg (2009). Anisotropic vesicle shapes suggest lower percolation thresholds than previous units (i.e. minimum vesicularity at which a connected pathway develops; Klug et al., 2002; Rust and Cashman 2011). Also, a "wormy" network (c.f., Mangan and Sisson 2000) of pore-spaces suggests slower decompression rates and/or bubble collapse relative to previous eruptions. The observations of glass chemistry and H_2O contents indicate very complex, probably polybaric crystallization, either with or without decompression, and microlites forming during syn-eruptive degassing. This is supported by the polymodal CSD and CCSD (**Appendix H3.3**) indicating multiple crystal nucleation and growth events.

The Oru textures suggest that shear strain rates larger than relaxation rates favoured the fragmentation of the partially-degassed magma (with the lowest porosity of all studied units; **Table 6.1**). An analogous model has been experimentally and numerically described by Dingwell (1996), Deubener et al. (2003), and Whittington et al. (2009). A very late decompression wave and vesiculation is also indicated, allowing time for melt migration into cracks within crystals, followed by expansion shortly before quenching.

6.2.4 The Okupata tephras pumice textures

Density and porosity: the macrotextural observations exposed in **Chapter 5.4** for the Lower (L-Okp) and Upper (U-Okp) Okupata tephras are corroborated by Gas-pycnometry data (**Appendix G; Table 6.1; Fig.6.13**). For these fall deposits, higher bulk densities (**Fig. 6.13a**) occurred in the basal deposit (1.15 $g \cdot cm^{-3}$) than the uppermost deposit (0.92 $g \cdot cm^{-3}$), reflecting higher bulk (**Fig. 6.13b**), connected (**Fig. 6.13c**), and isolated (**Fig. 6.13d**)

porosities in the latter. Density and porosity distributions are asymmetric with bulk density and isolated porosity being negatively skewed, while bulk and connected porosities are positively skewed (**Fig. 6.13e**).

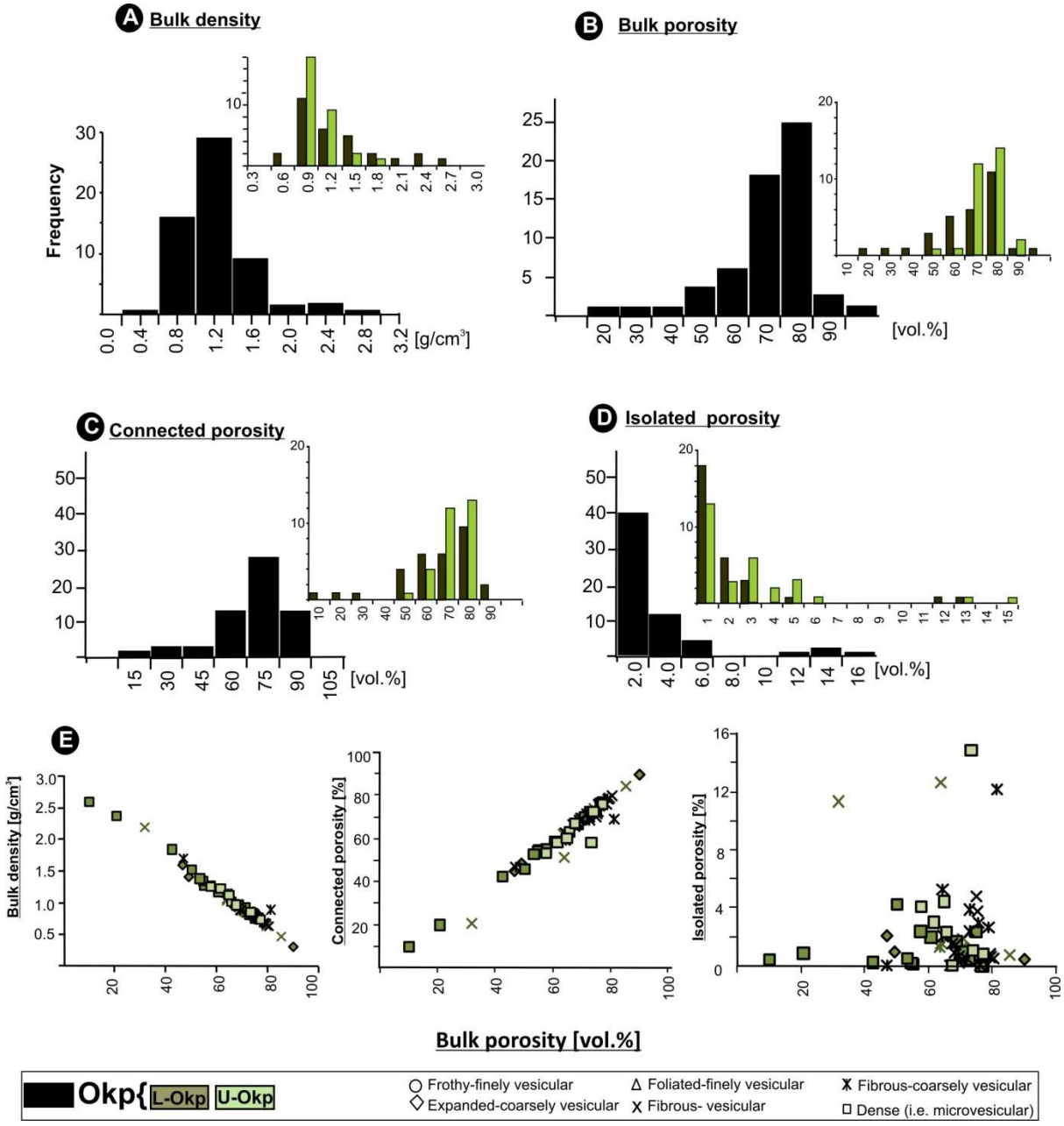

Figure 6.13 Porosity and density frequency distributions within the Okupata-Pourahu eruptive unit. The individual parameters were obtained from measurements of: **a)** bulk sample volume and envelop density; **b)** Connected + Isolated porosities relative to the bulk sample volume; **c)** skeletal density **d)** solid density determined in crushed samples; **e)** comparative plots of individual parameters against bulk porosity. Black histograms are for the total sample (n=60) and colour-coded distributions are for Lower (L-Okp) and Upper (U-Okp) subunits.

In general, all the parameters show narrow peaks, except the connected porosity, which is wider and polymodal in the L-Okp tephra, and positively skewed in the U-Okp tephra (**Fig. 6.13c**). The isolated porosity of L-Okp tephra is bimodal, which is also seen in plots of isolated vs. bulk porosity (**Fig. 6.13d, e**).

3D-Textures: due to the heterogeneity of textures within this unit, five samples were analysed: **a) microvesicular**-to-dense texture within the L-Okp (sample Ph-16a-5a) with 53 % vesicles, 4 % mafic crystals, and a microlitic matrix (**Fig. 6.14a-d; Appendices H.3.4, H4.4a**); **b)** two lapilli (samples B53-Ph161c-6a and B50Ph16b-3a) represent the U-Okp **dense**, coarsely porphyritic texture, with total vesicularity of 32 and 61 % and total mafic crystallinity of 17 and 19 %, respectively (**Fig. 6.14e-h; Appendices H.3.4, H4.4b**); and **c)** two samples (B50-Ph2-16b-1 and B50Ph-2-1d) of typical fibrous-to-**microfibrous,** coarsely **porphyritic** textures within the U-Okp, which are characterized by 10 to 50 μm ellipsoidal to highly sheared and distorted vesicles of different lengths (**Fig. 6.14i-n; Appendices H.3.4, H4.4c**).

Total vesicularity varies from 41 to 43 %, and total mafic crystallinity from 11 to 16 %. Larger vesicles are irregular and formed by coalescence of smaller vesicles: pore apertures vary from ~14 μm to 60 μm in width. In general, all samples are characterized by highly distorted and sharp vesicle outlines, with concave wall segments and V-shaped terminations (**Fig. 6.14c, f, m**). Vesicle walls vary from straight to highly wrinkled (**Fig. 6.14k, m**)**,** and are the thinnest of all the textural types found within the Bullot Formation (**Fig. 5.25**). Glass fibres are common into crystal cracks (**Fig. 6.14l; Appendix H4.4c**). Both microfibrous and dense end-members of the U-Okp deposit are coarsely porphyritic with crystals between 280-1000 μm. Mineral phases are the same as in previous units.

Five analysed samples each show an internal heterogeneity (**Appendix H.3.4; Table 6.2; Fig. 6.15**) with individual subvolumes showing different VVD's and VSD's. For this case, merging all data masks the internal textural domains. However, it is possible to recognize regions with common characteristics (**Fig. 6.15**), corroborated by digitally coring one of the samples into 20 different subvolumes (L-Okp sample; **Appendix H.3.4**). Individual and merged subvolumes show polymodal CSD's, stepped CCVD's, and power-law CCSD's (**Appendix H.3.4**).

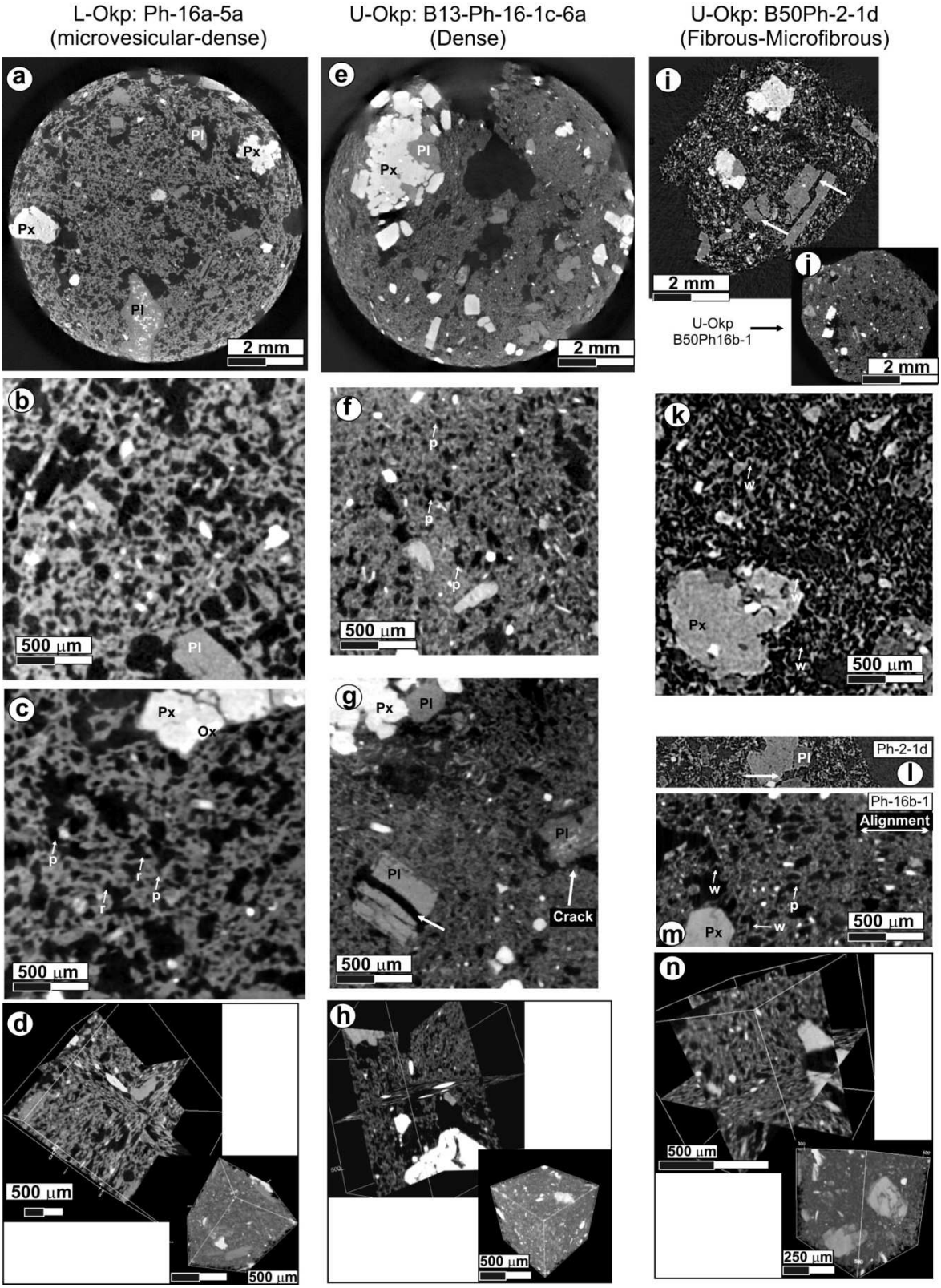

Figure 6.14 Reconstructed X-ray images of**: a-d)** microvesicular-dense clasts within the L-Okp (μCT scan 1 pixel = 4.2 μm); **e-h)** dense, coarsely porphyritic clasts within the U-Okp (μCT scan 1 pixel = 4.0 μm). Note the typical micro-jig-saw structures in crystals (arrow in **g**) and irregular voids with sharp edges surrounding feldspars (**g**). **i-n)** Microfibrous (**d**): synchrotron: 1 pixel = 1.8 μm; e: μCT scan: 1 pixel = 2.0 μm), coarsely porphyritic textures within the U-Okp, where vesicles have thin walls, commonly wrinkled (w); note the thin glass films crossing cracked feldspars (**l**) and the alignment of small vesicles and microcrysts (**m**); typically, all textures show highly distorted vesicles, many refolded (r) and with pinched terminations (p).

VSD's of both dense samples (B50Ph16b-3a and B13Ph161c-6a) studied for the U-Okp are exponential, with flat tails (**Fig. 6.15c**) and the CVSD show steps offsetting the curve from a perfect exponential-to-power-law trend (**Fig. 6.15d**). CVVD are distinctive, with a concave-up inflection (**Fig. 6.15b**). The microfibrous samples (B50-Ph16b-1 and Ph2-1d-5x) show a distinctive polymodal VVD (**Fig. 6.15a**), stepped CVVD (**Fig. 6.15b**), VSD (**Fig. 6.15c**), and concave-down (bi-partite) exponential CVSD (**Fig. 6.15d**) for individual and merged subvolumes (**Appendix H.3.4**). All samples from the U-Okp show two or more distinct populations within the CVD, with an anomalously large peak at equivalent diameters >790 μm, and some subvolumes show power-law CCSD (**Appendix H.3.4**).

From all data, the total vesicularity varies over a wide range (32-61 %), and mafic crystal content can reach the highest values seen (59% in the merged volume; **Appendix H.3.5**). N_v also shows the largest variation of the studied units, 10^4-10^6 cm^{-3}, whereas N_x remains within the 10^5-10^6 cm^{-3} range (**Table 6.2**). N_v reaches the highest values in the microfibrous clasts (10^6 cm^{-3}). Differences in textures correspond to different VVD: **a)** flattened, broad to bimodal for dense lapilli in the L-Okp; **b)** skewed and bimodal for the dense lapilli in the U-Okp, with one population locally flattened and a second peak of large vesicles; and **c)** polymodal for the microfibrous clasts of the U-Okp (**Fig. 6.15a**). This is also reflected in the CVVD, where small inflections are common in the dense clasts and multiple steps, or comparatively low slopes occur in the microfibrous clasts (**Fig. 6.15b**).

All samples have VSD highly offset from linear trends, with flat tails in the dense clasts, and inflections towards steeper slopes at large size classes for the microfibrous type. The main offsets from linearity occur for vesicles >100 μm (**Fig. 6.15c**). CVSDs are stepped, deviating from typically smooth curves. Merged subvolumes indicate a predominant power-law CVSD for the L-Okp sample, and exponential CVSD for the U-Okp samples. All CVSD have steeper slopes at higher vesicle sizes (**fig 6.15d**). Estimated GT is 6-18 μm, and the estimated initial number of nuclei per cm^3 varies from 18 to 21 in the dense clasts and from 22 to 24 in the microfibrous clasts (**Table 6.2**). For mafic crystals, all samples have polymodal CVD and power-law CCSD, with a distinctive population of anomalously large crystals with modal diameters of 119 μm (**Appendix H.3.4**).

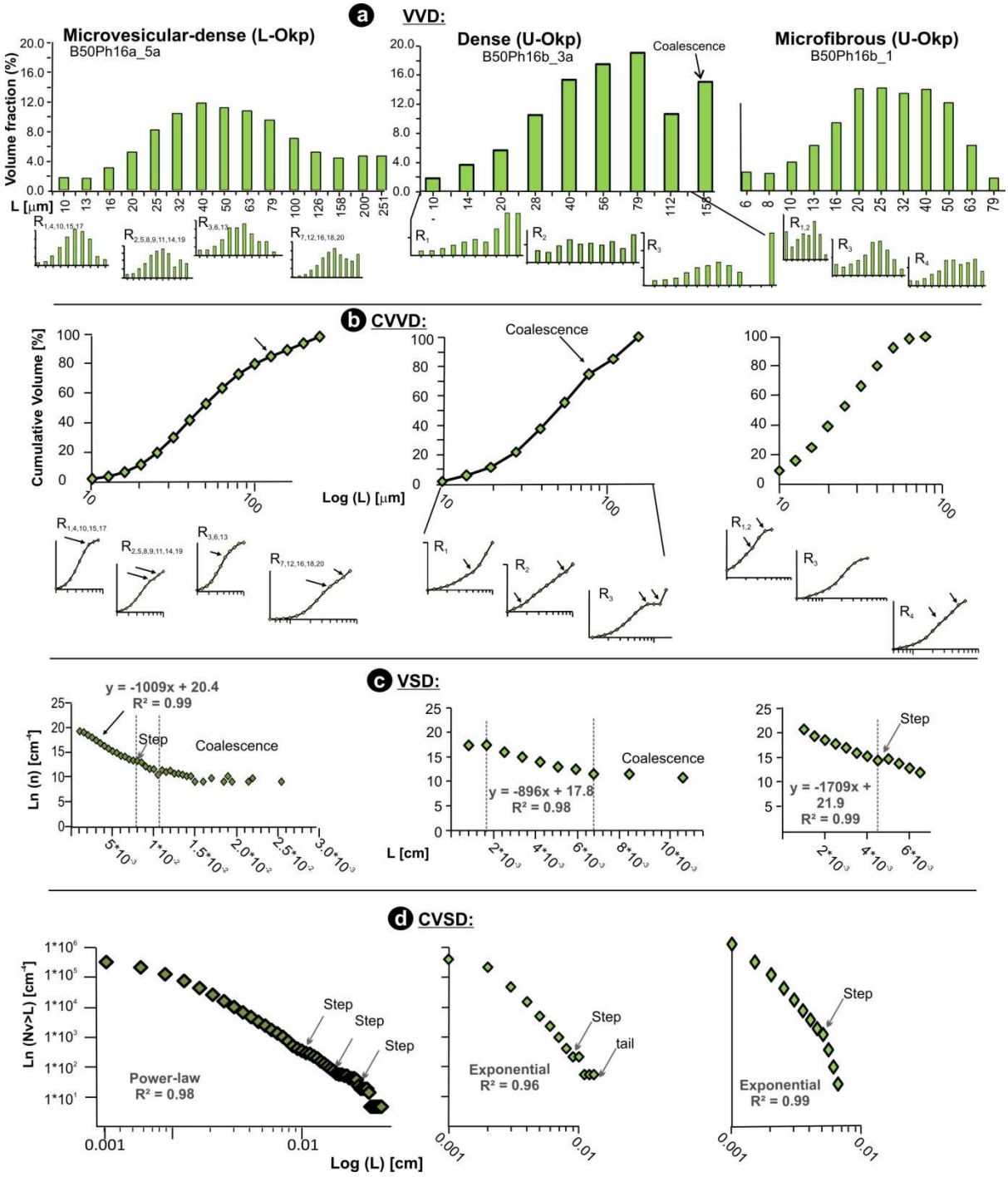

Figure 6.15 3D analysis results for: **a)** vesicle volume (VVD), **(b)** cumulative volume (CVVD), **(c)** vesicle size (VSD), and **(d)** cumulative vesicle size (CVSD) distributions obtained from Okupata Tephra samples. Note the high textural heterogeneity within any single clast. Arrows mark steps in the CVVD curves, above which coalescence occurs. Steps pointed with arrows in VSD and VSD mark more than one nucleation event.

Volatile content obtained from melt inclusions: FTIR spectra were obtained in 14 glass inclusions hosted in clino-and-orthopyroxene crystals of the L-Okp tephra (**Table 6.6; Appendix I; Fig. 6.16**). Glass compositions analysed by electron microprobe were obtained

in 15 different inclusions from the L-Okp tephra, varying from 67 to 72 wt.% SiO_2 (normalised); corresponding glass densities vary between 2.40 and 2.56 g·cm^{-3}. Microprobe analyses could not be completed in all the same inclusions where FTIR spectroscopy was carried out. Glass electron microprobe compositions are more mafic toward the core of the crystals. Assuming a mean silica concentration of 79 wt.% (normalised) and only considering the spectra of minimum noise (**Table 6.6; figure 6.16a**), dissolved total H_2O content calculated from the absorption peak at ~3550 cm^{-1} of 14 inclusions ranges between 1.4 and 5.4 wt.%. Molecular H_2O content calculated from the absorption peak at ~1630 cm^{-1} ranges between 0.5 and 1.9 wt.%.

Table 6.6 Summary of microprobe and micro-FTIR analyses on glass inclusions for the Okupata Tephra. Chemical data are given in wt.%; H_2O contents measured at 3550 and 1630 cm^{-1} are given in wt.%.

Sample	Host	# runs	SiO_2	TiO_2	Al_2O_3	FeO	MnO	MgO	CaO	Na_2O	K2O	P_2O_5	Calc Density [g/cm^3]	H_2O total @ 3550	H_2O mol @ 1630	Observations	Temperature ^{0}C (2Px geothermometer)	Liquid density [g/cm^3]	Calc. Saturation P [MPa]	Minimum saturation depth [km]	Melt viscosity [Pa*s]
Lower-Okupata Tephra																	977				
Residual Melt																		2.7			0.7
L-Okp-2	Opx	1	71.37	0.50	14.48	2.88	0.00	0.49	2.70	4.02	3.56	0.01	2.50								
L-Okp-3	Opx	2	71.58	0.63	13.97	3.10	0.08	0.56	2.53	3.69	3.79	0.08	2.50								
L-Okp-4	Opx	7	71.84	0.49	13.83	3.07	0.03	0.58	2.11	3.78	4.15	0.11	2.49								
L-Okp-5	Opx	2	67.68	0.83	16.04	3.26	0.01	0.97	3.42	3.98	3.52	0.30	2.53								
L-Okp-7	Opx	2	68.06	0.76	14.51	4.37	0.10	1.05	3.54	3.92	3.24	0.45	2.55								
L-Okp-8	Opx	1	80.60	0.12	9.30	2.42	0.00	0.17	0.85	2.91	3.62	0.02	2.40								
Avergage		*15*	*71.86*	*0.56*	*13.69*	*3.18*	*0.04*	*0.64*	*2.53*	*3.72*	*3.65*	*0.16*	*2.49*					2.4			0.7
Okp-1-2b-1	Opx	1*												3.23	1.15	Irregular, angular			88	3	
Okp-1-2b-2	Opx	2*												2.94	1.62	Irregular, angular, small			75	3	
Okp-1-4b-3	Opx	1*												2.89	0.76	Rounded			73	3	
Okp-1-4b-4	Opx	1*												3.06	1.33	Rounded			80	3	
Okp-1-5a-1	Opx	1*												3.77	1.76	Irregular			113	4	
Okp-1-10a-1	Opx	1*												3.58	1.33	Rounded			104	4	
Okp-1-10a-2	Opx	1*												2.62	0.81	Rounded			62	2	
Okp-1-10a-3	Opx	1*												3.76	1.08	Rounded			113	4	
Okp-1-10a-4	Opx	1*												3.12	1.22	Leaking			83	3	
Okp-1-10a-5	Opx	1*												**5.44**	**1.90**	Rounded			**199**	**7**	
Okp-1-9a-1	Opx	1*												1.57	0.65	Irregular, thick			25	1	
Okp-1-9a-2	Opx	1*												2.26	1.07	Elongated			67	2	
Okp-1-9a-3	Opx	1*												1.39	0.52	Elongated, irregular			20	1	
L-Okp-1	Opx	1*												3.60	1.00				105	4	
Upper-Okupata Tephra																					
Residual Melt																		2.7			0.6
U-Okp-3a-1	Opx	1*	71.50	0.53	14.31	2.91	0.16	0.53	2.64	3.72	3.55	0.15	2.49	3.48	1.16	Rounded		2.4	99	4	0.7
U-Okp-1		4	72.35	0.65	13.54	2.56	0.04	0.57	2.14	4.08	3.91	0.17	2.48								
U-Okp-2		3	71.59	0.71	13.65	2.91	0.04	1.11	2.09	3.78	4.02	0.10	2.50								
U-Okp-5		1	71.51	0.65	14.38	2.79	0.01	0.52	2.08	3.62	4.33	0.12	2.49								
U-Okp-8		2	68.80	0.40	15.95	2.12	0.04	1.25	2.96	4.42	3.89	0.18	2.51								
Avergage		*11*	*71.15*	*0.59*	*14.37*	*2.66*	*0.06*	*0.80*	*2.38*	*3.92*	*3.94*	*0.14*	*2.49*					2.4			0.7
U-Okp-3a-2	Opx	1*												**5.07**	**1.51**	Elongated			179	**7**	
U-Okp-5a-1	Opx	1*												2.81	1.28	Irregular			70	3	
U-Okp-6a-1	Opx	1*												1.53	0.92	Elongated			24	1	
U-Okp-6a2	Opx	1*												4.84	1.57	Small, rounded			167	6	
U-Okp-10a-1	Opx	1*												1.20	0.45	Small, rounded			15	1	
U-Okp-10a-2	Opx	1*												1.15	0.53				14	1	

Together with the fact that pyroxenes are commonly zoned, this might suggest polybaric crystallisation. Thus, the minimum H_2O content in the magma producing the pyroxenes crystallized was 5.4 wt.%.

FTIR spectra were recurrently noisy for the U-Okp and hence, estimated volatile contents are not precise. The only inclusion which could be both probed and analysed with FTIR is rhyolitic and contains 3 wt.% of total H_2O (**Fig. 6.16b**).

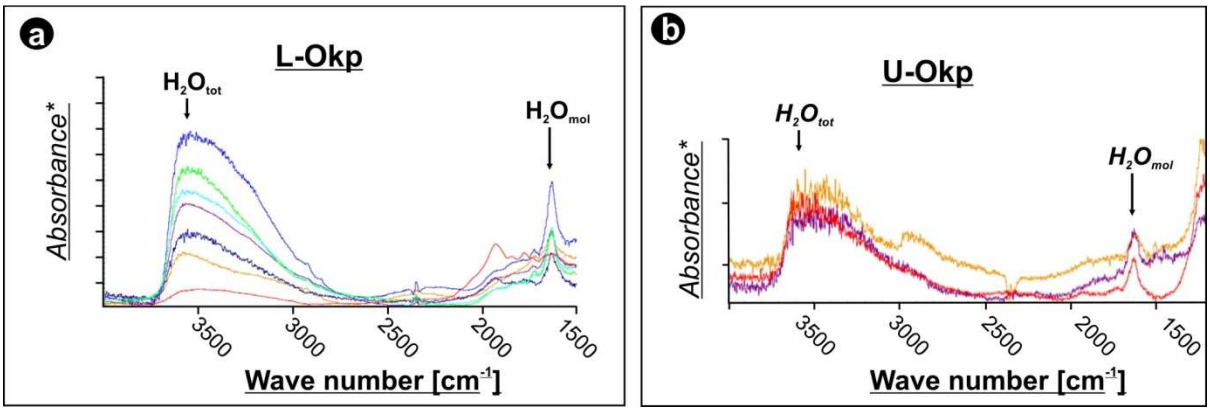

Figure 6.16 Mid-Infrared spectra obtained by microscopic FTIR in glass inclusions hosted in Cpx and Opx within the Okupata-Pourahu eruptive unit: **a)** total spectra showing the main peaks of total and molecular water; **b)** in the U-Okp tephra measurements did not produce clean spectra and calculated volatile contents shown in Table 6.6 represent rough estimations. Y-axis corresponds to absorbance (*), not to scale (See appendix A for values of individual measurement).

Interpretation: glass compositions within this unit (**Chapter 5.2.4**) indicate inclusions remained in contact with the decompressing melt until shortly prior to the eruption (c.f., Stewart and Pearce 2004; Signorelli et al., 1999). The measured 5.4 wt.% of total H_2O is here considered to represent the minimum pre-eruptive volatile content. Based on thermodynamic models and experimental data of H_2O solubilities in rhyolitic melt inclusions (Holloway and Blank 1994; Wallace and Anderson 2000; Newman and Lowenstern 2002), a minimum saturation pressure of ~2 kbar (7 km depth) is estimated (**Table 6.6**). Although initial, minimum pre-eruptive volatile content was high, pyroclasts were strongly degassed at the moment of fragmentation. Wrinkled thin vesicle walls indicate non-brittle rupture and permeability developed prior to quenching.

Individual and merged subvolumes of the L-Okp dense sample, at least two stages of bubble nucleation can be inferred, and the original distribution is interpreted to be modified by growth processes (i.e., coalescence and collapse; **Appendix H.3.4**). Coalescence is also indicated by the secondary peaks in the VVD, local inflections in the CVVD, flat to concave-up tails in the VSD, as well as the stepped VSD and CVSD (**Fig.6.15**). Bubble collapse as observed in thin sections is seen by flattened VVD when individual subvolumes are merged

(**Fig. 6.15a**). On the other hand, CVD and CSD indicate two to three stages of crystal nucleation and growth.

The U-Okp dense clasts are similar, indicating two stages of nucleation largely affected by coalescence and collapse. Individual subvolumes within each clast reflect textural heterogeneity, with local flattened and polymodal VVD's and inflections of the CVVD's, confirming bubble coalescence and collapse (**Appendix H.3.4**). For crystals, CVD and CCVD are consistent with a continuous nucleation and growth process, but anomalously populations of very large crystals occur (>500 μm to >790 μm; **Appendix H.3.4**). Microfibrous textures are dominant within the U-Okp, suggesting considerable strain before fragmentation (c.f., Rust and Cashman 2011). Two stages of nucleation modified by growth are indicated by polymodal VVD, bipartite VSD and CVSD with steeper slopes at larger class sizes (**Fig. 6.15d**). Some subvolumes also suggest advanced permeability driving bubble collapse as indicated by local flattened VVD (**Appendix H.3.4**; c.f., Klug et al., 2002; Shea et al., 2010).

The highly heterogeneous textures (also comprising the banded textures not analysed in 3D; **Fig. 5.25i-j**), show advanced deformation of vesicles, development of a "wormy" network, and high crystal contents. These features suggest high strain rates on a crystal-rich, relatively degassed magma compared to previous units, which had complex rheology at the fragmentation level (**Appendix F.2**). Vesicle shearing could have enhanced coalescence at low vesicularities, reducing the percolation threshold and increasing permeability (c.f., Okumura et al., 2006; Rust and Cashman 2004; Rust and Cashman 2011).

Together with the highest crystal and microlite content seen, this unit also has highly evolved groundmass glass compositions (**Chapter 5.2.4**), and high N_v. These observations imply a very slow ascent rate compared to Mgt and Sw eruptives. In addition, the higher crystal content and size at similar N_x relative to previous units indicates that crystal growth on pre-existing free crystals dominated over crystal nucleation. In some volumes (**Appendix H.3.4**) of the densest clasts, mafic crystallinity reached 59 %, which is already in the "rigid" regime of crystal-crystal interaction observed in domes by Dingwell (1998), similar to a conduit plug.

The data presented above indicate that the complex rheology of the Okp magma was mainly due to intense crystallisation and development of permeable, deformable vesicle networks across the conduit.

6.3 Microlite crystallization inferred from glass compositional trends

In the difficulty of thresholding feldspars and separate them from groundmass glass in 2D BSE images and 3D microtomography images, the groundmass glass compositions were plotted in Harker diagrams as an indirect way of visualizing the extent of microlite crystallization and study its variation from unit to unit. A trend of decreasing MgO, CaO and Al_2O_3 with increasing silica content (**Fig. 6.17a-c**), and a positive correlation between silica and K_2O (**Fig. 6.17d**) reflect plagioclase microlite crystallization. Considering the similar bulk-rock composition and phenocryst content of all studied units, a trend from older, microlite-poor units (Mgt), to younger, microlite-rich units (Oru and Okp) is suggested. When plotting groundmass glass compositions in the Qz-Ab-Or (Cashman and Blundy 2000; Martel and Schmidt 2003) ternary diagram (**Fig. 6.17e**), there is a trend from the eldest unit close to the Ab apex to the youngest units displaced towards the cotectic. Although the ternary diagram cannot be used to estimate closure pressures (c.f., Blundy and Cashman 2001; Hammer and Rutherford 2002; Cashman and McConnell 2005), because of the absence of modal quartz, the visualized trend also suggest increasing Pl crystallization with time. These observations indicate that the youngest magmas were subject to stalling at shallow levels in the conduit prior to eruption, possibly evolving into a progressively more open system.

Finally, variable concentrations of H_2O identified within each eruptive unit and within a single crystal as observed in Mt. Ruapehu samples, has been taken as evidence for magma mixing (e.g., Hervig and Dunbar 1992), crystal settling (e.g., Anderson et al., 2000), and degassing-induced crystallization (e.g., Sisson and Layne 1993), all to be considered for Ruapehu case.

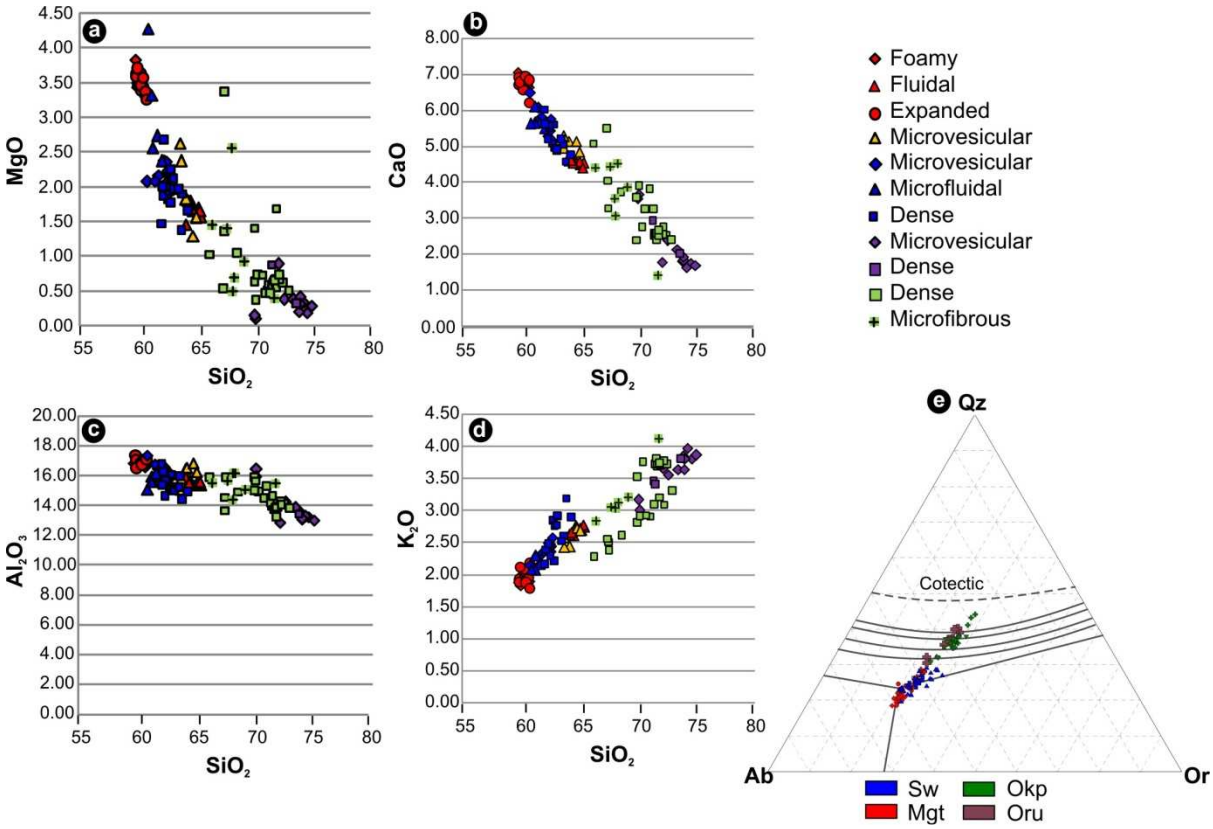

Figure 6.17 Glass composition in the selected eruptive units from Mt. Ruapehu projected in Harker diagrams (a-d) and in the Qz-Ab-Or ternary diagram (e) modified from Tuttle and Bowen (1958; in Cashman and Blundy 2000). Plots of individual units show a decreasing trend of MgO, CaO and Al_2O_3 with silica content and with stratigraphic position, whereas K_2O is positively correlated with silica. In (e), the variation with stratigraphic position is also represented in a trend away from Ab towards the cotectic. Data indicate progressively more crystallization of plagioclase microlites in youngest units related to the same eruption vent (i.e., from Mgt to Oru).

6.4 Discussion

6.4.1 Bubble nucleation mechanisms

X-ray microtomography results reported above gave N_x of ~10^5-10^6 cm^{-3}, which were similar or an order of magnitude higher than the corresponding N_v. This suggests that crystals acted as effective nucleation sites for bubbles and heterogeneous bubble nucleation occurred at low supersaturation pressures. This contrast to the homogeneous nucleation commonly reported in the literature for Plinian eruptions and indicates that bubble nucleation mechanism alone does not control the resulting eruptive style.

Although comparison between 2D and 3D methods are problematic (e.g., Shea et al., 2010; Giachetti et al., 2011), andesitic lapilli of Mt. Ruapehu have expected N_v and total vesicularity values intermediate between published data for rhyolitic-dacitic Plinian pumice and basaltic Strombolian lapilli (**Fig. 6.18**). Results obtained in this study are very similar to experimental data from rhyolites for both homogeneous and heterogeneous nucleation by Hurwitz and Navon (1994), Mangan and Sisson (2000), Burgisser and Gardner (2007), Cichy et al. (2010), and Hamada et al. (2010). Data plotted in this diagram are not referenced to the melt, since a complete dataset of crystallinity in the literature is not always available. These comparisons indicate that textural variability depends on glass composition(s) and textural maturity (**Fig. 6.18**).

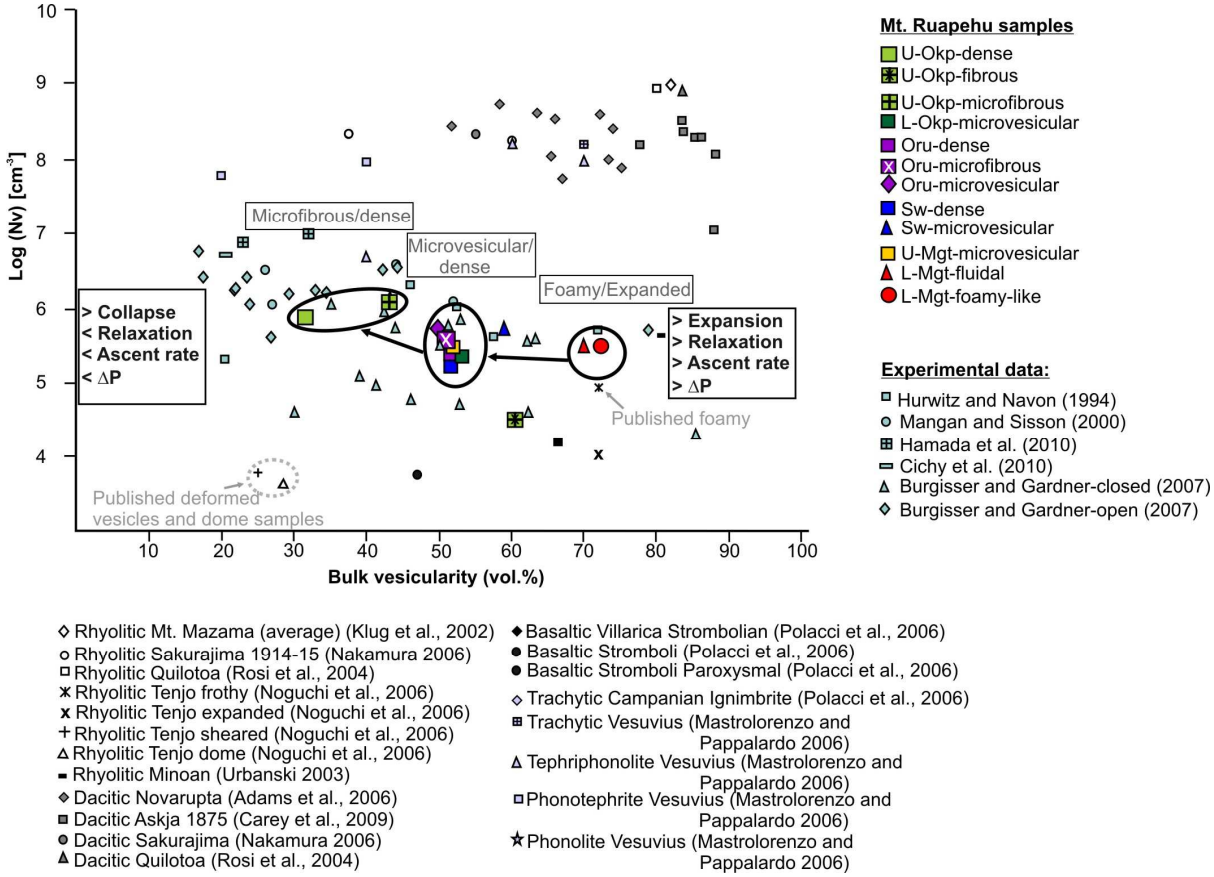

Figure 6.18 Comparison between studied Mt. Ruapehu samples and published data obtained both in natural samples and experimental samples. Textural variability seems to correspond to different glass composition and textural maturity: higher N_v are reached at higher SiO_2 content, whereas total vesicularity at similar N_v depend on textural maturity from initial conditions of free bubble expansion and growth, to intermediate conditions of restricted growth due to high crystallinity, and final conditions of extensive vesicle distortion and collapse.

Moreover, the plots shows two trends: (1) a trend for most of the rhyolitic and undersaturated pumice clasts where Nv are high and not affected by vesicularity, and (2), a trend for more mafic clasts where Bv decreases with increasing vesicularity. This second trend is expected for these mafic compositions where bubble expansion and coalescence occurs in correlation with increasing porosity. However, a detailed compilation of crystallinity in order to produce the same plots referenced to the melt would help to elucidate if (2) is a real trend or if it reflects the effect of not referencing Nv to the melt (c.f., Klug et al., 2002; Rust and Cashman, 2011).

Crystal volume distribution (CVD) and crystal size distributions (CSD) indicate multiple stages of mafic crystal nucleation and growth in all units. In conjunction with glass inclusion data, these patterns are explained as resulting from multiple magma storage levels (c.f., Cashman and McConnell 2005). Two different situations are considered:

1) Comprising Mgt and Sw magmas, where analyses indicate that crystallization of Px phenocrysts occurred in equilibrium with a rhyolitic melt in a pre-existent storage system and were later incorporated by the erupting, more mafic magmas.

2) In the case of the youngest Oru and Okp units, polybaric crystallization occurred during magma ascent. For these units, glass composition indicates shallow arrest prior to the eruption.

In both cases, the variation in N_x was strongly linked to the vesicle growth processes, interconnectivity, and record different degassing paths across the conduit.

6.4.2 Degassing processes in contrasting Plinian eruptions

Textural and glass compositional data of this study indicate progressively more viscous conditions in the younger Plinian deposits relative to older units of Mt. Ruapehu.

Nucleation rates could not be calculated directly from the obtained data as an eruption time is not available. However, estimated GT reaches average values >25 μm in the oldest Mgt and Sw units, and is <15 μm in the youngest Oru and Okp units (**Table 6.2**). In correlation with the observed pumice textures, GT values suggest that growth rates were higher in the oldest units and nucleation rates were more significant in the younger events.

Vesicle shapes and degree of coalescence give insights into the relative time scales of vesicle retraction (relaxation time) and solidification, which are directly linked with melt viscosity (Whittington et al., 2009). From Mgt to Okp, there is a general increase in N_v, crystal size, microlite content, deformation of vesicles, extension of coalescence and bubble collapse, and groundmass glass silica concentration, all consistent with advance degassing and slower decompression rates in the youngest events.

The microlite-poor L-Mgt lapilli indicate heterogeneous degassing and vesiculation, with magma regions rising at different rates in sheath or dyke-like structures within the conduit. During U-Mgt more homogeneous degassing conditions were reached, probably favoured by progressively slower decompression rates, extensive degassing and crystallisation, densification of the erupting magma, and reduction of the conduit diameter. Similar conditions prevailed during the eruption of the microlite-bearing Sw magma, which was chemically and physically homogeneous under general conditions of intermediate ascent/decompression rates. Oru and Okp microlite-rich lapilli indicate more viscous magmas rising at slow and highly variable decompression rates, with opportunity for intense shearing and segregation of magma with contrasting rheological properties across the conduit.

6.4.3 Implications for column stability

These textural parameters can be correlated to the eruptive parameters and lithofacies associations identified in the field, indicating that Oru unit signals a change in the typical, Late Pleistocene Plinian behaviour of Mt. Ruapehu. The oldest Mgt unit, having variable pumice textures, was accumulated from an eruption column fluctuating in height with time. The Sw unit, showing the most homogeneous pumice textures, was related to a steady column throughout the eruption. By contrast, Oru and younger deposits (until ~11.6 ka BP cal.) indicate that columns were unstable, with PDC deposits being interbedded with fall units. Pumice textures are the most heterogeneous (**Chapters 5 and 6.3**) and the compositional range of whole-rock major and trace element contents is wider relative to older units (**Appendix F**). The consequences of high rheological heterogeneity of the magma reaching the fragmentation level are important, since this condition could have contributed to the mismatch between magma supply, ascent, and discharge rates promoting column collapse. It is important to consider that the heterogeneity of pumice textures within the

deposit is reflecting an integrated-time sampling of clasts that were accumulated at the same time, not necessarily fragmented at the same time. Therefore, vertical variations in porosity/density within the conduit are not excluded and it is clear that clasts with different densities travel along different trajectories within the plume. However, the observations point to the conclusion that more viscous and degassed magmas affected by sheared and subject to shallow stalling and densification are prone to rise at variable ascent rates. Local variations in porosity and density can also promote differences in depth of the fragmentation front. All together, this conditions correlate with deposits related to column collapse.

Oru and Okp glass matrix compositions include high SiO_2 and K_2O, and low Al_2O_3, FeO, MgO, and CaO (**Fig. 5.3.3**; **Tables 6.5** and **6.6**), and a displacement towards the Qz apex within the haplo-granite diagram (**Fig. 6.17**). These observations are consistent with the progressively more effective crystallization of plagioclase and with the proposed slower decompression/ascent rates or increased degassing of latter events. Moreover, the significant drop in groundmass glass MgO content relative to previous units (**Appendix F**) is consistent with Ti-Mg oxides crystallization, which is usually favoured at slow decompression rates (i.e. <0.1 Pas^{-1} based on experimental models of Cichy et al., 2010).

Observations in natural and experimental samples by Burgisser and Gardner (2005), Cashman and Mangan (1994), Hamada et al. (2010), and Rust and Cashman (2011), showed that slow decompression rates favour coalescence and development of connectivity. This is consistent with the pattern observed at Mt. Ruapehu Plinian eruptions, with Oru and Okp lapilli textures indicating that magma ascent rate was slow enough, or that sufficient time passed to develop a progressively more open system to enhance vesicle-wall wrinkling, bubble connectivity and ultimate collapse. Subsequently Okp magma discharge rate and resulting column height were significantly lower than Oru (**Chapter 4**).

Within this context, how could a crystal-rich magma close to the crystal-crystal interaction erupt explosively instead of resulting in a dome-like emission? The answer to this question might lie in the competition between the eruption rate and the degassing process (c.f., Jaupart and Allegre 1991; Woods and Koyaguchi 1994). In Okp eruption the ascent rate could overcome the degassing rate because it was limited by the permeability of the conduit by lining/wall sealing as densification of magma occurred (c.f., Jaupart and Allegre 1991; Burgisser and Gardner 2005; Kennedy et al., 2010). Alternatively, it could have been erupted before enough degassing occur to become a conduit plug/dome by sudden decompression

(i.e., phreatic opening phase). Even though connectivity was high, the high overall viscosity and the crystallization of anhydrous phases could restrict bubble expansion, subsequently driving supersaturation and overpressure of small bubbles. The typically banded pumice textures within Oru, and more commonly in Okp, the strong alignment of vesicles and crystals, crystal grinding, and the incorporation of lithics entrapped within the pumice clasts, indicate advanced shear along the magma-conduit interface. Together with the low total vesicularity (31-60 vol.%), the viscous relaxation time of vesicles could be overprinted by the high deformation rate, inevitably driving the magma to fragmentation. The reader is referred to Dingwell and Webb (1990), Alidibirov and Dingwell (1996), Dingwell (1998), Mader (1998), Papale (1999), and Houghton et al. (2004) for the theoretical model behind these process.

On the other hand, Toramaru (2006) highlighted how vesicle collapse could trigger open-system degassing and transitions from explosive to effusive activity. It is highly probable that the erupting magma generating the Okp unit reached advanced permeability, ultimately leading to a transition into an effusive phase. This conclusion could be supported by the palaeomagnetic data reported by McClelland and Erwin (2003) on the coeval ~9 ka BP cal., collapse of Mt. Ruapehu, in which several clasts indicate the pre-existence of a dacitic dome.

6.5 Conclusions

Mt. Ruapehu andesitic Plinian eruptions where characterized by sudden decompression of volatile-rich magmas (minimum of 3.6-6.2 wt.% of total H_2O) stored at different levels, and experiencing heterogeneous bubble nucleation. Pumice textures reflect the dynamic processes of decompression and degassing. The different pumice textures found within a particular deposit correspond to variable N_v, VVD, VSD, and mafic crystal number density (N_x). There is a temporal trend with increasing average N_v and groundmass glass silica content in the youngest eruptive units, consistent with higher magma viscosities. All lapilli studied are characterized by polymodal mafic CVD and power-law CCSD, indicating multiple events of crystal nucleation and growth, with a distinctive population of anomalously large crystals in the youngest events.

Groundmass glass compositions plotted within the Qz-Ab-Or diagram show a clear temporal trend away from the Ab apex and progressively shifting towards the 0.1 MPa cotectic. This

tendency reflects the crystallisation of Pl at various pressures, and decreasing pre-eruptive storage depths in the youngest events. Vesicle nucleation and growth processes are intimately correlated with decompression rate.

Multiple bubble nucleation and growth processes inferred from polymodal distributions are likely to occur when N_x is an order of magnitude higher than N_v, under $<\Delta P$, allowing efficient bubble nucleation around Px and Ti-Mg oxide crystals at low supersaturation. Variations between subvolumes of a particular sample are dictated by the local effect of coalescence. The high total crystallinity increases the complexity of the vesiculation process, allowing populations that might experience coalescence and eventually, collapse.

The 3D textural analyses within the studied lapilli confirmed the hypothesis proposed from the study of ash-sized particles (**Chapter 5**), about variable fragmentation depths resulting from variable physical states (i.e., density) of the magma reaching the fragmentation level. This state is dictated by the undergoing degassing processes and local flow dynamics. The oldest Mgt unit indicates bubble expansion and acceleration at high decompression/ascent rates. This magma had the lowest density and highest isolated vesicularity, which could promote fragmentation at deeper levels relative to other units. The youngest Okp unit indicates shear strain at low ascent rates may have driven the melt towards the glass transition. Sw (expansion rate < decompression timescale) and Oru (strain rates > decompression/ascent rates) reflect intermediate conditions where vesicle growth rates could not keep pace with decompression rates, leading to magma fragmentation. It is possible that the complex flow conditions under high shear experimented by units younger than Oru are due to a change in conduit geometry after the high erosion/abrasion caused during the Sw episode (c.f., **Chapter 4**).

All units indicate a very late decompression wave and vesiculation, allowing time for melt migration between crystals crack-walls but shortly before quenching, as inferred from the recurrent feldspar and pyroxene phenocrysts with micro jig-saw structures, reflecting both vertical and lateral expansion.

The resulting eruption style and column behaviour during andesitic Plinian eruptions of Mt. Ruapehu did not depend much on the initial conditions, (all eruptions have similar initial estimated nuclei), but were strongly influenced by on the processes occurring between the exsolution level and the fragmentation level. These processes were controlled by the relative

timescales of vesicle nucleation, growth, relaxation, and shear in comparison to the overall magma ascent rate. It is well known that vesicle and mineral nucleation and growth are influenced by the magma decompression rate (e.g., Rutherford and Hill 1993; Hammer and Rutherford 2002; Martel and Schmidt 2003, Cichy et al., 2010). Magma degassing and ascent rate also controls the eruptive style (e.g., Sparks 1978; Hurwitz and Navon 1994), with groundmass textures preserving the decompression path within the conduit (Cichy et al., 2010). In Mt. Ruapehu Plinian eruptions, segregation of differential ascent rates across the conduit (with differential flow dynamics, degassing history, and relative viscosity), resulted in complex rheological conditions prior to fragmentation. The most heterogeneous rheology linked with column instability. Under low variability and relatively homogeneous fragmentation surfaces, eruption column is steady and sustained (e.g., Sw unit). Under intermediate variability, column height fluctuated during the eruption (e.g., Mgt unit), but greater variability (also leading to different fragmentation depths across the conduit according to local magma density; c.f., Spieler et al., 2004a) drove column collapse (e.g., Oru and Okp cases). Mt. Ruapehu Plinian eruptions are a typical example of magmas of similar bulk composition experiencing different rheological histories depending on crystal content, the evolution of the residual liquid composition, the bubble-crystal-melt interaction with different vesicle shapes, and the degassing path across and along the conduit.

CHAPTER 7. Discussion: an integrated model for the most violent explosive eruptions expected at Mt. Ruapehu

*This chapter summarizes the main findings of this study and discusses the new insights into Mt. Ruapehu's largest explosive eruptions. This discussion integrates data presented in **Chapters 3** to **6** and **Appendices A-I** following the methodology described in **Chapter 2**.*

7.1 Introduction

Previous studies indicate that the latest phase of large-scale explosive activity of Mt. Ruapehu took place during the Late Pleistocene (Topping 1973). Tephras mapped as the ~27 to ~10 ka BP cal., Bullot Formation (Donoghue 1991; Donoghue et al., 1995b; Neall et al., 1995; Cronin et al., 1996a, b; Cronin and Neall 1997) encompass the best-exposed deposits resulting from Plinian activity from this volcano. Similar Plinian to subplinian deposits are also known to date back to ~70 ka BP cal., but their deposits are only locally preserved at locations such as B14 (**Appendix A**) and along the Upper Waikato Stream (Cronin et al., 1996a). The study presented here is focused on the lithostratigraphic record of the Bullot Formation, and in particular on those units younger than the ~22 ka BP cal., Hokey Pokey Tephra (i.e. "*Hokey Pokey Lapilli*" of Donoghue 1991; Donoghue et al., 1995b). Within this record, 33 distinct eruptive units were identified, which were grouped into products of six periods to represent important variations in eruptive behaviour, particularly in column stability (**Chapter 3**).

Plinian eruptive units dated between 21,800 ± 500 cal years BP to shortly after 17,625 ± 425 cal years BP were named the *Rangipo Eruptive Period* (**Chapter 3.2.4**). These units were predominantly (but not exclusively) related to non-collapsing eruptive columns oscillating in height. The best example of this was the Mangatoetoenui Eruptive unit (Mgt), which involved a minimum erupted bulk volume of 0.3 km^3 and a 22 km-high column (**Chapter 4**). During this eruption, variation in column height (between 19 and 22 km) resulted in normally graded and shower-bedded fall deposits without associated pyroclastic density currents.

The following *Tukino Eruptive Period* (**Chapter 3.2.4**) was characterised by explosive eruptions being smaller and short-lived, mostly Vulcanian in style. This was followed by the *Karioi Eruptive Period* with a return to Plinian eruptions with three events prior to 13,625 ±

165 cal years BP, and the last one (i.e. Shawcroft Eruptive Unit) shortly afterwards. All *Karioi Period* eruptive units show depositional evidence for stable eruptive columns and deep conduit excavation of hydrothermally altered country rock. The youngest Shawcroft eruptive unit (Sw) has a minimum bulk volume of 0.6 km^3 and produced a 29 km-high column (**Chapter 4**).

The *Ohinewairua Eruptive Period* involved three major Plinian eruptions: Oruamatua (0.5 km^3, 37 km column height), unit XXVIII, and Akurangi (0.6 km^3; 35 km column height) (**Chapter 4**). The Oruamatua (Oru) and Akurangi (Ak) eruptive units are thus the largest explosive eruptions known for Ruapehu. These involved unsteady eruptive columns, reaching stratospheric levels (>30 km), but also partially collapsing to produce pyroclastic flows towards the east of the volcano (**Chapter 3.2.4**).

All the eruptive units up to this point were sourced at the northern crater of Mt. Ruapehu. Most produced bilobate plumes, indicating two predominant wind directions (from the NW and SW), varying: **(a)** with time, so that pauses between eruptive pulses/phases cannot be distinguished, and/or **(b)** with altitude in the atmosphere, so that higher portions of the plume could have been affected by north-westerlies, and the lower portion by south-westerlies (**Chapter 4**).

The last suite analyzed in this study represents the *Taurewa Eruptive Period*, comprising four eruptive units, of which the second one is the only Plinian event, termed the Okupata-Pourahu eruptive unit (Okp-Ph; **Chapter 3.2.4**). This unit includes two pumice fall deposits separated by a pyroclastic density current deposit and/or co-ignimbrite ash. The Lower and Upper Okupata fall units (0.4 km^3; 25 km column height; **Chapter 4**) are newly defined from original recognition of the 11,620 ± 190 cal years BP, Okupata Tephra of Topping (1973. The Okupata fallouts were accumulated from a bi-lobate plume, dispersed towards the north and southeast, and were sourced from the South Crater (**Chapter 4**). The small pyroclastic flow deposit related to this eruption equates to the unit described by Donoghue et al., (1995a, b) on the Rangipo Desert (i.e., *Op.Cit. Poruahu Member*), and is restricted to the Whangaehu valley consistent with a vent located to the south. Donoghue et al., (1999) defined the "Taurewa Eruptive Episode" as the largest event within the Late Pleistocene Ruapehu's history, producing the "only known" pyroclastic flow from this volcano, and was the last event before a ~8000 year period of repose in the eruptive activity (*Op.cit*). Complete revision of the pre-existing stratigraphy in this study (**Chapters 3-4**), shows that the largest

eruptions were the earlier Oruamatua and Akurangi eruptive units. The previous stratigraphic confusion probably resulted from the similar pumice colour, banding, textures, and silica content of the Oruamatua, Akuranki, and Okupata-Pourahu units. However, they are clearly differentiated on the eastern Ring Plain based on stratigraphic position and several intervening tephras (**Chapter 3**). Okp-Ph represents the last Plinian event known for Mt. Ruapehu, followed by tephras indicating progressively smaller-scaled eruptions, including the Ngamatea lapilli 1 and 2 (Donoghue 1991), and the minor orange lapilli fall beds found above the Mt. Tongariro sourced, ~11 ka cal years BP Pahoka Tephra (Donoghue 1991; Donoghue et al., 1995b; Moebis 2010; **Appendix A**).

The systematic change in lithofacies associations during the studied sequence was interpreted to result from transitions in the Plinian eruptive conditions over time (**Chapters 3-6**). Below, the discussion concentrates on interpretations based on the case-example eruptions for each eruptive period: **(1)** the Mangatoetoenui Eruptive Unit (Mgt), representing oscillating but stable eruptive columns; **(2)** the Shawcroft Eruptive Unit (Sw), representing stable, steady eruptive columns; **(3)** the Oruamatua (Oru) and **(4)** the Okupata-Pourahu (Okp-Ph) eruptive units, representing unsteady, collapsing columns. Changes in Plinian style and column behaviour resulted from evolution in the conditions within the storage system and the conduit, driving variations in the degassing and fragmentation processes.

7.2 Magma storage system

7.2.1 Whole rock Geochemistry

Whole-rock analyses of juvenile pumice clasts plot within a tight range of the basaltic andesite and andesite fields, overlapping with coeval Mangawhero (20-30 ka BP) and Whakapapa (2-15 ka BP) Formation lavas (c.f., Gamble et al., 1999, 2003; Price et al., 2012). The tephras, however, have overall lower SiO_2 and Na_2O contents, higher Al_2O_3 and FeO contents, and less chemical variability (**Fig. 7.1; Appendix F.1; Tables 7.1-7.4**).

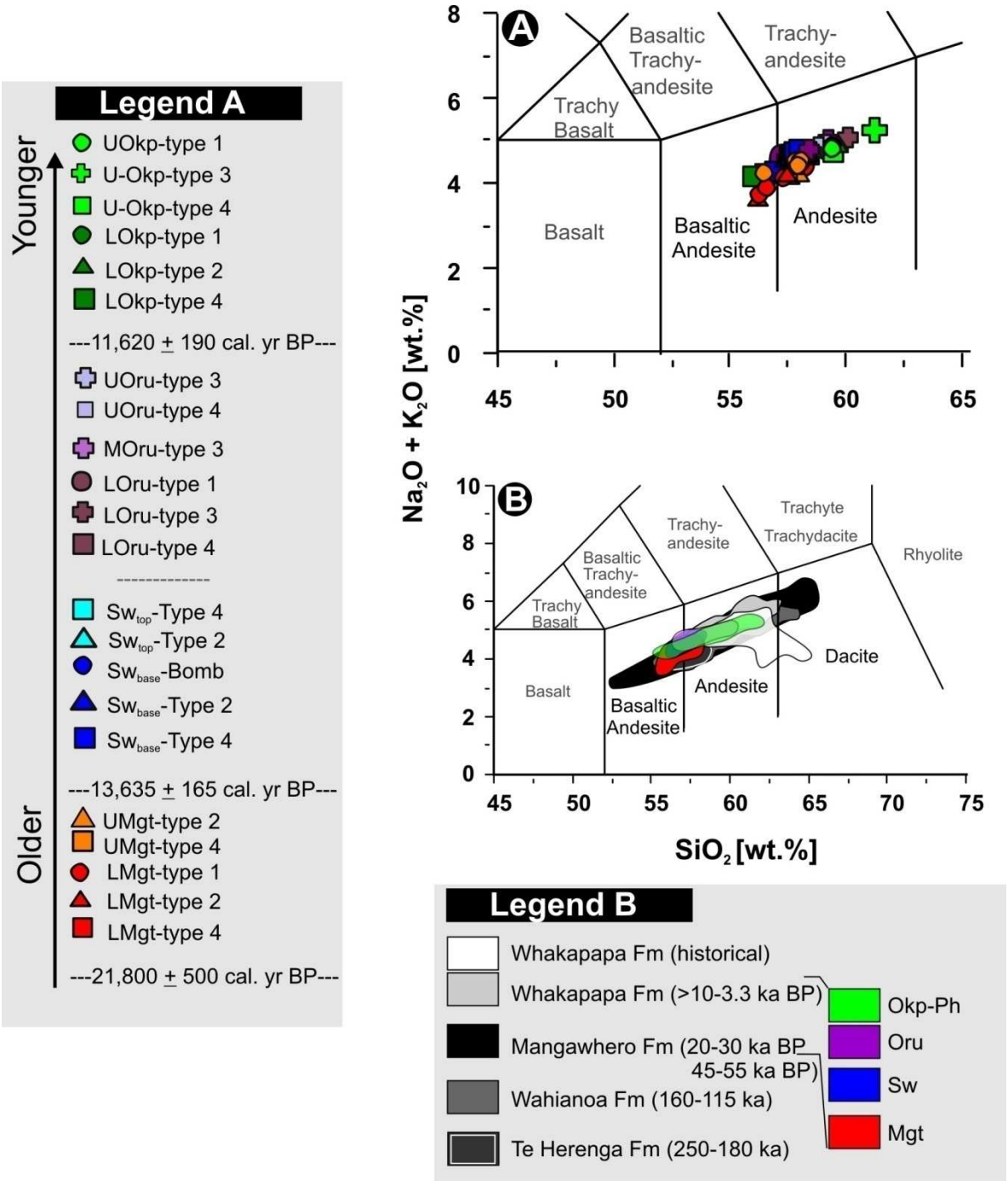

Figure 7.1 a) Juvenile Pumice whole-rock classification of the selected eruptive units following Le Bas et al. (1986). Different textural types are indicated in the legend as: **1)** foamy to expanded, consisting of sub-spherical vesicles. **2)** Fluidal, with predominantly elongated, ellipsoidal, and oriented vesicles. **3)** Fibrous, occasionally colour-banded, microlite-rich, with highly elongated vesicles showing very thin walls; collapsed vesicles are common. **4)** Dense, occasionally banded, microlite-rich pumice clasts with highly distorted, collapsed vesicles. **b)** Comparison between the studied tephras and the lava formations reported by Price et al. (2012, and references therein). Ar/Ar ages for lava formation are shown as reported by Gamble et al. (1999, 2003), and Price et al. (2012).

Table 7.1 Whole-rock, major (XRF) and trace element (LA-ICP-MS) data for the Mangatoetoenui Eruptive Unit pumice clasts.

	Lower Mangatoetoenui Eruptive Unit (L-Mgt)									Upper Mangatoetoenui Eruptive Unit (U-Mgt)							
Sample	**NP-1**	**NP-2**	**NP-3**	**NP-4**	**NP-5**	**NP-6**	**NP-7**	**NP-72**	**NP-73**	**NP-8**	**NP-9**	**NP-10**	**NP-11**	**NP-12**	**NP-13**	**NP-14**	**NP-74**
Type	**T1a**	**T1a**	**T2b**	**T2b**	**T1b**	**T1b**	**T4a**	**T2b**	**T2b**	**T2b**	**T4a**	**T2b**	**T1b**	**T4a**	**T2b**	**T1b**	**T2b**
Major Oxides (XRF)																	
SiO2	55.77	53.11	52.55	56.20	54.23	56.67	55.72	55.45	55.81	57.21	54.37	56.55	55.77	55.22	56.45	56.81	56.19
TiO2	0.69	0.71	0.75	0.72	0.72	0.71	0.72	0.73	0.71	0.72	0.75	0.75	0.72	0.74	0.73	0.72	0.71
Al2O3	15.96	16.64	16.94	16.85	16.58	16.40	16.36	16.61	16.57	16.68	17.99	16.74	16.84	16.79	16.82	16.91	16.75
Fe2O3	7.43	7.74	7.84	7.64	7.67	7.84	8.10	7.99	7.93	7.62	8.34	7.80	7.86	7.98	7.81	7.64	7.70
MnO	0.12	0.12	0.12	0.14	0.12	0.14	0.16	0.15	0.14	0.12	0.13	0.12	0.13	0.12	0.12	0.12	0.12
MgO	6.48	6.40	5.86	4.57	6.27	4.98	5.19	5.05	5.01	4.71	4.25	4.75	4.78	4.87	4.84	4.68	4.71
CaO	7.42	6.74	6.70	6.91	7.13	7.08	7.11	7.03	7.03	7.22	6.92	7.20	6.83	6.99	7.24	7.15	6.99
Na2O	2.79	2.45	2.39	2.80	2.62	2.82	2.69	2.70	2.75	2.98	2.78	2.91	2.72	2.65	2.86	2.92	2.79
K2O	1.21	1.04	1.01	1.47	1.07	1.48	1.40	1.36	1.42	1.52	1.23	1.49	1.41	1.37	1.42	1.47	1.45
P2O5	0.12	0.13	0.13	0.14	0.12	0.13	0.13	0.14	0.13	0.13	0.14	0.14	0.14	0.14	0.14	0.14	0.14
H2O	0.84	2.08	2.50	1.06	1.43	0.60	0.81	1.03	0.87	0.38	1.40	0.66	1.14	1.29	0.62	0.58	0.82
LOI	1.05	2.70	3.05	1.37	1.88	1.01	1.48	1.64	1.50	0.58	1.56	0.78	1.54	1.74	0.82	0.73	1.49
Total	99.85	99.86	99.83	99.86	99.83	99.87	99.87	99.87	99.87	99.88	99.87	99.88	99.89	99.88	99.87	99.88	99.86
Trace Elements (LA-ICP-MS)																	
Be	0.94	1.22	1.35	1.15	1.19	1.23	1.11	1.32	1.28	0.95	1.23	0.90	0.96	1.23	1.11	0.97	1.08
Sc	28.98	31.00	31.53	28.89	29.75	29.78	33.02	22.31	28.75	29.82	28.84	29.10	30.55	31.91	30.37	28.93	24.66
Ti	5082	5508	5735	5381	5373	5206	7046	4682	5284	6854	7164	6545	6576	6574	6362	6145	4436
V	183	177	175	195	173	201	206	171	219	200	209	193	195	205	204	198	179
Cr	304	344	312	120	311	137	153	73	84	121	74	122	130	133	128	118	89
Co	36.51	39.26	35.54	43.31	46.57	39.92	49.98	18.10	22.32	36.80	30.13	35.30	38.85	45.06	66.79	55.52	19.18
Ni	95.43	108.88	92.90	38.73	99.29	38.76	44.71	28.01	27.02	38.79	28.26	35.57	47.97	40.69	45.27	38.83	27.56
Cu	56.98	61.91	63.80	50.93	61.88	51.76	66.15	28.98	31.88	48.31	45.26	47.20	54.05	46.03	50.80	49.88	31.17
Zn	58.00	62.08	66.26	68.32	70.41	67.43	75.04	62.68	76.13	66.59	74.54	67.57	76.37	70.30	70.45	68.62	64.08
Ga	15.73	16.57	16.81	16.46	16.15	15.88	16.47	16.68	18.16	16.42	17.90	16.05	16.44	16.31	16.28	16.75	16.63
Rb	41.70	36.85	37.49	53.19	37.33	52.00	49.68	61.91	55.92	53.33	42.36	50.28	51.10	49.15	50.05	52.43	59.78
Sr	238	231	245	216	245	210	217	220	202	230	232	219	222	217	224	224	216
Y	19.07	25.61	22.61	20.91	20.02	19.98	21.99	17.65	16.96	20.22	21.18	20.28	21.54	22.03	20.35	20.00	17.68
Zr	102	110	117	120	106	109	121	157	157	118	115	117	122	124	116	115	147
Nb	3.89	4.16	4.51	5.01	4.00	4.66	4.89	6.38	6.52	4.77	4.70	4.69	5.02	5.05	4.78	4.86	6.02
Cs	2.63	2.73	2.81	3.23	2.72	3.14	2.93	3.82	3.50	3.19	2.44	2.97	3.03	2.97	2.84	2.98	3.52
Ba	284	312	424	306	488	291	304	336	309	314	283	296	329	296	301	300	327
La	12.37	16.06	14.55	13.90	12.75	13.09	14.50	13.92	10.87	13.33	13.27	13.33	14.15	14.22	13.33	13.56	13.38
Ce	24.18	28.49	28.50	29.13	25.48	27.11	30.54	30.32	24.56	27.18	27.57	26.94	29.12	28.06	27.36	27.16	28.92
Pr	3.18	4.11	3.93	3.58	3.35	3.28	3.66	3.64	2.79	3.43	3.54	3.41	3.63	3.59	3.44	3.46	3.49
Nd	13.67	17.53	16.74	14.97	14.55	14.14	15.71	14.85	11.28	14.78	15.03	14.63	15.43	15.57	14.93	14.72	14.45
Sm	3.13	3.93	3.76	3.62	3.27	3.37	3.76	3.36	2.67	3.48	3.65	3.63	3.52	3.60	3.42	3.47	3.35
Eu	0.85	1.04	1.02	0.89	0.90	0.85	0.92	0.78	0.86	0.88	0.95	0.86	0.93	0.94	0.90	0.87	0.77
Gd	3.26	4.47	4.21	3.63	3.60	3.52	3.91	3.28	2.75	3.65	3.95	3.62	3.74	3.90	3.65	3.37	3.34
Tb	0.51	0.67	0.62	0.56	0.53	0.54	0.60	0.51	0.47	0.57	0.61	0.55	0.57	0.60	0.56	0.57	0.53
Dy	3.36	4.20	4.05	3.68	3.48	3.53	4.05	3.29	3.10	3.78	4.04	3.73	3.97	3.89	3.80	3.63	3.35
Ho	0.68	0.88	0.81	0.76	0.72	0.73	0.85	0.68	0.62	0.78	0.82	0.79	0.81	0.81	0.79	0.74	0.70
Er	2.02	2.57	2.43	2.28	2.18	2.27	2.48	2.08	1.94	2.31	2.50	2.31	2.39	2.47	2.33	2.31	2.09
Tm	0.30	0.37	0.35	0.35	0.32	0.32	0.37	0.32	0.32	0.37	0.37	0.35	0.35	0.36	0.33	0.34	0.32
Yb	1.92	2.27	2.23	2.26	1.95	2.11	2.40	2.01	2.02	2.24	2.50	2.30	2.35	2.39	2.24	2.23	2.04
Lu	0.29	0.35	0.33	0.34	0.29	0.33	0.36	0.31	0.30	0.34	0.37	0.33	0.35	0.34	0.35	0.34	0.30
Hf	2.95	3.17	3.39	3.51	3.08	3.22	3.64	4.46	4.56	3.39	3.31	3.40	3.55	3.72	3.42	3.35	4.20
Ta	0.42	0.52	0.54	0.75	0.60	0.70	0.89	0.55	0.56	0.69	0.50	0.69	0.65	0.83	1.22	0.93	0.52
Pb	9.71	10.23	11.15	11.15	10.34	9.91	10.86	13.83	12.25	10.83	9.95	11.31	11.38	11.51	11.52	10.78	12.42
Th	4.92	5.35	5.69	6.30	5.06	5.73	6.49	9.01	8.66	6.28	5.99	6.19	6.50	6.58	6.04	6.04	8.46
U	1.29	1.41	1.48	1.65	1.30	1.53	1.62	1.95	1.87	1.58	1.51	1.57	1.64	1.64	1.56	1.53	1.91

Table 7.2 Whole-rock, major (XRF) and trace element (LA-ICP-MS) data for the Shawcroft Eruptive Unit pumice clasts.

	Shawcroft lapilli base											Shawcroft Lapilli top								
Sample	**NP-16**	**NP-17**	**NP-18**	**NP-19**	**NP-20**	**NP-21**	**NP-22**	**NP-23**	**NP-75**	**NP-76**	**NP-77**	**NP-24**	**NP-26**	**NP-27**	**NP-28**	**NP-29**	**NP-30**	**NP-78**	**NP-79**	**NP-80**
Type	**T1b**	**T2a**	**T2a**	**T2b**	**T4a**	**T4a**	**T4a**	**T2a**	**T2b**	**T4a**	**T2a**	**T2a**	**T2a**	**T2b**	**T4a**	**T2b**	**T2a**	**T4a**	**T4a**	**T2a**
Major Oxides (XRF)																				
SiO2	55.90	57.09	56.61	56.81	56.30	57.41	56.31	54.88	55.79	57.39	57.59	56.47	56.03	56.52	56.70	55.92	56.11	56.83	57.30	56.20
TiO2	0.79	0.78	0.79	0.77	0.80	0.76	0.82	0.80	0.79	0.78	0.79	0.81	0.80	0.80	0.77	0.79	0.81	0.77	0.80	0.81
Al2O3	17.75	17.54	17.54	17.60	17.46	16.75	17.61	17.61	17.89	17.18	17.14	17.54	17.68	17.52	17.43	17.97	17.62	17.47	17.31	17.40
Fe2O3	8.02	7.75	7.90	7.74	8.08	7.90	8.14	8.18	7.86	7.86	7.86	7.97	7.99	7.85	7.89	7.83	7.95	7.78	7.84	8.05
MnO	0.12	0.13	0.13	0.13	0.13	0.13	0.12	0.12	0.12	0.12	0.12	0.12	0.12	0.12	0.12	0.12	0.12	0.12	0.12	0.12
MgO	3.96	3.98	3.94	3.93	4.09	4.46	3.96	4.20	3.82	3.92	4.04	3.94	3.96	3.85	4.03	3.80	3.89	3.99	3.95	4.05
CaO	7.06	7.31	7.19	7.31	7.12	7.41	7.12	7.03	7.07	7.03	7.19	7.06	7.10	7.09	7.24	7.15	7.08	7.29	7.27	7.09
Na2O	3.00	3.19	3.08	3.16	3.03	3.11	3.07	2.81	3.00	3.10	3.23	3.07	3.01	3.10	3.11	3.03	3.05	3.15	3.21	3.04
K2O	1.39	1.50	1.48	1.47	1.44	1.51	1.44	1.29	1.39	1.52	1.55	1.47	1.41	1.50	1.47	1.38	1.44	1.46	1.52	1.43
P2O5	0.15	0.15	0.15	0.15	0.15	0.14	0.15	0.15	0.15	0.15	0.14	0.15	0.15	0.15	0.14	0.15	0.15	0.14	0.15	0.15
H2O	0.71	0.17	0.43	0.26	0.56	0.10	0.48	1.09	0.58	0.17	0.06	0.51	0.63	0.52	0.31	0.78	0.74	0.20	0.05	0.57
LOI	1.04	0.31	0.65	0.55	0.74	0.20	0.66	1.72	1.42	0.65	0.15	0.77	1.02	0.88	0.64	0.96	0.93	0.67	0.37	0.96
Total	99.89	99.90	99.89	99.88	99.89	99.87	99.88	99.88	99.88	99.88	99.88	99.88	99.89	99.88	99.87	99.87	99.89	99.88	99.88	99.87
Trace Elements (LA-ICP-MS)																				
Be	1.19	1.16	1.08	1.08	1.22	1.02	0.99	1.05	1.35	1.25	1.18	1.07	1.11	1.04	1.04	1.28	1.32	1.43	1.41	1.27
Sc	28.09	27.11	27.59	26.83	28.21	29.88	28.44	31.02	22.44	28.59	25.59	27.57	28.08	27.65	27.82	27.43	28.01	13.38	12.59	20.30
Ti	6515	6205	6282	5977	6128	5683	6002	5886	3909	4377	4163	5732	5536	5476	5250	5255	5293	2377	2257	3034
V	210	206	207	201	211	213	222	212	167	207	184	210	208	208	209	203	212	101	91	154
Cr	57	54	53	49	57	73	65	69	75	89	86	59	54	53	51	52	59	17	15	24
Co	30.47	49.27	50.78	69.93	36.80	39.61	64.18	61.06	16.86	21.97	19.37	38.56	31.34	40.77	39.53	43.06	54.72	9.78	23.38	29.05
Ni	18.13	20.52	20.09	17.64	20.07	20.92	21.88	25.49	23.76	28.04	28.39	21.95	20.64	18.91	19.01	20.24	21.41	8.32	7.87	10.07
Cu	30.58	28.60	30.99	30.84	33.75	25.10	32.30	33.18	25.13	39.58	24.94	30.10	31.82	30.99	27.56	29.19	36.07	14.22	14.55	20.68
Zn	70.13	72.18	71.64	71.63	71.71	72.63	72.99	71.30	60.44	67.66	66.30	72.24	73.23	73.16	72.22	70.51	74.03	63.34	64.97	72.08
Ga	17.62	17.39	17.14	16.96	17.15	16.24	17.48	17.38	15.51	16.95	16.44	17.17	17.35	17.17	17.05	17.30	16.96	14.50	14.41	15.96
Rb	45.74	48.75	48.98	47.39	47.24	49.41	47.71	43.71	67.91	50.58	58.23	48.41	47.00	50.53	47.89	45.69	47.47	56.10	58.64	48.46
Sr	258	265	258	263	255	255	267	248	205	222	216	262	264	262	263	264	257	210	225	240
Y	20.67	19.67	20.39	19.24	20.08	19.24	20.03	20.64	18.04	18.19	17.95	20.32	20.00	20.04	19.52	19.47	19.86	16.61	14.99	17.62
Zr	115	111	112	111	113	110	117	117	136	122	144	118	116	117	112	114	116	118	120	109
Nb	4.77	4.85	4.77	4.79	4.75	4.55	4.81	4.82	5.74	5.18	6.14	5.04	4.87	4.88	4.72	4.78	4.86	5.35	5.51	4.75
Cs	2.61	2.76	2.84	2.76	2.68	2.84	2.81	2.60	4.17	3.06	3.61	2.85	2.72	2.95	2.80	2.59	2.68	3.57	3.76	2.99
Ba	311	339	324	321	317	323	341	300	350	296	318	327	318	327	321	312	318	300	351	301
La	13.70	13.77	13.70	13.21	13.37	12.94	13.59	13.65	14.09	11.71	13.43	13.72	13.52	13.72	13.07	13.09	13.24	14.56	14.11	13.14
Ce	28.49	29.43	29.02	28.26	28.65	27.45	28.62	29.15	29.99	25.65	29.07	29.25	28.75	29.29	28.05	28.44	29.18	29.12	29.03	26.64
Pr	3.64	3.56	3.71	3.49	3.57	3.40	3.62	3.79	3.53	3.12	3.56	3.67	3.61	3.66	3.52	3.55	3.58	3.69	3.39	3.28
Nd	15.48	15.28	15.66	14.90	15.36	14.44	15.43	16.27	14.61	13.10	14.62	15.80	15.36	15.65	15.00	15.03	15.38	15.18	13.36	13.53
Sm	3.71	3.53	3.63	3.43	3.68	3.51	3.58	3.89	3.37	3.18	3.39	3.73	3.71	3.73	3.54	3.61	3.64	3.22	2.93	3.03
Eu	0.97	0.96	0.97	0.95	0.93	0.90	0.98	1.01	0.76	0.81	0.84	0.99	1.00	0.95	0.95	0.95	0.94	0.80	0.75	0.80
Gd	3.73	3.58	3.81	3.63	3.63	3.52	3.95	4.01	3.24	3.30	3.25	3.76	3.69	3.75	3.61	3.76	3.63	3.06	2.68	3.07
Tb	0.59	0.56	0.58	0.55	0.56	0.56	0.59	0.61	0.51	0.50	0.53	0.60	0.57	0.57	0.56	0.55	0.58	0.45	0.40	0.48
Dy	3.86	3.72	3.92	3.72	3.67	3.67	3.92	4.03	3.37	3.39	3.42	3.90	3.87	3.86	3.73	3.80	3.70	3.02	2.68	3.14
Ho	0.79	0.76	0.79	0.75	0.76	0.73	0.80	0.84	0.67	0.70	0.70	0.82	0.78	0.79	0.77	0.76	0.78	0.62	0.57	0.64
Er	2.41	2.24	2.40	2.29	2.34	2.24	2.37	2.47	2.05	2.15	2.13	2.35	2.37	2.37	2.27	2.22	2.34	1.94	1.72	2.07
Tm	0.35	0.34	0.34	0.32	0.34	0.34	0.36	0.37	0.31	0.34	0.31	0.36	0.35	0.35	0.36	0.34	0.35	0.31	0.28	0.31
Yb	2.36	2.22	2.34	2.14	2.23	2.20	2.35	2.36	2.09	2.23	2.06	2.41	2.36	2.29	2.22	2.28	2.25	2.06	1.87	2.14
Lu	0.36	0.32	0.33	0.32	0.33	0.31	0.35	0.36	0.31	0.30	0.31	0.33	0.34	0.33	0.32	0.33	0.33	0.32	0.29	0.32
Hf	3.36	3.19	3.23	3.13	3.27	3.16	3.46	3.43	3.94	3.59	4.08	3.42	3.44	3.40	3.23	3.24	3.36	3.32	3.28	3.13
Ta	0.49	1.16	0.96	1.68	0.69	0.75	1.42	1.40	0.49	0.42	0.52	0.81	0.64	0.89	0.83	1.03	1.07	0.48	0.84	0.76
Pb	10.66	10.10	10.34	13.24	10.22	10.86	11.50	13.47	11.78	10.42	13.30	12.07	13.41	12.81	12.18	12.02	12.93	13.86	12.76	11.49
Th	5.75	5.77	5.58	5.54	5.69	5.52	5.93	5.94	7.92	6.44	8.16	6.06	5.89	5.89	5.71	5.77	5.80	7.12	7.41	5.96
U	1.42	1.41	1.37	1.37	1.41	1.33	1.45	1.45	2.03	1.54	1.81	1.48	1.42	1.49	1.39	1.42	1.43	1.88	1.86	1.47

Table 7.3 Whole-rock, major (XRF) and trace element (LA-ICP-MS) data for the Oruamatua Eruptive Unit pumice clasts.

	Lower Oruamatua							Mid-Oruamatua			Upper-Oruamatua				
Sample	**NP-31**	**NP-32**	**NP-33**	**NP-34**	**NP-35**	**NP-36**	**NP-69**	**NP-38**	**NP-39**	**NP-40**	**NP-41**	**NP-42**	**NP-43**	**NP-44**	**NP-45**
Type	**T1a**	**T1a**	**T1a**	**T3a**	**T3a**	**T1b**	**T1b**	**T3a**	**T3a**	**T1b**	**T3a**	**T3a**	**T4a**	**T4a**	**T4a**
Major Oxides (XRF)															
SiO2	56.09	56.14	56.01	58.13	55.94	56.13	57.10	56.95	58.31	56.58	58.15	57.46	56.35	57.06	56.68
TiO2	0.72	0.72	0.81	0.72	0.76	0.73	0.73	0.75	0.71	0.74	0.72	0.73	0.69	0.73	0.72
Al2O3	18.35	18.53	17.66	16.67	18.33	18.04	17.45	16.90	16.53	18.08	17.00	17.00	18.57	17.51	17.89
Fe2O3	8.00	8.04	8.00	7.39	7.91	7.92	7.72	7.62	6.82	7.86	7.18	7.37	8.04	7.82	7.77
MnO	0.12	0.12	0.12	0.12	0.13	0.12	0.12	0.12	0.11	0.12	0.11	0.11	0.12	0.12	0.12
MgO	3.52	3.46	3.93	4.01	3.62	3.79	3.75	4.25	3.77	3.67	3.98	4.06	3.25	3.93	3.60
CaO	7.16	6.99	6.98	6.73	7.12	7.17	6.80	6.69	6.34	7.08	6.78	6.75	7.10	7.15	6.84
Na2O	3.14	3.17	3.02	3.21	3.14	3.13	3.16	3.00	3.08	3.19	3.18	3.09	3.21	3.15	3.13
K2O	1.26	1.26	1.41	1.69	1.29	1.31	1.48	1.57	1.83	1.35	1.62	1.59	1.24	1.42	1.39
P2O5	0.13	0.14	0.15	0.13	0.13	0.14	0.16	0.15	0.14	0.14	0.14	0.14	0.13	0.13	0.14
H2O	0.64	0.60	0.66	0.22	0.75	0.58	0.54	0.62	0.43	0.41	0.30	0.44	0.51	0.27	0.64
LOI	0.77	0.72	1.14	0.87	0.76	0.83	0.87	1.27	1.80	0.66	0.70	1.12	0.69	0.57	0.99
Total	99.89	99.89	99.90	99.89	99.89	99.88	99.88	99.89	99.88	99.89	99.87	99.87	99.91	99.87	99.90
Trace Elements (LA-ICP-MS)															
Be	1.06	1.15	1.14	1.17	1.10	1.05	1.16	1.08	1.22	0.91	1.01	1.07	1.00	0.93	1.14
Sc	24.67	23.71	27.65	24.93	25.76	26.43	30.19	27.72	25.65	25.51	25.47	25.67	22.16	26.72	24.63
Ti	4690	4583	5073	4362	4619	4410	5926	5565	5284	5378	5282	5346	5007	5360	5189
V	206	203	215	193	203	207	234	198	180	204	183	186	195	208	199
Cr	33	32	59	76	37	42	54	96	82	45	85	99	19	52	45
Co	33.36	49.12	33.05	44.86	41.43	34.98	28.52	30.18	21.27	41.26	40.92	21.32	70.66	38.71	37.78
Ni	13.95	13.28	21.78	25.01	16.42	16.71	24.55	29.73	27.36	18.25	29.85	31.94	10.53	20.52	16.29
Cu	25.96	36.71	40.12	28.11	32.98	31.58	37.01	33.74	29.32	28.89	24.40	37.38	21.71	27.52	25.83
Zn	73.89	76.72	73.79	73.57	74.07	72.47	73.48	71.94	66.71	74.11	69.68	70.72	79.16	98.90	74.44
Ga	17.29	17.98	17.27	16.31	17.50	17.11	19.49	16.71	16.28	16.97	16.50	16.58	17.34	16.79	17.01
Rb	41.20	42.04	47.26	57.51	42.16	42.52	40.37	55.71	66.39	44.39	56.74	56.29	40.28	48.14	47.09
Sr	247	246	255	235	242	240	245	244	240	247	249	251	250	245	240
Y	18.36	18.64	19.44	18.51	18.77	18.70	18.13	19.80	20.08	18.99	19.56	19.31	17.85	19.01	18.84
Zr	102	105	114	115	116	103	122	131	143	108	125	129	99	109	112
Nb	4.19	4.54	4.72	4.77	4.81	4.19	5.38	5.37	5.73	4.34	5.14	5.30	4.12	4.47	4.55
Cs	2.37	2.44	2.84	2.66	2.44	2.49	2.38	3.33	4.03	2.59	3.34	3.36	2.35	2.73	2.74
Ba	266	284	316	322	271	266	264	330	365	285	335	336	261	321	287
La	11.41	12.13	13.32	12.94	13.32	11.43	11.26	14.35	15.25	12.08	14.16	14.33	10.99	12.02	12.17
Ce	24.71	26.50	28.82	27.94	29.52	24.73	25.63	30.83	32.72	26.20	30.36	31.01	23.78	25.89	26.58
Pr	3.03	3.20	3.55	3.39	3.53	3.03	3.12	3.85	3.96	3.27	3.74	3.83	3.00	3.21	3.33
Nd	13.08	13.67	15.01	14.06	14.95	13.02	13.40	16.12	16.42	14.01	15.75	15.47	12.60	13.75	13.97
Sm	3.21	3.11	3.52	3.44	3.55	3.14	3.24	3.65	3.81	3.18	3.54	3.56	2.98	3.28	3.25
Eu	0.86	0.85	0.94	0.86	0.89	0.85	0.90	0.94	0.88	0.87	0.89	0.87	0.85	0.87	0.86
Gd	3.30	3.40	3.68	3.44	3.57	3.24	3.22	3.80	3.87	3.48	3.62	3.79	3.19	3.45	3.40
Tb	0.52	0.54	0.55	0.50	0.54	0.52	0.53	0.55	0.57	0.52	0.58	0.56	0.50	0.53	0.53
Dy	3.55	3.53	3.74	3.38	3.58	3.56	3.57	3.86	3.88	3.65	3.74	3.71	3.24	3.60	3.61
Ho	0.70	0.72	0.76	0.73	0.73	0.72	0.69	0.78	0.78	0.74	0.74	0.75	0.68	0.74	0.72
Er	2.19	2.20	2.28	2.08	2.20	2.22	2.21	2.35	2.36	2.24	2.25	2.20	2.13	2.20	2.20
Tm	0.33	0.33	0.34	0.32	0.34	0.31	0.35	0.35	0.35	0.35	0.35	0.34	0.32	0.32	0.32
Yb	2.14	2.13	2.24	2.07	2.23	2.18	2.19	2.31	2.33	2.20	2.27	2.16	2.07	2.20	2.17
Lu	0.32	0.32	0.32	0.31	0.33	0.32	0.33	0.33	0.34	0.33	0.31	0.33	0.31	0.33	0.33
Hf	2.93	3.00	3.32	3.33	3.31	2.95	3.54	3.87	4.19	3.10	3.58	3.75	2.84	3.16	3.23
Ta	0.54	1.17	0.54	0.83	0.89	0.42	0.52	0.62	0.50	0.83	0.81	0.44	1.63	0.80	0.79
Pb	11.63	12.39	12.07	11.20	11.51	10.73	11.74	13.51	15.24	13.56	14.74	15.50	13.24	16.38	12.46
Th	4.96	5.28	5.73	6.07	5.82	5.06	6.12	7.09	8.15	5.37	6.64	6.95	4.70	5.42	5.55
U	1.27	1.34	1.43	1.59	1.47	1.28	1.55	1.69	1.98	1.36	1.63	1.67	1.21	1.40	1.40

Table 7.4 Whole-rock, major (XRF) and trace element (LA-ICP-MS) data for the Lower and Upper Okupata pumice clasts.

	Lower Okupata Tephra								Upper Okupata Tephra							
Sample	**NP-46**	**NP-47**	**NP-49**	**NP-50**	**NP-51**	**NP-52**	**NP-53**	**NP-54**	**NP-55**	**NP-56**	**NP-57**	**NP-58**	**NP-59**	**NP-60**	**NP-61**	**NP-62**
Type	**T4a**	**T3a**	**T3a**	**T3a**	**T1b**	**T1b**	**T4a**	**T4a**	**T3b**	**T3b**	**T3b**	**T4a**	**T3a**	**T3a**	**T4a**	**T4a**
Major Oxides (XRF)																
SiO2	55.58	55.23	56.70	56.72	55.12	56.00	54.18	53.18	56.34	55.96	56.42	52.98	56.43	59.02	56.15	56.37
TiO2	0.72	0.72	0.74	0.72	0.77	0.75	0.75	0.79	0.76	0.70	0.73	0.79	0.73	0.70	0.75	0.74
Al2O3	17.91	18.17	17.12	17.52	18.41	17.82	18.49	18.69	17.08	17.52	17.41	18.10	17.00	16.35	17.21	16.81
Fe2O3	6.63	7.47	6.81	6.55	7.82	7.65	8.12	8.04	6.76	6.71	6.53	7.42	6.76	6.39	7.30	7.11
MnO	0.15	0.11	0.11	0.11	0.12	0.12	0.13	0.12	0.10	0.10	0.10	0.11	0.11	0.10	0.11	0.11
MgO	3.31	3.93	3.57	3.37	3.90	3.90	3.98	4.08	3.64	3.60	3.44	3.88	3.75	3.46	4.14	3.91
CaO	5.66	6.10	5.81	5.74	6.99	6.74	6.68	6.67	5.90	5.90	5.67	5.44	5.98	5.74	6.80	5.83
Na2O	2.93	2.73	2.92	2.97	2.91	3.04	2.88	2.81	2.88	2.89	2.92	2.58	2.87	3.06	2.94	2.87
K2O	1.61	1.30	1.69	1.71	1.22	1.36	1.15	1.11	1.68	1.59	1.70	1.47	1.64	1.97	1.43	1.60
P2O5	0.16	0.14	0.15	0.15	0.13	0.14	0.14	0.14	0.15	0.15	0.15	0.10	0.14	0.13	0.13	0.15
H2O	1.95	1.30	1.49	1.52	0.83	0.95	1.53	2.04	1.49	1.76	1.54	2.58	1.44	0.65	0.73	1.39
LOI	3.27	2.68	2.77	2.81	1.66	1.42	1.87	2.22	3.09	2.99	3.25	4.41	3.01	2.31	2.19	3.00
Total	99.87	99.89	99.87	99.88	99.88	99.88	99.89	99.88	99.87	99.86	99.87	99.87	99.86	99.88	99.88	99.88
Trace Elements (LA-ICP-MS)																
Be	1.35	0.99	1.15	1.43	1.25	1.02	1.11	1.11	1.25	1.41	1.37	1.28	1.11	1.44	1.25	1.20
Sc	23.14	25.98	24.52	22.49	28.25	27.73	27.93	28.95	25.06	24.38	23.20	28.65	25.32	23.97	28.58	26.14
Ti	5437	5338	5411	5280	5611	5543	5525	5682	5274	4817	4870	5266	4555	4176	4375	4253
V	175	183	183	171	199	205	219	224	191	181	178	218	184	178	207	188
Cr	66	84	79	67	52	50	49	52	85	83	76	84	91	80	89	88
Co	32.25	20.52	18.99	19.02	26.79	26.17	26.06	27.34	20.11	18.89	18.83	22.24	19.69	18.01	21.96	19.79
Ni	25.00	28.52	25.83	24.84	21.25	24.85	24.48	23.54	27.66	30.82	29.13	26.93	28.30	25.39	28.03	29.00
Cu	31.36	30.81	25.80	25.48	40.13	37.04	37.58	35.49	28.24	31.65	30.15	31.76	32.01	26.84	39.56	25.48
Zn	67.72	78.70	66.63	65.46	78.94	71.38	75.32	70.46	66.27	67.27	65.20	75.86	65.79	64.57	67.63	67.74
Ga	17.63	17.97	16.70	17.03	17.41	17.42	18.12	18.69	17.21	17.45	17.35	18.10	17.08	16.57	16.94	16.80
Rb	59.87	47.18	62.74	63.20	41.46	46.46	39.20	38.71	63.58	58.97	64.39	55.72	61.38	72.55	50.55	59.49
Sr	230	260	221	228	266	235	226	235	224	229	229	201	221	219	222	221
Y	19.20	18.11	18.63	18.40	19.61	19.79	17.95	17.39	18.54	17.89	18.36	16.90	18.15	19.27	18.18	18.34
Zr	153	133	149	150	115	118	109	117	158	151	163	156	151	145	122	147
Nb	6.49	5.63	6.24	6.31	4.82	4.97	4.44	5.16	6.56	6.22	6.64	6.50	6.19	6.13	5.18	6.27
Cs	3.70	3.16	3.93	3.88	2.77	2.86	2.29	2.28	3.81	3.66	3.97	3.48	3.61	4.45	3.06	3.69
Ba	334	367	336	342	316	289	252	253	342	328	350	308	335	374	296	325
La	14.31	13.18	14.00	14.16	12.83	12.32	10.70	10.80	14.07	13.68	14.48	10.83	13.74	15.06	11.71	13.72
Ce	36.56	29.18	30.74	31.28	27.78	27.34	24.28	24.57	30.57	29.77	31.54	24.48	29.69	32.04	25.64	29.70
Pr	3.79	3.45	3.65	3.70	3.41	3.30	2.99	3.00	3.71	3.60	3.79	2.78	3.58	3.77	3.12	3.64
Nd	15.65	14.26	15.38	15.03	14.44	13.88	12.98	12.85	15.05	15.18	15.45	11.24	14.84	15.61	13.09	14.94
Sm	3.57	3.39	3.52	3.51	3.46	3.43	3.18	3.10	3.56	3.48	3.50	2.66	3.44	3.60	3.17	3.47
Eu	0.89	0.84	0.82	0.87	0.91	0.90	0.84	0.87	0.83	0.85	0.82	0.85	0.79	0.82	0.81	0.86
Gd	3.52	3.37	3.45	3.42	3.62	3.49	3.15	3.08	3.37	3.44	3.41	2.74	3.43	3.46	3.29	3.32
Tb	0.53	0.50	0.53	0.54	0.55	0.56	0.52	0.51	0.55	0.55	0.53	0.46	0.54	0.55	0.50	0.54
Dy	3.56	3.35	3.53	3.42	3.74	3.76	3.42	3.42	3.52	3.49	3.42	3.09	3.44	3.60	3.39	3.49
Ho	0.71	0.70	0.71	0.69	0.77	0.79	0.73	0.67	0.72	0.69	0.71	0.62	0.72	0.71	0.70	0.72
Er	2.21	2.12	2.15	2.10	2.39	2.30	2.24	2.12	2.19	2.15	2.16	1.93	2.15	2.19	2.15	2.17
Tm	0.33	0.33	0.32	0.32	0.34	0.35	0.33	0.33	0.35	0.32	0.33	0.31	0.33	0.33	0.34	0.32
Yb	2.20	2.17	2.12	2.10	2.23	2.32	2.20	2.10	2.08	2.11	2.09	2.01	2.09	2.23	2.22	2.11
Lu	0.31	0.32	0.32	0.32	0.34	0.35	0.32	0.31	0.32	0.31	0.33	0.30	0.31	0.33	0.30	0.32
Hf	4.37	3.85	4.15	4.29	3.31	3.39	3.20	3.40	4.54	4.27	4.64	4.55	4.31	4.21	3.59	4.16
Ta	0.54	0.45	0.53	0.51	0.52	0.48	0.42	0.50	0.57	0.54	0.58	0.56	0.53	0.52	0.42	0.53
Pb	16.22	12.24	13.37	14.15	12.51	10.89	10.72	11.26	14.24	14.01	14.39	12.20	12.75	12.59	10.41	13.59
Th	8.73	7.21	8.42	8.49	5.68	6.05	5.38	5.87	9.14	8.68	9.37	8.63	8.69	8.46	6.44	8.34
U	1.98	1.60	1.94	1.96	1.34	1.48	1.37	1.49	2.03	2.00	2.03	1.87	1.96	2.17	1.54	1.85

The oldest Mgt and Sw units are the most mafic and with the most restricted range in compositions, whereas the youngest Oru and Okp-Ph eruptives show the widest compositional range, including the highest SiO_2 and K_2O contents (**Figs.7.1, 7.2; Tables 7.1-7.4; Appendix F.1**). The least variable unit, Sw, has the most homogeneous pumice textures

within any stratigraphic level. With increasing chemical variability, progressively more complex ranges in pumice textures occur at any stratigraphic level (**Fig. 7.2**).

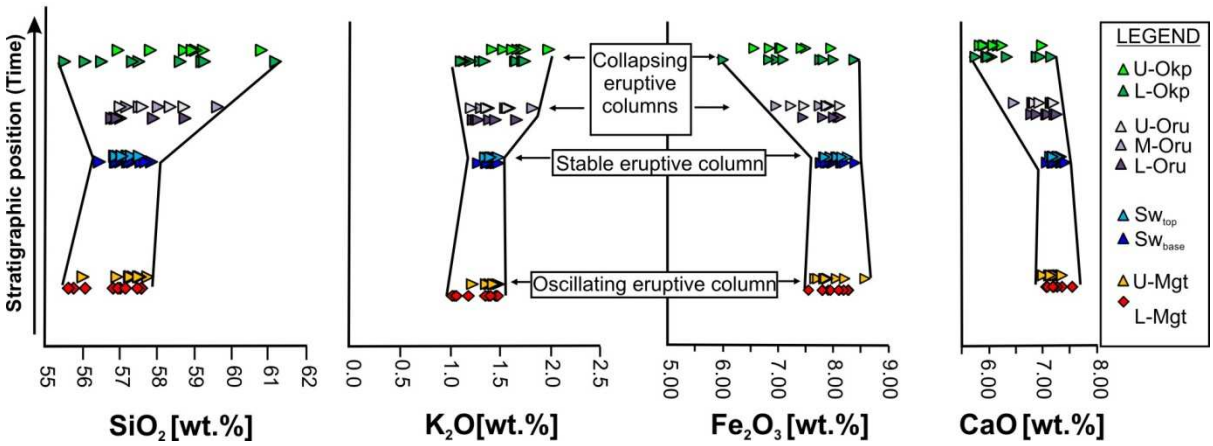

Figure 7.2 Variation in selected major oxide composition with time. Note a general trend towards more evolved compositions and wider compositional variability in the youngest eruptive units. This coincides with larger textural heterogeneity among pumice clasts in any stratigraphic level. Higher compositional variability is also correlated with collapsing eruption columns.

Harker diagrams of major oxides (**Fig. 7.3**) generally show roughly linear correlations with increasing silica content, suggesting that the rocks could be genetically related. There is some compositional variation between units that indicates petrogenetic variations between them. For example, the high MgO contents of some L-Mgt samples (**Fig. 7.3f**) show that this unit is more primitive than other units. Furthermore, differences in elemental trends between units reflect differences in the content of the crystallizing phases. In general, there are positive correlations between increasing SiO_2 and incompatible K_2O and Na_2O (to a lesser degree), while CaO, FeO_{total}, MgO, and TiO_2 show negative trends. The decrease in MgO, Fe_2O_3, and CaO is consistent with the crystallization of early-formed minerals from the cooling melt. MgO and Fe_2O_3 were incorporated into olivine and/or pyroxene, while CaO is incorporated into Ca-plagioclase and clinopyroxene. These composition correlations are consistent with the pumice mineralogy dominated by clino-and-ortho pyroxenes, Ca-plagioclase, and Fe-Mg-Ti-Oxides, as well as the absence of K-bearing phases. On the other hand, the negative correlation between TiO_2 and SiO_2 (**Fig. 7.3g**) indicates crystallization of titanomagnetite, which was not as important for Mgt and Ruapehu lavas.

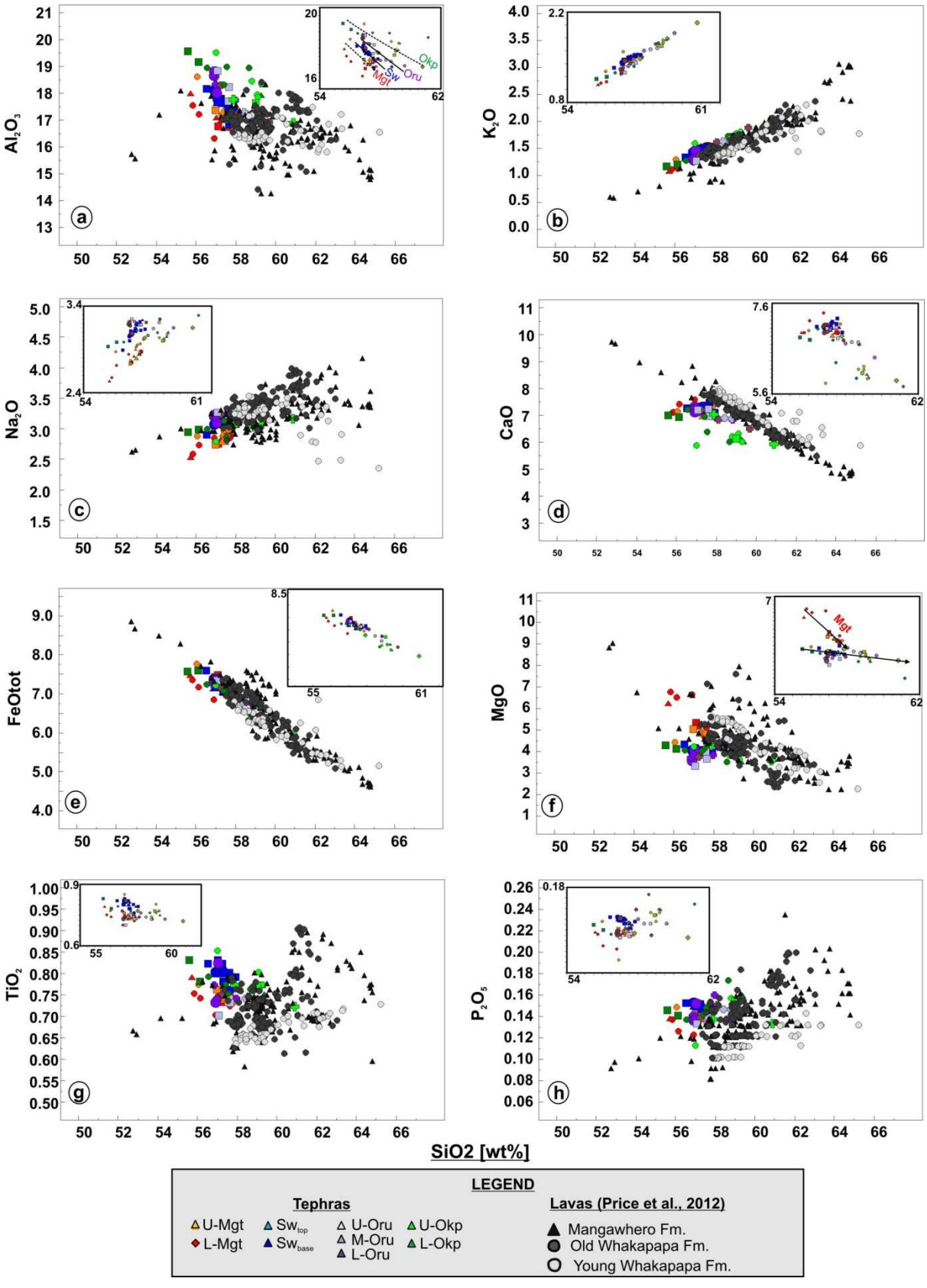

Figure 7.3 Harker diagrams of whole-rock composition from the studied Ruapehu tephras, showing the variation of major oxides with silica content and the comparison to published data on lava formations reported by Price et al. (2012). The colours correspond to the legend of Figs. 1 and 2. In inset boxes only tephra data are shown.

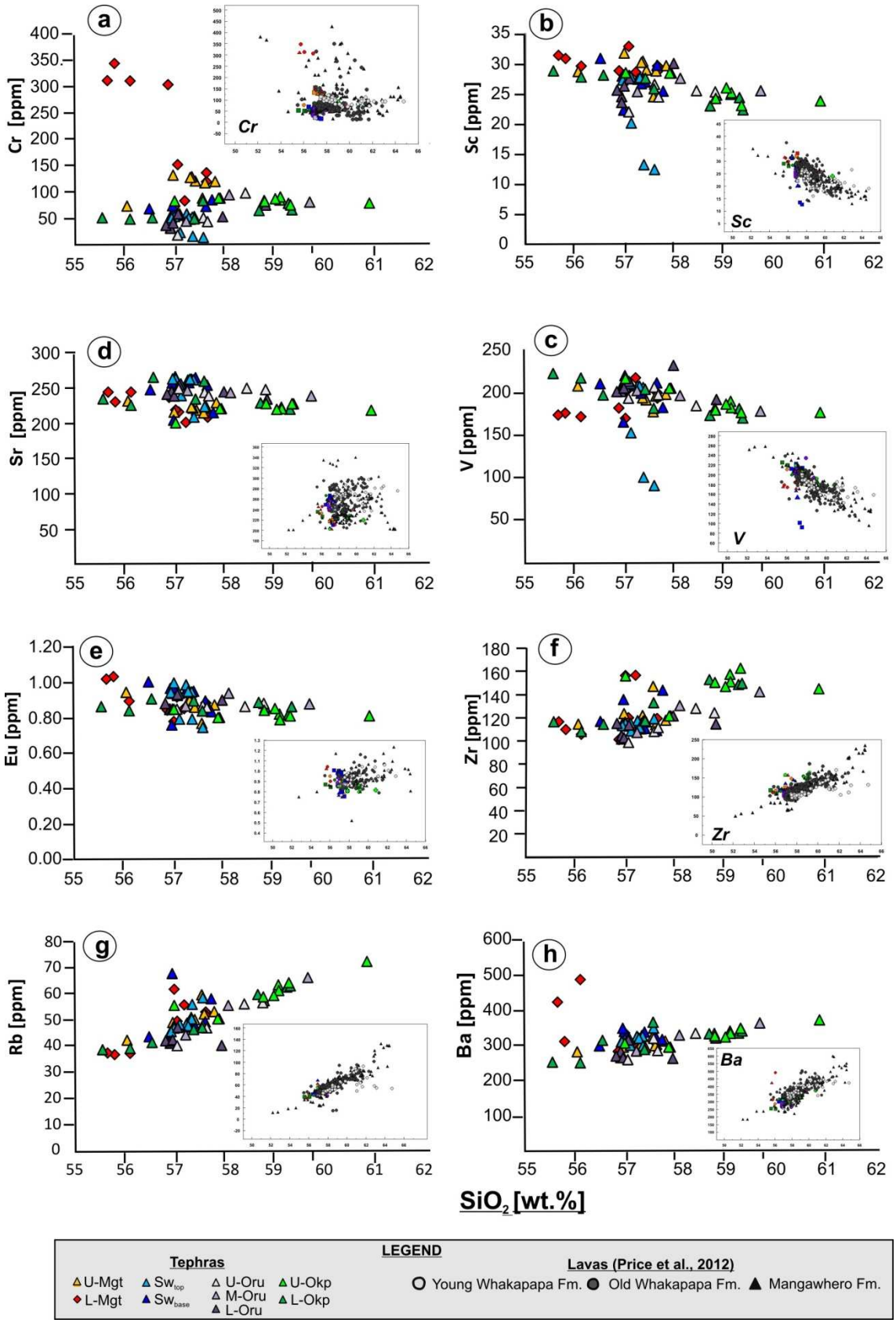

Figure 7.4 Harker diagrams showing the variation of trace elements with silica content. Note Ni and Cu show the same trend as Cr (**a**); Ti shows the same trend as Sc (**b**); Ga shows the same trend as V (**c**); Sr does not show significant variations with silica content (**d**); Gd, Tb, Dy, Ho, Er, Tm, Yb, Lu show the same trend as Eu (**e**); Nb, Y, Hf, Th, U show the same trend as Zr (**f**); Cs is incompatible as Rb (**g**); La, Ce, Pr, Nd, Sm show the same trend as Ba (**h**).

Variations in trace element concentration (**Fig. 7.4**) also show differences between eruptive units and indicate varying degrees of crystal fractionation within any given sample suite. For example, strongly decreasing concentrations of Cr and Ni with SiO_2 in Mgt samples indicate fractionation of olivine in this oldest, most primitive magma (**Fig. 7.4a**), but this trend does not occur in younger units (**Appendix F.1**). Pyroxene fractionation is indicated by the negative Sc against SiO_2 and Fe-Ti oxide fractionation is indicated by decreasing Ti and V with silica content (**Fig. 7.4b, c**). The crystallization of calcic plagioclase is also indicated by the negative trends of Sr and Eu (**Fig. 7.4d**). Other incompatible elements, such as Zr, Rb, and Ba show positive correlations with silica content (**Fig. 7.4g, h**).

The variation in composition with time is most obvious on Harker diagrams of major elements FeO_{tot}, CaO and Na_2O and trace elements Cr, Ni, Cu, Rb, Cs and Zr with MgO (**Fig. 7.5**). Both FeO_{tot} and CaO show two trends, differing before and after the Oruamatua eruptive unit. Incompatible trace elements generally decrease with increasing MgO (**Fig. 7.5e, f**).

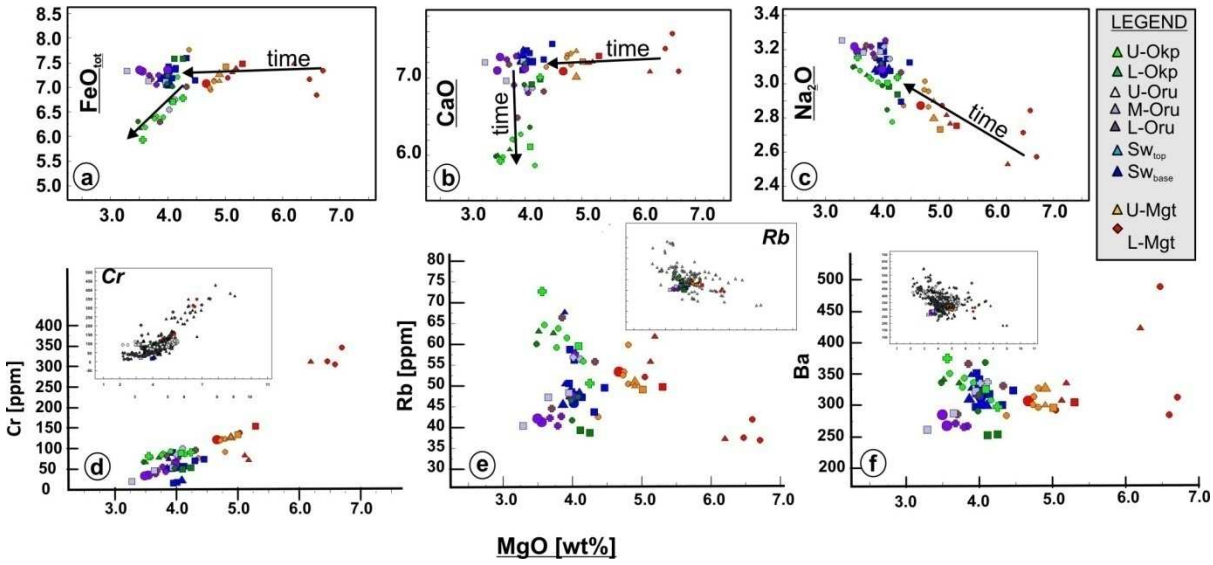

Figure 7.5 Harker diagrams of whole-rock geochemistry (See **Chapter 2.2.7** for analytical details) showing the variation of: **a)** FeO_{tot} [wt.%]; **b)** CaO [wt.%]; **c)** Na_2O [wt.%]; **d)** Cr, with Ni and Cu showing the same trend; **e)** Rb, with Cs and Zr showing the same trend; and **f**) Ba [ppm] with MgO content. The general trends indicated by data published by Price et al., (2012) on coeval lava formations are shown in inset boxes.

7.2.2 Groundmass glass and glass inclusions

The whole-rock chemical compositions are consistent with a single magma reservoir for each of the eruptives studied here. However, when integrated with textural data, groundmass and inclusion glass compositions, and volatile contents (**Fig. 7.6; Table 6.6; Appendices F** and **I**), more complex processes of polybaric crystallization are inferred. This is also indicated by the large plagioclase phenocrysts being both zoned/euhedral and sieved/subhedral-anhedral (**Appendix D.1**). Results presented in **Chapters 5** and **6** show that a majority of phenocrysts did not crystallize from the magma in which they were erupted. The decrease in silica content from melt inclusions to groundmass glass may alternatively indicate a rejuvenation of crystallising magma stored between 7 and 4 km in the crust (**Tables 6.3** and **6.4**), by injection of more primitive and hotter new magma. This process also explains the dissolved margins of many phenocrysts, such as micro-embayments of clinopyroxenes (**Appendix D.1**) and resorbed borders in plagioclase (**Appendix D.2**).

Sealed glass inclusions of similar chemical composition have variable volatile contents, indicating entrapment of melts at different pressures (c.f., Blundy and Cashman 2001). Some pyroxene crystals have higher volatile contents in the most siliceous glass inclusions, indicating that the magma was undersaturated in volatiles when these pyroxenes crystallized (c.f., Blundy and Cashman 2001). Therefore, solubility models give only minimum depths. In Mgt and Sw eruptives, these glass inclusions are more siliceous than groundmass glass (**Fig. 7.6a**). Considering measured volatile contents and precluding any post-entrapment modification of inclusions (e.g., Frezzotti 2001), these data suggest that crystallization occurred in pre-existing storage systems located at minimum depths of 7 km for the L-Mgt, 4 km for the U-Mgt, and 7 km for the Sw unit (**Tables 6.3** and **6.4**). These inclusion-bearing crystals were entrained by the later, more mafic erupting magma, which interacted with the shallow storage system, adding heat and pressure. Similar cases where new, hotter magmas enter partially crystallized magma reservoirs to remobilize the more evolved magmas are extensively documented (e.g., Venezky and Rutherford 1997; Murphy et al., 2000; Takeuchi and Nakamura 2001; Zellmer et al., 2003; Kennedy and Stix 2007).

All the lines of evidence point towards the Mgt and Sw events being triggered by the rejuvenation of a shallow storage system (**Figs. 7.7a, b**). Whole-rock data of Mgt (**Table 7.1; Figs. 7.3-7.5**) indicate that it was probably the deepest stored magma of the analysed series,

where olivine crystallized. Groundmass glass chemistry is consistent with the L-Mgt, involving both crystal-rich and crystal-poor magma components (**Fig. 7.6a**). The U-Mgt only involved the crystal-rich component, consistent with a shallow arrest and/or slowest magma ascent rate. By contrast, the Sw groundmass glass compositions (**Fig. 7.6b**) indicate a continuous crystal fractionation within a homogeneous reservoir. The melt inclusions that entrained pyroxenes were formerly in equilibrium with dacitic and rhyolitic melts.

In the case of the Oru unit, glass inclusion compositions plot within the same region as for Mgt and Sw (**Fig. 7.6c**), but are more mafic than associated groundmass glass. Okp glass inclusions are similar to the groundmass glass (**Fig. 7.6d**), indicating that they remained in contact with the melt until shortly prior to eruption, through capillary paths via crystal cleavage and/or twin planes (c.f., Stewart and Pearce 2004; Signorelli et al., 1999; Cashman and McConnell 2005). Although compositional data of Oru and Okp are consistent with "normal" crystal fractionation processes, the evolved composition of groundmass glass may be only the product of microlite crystallization. Eruptive units younger than Oru suggest late stage, syn-eruptive degassing-induced crystallization (e.g., Blundy and Cashman 2005) within the conduit, or at least, above the level recorded in non-leaky glass inclusions. Therefore, further studies on groundmass glass and melt inclusion trace elements, beyond the purpose of this study, could help to clarify if Oru and Okp were related to the shallow system where pyroxenes crystallized (i.e., true pre-eruptive storage system) or if the difference in groundmass glass composition is due to shallow conduit crystallization but the storage system was the same as Mgt and Sw. Magma temperatures estimated from clinopyroxene and orthopyroxene pairs, indicate that the youngest magmas where significantly colder than Mgt and Sw magmas. The extensive micro-jigsaw-cracked crystals and common disaggregated xenoliths, xenocrysts, and antecrysts (c.f., Jerram and Martin 2008) within Oru, Ak, and Okp-Ph pumice clasts appear to support "defrosting" of these crystal-rich magmas (c.f., Jerram et al., 2003; Huber et al., 2010).

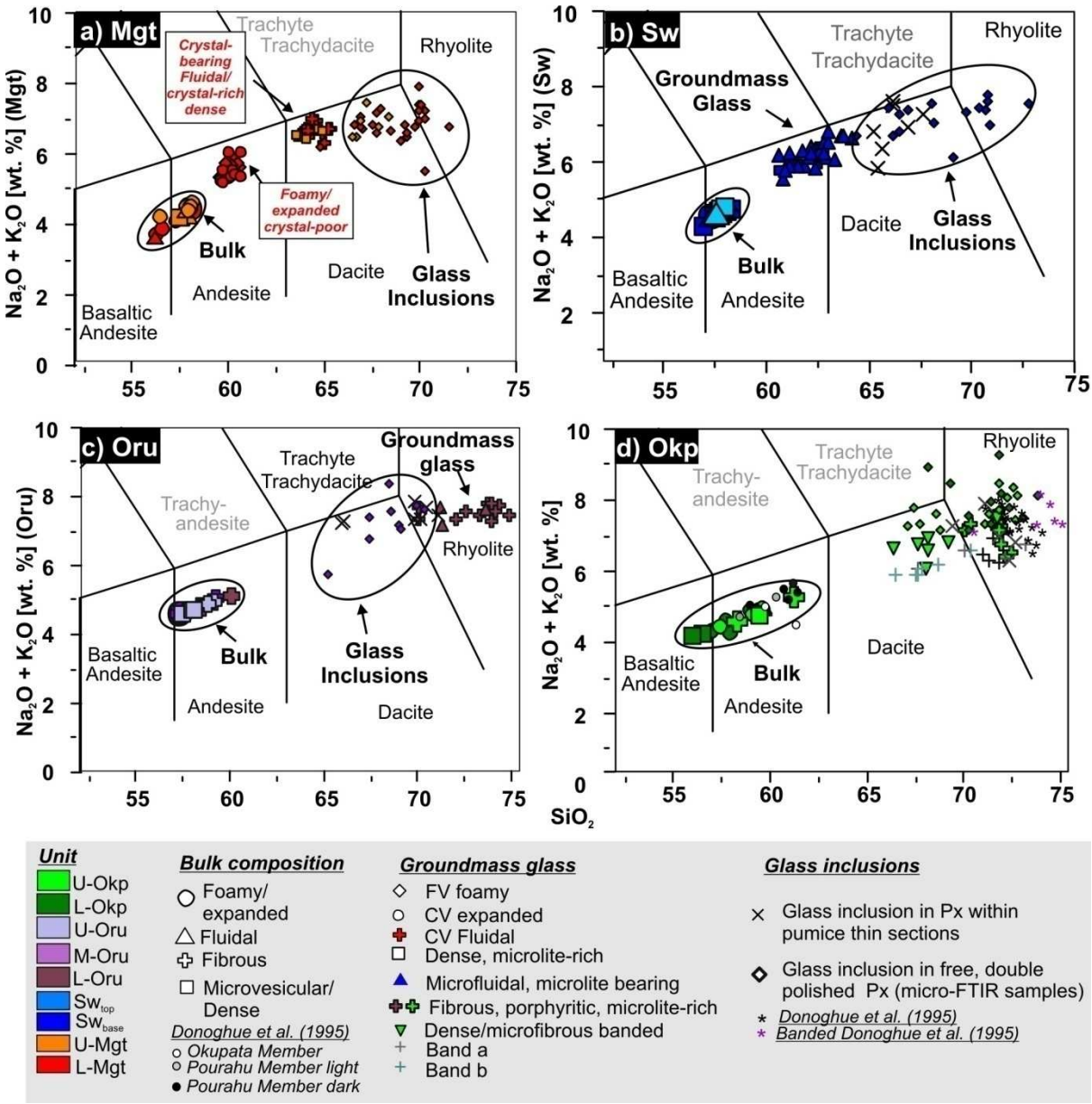

Figure 7.6 TAS diagrams (Le Bas et al., 1986) showing bulk, glass groundmass and glass inclusions compositions for: **a)** the Mangatoetoenui, **b)** Shawcroft, **c)** Oruamatua, and **d)** the Okupata-Poruahu eruptive units. The most silica-rich glass inclusions relative to groundmass glass are shown in **a**-and-**b**, and the change to more evolved residual glass compositions is seen in **c**-and-**d**.

This study (**Chapter 5, Appendices D, F**) indicates that pumice banding in Okp-Ph eruptives (and in the Oru and Ak units) resulted from shear between zones of contrasting rheology in the magma across its conduit, rather than mingling in the storage system. Local heterogeneous rheological conditions of the viscous magma reaching the base of the conduit were probably accentuated by degassing processes, with variable crystal and bubble growth stages, as well as variable vesicle shapes modulating the rheology of the rising magma and favouring local shear. Thus, the heterogeneous textures within these units are mainly a

consequence of conduit processes, including complex flow dynamics, viscous dissipation, local heating, crystal grinding, and resorption due to shearing at conduit walls (e.g., Rosi et al., 2004).

7.2.3 Storage and magma supply model for Ruapehu Plinian eruptions

Price et al., (2005, 2012) suggest that the storage system responsible for Ruapehu eruptions involves a range of connected and isolated magma reservoirs located in the mid-upper crust (**Fig. 7.7**).

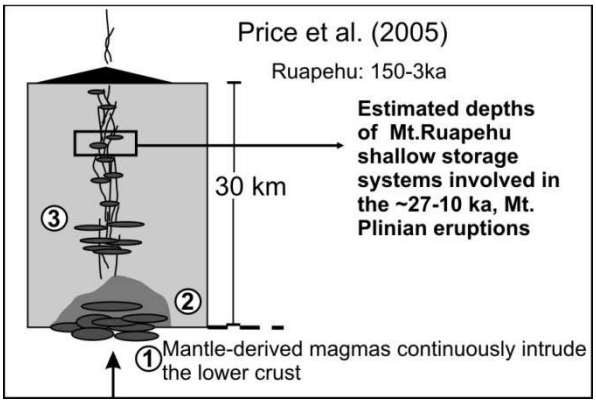

Figure 7.7 Schematic diagram proposed by Price et al., (2005) showing Mt. Ruapehu magmatic system. This system includes: 1) underplating basaltic magmas heating the lower crust; 2) fractionation of lower-crust magmas and interaction between them and mantle-derived magmas; 3) The generation of smaller and dispersed storage systems throughout the crust, subject to fractionation and crustal assimilation, mixing and mingling.

The tephra units studied here indicate that at least two to three connected upper-crustal magma reservoirs were involved in their eruption. A deeper reservoir (8-16 km considering the thickness of the quartzo-feldspathic crust above the "heavily intruded or underplated lower crust" in this region; Harrison and White 2006) provided the most mafic, crystal poor component. An overlying shallow-body, extending from 4-7 km in depth, was the site of mixing processes (**Fig. 7.8**). This upper region increased in geochemical and physical heterogeneity over the time frame studied here. The degree of mingling and mixing dictated the physical conditions of the magma supplied to the base of the eruption conduit.

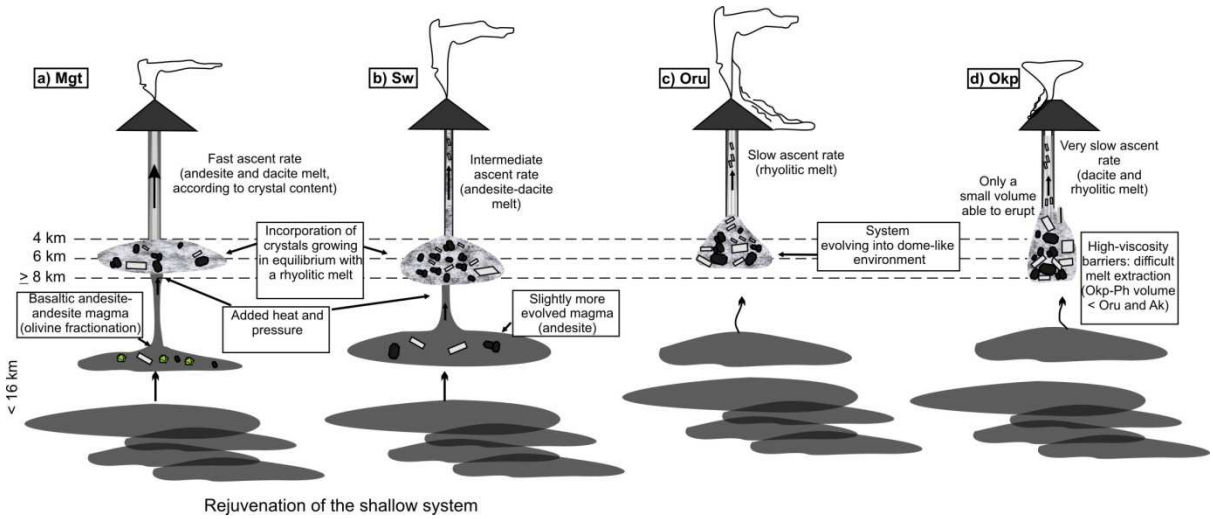

Figure 7.8 Schematic representation of the changes in magma storage system inferred for the Plinian eruptions of Mt. Ruapehu between ~27 and 10 ka BP cal. Different degrees of mingling and mixing occurred in the upper crustal magma reservoir producing: **a)** Mangatoetoenui; **b)** Shawcroft, **c)** Oruamatua, and **d)** Okupata-Pourahu eruptive units. The most chemically homogeneous system was associated with the Sw eruption.

7.3 Conduit dynamics during Ruapehu Plinian eruptions

The largest eruptions of composite volcanoes require conditions favourable for generating coupled degassing and corresponding delayed nucleation of vesicles during magma ascent (Nairn and Cole 1981; Froggatt and Lowe 1990; Klug and Cashman 1996; Cioni et al., 2000, 2003; Rosi et al., 2004; Rust and Cashman 2004; Sable et al., 2006; Gonnermann and Manga, 2007). These conditions can be achieved through internal limitations, mainly kinetic-viscosity barriers such as degassing-induced crystallization, or alternatively, external factors acting on the magma body, such as high ascent and decompression rates (Cashman et al., 2000). The detailed study of pyroclast textures over the past 20 years has revealed how variations in rheology of the fragmenting magma in the conduit may generate a strong influence on the eruption style. The coexistence of two to three juvenile pumice types, similar in mineralogy, glass and bulk composition, but contrasting in colour and texture, are extensively documented in andesitic-rhyolitic eruptions around the world (e.g., Gardner et al., 1998; Hammer et al., 1999; Polacci et al., 2001; Arce et al., 2005; Sable et al., 2006; Wright et al., 2007; Bouvet de Maisonneuve et al., 2009). Variations in textures and composition through a stratigraphic sequence may reflect transitions in eruptive dynamics with time (e.g., Gurioli et al., 2005), whereas a wide range in pumice textures at any stratigraphic level implies heterogeneity in

magma rheology across and throughout a conduit (e.g., Lirer et al., 1973; Waitt et al., 1981; Hoblitt and Harmon 1993; Gardner et al., 1998; Hammer et al., 1999; Polacci et al., 2001; 2003; Taddeucci and Wohletz 2001; Klug et al., 2002).

7.3.1 Vesiculation and crystallization processes

In the case of Mt. Ruapehu Plinian units studied, complex polybaric crystallization processes occurred to produce polymodal mafic crystal size (CSD) and cumulative crystal size distributions (CCSD) (**Appendix H.3**). Three-dimensional estimates of mafic crystal number densities of these units are 10^5-10^6 cm^{-3} (vesicle-free), which is very similar to, or one order of magnitude higher than corresponding vesicle number densities (10^4-10^6 cm^{-3}). This indicates that multiple events of crystal nucleation and growth favoured heterogeneous bubble nucleation (**Chapter 6.4.1**).

In the earlier phases of the Mangatoetoenui eruption (L-Mgt), vesicle coalescence, efficient vesicle wall retraction and high connected porosity was developed (**Chapter 6.2.1**), indicating that the bubble expansion rate of this magma was faster than permeable gas flow rates (c.f., Rust and Cashman 2011). This process caused rapid buoyant acceleration of the magma towards the surface. X-ray microtomography results (**Chapter 6.2.1**) indicate that bubble nucleation, diffusion, and expansion were variable across and along the conduit, generating a heterogeneous rheology (c.f., Jaupart 1998; Belien et al., 2010). A single bubble nucleation event but variable growth processes occurred in the central and/or deepest, crystal-poor conduit under the highest magma ascent/decompression rates. This was favoured by the low melt viscosity (melt: 0.4 Pa·s) and "primitive" composition of the Mgt magma (**Chapters 5.2.1** and **6.4.1**). Staged bubble nucleation and growth occurred in crystal-richer parts of the Mgt magma, rising more slowly closer to the conduit margin and/or stalled at shallow levels in the conduit. The Mgt event involved eruption of magma that travelled along different flow paths with variable ascent rates, experiencing a range in decompression rates, degassing and crystallization histories (**Fig. 7.9**).

In the U-Mgt eruption, magmas ascended more slowly and had a shallower and longer residence time in the conduit than the L-Mgt, as indicated by higher microlite crystallization and more siliceous glass compositions. This produced a greater density of initial bubble

nuclei relative to L-Mgt, but bubble growth and post-coalescence retraction was hindered by high melt viscosity (melt: 0.5 Pa·s). The microvesicular U-Mgt lapilli reflect that the magma underwent a single bubble nucleation and growth event, rapidly following decompression.

Microtextural and geochemical data indicates that the magma rising along the conduit feeding Sw eruption was chemically and physically homogeneous. The typical microvesicular and dense Sw lapilli indicate that the magma underwent a single bubble nucleation stage and the resulting bubble size distribution was mainly controlled by growth under decompression (i.e., coalescence and collapse). In addition, the high microlite content suggests syn-eruptive, degassing-induced crystallization.

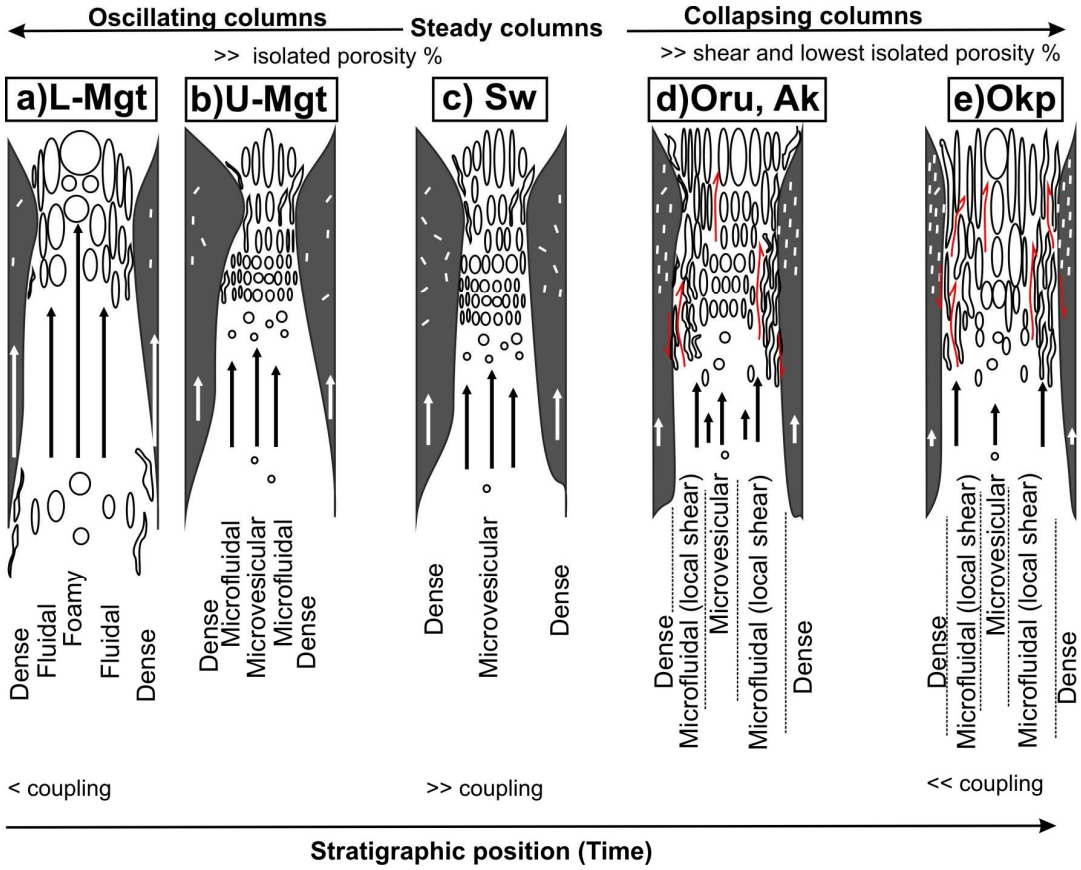

Figure 7.9 Schematic representation of the conduit processes occurred during the studied, Late Pleistocene, Mt. Ruapehu, Plinian eruptions. Dark grey zones correspond to the conduit lining material of slowest ascent rate (i.e. largest crystal content, densest clasts); Arrows point towards different ascent rates within and across the conduit: **(a)** L-Mgt-Highest ascent rates in the conduit centre; **(b)** U-Mgt-more degassed conditions with bubble expansion limited and microfluidal to dense zones being generated; **(c)** Sw-nearly homogeneous conditions, with vesicles forming under decompression at intermediate rates; **(d)** Oruamatua and **(e)** Okupata-Pourahu units where shearing bands developed along with slow ascent rates and variable bubble shapes, generating a complex flow regime. Local acceleration due to bubble shearing occurred in some zones (microfluidal); others had viscous stresses dominating, where subspherical vesicles behaved as rigid objects (microvesicular); friction occurred along conduit walls (dense/banded). In addition, for **(e)** intense shearing and very slow ascent rates favoured advanced bubble interconnection and development of permeable channels. The fragmentation front fluctuated with time and in space according to the local pressure (density) and balance between fragmentation speed and ascent rates.

The main difference between the Oru and Okp-Ph events compared to earlier eruptives studied here lies in the highly evolved groundmass glass chemistry (**Fig. 7.6**) and sheared pumice textures. Estimated melt viscosities are in the order of 0.6-0.7 Pa·s. Vesicle growth and shapes were highly affected by bubble-bubble and bubble-crystal interactions (c.f., Saar and Manga 1999; Martel and Schmidt 2003). The Oru and Okp-Ph magmas were rheologically extremely heterogeneous due to localised gas-pockets developed and segregated under shearing across the conduit (**Fig. 7.9**). Sheared (microfibrous) and dense, microlite-rich regions were developed towards the conduit margins. There, lithic incorporation from country-rock and crystal grinding also occurred.

The large plagioclase and pyroxene phenocryst size and high microlite contents (**Figs. 5.19, 5,21, 5.25-5.27; Appendix H.3**), together with the evolved groundmass glass composition indicate slow decompression rates and advanced degassed-induced crystallization (c.f., Cichy et al., 2011). Each zone within the differentially rising conduit (c.f., Sable et al., 2006; Bouvet de Maisonneuve et al., 2009) was subject to different bubble growth mechanisms, including elongation, coalescence, and collapse. These differences were most extreme in the Okp-Ph unit, because this magma had the highest exsolution depths and/or longer degassing times favouring multiple stages of bubble nucleation and growth with advanced coalescence and bubble collapse before fragmentation (**Tables 6.5** and **6.6**). The high melt viscosity and heterogeneous conditions across the conduit formed a variety of pumice textures, including banded clasts through shearing in Oru, Ak, and Okp-Ph.

7.3.2 Magma fragmentation and eruptive mechanisms

For all studied eruptions the opening phase was phreatic (Mgt) or phreatomagmatic (Sw-Okp; **Chapters 3 and 4**). Following the experimental models presented by Speiler et al., (2004a,b), fragmentation occurred at a deeper level for the most primitive, crystal-poor, highly vesicular L-Mgt magma. Apart from this, variable rheological states of the magma reaching the fragmentation level (c.f., Rust and Cashman 2011) in the youngest units, imply variable local density/porosity conditions which could drive variable fragmentation depths and speed across the conduit. This variability is proportional to column unsteadiness.

Two main fragmentation styles were identified in the studied units (**Chapter 5**), which could act separately or in combination:

1) **Decompression** dominated fragmentation, where the strain rate applied to the mixture exceeds the liquid viscous relaxation rate, forcing the bubbly magma to cross the glass transition boundary (e.g., Dingwell 1996; Deubener et al., 2003). Rapid changes in bubble internal pressure and expansion generate downward-propagating fragmentation waves. This process occurred during the L-Mgt where expanding vesicles provided weak surfaces (**Fig. 7.10a**), and dominated during the U-Mgt and Sw eruptions (**Fig. 7.10b**), where vesicle growth was restricted by other vesicles and crystals (i.e., where bubble overpressure was favoured). Phreatomagmatic interaction with hydrothermal fluids may have enhanced fragmentation efficiency in Sw as indicated by its high lithic content within the fine ash fractions (<3ϕ) and the glass-shards morphology (**Chapter 5**), but gas exsolution and decompression were dominant (i.e., magmatic processes were dominant).
2) **Shear** dominated fragmentation, where dense and low-vesicularity magmas are driven towards fragmentation by decompression and extreme shear rates (i.e., larger than relaxation, decompression, and ascent rates; e.g., Dingwell 1996; Deubener et al., 2003; Whittington et al., 2009; Gardner et al., 1996). Magma shear predominated or act in combination with decompression during the Oru and Okp-Ph eruptions, which had very viscous melts (0.7 Pa·s). Water-magma interaction also played a major role in increasing the fragmentation efficiency for Oru event (**Fig. 7.10c**). By contrast, the Okp-Ph was considerably more degassed at the moment of fragmentation (**Fig. 7.10d**) and no external water interaction occurred; therefore, fragmentation was least efficient.

Ash production and fragmentation

The L-Mgt unit dominantly contains ash with nearly spherical vesicles and a minor proportion with elongate vesicles (interpreted to originate from high shear conditions at the conduit margin; c.f., Rust et al., 2003). Rare, phenocryst and microlite-bearing, very finely to poorly vesicular ash was also produced from the outer, degassed areas of the conduit that underwent slow ascent rates (c.f., Massol and Jaupart 1999). Ductile deformation affected particles that underwent slow cooling after fragmentation, producing smooth, fluidal surfaces.

These particles, including some Pelée's tears, were likely derived from the regions of lowest viscosity and ejected under extreme exit velocities (c.f., Shimozuru 1994), (**Fig. 7.10a**).

The U-Mgt was characterised by finely vesicular, crystal-rich ash particles similar to the rare fragments from the outer conduit margins of the L-Mgt event. The U-Mgt ash (**Fig. 7.10b**) has more mature textures with collapsed vesicles and high crystal contents. These ash textures corroborate that the magma remaining after the L-Mgt was contained in a shallow level and subject to advanced undercooling, degassing, and crystallization (c.f., Tuttle and Bowen 1958, Nakada and Motomura 1995, Hammer et al., 1999).

The Shawcroft lapilli contained a high lithic content (up to 31 vol.% in the 3 ϕ size fraction), indicating conduit wall instability and extreme abrasion and erosion of the hydrothermally altered parts of the conduit (e.g., Macedonio et al., 1994; Woods 1995). This allowed the access of hot geothermal fluids (c.f., Papale et al., 1998; Houghton et al., 2004), but evidence of phreatomagmatic fragmentation is lacking (distinctive quenching cracks, abundant stepped-surfaces; c.f., Büttner et al., 1999; Dellino et al., 2001; **Chapter 5**) Instead, decompression stresses exceeding the relaxation rate of over-pressured bubbles (**Fig. 7.10b**), probably aided by fluid-instabilities generated during the contact with the hydrothermal fluids, drove highly explosive fragmentation (e.g., McBirney and Murase 1970; Alidibirov 1994; Koyaguchi and Mitani 2005; Koyaguchi et al., 2008). Abundant Pelée's tears and fused-shaped (c.f., Sheridan and Wohletz 1983) particles indicate common post-fragmentation, ductile behaviour, extreme exit velocities and slow quenching rates of the melt (>1000^{0}C in Mgt and Sw).

For the Oruamatua and following eruptions, slow ascent rates (**Fig.6.17**) and the non-Newtonian, complex flow dynamics with variable rates of magma ascent and degassing, produced highly variable rheologies of the magma reaching the fragmentation level (e.g., Caricchi et al., 2007; **Figs. 7.9d, e**). This promoted heterogeneous modes of fragmentation with multiple ash morphologies and variable fragmentation depths across the conduit, according to local density (**Fig. 7.10c**).

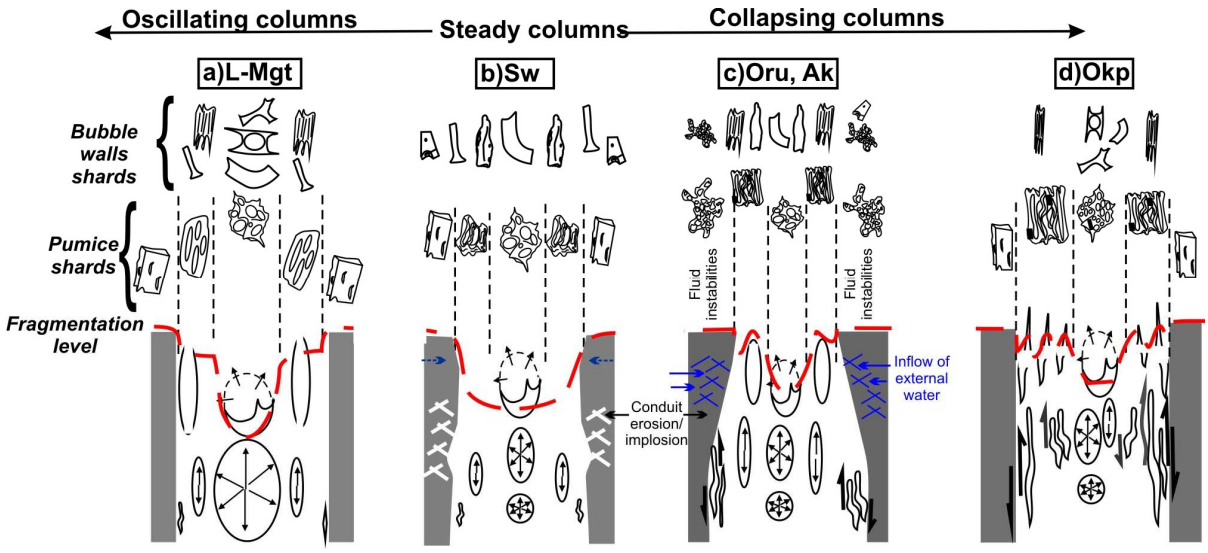

Figure 7.10 Schematic representation of the variation in fragmentation processes that occurred during the studied, Late Pleistocene, Mt. Ruapehu, Plinian eruptions. **(a)** Magma fragmentation of older eruptions, represented by the Mangatoetoenui Unit was expanded-acceleration dominated. **(b)** Following eruptions represented by the Shawcroft Unit were decompression-dominated; whereas **(c)** younger eruptions were characterized by shear-induced fragmentation with magma-water during the Oruamatua and Akurangi units and **(d)** dry, but weak fragmentation conditions during the Okupata-Pourahu eruption. The variability of fragments found within a particular unit reflects the heterogeneity of the magma reaching the fragmentation level at different rates.

Fibrous and tube-like shards show that high strain levels extended to the top of the conduit, while re-melted surfaces indicate that the particles remained deformable after fragmentation (c.f., Rust and Manga 2002; Stein and Spera 2002). Oru, Ak, and Okp-Ph ash morphologies indicate a feedback process operated, alternating between rapid decompression (e.g., Cashman et al., 2000), and shear-induced fragmentation (c.f., Dingwell 1996; Mader et al., 1996; Papale 1999; Zhang 1999). In addition, Oru ash also includes poorly vesicular, equant, moss-like and blocky to platy-shaped shards with distorted vesicles and thick walls, as well as hydrothermally altered lithic fragments (up to 23 % of the finest size fractions; **Appendix E**). Particles surface showing conchoidal fractures, grooves, stepped-surfaces and impact pits show that phreatomagmatism played a subsidiary role in the fragmentation of the dense, moderately vesicular Oru magma (**Table 6.1**). By contrast, a low degree of fragmentation is indicated by the grain-size distribution of Okp-Ph. A complex range of fragmentation mechanisms is indicated by the polymodal grain-size distribution, sheared-banded pumice textures, and the variability of ash morphologies (**Fig. 7.10d**).

7.4 Implications for column height, stability, and pyroclast dispersal

In the last three decades significant advances in the understanding of the physics of explosive volcanic eruptions have been made (e.g., Freundt and Rosi, 1998; Gilbert and Sparks, 1998; Sigurdsson et al., 2000). Drivers of explosive Plinian eruptions include: the kinetics and timescales of crystal nucleation and growth (e.g., Gardner et al., 1995; Rutherford and Devine 1996; Rutherford 1998), volatile content, speciation, and exsolution in magmas (e.g., Johnson et al., 1994; Lange 1994), rheology and rheological changes during ascent (e.g., Hess and Dingwell 1996; Giordano and Dingwell 2003), as well as conduit conditions. The main relevant conduit processes include coupled vs. decoupled degassing and development of magma permeability (e.g., Klug and Cashman 1996; Rust and Cashman 2004; Gonnermann and Manga 2007; Wright et al., 2007); degassing-induced crystallization (Geschwind and Rutherford 1995); development of localized strain, viscous dissipative heating, crystal fragmentation and resorbtion along conduit walls (Polacci et al., 2001, 2003; Rosi et al., 2004; Wright and Weinberg 2009).

The current models of explosive eruptions and column stability consider both magmatic and external factors (e.g., Cioni et al., 2003; Houghton et al., 2004). For example, factors known to control the steadiness of convective eruption columns include magma chemistry, volatile content, magma supply rate and its relation with magma discharge rate, conduit and vent geometry (Wilson 1976; Carey and Sirgudsson 1989; Woods 1995; Adams et al., 2006). These factors do not act independently but specific combinations of vent radius, gas velocity and gas content determine whether columns are buoyant or collapse (c.f., Sparks and Wilson 1976; Wilson et al., 1980), particularly if they lead to a disparity between magma supply and discharge rate (Bursik 1993; Cioni et al., 2000, 2003; Arce et al., 2005).

The Plinian units studied from Mt. Ruapehu show a correlation between chemical variability, rheology of the erupting magma, and the resulting eruptive behaviour. In eruptions involving narrow ranges in bulk composition, the most stable eruptive columns are formed, showing the narrowest range of pumice textures (e.g., Shawcroft eruption). For the most variable bulk compositions, partially or fully collapsing eruptive columns form, along with the most heterogeneous pumice textures (e.g., Oruamatua, Akurangi, and Okupata-Pourahu eruptions). Intermediate between these extremes and with intermediate ranges in composition, unsteady,

vertically variable, but non-collapsing columns are generated (e.g., Mangatoetoenui eruption), producing intermediate range in pumice textures.

The Ruapehu data show that physical uniformity of the magma at the base of the conduit varies in relation to the geochemical properties of the pre-eruptive storage system (**Chapter 7.2**). The magma supply rate is associated with the geochemical and related physical heterogeneities within the storage system (i.e. the nature of the mixture after varying degrees of mingling, mixing, crystal incorporation, crustal assimilation, etc., prior to the eruption). The complexity of eruptive discharge rates, in turn, is dictated by the segregation of magma across and along a conduit with differential ascent rates (e.g., Mader 1998; Massol and Jaupart 1999) and subsequent variable degassing mechanisms (**Chapter 7.3**). Ash morphologies produced at the fragmentation level respond to the local rheological state of the magma in a particular region within the conduit. Based on this understanding, the most geochemically heterogeneous storage systems hosting the most viscous (coldest) magmas, lead to the most variable supply rates and magma rheologies at the base of the conduit. These differences are accentuated along the conduit due to differential flow rates and also shear regimes developing along conduit margins. Collectively, these processes generate variably heterogeneous degassing in conduit cross-section and depth, along with widely variable vesicle (and crystal) nucleation and growth rates. The magnitude of these differences leads to different populations of pumice pyroclast textures observed in fall units.

The most complex magmatic conditions were predominant at Mt. Ruapehu between ~13 and 12 ka BP cal., producing the most violent eruptions known in the stratigraphic record (Oruamatua and Akurangi eruptive units). These were also associated with column instability and the generation of pyroclastic density currents. For the latest Plinian eruption (Okupata-Pourahu eruptive unit), related to a new conduit, the advanced degassed magma state at fragmentation, and therefore the shallow (and variable) fragmentation depth, was a crucial factor in generating a relatively low (25 km), collapsing column, but one which also collapsed to form pyroclastic density currents.

The influence of phreatomagmatism in the unsteadiness of the eruptive column has been widely documented in other volcanoes by Wilson et al. (1978), Cioni et al. (2003), Sulpizio et al. (2005), and Carey et al. (2010). External causes of column unsteadiness in the Ruapehu Plinian eruptions include water-magma interaction, as well as its temperature and depth of interaction. Despite inflow of hot, geothermal fluids associated with conduit erosion during

the Shawcroft eruption, a nearly steady high stratospheric column (29 km) persisted during the eruption. Higher, but partly unstable eruption columns during the Oruamatua and Akurangi eruptions were possibly influenced by interaction of cold groundwater to shallow levels of the conduit.

From theoretical models (Wilson et al., 1978), it is well established that the rate of thermal energy release is dependent on vent radius, density, and temperature of the erupting mixture. Conditions favouring the Shawcroft and Oruamatua column heights include the restricted bubble-growth, indicating high bubble-overpressure dramatically disrupted under decompression, the more "coupled" degassing relative to Mgt and Okp-Ph, and the fine fragmentation of pyroclasts. High degrees of fragmentation and high exit velocities in Shawcroft eruption point towards a greater dilution of the pyroclastic mixture which could easily enter the convection zone (c.f., Wilson et al., 1980). An external factor contributing to high columns, difficult to prove from ancient deposits, could be a reduced conduit/vent diameter (c.f., Kaminski and Jaupart 1997) relative to Mgt and Okp-Ph. A first estimation of temperatures based on Putirka (2008) 2-Px geothermometer (**Table 7.6**) indicates that magma temperature decreases with time. Therefore, for the case of Ruapehu, temperature effects where minimized by other factors controlling eruption height. Instead, it could play a significant role in favouring column unsteadiness, since temperature is known to be one of the major factors controlling viscosity (consistent with the resulting pumice textures).

7.5 Summary

The transitions observed in the lithofacies associations of Plinian eruption deposits from Mt. Ruapehu can be readily correlated to the microtextural and geochemical properties of the erupting magmas. The inferred eruptive parameters and column behaviour are intimately linked to pre-eruptive storage, conduit, and fragmentation conditions (**Tables 7.5** and **7.6; Figs. 7.6, 7.8-7.10**).

Table 7.5 Eruptive parameters calculated from field data and average componentry results (from counts on binocular and scanning electron microscope (SEM)) for the Mangatoetoenui (Mgt), Shawcroft (Sw), Oruamatua (Oru), and Okupata (Okp) eruptive units.

Unit	Eruptive parameters from field data										Sieving	Componentry + SEM						
Mgt	**Whole deposit volume [km^3]**	**Bscalc [km]**	**D [km2]**	**bt**	**bc**	**bc/ bt**	**Highest lobe HT [km]**	**MDR [kg/s]**	**Log (MDR)**	**M [kg]**	**Mz [mm]**	**G**	**X**	**L**	**A1**	**A2**	**A3**	**A4**
Average	0.3	31.4	2254	4.0	6.5	1.6	22	6.8E+07	7.8	4.4	**6**	**53**	**29**	**19**	**34**	**28**	**3**	**36**
L-Mgt$_{base}$											8	56	24	20	41	29	6	24
L-Mgt$_{top}$											5	32	53	15	26	26	0	47
U-Mgt											6	70	9	21				
Sw	**Whole deposit volume [km3]**	**Bscalc [km]**	**D [km2]**	**bt**	**bc**	**bc/ bt**	**Highest lobe HT [km]**	**MDR [kg/s]**	**Log (MDR)**	**M [kg]**	**Mz [mm]**	**G**	**X**	**L**	**A1**	**A2**	**A3**	**A4**
Average	0.6	59.3	8483	7.8	5.6	0.7	29	1.5E+08	8.2	4.9	**10**	**42**	**28**	**31**	**22**	**18**	**26**	**34**
Sw-base											9	38	32	31	10	23	19	48
Sw-Top											11	45	24	31	33	13	33	20
Oru	**Whole deposit volume [km3]**	**Bscalc [km]**	**D [km2]**	**bt**	**bc**	**bc/ bt**	**Highest lobe HT [km]**	**MDR [kg/s]**	**Log (MDR)**	**M [kg]**	**Mz [mm]**	**G**	**X**	**L**	**A1**	**A2**	**A3**	**A4**
Average	0.5	62.9	9600	8.3	9.8	1.2	37	6.0E+08	8.8	4.9	**3**	**38**	**38**	**24**	**25**	**13**	**19**	**42**
L-Oru											6	43	39	18	33	33	22	11
M-Oru											1	33	41	25	13	6	16	65
U-Oru											3	37	33	30	30	0	20	50
Okp	**Whole deposit volume [km3]**	**Bscalc [km]**	**D [km2]**	**bt**	**bc**	**bc/ bt**	**Highest lobe HT [km]**	**MDR [kg/s]**	**Log (MDR)**	**M [kg]**	**Mz [mm]**	**G**	**X**	**L**	**A1**	**A2**	**A3**	**A4**
Average	0.4	45.7	4943	6.0	9.8	1.6	25	7.5E+07	7.9	4.6	**4**	**47**	**31**	**23**	**53**	**22**	**15**	**11**
L-Okp											3	51	26	23	68	0	11	21
U-Okp											5	42	35	23	38	44	19	0

Calculated whole deposit volume and break in slope (Bscalc) are given following Sulpizio (2005)
D = Fragmentation index proposed by Walker (1973)
bt = thickness half distance
bc = lithic clast half distance
bc/bt= half distance ratio: fragmentation index proposed by Pyle (1989)
HT = total column height estimated from the lobe of highest HT, following Sulpizio (2005)
M = eruptive magnitude as calculated from Pyle (2000)
Mz = Mean diametre from grain size analysis
Glass (G), Crystals (X), and Lithic(L) content in the 3 ϕ size fraction
A1: highly vesichular ash shard; A2: Fluidal shard; A3: Fused/Pelean shard; A4= poorly vesicular/blocky shard
Ves*: Average vesicularity corrected for phenocrysts and microlite contents, and based on relative proportion of each textures in each unit

Table 7.6 Textural and geochemical parameters obtained from He-Pycnometry, X-ray microtomography, X-ray fluorescence (XRF) and Electron Microprobe (EMP) in correlation with the fragmentation index D (Walker 1973), and volatile content obtained with infrared microscopy (micro-FTIR).

	Envelope and gas-pycnometry						X-ray microtomography							XRF	EMPA		FTIR		
Mgt	**Bulk density [g/cm^3]**	**Skeletal density [g/cm^3]**	**Solid density [g/cm^3]**	**Bulk porosity [vol.%]**	**Connected porosity [vol.%]**	**Isolated porosity [vol.%]**	**Ves* [%] gas pyc**	**Ves* [%]**	**Mafic X_{melt} [%]**	**Mean vesicle diameter [µm]**	**Nv* [mm^{-3}]**	**mafic Nx_{melt}* [mm^{-3}]**	**Oxide Nxmelt* [mm-3]**	**SiO_2 bulk [wt.%]**	**SiO_2 groundmass glass [%]**	**SiO_2 glass inclusions [%]**	**H2O [wt.%]**	**Estimated pressure (Mpa)**	**Calc. T [°C]2Px**
AVERAGE	**0.93**	**2.71**	**3.50**	**73.03**	**64.91**	**8.99**	**54**	**47**	**24**		**312**	**2734**	**213**	57.5	63.07	68.2			1120
L-Mgt$_{base}$	0.64	2.23	3.20	79.91	68.77	11.15	57	51			312	3114	291	57.3	61.45	69.1	5.3	192	
L-Mgt$_{top}$	0.79	3.27	3.50	76.88	74.01	2.87					312	2355	135		64.27	67.3	3.6	106	
U-Mgt	1.28	3.24	3.80	64.42	59.51	4.91	52	42						57.8					
Foamy	0.86	2.79	3.30	73.88	67.49	6.39	64	62	18		302	4216	0	57.6	60.25				
Fluidal	0.88	2.60	3.40	73.79	65.54	8.25	55	51	16		312	2953	303	57.4	64.70				
Microfluidal	1.08	2.83	3.70	70.73	60.92	9.81	43	23	37		316	96	58	57.5	64.27				
Sw	**Bulk density [g/cm^3]**	**Skeletal density [g/cm^3]**	**Solid density [g/cm^3]**	**Bulk porosity [vol.%]**	**Connected porosity [vol.%]**	**Isolated porosity [vol.%]**	**Ves* [%] gas pyc**	**Ves* [%]**	**X_{melt}[%]**	**Mean vesicle diameter [µm]**	**Nv [mm^{-3}]**	**Nx [mm^{-3}]**	**Oxide Nxmelt* [mm-3]**	**SiO_2 bulk [wt.%]**	**SiO_2 groundmass glass [%]**	**SiO_2 glass inclusions [%]**	**H2O [wt.%]**	**Estimated pressure (Mpa)**	**Calc. T [oC]**
AVERAGE	**1.25**	**3.07**	**3.40**	**62.52**	**58.93**	**4.53**	**41**	**36**	**17**		**300**	**3142**	**183**	57.7	62.34	66.1	5.4	198	1013
Sw-base	1.29	3.11	3.50	62.45	58.06	4.38								57.7					
Sw-Top	1.22	3.04	3.30	62.59	59.72	2.88								57.7					
Foamy	1.15	3.21	3.50	66.79	63.82	2.98	64	62											
Microfluidal	1.27	3.07	3.30	61.45	58.37	3.09	36	33	13		535	6621	173	57.8	62.15				
Dense	1.26	3.02	3.40	62.52	58.01	4.52	30	19	22		162	873	45	57.8	62.52				
Oru	**Bulk density [g/cm^3]**	**Skeletal density [g/cm^3]**	**Solid density [g/cm^3]**	**Bulk porosity [vol.%]**	**Connected porosity [vol.%]**	**Isolated porosity [vol.%]**		**Ves [%]**	**X_{melt}[%]**	**Mean vesicle diameter [µm]**	**Nv [mm^{-3}]**	**Nx [mm^{-3}]**	**Oxide Nxmelt* [mm-3]**	**SiO_2 bulk [wt.%]**	**SiO_2 groundmass glass [%]**	**SiO_2 glass inclusions [%]**	**H2O [wt.%]**	**Estimated pressure (Mpa)**	**Calc. T [oC]**
AVERAGE	**1.26**	**2.87**	**3.00**	**57.81**	**56.04**	**2.74**	**41**	**35**	**14**		**354**	**2639**	**80**	58.2	72.62	69.3	1.8	36	974
L-Oru	1.33	2.84	3.00	54.95	53.16	1.79								58.0					
M-Oru	1.13	2.92	3.00	62.55	61.11	1.44								58.8					
U-Oru	1.29	2.86	3.00	56.89	54.82	2.07								58.4					
Foamy	1.27	2.88	3.00	57.07	55.96	1.11	64	62						57.5					
Fluidal	1.17	2.88	3.00	61.60	59.59	2.01	45	33	6		533	1386	92						
Fibrous	1.17	2.87	3.00	60.68	59.04	1.64	44	34	20		518	3446	61	58.6	73.10				
Dense	1.32	2.87	3.00	55.85	53.80	2.05	33	29	15		226	1061	110	57.9	72.18				
Okp	**Bulk density [g/cm^3]**	**Skeletal density [g/cm^3]**	**Solid density [g/cm^3]**	**Bulk porosity [vol.%]**	**Connected porosity [vol.%]**	**Isolated porosity [vol.%]**		**Ves [%]**	**X_{melt} [%]**	**Mean vesicle diameter [µm]**	**Nv [mm^{-3}]**	**Nx [mm^{-3}]**	**Oxide Nxmelt* [mm-3]**	**SiO_2 bulk [wt.%]**	**SiO_2 groundmass glass [%]**	**SiO_2 glass inclusions [%]**	**H2O [wt.%]**	**Estimated pressure (Mpa)**	**Calc. T [oC]**
AVERAGE	**1.04**	**2.90**	**3.10**	**66.23**	**64.02**	**2.21**	**39**	**19**	**27**		**2234**	**4061**	**69**	58.7	69.61	71.5			977
L-Okp	1.16	2.91	3.00	61.75	59.96	1.80	44	25	8		422	422	81	58.0	70.72	70.1	5.4	199	
U-Okp	0.92	2.90	3.20	70.71	68.09	2.62	34	12	32		4047	4047	57	**58.7**	68.50	71.2	5.1	179	
Foamy	1.11	2.86	3.00	62.01	60.86	1.15	40	32			313	694	28	58.6					
Fibrous	0.92	2.90	3.10	70.59	68.19	2.41	51	41	22		3224	2217	153	59.8	68.50				
Dense	1.21	2.91	3.10	60.34	58.28	2.06	40	12	31		393	5760	34	57.4	70.72				

Ves: vesicularity; x: mafic crystallinity; N_v and N_x: vesicle and mafic crystal number density, respectively. Ves L= vesicle dominant diameter; n_o=initial vesicle nuclei; GT = growth rate (G) in a given timescale (T); XL= mafic crystal dominant diameter; liquid density (δ_{liq}), melt viscosity (ν) was calculated with the software norm x4, based on geochemical data. Magma temperature (T) was estimated from clinopyroxene and orthopyroxene pairs following Putirka (2008).

Over the period examined, the changes in eruption behaviour showed a consistent evolutionary pattern at Mt. Ruapehu. Initially, oscillating but non-collapsing Plinian columns (L-Mgt) were predominant. They occurred when mafic, rapidly rising magmas interacted with a shallower storage system (in equilibrium with dacitic to rhyolitic melts), incorporating phenocrysts, and experiencing different degassing mechanisms, causing variations in conduit diameter and reaching variable magma rheology at the fragmentation level (c.f., Cioni et al., 2000). In these cases, fragmentation was decompression-dominated and the local porosity-conditions may have played a significant role in causing spatial variations (c.f., Spieler et al., 2004) of the fragmentation depth across the conduit. Stable column conditions (e.g., U-Mgt, Sw) were reached when the magma was extracted from the most homogeneous systems after mixing and incorporation of crystals, and rising along the conduit at intermediate magma ascent/decompression rates to reaching the fragmentation level. In this case, fragmentation was also decompression-dominated, but the fragmentation depth was relatively uniform across the conduit.

Later, collapsing columns (e.g., Oru to Okp-Ph units) occurred when viscous magmas were extracted from crystal-rich (up to 23 %) reservoir and ascended very slowly. In these cases, differential decompression rates and multiple degassing mechanisms, within and across the conduit developed connected porosities and consistently lower isolated porosities than in the steady column cases. This also produced extreme rheological heterogeneity at the fragmentation level, with fragmentation being induced by decompression, strong shearing and in some cases, influenced by magma-water interaction. Following experimental modelling by Spieler et al., (2004), the high porosity unevenness across the conduit could have caused extreme variability of the fragmentation depth across the conduit favouring column collapse.

The highest eruption columns at Mt. Ruapehu produced deposits containing the lowest bulk and connected porosities (**Fig. 7.11**). For the Shawcroft and Oruamatua units, bulk porosities of 58-63 % indicate lower percolation thresholds than in the Mangatoetoenui and Okupata-Pourahu eruptions, where bulk pumice porosities are in the order of 73 and 66 %, respectively. This can be explained by the more mafic melt composition and low viscosity of the L-Mgt, which favoured almost de-coupled degassing mechanisms (c.f., Wilson et al., 1980; Papale et al., 1998; Sparks et al., 1994; Sable et al., 2006). By contrast advanced, pre-fragmentation permeability, with multiple bubble deformation processes (including collapse)

was advanced for Okp-Ph. Both conditions led to lower degrees of fragmentation relative to the Sw and Oru cases.

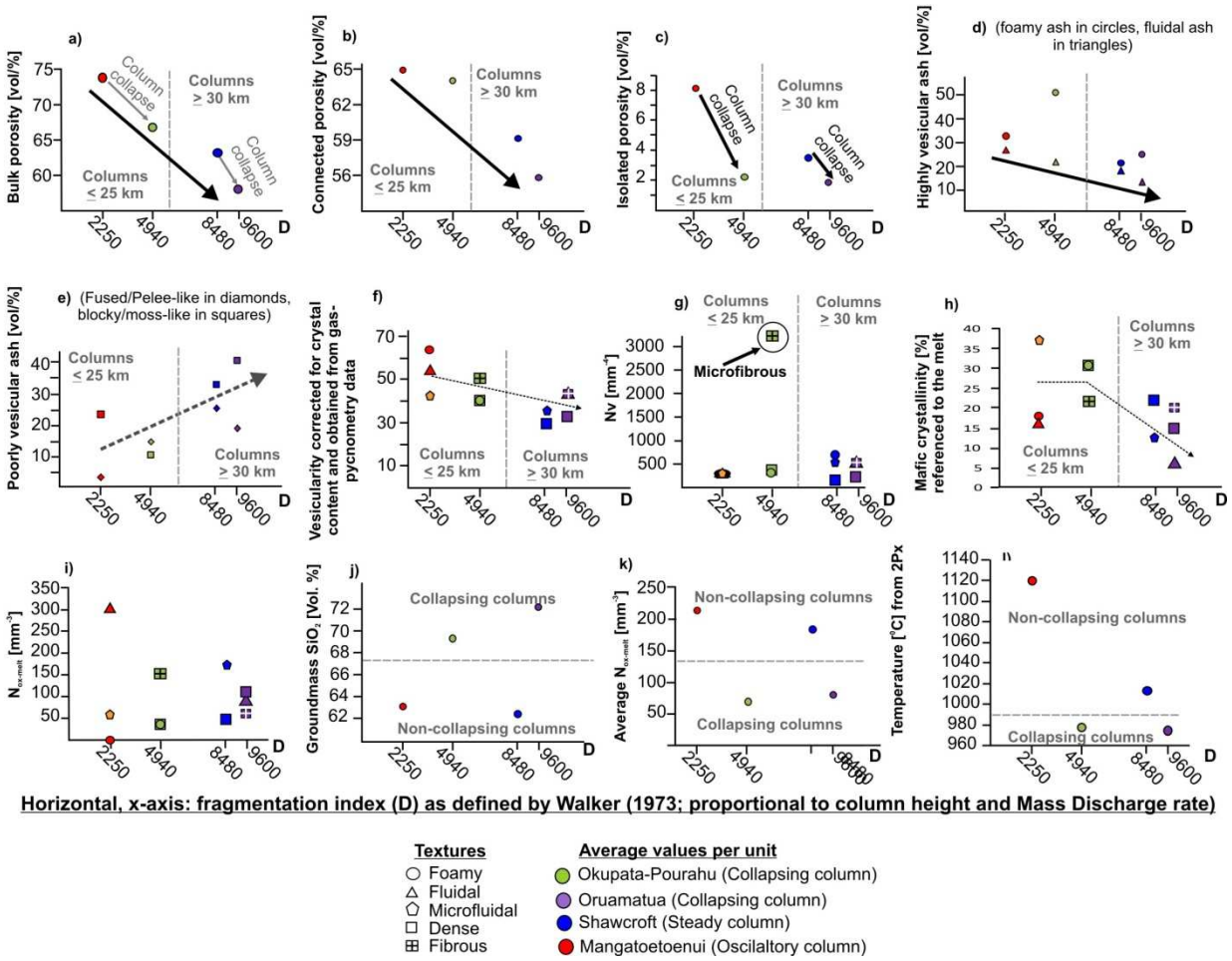

Figure 7.11 Correlation between the non-dimensional fragmentation Index (D) as a measure of eruptive violence and textural, componentry and geochemical parameters obtained in this study.

The total juvenile glass components, together with highly vesicular foamy, fluidal, and fibrous ash textures, are most abundant in Mgt and Okp deposits. By contrast, dominantly poorly vesicular ash shards are derived from intensive fragmentation and bubble wall rupture in the Sw and Oru units, along with high contents of non-juvenile lithics in fine size fractions. Pelée's tears (e.g., Mgt and Sw) appear to be related to high magma temperature of the oldest magmas. Platy shards, instead, could be attributed to fragmentation from degassed regions of slow magma ascent rates.

From the correlated parameters shown in **Fig. 7.11**, column height appeared to be controlled by the bulk porosity (**Fig. 7.11a-f**). This could reflect an effect of vesicle-size, with highest

columns (i.e., Sw and Oru) related to those magmas where bubble growth was inhibited, favouring high over-pressures. The correlation of dense glass particles (and lithic content) with column height (**Fig. 7.11d,e**), suggests that another factor controlling eruption column height could be the fragmentation index enhanced by interaction with external water. Fine fragmentation aided by such process (weak in Sw but clearly identified for Oru) could promote the production of fine particles of low settling velocity, able to rise higher in the eruption cloud (c.f., Kaminski et al., 2011). The low density of the erupted mixture is also indirectly reflected by the lowest contents of mafic crystallinity (**Fig. 7.11h**). On the other hand, an interesting parameter involved in column steadiness appears to be the evolution of the residual liquid (**Fig. 7.11j**). Groundmass glass composition indirectly suggests that microlite crystallization, and hence, shallow magma stalling and degassing occurred in case of unsteady eruption columns. These factors together with the lowest temperatures calculated for the youngest units (**Fig. 7.11l**), indicate that andesitic magmas within the high viscosity ranges are prone to rise at slow ascent rates and are susceptible to experience heterogeneous degassing processes and shear, developing rheologically complex flows during ascent. This will also have an effect on the fragmentation speed (c.f., Spieler et al., 2004) and the variable depth of the fragmentation front across the conduit. All together, these factors result in column collapse.

7.6 Hazard implications

During the past ~3 ka BP cal., Mt. Ruapehu eruptions have been two orders of magnitude less explosive than those examined for the Late Pleistocene, with the greatest hazards related to lahars along the Whangaehu and Whakapapa catchments (e.g., 1861, 1895, 1945-Tangiwai Disaster, 1953, 1968-1975; in Neall 1990; Neall et al., 1999; Lecointre et al., 2004). Hence, most of the mitigation management (Montgomery and Keys 1993; Cronin and Neall 2004) and emergency/contingency plans are currently focused on the potential activity of Crater Lake and major consequences of its rim collapse, or its disruption by eruptions. The largest explosive event ever seen by New Zealanders from Mt. Ruapehu was the 1995-1996 phreatomagmatic eruption, which developed two 10-12 km high eruptive columns, distributing 5-25 x 10^6 m^3 of ash (Cronin et al., 1998). This study reveals that Mt. Ruapehu is capable of producing events of magnitudes 4 to 5, with eruptive columns reaching stratospheric levels (>30 km). Thus, Ruapehu is capable of producing eruptions of the scale

of the Askja 1875 and Chaitén 2008 eruptions, up to 10-15 km higher than the 18 May 1980 Mt. St Helens eruption.

The mapping of the tephras during this study highlighted the complexity of New Zealand wind patterns complicates in estimating areas potentially affected by tephra fall. There is a high probability of cross-winds and shifts in the wind direction within the course of a few hours, causing multiple depositional lobes, as seen during the 1995-1996 eruption (Cronin et al., 1998, 2003; Turner and Hurst 2001) and similarly reflected by the Late Pleistocene tephra record. In the past, north-westerly winds have dominated during major eruptions, causing repeated accumulation of lapilli fallouts on the eastern ring plain and towards Waiouru. Ohakune and Taihape have been, by contrast, subject to ash deposition less frequently (**Fig. 7.12**). Turangi is currently the main urban area that has been affected by past eruptions during dominant south-westerlies. The Late Pleistocene Plinian eruption record suggests that fine ash could easily be dispersed towards Napier, Hastings, and Central North Island, and even reaching the Pacific Ocean.

The most violent eruptions identified within the last ~27 ka BP cal., at Ruapehu occurred between ~13 and 11 ka BP cal., involving columns reaching more than 35 km height, at mass discharge rates of 10^8 kg/s, and producing pyroclastic density currents. This was the most common eruption style before a transition to subplinian and Vulcanian to phreatomagmatic eruptions that have predominated since ~10 ka BP cal. When considering the long term eruption record of variable scale and small scale eruptions at Ruapehu (Cronin et al., 1996a, c), a return to these large-scale Plinian eruptions types must be considered as possible.

Considering the entire ~27-11 ka BP cal., Plinian eruption record at Mt. Ruapehu, textural and geochemical analyses (**Chapters 6.3** and **6.4**) indicate a systematic reduction in magma ascent/decompression rate with time. Villamor et al., (2010) identified variations in single-event slip rates within the Rangipo fault, occurring in concert with volcanic activity.

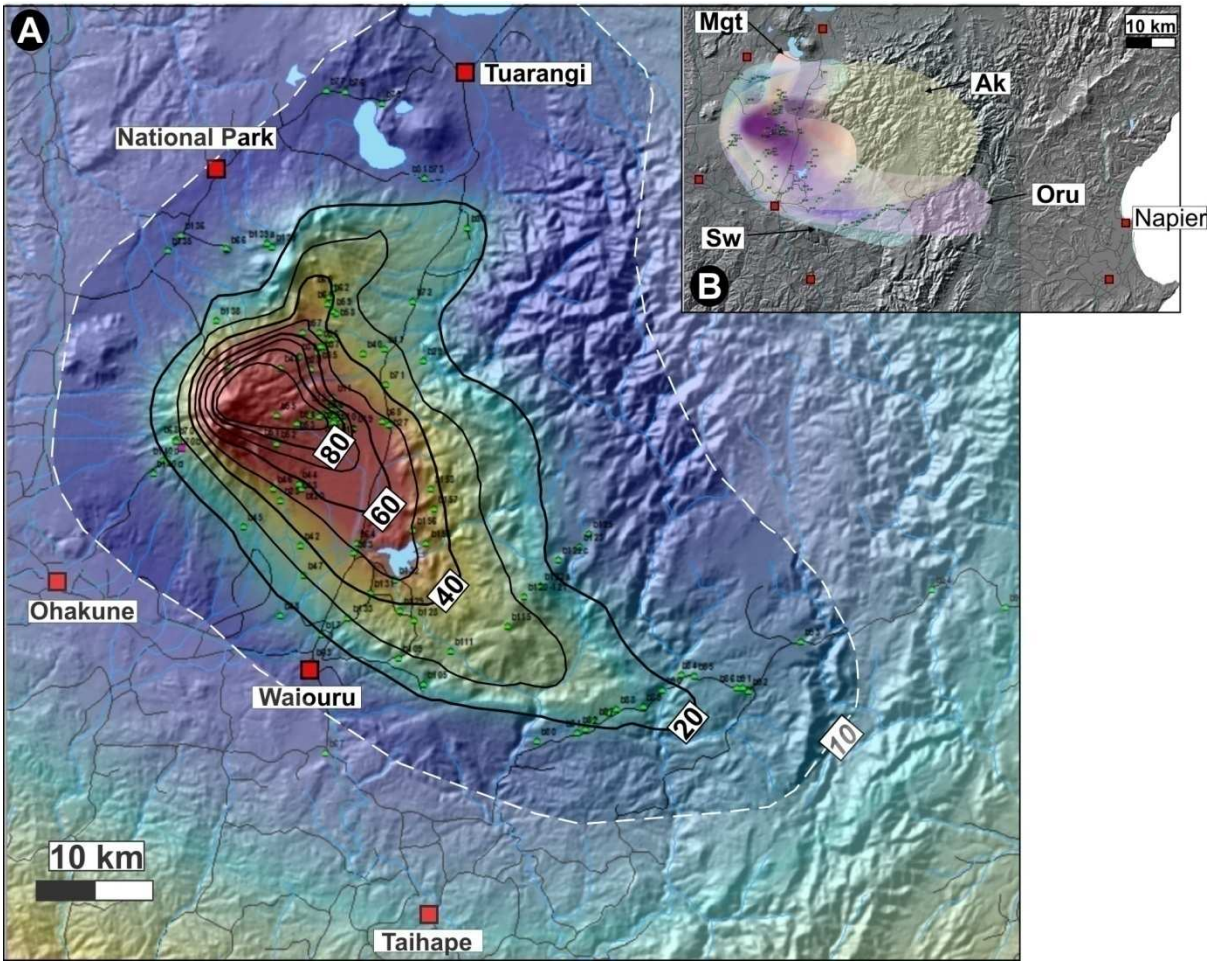

Figure 7.12 Accumulated thickness in cm for major Plinian fallouts during the Late Pleistocene: Mgt: Mangatoetoenui; Sw: Shawcroft: Oru: Oruamatua, and Ak: Akurangi eruptive units. Okupata-Pourahu is here excluded for simplicity (See the corresponding isopachs in Fig. 4.2); **a)** the Tongariro National park and the main urban centres repeatedly affected during Late Pleistocene eruptions; **b)** overview showing the extent of mapped tephras towards the east coast of North Island.

Although a detailed correlation with paleoseismology data is outside the scope of this study, there is an interesting first-order relationship between high slip rates along the Rangipo, Shawcroft Road, and possibly the Karioi faults before 11 ka BP cal., (Villamor, *personal communication*) and the generation of the largest eruptive events known from Mt. Ruapehu. After ~11 ka BP cal., a substantial reduction in the slip rate occurred along these faults. As a preliminary hypothesis and based on the data presented in this study, magma decompression or instability of the shallow magmatic system may have been triggered in response to changes in the local stress regime and/or stress field orientation. Progressively decreasing fault slip-rates with time could lead the Late-Pleistocene storage system towards advanced crystallization and "freezing" and/or a re-configuration of the storage system into new,

smaller magma batches sparse in the upper-crust. Decreasing deformation rates at faults affecting Mt. Ruapehu shallow storage systems could have driven the transition toward smaller eruptions in the Holocene. In turn, the deceleration of faults affecting Mt. Ruapehu shallow crustal storage system may have activated neighbouring faults affecting the Mt. Tongariro storage systems, triggering the following Holocene, Pahoka-Mangamate eruptive sequence. For instance, the local tectonic stresses in interaction with the surface heat flow and the role of the local rheological boundaries have been identified as important factors on magma emplacement depth and size (c.f. Watanabe et al., 1999). In addition, the residence time of magma at a certain level and magma-filled crack ascent velocity also depend on density barriers and changes of the stress field (c.f., Scandone et al., 2007). Therefore, a high-resolution paleoseismological study on the faulted tephras exposed on the eastern slopes of Ruapehu and its eastern ring Plain is needed to clarify the relationship between local tectonics and volcanism.

8. CONCLUSIONS: A new understanding of Mt. Ruapehu Plinian eruptions

8.1 Summary

Andesite volcanoes have been responsible for most of the major historic volcanic disasters throughout the world. The reasons for this are their sporadic eruptions interposed by variable repose periods, as well as their wide range in eruption styles. Of particular importance are the most-explosive sub-Plinian to Plinian eruption styles, which produce widespread tephra falls and pyroclastic flows. An important result arising from the research presented in this thesis is that andesitic Plinian eruptions are primarily controlled by physical processes within the conduit, such as vesiculation and crystallization, which affect the rheology of the rising magma. These processes control the height of Plinian columns and also whether they may collapse or not to form pyroclastic flows. The bulk chemical characteristics of the system as a whole are by contrast, only secondary influences. This research extends the traditional understanding of eruption column stability (c.f., Suzuki and Koyaguchi 2012), by quantifying the role of rheological heterogeneity in the magma ascent and fragmentation processes.

This study identified the physical processes driving the largest explosive eruptions of Mt. Ruapehu. An integrated approach using a wide range of analytical techniques was required, including: detailed unit stratigraphy, distribution mapping, granulometry, componentry, porosimetry and density determinations, as well as petrography, textural studies using high resolution X-Ray micro-tomography, and chemical determinations with Fourier-Infrared-Spectroscopy, X-ray fluorescence and Electron Microprobe. From these data, the conditions in the pre-eruptive magma storage system and volcanic conduit, including the magma volatile saturation, vesiculation, degassing and fragmentation processes, were derived and correlated with external factors such as conduit geometry and wall-stability, vent location, and interaction of magma with hydrothermal systems and groundwater.

An important result of the study has been the determination of the range and upper limits of eruptive parameters that might be expected from this volcano in future eruptions. Additionally, it has demonstrated how from a single andesitic volcano, magmas of similar bulk composition and initial volatile content may experience different dynamic processes as they rise to the surface, resulting in contrasting eruption styles.

In the studied sequence from Mt. Ruapehu, there is an evolution from oscillatory, to stable, and to collapsing columns over time. **Oscillating** (but non-collapsing) columns occur when the magma ascent/decompression rate is extremely high and a rising magma body experiences variable vesiculation mechanisms, due to differential ascent rates across the conduit (i.e., influenced by frictional drag against conduit walls). Expansion-acceleration processes dominate the magma fragmentation in this situation, but strongly variable magma rheology continuously changes the energy release into the column. **Stable** columns are generated at intermediate magma ascent/decompression rates, when magma reaching the fragmentation level in the conduit is chemically and physically homogeneous. In this case, fragmentation is dominantly decompression-dominated. **Collapsing** columns occur when viscous magma rises slowly and shearing induces strongly variable decompression rates and degassing mechanisms across the conduit. In this case, fragmentation is induced by shearing and may in some cases, be influenced by water-magma interaction.

This study proves that the rheological state of magma within the conduit as it reaches the fragmentation level is a critical control of eruption outcome. The physical state of the magma is reflected in the pyroclast textures (c.f., Stein and Spera 1992), vesicle and crystal content and crystal number density (degree of undercooling), and the chemistry of the residual liquid (c.f., Whittington et al., 2009). Plinian eruptions are mostly considered to be the result of homogeneous bubble nucleation, but it is shown that heterogeneous bubble nucleation is more common for Ruapehu cases. At this volcano, mafic crystal (i.e. pyroxene and Ti-oxide) number densities in erupting magmas are equal or exceed vesicle number densities, and phenocrysts become effective sites for heterogeneous bubble nucleation at low supersaturation pressures. Therefore, andesitic magmas do not need to be over-saturated in volatiles at the base of a conduit to ultimately drive highly explosive eruptions.

In addition, this study shows that total vesicularity (and hence, bulk density) is not a critical factor driving Plinian column collapse. Rather, column collapse occurs when isolated porosities are below a critical threshold (<3 % in Ruapehu studied cases) and when ascending magmas experience intense shear within the conduit at slow decompression rates. Under polybaric crystallization and multiple stages of crystal nucleation and growth, vesicle nucleation and growth mechanisms, as well as the resulting vesicle and crystal size distributions, determine the rheological conditions within the conduit, and these control the steadiness of magma discharge at the vent.

8.2 Specific findings of this study

8.2.1 Identification of a systematic change in the dominant lithofacies association, Plinian style, vent location, and eruptive column behaviour over time of deposition of the Bullot Formation

The lithofacies associations of Plinian deposits within the oldest *Rangipo Eruptive Period* (~22-17 ka BP cal.), indicate non-collapsing but oscillatory eruptive columns. Those of deposits within the *Karioi Eruptive Period* (~17-13 ka BP cal.) show evidence for steady eruption columns, involving extreme conduit erosion. Most of the younger Plinian deposits (up to ~11 ka BP cal.) have lithofacies associations that indicate unsteady eruption conditions and collapsing columns. All of these eruptions were sourced at the North Crater of Mt. Ruapehu, with a shift to the South Crater for the last major Plinian eruption, the Okupata-Pourahu event.

8.2.2 Clarification of the source of the Pahoka Tephra

The lowermost unit of the ~11 ka BP cal., Pahoka-Mangamate Sequence (Nairn et al., 1998), known as the Pahoka Tephra, had been attributed variously to Mt. Ruapehu, Mt. Tongariro, or a vent located between the two, known as the "Saddle Cone" (Topping 1973; Donoghue 1991; Nairn et al., 1998). Lithofacies and detailed mapping during this study clearly demonstrates that it was sourced from Mt. Tongariro, with a vent location most probably below the current Mt. Ngauruhoe edifice.

8.2.3 (Re)Definition of the largest Plinian eruption of Mt. Ruapehu

The Okupata-Pourahu eruptive is not the largest Plinian event of Mt. Ruapehu, as previously concluded by Donoghue et al. (1995a). Based on the mapping and eruptive parameters derived from distributed tephra, it is clear that the largest eruptions produced by Mt. Ruapehu were earlier, occurring shortly after 13,625 ± 165 cal years BP and before 11,620 ± 190 cal years BP. In particular, the Oruamatua and Akurangi eruptive units represent the largest events, producing eruption columns as high as 37 km, with widespread tephra fall to the east of the volcano as well as pyroclastic flows on the upper eastern volcanic flanks. The pumice colour, textures, and chemistry of the Oruamatua, Akurangi, and Okupata-Pourahu are very

similar. They all contain banded pumice clasts, which had been formerly used as an exclusive field criterion for identifying Okupata-Pourahu. The stratigraphic record between the Oruamatua and the Okupata-Pourahu eruptive units was incorrectly conflated during the correlation of Donoghue et al. (1999), and the units were grouped as a single, short-lived, "*Taurewa Eruptive Episode*". The stratigraphy presented in this study shows many separate eruption events and time-breaks occurred between these eruptives and that each of them was individually a major eruptive episode. The latest, Okupata-Pourahu event was smaller in volume and also produced a lower eruption column (25 km) than many of the earlier events of this volcano.

8.2.4 Metrics of the largest Ruapehu Plinian eruptions

The Mangatoetoenui Eruptive Unit was the smallest of the Plinian eruptions described in detail in this study, involving a minimum erupted volume of 0.3 km^3 and a column height of 22 km at erupted mass discharge rates of $6.8x10^7$ kg/s. This case-example is typical of the Rangipo eruptive period, where eruption columns varied greatly in height but did not collapse. Assuming a bulk density of 990 kg/m^3 (measured in the field), the estimated duration of the climactic phase of this eruption was around 1.1 hour.

An intermediate sized eruption is exemplified by the Okupata-Pourahu unit, producing a minimum erupted volume of 0.4 km^3 and a column height of 25 km at erupted mass discharge rates of $7.5x10^7$ kg/s. This is a typical example of a dense, collapsing eruption column. Assuming a bulk density of 1157 kg/m^3 (measured in the field), the Plinian phase of this eruption lasted around 1.5 hour.

The largest eruptions were the Shawcroft unit (steady column), Oruamatua, and Akurangi units (partly collapsing columns), which erupted 0.5-0.6 km^3 of magma, producing column heights of 29, 35 and 37 km respectively, corresponding to mass discharge rates of ~10^8 kg/s. Estimated climactic phase durations were around 1.4 hours for Shawcroft (considering an average bulk density of 1350 kg/m^3), 0.4 hours for Oruamatua (with an average bulk density of 1450 kg/m^3) and 5.8 hours for Akurangi (with an average bulk density of 1380 kg/m^3). These three units demonstrate the uppermost limits of eruptive conditions and related hazards from Mt. Ruapehu. Akurangi and Oruamatua units are the best reference models to approximate the maximum eruptive scenario expected for this volcano, with stratospheric-

height columns and partly collapsing columns generating pyroclastic flows with minimum run-out distances of 15 km.

8.2.5 Tephra distribution patterns of Plinian eruptions at Mt. Ruapehu

All studied Plinian tephra units show bilobate isopach and isopleth distribution patterns, suggesting two predominant wind directions (from NW and SW), varying: **a)** for longer eruptions, with time, such that pauses between eruptive pulses/phases cannot be distinguished, or **b)** for brief (<2 hours) eruptions, with altitude in the atmosphere, such that higher portions of the plume were affected by north-westerlies, and lower portions by south-westerlies. Both options are very likely in the North Island, where wind direction and speed can significantly change within a few hours of an eruption (c.f., Cronin et al., 1998, Turner and Hurst 2001).

8.2.6 Relationships between chemical and eruption variability of Mt. Ruapehu Plinian eruptions

This study demonstrates that there is a correlation between chemical variability and the rheology of the erupting magma (as reflected by juvenile pumice textures), to the subsequent eruptive behaviour. In the studied tephra sequence at Mt. Ruapehu, the most restricted bulk compositions and lowest textural variability are found in deposits related to the most stable eruptive columns (e.g., Shawcroft Eruptive Unit). On the other hand, the most variable bulk compositions and textures are correlated to the deposits from unstable, collapsing eruptive columns (e.g., Oruamatua, Akurangi, and Okupata-Pourahu eruptive units). In intermediate situations, where different clusters of groundmass glass chemistry relate to variations in crystal content and time, variable height, but non-collapsing columns formed (e.g., Mangatoetoenui Eruptive Unit).

8.2.7 Evolution of the eruptive/magmatic system at Mt. Ruapehu

Over the examined ~27-11 ka BP cal., stratigraphic record, there is a trend of decreasing isolated porosities and temperatures, increasing magma viscosity, and slower magma ascent/decompression rates with time. These changes are reflected in features such as increasing: average vesicle number density, crystal size, microlite content and groundmass glass silica content over time, along with the degree of vesicle deformation, inferred extension of coalescence and bubble collapse.

Earlier eruptions occurred under rapid-ascent conditions from deeper magma reservoirs. The Lower Mangatoetoenui subunit, involved a mafic magma with low-viscosity where bubble surface tension was large, favouring high bubble growth rates, expansion, and relaxation under low-kinetic barriers. Close to the conduit margins and/or at shallower levels in the conduit, where mafic crystal number density was higher, multiple events of bubble nucleation and growth were enhanced. High isolated porosity shows that gas exsolution and expansion rates exceeded permeable flow.

The following eruptions produced the highest eruption columns with pumice lapilli showing the highest bulk densities, and lowest bulk and connected porosities. Shawcroft magma showed a single bubble nucleation but limited growth under kinetic barriers, due to advanced crystallisation at slower decompression rates than during the Mangatoetoenui eruption. During this eruption, the conduit walls were highly unstable and intense conduit erosion modified the pre-existent geometry. This modification was an additional factor modulating the subsequent eruption styles. The youngest Oruamatua (also Akurangi), and Okupata-Pourahu magmas showed the most heterogeneous degassing processes, where strong shearing at the slowest decompression rate led to variable processes of bubble nucleation and growth, and extremely variable rheology across the conduit. This led to very unstable, collapsing eruption columns producing pyroclastic density currents. In the Okupata magma, advanced degassing and formation of permeable networks under intense shear had developed prior to fragmentation, leading to lower magma discharge rates and a lower eruption column relative to Oruamatua and Akurangi.

8.2.8 Glass transition and fragmentation style changes

Fast decompression of expanding (Lower Mangatoetoenui) and over-pressured (Upper Mangatoetoenui and Shawcroft) bubbles exceeded the liquid viscous relaxation rate, driving the magma across the glass transition and fragmentation. In the youngest Oruamatua, Akurangi, and Okupata-Pourahu eruption, shear stress was an additional mechanism during which the viscous relaxation time of vesicles was overprinted by the high deformation rate, driving magma to fragmentation. Furthermore, the Oruamatua and Akurangi eruptions involved magma-water interaction, which enhanced fragmentation. The earliest Mangatoetoenui magma was considerably more vesicular than other magmas, favouring a deeper fragmentation front relative to young, dense magmas. In addition, the homogeneous physical state (porosity) of Shawcroft (steady column), promoted a relatively constant

fragmentation depth across the conduit, whereas the spatial variation of the fragmentation front depth (and speed) increased in proportion to the physical variability (Mangatoetoenui <Oruamatua, Okupata-Pourahu) of the magmas producing unstable columns.

8.2.9 Controls on eruption column height and steadiness

Developing high eruption columns depends on the retention of dissolved volatiles in magmas until high levels in the crust (coupled degassing), the degree of fragmentation, the exit velocity, and temperature of the pyroclastic mixture (which promotes buoyancy). At Ruapehu, column stability was a function of the rheological heterogeneity of the magma reaching the fragmentation level. The most stable conditions were reached during the Shawcroft event, where a balance between high temperature, low silica content, and low mafic crystal number density allowed late vesiculation under intermediate magma ascent/decompression rates, leading to a homogeneous rheology across a narrow conduit. The sharp density and porosity peaks in Shawcroft pyroclasts show that the magma was chemically and physically homogeneous at the fragmentation level, favouring sustained eruption conditions.

The high degree of conduit erosion during the Shawcroft eruption episode changed the conduit geometry, promoting more complex flow conditions under high shear for subsequent eruptions. Oruamatua and younger Plinian events involved wider physical and chemical heterogeneity leading to variable discharge rates and/or fragmentation fronts (and speeds) of variable depth across the conduit, ultimately resulting in column collapse. Slow ascent rates also gave more opportunity for magma/water interaction, which may have been an additional, external factor promoting column collapse and generation of pyroclastic density currents.

The results of this study suggest that the time interval between the levels of gas exsolution and magma fragmentation determines the extent of bubble interconnectivity and magma permeability. If these intervals are small, the degassing processes of the rising magma are roughly homogeneous, enough isolated vesicles are retained until shallow levels, and stable columns are favoured. Under larger time intervals, degassing processes approach almost de-coupled and open conditions, reducing the proportion of isolated vesicles. In this case, the rheological heterogeneity of the magma reaching the fragmentation level is greater, causing a

disparity between magma supply and discharge rates at the vent and leading to column collapse.

8.3 Concluding statement and future research questions

The final eruption style and column behaviour during the andesitic Plinian eruptions of Mt. Ruapehu were a function of the conditions occurring between the levels of gas exsolution and magma fragmentation, as well as of the conduit geometry. The conduit processes were controlled by the relative rates of vesicle nucleation, growth, interconnection, relaxation, and shear in comparison to the overall magma ascent/decompression rates. In addition, shifts in vent location and the opening of a new conduit during the youngest Plinian event (Okp-Ph), led to a slow magma ascent where magma shear was a greater factor in development of permeability prior to fragmentation.

As a hypothesis for future research, it is very likely that decompression rates have responded to changes in the local stress regime, such as its orientation, or local deformation/extension rate. Volcanic rejuvenation, increased heat and development of overpressure of intermediate-size, shallow-crust reservoirs may be tectonically controlled. The observation of progressively decreasing fault slip-rates with time in this region over and following the time range studied here (c.f.,Villamor et al., 2010), could have led to decreasing magma decompression rates, favouring the arrest of magmas at shallow depths, driving the storage system towards advanced crystallization and “freezing”. This could have driven the transition toward smaller eruptions characteristic during the Holocene at Mt. Ruapehu (c.f., Moebis et al., 2011). An intermediate step could have followed the deceleration of faults affecting Mt. Ruapehu shallow crustal storage system, where Mt. Tongariro faults were activated, triggering the sudden and short-lived episode of the Pahoka-Mangamate Plinian eruptions.

The data presented here demonstrate long-period transitions in the eruption behaviour at Mt. Ruapehu. This shows that time-varying approaches are needed to adequately forecast future eruption potential for this and similar andesitic volcanoes. These must take into account evolution in the magmatic and conduit system feeding large-scale eruptions, but also short-term variable factors, including the stress regime affecting the volcano.

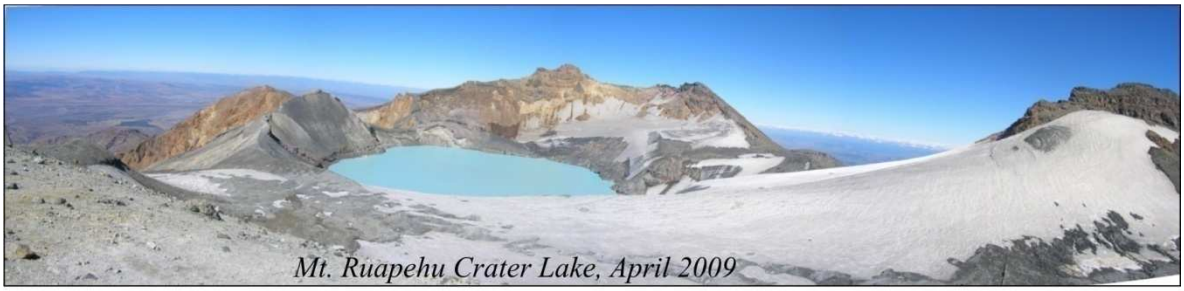

Mt. Ruapehu Crater Lake, April 2009

What are your secrets, sacred Mountain?

Te koru: the spiral geometry of Life according to Maori tradition. It symbolizes the continuous unfolding of life, renewal, and hope for the future. It was a permanent source of inspiration during this "PhD process"

Tihei Mauri ora!

REFERENCES

Adams NK, Houghton BF, Hildreth W (2006) Abrupt transitions during sustained explosive eruptions: examples from the 1912 eruption of Novarupta, Alaska. Bull Volcanol 69: 189-206

Alidibirov M (1994) A model for viscous magma fragmentation during volcanic blasts. Bull Volcanol 56: 459-465

Alidibirov M, Dingwell DB (1996) Magma fragmentation by rapid decompression. Nature 380: 146-149

Alidibirov M, Dingwell DB (2000) Three fragmentation mechanisms for highly viscous magma under rapid decompression. J. Volcanol. Geotherm. Res. 100: 413-421

Anderson AT, Davis AM, Fangqiong LU (2000) Evolution of Bishop Tuff Rhyolitic Magma Based on Melt and Magnetite Inclusions and Zoned Phenocrysts. J. Petrol. 41 (3): 449-473

Anilkumar AV, Sparks RSJ, Sturtevant B (1993). Geological implications and applications of high velocity two-phase flow experiments. J. Volcanol. Geotherm. Res. 56: 145-160

Arana-Salinas L, Siebe C, Macías JL (2010) Dynamics of the ca. 4965 yr ^{14}C BP "Ochre Pumice" Plinian eruption of Popocatépetl volcano, México. J. Volcanol. Geotherm. Res. 192: 212-231

Arce JL, Cervantes KE, Macías JL, Mora JC (2005) The 12.1 ka middle Toluca pumice: a dacitic Plinian-subplinian eruption of Nevado de Toluca in Central México: J. Volcanol. Geotherm. Res. 147: 125-143

Arce JL, Macías JL, Vázquez SL (2003) The 10.5 Ka Plinian eruption of Nevado de Toluca, México: stratigraphy and hazard implications: Geol. Soc. Am. Bull. 115 (2): 230-248

Asimow PD (2000) Melting the Mantle. In: Sigurdsson H, Houghton BF, McNutt SR, Rymer H, Stix J (eds) Encyclopedia of Volcanoes. Academic Press, San Diego: 55-68

Baker DR, Polacci M, LaRue A (2011) A study on the reproducibility of counting vesicles in volcanic rocks. Geosphere 7: 79-86

Belien I, Cashman KV, Rempel AW (2010) Gas accumulation in particle-rich suspensions and implications for bubble populations in crystal-rich magma. Earth Planet. Sci. Lett. 297: 133-140

Best MG (2003) Igneous and Metamorphic Petrology. Blackwell Science Ltd (ed), 733p.

Biass S, Bonadonna C (2010) A quantitative uncertainty assessment of eruptive parameters derived from tephra deposits: the example of two large eruptions of Cotopaxi volcano, Ecuador. Bull Volcanol 73: 73-90

Blake S (1984) Volatile oversaturation during the evolution of silicic magma chambers as an eruption trigger. J. Geophys. Res. 89: 8237-8244

Blower JD, Keating JP, Mader HM, Phillips JC (2001) Inferring volcanic degassing processes from vesicle size distributions. Geophys. Res. Lett. 28 (2): 347–350

Blower JD, Keating JP, Mader HM, Phillips JC (2002) The evolution of bubble size distributions in volcanic eruptions. J. Volcanol. Geotherm. Res. 120: 1-23

Blundy J, Cashman KV (2001) Ascent-driven crystallization of dacite magmas at Mount St Helens 1980-1986. Contrib. Mineral. Petrol. 120: 631-650

Blundy J, Cashman KV (2005) Rapid decompression-driven crystallization recorded by melt inclusions from Mount St. Helens volcano. Geology 33 (10): 193-196

Bonadonna C, Ernst GGJ, Sparks RSJ (1998) Thickness variations and volume estimates of tephra fall deposits: the importance of particle Reynolds number. J. Volcanol. Geotherm. Res. 81: 173-187

Bonadonna C, Houghton BF (2005) Total grain-size distribution and volume of tephra-fall deposits. Bull Volcanol 67: 441-456

Bouvet de Maisonneuve C, Bachmann O, Burgisser A (2009) Characterization of juvenile pyroclasts from the Kos Plateau Tuff (Aegean Arc): insights into the eruptive dynamics of a large rhyolitic eruption. Bull Volcanol 71: 643-658

Brazier S, Sparks RSJ, Carey SN, Sigurdsson H, and Westgate JA (1983) Bimodal grain-size distribution and secondary thickening in air-fall ash layers. Nature 301 (5896): 115-119

Brown RJ, Branney MJ, Maher C, Dávila-Harris P (2010) Origin of accretionary lapilli within ground-hugging density currents: Evidence from pyroclastic couplets on Tenerife. GSA Bull 122: 305-320

Burgisser A, Gardner JE (2005) Experimental constraints on degassing and permeability in volcanic conduit flow. Bull Volcanol 67: 42-56

Bursik MI (1993) Subplinian eruption mechanisms inferred from volatile and clast dispersal data. J. Volcanol. Geotherm. Res. 57: 47-60

Bursik MI (1998) Tephra dispersal. In: Gilbert, J.S., Sparks, R.S.J. (Eds.). The physics of explosive volcanic eruptions, Geol. Soc. Lon. Spec. Publ. 145: 115-144

Bursik MI, Sparks RSJ, Gilbert JS, and Carey SN (1992) Sedimentation of tephra by volcanic plumes I, Theory and its comparison with a study of the Fogo A Plinian deposit, Sao Miguel (Azores). Bull Volcanol 54: 329-344

Büttner R, Dellino P, Zimanowski B (1999) Identifying modes of magma/water interaction from the surface features of ash particles. Nature 401: 688-690

Carey S, Sirgudsson H (1989) The intensity of Plinian eruptions. Bull Volcanol 51: 28-40

Carey S, Sparks RSJ (1986) Quantitative models of the fall and dispersal of tephra from volcanic eruption columns. Bull Volcanol 48: 109-125

Carey S, Gardner J. Sigurdsson H (1995) The intensity and magnitude of Holocene Plinian eruptions from Mount St. Helens volcano. J. Volcanol. Geotherm. Res. 66: 185-202

Carey RJ, Houghton BF, Thordarsson T (2010). Abrupt shifts between wet and dry phases of the 1875 eruption of Askja Volcano: Microscopic evidence for macroscopic dynamics. J. Volcanol. Geotherm. Res. 184: 256-270

Caricchi L, Burlini L, Ulmer P, Gerya T, Vassalli M, Papale P (2007) Earth Planet. Sci. Lett. 264 (3-4): 402-419

Carn SA, Pallister JS, Lara L, Ewert JW, Watt S, Prata AJ, Thomas RJ, Villarosa (2009) The unexpected awakening of Chaitén Volcano, Chile. EOS Transactions, AGU 90 (24): 205-206

Cas RAF, Wright JV (1987) Volcanic successions. Allen and Unwin. 528p.

Cashman KV, Blundy J (2000) Degassing and crystallization of ascending andesite and dacite. Phil. Trans. Roy. Soc. 358: 1487-1513

Cashman KV, Cronin SJ (2008) Welcoming a monster to the world: Myths, oral tradition, and modern societal response to volcanic disasters. J. Volcanol. Geotherm. Res. 176: 407-418

Cashman KV, Ferry JM (1988) Crystal size distribution (CSD) in rocks and the kinetics and dynamics of crystallization. Contrib. Mineral. Petrol. 99: 401-415

Cashman KV, Giordano G (2008) Volcanoes and human history. J. Volcanol. Geotherm. Res. 176: 325-329

Cashman KV, Mangan MT (1994) Physical aspects of magmatic degassing II. Constraints on vesiculation processes from textural studies of eruptive products. In: Carroll MR, Holloway JR (eds) Volatiles in magmas. Rev Mineral 30: 447-478

Cashman KV, McConnell SM (2005) Multiple levels of magma storage during the 1980 summer eruptions of Mount St. Helens, WA. Bull Volcanol 68: 57-75

Cashman KV, Sturtevant B, Papale P, Navon O (2000). Magmatic fragmentation. In: Sigurdsson H, Houghton BF, McNutt SR, Rymer H, Stix J (eds) Encyclopedia of volcanoes. Academic Press, San Diego, CA: 421-430

Christenson BW, Wood CP (1993) Evolution of a vent-hosted hydrothermal system beneath Ruapehu Crater Lake, New Zealand. Bull Volcanol 55: 547-565

Cichy SB, Botcharnikov RW, Holtz F, Behrens H (2011) Vesiculation and Microlite Crystallization Induced by Decompression: a Case Study of the 1991-1995 Mt Unzen Eruption (Japan). J. Petrol. 52 (7-8): 1469-1492

Cioni R, Marianelli P, Stantacroce R, Sbrana A (2000) Plinian and subplinian eruptions. In: Sigurdsson H, Houghton BF, McNutt SR, Rymer H, Stix J (eds) Encyclopedia of Volcanoes. Academic Press, San Diego: 477-494

Cioni R, Sulpizio R, Garruccio N (2003) Variability of the eruption dynamics during a Subplinian event: Greenish Pumice eruption of Somma-Vesuvius (Italy). J. Volcanol. Geotherm. Res. 124: 89-114

Cluzel N, Laporte D, Provost A, Kannewischer I (2008) Kinetics of heterogeneous bubble nucleation in rhyolitic melts: implications for the number density of bubbles in volcanic conduits and for pumice textures. Contrib. Mineral. Petrol. 156: 745-763

Cole JW (1978) Andesites of Tongariro Volcanic Centre, North Island, New Zealand. J. Volcanol. Geotherm. Res. 3: 121-153

Cole JW (1979) Structure, petrology, and genesis of Cenozoic volcanism, Taupo Volcanic Zone, New Zealand-a review. NZ J Geol Geophys 22 (6): 631-657

Cole JW, Graham IJ, Hackett WR, Houghton BF (1986) Volcanology and petrology of the Quaternary composite volcanoes of Tongariro Volcanic Centre, Taupo Volcanic Zone. In: Smith, I.E.M. (Ed.), 'Late Cenozoic Volcanism in New Zealand'. Roy Soc New Zealand: 222-250

Cole JW, Nairn IAI (1975) Catalogue of the active volcanoes of the world 22: New Zealand. International Association of Volcanology and Chemistry of the Earth's Interior (IAVCEI), Naples: 1-152

Cole JW, Thordarson T, Burt RM (2000) Magma origin and evolution of White Island (Whakaari) Volcano Bay of Plenty, New Zealand. J. Petrol. 41: 867-895

Coltelli M, Del Carlo P, Vezzoli L (2000) Stratigraphic constrains for explosive activity in the past 100 ka at Etna volcano, Italy. Int. J. Earth Sci. 89: 665-677

Costa A (2006) Permeability-porosity relationship: A re-examination of the Kozeny-Carman equation based on a fractal pore-space geometry assumption: Geophys. Res. Lett., 33: L02318

Costa A Macedonio G (2005) Viscous heating effects in fluids with temperature dependent viscosity: triggering of secondary flows. J. Fluid Mech. 540: 21-38

Couch S, Sparks RSJ, Carroll MR (2001) Mineral disequilibrium in lavas explained by convective self-mixing in open magma chambers. Nature 411: 1037-1039

Cronin SJ, Hedley MJ, Neall VE, Smith G (1998) Agronomic impact of tephra fallout from 1995 and 1996 Ruapehu volcano eruptions, New Zealand. Environ. Geol. 34: 21-30

Cronin SJ, Hodgson KA, Neall VE, Palmer AS, Lecointre JA (1997a). 1995 Ruapehu lahars in relation to the late Holocene lahars of Whangaehu River, New Zealand. NZ J Geol Geophys 40: 507-520

Cronin SJ, Neall VE (1997) A late Quaternary stratigraphic framework for the northeastern Ruapehu and eastern Tongariro ring plains, New Zealand. NZ J Geol Geophys 40: 179-191

Cronin SJ, Neall VE (2004) Understanding the Volcanic Risk. Tephra 21: Living with volcanoes. Ministry of civil Defence and Emergency Management, Wellington, New Zealand: 26-31

Cronin SJ, Neall VE, Lecointre JA, Hedley MJ, Loganathan P (2003) Environmental hazards of fluoride in volcanic ash: a case study from Ruapehu volcano, New Zealand. J. Volcanol. Geotherm. Res. 121: 271-291

Cronin SJ, Neall VE, Palmer AS (1996a) Geological history of the northeastern ring plain of Ruapehu volcano, New Zealand. Quat. Int. 34/36: 21-28

Cronin SJ, Neall VE, Palmer AS (1996b) Investigation of an aggrading paleosol developed into andesitic ring plain deposits, Ruapehu volcano, New Zealand. Geoderma 69: 119-135

Cronin SJ, Neall VE, Palmer AS, Stewart RB (1997b). Methods of identifying late Quaternary rhyolitic tephras on the ring plains of Ruapehu and Tongariro volcanoes, New Zealand. NZ J Geol Geophys 40: 175-184

Cronin SJ, Neall VE, Stewart RB, Palmer AS (1996c). A multiple-parameter approach to andesitic tephra correlation, Ruapehu volcano, New Zealand. J. Volcanol. Geotherm. Res. 72: 199-215

Del Carlo P, Pompilio M (2004) The relationship between volatile content and the eruptive style of basaltic magma: the Etna case. Annals of Geophysics 47: 1423-1432

Dellino P, Isaia R, La Volpe L, Orsi G (2001) Statistical analysis of textural data from complex pyroclastic sequences: implications for fragmentation processes of the Agnano-Monte Spina Tephra (4.1 ka), Phlegraean Fields, southern Italy. Bull Volcanol 63: 443-461

Degruyter W, Bachmann O, Burgisser A (2010) Controls on magma permeability in the volcanic conduit during the climactic phase of the Kos Plateau Tuff eruption (Aegean Arc). Bull Volcanol 72 (1): 63-74

Deubener J, Mueller R, Behrens H, Heide G (2003) Water and the glass transition temperature of silicate melts. J. Non-Cryst. Solids 330: 268-73

Devine JD, Gardner JE, Brack HP, Layne GD, and Rutherford MJ (1995). Comparison of microanalytical methods for estimating H_2O contents of silicic volcanic glasses. Am. Mineral. 80: 319-328

Dingwell DB (1996) Volcanic Dilemma: Flow or Blow?. Science 273 (5278): 1054-155

Dingwell DB (1998) The glass transition in hydrous granitic melts. Phys. Earth Planet. Inter. 107: 1-8

Dingwell DB, Webb SL (1989) Structural relaxation in silicate melts and non-Newtonian melt rheology in geological processes. Phys. Chem. Miner. 16: 508-516

Dixon J E (1997) Degassing of alkalic basalts. Am. Mineral. 82: 368-378

Donoghue SL (1991) Late Quaternary volcanic stratigraphy of the southeastern sector of the Ruapehu ring plain, New Zealand. PhD thesis Massey University, Palmerston North, New Zealand. 615p.

Donoghue SL, Gamble JG, Palmer AS, Stewart RB (1995a) Magma mingling in an andesite pyroclastic flow of the Pourahu Member, Ruapehu volcano, New Zealand. J. Volcanol. Geotherm. Res. 68: 177-191

Donoghue SL, Neall VE (2001) Late Quaternary constructional history of the southeastern Ruapehu ring plain, New Zealand. NZ J Geol Geophys 44: 43-66

Donoghue SL, Neall VE, Palmer AS (1995b) Stratigraphy and chronology of late Quaternary andesitic tephra deposits, Tongariro Volcanic Centre, New Zealand. Roy Soc New Zealand 25 (2): 112-206

Donoghue SL, Neall VE, Palmer AS, Stewart RB (1997) The volcanic history of Ruapehu during the last 2 millennia based on the record of the Tufa Trig Tephras. Bull Volcanol 59: 136-146

Donoghue SL, Palmer AS, McClelland EA, Hobson K, Stewart RB, Neall VE, Lecointre J, Price R (1999) The Taurewa Eruptive Episode: Evidence for climactic eruptions at Ruapehu Volcano, New Zealand. Bull Volcanol 60: 223-240

Donoghue S, Vallance J, Smith IEM, Stewart RB (2007) Using geochemistry as a tool for correlating proximal andesitic tephra: case studies from Mt Rainier (USA) and Mt. Ruapehu (New Zealand). Journal of Quaternary Science 22 (4): 395-410

Dungan MA, Wulff A, Thompson R (2001) Eruptive stratigraphy of the Tatara–San Pedro Complex, 36 8S, southern volcanic zone, Chilean Andes: reconstruction method and implications for magma evolution at long-lived arc volcanic centres. J. Petrol. 42: 555-626

Eggins SM, Kinsley LPJ, and Shelley JMG (1998a) Deposition and element fractionation processes during atmospheric pressure laser sampling for analysis by ICP-MS: Applied Surface Science 127/129: 278-286

Eggins SM, Rudnick RL, and McDonough WF (1998b) The composition of peridotites and their minerals: a laser-ablation ICP-MS study: Earth Planet. Sci. Lett. 154: 53-71

Eichelberger JC (1995) Silicic volcanism: ascent of viscous magmas from crustal reservoirs. Annu. Rev. Earth Planet. Sci. 23:41–63

Escher BG (1933) On a classification of central eruptions according to gas pressure of the magma and viscosity of the lava. Leidsche Geol. Meded., Deel VI,. Afl., I: 45-48

Fagents SA, Wilson L (1993) Explosive eruptions-VII. The ranges of pyroclasts ejected in transient volcanic explosions. Geophys. J. Int. 113 (2): 359-370

Fierstein J, Nathenson M (1992) Another look at the calculation of fallout tephra volumes. Bull Volcanol 54: 156-167.

Fisher R, Schmincke HU (1984) Pyroclastic Rocks, Springer-Verlag, Berlin. 472 p.

Folk RL, and Ward WC (1957) Brazos river bar: a study of the significance of the grainsize parameters. J. Sed. Petrol. 27: 3-26

Frezzotti ML (2001) Silicate-melt inclusions in magmatic rocks: applications to petrology. Lithos 55: 273-299

Freundt A, Rosi M (1998) From magma to tephra: modelling physical processes of explosive volcanic eruptions. Elsevier, 334p.

Froggatt PC, Lowe DJ (1990) A review of late Quaternary silicic and some other tephra formations from New Zealand: their stratigraphy, nomenclature, distribution, volume, and age. NZ J Geol Geophys 33: 89-109

Gamble JA, Price RC, Smith IEM, McIntosh WC, Dunbar NW (2003) 40Ar/39Ar geochronology of magmatic activity, magma flux and hazards at Ruapehu volcano, Taupo Volcanic Zone, New Zealand. J. Volcanol. Geotherm. Res. 120: 271-287

Gamble JA, Smith IEM, McCulloch IJ, Graham IJ, Kokelaar BP (1993) The geochemistry and petrogenesis of basalts from the Taupo Volcanic Zone and Kermadec Island Arc, S.W. Pacific. J. Volcanol. Geotherm. Res. 54 (3-4): 265-290

Gamble JA, Wood CP, Price RC, Smith IEM, Stewart RB, Waight T (1999). A fifty year perspective of magmatic evolution on Ruapehu volcano, New Zealand: Verification of open system behavior in an arc volcano. Earth Planet. Sci. Lett. 170: 301-314

Gardner CA, Cashman KV, Neal CA (1998) Tephra-fall deposits from the 1992 eruption of Crater Peak, Alaska: implications of clast textures for eruptive processes. Bull Volcanol 59: 537-555

Gardner JE (2007) Heterogeneous bubble nucleation in highly viscous silicate melts during instantaneous decompression from high pressure. Chem. Geol. 236: 1-12

Gardner JE, Denis MH (2004) Heterogeneous bubble nucleation on Fe-Ti oxide crystals in high-silica rhyolitic melts. Geochim. Cosmochim. Acta 68: 3587-3597

Gardner JE, Hilton M, Carrol MR (1999) Experimental constraints on degassing of magma: Isothermal bubble growth during continuous decompression from high pressure. Earth Planet. Sci. Lett. 168: 201-218

Gardner JE, Rutherford M, Carey S, Sigurdsson H (1995) Experimental constraints on pre-eruptive water contents and changing magma storage prior to explosive eruptions of Mount St. Helens volcano. Bull Volcanol 57: 1-17

Gardner JE, Thomas RME, Jaupart C, Tait S (1996) Fragmentation of magma during Plinian volcanic eruptions. Bull Volcanol 58 (2-3): 144-162

Giachetti T, Burgisser A, Arbaret L, Druitt TH, Kelfoun K (2011) Quantitative textural analysis of Vulcanian pyroclasts (Montserrat) using multi-scale X-ray computed microtomography: comparison with results from 2D image analysis. Bull Volcanol 73: 1295-1309

Giachetti T, Druitt TH, Burgisser A, Arbaret L, Galven C (2010) Bubble nucleation and growth during the 1997 Vulcanian explosions of Soufrière Hills Volcano, Montserrat. J. Volcanol. Geotherm. Res. 193 (3-4): 215-231

Gill JB (1981) Orogenic Andesites and Plate Tectonics. Berlin, Springer-Verlag, 336p.

Gilbert and R.S.J. Sparks eds. (1998) The physics of explosive volcanic eruptions. Geol. Soc. Lon. Spec. Publ 145, 186p.

Giordano D, Dingwell DB (2003) Viscosity of hydrous Etna basalt: implications for Plinian-style basaltic eruptions. Bull Volcanol 65: 8-14

Gonnermann HM, Manga M (2005) Flow banding in obsidian: A record of evolving textural heterogeneity during magma deformation. Earth Planet. Sci. Lett. 236: 135-147

Gonnermann HM, Manga M (2007) The Fluid Mechanics Inside a Volcano. Annu. Rev. Fluid Mech. 39: 321-356

Graham LJ, Blattner P, McCulloch MT (1990) Metaigneous granulite xenoliths from Mount Ruapehu, New Zealand: Fragments of altered oceanic crust? Contrib. Mineral. Petrol. 105: 650-661

Graham IJ, Cole JW, Briggs RM, Gamble JA, Smith IEM (1995) Petrology and petrogenesis of volcanic rocks from the Taupo Volcanic Zone: a review. J. Volcanol. Geotherm. Res. 68: 59-87

Graham IJ, Hackett WR (1987) Petrology of calc-alkaline lavas from Ruapehu Volcano and related vents, Taupo Volcanic Zone, New Zealand. J. Petrol. 28: 531-567

Gregg DR (1960) The geology of Tongariro Subdivision. N.Z. Geol. Surv. Bull. 40

Gregg DR (1961) Volcanoes of Tongariro National Park. In: N.Z. Department of Scientific and Industrial Research (eds). New Zealand Geological Survey Handbook, Information Series 28

Geschwind CH and Rutherford MJ (1995) Crystallisation of microlites during magma ascent: the fluid mechanics of 1980-1986 at Mount St Helens. Bull Volcanol 57: 356-370

Gualda GAR, Baker DR, Polacci M (2010a) Introduction: Advances in 3D imaging and analysis of geomaterials. Geosphere 6: 468-469

Gualda GAR, Pamukcu AS, Claiborne LL, Rivers ML (2010b) Quantitative 3D petrography using X-ray tomography 3: Documenting accessory phases with differential absorption tomography. Geosphere 6 (6): 782-292

Gualda GAR, Rivers M (2006) Quantitative 3D petrography using X-ray tomography: Application to Bishop Tuff pumice clasts. J. Volcanol. Geotherm. Res. 154 (1-2): 48-62

Gurioli L, Houghton BF, Cashman KV, Cioni R (2005) Complex changes in eruption dynamics during the 79 AD eruption of Vesuvius. Bull Volcanol 67: 144-159

Hackett WR (1985) Geology and Petrology of Ruapehu Volcano and Related Vents. PhD. Thesis, Victoria University of Wellington, 312 p.

Hackett WR, Houghton BF (1989) A facies model for a Quaternary andesitic composite volcano, Ruapehu, New Zealand. Bull Volcanol 51: 51-68

Hale A, Mühlhaus HB (2007) Modelling shear bands in a volcanic conduit: Implications for over-pressures and extrusion-rates. Earth and Planet. Sci. Lett. 263: 74-87

Hamada M, Laporte D, Cluzel N, Koga KT, Kawamoto T (2010) Simulating bubble number density of rhyolitic pumices from Plinian eruptions: constraints from fast decompression experiments. Bull Volcanol 72: 735-746

Hammer JE, Cashman KV, Hoblitt RP, Newman S (1999) Degassing and microlite crystallization during pre-climactic events of the 1991 eruption of Mt. Pinatubo, Philippines. Bull Volcanol 60: 355-380

Hammer JE and Rutherford (2002) An experimental study of the kinetics of decompression-induced crystallization in silicic melt: J. Geophys. Res. 107, 0.1029/2001JB00281

Harrison A, and White RS (2006) Lithospheric structure of an active backarc basin: the Taupo Volcanic Zone, New Zealand. Geophys. J. Int. 167: 968-990

Heiken G H (1972) Morphology and petrography of volcanic ashes. Geol. Sot. Bull. 83: 1961-1988

Higgins MD (2000) Measurement of crystal size distributions. Am. Mineral. 85: 1105-1116

Healy J, Lloyd EF, Rishworth DEH, Wood CP, Glover RB, Dibble RR (1978) The eruption of Ruapehu New Zealand on 22 June 1969. New Zealand Department of Scientific and Industrial Research Bulletin 224, 80p.

Hervig RL, Dunbar NW (1992) Cause of chemical zoning in the Bishop (California) and Bandelier (New Mexico) magma chambers. Earth Planet. Sci. Lett. 111: 97-108

Hess KU, Dingwell DB (1996) Viscosities of hydrous leucogranitic melts: A non-Arrhenian model. Am. Mineral. 81: 1297-1300

Hitchcock DW, Cole JW (2007) Potential impacts of a widespread subplinian andesitic eruption from Tongariro volcano, based on a study of the Poutu Lapilli. NZ J Geol Geophys 50 (1): 53-66

Hobden BJ (1997) Modelling magmatic trends in time and space: Eruptive and magmatic history of the Tongariro Volcanic Complex, New Zealand. PhD thesis, University of Canterbury, Christchurch, New Zealand, 509p.

Hobden BJ, Houghton BF, Davidson JP, Weaver SD (1999) Small and short-lived magma batches at composite volcanoes: time windows at Tongariro volcano, New Zealand. J Geol Soc Lond 156:865-868

Hobden BJ, Houghton BF, Lanphere MA, Nairn IA (1996) Growth of the Tongariro volcanic complex: New evidence from K/Ar age determinations. NZ J Geol Geophys 39: 151-154

Hoblitt RP, Harmon RS (1993) Bimodal density distribution of cryptodome dacite from the eruption of Mount St. Helens, Washington. Bull Volcanol 55: 421-437

Hoblitt RP, Wolfe EW, Scott WE, Couchman MR, Pallister JS, Javier D (1996) The preclimactic eruptions of Mount Pinatubo, June 1991. In: Newhall CG, Punongbayan RS (eds.), Fire and Mud: Eruptions and Lahars of Mount Pinatubo, Philippines. University of Washington Press, Hong Kong: 457-511

Holloway JR, Blank JG (1994) Application of experimental results to C-O-H species in natural melts. In: Carroll MR, Holloway JR (eds) Volatiles in magmas. Rev Mineral 30: 188-230

Houghton BF, Latter JH, Hackett WR (1987) Volcanic hazard assessment for Ruapehu composite volcano, Taupo Volcanic Zone, New Zealand. Bull Volcanol 49: 737-751

Houghton BF, Wilson CJN (1989) vesicularity index for pyroclastic deposits. Bull Volcanol 51: 451-462

Houghton BF, Wilson CJN, Del Carlo P, Coltelli M, Sable JE, Carey R (2004) The influence of conduit processes on changes in style of basaltic Plinian eruptions: Tarawera 1886 and Etna 122 BC. J. Volcano. Geotherm. Res. 137: 1-14

Huber C, Bachmann O, Manfa M (2010) Two competing effects of volatiles on heat transfer in crystal-rich magmas: thermal insulation vs defrosting. J. Petrol. 51: 847-867

Huber C, Bachman O, Dufek J (2011). Thermo-mechanical reactivation of locked crystal mushes: Melting-induced internal fracturing and assimilation processes in magmas. Earth Planet. Sci. Lett. 304: 443-454

Hurwitz S, Navon O (1994) Bubble nucleation in rhyolitic melts: experiments at high pressure, temperature and water content. Earth Planet. Sci. Lett. 122: 267-280

Ihinger PD, Hervig RL, and McMillan PF (1994) Analytical Methods for Volatiles in Glasses. In: Carroll MR, Holloway JR (eds) Volatiles in magmas. Rev Mineral 30: 67-121

Inman DL (1952) Measures for describing the size distribution of sediments. F. Sed. Petrol. 22: 125-45

Jaupart C (1998) Gas loss from magmas through conduit walls during eruption, Geol. Soc. Lon. Spec. Publ 145: 73-90

Jaupart C, Allegre CJ (1991) Gas content, eruption rate and instabilities of eruption regime in silicic volcanoes. Earth Planet. Sci. Lett. 102: 413-429

Jeanloz R (2000) Mantle of the Earth. In: Sigurdsson H, Houghton BF, McNutt SR, Rymer H, Stix J (eds) Encyclopedia of volcanoes. Academic Press, San Diego, CA: 41-54

Jerram DA, Cheadle MJ, Philpotts AR (2003) Quantifying the building blocks of igneous rocks: are clustered crystal frameworks the foundation?. J. Petrol. 44: 2033-2051

Jerram DA, Martin VM (2008) Understanding crystal populations and their significance through the magma plumbing system. In: Dynamics of crustal Magma Transfer, Storage and Differentiation (Annen and Zellmer Eds). Geological Society Special Publication 304: 144-148

Johnson MC, Anderson AT, Rutherford MJ (1994) Pre-eruptive volatile contents of magmas. In: Carroll MR, Holloway JR (eds) Volatiles in magmas. Rev Mineral 30: 281-330

Johnston DM, Houghton BF, Neall VE, Ronan KR, and Paton D (2000) Impacts of the 1945 and 1995-1996 Ruapehu eruptions, New Zealand: An example of increasing societal vulnerability. GSA Bulletin 112 (5): 720-726

Kaminski E, Jaupart C (1997) Expansion and quenching of vesicular magma fragments in Plinian eruptions. J. Geophys. Res. 102: 12,187-12,203

Kaminski E, Tait S, Ferrucci F, Martet M, Hirn B, Husson P (2011) Estimation of ash injection in the atmosphere of basaltic volcanic plumes: The case of the Eyjafjallajökull 2010 eruption. J. Geophys. Res. 116, B00C02.

Kennedy B, Jellinek AM, Russel JK, Nichols ARL, Vigouroux N (2010) Time-and temperature-dependent conduit wall porosity: a key control on degassing and explosivity at Taurewa volcano, New Zealand. Earth. Planet. Sci. Lett 299: 126-137

Kennedy B, Spieler O, Scheu B, Kueppers U, Taddeucci J, and Dingwell DB (2005). Conduit implosion during Vulcanian eruptions. Geology 33 (7): 581-584

Kennedy B, Stix J (2007) Magmatic processes associated with caldera collapse at Ossipee ring dike, New Hampshire. GSA Bull 119: 3-17

Kerr P (1977) Optical Mineralogy. McGraw Hill, 442p.

Ketcham RA (2005) Three-dimensional textural measurements using high-resolution X-ray computed tomography. J. Struct. Geol. 27: 1217-1228

Ketcham RA, and WD Carlson (2001) Acquisition, optimization and interpretation of X-ray computed tomographic imagery: applications to the geosciences. Computers & Geosciences 27: 381-400

Kilgour G, Manville V, Della Pasqua F, Graettinger A, Hodgson KA, Jolly GE (2010) The 25 September 2007 eruption of Mount Ruapehu, New Zealand: Directed ballistics, surtseyan jets, and ice-slurry lahars. J. Volcanol. Geotherm. Res. 191:1-14

King PL, Holloway JR (2002). CO_2 solubility and speciation in intermediate (andesitic) melts: the role ofH2Oand composition. Geochim. Cosmochim. Acta 66 (9); 1627-1640

Klug C, Cashman KV (1994) Vesiculation of May 18, 1980. Mount St. Helens magma. Geology 22: 468-472

Klug C, Cashman KV (1996) Permeability development in vesiculating magmas: implications for fragmentation. Bull Volcanol 58: 87-100

Klug C, Cashman KV, Bacon CR (2002). Structure and physical characteristics of pumice from the climactic eruption of Mt Mazama (Crater Lake), Oregon. Bull Volcanol 64: 486-501

Kohn BP, Topping WW (1978) Time-space relationships between late Quaternary rhyolitic and andesitic volcanism in the southern Taupo volcanic zone, New Zealand. Geol. Soc. Am. Bull. 89: 1265-1271

Koyaguchi T, Mitani NK (2005) A theoretical model for fragmentation of viscous bubbly magmas in shock tubes. J. Geophys. Res. 110, B10202: doi:10.1029/2004JB003513

Koyaguchi T, Schew B, Mitani N, Melnik O (2008) A fragmentation criterion for highly viscous bubbly magmas estimated from shock tube experiments. J. Volcanol. Geotherm. Res. 178: 58-71

Koyaguchi T, Tokuno M (1993) Origin of the giant eruption cloud of Pinatubo, June 15, 1991. J. Volcanol. Geotherm. Res. 55: 85-96

Kratzmann DJ, Carey SN, Fero J, Scasso RA, Naranjo JA (2010) Simulations of tephra dispersal from the 1991 explosive eruptions of Hudson volcano, Chile. J. Volcanol. Geotherm. Res. 190: 337-352

Lambert IB and Wyllie PJ (1972) Melting of gabbro (quartz eclogite) with excess water to 35 kilobars with geological applications. J. Geol. 80: 693-708

Lange RA (1994) The effect of H2O, CO2 and F on the density and viscosity of silica melts In: Carroll MR, Holloway JR (eds) Volatiles in magmas. Rev Mineral 30: 331-370

Lange RA (1997) A revised model for the density and thermal expansivity of Na_2O-K_2O-CaO-MgO-FeO-Fe_2O_3-Al_2O_3-TiO_2-SiO_2 liquids between 713 and 1896 K: extension to crustal magmatic temperatures. Contrib. Mineral. Petrol. 130: 1-11

Lange RA and Carmichael ISE (1987) Densities of Na_2O-K_2O-CaO-MgO-FeO-Fe_2O_3-Al_2O_3-TiO_2-SiO_2 liquids: new measurements and derived partial molar properties. Geochim. Cosmochim. Acta 53: 2195-2204

Lara L (2009) The 2008 eruption of the Chaitén Volcano, Chile: a preliminary report. Andean Geology 36 (1): 125-129

Larsen JR, Gardner JE (2000) Experimental constraints on bubble interactions in rhyolite melts: implications for vesicle size distributions. Earth Planet. Sci. Lett. 180: 201-214

Lavallée Y, Meredith PG, Dingwell DB, Hess KU, Wassermann J, Cordonnier B, Gerik A, Kruhl JH (2008) Seismogenic lavas and explosive eruption forecasting. Nature letters 453: 507-510

Le Bas M J, Le Maitre RW, Streckeisen A, Zanettin B (1986). A chemical classification of volcanic rocks based on the total alkali-silica diagram. J. Petrol. 27**:**745-750

Lecointre J, Hodgson K, Neall V, Cronin SJ (2004) Lahar-triggering mechanisms and hazard at Ruapehu Volcano, New Zealand. Natural Hazards 31: 85-109.

Lecointre JA, Nell VE, Palmer A (1998) Quaternary lahar stratigraphy of the western Ruapehu ring plain, New Zealand. NZ J Geol Geophys 41: 225-245

Lecointre JA, Nell VE, Wallace RC (2004) Late Quaternary evolution of the Rotoaira Basin, northern Tongariro ring plain, New Zealand. NZ J Geol Geophys 47: 549-565

Libowitzky E, Rossman GR (1997) An IR absorption calibration for water in minerals. Amer. Mineral. 82 (11-12): 1111-1115

Lipman P, Mullineaux D (1981) The 1980 Eruptions of Mount St. Helens, Washington. U.S. Geol. Surv. Prof. Pap. 1250, 844p.

Lirer L, Pescatore T, Booth B, Walker GPL (1973) Two Plinian pumice fall deposits from Somma-Vesuvius, Italy. Geol. Soc. Am. Bull. 84: 759-772

Lorenz V (1973) On the formation of maars. Bulletin Volcanologique 37: 183-204

Lowe DJ, Shane PAR, Alloway BV, Newnham RM (2008) Fingerprints and age models for widespread New Zealand tephra marker beds erupted since 30,000 years ago: a framework for NZ-INTIMATE. Quat. Sci. Rev. 27: 95-126

Lowenstern JB (1995) Applications of silicate melt inclusions to the study of magmatic volatiles. In: JFH Thompson (ed). Magmas, Fluids and Ore Deposits. Mineralogical Association of Canada Short Course 23: 71-99

Lube G, Cronin SJ, Procter J (2009) Explaining the extreme mobility of volcanic ice-slurry flows, Ruapehu volcano, New Zealand. Geology 37 (1): 15-18

Lyakhovsky V, Hurwitz S, Navon O (1996). Bubble growth in rhyolitic melts: experimental and numerical investigation. Bull Volcanol 58: 19-32

Macedonio G, Dobran F, Neri A (1994) Erosion processes in volcanic conduits and application to the AD 79 eruption of Vesuvius. Earth Planet. Sci. Lett. 121 (1-2): 137-152

Macías JL, Arce JL, Mora JC, Espíndola JM, Saucedo R, Manetti P (2003) A 550-year-old Plinian eruption at El Chichón Volcano, Chiapas, Mexico: explosive volcanism linked to reheating of the magma reservoir. J. Geophys. Res. 108 (B12), 2569

Mader HM (1998) Conduit flow and fragmentation. In: J.S. Gilbert and R.S.J. Sparks (Editors), The physics of explosive volcanic eruptions. Geol. Soc. Lon. Spec. Publ 145: 51-71

Mader HM, Phillips JC, Sparks RSJ, Sturtevant B (1996) Dynamics of explosive degassing of magma: Observations of fragmenting two-phase flows. J. Geophys. Res. 101B: 5547-5560

Mader HM, Zgang Y, Phillips JC, Sparks RSJ, Sturtevant B, Stolper E (1994) Experimental simulations of explosive degassing of magma. Nature 372: 85-88

Mandeville CW, Webster JD, Rutherford MJ, Taylor BE, Timbal A., Faure K (2002). Determination of molar absorptivities for infrared absorption bands of H_2O in andesitic glasses. Am. Mineral. 87: 813-821

Mangan MT, Cashman KV (1996) The structure of basaltic scoria and reticulite and inferences for vesiculation, foam formation, and fragmentation in lava fountains. J. Volcanol. Geotherm. Res. 73: 1-18

Mangan M, Mastin L, Sisson T (2004) Gas evolution in eruptive conduits: combining insights from high temperature and pressure decompression experiments with steady-state flow modelling. J. Volcanol. Geotherm. Res. 129 (1-3): 23-36

Mangan MT, Sisson T (2000) Delayed, disequilibrium degassing in rhyolite magma: decompression experiments and implications for explosive volcanism. Earth Planet. Sci. Lett. 183: 441-455

Manville V, Hodgson K A, Houghton BF, Keys JR, White JD (2000) Tephra, snow and water: Complex sedimentary responses at an active snow-capped stratovolcano, Ruapehu, New Zealand. Bull Volcanol 62: 278-293

Manville V, Németh K, Kano K (2009). From source to sink: a review of three decades of progress in the understanding of volcaniclastic processes, deposits, and hazards. Sedimentary Geology 220: 136-161

Martel C, Schmidt BC (2003) Decompression experiments as an insight into ascent rates of silicic magmas. Contrib. Mineral. Petrol. 144: 397-415

Marziano GI, Schmidt BC, Dolfi D (2007) Equilibrium and disequilibrium degassing of phonolitic melt (Vesuvius AD 79 ‘‘white pumice’’) simulated by decompression experiments. J. Volcanol. Geotherm. Res. 161:151-164

Massol H, Jaupart C (1999) The generation of gas overpressure in volcanic eruptions. Earth Planet. Sci. Lett. 166: 57-70

Mathews WH (1967) A contribution to the geology of the Mount Tongariro massif, North Island, New Zealand. NZ J Geol Geophys 10: 1027-1038

McBirney AR (1973) Factors governing the intensity of explosive andesitic eruptions: Bull Volcanol 37: 443-453

McBirney AR (1977) Mixing and unmixing of magmas. J. Volcanol. Geotherm. Res. 7: 357-371

McBirney AR, Murase T (1970) Factors governing the formation of pyroclastic rocks. Bull Volcanol 34: 372-384

McClelland E, Erwin PS (2003) Was a dacite dome implicated in the 9,500 B.P. collapse of Mt Ruapehu? A palaeomagnetic investigation. Bull Volcanol 65: 294-305

McMillan PF (1994) water solubility and speciation models. In: Carroll MR, Holloway JR (eds) Volatiles in magmas. Rev Mineral 30: 131-156

Melnik O (2000) Dynamics of two-phase conduit flow of high viscosity gas-saturated magma: large variations of sustained explosive eruption intensity. Bull Volcanol 62(3):153-170

Mess F, Swennen R, Van Geet M, Jacobs P (2003) Applications of X-ray computed tomography in the geosciences. Geol. Soc. Lon. Spec. Publ., 215p

Miall A (1996) The Geology of Fluvial Deposits. Sedimentary Facies, Basin Analysis, and Petroleum Geology. Springer (eds), 582p.

Moebis A (2010) Understanding the Holocene explosive eruption record of the Tongariro Volcanic Centre, New Zealand. PhD Thesis (Massey University, Palmerston North, New Zealand), 381p.

Moebis A, Cronin SJ, Neall VE, Smith IE (2011) Unravelling a complex volcanic history from fine-grained, intricate Holocene ash sequences at the Tongariro Volcanic Centre, New Zealand. Quat. Int. 246: 352-363

Montgomery RL, Keys HJR (1993) Volcanic Hazard management in Tongariro National Park. Science and research series 61. Dept. of Conservation, Wellington, N.Z. Head Office, 12p.

Morris JD, Leeman WP, Tera F (1990) The subducted component in island arc lavas: constraints from Be isotopic and B-Be systematic. Nature 344: 31-36

Morrissey MM, Mastin LG (2000) Vulcanian eruptions. In: Sigurdsson H, Houghton BF, McNutt SR, Rymer H, Stix J (eds) Encyclopedia of volcanoes. Academic Press, San Diego, CA: 463-475

Mourtada-Bonnefoi and Laporte (1999) Experimental study of homogeneous bubble nucleation in rhyolitic magmas. Geophys. Res. Lett. 26: 3505-3508

Mueller S, Llewellin EW, Mader HM (2009) The rheology of suspensions of solid particles. Proc. R. Soc. A. 466 (2116): 1201-1228, doi: 10.1098/rspa.2009.0445

Mueller S, Melnik O, Spieler O, Scheu B, Dingwell DB (2005) Permeability and degassing of dome lavas undergoing rapid decompression: an experimental determination. Bull Volcanol 67 (6): 526-538

Mueller S, Scheu B, Spieler O, Dingwell DB (2008). Permeability control on magma fragmentation. Geology 36 (5): 399-402

Murphy MD, Sparks RSJ, Barclay J, Carroll MR, Brewer TS (2000) Remobilization of Andesite magma by intrusion of mafic magma at the Soufrier Hills Volcano, Montserrat, west Indies. J. Petrol. 41 (1): 21-42

Narin IA, Cole JW (1981) Basalt dikes in the 1886 Tarawera Rift. NZ J Geol Geophys 24 (5-6): 585-592

Nairn IA, Kobayashi T, Nakagawa M (1998) The ~10 ka multiple vent pyroclastic eruption sequence at Tongariro Volcanic Centre, Taupo Volcanic Zone, New Zealand: Part 1. Eruptive processes during regional extension. J. Volcanol. Geotherm. Res. 86 (1- 4): 19-44

Nairn IA, Wood CP, Hewson CAY (1979) Phreatic eruptions of Ruapehu: April 1975. NZ J Geol Geophys 22: 155-173

Nakada S, Motomura Y (1999) Petrology of the 1991-1995 eruption at Unzen: effusion pulsation and groundmass crystallization. J. Volcanol. Geotherm. Res. 89: 174-196

Nakagawa M, Nairn IA, Kobayashi T (1998) The ~10 ka multiple vent pyroclastic eruption sequence at Tongariro Volcanic Centre, Taupo Volcanic Zone, New Zealand, part 2. Petrological insights into magma storage and transport during regional extension. J. Volcanol. Geotherm. Res. 86: 45-65

Nakagawa M, Wada K, Thordarson T, Wood CP, Gamble JA (1999) Petrologic investigations of the 1995 and 1996 eruptions of Ruapehu volcano, New Zealand: formation of discrete and small magma pockets and their intermittent discharge. Bull Volcanol 61:15-31

Nakagawa M, Wada K, Wood PC (2002) Mixed magmas, mush chambers and eruption triggers: Evidence from zoned clinopyroxene phenocrysts in andesitic scoria from the 1995 eruptions of Ruapehu Volcano, New Zealand. J. Petrol. 43 (12): 2279-2303

Namiki A, Manga M (2008) Transition between fragmentation and permeable outgassing of low viscosity magmas. J. Volcanol. Geotherm. Res. 169: 48-60

Navon O and Lyakhovsky V (1998) Vesiculation processes in Silicic Magmas. In: Gilbert, J. and Sparks R.S.J. (eds.) The Physics of Explosive Volcanism Geol. Soc. Lond., Spec. Publ. 145: 29-52

Neall VE (1990) Natural Hazard assessment in New Zealand. Research School of Earth Sciences Victoria University of Wellington. Natural Hazards 90: 24-28

Neall VE, Cronin SJ, Donoghue SL, Hodgson KA, Lecointre JA, Palmer AS, Purves AM, Stewart RB (2001) Lahar Hazards Map for Ruapehu Volcano. Institute of Natural Resources – Massey University, Soil and Earth Sciences Occasional Publication No. 1

Neall VE, Cronin SJ, Donoghue SL, Hodgson KA, Lecointre JA, Purves AM (1995) The Potential volcanic threat at Ruapehu. New Zealand Ministry of Civil Defense (eds) Tephra 14 (2): 18-21

Neall VE, Houghton BF, Cronin SJ, Donoghue SL, Hodgson KA, Johnston DM, Lecointre JA, Mitchell AR (1999). Volcanic Hazards at Ruapehu Volcano. Ministry of Civil Defence, Wellington, Volcanic hazards information series 8, 30p.

Nelson ST, Montana A (1992) Sieve-textured plagioclase in volcanic rocks produced by rapid decompression. Am. Mineral. 77: 1242-1249

Neri A, Papale P, Macedonio G (1998) The role of magma composition and water content in explosive eruptions: 2. Pyroclastic dispersion dynamics. J. Volcanol. Geotherm. Res. 87: 95-115

Neri A, Papale P, Seppia DD, Santacroce R (2002) Coupled conduit and atmospheric dispersal dynamics of the AD 79 Plinian eruption of Vesuvius. J. Volcanol. Geotherm. Res. 120: 141-160

Newman S, Lowerstern JB (2002) VolatileCalc: A silicate melt-H_2O-CO_2 solution model written in Visual Basic for Excel. Comp Geosci 28: 597-604

Newman S, Stolper EM, Epstein S (1986) Measurement of water in rhyolitic glasses: calibration of an infrared spectroscopic technique. Am. Mineral. 71: 1527-1541

Newnham RM, Eden DN, Lowe DJ, Hendy CH (2003) Rerewhakaaitu Tephra, a land–sea marker for the Last Glacial Termination in New Zealand, with implications for global climate change. Quat. Sci. Rev. 22: 289-308

Newnham RM, Lowe DJ (2000) Fine-resolution pollen record of late glacial climate reversal from New Zealand. Geology 28: 759-762

Nichols ARL, and Wysoczansk RJ (2007) Using micro-FTIR spectroscopy to measure volatile contents in small and unexposed inclusions hosted in olivine crystals. Chem. Geol. 242: 371-384

Nielsen CH and Sigurdsson H (1981) Quantitative methods for electron microprobe analysis of sodium in natural and synthetic glasses. Am. Mineral. 66: 547-552

Norrish K and Chappell BW (1977) X-ray fluorescence spectrometry. In: Zussman J (ed) Physical methods in determinative mineralogy. London, Academic Press: 201-272

Ochs FA III and Lange RA (1997) The partial molar volume, thermal expansivity, and compressibility of H_2O in $NaAlSi_3O_8$ liquid: new measurements and an internally consistent model. Contrib. Mineral. Petrol. 179: 155-165

Ohlhorst S, Behrens H, Holtz F (2001) Compositional dependence of molar absorptivities of near-infrared OH^- and H_2O bands in rhyolitic to basaltic glasses. Chem. Geol. 174: 5-20

Okumura S, Nakamura M, Tsuchiyama A (2006) Shear-induced bubble coalescence in rhyolitic melts with low vesicularity. Geophys. Res. Lett. 33 (20): 1-5

Orsi G, Gallo G, Heiken G, Wohletz K, Yu E, Bonani G (1992) A comprehensive study of pumice formation and dispersal: the Cretaio Tephra of Ischia (Italy). J. Volcanol. Geotherm. Res. 53: 329-354

Palladino DM, Simei S, Kyriakopoulos K (2008) On magma fragmentation by conduit shear stress: Evidence from the Kos Plateau Tuff, Aegean Volcanic Arc. J. Volcanol. Geotherm. Res. 178: 807-817

Palmer BA (1991) Holocene lahar deposits in the Whakapapa catchment, northwestern ring plain, Ruapehu volcano (North Island, New Zealand). NZ J Geol Geophys 34: 177-190

Palmer BA, Neall VE (1989) The Murimotu Formation, ~9500 year old deposits of a debris avalanche and associated lahars, Mount Ruapehu, North Island, New Zealand. NZ J Geol Geophys 32: 477-486

Papale P (1999). Strain-induced magma fragmentation in explosive eruptions: Nature 397: 425-428

Papale P, Dobran F (1993) Modelling of the ascent of magma during the plinian eruption of Vesuvius in A.D. 79. J. Volcanol. Geotherm. Res. 58: 101-132

Papale P, Neri A, Macedonio G (1998) The role of magma composition and water content in explosive eruptions, 1. Conduit ascent dynamics. J. Volcanol. Geotherm. Res. 87: 75-93

Parfitt EA, Wilson L (2008) Fundamentals of Physical Volcanology. Oxford, Blackwell, 256p.

Pardo N, Cronin SJ, Palmer A, Németh K (2012a) Reconstructing the largest explosive eruptions of Mt. Ruapehu, New Zealand: lithostratigraphic tools to understand subplinian-Plinian eruptions at andesitic volcanoes. Bull Volcanol 74: 617-640. doi:10.1007/s00445-011-0555-z (appendix J.1)

Pardo N, Cronin SJ, Palmer A, Procter J, Smith I (2012b, in press). Andesitic Plinian eruptions at Mt. Ruapehu: quantifying the uppermost limits of eruptive parameters. Bull Volcanol 74: 1161-1185. doi: 0.1007/s00445-012-0588-y (appendix J.2)

Pearce TH, Kolisnik AM (1990) Observations of plagioclase zooming using interference imaging. Earth Sci. Rev. 29: 9-26

Pearce NJG, Denton JS, Perkins WT, Westgate JA, and Alloway BV (2007) Correlation and characterisation of individual glass shards from tephra deposits using trace element laser ablation ICP-MS analyses: current status and future potential. J. Quat. Sci. 22(7): 721-736

Pérez W, Freundt A, Kutterolf S, Schmincke HU (2009) The Masaya Triple Layer: A 2100 year old basaltic multi-episodic Plinian eruption from the Masaya Caldera Complex (Nicaragua). J. Volcanol. Geotherm. Res. 179: 191-205

Perfit MR, Davidson JP (2000) Plate Tectonics and Volcanism. In: Sigurdsson H, Houghton BF, McNutt SR, Rymer H, Stix J (eds) Encyclopedia of volcanoes. Academic Press, San Diego, CA: 89-113

Platz T (2007) Understanding Aspects of Andesitic Dome-forming Eruptions through the Last 1000 yrs of volcanism at Mt. Taranaki, New Zealand. PhD-Thesis. Massey University, Earth Sciences, Palmerston North, New Zealand, 203p.

Platz T, Cronin SJ, Cashman KV, Stewart RB, Smith IEM (2007) Transitions from effusive to explosive phases in andesite eruptions-A case-study from the AD 1655 eruption of Mt. Taranaki, New Zealand. J. Volcanol. Geotherm. Res. 161: 15-34

Polacci M, (2005) Constraining the dynamics of volcanic eruptions by characterization of with Vp and Vp/Vs. Geophys. J. Int., 165: 565–583imaging. Earth Sci. Rev. 29: 9-26

Polacci M, Baker DR, Bai L, Mancini L (2008) Large vesicles record pathways of degassing at basaltic volcanoes. Bull Volcanol 70: 1023-1029

Polacci M, Baker DR, Mancini L, Favretto S, Hill RJ (2009a) Vesiculation in magmas from Stromboli and implications for normal Strombolian activity and paroxysmal explosions in basaltic systems. J. Geophys. Res. 114: B01206, doi:10.1029/2008JB005672

Polacci M, Baker DR, Mancini L, Tromba G, Zanini F (2006) Three-dimensional investigation of volcanic textures by X-ray microtomography and implications for conduit processes. Geophys. Res. Lett. 33(13): L13312

Polacci M, Burton MR, La Spina A, Muré F, Favretto S, Zanini F (2009b) The role of syn-eruptive vesiculation on explosive basaltic activity at Mt. Etna, Italy. J. Volcanol. Geotherm. Res. 179: 265-269

Polacci M, Papale P, Rosi M (2001) Textural heterogeneities in pumices from the climactic eruption of Mount Pinatubo, 15 June 1991, and implications for magma ascent dynamics. Bull Volcanol 63: 83-97

Polacci M, Pioli L, Rosi M (2003) The Plinian phase of the Campanian Ignimbrite eruption (Phlegrean Fields, Italy): evidences from density measurements and textural characterization of pumice. Bull Volcanol 65: 418-432

Price RC, Gamble JA, Smith IEM, Stewart RB, Eggins S, Wright IC (2005). An integrated model for the temporal evolution of andesites and rhyolites and crustal development in New Zealand's North Island. J. Volcanol. Geotherm. Res. 140 (1-3): 1-24

Price R, Gamble JA, Smith IEM, Maas R, Waight T, Stewart RB, Woodhead J (2012). The anatomy of an andesite volcano: A time-stratigraphic study of andesite petrogenesis and crustal evolution at Ruapehu volcano, New Zealand. J. Petrol. (in press)

Procter JN, Cronin SJ, Zernack AV (2010) Landscape and sedimentary response to catastrophic debris avalanches, Western Taranaki, New Zealand, Sedimentary Geology 38 (1): 67-70

Proussevitch AA, Mulukutla GK, Sahagian DL (2011) A new method of measuring bubble size distributions from vesicle fragments preserved on surface of volcanic ash particles. Geosphere 7: 62-69

Proussevitch AA, Sahagian DL, Anderson AT (1993) Dynamics of diffusive bubble growth in magmas: isothermal case. J. Geophys. Res. 98 (B12): 22283-22307

Proussevitch AA, Sahagian DL, Tsentalovich EP (2007) Statistical analysis of bubble and crystal size distributions: Formulations and procedures. J. Volcanol. Geotherm. Res. 164: 95-111

Putirka KD (2008) Thermometers and barometers for volcanic systems. Rev Min Geochem 69, 61-120

Pyle DM (1989) The thickness, volume and grainsize of tephra fall deposits. Bull Volcanol 51: 1-15

Pyle DM (2000) Sizes of volcanic eruptions. In: Sigurdsson H, Houghton BF, McNutt SR, Rymer H, Stix J (eds) Encyclopedia of volcanoes. Academic Press, San Diego, CA: 263-269

Reyners M, Eberhart-Phillips D, Graham S, Yuichi N (2006) Imaging subduction from the trench to 300 km depth beneath the central North Island, New Zealand, with Vp and Vp/Vs. Geophys J Int 165: 565-583

Rosi M (1998) Plinian eruption columns: particle transport and fallout. In: Freundt A, Rosi M (eds) From magma to tephra. Elsevier, Amsterdam: 139-172

Rosi M, Landi P, Polacci M, Di Muro A, Zandomeneghi D (2004) Role of conduit shear on ascent of the crystal-rich magma feeding the 800-year-BP Plinian eruption of Quilotoa volcano (Ecuador). Bull Volcanol 66: 307-321

Rosi M, Palladio-Melosantos ML, Di Muro A, Leoni R, Bacolcol T (2001) Fall vs flow activity during the 1991 climatic eruption of Pinatubo Volcano (Philippines) Bull Volcanol 62: 549-566

Rutherford MJ and Hill PM (1993) Magma ascent rates from amphibole breakdown: An experimental study applied to the 1980-1986 Mount St. Helens eruptions. J. Geophys. Res. 98: 19667-19685

Rutherford MJ, Devine JD (1996) Preeruption pressure-temperature conditions and volatiles in the 1991 dacitic magma of Mount Pinatubo. In: Newhall CG, Punongbayan RS (eds) Fire and Mud: Eruptions and lahars of Mount Pinatubo, Philippines. University of Washington Press, Seattle and London, 1126p.

Rutherford MJ, Devine JD, Barclay J (1998) Changing magma conditions and ascent rates during the Soufriére Hills eruption on Montserrat. GSA Today 8: 1-7

Rust AC, Cashman KV (2004). Permeability of vesicular silicic magma: Inertial and hysteresis effects, Earth Planet. Sci. Lett. 228: 93-107

Rust AC, Cashman KV (2011) Permeability controls on expansion and size distributions of pyroclasts. J. Geophys. Res. 116, B11202, 17p. doi:10.1029/2011JB008494

Rust A, Manga M (2002) Bubble shapes and orientation in low Re simple shear flow. J Colloid Interface Sci 249: 476

Saar MO, Manga M (1999). Permeability-porosity relationship in vesicular basalts. Geophys. Res. Lett. 26: 111-14

Sable JE, Houghton BF, Wilson CJN, Carey RJ (2006) Complex proximal sedimentation from Plinian plumes: the example of Tarawera 1886. Bull Volcanol 69: 89-103

Sahagian DL, and Proussevitch AA (1998) 3D Particle size distributions from 2D observations: stereology for natural applications, J. Volcanol. Geotherm. Res. 84: 173-196

Saucedo R, Macías JL, Gavilanes JC, Arce JL, Komorowski JC, Gardner JE, Valdez-Moreno G (2010) Eyewitness, stratigraphy, chemistry, and eruptive dynamics of the 1913 Plinian eruption of Volcán de Colima, México. J. Volcanol. Geotherm. Res. 191: 149-166

Scandone R, Malone SD (1985) Magma supply, magma discharge and readjustment of the feeding system of Mount St. Helens during 1980. J. Volcanol. Geotherm. Res. 23: 239-262

Scandone R, Cashman KV, Malone SD (2007) Magma supply, magma ascent and the style of volcanic eruptions. Earth Planet. Sci. Lett. 253: 513-529

Scheu B, Spieler O, Dingwell DB (2006) Dynamics of explosive volcanism at Unzen volcano: an experimental contribution. Bull Volcanol 69: 175-187

Schipper CI (2010) A Practical guide to FTIR microanalysis of volatiles in volcanic samples. INR, Massey University, Palmerston North, new Zealand (*unpublished*), 47p.

Schmidt MW, Poli S (1998) Experimentally based water budgets for dehydrating slabs and consequences for arc magma generation. Earth Planet. Sci. Lett. 163: 361-379

Shane P, Doyle LR, Nairn IA (2008) Heterogeneous andesite–dacite ejecta in 26–16.6 ka pyroclastic deposits of Tongariro Volcano, New Zealand: the product of multiple magma-mixing events. Bull Volcanol 70: 517-536

Shea T, Houghton BF, Gurioli L, Cashman KV, Hammer JE, Hobden BJ (2010) Textural studies of vesicles in volcanic rocks: An integrated methodology. J. Volcanol. Geotherm. Res. 190: 271-289

Sheridan MF, Wohletz KH (1983). Hydrovolcanism: basic considerations and review. In: Explosive Volcanism (MF Sheridan and F Barberi Eds). J Volcanol. Geotherm. Res. 17: 1-29

Shimozuru (1994) Physical parameters governing the formation of Pele's hair and tears. Bull Volcanol 56: 217-219

Sieh K, Bursik M (1986) Most recent eruption of the Mono Craters, eastern central California. J. Geophys. Res. 91: 12539-12571

Siebe C, Macías JL, Abrams M, Rodríguez S, Castro R (1997) Catastrophic prehistoric eruptions at Popocatépetl and Quaternary explosive volcanismin the Serdán-Oriental basin, east-central México. Pre-meeting excursion fieldtrip guidebook No 4, January 12–18: Puerto Vallarta, México, International Association of Volcanology and Chemistry of the Earth's Interior (IAVCEI) General Assembly, 88p.

Signorelli S, Vaggelli G, Francalanci L, Rosi M (1999) Origin of magmas feeding the Plinian phase of the Campanian Ignimbrite eruption, Phlegrean Fields (Italy): constraints based on matrix-glass and glass-inclusion compositions. J. Volcanol. Geotherm. Res. 91: 199-220

Sigurdsson H, Carey S, Espíndola JM (1984) The 1982 eruption of El Chichón volcano, Mexico; stratigraphy of pyroclastic deposits. J. Volcanol. Geotherm. Res. 23: 11-37

Sigurdsson H, Houghton BF, McNutt SR, Rymer H, Stix J (eds) (2000) Encyclopedia of Volcanoes. Academic Press, San Diego, CA, 1417 p.

Simkin T, Siebert L (2000) Earth's volcanoes and eruptions: an overview. In: Sigurdsson H, Houghton BF, McNutt SR, Rymer H, Stix J (eds) Encyclopedia of volcanoes. Academic Press, San Diego: 249-261

Sisson TW, Layne GD (1993) H2O in basalt and basaltic andesite glass inclusions from four subduction-related volcanoes, Earth Planet. Sci. Lett. 117: 619-635

Smith GA (1991) Facies sequences and geometries in continental volcaniclastic sediments. In: Fisher RV, Smith GA (eds). Sedimentation in Volcanic Settings, Society of Economic Paleontologists and Mineralogist Special Publications 45, Tulsa, Ok: 10-25

Sohn YK, and Cough SK (1989) Depositional processes of the Suwolbong tuff ring, Cheju Island (Korea), Sedimentology 36: 837-855

Song SR, Jones KW, Lindquist WB, Dowd BA, and Sahagian DL (2001) Synchrotron X-ray computed microtomography: studies on vesiculated basaltic rocks, Bull Volcanol 63 (4): 252-263

Sosa-Ceballos G, Gardner JE, Siebe C, Macías JL (2012) A caldera-forming eruption ~14,100 14C yr BP at Popocatéptl volcano, México: Insights from eruption dynamics and magma mixing. J. Volcanol. Geotherm. Res. 213-214: 27-40

Sparks RSJ (1978) The dynamics of bubble formation and growth in magmas: a review and analysis. J. Volcanol. Geotherm. Res. 3: 1-37

Sparks RSJ (1986) The dimension and dynamics of volcanic eruption columns. Bull Volcanol 48: 13-15

Sparks RSJ, Barclay J, Jaupart C, Mader HM, Phillips JC (1994) Physical aspects of magma degassing I. Experimental and theoretical constraints on vesiculation. In: Carroll MR, Holloway JR (eds) Volatiles in magmas. Rev Mineral 30: 413-445

Sparks RSJ, Brazier S (1982) New evidence for degassing processes during explosive eruptions. Nature 295: 218-220

Sparks RSJ, Bursik M, Carey SN, Gilbert JS, Glaze LS, Sigurdsson H, Woods AW (1997) Volcanic plumes. Wiley, Chichester, 574 p.

Sparks RSJ and Wilson L (1976) A model for the formation of ignimbrite by gravitational column collapse. J Geol. Soc. Lond. 132: 441-451

Spieler O, Dinwell DB, Alidibirov M (2004a) Magma fragmentation speed: an experimental determination. J. Voclanol. Geotherm. Res. 129: 109-123

Spieler O, Kennedy B, Kueppers U, Dingwell DB, Scheu B, Taddeucci J (2004b) The fragmentation threshold of pyroclastic rocks. Earth Planet. Sci. Lett. 226: 139-148

Spinks KD, Acocella V, Cole JW, Bassett KN (2005) Structural control of volcanism and caldera development in the transtensional Taupo Volcanic Zone, New Zealand. J. Volcanol. Geoherm. Res. 144: 7-22

Statistics New Zealand (2007) Regional Gross Domestic Product http://www.stats.govt.nz/reports/analytical-reports/regional-gross-domestic-product.aspx. Retrieved 18 February 2010)

Statistics New Zealand (2009) Subnational Population Estimates: At 30 June 2009 http://www.stats.govt.nz/methods_and_services/access-data/tables/subnational-pop-estimates.aspx. Retrieved 2009-10-23

Stein D J, Spera FJ (1992) Rheology and microstructure of magmatic emulsions: theory and experiments. J. Volcanol. Geotherm. Res. 49: 157-174

Stein DJ, Spera FJ (2002) Shear viscosity of rhyolite-vapor emulsions at magmatic temperatures by concentric cylinder rheometry. J. Volcanol. Geotherm. Res. 113: 243-58

Stewart M, Pearce T (2004) Sieve-textured plagioclase in dacitic magma: Interference imaging results. Am. Mineral. 89: 348-351

Stewart RB, Price RC, Smith IEM (1996) Evolution of high-K arc magma, Egmont volcano, Taranaki, New Zealand: evidence from mineral chemistry. J. Volcanol. Geotherm. Res. 74: 275-295

Stix J, Trres RC, Narváez LM, Cortés GP, Raigosa JA, Gómez D, Castonguay R (1997) A model of vulcanian eruptions at Galeras volcano, Colombia. J. Volcanol. Geotherm. Res. 77: 285-303

Stolper EM (1982) Water in silicate glasses: An infrared spectroscopic study. Contrib. Mineral. Petrol. 81: 1-17

Sugioka I, Bursik M (1995) Explosive fragmentation of erupting magma. Nature 373: 689-692

Sulpizio R (2005) Three empirical methods for the calculation of distal volume of tephra-fall deposits. J. Volcanol. Geotherm. Res. 145 (3-4): 315-33

Sulpizio R, Mele D, Dellino P, La Volpe L (2005) A complex, subplinian-type eruption from low-viscosity, phonolitic to tephri-phonolitic magma: the AD 472 (Pollena) eruption of Somma-Vesuvius, Italy. Bull Volcanol 76: 743-767

Susuki YJ, Koyaguchi T (2012) 3-D numerical simulations of eruption column collapse: effects of vent size on pressure-balance jet/plumes. J. Volcanol. Geitherm. Res. 221-222: 1-13

Symonds RB, Rose WI, Bluth GJS, Gerlach TM (1994) Volcanic-gas studies: methods, results, and applications. In: Carroll MR, Holloway JR (eds) Volatiles in magmas. Rev Mineral 30: 10-66

Taddeucci J, Wohletz KH (2001) Temporal evolution of the Minoan eruption (Santorini, Greece), as recorded by its Plinian fall deposit and interlayered ash flow beds. J. Volcanol. Geotherm. Res. 109: 299-317

Tait S (1992) Selective preservation of melt inclusions in igneous phenocrysts, Am. Mineral. 77: 146-155

Tait S, Jaupart C, and Vergniolle S (1989) Pressure, gas content and eruption periodicity of a shallow crystallizing magma chamber. Earth Planet. Sci. Lett. 92: 107-123

Takeuchi S, Nakamura M (2001) Role of precursory less-viscous, mixed magma in the eruption of phenocryst-rich magma: evidence from the Hokkaido-Komagatake 1929 eruption. Bull Volcanol 63: 365-376

Takeuchi S, Tomiya A, Shinohara H (2009) Degassing conditions for permeable silicic magmas: Implications from decompression experiments with constant rates. Earth Planet. Sci. Lett. 283 (1-4): 101-110

The Treasury (2010) **New Zealand Economic and Financial Overview 2010. 60P.** ISSN: 1173-2334. http://www.treasury.govt.nz/economy/overview/2010

Thomas N, Jaupart C, Vergniolle (1004) On the vesicularity of pumice. J. Geophys. Res. 99: 15633-15644

Thomas RME, Sparks RSJ (1992) Cooling of tephra during fallout from eruption columns. Bull Volcanol 54: 542-553

Thorarinsson S, Sigvaldason GE (1972) The Hekla eruption of 1970. Bull Volcanol 36: 1-20

Thouret JC, Juvigné E, Gourgaud A, Boivin P, Dávila J (2002) reconstruction of the AD Huaynaputina eruption based on the correlation of geologic evidence with early Spanish Chronicles. . J. Volcanol. Geotherm. Res. 115: 529-570

Topping WW (1973) Tephrostratigraphy and chronology of late Quaternary eruptives from the Tongariro Volcanic Centre. New Zealand. NZ J Geol Geophys 16: 397-423

Topping WW (1974) Some aspects of Quaternary history of Tongariro Volcanic Centre. PhD thesis, Victoria University of Wellington, New Zealand. 347p.

Toramaru A (1989) Vesiculation process and bubble size distributions in ascending magmas with constant velocities. J. Geophys. Res. 94: 17523-17542

Toramaru A (1990) Measurement of bubble-size distributions in vesiculated rocks with implications for quantitative estimation of eruption processes. J. Volcanol. Geotherm. Res. 43: 71-90

Toramaru A (2006) BND (bubble number density) decompression rate meter for explosive volcanic eruptions. J. Volcanol. Geotherm. Res. 154: 303-316

Turner R, Hurst T (2001) Factors influencing volcanic ash dispersal from the 1995 and 1996 Eruptions of Mount Ruapehu, New Zealand. Appl. Meteor. 40: 56-69

Tuttle OF, Bowen NL (1958) Origin of granite in the light of experimental studies in system $NaAlSi_3O_8$-$KAlSi_3O_8$-SiO_2-H_2O. Geol Soc Am Mem 74, 153 p.

Udden JA (1914) Mechanical composition of clastic sediments. Geol. Soc. Am. Bull. 25: 655-744

Underwood EE (1970) Quantitative stereology. Addison-Wesley, Cambridge Massachusetts. USA, 274p.

Varekamp JC (1993) Some remarks on volcanic vent evolution during Plinian eruptions. J. Volcanol. Geotherm. Res. 54: 309-318

Venezky DY, Rutherford MJ (1997) Preeruption conditions and timing of dacite-andesite magma mixing in the 2.2 ka eruption at Mt. Ranier. J. Geophys. Res. 102: 20069-20086

Verhoogen J (1951) Mechanics of ash formation. Am. J. Sci. 249:729-739

Villamor P, Van Dissen R, Alloway BV, Palmer AS, Litchfield N (2010) The Rangipo fault, Taupo rift, New Zealand: An example of temporal slip-rate and single-event displacement variability in a volcanic environment. Geol. Soc. Am. Bull. 119: 529-547

Waight TE, Price RC, Stewart RB, Smith IEM, Gamble JA (1999) Stratigraphy and geochemistry of the Turoa area, with implications for andesite petrogenesis at Mt Ruapehu, Taupo Volcanic Zone, New Zealand. NZ J Geol Geophys 42:513-532

Waitt RB, Hansen VL, Sarna-Wojcicki AM, Wood SH (1981) Proximal air-fall deposits of eruptions between May 24 and August 7, 1980-stratigraphy and field sedimentology. US Geol Surv Prof Pap 1250: 617-628

Wallace P (2001) Volcanic SO_2 emissions and the abundance and distribution of exsolved gas in magmas. J. Volcanol. Geotherm. Res. 108: 85-106

Wallace PJ, Anderson AT, and Davis AM (1995) Quantification of pre-eruptive exsolved gas contents in silicic magmas: Nature 377: 612-616

Wallace PJ, Anderson AT (1998) Effects of eruption and lava drain back on the H_2O contents of basaltic magmas at Kilauea volcano. Bull Volcanol 59: 327-344

Wallace P, Anderson AT (2000) Volatiles in Magmas. In: Sigurdsson H, Houghton BF, McNutt SR, Rymer H, Stix J (eds) Encyclopedia of volcanoes. Academic Press, San Diego, CA: 149-170

Walker GPL (1973) Explosive Volcanic Eruptions -A new Classification Scheme. Geologiche Rundshau 62: 431-446

Walker GPL (1989) Spongy pahoehoe in Hawaii: a study of vesicle-distribution patterns in basalt and their significance. Bull Volcanol 51: 199-209

Walker GPL (1980) The Taupo Pumice: product of the most powerful known (ultraplinian) eruption? J. Volcanol. Geotherm. Res. 8: 69-94

Walker GPL, Croasdale R (1971) Two Plinian-type eruptions in The Azores. J Geol Soc Lond 127:17-55

Watanabe K, Danhara T, Watanabe K, Terai K, Yamashita T (1999) Juvenile volcanic glass erupted before the appearance of the 1991 lava dome, Unzen volcano, Kyushu, Japan. J. Volcanol. Geotherm. Res. 89: 113-121

Watt SFL, Pyle DM, Tamsin AM, Martin RS, Matthews NE (2009) Fallout and distribution of volcanic ash over Argentina following the May 2008 explosive eruption of Chaitén, Chile. J. Geophys. Res. 114: B04207, doi:10.1029/2008JB006219

Wehrmann H., Bonadonna C., Freundt A., Houghton BF, Kutterolf S (2006) Fontana Tephra: a basaltic Plinian eruption in Nicaragua. In: Rose WI, Bluth G, Carr MJ, Ewert J, Patino L, Vallance J (eds) Volcanic hazards in Central America. Geol Soc Am Spec Paper 412: 209-223

Wentworth CK (1922) A scale of grade and class terms for clastic sediments. J. Geol. 30: 377-392

White JDL (1991) Maar-diatreme phreatomagmatism at Hopi Buttes, Navajo Nation (Arizona), USA. Bull Volcanol 53: 239-258

White JDL, Houhghton BF (2006) Primary volcaniclastic rocks. Geology 34: 677-680

Whitham AG, Sparks RSJ (1986) Pumice. Bull Volcanol 48: 209-223

Whittington AG, Hellwig M, Behrens H, Joachim B, Stechern A, Vetere F (2009) The viscosity of hydrous dacitic liquids: implications for the rheology of evolving silicic magmas. Bull Volcanol 71: 185-199

Williams SN (1983) Plinian airfall deposits of basaltic composition. Geology 11: 211-214

Wilson CJN, Houghton BF, McWilliams MO, Lanphere MA, Weaver SD, Briggs RM (1995) Volcanic and structural evolution of Taupo Volcanic Zone, New Zealand: a review. J. Volcanol. Geotherm. Res. 68: 1-28

Wilson CJN, Rogan AM, Smith IEM, Northey DJ, Naim LA, Houghton BF (1984) Caldera volcanoes of the Taupo Volcanic Zone, New Zealand. J. Geophys. Res. 89: 8463-8484

Wilson CJN, Switsur RV, Ward AP (1988) A new ^{14}C age for the Oruanui (Wairakei) eruption, New Zealand. Geological Magazine 125: 297-300

Wilson CJN (2001) The 26.5 ka Oruanui eruption, New Zealand: an introduction and overview. J. Volcanol. Geotherm. Res. 112: 133-174

Wilson L (1972) Explosive volcanic eruptions-II: the atmospheric trajectories of pyroclasts. Geophys J Royal Astronom Soc 30: 381-392

Wilson L (1976) Explosive volcanic eruptions III. Plinian eruption columns. Geophys J Royal Astronom Soc 45: 543-56

Wilson L (1999) Explosive volcanic eruptions-X. The influence of pyroclast size distributions and released magma gas contents on the eruption velocities of pyroclasts and gas in Hawaiian and Plinian eruptions. Geophys. J. Int. 136: 609-619

Wilson L, Sparks RSJ, Huang TC, Watkins ND (1978) The control of volcanic column heights by eruption energetics and dynamics, J. Geophys. Res. 83 (B4): 1829-1836

Wilson L, Sparks RSJ, Walker GPL (1980) Explosive volcanic eruptions - IV. The control of magma properties and conduit geometry on eruption column behaviour. Geophys J Royal Astronom Soc 63: 117-148

Winter JDN (2010) An introduction to Igneous and Metamorphic Petrology. Prentice Hall, 702p.

Wohletz KH (1983) Mechanisms of hydrovolcanic pyroclast formation: size, scanning electron microscopy, and experimental studies. In: Explosive Volcanism (MF Sheridan and F Barberi, Eds). J. Volcanol. Geotherm. Res. 17: 31-63.

Wohletz KH (1986) Explosive magma-water interactions: thermodynamics, explosion mechanisms, and field studies. Bull Volcanol 48: 245-264

Wohletz K, Heiken G (1992) Volcanology and Geothermal Energy. California Press, Berkeley, 432p.

Wohletz KH, Krinsley D (1982) Scanning electron microscopy of basaltic hydromagmatic ash. Los Alamos National Laboratory Report LA-UR 82-1433, 26 p.

Wohletz KH, Sheridan MF (1983) Hydrovolcanic explosions; II. Evolution of basaltic tuff rings and tuff cones: Am. J. Sci. 283: 385-413

Wohletz KH, Sheridan MF, Brown WK (1989) Particle-size distributions and the sequential fragmentation/transport theory applied to volcanic ash. J. Geophys. Res. 94 (B11): 15703-15721

Woods AW (1995) The dynamics of explosive volcanic eruptions. Reviews of Geophysics 33: 495-530

Woods AW and Koyaguchi T (1994) Transitions between explosive and effusive eruptions of silicic magma. Nature 370: 641-644

Wright HMN, Cashman KV, Rosi M, Cioni R (2007) Breadcrust bombs as indicators of Vulcanian eruption dynamics at Guagua Pichincha volcano, Ecuador. Bull Volcanol 69: 281-300

Wright HMN, Roberts JJ, Cashman KV (2006) Permeability of anisotropic tube pumice: Model calculations and measurements. Geophys. Res. Lett. 33: L17316, doi:10.1029/2006GL027224

Wright HMN, Weinberg RF (2009) Strain localization in vesicular magma: Implications for rheology and fragmentation. Geology 37: 1023-1026

Zandomeneghi D, Voltolini M, Macini L, Brun F, Dreossi D, Polacci M (2010) Quantitative analysis of X-ray microtomography images of geomaterials: Application to volcanic rocks. Geosphere 6 (6): 793-804

Zellmer GF, Sparks RSJ, Hawkesworth CJ, Wiedenbeck (2003) Magma Emplacement and remobilization Timescales Beneath Montserrat: Insights from Sr and Ba zonation in plagioclase phenocrysts. J. Petrol. 44 (8): 1413-1431

Zhang YX (1999) A criterion for the fragmentation of bubbly magma based on brittle failure theory. Nature 402: 648-650

Zimanowski B, Büttner R, Lorenz V, Häfele HG (1997) Fragmentation of basaltic melt in the course of explosive volcanism. J. Geophys. Res. 102: 803-814

Zimanowski B, Fröhlich G, Lorenz V (1991) Quantitative experiments on phreatomagmatic explosions. J. Volcanol. Geotherm. Res. 48: 341-358